PORTOFOLIU CU LUCRĂRI ŞTIINŢIFICE RELEVANTE

CS I DR. Georgeta-Camelia COZARU

Nr. Crt.	**Articol**	**Factor de impact**
1.	Caraban BM, Matei E, **Cozaru G.C**, Aşchie M, Deacu M, Enciu M, Bălţătescu GI, Chisoi A, Dobrin N, Petcu L, Gheorghe E, Hangan L-T, Roşu MC, Orasanu CI, Nicolau A-A. (**2023**) *PD-L1, CD4+, and CD8+ Tumor-Infiltrating Lymphocytes (TILs) Expression Profiles in Melanoma Tumor Microenvironment Cells*. Journal of Personalized Medicine.; 13(2):221., https://doi.org/10.3390/jpm13020221 Category Quartile (**Q2**) https://www.mdpi.com/2075-4426/13/2/221 WOS:000941363600001 **(autori cu contribuție egală)**	**3.4**
2.	Popovici, V., Matei, E., **Cozaru, G.C.,** Bucur, L., Gîrd, C. E., Schröder, V., ... & Badea, V. (**2022**). *In Vitro Anticancer Activity of Mucoadhesive Oral Films Loaded with Usnea barbata (L.) FH Wigg Dry Acetone Extract, with Potential Applications in Oral Squamous Cell Carcinoma Complementary Therapy.* Antioxidants, 11(10), 1934., DOI10.3390/antiox11101934, Category Quartile (**Q1**) https://www.mdpi.com/2076-3921/11/10/1934 WOS:000874144600001 **(contribuție egală cu primul autor)**	**7**
3.	Popovici, V., Matei, E., **Cozaru, G. C.**, Bucur, L., Gîrd, C. E., Schröder, V., ... & Badea, V. (**2022**). *Design, Characterization, and Anticancer and Antimicrobial Activities of Mucoadhesive Oral Patches Loaded with Usnea barbata (L.) FH Wigg Ethanol Extract F-UBE-HPMC.* Antioxidants, 11(9), 1801, DOI10.3390/antiox11091801, Category Quartile (**Q1**) https://www.mdpi.com/2076-3921/11/9/1801 WOS:000858531900001 **(contribuție egală cu primul autor)**	**7**
4.	Popovici, V., Matei, E., **Cozaru, G.C.,** Bucur, L., Gîrd, C. E., Schröder, V., ... & Badea, V. (**2022**). *Formulation and Development of Bioadhesive Oral Films Containing Usnea barbata (L.) FH Wigg Dry Ethanol Extract (F-UBE-HPC) with Antimicrobial and Anticancer Properties for Potential Use in Oral Cancer Complementary Therapy.* Pharmaceutics, 14(9), 1808., DOI10.3390/pharmaceutics14091808, Category Quartile (**Q1**) https://www.mdpi.com/1999-4923/14/9/1808 WOS:000857548300001 **(contribuție egală cu primul autor)**	**5.4**
5.	Popovici, V., Matei, E., **Cozaru, G.C.,** Bucur, L., Gîrd, C. E., Schröder, V., ... & Badea, V. **(2022).** *Evaluation of Usnea barbata (L.) Weber ex FH Wigg Extract in Canola Oil Loaded in Bioadhesive Oral Films for Potential Applications in Oral Cavity Infections and Malignancy.* Antioxidants, 11(8), 1601., DOI10.3390/antiox11081601, Category Quartile (**Q1**)	**7**

	https://www.mdpi.com/2076-3921/11/8/1601 WOS:000846960000001 **(contribuție egală cu primul autor)**	
6.	Ionescu, C. A., Aschie, M., Matei, E., **Cozaru, G. C.**, Deacu, M., Mitroi, A. F., ... & Enciu, M. **(2022).** *Characterization of the Tumor Microenvironment and the Biological Processes with a Role in Prostatic Tumorigenesis.* Biomedicines, 10(7), 1672. (Q2), DOI10.3390/biomedicines10071672, Category Quartile (**Q2**) https://www.mdpi.com/2227-9059/10/7/1672 WOS:000832323700001 **(autori cu contribuție egală)**	**4.7**
7.	Popovici, V.; Bucur, L.; Gîrd, C.E.; Popescu, A.; Matei, E.; **Cozaru, G.C**.; Schröder, V.; Ozon, E.A.; Fit,a, A.C.; Lupuliasa, D.; et al. **(2022)** *Phenolic Secondary Metabolites and Antiradical and Antibacterial Activities of Different Extracts of Usnea barbata (L.) Weber ex F.H.Wigg from Călimani Mountains*, Romania. Pharmaceuticals, 15, 829, https://doi.org/10.3390/ph15070829, Category Quartile (**Q2**) https://www.mdpi.com/1424-8247/15/7/829 WOS:000832007100001 **(contribuție egală cu primul autor)**	**4.6**
8.	Popovici V, Matei E, **Cozaru G.C**, Aschie M, Bucur L, Rambu D, Costache T, Cucolea IE, Vochita G, Gherghel D, Caraiane A, Badea V. (**2021)** *Usnic Acid and Usnea barbata (L.) F.H. Wigg. Dry Extracts Promote Apoptosis and DNA Damage in Human Blood Cells through Enhancing ROS Levels. Antioxidants*.; 10(8):1171, https://doi.org/10.3390/antiox10081171 Category Quartile (**Q1**) https://www.mdpi.com/2076-3921/10/8/1171 WOS:000688580400001 **(contribuție egală cu primul autor)**	**7**
9.	Brînzan, C., Aşchie, M., **Cozaru, G.,** Dumitru, E., & Mitroi, A. (**2020**). *The diagnostic value of miR-92a,-143, and-145 expression levels in patients with colorectal adenocarcinoma from Romania. Medicine*, *99*(35). ISSN / eISSN: 0025-7974 / 1536-5964**,** DOI:10.1097/MD.0000000000021895 Category Quartile (**Q3**) https://journals.lww.com/md-journal/Fulltext/2020/08280/The_diagnostic_value_of_miR_92a,__143,_and__145.63.aspx WOS:000579132500063 **(autori cu contribuție egală)**	**1.889**
10.	Brînzan, C., Aşchie, M., Matei, E., Mitroi, A., & **Cozaru, G.** (**2019**). *Molecular expression profiles of selected microRNAs in colorectal adenocarcinoma in patients from south-eastern part of Romania.* Medicine 98(47):p e18122, November 2019. | DOI: 10.1097/MD.0000000000018122 Category Quartile (**Q3**) https://journals.lww.com/md-journal/Fulltext/2019/11220/Molecular_expression_profiles_of_selected.84.aspx WOS:000507864900084 **(ultim autor)**	**1.552**

Journal of
*Personalized
Medicine*

Article

PD-L1, CD4+, and CD8+ Tumor-Infiltrating Lymphocytes (TILs) Expression Profiles in Melanoma Tumor Microenvironment Cells

Bogdan Marian Caraban [1], Elena Matei [2,*], Georgeta Camelia Cozaru [2,3], Mariana Aşchie [2,3], Mariana Deacu [1,3], Manuela Enciu [1,3], Gabriela Izabela Băltăţescu [2,3], Anca Chisoi [2,3], Nicolae Dobrin [3], Lucian Petcu [4], Emma Gheorghe [1], Laurenţiu-Tony Hangan [1], Mihai Cătălin Roșu [2], Cristian Ionuț Orasanu [2,3] and Antonela-Anca Nicolau [2,3]

[1] Faculty of Medicine, "Ovidius" University of Constanta, 900470 Constanta, Romania
[2] Center for Research and Development of the Morphological and Genetic Studies of Malignant Pathology, "Ovidius" University of Constanta, 900591 Constanta, Romania
[3] Clinical Service of Pathology, "Sf. Apostol Andrei" Emergency County Hospital, 900591 Constanta, Romania
[4] Dental Medicine Faculty, "Ovidius" University of Constanta, 900470 Constanta, Romania
* Correspondence: sogorescuelena@gmail.com; Tel.: +40-723943559

Abstract: (1) Background: Because melanoma is an aggressive tumor with an unfavorable prognosis, we aimed to characterize the PD-L1 expression in melanomas in association with T cell infiltrates because PD-1/PD-L1 blockade represents the target in treating melanoma strategy. (2) Methods: The immunohistochemical manual quantitative methods of PD-L1, CD4, and CD8 TILs were performed in melanoma tumor microenvironment cells. (3) Results: Most of the PD-L1 positive, expressing tumors, have a moderate score of CD4+ TILs and CD8+TILs (5−50% of tumor area) in tumoral melanoma environment cells. The PD-L1 expression in TILs was correlated with different degrees of lymphocytic infiltration described by the Clark system ($X^2 = 8.383$, $p = 0.020$). PD-L1 expression was observed often in melanoma cases, with more than 2−4 mm of Breslow tumor thickness being the associated parameters ($X^2 = 9.933$, $p = 0.014$). (4) Conclusions: PD-L1 expression represents a predictive biomarker with very good accuracy for discriminating the presence or absence of malign tumoral melanoma cells. PD-L1 expression was an independent predictor of good prognosis in patients with melanomas.

Keywords: PD-L1; CD4+; CD8+; tumor-infiltrating lymphocytes; melanoma tumor microenvironment cells

check for updates

Citation: Caraban, B.M.; Matei, E.; Cozaru, G.C.; Aşchie, M.; Deacu, M.; Enciu, M.; Băltăţescu, G.I.; Chisoi, A.; Dobrin, N.; Petcu, L.; et al. PD-L1, CD4+, and CD8+ Tumor-Infiltrating Lymphocytes (TILs) Expression Profiles in Melanoma Tumor Microenvironment Cells. *J. Pers. Med.* **2023**, *13*, 221. https://doi.org/10.3390/jpm13020221

Academic Editors: Carolina Constantin, Sabina Zurac and Monica Neagu

Received: 20 December 2022
Revised: 21 January 2023
Accepted: 25 January 2023
Published: 27 January 2023

1. Introduction

Melanoma is a highly aggressive tumor, most often with a cutaneous presentation with an immunogenic character, unfavorable prognosis, and raised mortality rate. Older fair-skinned males represent the high-risk population with a personal or family history of melanoma and with chronic UV exposure [1,2]. In recent years, significant progress in targeted therapy development [3,4] and novel prognostic biomarkers have been necessary for patient treatment strategy tailoring [5].

It is recognized that the immune inhibitory signaling pathways have an important role in immunosuppressive microenvironment maintenance, which favor cancer development [6]. An important co-inhibitory pathway is the programmed death-ligand 1 (PD-L1) and programmed death-1 (PD-1) axis [7]. The expression of PD-1 is induced on effector T-cells in response to inflammatory signals, and PD-L1 (B7-H1 or CD274) was the first identified ligand of PD-1 and is expressed in lymphocytes, vascular endothelium, mesenchymal stem cells, neuronal cells, and tumor cells [8]. PD-1/PD-L1 interactions have roles in T-cell-mediated immune responses inhibiting, cytokine production limiting, and tumor immune escape promotion [5,9]. PD-L1 binding to PD-1 suppresses the immune response through CD8+ T cell inhibition and CD4+T-regulatory lymphocyte activation, and melanoma tumor cells use this mechanism [10,11]. PD-L1 is expressed in the tumor microenvironment cells facilitating immune evasion, a predictive biomarker for malignant melanoma evolution [12–14]. PD-L1 expression in tumor cells is the most studied predictive biomarker, but a correlation with a therapeutic response is insufficient for melanoma for clinical use. PD-L1 overexpression is examined as a prognostic factor in diverse cancers, such as lung cancer [15], gastric cancer [16], ovarian cancer [17], breast cancer [18], prostate cancer [19], bladder cancer [20], cervical cancer [21], colorectal cancer [22], pancreatic cancer [23], and renal cell carcinoma [24]. Various studies reported the prognostic value of PD-L1 expression in melanoma patients [5,25–37].

Other predictive biomarkers studied in melanoma tumors include T cell receptors and T cell infiltrates. CD8+ T cell presence in the melanoma periphery is associated with a better response to PD-1 inhibitors [38,39]. Most malignant melanocytic tumors evolved despite immune cell presence in the tumor microenvironment, suggesting that these lymphocytes fail to control tumor growth [7,40,41]. The tumor-infiltrating lymphocytes (TILs) were a part of many studies in the past few years [42], bringing important evidence that a high number of lymphocytes are present in the development site of a tumor, with numerous CD8-positive T lymphocytes. These lymphocytes present in melanoma must be differentiated from lymphocytes in a skin lymphoma that has immunoreactivity for CD20 but a negative reaction for CD30 and CD45 [43]. A statistically significant correlation between skin melanoma survivors and increased risk of Non-Hodgkin Lymphoma was observed in the first three years after the diagnosis of skin melanoma [44].

In this study, we used a melanoma patient cohort to characterize the PD-L1 expression in melanoma cases associated with T-cell infiltrates, with roles in diagnosis and prognosis.

2. Materials and Methods

2.1. Patient Group

This study collected the cases from the electronic database of the Pathology Department of ”St. Andrew’s” Clinical Emergency County Hospital of Constanta diagnosed with different forms of melanoma in the last two years. We identified 61 patients with surgically removed skin melanocytic tumors upon dermatological recommendation that proved to be melanomas before any oncological treatment. The histologic diagnosis for each specimen was confirmed on Hematoxylin Eosin (HE) stain slides by two experienced pathologists, with a concordance of measurements between 80−90%. We kept a representative tissue block to use for additional studies. Clinico-morphologic features were taken from the pathological reports, including age, gender, Clark level, Brelow thickness, TILs, and vascular and perineural invasion.

Our study followed these criteria: (1) inclusion of patients diagnosed with histologically confirmed melanoma; (2) detection of PD-L1, CD4, and CD8 TILs immunohistochemical expression in the melanomas (IHC) analysis; (3) identification of predictive biomarkers as PD-L1, CD4, CD8 tumor-infiltrating lymphocytes expression patterns; and calculation of the hazard ratio (HR) and 95% confidence interval (95% CI).

2.2. TILs Evaluation

TILs evaluation was performed on Hematoxylin Eosin (HE) stain using the Clark scoring system, classifying immune infiltrate as brisk (TILs present throughout the vertical growth), non-brisk (TILs in one or more foci of the vertical growth phase), or absent.

2.3. Immunohistochemical (IHC) Analysis

The immunohistochemical evaluation was performed with a panel of three antibodies from Master Diagnostica (Granada, Spain) (ready-to-use): PD-L1 (CAL10-clone, rabbit monoclonal antibody), CD4 (EP204-clone, rabbit monoclonal antibody), CD8 (SP16-clone, rabbit monoclonal antibody). We used formalin-fixed paraffin-embedded blocks to obtain four µm-thick sections, 3, 3′diaminobenzidine (DAB) as chromogen, with brown staining.

The sections were finally counterstained with Mayer's Hematoxylin and mounted. For positive and negative quality controls, we used tonsil tissue according to the manufacturer's recommendation. The three immunohistochemical biomarkers were evaluated using optic microscopy, considering the positive reaction ≥5%. The degrees of intensities were considered: weakly positive (1+), moderate positive (2+), and intense positive (3+). We assessed the PD-L1 expression in melanoma cells, and TIL's and CD4 and CD8 TIL's expression in melanoma tumor microenvironment cells.

2.4. Statistical Analysis

The experimental data were analyzed using IBM SPSS Statistics Version 26 (Armonk, NY: IBM Corp). The procedures used were descriptive statistics (for characterization of the discreet and continuous variables defined in the database), parametric test (Independent Sample t Test with Levene's Test and One Way ANOVA with posthoc Tukey's range test and Games-Howell Test), Nonparametric tests (Pearson Chi-Square with Cramer's V test for the association between categorical variables, Mann-Whitney U Test and Kruskal-Wallis H Test for continuous variables). All *p*-values below 0.05 were considered statistically significant. Receiver operating characteristic (ROC) and area under the curve (AUC) made by MedCalc v20.111 Software Ltd. (Ostend, Belgium) were used to establish the accuracy of the biomarkers in melanoma diagnoses. The sensitivity and specificity of biomarkers are represented by the Youden index, which is the optimal cut-off point as the value that maximizes the area under the ROC curve [45,46]. Furthermore, multivariate Cox-proportional hazard regression was performed to determine the potential prognostic values of PD-L1, CD4, and CD8 TILs in melanoma patients.

3. Results

3.1. Clinico-Pathological Analysis of Melanoma Tumor Microenvironment Cells, Associated with IHC Patterns of PD-L1 (+/-) Expression

PD-L1 (+/-) expression patterns in patients with acral, cervical-cranial, and limb localization of melanomas are summarized in Table 1. The incidence of PDL-1 positive expressions for patients with acral and cervico-cranial localization of melanoma was notably lower than for patients with upper body and limbs localizations of melanoma (TILs-A:5.41%; CC:8.11% vs. UB:51.35%; L:35.14%, $p < 0.05$; MTCs-A:7.10%; CC:17.86% vs. UB:53.62%; L:21.43%, $p \geq 0.05$). We observed PD-L1 positive expression patterns in 56.76% of TILs and 46.43% in MTCs ($p \geq 0.05$) for IV grade of Clark level of invasion in melanoma samples from 61 patients when a TILs threshold of positive reaction ≥5%.

Table 1. Melanoma tumor microenvironment characterization in the function of PD-L1 (+/-) expression.

Nb.	**Clinico-Pathological Aspects**	**PD-L1 Expression in TILs**		**χ^2 Score**	***p*-Value**	**PD-L1 Expression in MTCs**		**χ^2 Score**	***p*-Value**
		Negative *n* (%)	**Positive *n* (%)**			**Negative *n* (%)**	**Positive *n* (%)**		
	Age								
1.	<65 years	8 (33.33%)	20 (54.05%)	2.517	0.126	17 (51.52%)	11 (39.29%)	0.912	0.243
	>65 years	16 (66.67%)	17 (54.95%)			16 (48.48%)	17 (60.71%)		
	Gender								
2.	Males	9 (37.50%)	22 (59.46%)	2.809	0.120	15 (45.45%)	16 (57.14%)	0.828	0.444
	Females	15 (62.50%)	15 (40.54%)			18 (54.55%)	12 (42.86%)		
	Localization								
3.	Acral	3 (12.5%)	2 (5.41%)	*9.603 **	*0.018*	3 (9.1%)	2 (7.1%)	2.791	0.443
	Upper body	7 (29.17%)	19 (51.35%)			11 (33.33%)	15 (53.62%)		
	Cervico-cranial	9 (37.5%	3 (8.11%)			7 (21.2%)	5 (17.86%)		
	Limbs	5 (20.83%)	13 (35.14%)			12 (36.36%)	6 (21.43%)		

Table 1. *Cont.*

Nb.	**Clinico-Pathological Aspects**	**PD-L1 Expression in TILs**		**X^2 Score**	***p*-Value**	**PD-L1 Expression in MTCs**		**X^2 Score**	***p*-Value**
		Negative *n* (%)	**Positive *n* (%)**			**Negative *n* (%)**	**Positive *n* (%)**		
4.	**Clark level of invasion**			3.584	0.494			8.819	0.068
	I	6 (25%)	3 (8.11%)			7 (21.22%)	2(7.14%)		
	II	2 (8.33%)	4 (10.81%)			1 (3.03%)	5 (17.86%)		
	III	4(16.67%)	6(16.22%)			3 (9.09%)	7 (25.00%)		
	IV	11(45.83%)	21 (56.76%)			19 (57.58%)	13 (46.43%)		
	V	1(4.17%)	3 (8.11%)			3 (9.09%)	1 (3.57%)		
5.	**Breslow tumor thickness**			6.851	0.086			*9.933* *	*0.014*
	<1 mm	4 (16.67%)	2 (5.41%)			6 (18.18%)	0 (0%)		
	1–2 mm	0 (0%)	3 (8.11%)			0 (0%)	3 (10.71%)		
	2–4 mm	3 (12.50%)	12 (32.43%)			6 (18.18%)	9 (32.14%)		
	>4 mm	17 (70.83%)	20 (54.05%)			21 (63.64%)	16 (57.14%)		
6.	**Lymphovascular invasion**			3.175	0.113			1.533	0.216
	Present	10 (41.67%)	24 (64.86%)			16 (48.48%)	18 (64.29%)		
	Absent	14(52.14%)	13(35.14%)			17 (51.52%)	10 (35.71%)		
7.	**Perineural invasion**			1.163	0.298			0.009	0.926
	Present	5 (20.83%)	9 (14.75%)			5 (15.15%)	4 (14.29%)		
	Absent	19 (79.17%)	33 (89.19)			28 (84.85%)	24 (85.71%)		

PD-L1- Programmed cell death ligand-1; TILs-tumor-infiltrating lymphocytes; MTCs-melanoma tumor cells; * $p < 0.05$ represents statistically significant differences between cases made by Pearson Chi-Square with Cramer's V test for the association between categorical variables, Mann-Whitney U Test and Kruskal-Wallis H Test for Continuous variables (X^2 Score).

When comparing the Breslow tumor thickness between TILs with MTCs, were observed the lowest proportion of PD-L1 (+) expression, at 5.41% (TILs) and 0% (MTCs) for <1 mm diameter, while the highest proportion of PD-L1 (+) specimens was seen for >4mm diameter, at 54.05% (TILs, $p \geq 0.05$) and 57.14% (MTCs, $p < 0.05$) from cases.

The association between PD-L1 expression and clinicopathological features was analyzed, age (≥65 vs. <65 years), gender (male vs. female), localization (acral, upper body, cervico-cranial, limb), Clark level of invasion (I, II, III, IV, V), Breslow tumor thickness (<1 mm; 1–2 mm; 2–4 mm; >4 mm), lymphovascular invasion (present, absent), perineural invasion (present, absent) (Table 1).

PD-L1 expression was significantly correlated with melanoma localizations in infiltrating immune cells ($X^2 = 9.603$, $p = 0.018$) and Breslow tumor thickness in melanoma tumor cells ($X^2 = 9.933$, $p = 0.014$), but no significant relationship between PD-L1 expression and age, gender, or morphological characteristics was seen (Clark level of invasion, lymphovascular invasion, and perineural invasion).

3.2. PD-L1 Expression in Tumor Cells and Immune-Infiltrating Cells in Various Morphological Types of Melanoma and Tils Quantification and Characterization

PD-L1 (+/-) expression patterns were observed in the different morphological types of melanomas as lentigo maligna melanoma (LMM), superficial spreading melanoma (SSM), superficial spreading melanoma with vertical growth nodule (SSM-VGN), and nodular melanoma (NM), being presented in Table 2.

The highest incidences of PD-L1 (+) in TILs were observed for SSM (37.84%) and SSM-VGN (37.84%, $p \geq 0.05$). Superficial spreading melanoma has in MTCs the highest incidence (46.43%, $p \geq 0.05$). PD-L1 (+/-) expressions in TILs were observed in strong association with CD8+ and CD4+ T-lymphocytes ($X^2 = 11.238$, $p = 0.003$; $X^2 = 12.614$, $p = 0.001$, Table 2).

PD-L1 (+) patterns associated with moderate to severe CD8+ and CD4+ lymphocytes intensities (CD8+TILs: 69.57%; MTCs: 75.00%; CD4+TILs: 97.30%; MTCs: 85.71%) compared to mild (CD8+TILs: 2.79%; MTCs: 7.14%, CD4+TILs: 0.00%; MTCs: 3.57%, $p < 0.05$) were observed in the majority of morphological types of melanomas (Table 2) (Figures 1–5).

Melanomas negative for PD-L1 show a significant degree of staining (2+) by CD4 and CD8 infiltrating lymphocytes (CD8+TILs: 58.53%; MTCs: 75.76%, CD4+TILs: 70.83%; MTCs: 87.88%, $p < 0.05$).

Table 2. Association between PD-L1 (+/-) expressions in tumor microenvironment cells and CD4 and CD8 tumor-infiltrating lymphocytes.

Nb.	**Morphological Features**	**Infiltrating Immune Cells**		**χ^2 Score**	***p*-Value**	**Melanoma Tumor Cells**		**χ^2 Score**	***p*-Value**
		PD-L1 (-) ***n* (%)**	**PD-L1 (+)** ***n* (%)**			**PD-L1 (-)** ***n* (%)**	**PD-L1 (+)** ***n* (%)**		
1.	**Morphologic type**			3.305	0.332			5.678	0.144
	LMM	2 (8.33%)	1 (2.70%)			3 (9.09%)	0 (0%)		
	SSM	7 (29.17%)	14 (37.84%)			8 (24.24%)	13 (46.43%)		
	SSM with VGN	6 (25%)	14 (37.84%)			13 (39.39%)	7 (25%)		
	NM	9 (37.50%)	8 (21.62%)			9 (27.27%)	8 (28.57%)		
2.	**TILs evaluation**			_8.383 *_	_0.020_			2.425	0.287
	Absent	8 (33.33%)	2 (5.41%)			7 (21.21%)	3 (10.71%)		
	Brisk	3 (12.50%)	8 (21.62%)			4 (12.12%)	7 (25%)		
	Non-brisk	13 (54.17%)	27 (72.97%)			22 (66.67%)	18 (64.29%)		
3.	**CD8 TIL's**			_11.238 **_	_0.003_			2.775	0.514
	Negative	9(37.50%)	2 (5.41%)			7 (21.21%)	4 (14.29%)		
	<5%	1(4.17%)	1 (2.70%)			0(0.00%)	2 (7.14%)		
	5–50%	14(58.33%)	32 (69.57%)			25 (75.76%)	21 (75.00%)		
	>50%	0 (0.00%)	2 (5.41%)			1 (50.00%)	1 (50.00%)		
4.	**CD4 TIL's**			_12.614 **_	_0.001_			2.076	0.906
	Negative	6 (25.00%)	0 (0.00%)			3 (9.09%)	3 (10.71%)		
	<5%	1 (4.17%)	0 (0.00%)			0 (0.00%)	1 (3.57%)		
	5–50%	17 (70.83%)	36 (97.30%)			29 (87.88%)	24 (85.71%)		
	>50	0 (0.00%)	1 (2.70%)			1 (3.03%)	0 (0.00%)		

PD-L1- Programmed cell death ligand-1; TILs- tumor-infiltrating lymphocytes; LMM- lentigo maligna melanoma; SSM- Superficial spreading melanoma; SSM-VGN- superficial spreading melanoma with vertical growth nodule; NM- nodular melanoma; * $p < 0.05$ and ** $p \leq 0.001$ represent statistically significant differences between cases made by Pearson Chi-Square with Cramer's V test for the association between categorical variables, Mann-Whitney U Test and Kruskal-Wallis H Test for Continuous variables (X^2 Score).

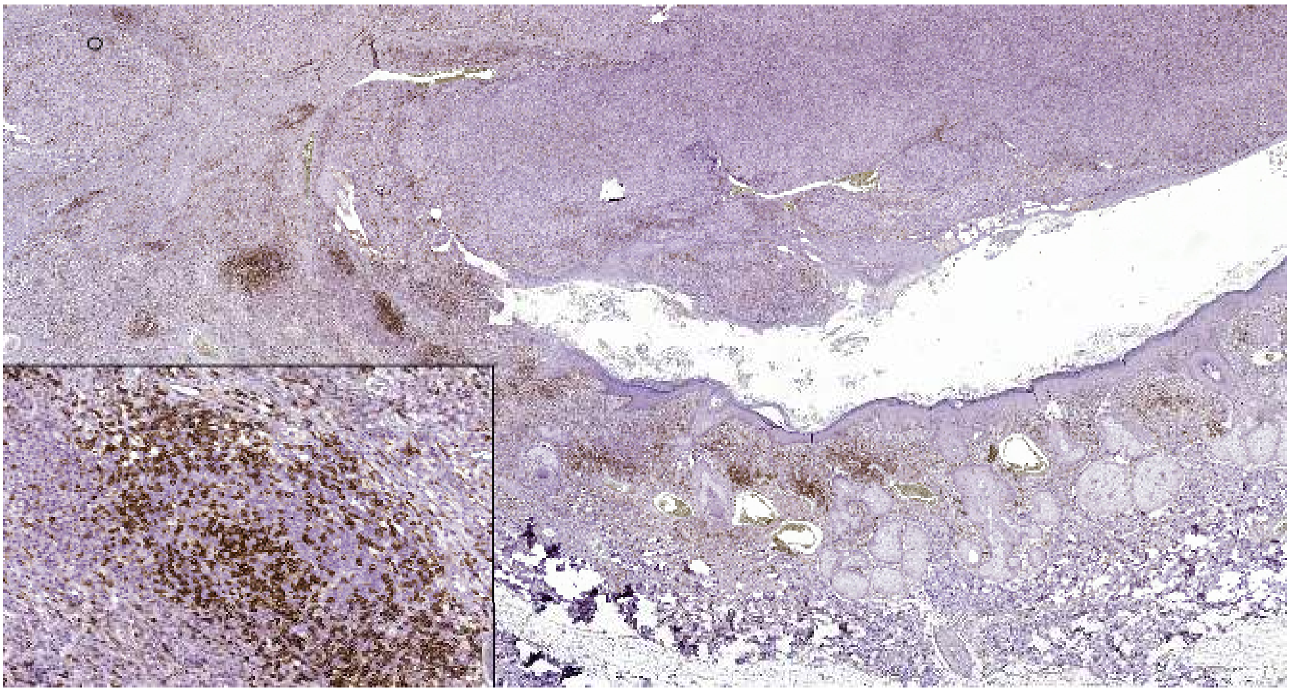

Figure 1. In nodular polypoid melanoma, CD4 intense membranous expression in intra and peritumoral lymphocytes (CD4 monoclonal antibody, clone EP204). In the lower left side detail, obx200.

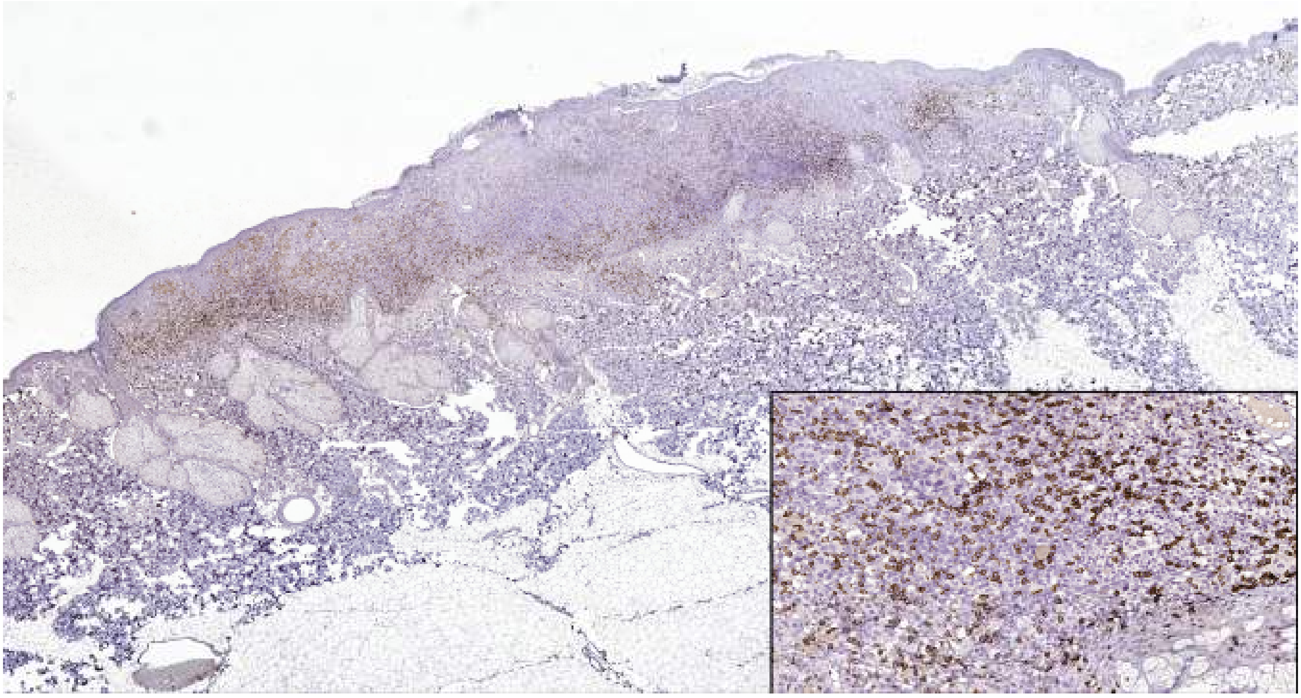

Figure 2. CD8 intense positive reaction in superficial spreading melanoma (CD8 Monoclonal Antibody, clone SP16, scanned image). In the lower right side, detail ob.x200.

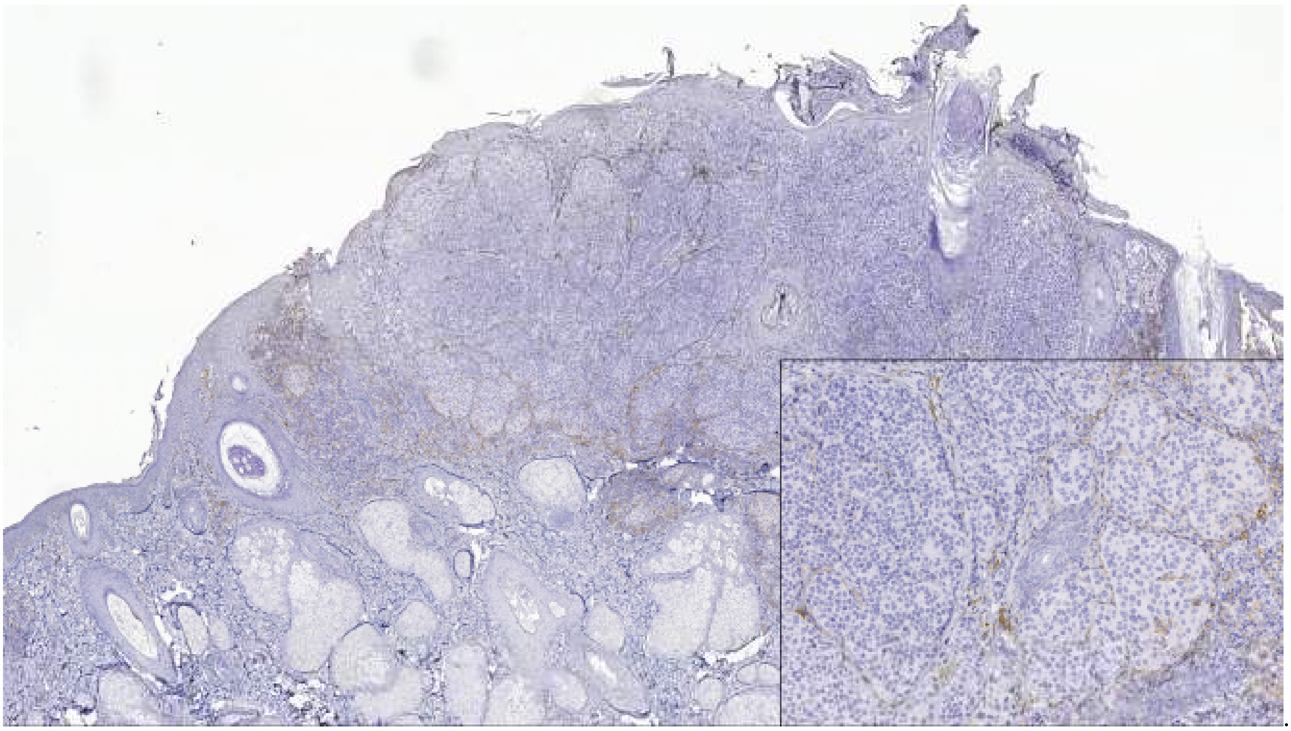

Figure 3. PD-L1 negative expression in tumor cells and TILs of nodular melanoma (PD-L1 Monoclonal Antibody, Clone CAL10). The brown staining is due to melanin pigment and melanophages. In the lower right side, detail ob.x100.

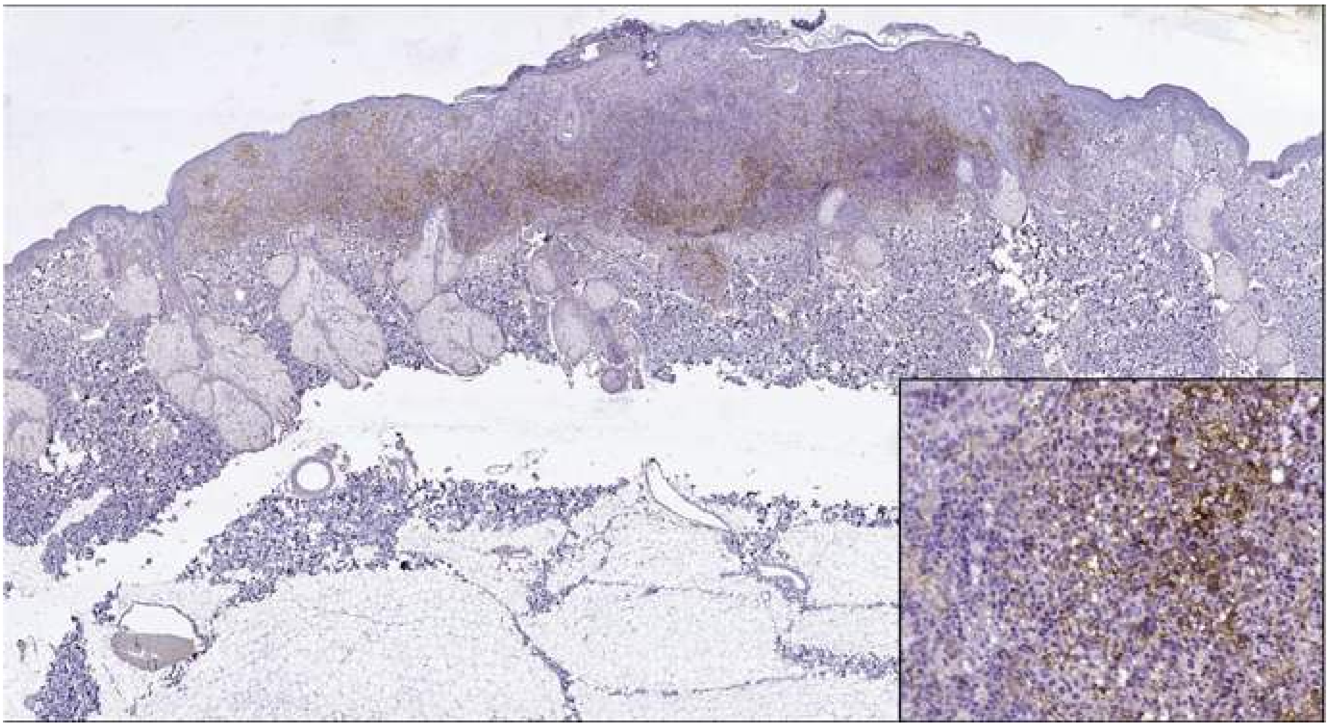

Figure 4. PD-L1 positive expression in melanoma cells of a superficial spreading melanoma (PD-L1 Monoclonal Antibody, Clone CAL10). Lower right side, detail, ob.x200.

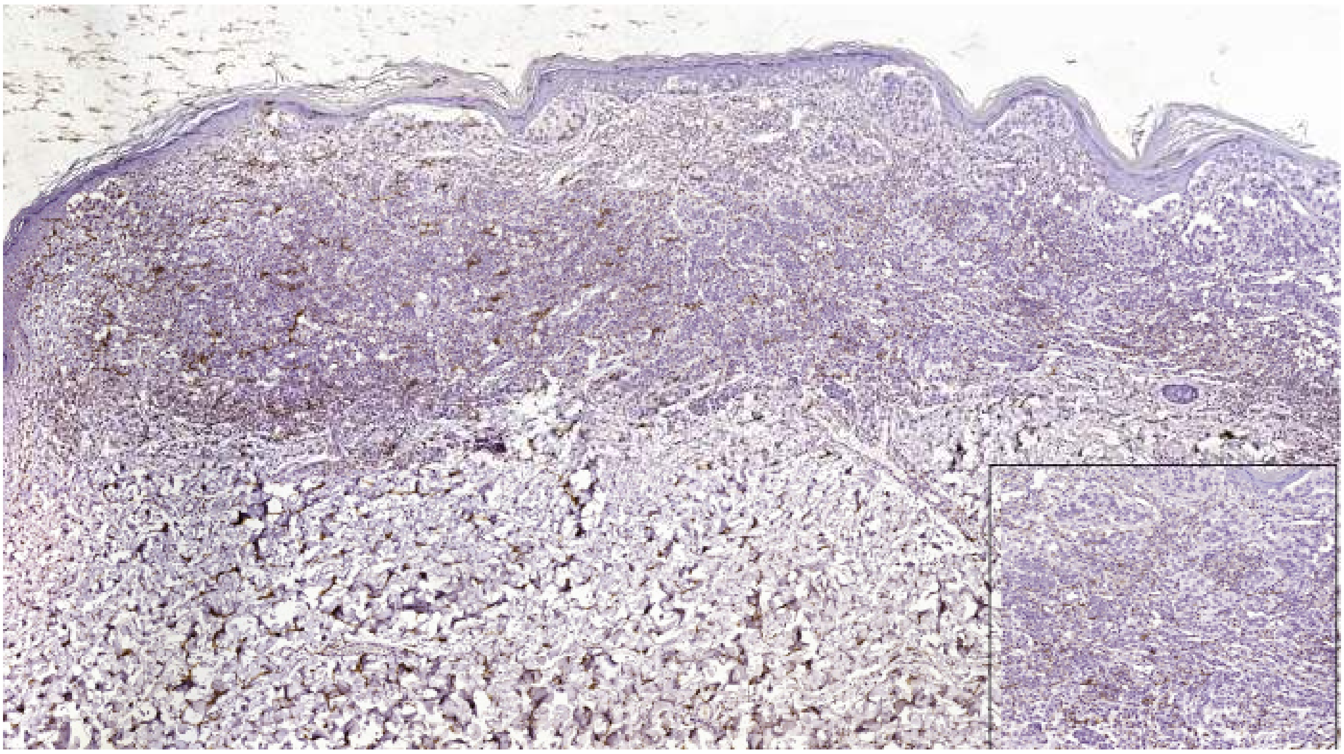

Figure 5. PD-L1 negative expression in tumor cells and focally positive in TILs in a case of superficial spreading melanoma (PD-L1 Monoclonal Antibody, Clone CAL10). Lower right side, detail, ob.x400.

Although PD-L1 expression associated with no TILs was not observed in melanoma tumor cells ($X^2 = 2.775$, $p = 0.514$), PD-L1 was expressed in T lymphocytes ($X^2 = 8.383$,

p = 0.020). In our study, PD-L1 showed intertumoral heterogeneity. PD-L1, CD4 TILs, and CD8TILs biomarkers intensities were observed in Figures 1–5.

3.3. Predictive and Prognostic Roles of PD-L1, CD4, and CD8 Tumor-Infiltrating Lymphocytes Biomarkers in Melanoma Tumor Microenvironment Cells

To establish the laboratory diagnostic, the predictive model (ROC curves) is used to estimate the risk of patient adverse outcomes in medical research and to use as a discriminatory tool for true positive values (sensitivity) and true negative values (specificity) [45]. ROC curves were used to show the accuracy of the methods by interpreting the true positive results (TPR, sensitivity) and false positive results (FPR, 100-specificity) for each biomarker with two overlapping distributions (negative, positive) (Table 3, Figure 6). Sensitivities of methods in patients with melanoma were very good for PD-L1, CD8TILs, and CD4TILs biomarkers (TILs: 97.30%; M: 96.43%, 89.13%, and 84.31%, $p < 0.001$ (Table 3, Figure 6). Also, specificities of analyzed biomarkers in melanoma tumor microenvironment cells were very good for PD-L1 (TILs: 91.67%; M: 96.97%), CD8 (86.67%), CD4 (90.00%, $p < 0.001$) (Table 3, Figure 6). The area under the curve (AUC) for our studied biomarkers (PD-L1, CD4 TILs, and CD8 TILs) starts from 0.941 to 0.975, which means a very good ability of the ROC test to discriminate the presence or absence of malign tumoral melanoma cells.

Table 3. Receiver operating characteristic (ROC) analysis of PD-L1, CD4, and CD8 tumor-infiltrating lymphocyte biomarkers in melanoma patients.

Nb.	Biomarkers	AUC	95% CI *	*p*-Value	Youden J Index	Cut-Off Value	Sensitivity	Specificity
1.	**PD-L1 TILs**	0.959	0.875 to 0.993	<0.001	0.889	>3	97.30	91.67
2.	**PD-L1 M**	0.975	0.898 to 0.998	<0.001	0.934	>0	96.43	96.97
3.	**CD4 M**	0.950	0.862 to 0.989	<0.001	0.743	>15	84.31	90.00
4.	**CD8 M**	0.941	0.850 to 0.985	<0.001	0.758	>10	89.13	86.67

UC = area under the curve; ROC = receiver operating characteristic; * Confidence interval; Youden J = sensitivity + specificity – 100; PD-L1- Programmed cell death ligand-1; TILs- tumor-infiltrating lymphocytes; M- melanoma tumor cells.

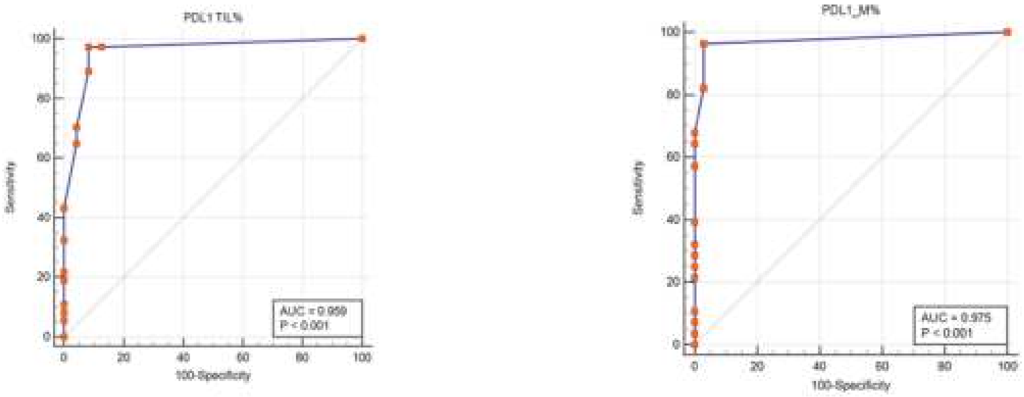

Figure 6. *Cont.*

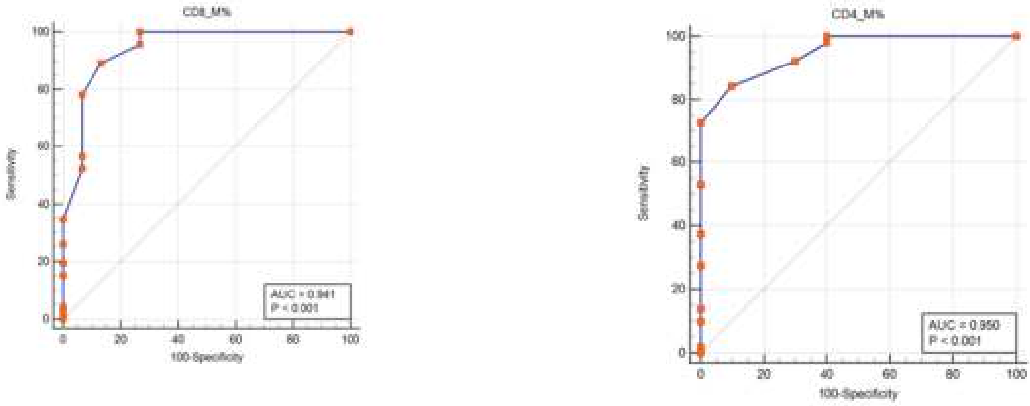

Figure 6. PD-L1, CD4, and CD8 tumor-infiltrating lymphocytes expressions patterns as potential biomarkers in melanoma diagnosis. Receiver operating curve (ROC) analyses were generated from 61 patients and had a value of the area under the curve (AUC) for PD-L1 (TILs: sensitivity: 97.30%, specificity: 91.67%; $p < 0.001$; M: sensitivity: 96.43%, specificity: 96.97%; $p < 0.001$), CD8 tumor-infiltrating lymphocytes (M: sensitivity: 89.13%, specificity: 86.67%; $p < 0.001$), and CD4 tumor-infiltrating lymphocytes (M: sensitivity: 84.31%, specificity: 90.00%; $p < 0.001$), respectively.

Furthermore, multivariate analysis Cox-proportional hazard regression analyzed the following parameters as the PD-L1, CD4, and CD8 TILs expression patterns to observe their potential prognostic roles in melanoma tumor microenvironment cells (Table 4). In our analysis, we observed that PDL-1 represents a favorable prognostic biomarker, an independent predictor factor implied in the prognosis of the melanoma patients.

Table 4. Logistic regression of potential prognostic values of PD-L1, CD4, and CD8 TILs in melanoma tumor microenvironment cells.

Nb.	Clinical Variables	Multivariate Analysis		
		Melanoma Tumor Microenvironment Cells		
		Hazard Ratio	p-Value	95% CI *
1.	Lymphovascular invasion	3.049	0.528	0.095−97.914
2.	Perineural invasion	0.026 *	***0.023***	0.001−0.607
3.	PD-L1	2.700	0.455	0.198−36.683
4.	CD4 TILs	11.838 *	***0.023***	1.386−101.108
5.	CD8 TILs	7.748 *	***0.018***	1.408−42.622

CI*- Confidence interval; * $p < 0.05$ represents statistically significant differences between variables made by Cox Logistic & Snell regression (Cox & Snell R^2). PDL-1 in MTC-$R^2 = 0.23$, $p = 0.43$; CD8 TILs in MTC – $R^2 = 0.49$, $p < 0.0001$; CD4 TILs in MTC - $R^2 = 0.38$, $p = 0.002$.

4. Discussion

Immunotherapy has proved in the past few years to have a real success for many types of cancer. So far, the most effective immunotherapies are the monoclonal antibodies targeting the checkpoint molecules CTLA-4 (cytotoxic T lymphocytes-associated protein 4) and PD-1 (programmed cell death protein 1) and its ligand PD-L1. Antibody blockade of PD-1 and its ligand PD-L1 have antitumor efficacy and durability of responses in melanoma patients [14]. PD-L1 expression by melanoma tumor cells is heterogeneous and contiguous to tumor-infiltrating lymphocyte areas [11]. Melanomas may express PD-L1 against antitumor immune effector cells, facilitating immune evasion even if the B7-H1 costimulatory molecule is present on the surface of tumor cells. This regulates the cellular and humoral immune responses through the PD-1 receptor on activated T and B cells. Also, it was observed that in vitro, the B7-H1 tumor cell lines might increase the apoptosis of antigen-specific human T-cells, which means the apoptotic effects of B7-H1 are mediated by one or more receptors other than PD-1 [10]. TILs recognize tumors and secrete pro-inflammatory cytokines with a role in the upregulation of PD-L1 expression in the TME. PD-L1 ligates PD-1 on TILs determining their downregulation [47]. The PD-L1 expression in TILs is interesting to keep in observation because PD-L1 was correlated with different degrees of lymphocytic infiltration described by the Clark system ($X^2 = 8.383$, $p = 0.020$), according to references [48].

PD-L1 (+) expression shows a higher incidence in cases with superficial spreading melanoma, superficial spreading melanoma with vertical growth nodules, and a lower incidence rate in lentigo maligna melanoma and nodular melanomas, in conformity with references [49,50].

In the studies on melanomas, a high Breslow tumor thickness represents an indicator of poor prognosis [51–53]. PD-L1 expression was observed often in melanoma cases with more than 2−4 mm of Breslow tumor thickness [54,55]. According to the references, our study shows a significant correlation between the PD-L1 expression and Breslow tumor thickness in melanoma tumor cells ($X^2 = 9.933$, $p = 0.014$).

Tumor-infiltrating lymphocytes (TILs) infiltrate tumor cells. The degree of infiltration is described by the TIL infiltrate's extent and intensity. The most applied grading scheme for assessing the presence of TILs is the Clark system, as follows: 1; absent TILs infiltrate. 2; non-brisk TILs infiltrate: focal areas of lymphocytic infiltration in the tumor. 3; brisk TILs infiltrate: TILs infiltration of the entire tumor base or diffuse permeation of the tumor. Other systems for grading TILs infiltrates have been proposed based on their density and distribution but have not been validated [51–53]. TILs are an essential histopathological feature in diagnosing melanocytic tumors, composed of a series of cells, including T lymphocytes [56].

CD8+ cytotoxic and CD4+ T cells are important for the action of immune checkpoint inhibitors [38]. PD-L1 (+/-) expression patterns were observed on both tumor and immune cells. They were differentiated in the function of morphologic features, and tumors were considered to be PD-L1 positive when ≥5% of tumor cells presented membrane staining [57,58]. The presence of CD8+ TILs was scored as 0 (negative), weak (1+, positive cells focally at the edge of tumor or perivascular, 5% of tumor area), moderate (2+, infiltrating tumor by extending away from intratumoral vessels, 5−50% of tumor area), or intense (3+, broad infiltration by TILs, more than 50% of tumor area). Our study presented that PD-L1 expression was associated with CD8 TILs and CD4 TILs in the tumor immune microenvironment ($X^2 = 11.238$, $p = 0.003$; $X^2 = 12.614$, $p = 0.001$). These results are in accordance with multiple previous studies showing how PD-L1 positive expression represents an adaptive mechanism of expression induced by the host immune antitumor response [40,50,59,60].

In melanoma, PD-L1 is expressed by activated lymphocytes, presumably to decrease inflammation [61,62]. PD-L1 in stromal cells interacts with PD-1 on effector T cells, inhibiting their function. Moreover, in the tumor microenvironment, PD-L1 expression might be induced by interferon-gamma secretion via effector T cells [12]. Responding to immune checkpoint inhibitors may depend on active interaction between PD-1 on CD8 cells and PD-L1 in stromal cells [63].

PD-L1 plays an important role in the immune response regulation in the tumor microenvironment [64]. When PD-L1 binds to PD-1, it determines the T cell proliferation inhibition and its secretion of cytokines [65]. PD-1/PD-L1 blockade represents an essential strategy with therapeutic goals [66].

PD-L1 status was examined in TILs and MTCs cells, and cut-off values were calculated by the ROC curve method. Sensitivities of methods for PD-L1, CD8, and CD4 biomarkers, in patients with melanoma, were from 84.31% to 97.30%, and specificities of these analyzed biomarkers in melanoma tumor microenvironment cells were from 86.67% to 96.97%, offering the possibility to be biomarkers with predictive accuracy in melanomas. The area under the curve (AUC) for PD-L1, CD4, and CD8 biomarkers was from 0.941 to 0.975, which means a very good ability of the ROC test to discriminate the presence or absence of malign tumoral melanoma cells. To obtain more accurate measurements of PD-L1 expression, an IHC quantitative method associated with TILs characterization by CD4 and CD8 TILs expression was used, in conformity with other studies [67–69]. To verify antibody specificity, we used quality negative and positive controls for PD-L1 containing placental and tonsil tissue as previously described studies [57,67]. Many clinical assays develop predictive biomarkers by comparing the expression of PD-L1 in the tumor microenvironment cells in samples from patients treated with immune checkpoint inhibitors. Expressing these biomarkers in the tumor microenvironment predicts a better response to therapy [39].

One of the challenges to assessing the potential role of PD-L1 expression as a predictive biomarker was the variation in assays used across studies. Most studies used chromogenic IHC assays and obtained results of PD-L1 expression were interpreted by pathologists by reporting the percentage of tumor cells and immune cells demonstrating expression [14]. Other predictive biomarker studies involving PD-L1 expression used standard immunohistochemistry (IHC) as references [63,70–72].

We assessed the PD-L1, CD4, and CD8 lymphocytes infiltrations expression patterns, lymphovascular invasion, and perineural invasion in MTCs by multivariate analysis of Cox-proportional hazard regression. We observed that PDL-1 represents a favorable prognostic biomarker, being an independent predictor factor implied in the prognosis of the melanoma patients.

The association between PD-L1 expression and prognosis in melanoma has been explored extensively in previous studies [32,33,40,57]. PD-L1 expression was an independent predictor of good prognosis in patients with melanomas. In some studies, PD-L1 expression was correlated with the treatment response, but other studies show it must be complemented by additional biomarkers for immune profiling of the CD8+ T cells [32,40,50,58,73].

Other studies demonstrated that a high expression rate of PD-L1 with a dense and diffuse T-cell inflammatory infiltrate is a characteristic feature of melanoma and represents a good prognostic marker for metastatic melanoma [74–76]. Adaptive PD-L1 expression in melanoma microenvironment pretreatment is associated with a good prognosis [57] and biomarker predictive of response to anti-PD-1/PD-L1 therapies in melanoma [38,70,72].

It is unclear if the PD-L1 negative status in advanced melanoma determines phenotypic differences in immune responses or is an intrinsic tumor quality, and PD-L1–negative tumors are frequently associated with TILs. Melanoma with PD-L1–negative expression has a worse prognosis and responds less frequently to immune checkpoint therapies [11].

Lymphovascular invasion represents the presence of melanoma cells within the lamina of blood vessels or lymphatics, or both and is recorded as absent or present. Neurotropism represents the presence of melanoma cells close to the nerve sheaths. It is best identified at the periphery of the tumor and is associated with an increased local recurrence rate or local persistence. The density of lymphatic vessels within or surrounding growing tumors correlates with poor patient outcomes, being observed in many types of solid tumors [77,78]. Our data shows that lymphovascular and perineural invasion, both reliable morphologic prognostic features, did not correlate with PD-L1 expression and may not be considered an unfavorable prognostic marker.

Many studies have investigated the impact of PD-L1 on the prognosis of solid tumors [79]. PD-L1 expression was an independent prognostic factor in renal cell carcinoma [80]. A high PD-L1 expression was a poor prognostic biomarker in patients with non-Hodgkin lymphoma [5,81].

Our results might have limitations such as a limited sampling, the lack of consensus method in the evaluation of PD-L1 expression (only quantitative in our study), not considering more categories of positivity depending on the amount and distribution of positive melanoma cells, and the fact that the immunohistochemical tests were performed on tissue fragments prior to any treatment. Other study limitations in the association between PD-L1 and melanoma prognosis are the heterogeneity, patient ethnicity, and treatment, which could influence patient survival. In further studies, we propose working with a larger cohort of melanoma patients to have meaningful results to validate the immuno-histochemical PD-L1 expression with roles in diagnosis and prognosis.

5. Conclusions

In this study, we used a melanoma patient cohort to characterize the PD-L1 expression in melanoma in the context of T-cell infiltrates because the PD-1/PD-L1 blockade represents the target in treating melanoma strategy. Most of the PD-L1 positive expressing tumors have a moderate score of CD4+ TILs and CD8+TILs (5-50% of tumor area) in tumoral melanoma environment cells. PD-L1 expression represents a predictive biomarker with very good accuracy to discriminate the presence or absence of malign tumoral melanoma cells. PD-L1 expression was an independent predictor of good prognosis in patients with melanomas.

Author Contributions: All authors contributed equally to this study and shared the first authorship. Conceptualization, B.M.C., A.-A.N., E.M., M.E., M.A., M.D., E.G., L.-T.H. and G.C.C.; methodology, M.E., M.A., G.I.B., A.-A.N., A.C. and M.D.; software, E.M., L.-T.H., N.D. and L.P.; validation, E.M., L.-T.H.; formal analysis, M.E.; investigation B.M.C., A.-A.N., G.I.B., M.E. and C.I.O.; resources, A.-A.N. and M.E.; writing—original draft preparation, E.M., A.-A.N., B.M.C., M.E., A.C., M.A., M.D., M.C.R. and G.C.C.; writing—review and editing, E.M., A.-A.N. and M.E.; visualization, N.D. and G.C.C.; supervision, M.D. and M.A.; project administration, A.-A.N. and M.E.; funding acquisition, A.-A.N., M.D. and G.C.C. All authors have read and agreed to the published version of the manuscript.

Funding: This study is part of the result indicators assumed within a SEPMEL grant, contract number 06/14 November 2018. This grant was won in the biomedical competition organized into the CNFIS-FDI-2018-0462 project entitled “Excellence, performance, and competitiveness in biomedical research at the Ovidius University of Constanta”.

Institutional Review Board Statement: All aspects of ethics approval and consent to participate of patients in this study are made in conformity with the declaration of Helsinki 2000 and approved by the Ethics Committee of “Ovidius” University of Constanta, Romania, 5418/14 December 2018.

Informed Consent Statement: Informed consent was obtained from all patients involved in the study.

Data Availability Statement: Data are contained within the article.

Conflicts of Interest: The authors declare no conflict of interest.

References

1. O’Neill, C.H.; Scoggins, C.R. Melanoma. *J. Surg. Oncol.* **2019**, *120*, 873–881. [CrossRef] [PubMed]
2. Rodić, N.; Anders, R.A.; Eshleman, J.R.; Lin, M.-T.; Xu, H.; Kim, J.H.; Beierl, K.; Chen, S.; Luber, B.S.; Wang, H.; et al. PD-L1 expression in melanocytic lesions does not correlate with the BRAF V600E mutation. *Cancer Immunol. Res.* **2015**, *3*, 110–115. [CrossRef]
3. Fujimura, T.; Fujisawa, Y.; Kambayashi, Y.; Aiba, S. Significance of BRAF kinase inhibitors for melanoma treatment: From bench to bedside. *Cancers* **2019**, *11*, 1342. [CrossRef] [PubMed]
4. Weiss, S.A.; Wolchok, J.D.; Sznol, M. Immunotherapy of melanoma: Facts and hopes. *Clin Cancer Res.* **2019**, *25*, 5191–5201. [CrossRef]
5. Yang, J.; Dong, M.; Shui, Y.; Zhang, Y.; Zhang, Z.; Mi, Y.; Zuo, X.; Jiang, L.; Liu, K.; Liu, Z.; et al. A pooled analysis of the prognostic value of PD-L1 in melanoma: Evidence from 1062 patients. *Cancer Cell Int.* **2020**, *20*, 96. [CrossRef]
6. Chen, J.; Jiang, C.C.; Jin, L.; Zhang, X.D. Regulation of PD-L1: A novel role of pro-survival signalling in cancer. *Ann. Oncol.* **2016**, *27*, 409–416. [CrossRef] [PubMed]
7. Wei, R.; Guo, L.B.; Wang, Q.S.; Miao, J.; Kwok, H.F.; Lin, Y. Targeting PD-L1 protein: Translation, modification and transport. *Curr. Protein Pept. Sci.* **2019**, *20*, 82–91. [CrossRef]
8. Jiang, X.J.; Wang, J.; Deng, X.Y.; Xiong, F.; Ge, J.S.; Xiang, B.; Wu, X.; Ma, J.; Zhou, M.; Li, X.L.; et al. Role of the tumor microenvironment in PD-L1/PD-1-mediated tumor immune escape. *Mol. Cancer* **2019**, *18*, 1–7. [CrossRef]
9. Chen, L.P.; Han, X. Anti-PD-1/PD-L1 therapy of human cancer: Past, present, and future. *J. Clin. Investig.* **2015**, *125*, 3384–3391. [CrossRef] [PubMed]
10. Dong, H.; Strome, S.E.; Salomao, D.R.; Tamura, H.; Hirano, F.; Flies, D.B.; Roche, P.C.; Lu, J.; Zhu, G.; Tamada, K.; et al. Tumor-associated B7-H1 promotes T-cell apoptosis: A potential mechanism of immune evasion. *Nat. Med.* **2002**, *8*, 793–800. [CrossRef]
11. Madore, J.; Strbenac, D.; Vilain, R.; Menzies, A.M.; Yang, J.Y.H.; Thompson, J.F.; Long, G.V.; Mann, G.J.; Scolyer, R.A.; Wilmott, J.S. PD-L1 Negative Status is Associated with Lower Mutation Burden, Differential Expression of Immune-Related Genes, and Worse Survival in Stage III Melanoma. *Clin. Cancer Res.* **2016**, *22*, 3915–3923. [CrossRef]
12. Robert, C.; Long, G.V.; Brady, B.; Dutriaux, C.; Maio, M.; Mortier, L.; Hassel, J.C.; Rutkowski, P.; McNeil, C.; Kalinka-Warzocha, E.; et al. Nivolumab in previously untreated melanoma without BRAF mutation. *N. Engl. J. Med.* **2015**, *372*, 320–330. [CrossRef] [PubMed]
13. Weber, J.S.; D’Angelo, S.P.; Minor, D.; Hodi, F.S.; Gutzmer, R.; Neyns, B.; Hoeller, C.; Khushalani, N.I.; Miller, W.H., Jr.; Lao, C.D.; et al. Nivolumab versus chemotherapy in patients with advanced melanoma who progressed after anti-CTLA-4 treatment (CheckMate 037): A randomized, controlled, open-label, phase 3 trial. *Lancet Oncol.* **2015**, *16*, 375–384. [CrossRef] [PubMed]

14. Sunshine, J.C.; Nguyen, P.L.; Kaunitz, G.J.; Cottrell, T.R.; Berry, S.; Esandrio, J.; Xu, H.; Ogurtsova, A.; Bleich, K.B.; Cornish, T.C.; et al. PD-L1 Expression in Melanoma: A Quantitative Immunohistochemical Antibody Comparison. *Clin. Cancer Res.* **2017**, *23*, 4938–4944. [CrossRef]
15. Yu, H.; Boyle, T.A.; Zhou, C.; Rimm, D.L.; Hirsch, F.R. PD-L1 expression in lung cancer. *J. Thorac. Oncol.* **2016**, *11*, 964–975. [CrossRef]
16. Liu, Y.X.; Wang, X.S.; Wang, Y.F.; Hu, X.C.; Yan, J.Q.; Zhang, Y.L.; Wang, W.; Yang, R.J.; Feng, Y.Y.; Gao, S.G.; et al. Prognostic significance of PD-L1 expression in patients with gastric cancer in East Asia: A meta-analysis. *Oncotarg. Ther.* **2016**, *9*, 2649–2654.
17. Huang, L.J.; Deng, X.F.; Chang, F.; Wu, X.L.; Wu, Y.; Diao, Q.Z. Prognostic significance of programmed cell death ligand 1 expression in patients with ovarian carcinoma A systematic review and meta-analysis. *Medicine* **2018**, *97*, 43.
18. Wu, Z.; Zhang, L.; Peng, J.; Xu, S.; Zhou, L.; Lin, Y.; Wang, Y.; Lu, J.; Yin, W.; Lu, J. Predictive and prognostic value of PDL1 protein expression in breast cancer patients in neoadjuvant setting. *Cancer Biol. Ther.* **2019**, *20*, 941–947. [CrossRef]
19. Gevensleben, H.; Dietrich, D.; Golletz, C.; Steiner, S.; Jung, M.; Thiesler, T.; Majores, M.; Stein, J.; Uhl, B.; Muller, S.; et al. The immune checkpoint regulator PD-L1 is highly expressed in aggressive primary prostate cancer. *Clin. Cancer Res.* **2016**, *22*, 1969–1977. [CrossRef] [PubMed]
20. Wang, B.; Pan, W.; Yang, M.; Yang, W.; He, W.; Chen, X.; Bi, J.; Jiang, N.; Huang, J.; Lin, T. Programmed death ligand-1 is associated with tumor infiltrating lymphocytes and poorer survival in urothelial cell carcinoma of the bladder. *Cancer Sci.* **2019**, *110*, 489–498. [CrossRef]
21. Gu, X.; Dong, M.; Liu, Z.; Mi, Y.; Yang, J.; Zhang, Z.; Liu, K.; Jiang, L.; Zhang, Y.; Dong, S.; et al. Elevated PD-L1 expression predicts poor survival outcomes in patients with cervical cancer. *Cancer Cell Int.* **2019**, *19*, 146. [CrossRef]
22. Lee, L.H.; Cavalcanti, M.S.; Segal, N.H.; Hechtman, J.F.; Weiser, M.R.; Smith, J.J.; Garcia-Aguilar, J.; Sadot, E.; Ntiamoah, P.; Markowitz, A.J.; et al. Patterns and prognostic relevance of PD-1 and PD-L1 expression in colorectal carcinoma. *Mod. Pathol.* **2016**, *29*, 1433–1442. [CrossRef]
23. Liang, X.; Sun, J.; Wu, H.; Luo, Y.; Wang, L.; Lu, J.; Zhang, Z.; Guo, J.; Liang, Z.; Liu, T. PD-L1 in pancreatic ductal adenocarcinoma: A retrospective analysis of 373 Chinese patients using an in vitro diagnostic assay. *Diagn. Pathol.* **2018**, *13*, 5. [CrossRef] [PubMed]
24. Motoshima, T.; Komohara, Y.; Ma, C.; Dewi, A.K.; Noguchi, H.; Yamada, S.; Nakayama, T.; Kitada, S.; Kawano, Y.; Takahashi, W.; et al. PD-L1 expression in papillary renal cell carcinoma. *BMC Urol.* **2017**, *17*, 8. [CrossRef] [PubMed]
25. Cho, J.; Ahn, S.; Yoo, K.H.; Kim, J.H.; Choi, S.H.; Jang, K.T.; Lee, J. Treatment outcome of PD-1 immune checkpoint inhibitor in Asian metastatic melanoma patients: Correlative analysis with PD-L1 immunohistochemistry. *Invest. N. Drugs* **2016**, *34*, 677–684. [CrossRef] [PubMed]
26. Gadiot, J.; Hooijkaas, A.I.; Kaiser, A.D.M.; van Tinteren, H.; van Boven, H.; Blank, C. Overall survival and PD-L1 expression in metastasized malignant melanoma. *Cancer* **2011**, *117*, 2192–2201. [CrossRef] [PubMed]
27. Johnson, D.B.; Bordeaux, J.; Kim, J.Y.; Vaupel, C.; Rimm, D.L.; Ho, T.H.; Joseph, R.W.; Daud, A.I.; Conry, R.M.; Gaughan, E.M.; et al. Quantitative spatial profiling of PD-1/PD-L1 interaction and HLA-DR/IDO-1 predicts improved outcomes of anti-PD-1 therapies in metastatic melanoma. *Clin. Cancer Res.* **2018**, *24*, 5250–5260. [CrossRef] [PubMed]
28. Madonna, G.; Ballesteros-Merino, C.; Feng, Z.; Bifulco, C.; Capone, M.; Giannarelli, D.; Mallardo, D.; Simeone, E.; Grimaldi, A.M.; Caraco, C.; et al. PD-L1 expression with immune-infiltrate evaluation and outcome prediction in melanoma patients treated with ipilimumab. *Oncoimmunology* **2018**, *7*, e1405206. [CrossRef]
29. Madore, J.; Vilain, R.E.; Menzies, A.M.; Kakavand, H.; Wilmott, J.S.; Hyman, J.; Yearley, J.H.; Kefford, R.F.; Thompson, J.F.; Long, G.V.; et al. PD-L1 expression in melanoma shows marked heterogeneity within and between patients: Implications for anti-PD-1/PD-L1 clinical trials. *Pigment Cell Melanoma Res.* **2015**, *28*, 245–253. [CrossRef] [PubMed]
30. Massi, D.; Brusa, D.; Merelli, B.; Falcone, C.; Xue, G.; Carobbio, A.; Nassini, R.; Baroni, G.; Tamborini, E.; Cattaneo, L.; et al. The status of PD-L1 and tumor infiltrating immune cells predict resistance and poor prognosis in BRAF treated melanoma patients harboring mutant BRAFV600. *Ann. Oncol.* **2015**, *26*, 1980–1987. [CrossRef] [PubMed]
31. Morrison, C.; Pabla, S.; Conroy, J.M.; Nesline, M.K.; Glenn, S.T.; Dressman, D.; Papanicolau-Sengos, A.; Burgher, B.; Andreas, J.; Giamo, V.; et al. Predicting response to checkpoint inhibitors in melanoma beyond PD-L1 and mutational burden. *J. Immunother. Cancer* **2018**, *6*, 32. [CrossRef] [PubMed]
32. Obeid, J.M.; Erdag, G.; Smolkin, M.E.; Deacon, D.H.; Patterson, J.W.; Chen, L.; Bullock, T.N.; Slingluff, C.L. PD-L1, PD-L2 and PD-1 expression in metastatic melanoma: Correlation with tumor-infiltrating immune cells and clinical outcome. *Oncoimmunology* **2016**, *5*, e1235107. [CrossRef] [PubMed]
33. Ren, M.; Dai, B.; Kong, Y.Y.; Lv, J.J.; Cai, X. PD-L1 expression in tumour-infiltrating lymphocytes is a poor prognostic factor for primary acral melanoma patients. *Histopathology* **2018**, *73*, 386–396. [CrossRef]
34. Ren, Y.; Lv, Q.; Yue, W.; Liu, B.; Zou, Z. The programmed cell death protein-1/programmed cell death ligand 1 expression, CD3+ T cell infiltration, NY-ESO-1 expression, and microsatellite instability phenotype in primary cutaneous melanoma and mucosal melanoma and their clinical significance and prognostic value: A study of 89 consecutive cases. *Melanoma Res.* **2019**, *30*, 85–101.
35. Schaper-Gerhardt, K.; Okoye, S.; Herbst, R.; Ulrich, J.; Terheyden, P.; Pfohler, C.; Utikal, J.S.; Kreuter, A.; Mohr, P.; Dippel, E.; et al. PD-L1 status does not predict the outcome of BRAF inhibitor therapy in metastatic melanoma. *Eur. J. Cancer* **2018**, *88*, 67–76. [CrossRef]
36. Thierauf, J.; Veit, J.A.; Affolter, A.; Bergmann, C.; Grunow, J.; Laban, S.; Lennerz, J.K.; Grunmuller, L.; Mauch, C.; Plinkert, P.K.; et al. Identification and clinical relevance of PD-L1 expression in primary mucosal malignant melanoma of the head and neck. *Melanoma Res.* **2015**, *25*, 503–509. [CrossRef] [PubMed]
37. Wang, H.Y.; Wu, X.Y.; Zhang, X.; Yang, X.H.; Long, Y.K.; Feng, Y.F.; Wang, F. Prevalence of NRAS mutation, PD-L1 expression and amplification, and overall survival analysis in 36 primary vaginal melanomas. *Oncologist* **2019**, *25*, e291–e301. [CrossRef]

38. Tumeh, P.C.; Harview, C.L.; Yearley, J.H.; Shintaku, I.P.; Taylor, E.J.M.; Robert, L.; Chmielowski, B.; Spasic, M.; Henry, G.; Ciobanu, V.; et al. PD-1 blockade induces responses by inhibiting adaptive immune resistance. *Nature* **2014**, *515*, 568–571. [CrossRef] [PubMed]
39. Kluger, H.M.; Zito, C.R.; Turcu, G.; Baine, M.K.; Zhang, H.; Adeniran, A.; Sznol, M.; Rimm, D.L.; Kluger, Y.; Chen, L.; et al. PD-L1 Studies Across Tumor Types, its Differential Expression and Predictive Value in Patients Treated with Immune Checkpoint Inhibitors. *Clin. Cancer Res.* **2017**, *23*, 4270–4279. [CrossRef] [PubMed]
40. Kakavand, H.; Rawson, R.V.; Pupo, G.M.; Yang, J.Y.H.; Menzies, A.M.; Carlino, M.S.; Kefford, R.F.; Howle, J.R.; Saw, R.P.; Thompson, J.F.; et al. PD-L1 expression and immune escape in melanoma resistance to MAPK inhibitors. *Clin. Cancer Res.* **2017**, *23*, 6054–6061. [CrossRef] [PubMed]
41. Cancer Genome Atlas Network. Genomic Classification of Cutaneous Melanoma. *Cell* **2015**, *161*, 1681–1696. [CrossRef] [PubMed]
42. Ionescu, C.A.; Aschie, M.; Matei, E.; Cozaru, G.C.; Deacu, M.; Mitroi, A.F.; Baltatescu, G.I.; Nicolau, A.A.; Mazilu, L.; Tuta, L.A.; et al. Characterization of the Tumor Microenvironment and the Biological Processes with a Role in Prostatic Tumorigenesis. *Biomedicines* **2022**, *10*, 1672. [CrossRef] [PubMed]
43. Bosoteanu, C.; Bosoteanu, M.; Aschie, M. Differential diagnosis issues in a case of gastric carcinoma associated with leukemoid reaction. *Rom. J. Morphol. Embryol.* **2009**, *50*, 701–705.
44. Goggins, W.B.; Finkelstein, D.M.; Tsao, H. Evidence for an association between cutaneous melanoma and non-Hodgkin lymphoma. *Cancer* **2001**, *91*, 874–880. [CrossRef] [PubMed]
45. Matei, E.; Aschie, M.; Mitroi, A.F.; Ghinea, M.M.; Gheorghe, E.; Petcu, L.; Dobrin, N.; Chisoi, A.; Mihaela, M. Biomarkers involved in evaluation of platelets function in South-Eastern Romanian patients with hematological malignancies subtypes. *Medicine* **2021**, *100*, e25944. [CrossRef] [PubMed]
46. Brinzan, C.; Așchie, M.; Matei, E.; Mitroi, A.F.; Cozaru, G.C. Molecular expression profiles of selected microRNAs in colorectal adenocarcinoma in patients from south-eastern part of Romania. *Medicine* **2019**, *98*, e18122. [CrossRef]
47. Karydis, I.; Chan, P.Y.; Wheater, M.; Arriola, E.; Szlosarek, P.W.; Ottensmeier, C. Clinical activity and safety of Pembrolizumab in Ipilimumab pre-treated patients with uveal melanoma. *Oncoimmunology* **2016**, *5*, e1143997. [CrossRef]
48. Lee, S.-J.; Lim, H.J.; Choi, Y.H.; Chang, Y.H.; Lee, W.J.; Kim, D.W.; Yoon, G.S. The clinical significance of tumor infiltrating lymphocytes and microscopic satellites in acral melanoma in a Korean population. *Ann. Dermatol.* **2013**, *25*, 61–66. [CrossRef]
49. Song, H.; Wu, Y.; Ren, G.; Guo, W.; Wang, L. Prognostic factors of oral mucosal melanoma: Histopathological analysis in a retrospective cohort of 82 cases. *Histopathology* **2015**, *67*, 548–556. [CrossRef]
50. Kaunitz, G.J.; Cottrell, T.R.; Lilo, M.; Muthappan, V.; Esandrio, J.; Berry, S.; Xu, H.; Ogurtsova, A.; Anders, R.A.; Fischer, A.H.; et al. Melanoma subtypes demonstrate distinct PD-L1 expression profiles. *Lab. Investig.* **2017**, *97*, 1063–1071. [CrossRef]
51. Elder, D.E.; Massi, D.; Scolyer, R.; Willemze, R. *WHO Classification of Skin Tumours*, 4th ed.; World Health Organization: Geneva, Switzerland, 2018.
52. Elder, D.E. *Lever's Histopathology of the Skin*, 11th ed.; Wolters-Kluwer: Alphen aan den Rijn, The Netherlands, 2014; pp. 488–547.
53. Calonje, E.; Brenn, T.; Lazar, A. *McKee PH McKee's Pathology of the Skin*, 4th ed.; Elsevier: Amsterdam, The Netherlands, 2012; pp. 1126–1267.
54. Massi, D.; Brusa, D.; Merelli, B.; Ciano, M.; Audrito, V.; Serra, S.; Buonincontri, R.; Baroni, G.; Nassini, R.; Minocci, D.; et al. PD-L1 marks a subset of melanomas with a shorter overall survival and distinct genetic and morphological characteristics. *Ann. Oncol.* **2014**, *25*, 2433–2442. [CrossRef]
55. Schramm, S.J.; Mann, G.J. Melanoma prognosis: A REMARK-based systematic review and bioinformatic analysis of immunohistochemical and gene microarray studies. *Mol. Cancer Ther.* **2011**, *10*, 1520–1528. [CrossRef]
56. Nicolau, A.A.; Caraban, B.M.; Gheorghe, E.; Hangan, T.L.; Cojocaru, O.; Orasanu, C.I.; Voda, R.I. Proteomic Implications of Tumoral Infiltrating Lymphocytes in Melanoma: PD-L1, CD4 and CD8—Short Review. *ARS Med. Tomitana* **2020**, *3*, 117–121. [CrossRef]
57. Taube, J.M.; Anders, R.A.; Young, G.D.; Xu, H.; Sharma, R.; McMiller, T.L.; Chen, S.; Klein, A.P.; Pardoll, D.M.; Topalian, S.L.; et al. Colocalization of inflammatory response with B7-H1 expression in human melanocytic lesions supports an adaptive resistance mechanism of immune escape. *Sci. Transl. Med.* **2012**, *4*, 127ra37. [CrossRef] [PubMed]
58. Taube, J.M.; Klein, A.; Brahmer, J.R.; Xu, H.; Pan, X.; Kim, J.H.; Chen, L.; Pardoll, D.M.; Topalian, S.L.; Anders, R.A. Association of PD-1, PD-1 ligands, and other features of the tumor immune microenvironment with response to anti-PD-1 therapy. *Clin. Cancer Res.* **2014**, *20*, 5064–5074. [CrossRef]
59. Ahmadzadeh, M.; Johnson, L.A.; Heemskerk, B.; Wunderlich, J.R.; Dudley, M.E.; White, D.E.; Rosenberg, S.A. Tumor antigen-specific CD8 T cells infiltrating the tumor express high levels of PD-1 and are functionally impaired. *Blood* **2009**, *114*, 1537–1544. [CrossRef] [PubMed]
60. Mandala, M.; Merelli, B.; Massi, D. PD-L1 in melanoma: Facts and myths. *Melanoma Manag.* **2016**, *3*, 187–194. [CrossRef]
61. Bønnelykke-Behrndtz, M.L.; Steiniche, T.; Damsgaard, T.E.; Georgsen, J.B.; Danielsen, A.; Bastholt, L.; Møller, H.J.; Nørgaard, P.H.; Schmidt, H. Melanoma negative spindle-cell associated melanoma, a distinct inflammatory phenotype correlated with dense infiltration of CD163 macrophages and loss of E-cadherin. *Melanoma Res.* **2015**, *25*, 113–118. [CrossRef]
62. Le, D.T.; Uram, J.N.; Wang, H.; Bartlett, B.R.; Kemberling, H.; Eyring, A.D.; Skora, A.D.; Luber, B.S.; Azad, N.S.; Laheru, D.; et al. PD-1 blockade in tumors with mismatch-repair deficiency. *N. Engl. J. Med.* **2015**, *372*, 2509–2520. [CrossRef]

63. Robert, C.; Ribas, A.; Wolchok, J.D.; Hodi, F.S.; Hamid, O.; Kefford, R.; Weber, J.S.; Joshua, A.M.; Hwu, W.-J.; Gangadhar, T.C.; et al. Anti-programmed-death-receptor 1 treatment with pembrolizumab in ipilimumab-refractory advanced melanoma: A randomised dose-comparison cohort of a phase 1 trial. *Lancet* **2014**, *384*, 1109–1117. [CrossRef] [PubMed]
64. Dermani, F.K.; Samadi, P.; Rahmani, G.; Kohlan, A.K.; Najafi, R. PD-1/PD-L1 immune checkpoint: Potential target for cancer therapy. *J. Cell Physiol.* **2019**, *234*, 1313–1325. [CrossRef]
65. Zou, W.P.; Wolchok, J.D.; Chen, L.P. PD-L1 (B7-H1) and PD-1 pathway blockade for cancer therapy: Mechanisms, response biomarkers, and combinations. *Sci. Transl. Med.* **2016**, *8*, 328. [CrossRef]
66. Clark, C.A.; Gupta, H.B.; Sareddy, G.; Pandeswara, S.; Lao, S.; Yuan, B.; Drerup, J.M.; Padron, A.; Conejo-Garcia, J.; Murthy, K.; et al. Tumor-intrinsic PD-L1 signals regulate cell growth, pathogenesis, and autophagy in ovarian cancer and melanoma. *Cancer Res.* **2016**, *76*, 6964–6974. [CrossRef]
67. Jilaveanu, L.B.; Shuch, B.; Zito, C.R.; Parisi, F.; Barr, M.; Kluger, Y.; Chen, L.; Kluger, H.M. PD-L1 expression in clear cell renal cell carcinoma: An analysis of nephrectomy and sites of metastases. *J Cancer* **2014**, *5*, 166–172. [CrossRef]
68. Schalper, K.A.; Velcheti, V.; Carvajal, D.; Wimberly, H.; Brown, J.; Pusztai, L.; Rimm, D.L. In situ tumor PD-L1 mRNA expression is associated with increased TILs and better outcome in breast carcinomas. *Clin. Cancer Res.* **2014**, *20*, 2773–2782. [CrossRef] [PubMed]
69. Velcheti, V.; Schalper, K.A.; Carvajal, D.E.; Anagnostou, V.K.; Syrigos, K.N.; Sznol, M.; Herbst, R.S.; Gettinger, S.N.; Chen, L.; Rimm, D.L. Programmed death ligand-1 expression in non-small cell lung cancer. *Lab. Investig.* **2014**, *94*, 107–116. [CrossRef]
70. Topalian, S.L.; Sznol, M.; McDermott, D.F.; Kluger, H.M.; Carvajal, R.D.; Sharfman, W.H.; Brahmer, J.R.; Lawrence, D.P.; Atkins, M.B.; Powderly, J.D.; et al. Survival, durable tumor remission, and long-term safety in patients with advanced melanoma receiving nivolumab. *J. Clin. Oncol.* **2014**, *32*, 1020–1030. [CrossRef] [PubMed]
71. Ribas, A.; Puzanov, I.; Dummer, R.; Schadendorf, D.; Hamid, O.; Robert, C.; Hodi, F.S.; Schachter, J.; Pavlick, A.C.; Lewis, K.D.; et al. Pembrolizumab versus investigator-choice chemotherapy for ipilimumab-refractory melanoma (KEYNOTE-002): A randomised, controlled, phase 2 trial. *Lancet Oncol.* **2015**, *16*, 908–918. [CrossRef] [PubMed]
72. Topalian, S.L.; Drake, C.G.; Pardoll, D.M. Immune checkpoint blockade: A common denominator approach to cancer therapy. *Cancer Cell* **2015**, *27*, 450–461. [CrossRef]
73. Kwong, F.N.K.; Laggner, U.; McKinney, O.; Croud, J.; Rice, A.; Nicholson, A.G. Expression of PD-L1 correlates with pleomorphic morphology and histological patterns of non-small-cell lung carcinomas. *Histopathology* **2018**, *72*, 1024–1032. [CrossRef]
74. Ghebeh, H.; Mohammed, S.; Al-Omair, A.; Qattant, A.; Lehe, C.; Al-Qudaihi, G.; Elkum, N.; Alshabanah, M.; Bin Amer, S.; Tulbah, A.; et al. The B7-H1 (PD-L1) T lymphocyte-inhibitory molecule is expressed in breast cancer patients with infiltrating ductal carcinoma: Correlation with important high-risk prognostic factors. *Neoplasia* **2006**, *8*, 190–198. [CrossRef] [PubMed]
75. Hino, R.; Kabashima, K.; Kato, Y.; Yagi, H.; Nakamura, M.; Honjo, T.; Okazaki, T.; Tokura, Y. Tumor cell expression of programmed cell death-1 ligand 1 is a prognostic factor for malignant melanoma. *Cancer* **2010**, *116*, 1757–1766. [CrossRef] [PubMed]
76. Krönig, H.; Falchner, K.J.; Odendahl, M.; Brackertz, B.; Conrad, H.; Muck, D.; Hein, R.; Blank, C.; Peschel, C.; Haller, B.; et al. PD-1 expression on Melan-A-reactive T cells increases during progression to metastatic disease. *Int. J. Cancer* **2012**, *130*, 2327–2336. [CrossRef] [PubMed]
77. Fujimoto, N.; Dieterich, L.C. Mechanisms and Clinical Significance of Tumor Lymphatic Invasion. *Cells* **2021**, *10*, 2585. [CrossRef] [PubMed]
78. Brinzan, C.; Așchie, M.; Grasa, C.N.; Mitroi, A.F.; Matei, E.; Cozaru, G.C. The Mutation Profiles of KRAS and BRAF Genes in a Romanian Colorectal Cancer Cohort. *Rev. Chim.* **2019**, *70*, 1346–1350. [CrossRef]
79. Iacovelli, R.; Nole, F.; Verri, E.; Renne, G.; Paglino, C.; Santoni, M.; Rocca, M.C.; Giglione, P.; Aurilio, G.; Cullura, D.; et al. Prognostic role of PD-L1 expression in renal cell carcinoma. a systematic review and meta-analysis. *Target. Oncol.* **2016**, *11*, 143–148. [CrossRef]
80. Pyo, J.S.; Kang, G.; Kim, J.Y. Prognostic role of PD-L1 in malignant solid tumors: A meta-analysis. *Int. J. Biol. Markers* **2017**, *32*, E68–E74. [CrossRef]
81. Zhao, S.; Zhang, M.H.; Zhang, Y.; Meng, H.X.; Wang, Y.; Liu, Y.P.; Jing, J.; Huang, L.; Sun, M.Q.; Zhang, Y.; et al. The prognostic value of programmed cell death ligand 1 expression in non-Hodgkin lymphoma: A meta-analysis. *Cancer Biol. Med.* **2018**, *15*, 290–298.

antioxidants

MDPI

Article

In Vitro Anticancer Activity of Mucoadhesive Oral Films Loaded with *Usnea barbata* (L.) F. H. Wigg Dry Acetone Extract, with Potential Applications in Oral Squamous Cell Carcinoma Complementary Therapy

Violeta Popovici [1,†], Elena Matei [2,*], Georgeta Camelia Cozaru [2,3,†], Laura Bucur [4,†], Cerasela Elena Gîrd [5,†], Verginica Schröder [6,*], Emma Adriana Ozon [7,*], Adina Magdalena Musuc [8,*], Mirela Adriana Mitu [7,*], Irina Atkinson [8], Adriana Rusu [8], Simona Petrescu [8], Raul-Augustin Mitran [8], Mihai Anastasescu [8], Aureliana Caraiane [9], Dumitru Lupuliasa [7,‡], Mariana Aschie [2,3,‡] and Victoria Badea [1,‡]

[1] Department of Microbiology and Immunology, Faculty of Dental Medicine, Ovidius University of Constanta, 900684 Constanta, Romania
[2] Center for Research and Development of the Morphological and Genetic Studies of Malignant Pathology, Ovidius University of Constanta, CEDMOG, 900591 Constanta, Romania
[3] Clinical Service of Pathology, Sf. Apostol Andrei Emergency County Hospital, 900591 Constanta, Romania
[4] Department of Pharmacognosy, Faculty of Pharmacy, Ovidius University of Constanta, 900001 Constanta, Romania
[5] Department of Pharmacognosy, Phytochemistry, and Phytotherapy, Faculty of Pharmacy, Carol Davila University of Medicine and Pharmacy, 020956 Bucharest, Romania
[6] Department of Cellular and Molecular Biology, Faculty of Pharmacy, Ovidius University of Constanta, 900001 Constanta, Romania
[7] Department of Pharmaceutical Technology and Biopharmacy, Faculty of Pharmacy, Carol Davila University of Medicine and Pharmacy, 020956 Bucharest, Romania
[8] Ilie Murgulescu" Institute of Physical Chemistry, Romanian Academy, 060021 Bucharest, Romania
[9] Department of Oral Rehabilitation, Faculty of Dental Medicine, Ovidius University of Constanta, 900684 Constanta, Romania
* Correspondence: sogorescuelena@gmail.com (E.M.); verginica.schroder@univ-ovidius.ro (V.S.); emma.budura@umfcd.ro (E.A.O.); amusuc@icf.ro (A.M.M.); mirela.mitu@umfcd.ro (M.A.M.)
† These authors contributed equally to this work.
‡ These authors contributed equally to this work.

Citation: Popovici, V.; Matei, E.; Cozaru, G.C.; Bucur, L.; Gîrd, C.E.; Schröder, V.; Ozon, E.A.; Musuc, A.M.; Mitu, M.A.; Atkinson, I.; et al. In Vitro Anticancer Activity of Mucoadhesive Oral Films Loaded with *Usnea barbata* (L.) F. H. Wigg Dry Acetone Extract, with Potential Applications in Oral Squamous Cell Carcinoma Complementary Therapy. *Antioxidants* **2022**, *11*, 1934. https://doi.org/10.3390/antiox11101934

Academic Editor: Stanley Omaye

Received: 28 July 2022
Accepted: 23 September 2022
Published: 28 September 2022

Abstract: Oral squamous cell carcinoma (OSCC) is the most frequent oral malignancy, with a high death rate and an inadequate response to conventional chemotherapeutic drugs. Medical research explores plant extracts' properties to obtain potential nanomaterial-based anticancer drugs. The present study aims to formulate, develop, and characterize mucoadhesive oral films loaded with *Usnea barbata* (L.) dry acetone extract (F-UBA) and to investigate their anticancer potential for possible use in oral cancer therapy. *U. barbata* dry acetone extract (UBA) was solubilized in ethanol: isopropanol mixture and loaded in a formulation containing hydroxypropyl methylcellulose (HPMC) K100 and polyethylene glycol 400 (PEG 400). The UBA influence on the F-UBA pharmaceutical characteristics was evidenced compared with the references, i.e., mucoadhesive oral films containing suitable excipients but no active ingredient loaded. Both films were subjected to a complex analysis using standard methods to evaluate their suitability for topical administration on the oral mucosa. Physico-chemical and structural characterization was achieved by Fourier transform infrared spectroscopy (FTIR), X-ray diffraction (XRD), thermogravimetric analysis (TGA), scanning electron microscopy (SEM), and atomic force microscopy (AFM). Pharmacotechnical evaluation (consisting of the measurement of specific parameters: weight uniformity, thickness, folding endurance, tensile strength, elongation, moisture content, pH, disintegration time, swelling rate, and *ex vivo* mucoadhesion time) proved that F-UBAs are suitable for oral mucosal administration. The brine shrimp lethality (BSL) assay was the F-UBA cytotoxicity prescreen. Cellular oxidative stress, caspase 3/7 activity, nuclear condensation, lysosomal activity, and DNA synthesis induced by F-UBA in blood cell cultures and oral epithelial squamous cell carcinoma (CLS-354) cell line were investigated through complex flow cytometry analyses. Moreover, F-UBA influence on both cell type division and proliferation was determined.

Finally, using the resazurin-based 96-well plate microdilution method, the F-UBA antimicrobial potential was explored against *Staphylococcus aureus* ATCC 25923, *Pseudomonas aeruginosa* ATCC 27353, *Candida albicans* ATCC 10231, and *Candida parapsilosis* ATCC 22019. The results revealed that each UBA-loaded film contains 175 µg dry extract with a usnic acid (UA) content of 42.32 µg. F-UBAs are very thin (0.060 ± 0.002 mm), report a neutral pH (7.01 ± 0.01), a disintegration time of 146 ± 5.09 s, and an ex vivo mucoadhesion time of 85 ± 2.33 min, and they show a swelling ratio after 6 h of 211 ± 4.31%. They are suitable for topical administration on the oral mucosa. Like UA, they act on CLS-354 tumor cells, considerably increasing cellular oxidative stress, nuclear condensation, and autophagy and inducing cell cycle arrest in G0/G1. The F-UBAs inhibited the bacterial and fungal strains in a dose-dependent manner; they showed similar effects on both *Candida* sp. and higher inhibitory activity against *P. aeruginosa* than *S. aureus*. All these properties lead to considering the UBA-loaded mucoadhesive oral films suitable for potential application as a complementary therapy in OSCC.

Keywords: *Usnea barbata* (L.) F. H. Wigg dry acetone extract; oral squamous cell carcinoma; mucoadhesive oral films; usnic acid; CLS-354 cell line; blood cell cultures; oxidative stress; anticancer potential; antimicrobial activity

1. Introduction

Approximately 3–10% of all cancer mortality is known to be contributed by oral cancer [1]. Oral cancer incidence increases due to environmental conditions and harmful habits of the modern lifestyle: pollution, diet and nutrition, tobacco smoking [2], betel quid chewing [3], and alcohol consumption [4,5]. These factors, associated with a hereditary predisposition, chronic inflammation, and infectious diseases, have contributed to the increased risk of developing oral cavity malignancies [6]. Oral squamous cell carcinoma (OSCC) represents 90% of oral neoplasia [7]; it is the sixth most common cancer in the world [8] and has an overall 5-year survival rate below 50% [9] due to its modest outcomes, tardive diagnosis, and inadequate response to chemoradiation therapy [10]. Furthermore, after the current treatment protocol [10], the quality of life of patients with oral cancer is substantially diminished [11], and restrictions on food intake could lead to malnutrition [12].

Consequently, global medical research focuses on discovering and developing alternative therapies against cancer, investigating the properties of plant extracts to obtain potential nanomaterial-based anticancer drugs. According to Dehelean et al. [13], the anticancer potential of natural products could be expressed as chemotherapeutic effects (due to their innate antitumor activity), chemopreventive action (maintaining a low risk of developing cancer or keeping it from coming back), and sensitizers in multidrug resistance.

In a recent comprehensive review, Prakash et al. [14] described various medicinal plants with beneficial effects against oral cancer (*Ocimum sanctum* L., *Curcuma longa* L., *Vaccinium corymbosum* L., *Vaccinium macrocarpon* Aiton, *Momordica charantia* L., *Azadirachta indica* A. Juss, *Senegalia Catechu* (L.f.) P.J.H. Hurter & Mabb., *Dracaena cinnabari* Balf.f., *Piper nigrum* L., and *Zingiber officinale* Roscoe) and their active secondary metabolites (curcumin, nimbolide, resveratrol, anthocyanins, piperine, and eugenol). Their list could be completed with *Melissa officinalis* L. [15], *Gracilaria tenuistipitata* C.F. Chang & B.M. Xia [16], *Cynara cardunculus* L. [17], *Imperata cylindrica* (L.) P.Beauv. [18], *Caesalpinia sappan* L. [19], *Angelica gigas* Nakai [20], *Aloe barbadensis* Miller [21], *Padina gymnospora* [22] and *Usnea barbata* (L.) F.H.Wigg [23–25]. The principal mechanism triggered in the OSCC tumor cell line is oxidative stress, which induces DNA damage and cell cycle arrest, leading to apoptotic cell death [16,17,23,24]. Moreover, these medicinal plants could also be helpful in oral cancer chemoprevention due to other associated bioactivities (such as antimicrobial, anti-inflammatory, antioxidant, and wound-healing effects).

Numerous studies described plant-based oral formulations tested for their efficacy in improving oral hygiene, salivary microbial flora, and gingival health. Pérez Zamora et al. developed herbal buccal films with in vitro antibacterial and anti-inflammatory effects containing *Lippia turbinata* Griseb. and *Lippia alba* (Mill.) Britton & P.Wilson extracts [26]. Pagano et al. [27] incorporated grape seed extract in bioadhesive patches with a combination of acacia gum/PVP/cyclic dextrin, aiming for a wound dressing effect. Utama-ang et al. [28] developed Thai rice films loaded with ginger extract for oral antimicrobial properties.

Other authors formulated fast-dissolving herbal films with *Eclipta prostrata* (L.) leaves extract for mouth ulcers [29] and oral patches containing *Glycyrrhiza* complex herbal extract [30], and *Myrtus communis* L. (Myrtle) [31] for aphthous stomatitis. Nam et al. [32] proposed *Angelica gigas* Nakai extract-loaded fast-dissolving nanofiber based on poly(vinyl alcohol) and Soluplus for oral cancer therapy. Recently, Chiaoprakobkij et al. [33] examined in vitro anticancer and antibacterial effects of *Garcinia mangostana* L. extract incorporated in bacterial cellulose-gelatin films.

The present study aimed to develop and characterize mucoadhesive oral films based on HPMC and PEG 400 containing *U. barbata* dry acetone extract. Moreover, our work investigated in vivo cytotoxicity on an animal model and in vitro antitumor and antimicrobial activities of F-UBA for potential application in oral cancer prevention and therapy.

2. Materials and Methods

2.1. Materials

All chemicals, reagents, and standards used in this study were of analytical grade. Polyethylene glycol 400 (PEG 400), hydroxypropyl methylcellulose (HPMC), usnic acid standard 98.1% purity, propidium iodide (PI) 1.0 mg/mL, dimethyl sulfoxide (DMSO), and antibiotics mix solution 100 μL/mL with 10 mg streptomycin, 10,000 U penicillin, 25 μg amphotericin B per 1 mL were provided by Sigma-Aldrich Chemie GmbH (Taufkirchen, Germany). Annexin V Apoptosis Detection Kit and flow cytometry staining buffer (FCB) were purchased from eBioscience™ (Frankfurt am Main, Germany) and RNase A 4 mg/mL from Promega (Madison, WI, USA). Magic Red® Caspase-3/7 Assay Kit, Reactive Oxygen Species (ROS) Detection Assay Kit, and EdU i-Fluor 488 Kit were supplied by Abcam (Cambridge, UK).

The OSCC cell line (CLS-354) and the culture medium Dulbecco's Modified Eagle's Medium (DMEM) High Glucose basic supplemented with 4.5 g/l glucose and L-glutamine and 10% fetal bovine serum (FBS) were provided by CLS Cell Lines Service GmbH (Eppelheim, Germany). Trypsin-ethylenediamine tetra acetic acid (Trypsin EDTA) and the media for blood cells Dulbecco's phosphate-buffered saline with $MgCl_2$ and $CaCl_2$, FBS, and L-Glutamine (200 mM) solution were purchased from Gibco™ Inc (Billings, MT, USA).

The blood samples were collected from a non-smoker healthy donor (B Rh+ blood type), according to Ovidius University of Constanta Ethical approval code 7080/10 June 2021 and Donor Consent code 39/30 June 2021.

Artemia salina eggs and Artemia salt (Dohse Aquaristik GmbH & Co. Gelsdorf, Germany) were purchased online from https://www.aquaristikshop.com/ (accessed on 5 May 2022).

The microbial cell lines (*S. aureus* ATCC 25923, *P. aeruginosa* ATCC 27353, *C. albicans* ATCC 10231, and *C. parapsilosis* ATCC 22019) were obtained from the Microbiology Department, S.C. Synevo Romania SRL, Constanta Laboratory, under partnership agreement No 1060/25 January 2018 with the Faculty of Pharmacy, Ovidius University of Constanta. Culture medium Mueller-Hinton agar (MHA) was supplied by Thermo Fisher Scientific, GmbH, Dreieich, Germany; RPMI 1640 Medium and Resazurin solution (from In Vitro Toxicology Assay Kit, TOX8-1KT, Resazurin based) were purchased from Sigma-Aldrich Chemie GmbH (Taufkirchen, Germany).

U. barbata lichen was harvested in March 2021 from the forest localized in the Călimani Mountains (47 °29′ N, 25 °12′ E, and 900 m altitude). It was identified by the Department of Pharmaceutical Botany of the Faculty of Pharmacy, Ovidius University of Constanta, using standard methods. A voucher specimen is maintained in the Herbarium of Pharmacognosy Department, Faculty of Pharmacy, Ovidius University of Constanta (Popovici 3/2021, Ph-UOC).

2.2. Lichen Extract

The dried lichen was ground in an LM 120 laboratory mill (PerkinElmer, Waltham, MA, USA) and passed through the no. 5 sieve [34]. The obtained moderately fine lichen powder (particle size ≤ 315 µm) was subjected to Soxhlet extraction in acetone at 55–60 °C for 8 h, followed by solvent evaporation; the method is described in a previously published study [34]. The *U. barbata* dry acetone extract (UBA) was preserved in a freezer (Sirge® Elettrodomestici—SAC Rappresentanze, Torino, Avigliana, Italy) at −18 °C until used for mucoadhesive oral films preparation [34].

2.3. Formulation and Manufacturing of Mucoadhesive Oral Films

Because the UBA-loaded mucoadhesive films are designated for oral administration and residual amounts of acetone may be found in the final pharmaceutical product, it was decided to select a more appropriate solvent for *U. Barbata* dry acetone extract. Thus, a mix of 1:1 (*w*/*w*) ethyl alcohol and isopropyl alcohol was used for UBA solubilization. The solubility of UBA in the previously mentioned combination was 2.5% (*w*/*w*); thus, UBA dosage in the developed films was established. A Mettler Toledo AT261 balance (with 0.01 mg sensitivity) was used to weigh the ingredients.

HPMC K100 [35] with a viscosity of 100 mPa was chosen for the film matrix formation, considering its high hydrophilic character, stability, and biocompatibility [36–38]. PEG 400 was used as a plasticizer because it offers excellent flexibility to the polymer base [39,40].

Without UBA, the references (R) were prepared to investigate the active ingredient's influence on the mucoadhesive oral films' physicochemical and pharmacotechnical characteristics and evaluate the extract's efficacy. HPMC dispersion was prepared by adding the weighted polymer to water at room temperature and stirring for 30 min at 700 rpm, using a Heidolph MR 3001K magnetic stirrer (Schwabach, Germany). PEG 400 was incorporated into the polymer matrix. The lichen extract solution was obtained by dissolving UBA in the ethanol: isopropanol mixture and then poured over the polymer dispersion under continuous stirring in the same conditions. The formed gel systems were left overnight for deaeration in ambient conditions. The dispersions were placed in a thin layer on Petri glass plates and dried for 24 h at room temperature. Next, the dried films were detached from the glass plate surface and cut into patches of 1.5 × 2 cm sizes.

2.4. Physico-Chemical Characterization of the UBA-Loaded Mucoadhesive Oral Films

2.4.1. Fourier Transform Infrared Spectroscopy

Fourier transform infrared spectroscopy (FTIR) measurements were performed using a NICOLET 6700 FTIR Spectrometer (Grayslake, IL, USA) with a Smart DuraSamplIR HATR (Horizontal Attenuated Total Reflectance) accessory and a laminated–diamond crystal (Thermo Electron Corporation, Waltham, MA, USA). The FTIR spectra were assessed in the range of 4000–400 cm^{-1} using a DTGS KBr detector at a resolution of 4 cm^{-1}. All spectra were plotted in transmittance mode.

2.4.2. Powder X-ray Diffractometry

Powder X-ray diffraction (XRD) measurements were recorded using a Rigaku Ultima IV diffractometer (Rigaku Corporation, Tokyo, Japan) in parallel beam geometry with a step size of 0.02° and a speed of 2°/min over a range of 5–60°. A CuKα tube (λ = 1.54056 Å) operating at 40 kV and 30 mA was the source of the X-rays.

2.4.3. TG/DTA Measurements

The conditions of both analyses—thermogravimetric analysis (TGA) coupled with differential thermal analyses (DTA)—comprised a synthetic air atmosphere with a heating rate of 10 °C min^{-1} and a flow rate of 80 mL/ min. Both films' thermogravimetric curves were carried out on a Mettler Toledo TGA/SDTA 851^e thermogravimetric analyzer (Mettler-Toledo GmbH, Greifensee, Switzerland).

2.4.4. Scanning Electron Microscopy (SEM)

Morphological analysis was made on a high-resolution scanning electron microscope FEI Quanta3D FEG (Thermo Fisher Scientific, GmbH, Dreieich, Germany).

2.4.5. Atomic Force Microscopy (AFM)

AFM analysis was made using an XE-100 microscope from Park Systems (Suwon-si, South Korea) in non-contact mode. Sharp tips, NCHR from NanosensorsTM, with typically ~8 nm radius of curvature, ~125 mm mean length, 30 mm mean width, ~42 N/m force constant, and ~330 kHz resonance frequency was used. The image processing and roughness evaluation were performed using the XEI program (v 1.8.0) from Park Systems. The detailed surface profile of the scanned films was presented in "enhanced contrast" view mode.

2.5. Pharmacotechnical Analysis of the UBA-Loaded Mucoadhesive Oral Films

2.5.1. Weight Uniformity

The weight uniformity was achieved on 20 films of each type (F-UBA and R) that were individually weighed, and the average was calculated.

2.5.2. Thickness

This parameter was assessed with a Yato Trading CO., Ltd., Shanghai, China, digital micrometer with a 0–25 mm measurement range and 0.001 mm resolution on 20 films of each formulation. The mean and the standard deviation were calculated.

2.5.3. Folding Endurance

To test folding endurance, 10 films of each formulation were folded and rolled repeatedly, at the same place, until they broke, or up to 300 times [41]. The folding times were recorded and reported as folding endurance values.

2.5.4. Tensile Strength and Elongation Ability

Both parameters were determined using an LR 10K Plus digital tensile force tester for universal materials (Lloyd Instruments Ltd., West Sussex, UK). For the test, 5 films of each type (F-UBA and R) were placed in a vertical position between apparatus 2 braces, and then the test was performed at a speed of 30 mm/min from a distance of 30 mm.

The tensile strength (kg/mm^2) and elongation at break (%) were calculated using the following equations:

$$Tensile\ strength\left(\text{kg}/\text{mm}^2\right) = \frac{Force\ at\ breakage\ (\text{kg})}{Film\ thickness\ (\text{mm}) \times Film\ width\ (\text{mm})} \tag{1}$$

$$Elongation\ \% = \frac{Increase\ in\ film\ length\ (\text{cm})}{Inital\ film\ length\ (\text{cm})} \times 100 \tag{2}$$

2.5.5. Moisture Content

The moisture content was evaluated as the loss on drying using a thermogravimetric method with an HR 73 Mettler Toledo halogen humidity analyzer (Mettler-Toledo GmbH, Greifensee, Switzerland) [42]. Five films of each formulation (F-UBA and R) were tested.

2.5.6. Surface pH Value

For pH testing, 5 films of each formulation (F-UBA and R) were moistened for 5 min at room temperature with 1 mL distilled water (pH 6.5 ± 0.5). The pH was registered by touching the film surface with the electrode of a CONSORT P601 pH-meter (Consort bvba, Turnhout, Belgium).

2.5.7. In Vitro Disintegration Time

This parameter was assessed on 6 films of each formulation (F-UBA and R) in simulated saliva phosphate buffer pH 6.8 at 37 ± 2 °C [43], using an Erweka DT 3 apparatus (Erweka® GmbH, Langen, Germany). The time required for both films' total disintegration was registered.

2.5.8. Swelling Ratio

The films were placed in Petri plates on a 1.5% agar gel and incubated at 37 ± 1 °C. They were weighed every 30 min for 6 h, and the swelling ratio was calculated according to the following equation:

$$Swelling\ ratio = \frac{Wt - Wi}{Wi} \times 100 \tag{3}$$

where Wt is the film weight at time t after the incubation and Wi is the initial weight [44–46].

2.5.9. Ex Vivo Mucoadhesion Time

The method used to determine the residence time on a detached porcine oral mucosa was adapted to those described by Gupta et al. [47]. The fat layer and any tissue residue were removed from the membrane surface, then rinsed with distilled water and a phosphate buffer pH of 6.8 at 37 °C and fixed on a glass plate. Each film was hydrated in the center with 15 µL phosphate buffer and pressed on the membrane surface for 30 s. The glass plate was in a 200 mL phosphate buffer of pH 6.8 and kept at 37 °C for 2 min. The paddle with a stirring rate of 28 rpm was operated to reproduce the oral cavity conditions. The bioadhesion time was established by measuring the necessary time for each film to detach from the oral mucosa. All tests were performed in triplicate.

2.6. Evaluation of the Cytotoxic Activity of UBA-Loaded Mucoadhesive Oral Films on A. salina Larvae

2.6.1. Sample Preparation

The F-UBA was placed in a diluted buffer (1 mL) and incubated for 15 min at 37 °C; then, its homogenous dispersion in the buffer solution was observed.

2.6.2. BSL Assay

Artemia salina (brine shrimp) was used as an animal model for the UBA-loaded mucoadhesive oral films' cytotoxicity investigation, adapted from Nazir et al. [48]. The *A. salina* larvae were obtained under continuous light and aeration conditions, at a temperature of 20 °C, by introducing the cysts of *A. salina* for 24–48 h in a saline solution of 0.35%. The brine shrimp larvae in the first stage (instar I) were introduced in 0.3% saline solution into experimental pots (with a volume of 1 mL) [49]. The analysis was compared with a blank (untreated nauplii) to obtain accurate results regarding the F-UBA cytotoxic effects. The nauplii were not fed during the test to not interfere with the tested extracts. Their evolution was investigated after 24 h and 48 h; the larvae had embryonic energy reserves as lipids throughout this period.

Morphological changes of brine shrimp larvae [50,51] after 24 and 48 h were observed at VWR microscope VisiScope 300D (VWR International, Radnor, PA, USA).

2.6.3. Fluorescent Microscopy

After 48 h, the brine shrimp larvae were stained with 3% acridine orange (Merck Millipore, Burlington, MA, USA) for 5 min. The samples were subjected to drying for 15 min in darkness and placed on the microscope slides.

2.6.4. Data Processing

The microscopic images were achieved using a VWR microscope VisiScope 300D (VWR International, Radnor, PA, USA) with a Visicam X3 camera (VWR International Radnor, PA, USA) at 100× and 400× magnifications and processed with VisiCam Image Analyzer 2.13.

Using an OPTIKA B-350 microscope (Ponteranica, BG, Italy) blue filter (λex = 450–490 nm; λem = 515–520 nm) and green filter (λex = 510–550 nm; λem = 590 nm), fluorescent microscopy images were obtained [52]. The FM images at 200× and 400× magnification were processed with Optikam Pro 3 Software (OPTIKA S.R.L., Ponteranica, BG, Italy).

All observations were performed in triplicate.

2.7. In Vitro Analysis of the Effects of UBA-Loaded Mucoadhesive Oral Films on Human Normal Blood Cells and OSCC CLS-354 Cell Line

2.7.1. Equipment

The Attune Acoustic focusing cytometer (Applied Biosystems, Bedford, MA, USA) was the platform for the in vitro cytotoxicity analysis of UBA-loaded mucoadhesive oral films. Before cell analysis, the flow cytometer was first set by using fluorescent beads Attune performance tracking beads, labeling, and detection (Life Technologies, Europe BV, Bleiswijk, Netherlands) [53], with a standard size (four intensity levels of beads population). The cell amount was established by enumerating cells below 1 µm [54]. Using forward scatter (FSC) and side scatter (SSC), more than 10,000 cells per sample for each analysis were gated.

2.7.2. Data Processing

Flow cytometry data were achieved using Attune Cytometric Software v.1.2.5, Applied Biosystems 2010 (Bedford, MA, USA).

2.7.3. Human Blood Cells Cultures

The blood sample was collected into heparin vacutainers. Then, the heparinized blood (1.0 mL) was added to untreated Nunclon Vita Cell culture 6-well plates (Kisker Biotech GmbH & Co.KG, Steinfurt, Germany), together with 6.0 mL of Dulbecco's phosphate-buffered saline with $MgCl_2$ and $CaCl_2$ medium supplemented with 10% bovine fetal serum, L-glutamine, and antibiotics mix solution. They were incubated in a Steri-Cycle™ i160 CO_2 Incubator (Thermo Fisher Scientific Inc., Waltham, MA, USA) with 5% CO_2 at 37 °C. After 72 h, the blood cell cultures were treated with the samples and controls. Then, the cells were subjected to 24 h of incubation in the same conditions [53]. All flow cytometry analyses were performed after this incubation time.

2.7.4. CLS-354 Cell Line, Cells Culture

The CLS-354 tumor cells were cultured in DMEM high glucose supplemented with antibiotic mix solution in humidity conditions of 5% CO_2 at 37 °C for 7 days [55]. Then, the cells were dissociated with trypsin-EDTA, centrifugated at 3000 rpm for 10 min in a Fisher Scientific GT1 centrifuge (Thermo Fisher Scientific Inc., Waltham, MA, USA), and distributed in Millicell™ 24-Well Cell Culture Microplates (Thermo Fisher Scientific Inc., Waltham, MA, USA). After treatment, the cells were incubated for 24 ore in the same conditions [25]. All the flow-cytometry analyzes were performed after this incubation period.

2.7.5. Samples and Control Solutions

The UBA-loaded mucoadhesive oral films were dissolved in the suitable culture medium for both types of cells, with 1% DMSO. As a positive control, usnic acid (125 µg/mL in 1% DMSO) was selected, and the negative control was 1% DMSO.

2.8. Evaluation of Total ROS Activity

ROS assay stain solution (100 µL) was added to each 1 mL of cell culture in flow cytometry tubes and well-mixed. Then, the cells were incubated in a 5% CO_2 atmosphere at 37 °C for 60 min. After this process, the cells were analyzed by flow cytometry, using a 488 nm excitation and green emission for ROS (BL1 channel).

2.9. Evaluation of Caspase 3/7 Activity

Both cell cultures (300 µL) were transferred in flow cytometry tubes; then, 20 µL of a Magic Red® Caspase-3/7 Substrate—MR-(DEVD)2-solution—was added and well-mixed with the cells. Next, 20 µL of PI was added. After incubation, 1 mL FCB was added. Then, the early stages of cell apoptosis by activating caspases 3/7 (DEVD-ases) [56] were analyzed through flow cytometry using a 488 nm excitation, red emission for MR-(DEVD)2—BL3 channel, and orange emission for PI—BL2 channel.

2.10. Evaluation of Nuclear Condensation and Lysosomal Activity

Magic Red® Caspase-3/7 Assay Kit contains Hoechst 33,342 stain (200 µg/mL) and acridine orange (AO, 1.0 µM). Hoechst 33,342 is a cell-permeant nuclear stain [57]; when it is linked to double-chain DNA, it emits blue fluorescence, highlighting condensed nuclei in apoptotic cells. Acridine orange is a chelating dye that can be used to reveal lysosomal activity [58]. Here, 300 µL of each cell culture was introduced in flow cytometry tubes; then, 2 µL of Hoechst 33,342 stain was added, and the cells were mixed well [53]. After these operations, 50 µL of 1.0 µM AO was added; the cells were incubated at room temperature into darkness for 30 min. After incubation, 1 mL FCB was added; the cells were examined at the flow cytometer under the following conditions: an excitation of 488 nm, the UV excitation, and blue emission for Hoechst 33,342 (VL2), and green emission acridine orange (BL1 channel) [53].

2.11. Cell Cycle Analysis

A cell culture volume of 1 mL was washed in FCB, introduced in flow cytometry tubes, and fixed with 50 µL ethanol for 30 min [53]. Next, the cells were treated with PI (20 µg/mL) and RNase A (30 µg/mL) and incubated at room temperature, into darkness, for 30 min [53]. Then, 1 mL FCB was added, and the cell cycle distribution was detected at the flow cytometer in the following conditions: a 488 nm excitation and orange emission for PI (BL2 channel) [53].

2.12. Annexin V-FITC Apoptosis Assay

The blood cells and CLS-354 tumor cells were incubated in flow cytometry tubes with 2 µL Annexin V-FITC and 2 µL PI (20 µg/mL) for 30 min, at room temperature, in darkness. After incubation, 1 mL of FCB was added. All viable cells, early apoptotic cells, late apoptotic cells, and necrotic cells were examined at a flow cytometer using the following conditions: an excitation of 488 nm and two emission types: green for Annexin V-FITC (BL1 channel) and orange for PI (BL2 channel) [53].

2.13. Evaluation of Cell Proliferation

Volumes of 1 mL of both cell cultures were incubated with 50 µM EdU (500 µL) at 37 °C for 2 h. Then, both cell types were fixed with 4% paraformaldehyde in PBS (100 µL) and permeabilized with Triton X-100 (100 µL). After washing in 3% buffer sodium azide (BSA) and centrifuging at 300 rpm for 5 min, at 4 °C, the cells were incubated with a reaction mix (500 µL) for 30 min at room temperature into darkness. Then, they were washed in permeabilization buffer and centrifuged at $300\times g$ rpm for 5 min, at 4 °C. After these procedures, 1 mL FCB was added, and the cells were examined by flow cytometry, using a 488 nm excitation and green emission for EdU-iFluor 488 (BL1).

2.14. Antimicrobial Activity Evaluation by Resazurin-Based 96-Well Plate Microdilution Method

2.14.1. Inoculum Preparation

The direct colony suspension method (CLSI) was used for preparing the bacterial inoculum. First, bacterial colonies selected from a 24 h agar plate were suspended in an MHA medium. The bacterial inoculum was accorded to the 0.5 McFarland standard, measured at Densimat Densitometer (Biomerieux, Marcy-l'Étoile, France) with around 10^8 CFU/mL (CFU = colony-forming unit). The fungal inoculum was prepared using the same method, adjusting the RPMI 1640 with fungal colonies to the 1.0 McFarland standard, with 10^6 CFU/mL.

2.14.2. Samples and Standards

The F-UBA was dissolved in 1 mL of diluted phosphate buffer. As standards, Ceftriaxone (Cefort 1 g Antibiotice SA Iasi, Romania) solutions 30 mg/mL and 122 mg/mL in distilled water were used for bacteria. Cefort powder was weighted at Partner Analytical balance (Fink & Partner GmbH, Goch, Germany) and dissolved in distilled water. Terbinafine solution 10.1 mg/mL (Rompharm Company S.R.L., Otopeni, România) was selected as standard for *Candida* sp.

2.14.3. Resazurin-Based 96-Well Plate Microdilution Method

All successive steps were performed in an Aslair Vertical 700, laminar flow, microbiological protection cabinet (Asal Srl, Cernusco (MI) Italy). In four 96-well plates, we performed seven serial dilutions, adapting the protocol described by Fathi et al. [59] and Elshikh et al. [60].

The 96-well plates were incubated for 24 h at 37 °C for bacteria and 35 °C for yeasts in a My Temp mini Z763322 Digital Incubator (Benchmark Scientific Inc., Sayreville, NJ, USA).

2.14.4. Reading and Interpreting

After 24 h incubation, the colors from 96-well plates were examined to see the differences between standard and samples [61]. Moreover, they were evaluated at the Smart LED Illuminator (Kaneka Eurogentec S.A., Seraing, Belgium) at the wavelength of 470 nm, and the active sample concentrations were compared with the Standard antibiotic ones. The F-UBA microdilutions whose color was similar to standard antibiotic ones were highlighted. For yeasts, the color chart of the resazurin dye reduction method was used [62,63].

2.15. Data Analysis

All analyses were performed in triplicate, and the results were presented as means ± standard deviations (SD). They are expressed as percent (%) of the cells for apoptosis, caspase 3/7 activity, nuclear condensation, autophagy, cell cycle, DNA synthesis, and count ($\times 10^4$) of ROS for cellular oxidative stress. The flow cytometry data were collected with SPSS v.23, 2015 (IBM, Armonk, NY, USA). The Levene test was analyzed for the homogeneity of sample variances. The paired t-test was used ($p < 0.05$ was considered statistically significant) to establish the differences between samples and controls. The principal component analysis (PCA) was performed using XLSTAT 2022.2.1. by Addinsoft (New York, NY, USA) [34].

3. Results

3.1. Physico-Chemical Characterization of the UBA-Loaded Mucoadhesive Oral Films

The composition of R and F-UBA is illustrated in Table 1.

Table 1. Composition, physico-chemical properties, and pharmacotechnical characterization of mucoadhesive oral films (F-UBA and R).

Variable		**F-UBA**	**R**
Composition			
UBA (g)		0.25	-
Ethyl alcohol 96% (*v*/*v*) (g)		5	5
Isopropyl alcohol (g)		5	5
PEG 400 (g)		5	5
HPMC 15% water dispersion (*w*/*w*) (g)		84.75	85
Physico-chemical properties-TG/DTA parameters			
1st Step (%)	TG (%)	2.50%	1.20%
2nd Step (%)	TG (%)/Tmax (°C)	85.5%/355.2 °C	86.9%/360.5 °C
3rd Step (%)	TG (%)/Tmax (°C)	12.1%/461.8 °C	11.9%/454.7 °C
Pharmacotechnical properties			
Weight uniformity (mg)		70 ± 3.54	66 ± 4.18
Thickness (mm)		0.060 ± 0.002	0.058 ± 0.003
Folding endurance value		>300	>300
Tensile strength (kg/mm^2)		3.02 ± 2.39	2.88 ± 3.43
Elongation %		47.26 ± 2.16	49.25 ± 2.24
Moisture content % (*w*/*w*)		4.11 ± 0.35	3.98 ± 1.02
pH		7.01 ± 0.01	7.04 ± 0.02
Disintegration time (seconds)		146 ± 5.09	138 ± 4.67
Swelling ratio (% after 6 h)		211 ± 4.31	204 ± 3.29
Ex vivo bioadhesion time (minutes)		85 ± 2.33	82 ± 2.61

F-UBA—mucoadhesive oral films loaded with *U. barbata* dry acetone extract; R—Reference (films without UBA); UBA—*U. barbata* dry acetone extract; PEG 400—polyethylene glycol 400; HPMC—hydroxypropyl methylcellulose.

Both formulations (F-UBA and reference) led to thin, non-sticky, transparent, and homogenous mucoadhesive with smooth and uniform surfaces; no cracks or air bubbles were visible. UBA-loaded mucoadhesive oral films have a yellowish-greenish-faint brown color (due to UBA), and R ones are colorless (Figure S1 from Supplementary Material). The final F-UBA has 175 µg UBA, with 42.32 µg usnic acid, from a total phenolic content of 150.997 µg.

3.1.1. FTIR Spectra

The FTIR spectra of reference (R) and UBA-loaded mucoadhesive oral films are presented in Figure 1a.

The broad absorbance peak at 3443 cm^{-1} corresponds to the O-H stretching vibration of HPMC [64]. The absorption peak at 2915 cm^{-1} is assigned to the stretching vibration of the C–H band, and the peaks at 1455 cm^{-1} correspond to the deformation vibration of C–H$_2$ [65]. The absorption peaks at 1118 cm^{-1} and 940 cm^{-1} are attributed to the C–O–C asymmetric stretching vibrations and β-glycosidic linkages, respectively [66,67].

Instead, the FTIR spectrum of F-UBA (Figure 1a, magenta line) shows the presence of the same peaks found in the reference (Figure 1a, black line), with a slight displacement and lower intensities. These observations proved the dispersion of UBA in the polymer matrix.

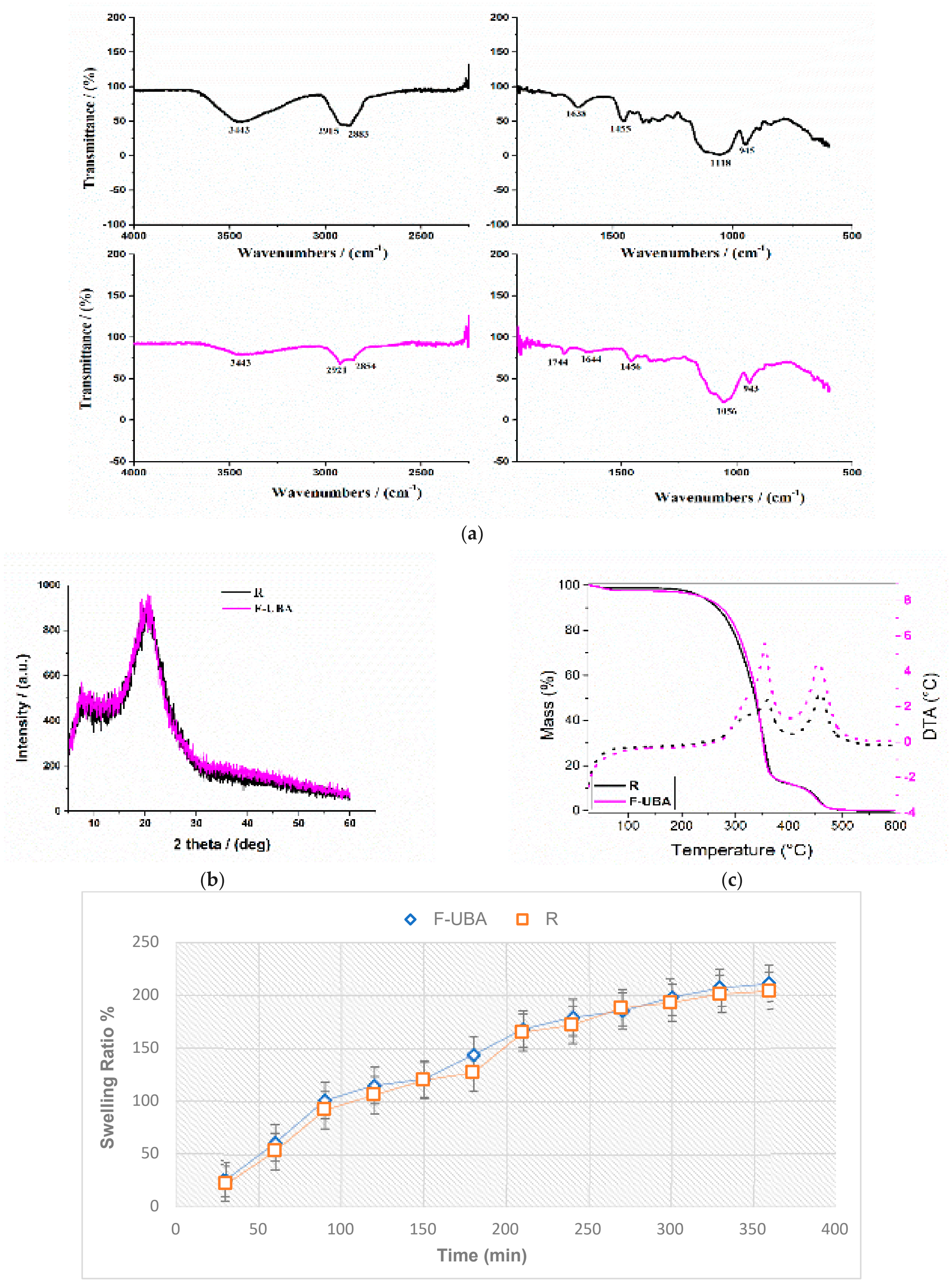

Figure 1. (**a**) FTIR spectra of mucoadhesive oral films R (black line) and F-UBA (magenta line); (**b**) XRD pattern and (**c**) TG/DTA curves; (**d**) swelling ratio over 6 h of both mucoadhesive films (F-UBA and R). F-UBA—UBA-loaded mucoadhesive oral film; R—Reference (mucoadhesive oral film without UBA); UBA—*U. barbata* dry acetone extract.

3.1.2. XRD Analysis

The X-ray diffraction patterns of reference and F-UBA are shown in Figure 1b. The diffraction patterns obtained for the UBA-loaded polymer matrix (F-UBA) are similar to that of the reference, with a change in intensity. The reference shows the diffraction pattern of HPMC film with two vast diffraction peaks at 7.94° and 20.55°, which indicate its semi-crystalline nature [68,69].

These peaks are characteristic of planes (101) and (002). The UBA incorporation does not affect the parent HPMC matrix.

3.1.3. TG/DTA Measurements

The thermogravimetric method was performed in a linear heating program under an air atmosphere to study the films' thermal behavior. Thermal analysis of the films shows several steps of mass loss (Table 1 and Figure 1c).

The first step, similar for both films (reference and F-UBA), occurs up to 100 °C and is mainly due to the dehydration process (the used solvent and physisorbed water). The reference lost about 1.2%, while F-UBA lost about 2.5%.

In the second step, R lost about 86.9% of the mass, while F-UBA lost about 85.5%. The decomposition of the organic compounds occurs between 200 and 400 °C (in the films, the thermal degradation of HPMC polymer) [70].

The third step, between 400 and 500 °C, is due to the thermal decomposition of the other more stable organic groups.

The thermodynamic parameters (mass losses and maximum decomposition temperatures obtained from DTA curves) associated with the three decomposition steps are registered in Table 1.

3.1.4. SEM Analysis

SEM images of reference (R) and UBA-loaded mucoadhesive oral films are shown in Figure 2a,b. The reference (Figure 2a) shows a smooth surface morphology with some small round particles. When UBA was added to the reference, a difference could be observed in the F-UBA's morphology. Compared with the reference, a rougher surface was noted for the mucoadhesive film with UBA incorporated (Figure 2b).

3.1.5. AFM Measurements

The reference (Figure 2c) exhibits a surface with smaller features, particle-like, as can be observed mainly in the lower part of Figure 2c, in the dashed circle surrounding such an area of particles. Nevertheless, some large pits (surface cavities) are observed on the reference's surface. The arbitrary lines plotted below the AFM images of the R film suggest a similar Z-scale (oscillations level) of about 120 nm. (Figure 2e)

Figure 2d shows the UBA-loaded mucoadhesive oral film. Its morphology is less uniform than the reference, exhibiting small protuberances. F-UBA roughness and peak-to-valley parameters increase compared with R (Figure 2f).

Calculating the corrugation parameters using the whole scanned area, i.e., 8 × 8 μm^2, highlights the rougher morphology of F-UBA (Figure 2h). Using the scale of 3 × 3 μm^2 (Figure 2g,h), it was observed that the roughness shows the same trend for the small areas: from the morphological point of view, the films are relatively uniform. The AFM images accord with the SEM analysis regarding both films' morphology.

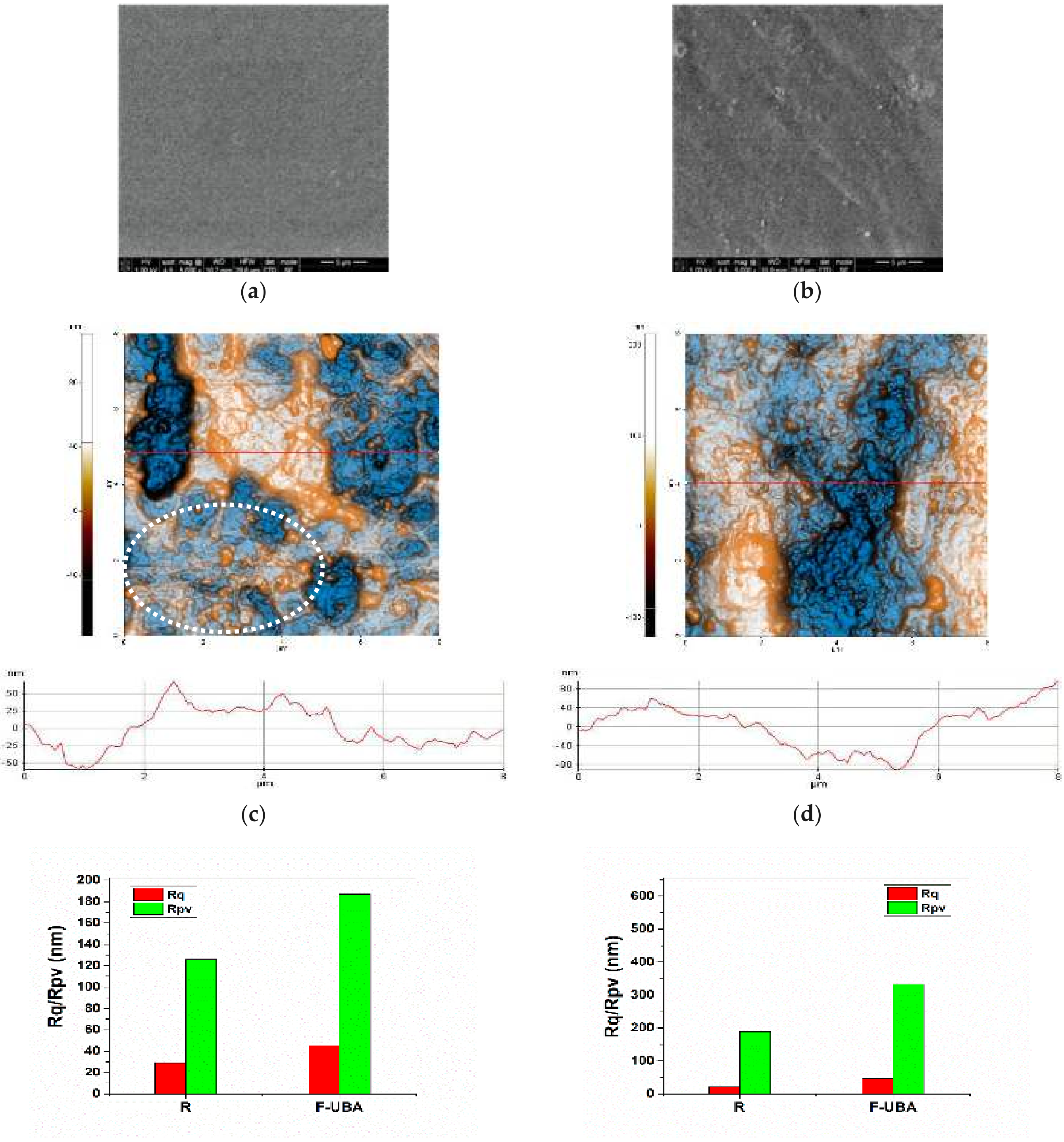

(**a**) (**b**)

(**c**) (**d**)

(**e**) (**f**)

Figure 2. *Cont.*

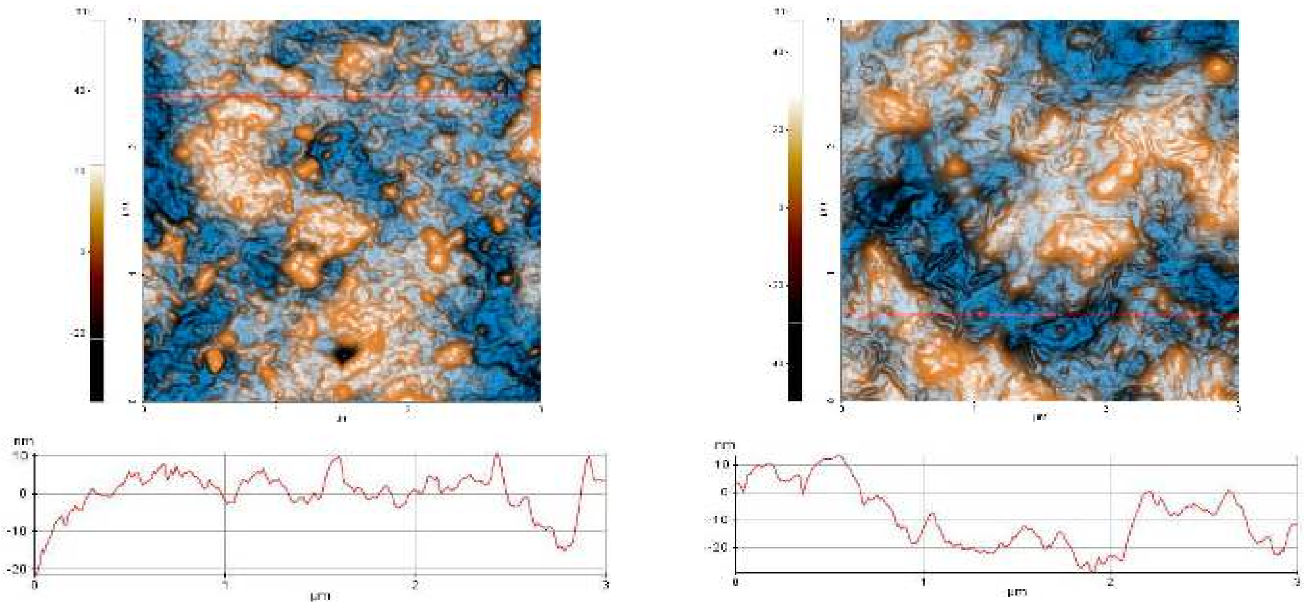

(g) (h)

Figure 2. SEM and AFM images of mucoadhesive oral films. SEM micrographs (**a**,**b**) of both mucoadhesive oral films: (**a**) reference (R); (**b**) F-UBA. 2D AFM images (**c**,**d**) in enhanced contrast view at the scale of (8 × 8) µm^2 together with representative line scans for films: (**c**) R, (**d**) F-UBA; Roughness (Rq), and peak-to-valley (Rpv) parameters (**e**) along the line-scans and (**f**) for the whole scanned areas; and at the scale of (3 × 3) µm^2 together with representative line-scans for films (**g**) R and (**h**) F-UBA. R—Reference (mucoadhesive oral film without UBA); F-UBA—UBA-loaded mucoadhesive oral film; UBA—*U. barbata* dry acetone extract.

3.2. Pharmacotechnical Characterization of UBA-Loaded Mucoadhesive Oral Films

The pharmacotechnical properties of both films—F-UBA and reference (R)—are displayed in Table 1.

Reference has around 66 mg, while F-UBA shows an average weight of 70 mg, containing 175 mg UBA with a usnic acid content of 42.32 µg.

Both films are very thin, between 0.058 and 0.060 mm.

The folding endurance values were above 300 for both types of films.

F-UBA has a tensile strength of 3.02 kg/mm^2 and a 47.26% elongation, while the R values were 2.88 kg/mm^2 and 49.25%, respectively.

F-UBA has a moisture content of 4.11%, while R presents a 3.98% loss on drying.

Both films present a neutral pH (7.01 for F-UBA and 7.04 for R), indicating good biocompatibility with the buccal mucosa and high tolerability.

The F-UBA displayed an in vitro disintegration time in a simulated saliva medium of 146 s, compared to R one of 138 s.

All data obtained reported no significant differences between F-UBA and R ($p > 0.05$).

The swelling ratio registered for mucoadhesive oral films (F-UBA and R) over the 6 h is shown in Figure 1d.

The swelling behavior of the two films (F-UBA and R) was similar, with a higher swelling rate in the first 150 min. The hydration process continued with a much slower profile, with erosion occurring after 6 h. The swelling index of F-UBA was 211% after 6 h, and that of R, 204% (Table 1, Figure 1d)

Both mucoadhesive films exhibited good retention times on the oral mucosa: 85 min for F-UBA and 82 min for R; it could be observed that UBA incorporation slightly increased the bioadhesion time by 3 min (Table 1).

3.3. BSL Assay

After 24 h, all the larvae were alive, swimming, and showing normally visible movements. After 48 h, 68.88% of larvae were active, and 4.44% were in the sublethal stage; the registered mortality was 26.66%. We investigated them under a microscope to observe the changes after 24 and 48 h of exposure. All these microscopic images are presented in Figure 3a–p.

Figure 3 shows that *A salina* larvae are progressively affected by lipid metabolism disturbances, which begin to be visible after 24 h of exposure to F-UBA, compared with blank (Figure 3a–h). Lipid accumulation in the digestive tract and penetration into the neighboring tissues can be observed (Figure 3e–g). In the lower extremity, a slight detachment of the external cuticle from larval tissues is also observed (Figure 3h). After 48 h of exposure, the larval tissues are massively invaded, and the damage continues with digestive blockage and significant tissue destruction (Figure 3m–p) that lead to larvae death. In addition, at the intracellular level, activated lysosomes in cell death processes could be observed using AO staining (Figure 3t–v).

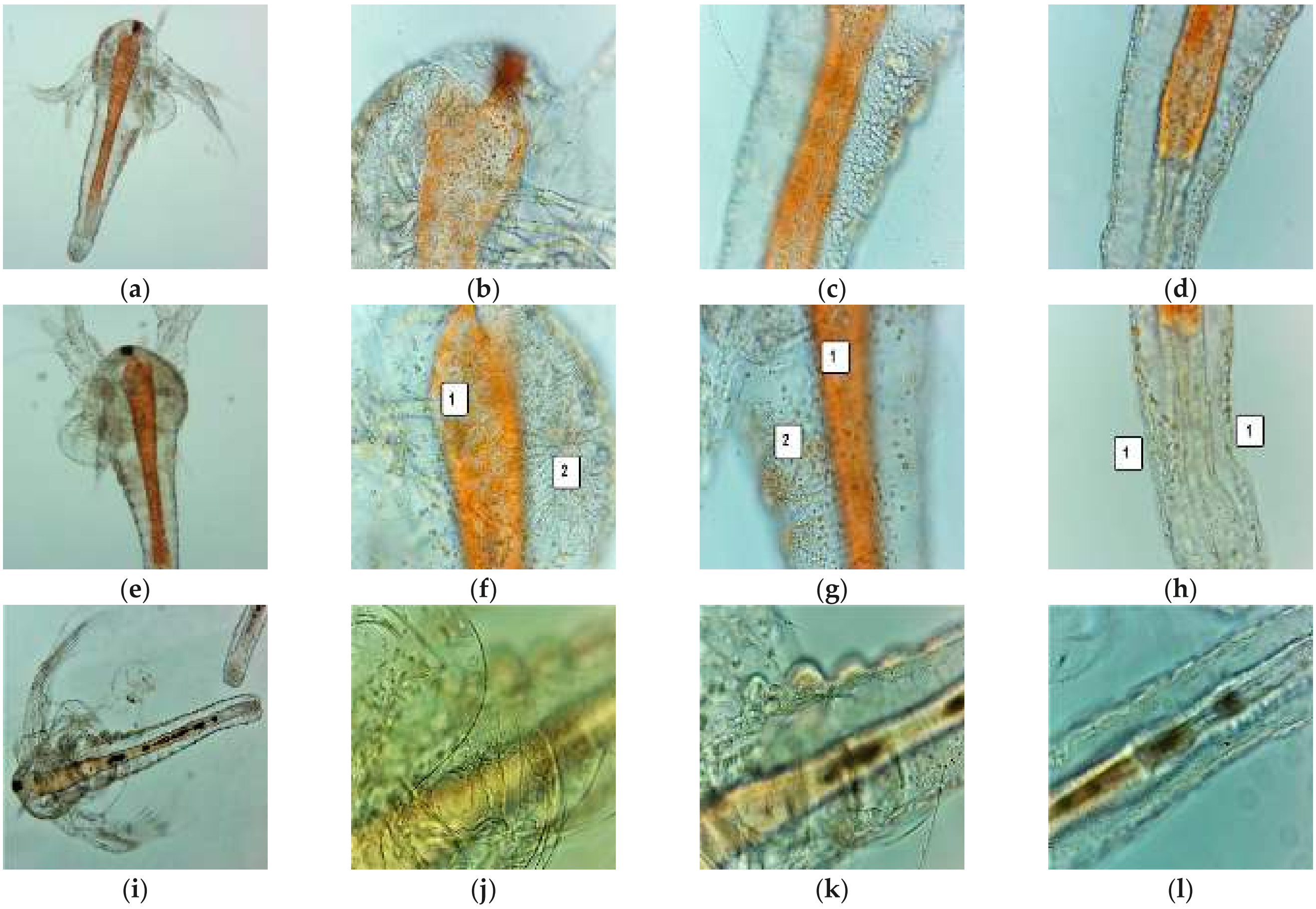

Figure 3. *Cont.*

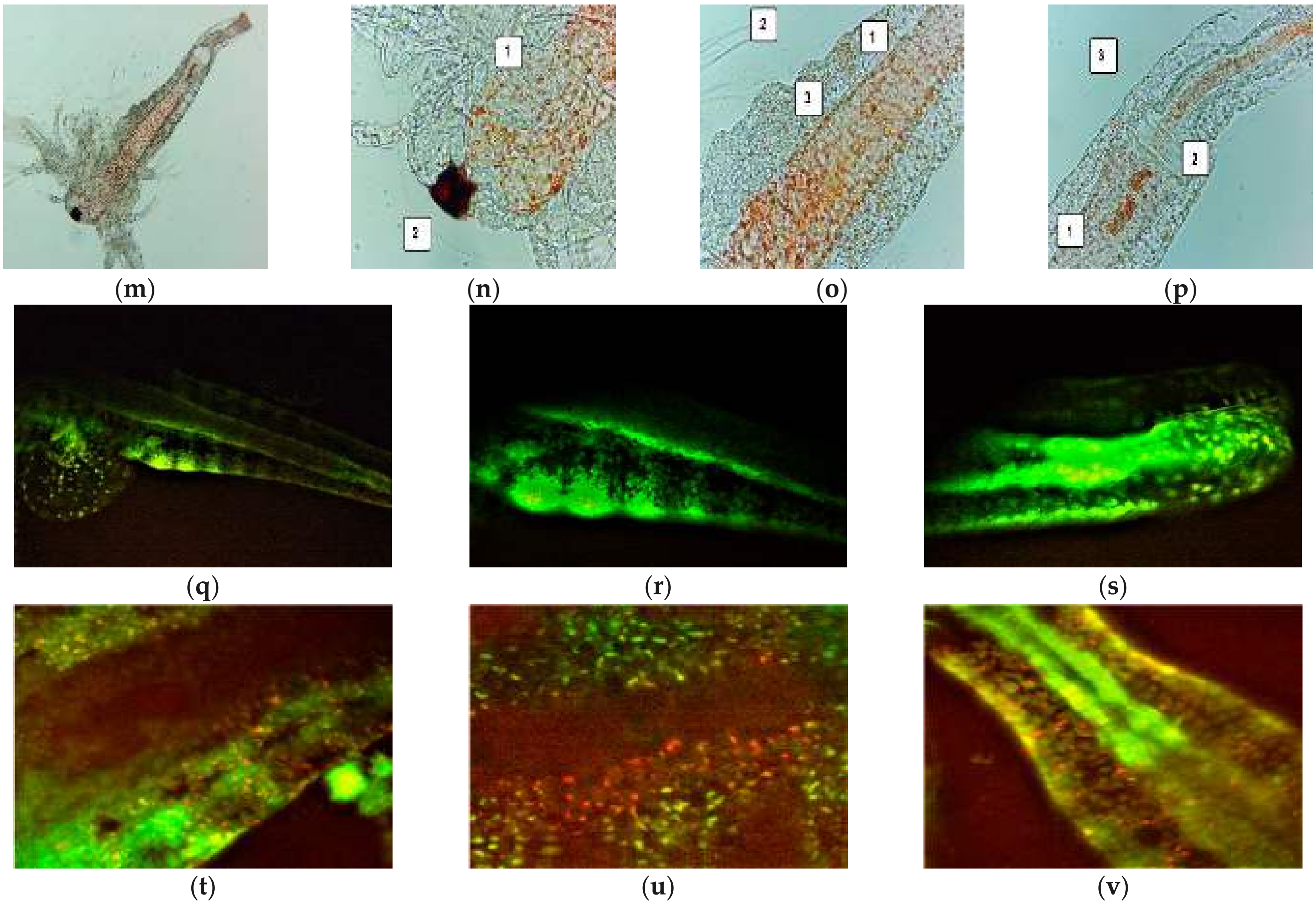

Figure 3. (**a**–**p**) *A. salina* larvae after the exposure period of 24 and 48 h to F-UBA—microscopic images at 100× (**a**,**e**,**i**,**m**) and 400× (**b**–**d**,**f**–**h**,**j**–**l**,**n**–**p**). After 24 h: blank (**a**–**d**) and F-UBA (**e**–**g**); after 48 h: blank (**i**–**l**) and F-UBA (**m**–**p**). The following changes after 24 h can be observed compared with blank: (**f**–**g**) lipids accumulation in the digestive tract (1), lipids penetration into the neighboring tissues (2); (**h**) a low detachment of the cuticle from larval tissues (1); (**n**) cell damage with large intercellular spaces and tissue destruction (1) and considerable detachment of the cuticle from larval tissues (2); (**o**) detachment of the membrane that separates the digestive tube from the neighboring tissues (1), lipid penetration in the adjacent tissues (2), and considerable detachment of the external cuticle from larval tissues (3); (**p**) digestive blockage (1) with massive tissue destruction (2) and high detachment of the external cuticle from larval tissues (3). (**q**–**v**) FM images of *A. salina* larvae after 48 h of exposure at F-UBA—stained with Acridine Orange 400× (**q**–**s**) and 200× (**t**–**v**); (**q**-**s**)—blank; (**t**–**v**)—F-UBA. The red fluorescence shows intracellular lysosomes activated in cell death processes (**t**–**v**). F-UBA—UBA-loaded mucoadhesive oral film; UBA—*U. barbata* dry acetone extract.

3.4. In Vitro Analysis of the Effects of UBA-Loaded Mucoadhesive Oral Films on Human Normal Blood Cells and OSCC CLS-354 Cell Line

The effects of F-UBA on biological processes represented by oxidative stress, caspase 3/7 activity, nuclear shrinkage, autophagy, cell cycle, apoptosis, and DNA synthesis and fragmentation were investigated in blood cell cultures and CLS-354 tumor cell line. All these flow-cytometry analyses follow our preliminary studies about the effects of *U. barbata* dry acetone extract on normal and tumor cells [24,25,53].

3.4.1. ROS Levels

The F-UBA induced cellular oxidative stress in blood cell cultures and CLS-354 tumor cell lines. Total ROS levels were determined through flow cytometry (Figure 4).

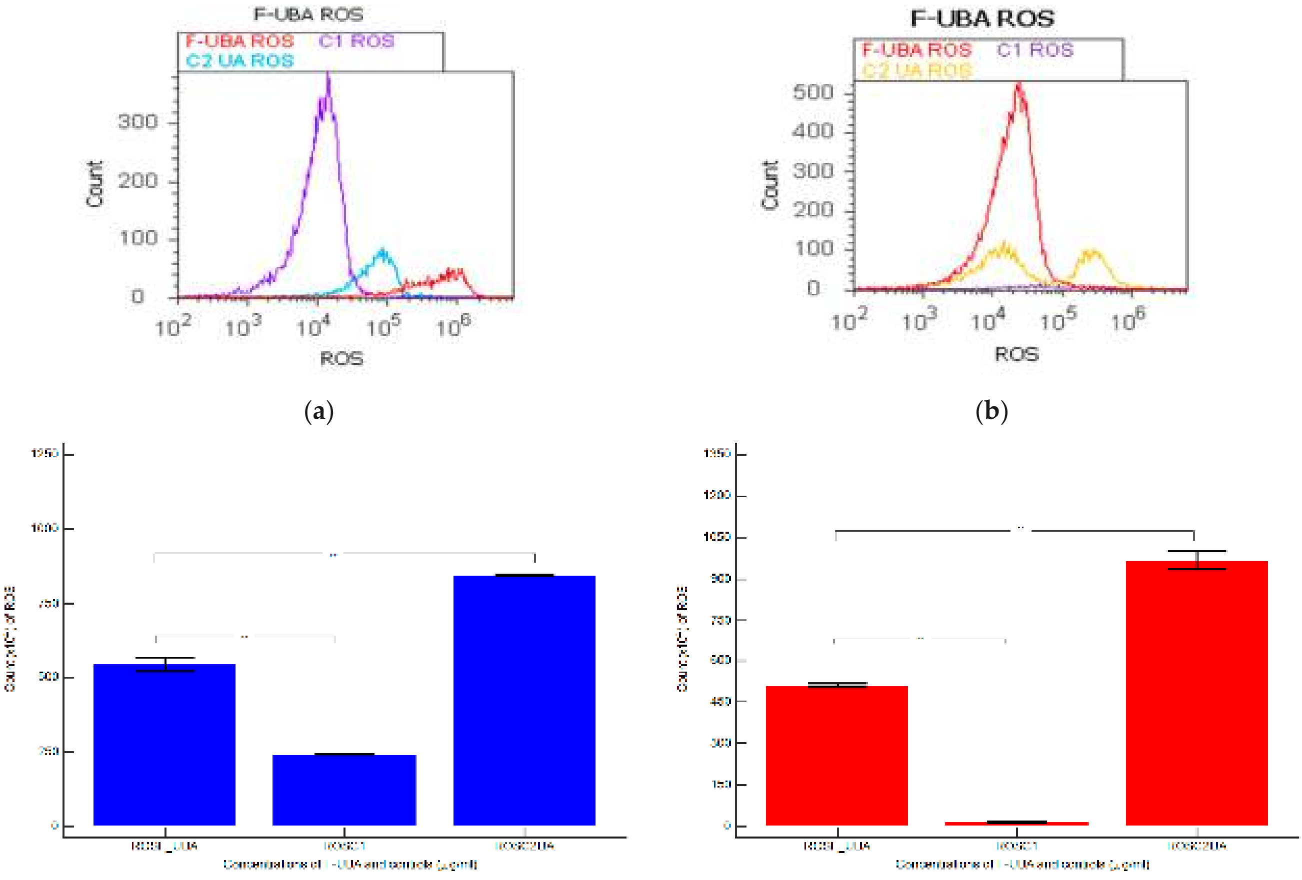

(**a**) (**b**)

(**c**) (**d**)

Figure 4. Reactive oxygen species (ROS) in blood cells (**a**) and CLS-354 tumor cells (**b**) after 24 h treatment with F-UBA; C1—1% DMSO negative control; C2—125 µg/mL UA positive control; Statistical analysis of reactive oxygen species (ROS) in blood cell cultures (**c**) and CLS-354 tumor cell line (**d**), after 24 h treatment with F-UBA; ** $p < 0.01$ represents significant statistical differences between controls and sample made by paired samples *t*-test. C1—negative control with 1% dimethyl sulfoxide (DMSO); C2UA—positive control with 125 µg/mL usnic acid (UA); F-UBA—UBA-loaded mucoadhesive oral film; UBA—*U. barbata* dry acetone extract.

In the blood cells treated with F-UBA, ROS levels were substantially higher ($543.33 \times 10^4 \pm 40.41$) than 1% DMSO negative control ($242.00 \times 10^4 \pm 2.00$, $p < 0.01$) and significantly lower than 125 µg/mL of UA positive control: $846.66 \times 10^4 \pm 5.77$; $p < 0.01$ (Figure 4a,c)

Oxidative stress appreciably increased in the CLS-354 tumor cell line treated with F-UBA ($510.00 \times 10^4 \pm 10.00$) compared with negative control ($15.66 \times 10^4 \pm 4.04$; $p < 0.01$). However, C3UA positive control induced the highest ROS production: $966.66 \times 10^4 \pm 57.73$, $p < 0.01$ (Figure 4b,d).

3.4.2. Caspase 3/7 Activity

Effector caspase 3/7 enzymatic activity implied in apoptosis was observed after F-UBA treatment for 24 h in normal blood cells and OSCC tumor cells (Figure 5).

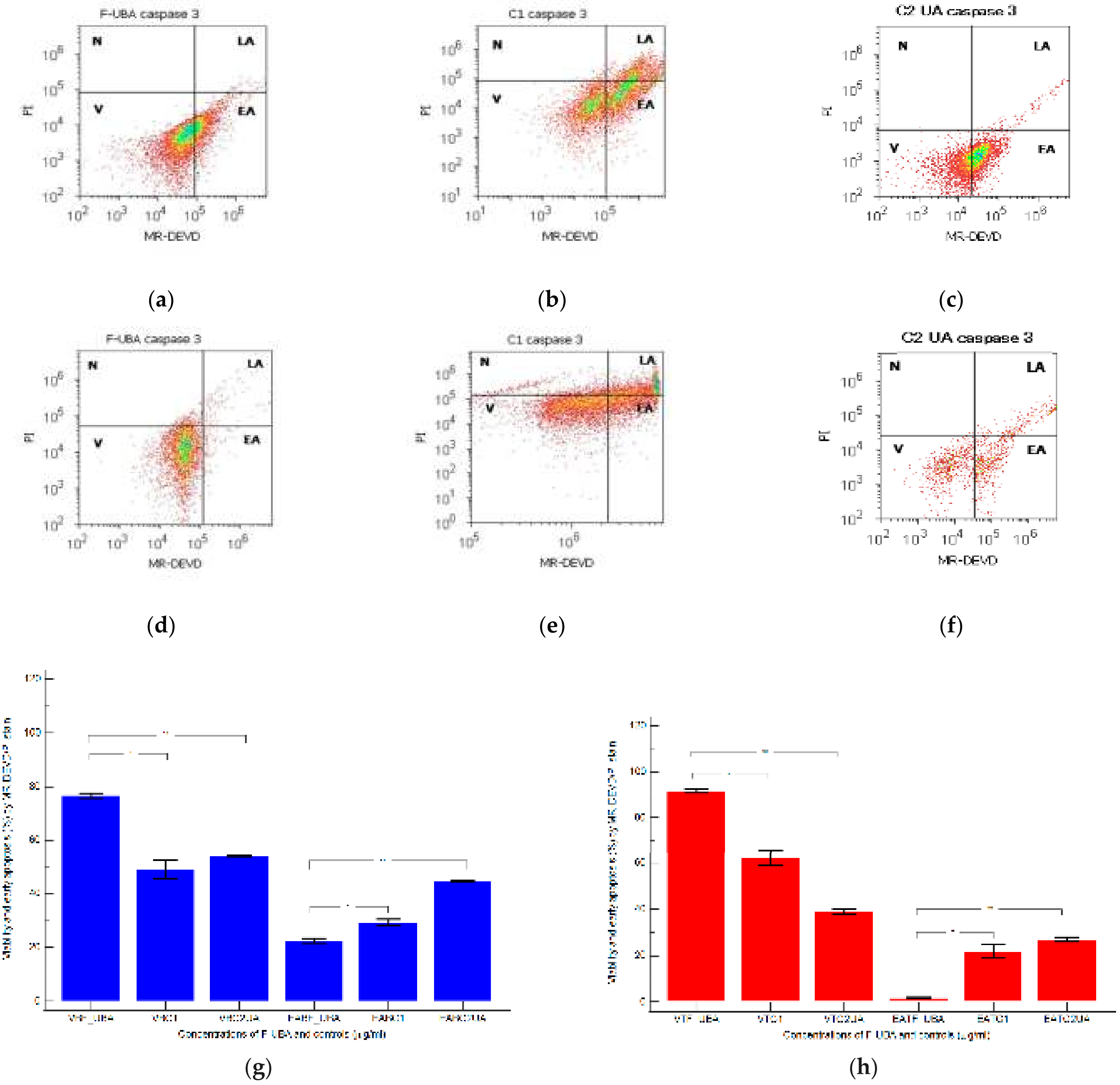

(**a**) (**b**) (**c**)

(**d**) (**e**) (**f**)

(**g**) (**h**)

Figure 5. Activity of 3/7 effector caspases in blood cells (**a**–**c**,**g**) and CLS-354 tumor cells (**d**–**f**,**h**) after 24 h treatment with F-UBA. MR-DEVD/PI patterns of F-UBA (**a**,**d**), 1% DMSO negative control (**b**,**e**); 125 µg/mL UA positive control (**c**,**f**). Statistical analysis of 3/7 caspases activity in blood cells (**g**) and CLS-354 tumor cells (**h**) after 24 h treatment with F-UBA; * $p < 0.05$ and ** $p < 0.01$ represent significant statistical differences between controls and film made by paired samples *t*-test. V—viability; EA—early apoptosis; C1—negative control with 1% dimethyl sulfoxide (DMSO); C2UA—positive control with 125 µg/mL usnic acid (UA); F-UBA—UBA-loaded mucoadhesive oral film; UBA—*U. barbata* dry acetone extract.

In blood cell cultures, after 24 h treatment with F-UBA, we observed significantly decreased values of caspase-3/7 activation mechanisms compared with negative and positive controls: 22.54 ± 1.57 vs. C1: 29.26 ± 1.97, $p < 0.05$; C2UA: 44.74 ± 0.41, $p < 0.01$ (Figure 5a–c,g).

Proapoptotic signal after F-UBA treatment in CLS-354 tumor cell line had significant increasing relative to 1% DMSO negative control and 125 µg/mL UA positive control: 1.79 ± 0.45; vs. 21.88 ± 5.09, $p < 0.05$; 27.02 ± 1.64, $p < 0.01$ (Figure 5d–f,h).

3.4.3. Nuclear Shrinkage and Autophagy

The presence of pyknotic nuclei (stained with Hoechst 33342) and lysosomal activity (evidenced with AO) in blood cells and CLS-354 tumor cells after 24 h treatment with F-UBA is displayed in Figure 6.

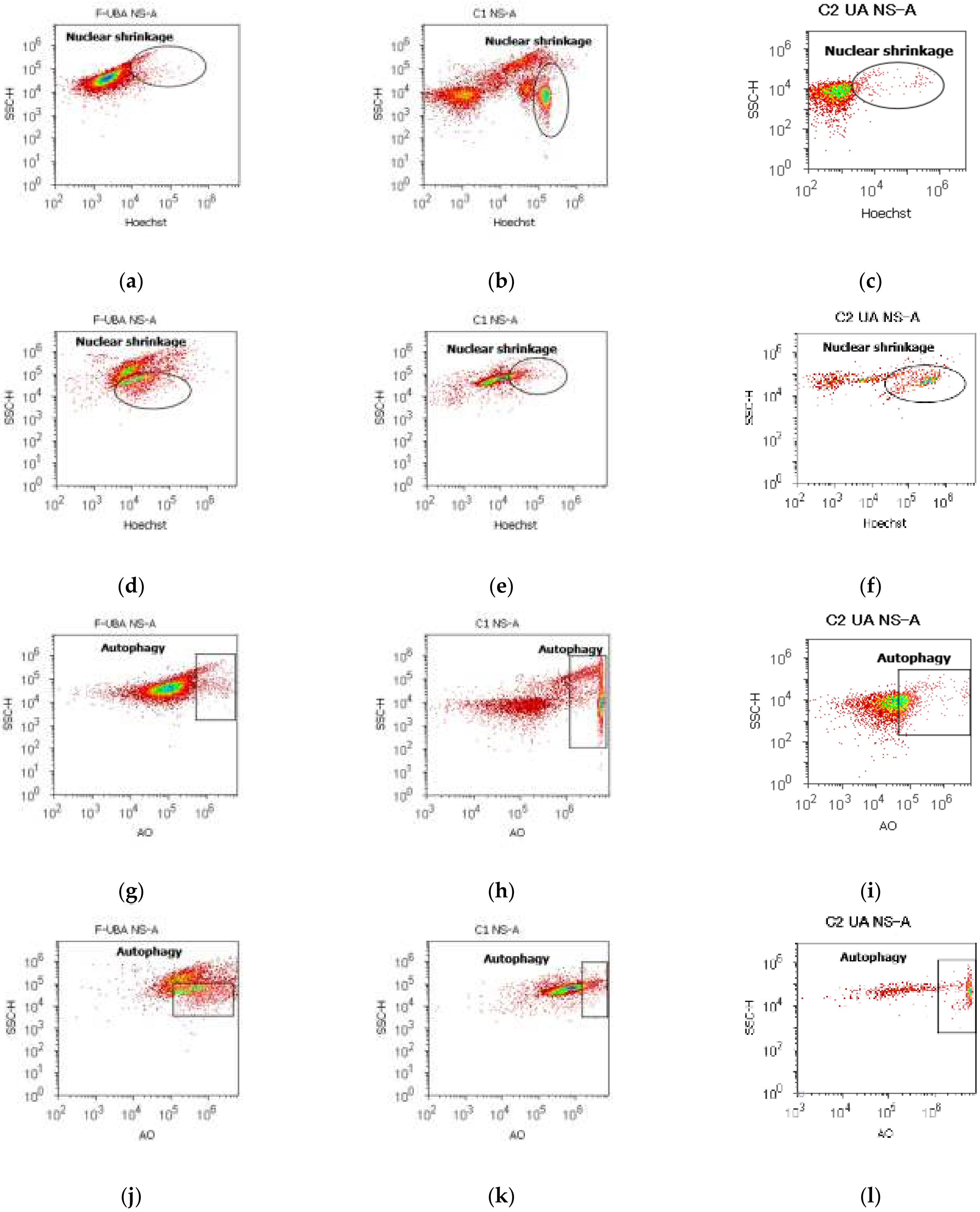

(**a**) (**b**) (**c**)

(**d**) (**e**) (**f**)

(**g**) (**h**) (**i**)

(**j**) (**k**) (**l**)

Figure 6. *Cont.*

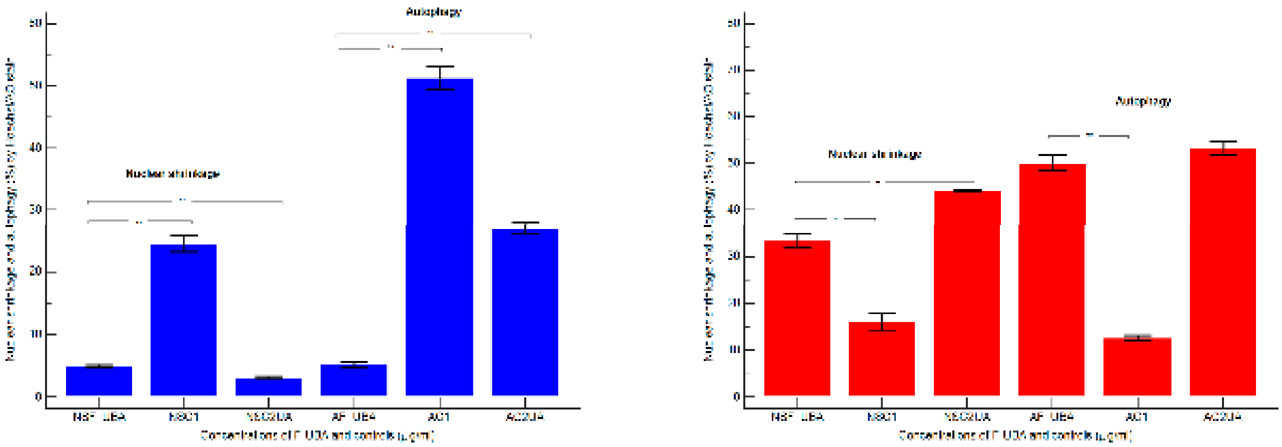

(**m**) (**n**)

Figure 6. Nuclear shrinkage (**a**–**f**) and lysosomal activity (**g**–**l**) in blood cells (**a**–**c**,**g**–**i**) and CLS-354 tumor cells (**d**–**f**,**j**–**l**) after 24 h treatment with F-UBA. Hoechst patterns of F-UBA (**a**,**d**); acridine range patterns of F-UBA (**g**,**j**); 1% DMSO negative control (**b**,**e**,**h**,**k**); 125 µg/mL UA positive control (**c**,**f**,**i**,**l**). F-UBA—UBA-loaded mucoadhesive oral film; UBA—*U. barbata* dry acetone extract. Statistical analysis of nuclear shrinkage and autophagy in normal blood cells (**m**) and CLS-354 tumor cells (**n**) after 24 h treatment with F-UBA; * $p < 0.05$ and ** $p < 0.01$ represent significant statistical differences between controls and sample made by paired samples *t*-test. NS—nuclear shrinkage; A—autophagy; C1—negative control with 1% dimethyl sulfoxide (DMSO); C2UA—positive control with 125 µg/mL usnic acid (UA); F-UBA—UBA-loaded mucoadhesive oral film; UBA—*U. barbata* dry acetone extract.

In normal blood cells, F-UBA remarkably diminished the nuclear condensation (4.94 ± 0.39, $p < 0.01$) compared to 1% DMSO negative control (24.50 ± 2.21), as shown in Figure 6a,b,m. However, NS are higher than 125 µg/mL UA positive control (3.19 ± 0.30, $p < 0.01$). The levels of lysosomal activity were considerably lower than the controls: 5.22 ± 0.77; vs. C1: 51.30 ± 3.25; C2UA: 27.05 ± 1.52, $p < 0.01$ (Figure 6g–i,n).

In CLS-354 tumor cells, after F-UBA treatment, the chromatin shrinkage (NS), and autophagy (A) by Hoechst 33342/AO dual stain, recorded a substantial augmentation compared to C1DMSO negative control: NS: 33.31 ± 2.69 vs. 16.11 ± 3.11, $p < 0.05$; A: 50.07 ± 2.89 vs. 12.57 ± 0.92, $p < 0.01$ (Figure 6d,e,j,k,n). However, the nuclear condensation induced by F-UBA was significantly lower than C2UA positive control: 33.31 ± 2.69 vs. 44.03 ± 0.36; $p < 0.05$ (Figure 6d,f,n).

3.4.4. Cell Cycle Analysis

Cell cycle analysis was performed by PI/RNase stain (Figure 7) to explore the effects of UBA-loaded mucoadhesive oral films in normal blood cells and CLS-354 tumor cells.

In blood cells (Figure 7a,b,g,i) F-UBA induced a lower cell cycle arrest in G1/G0 phase (85.87 ± 1.30, $p < 0.05$) and DNA synthesis (1.40 ± 0.65, $p < 0.05$) than C1DMSO negative control (88.52 ± 0.54, respectively 4.76 ± 0.68).

In CLS-354 tumor cells, F-UBA treatment reported slowly higher values of cell cycle arrest in G0/G1 than negative control: 93.33 ± 2.42 vs. 92.13 ± 1.61, $p \geq 0.05$ (Figure 7d,e,h,j). However, DNA synthesis significantly decreased compared to 1% DMSO: 1.05 ± 0.14 vs. 5.47 ± 0.83, $p < 0.05$ (Figure 7d,e,h,j).

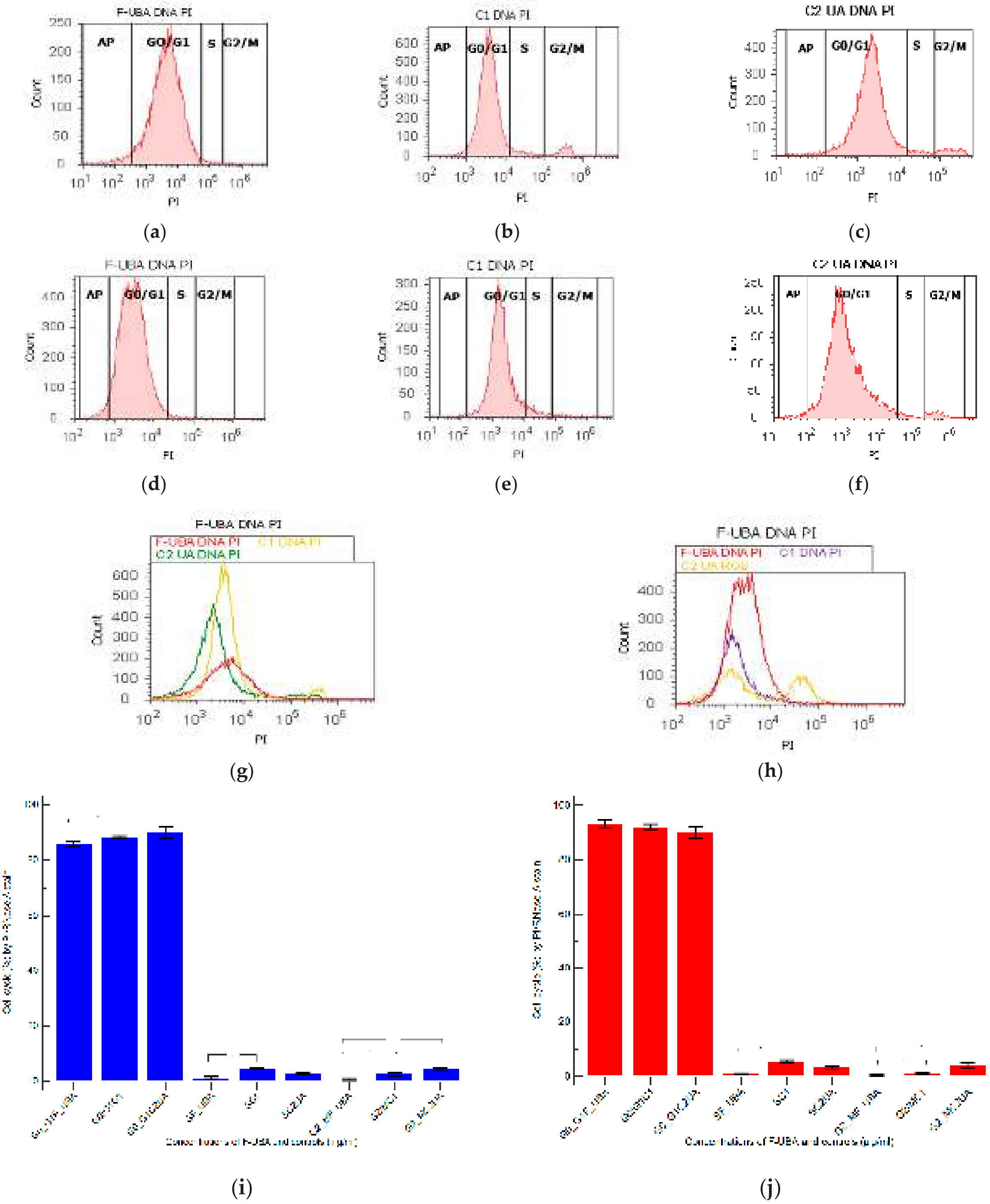

(**a**) (**b**) (**c**)

(**d**) (**e**) (**f**)

(**g**) (**h**)

(**i**) (**j**)

Figure 7. Cell cycle analysis in normal blood cells (**a**–**c**) and CLS-354 tumor cells (**d**–**f**) after 24 h treatment with F-UBA; PI/RNase patterns of F-UBA (**a**,**d**); 1% DMSO negative control (**b**,**e**); 125 µg/mL UA positive control (**c**,**f**); F-UBA and both controls extrapolated on PI axis (**g**,**h**). AP—apoptosis (subG0/G1); PI—propidium iodide; S—synthesis of cell cycle phases. Statistical analysis of G0/G1, synthesis (S), and G2/M phases of cell cycle in normal blood cell cultures (**i**) and CLS-354 tumor cell line (**j**) after 24 h treatment with F-UBA; * $p < 0.05$ and ** $p < 0.01$ represent significant statistical differences between controls and sample made by paired samples *t*-test. C1—negative control with 1% dimethyl sulfoxide (DMSO); C2UA—positive control with 125 µg/mL usnic acid (UA); F-UBA—UBA-loaded mucoadhesive oral film; UBA—*U. barbata* dry acetone extract.

3.4.5. Apoptosis

Morphology and cell membrane integrity examination with annexin V-FITC/ PI staining after 24 h treatment with F-UBA in normal blood cells and CLS-354 tumor cells are presented in Figure 8.

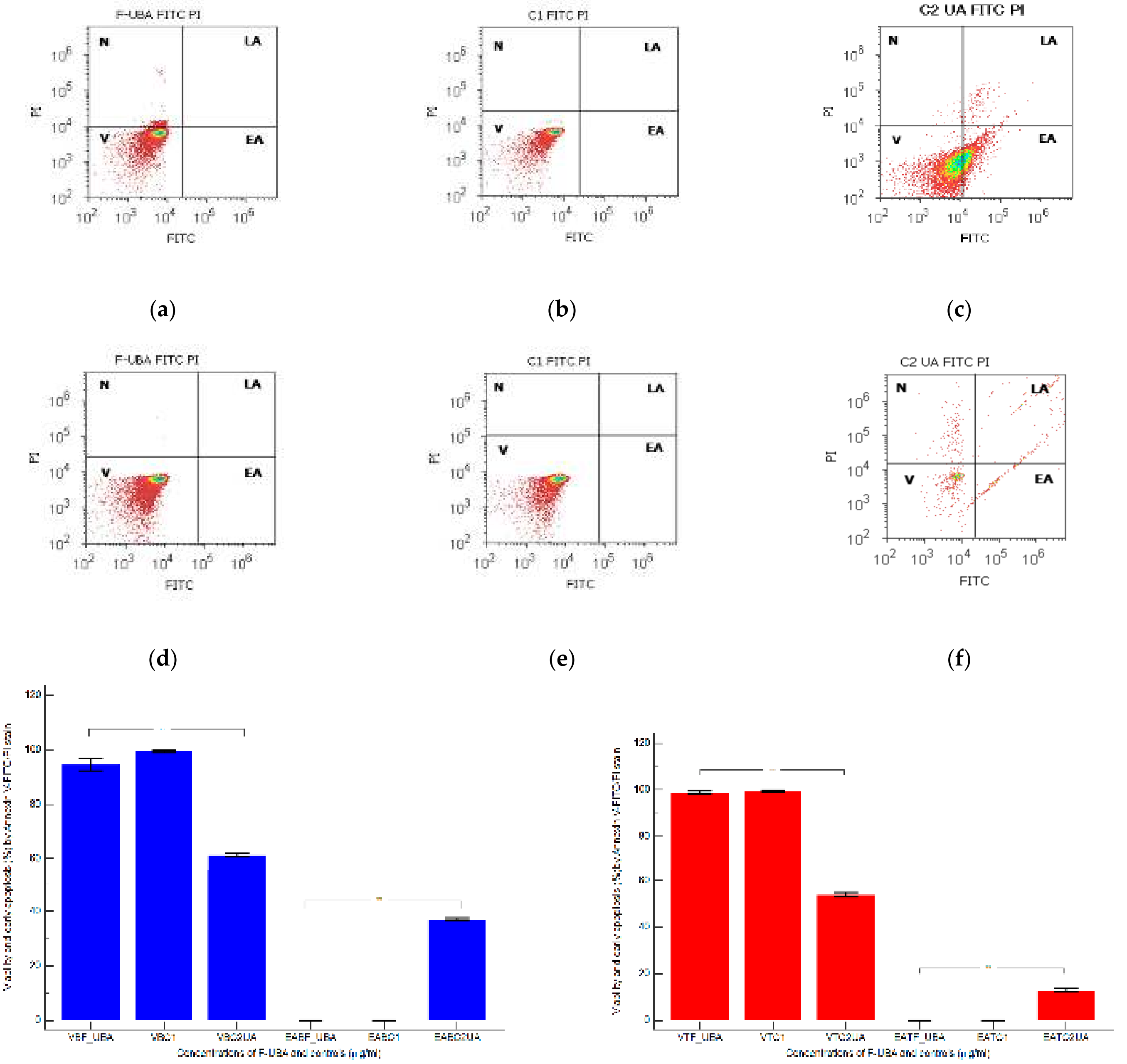

(**a**) (**b**) (**c**)

(**d**) (**e**) (**f**)

(**g**) (**h**)

Figure 8. Cell apoptosis in normal blood cells (**a**–**c**) and CLS-354 tumor cells (**d**–**f**) after 24 h treatment with F-UBA; Annexin V-FITC/PI patterns of F-UBA (**a**,**d**); 1% DMSO negative control (**b**,**e**); 125 μg/mL UA positive control (**c**,**f**). Statistical analysis of cell apoptosis in normal blood cell cultures (**g**) and CLS-354 tumor cell line (**h**) after 24 h treatment with F-UBA; ** $p < 0.01$ represents significant statistical differences between controls and sample made by paired samples *t*-test. V—viability; EA—early apoptosis; C1—negative control with 1% dimethyl sulfoxide (DMSO); C2UA—positive control with 125 μg/mL usnic acid (UA); F-UBA—UBA-loaded mucoadhesive oral film; UBA—*U. barbata* dry acetone extract.

The F-UBA treatment did not induce early cell apoptosis (EA) in normal blood cells compared to C2UA positive control, which determined a considerable level of EA: 37.04 ± 0.66, $p < 0.01$. Therefore, cell viability after F-UBA treatment is significantly higher than 125 µg/mL UA positive control: 94.52 ± 3.85 vs. 61.43 ± 0.88, $p < 0.01$ (Figure 8a,c,g).

The CLS-354 tumor cell viability after F-UBA treatment remained substantially augmented than positive control C2UA: 98.77 ± 1.15 vs. 54.05 ± 1.68, $p < 0.01$ (Figure 8d,f,h). In the CLS-354 tumor cell line, only C2UA determined early apoptosis. EA level is lower than normal blood cells but significantly higher than F-UBA and 1% DMSO (12.92 ± 1.35 vs. 0.00 ± 0.00 $p < 0.01$).

3.4.6. Cell Proliferation

The effects of F-UBA in normal blood cells and CLS-354 tumor cells (DNA synthesis and fragmentation) by EdU incorporation were displayed in Figure 9.

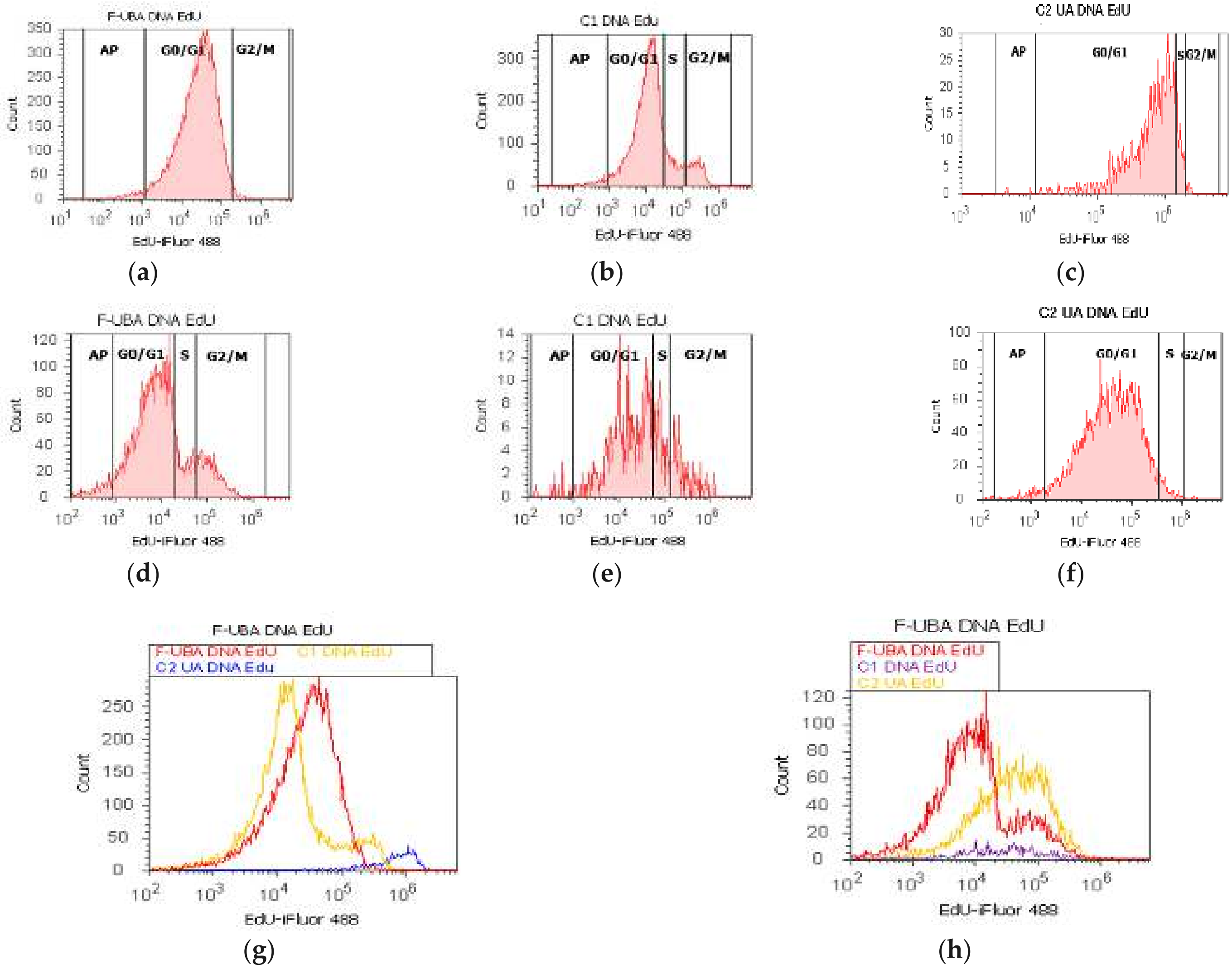

(a) (b) (c)

(d) (e) (f)

(g) (h)

Figure 9. *Cont.*

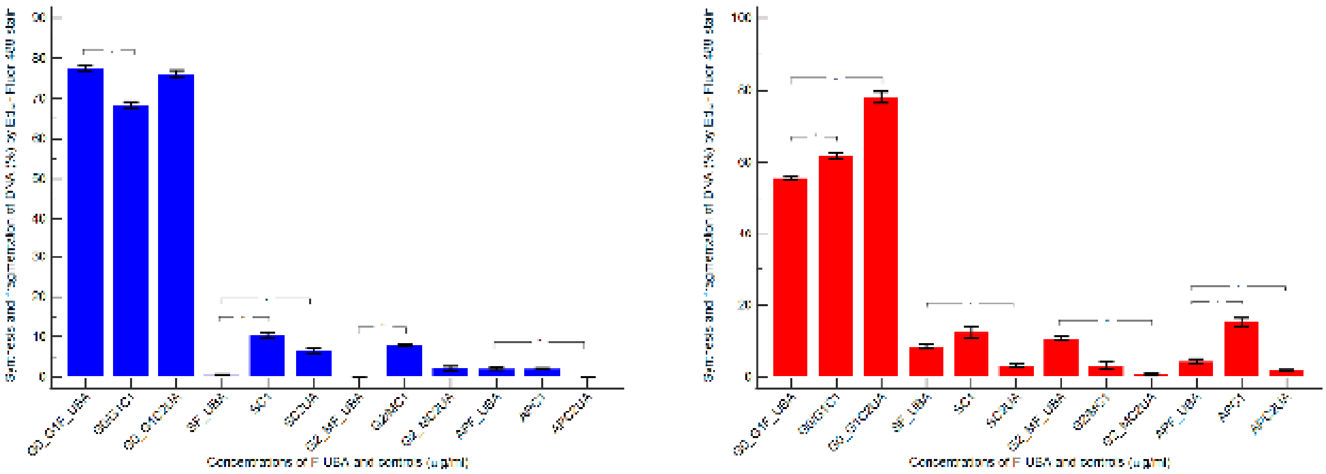

(i) (j)

Figure 9. Synthesis (S) and fragmentation of DNA (subG0/G1) in normal blood cells (**a**–**c**) and CLS-354 tumor cells (**d**–**f**) after 24 h treatment with F-UBA; EdU-iFluor 488 patterns of F-UBA (**a**,**d**); 1% DMSO negative control (**b**,**e**); 125 µg/mL UA positive control (**c**,**f**). F-UBA and controls extrapolated on EdU-iFluor 488 axis (**g**,**h**). AP—apoptosis (subG0/G1). Statistical analysis of cell proliferation in blood cell cultures (**i**) and CLS-354 tumor cell line (**j**) after 24 h treatment with F-UBA; * $p < 0.05$ and ** $p < 0.01$ represent significant statistical differences between controls and sample made by paired samples *t*-test. C1—negative control with 1% dimethyl sulfoxide (DMSO); C2UA—positive control with 125 µg/mL usnic acid (UA); F-UBA—UBA-loaded mucoadhesive oral film; UBA—*U. barbata* dry acetone extract.

Levels of DNA synthesis, after 24 h of F-UBA treatment in normal blood cells, were considerably diminished than both controls (0.59 ± 0.05 vs. C1: 10.36 ± 1.21; $p < 0.01$; C2UA: 6.49 ± 1.25, $p < 0.05$). Fractional DNA implied in apoptosis, reported significantly higher values compared to positive control: 2.11 ± 0.56 vs. 0.00 ± 0.00, $p < 0.05$ (Figure 9a–c,g,i).

On the other hand, in CLS-354 tumor cells, UBA-loaded mucoadhesive oral films determined slowly lower levels of DNA synthesis than 1% DMSO negative control (8.55 ± 0.96 vs. C1: 12.44 ± 2.80, $p \geq 0.05$) and significantly higher than positive control with 125 µg/mL usnic acid (8.55 ± 0.96 vs. 3.14 ± 0.50, $p < 0.05$). However, fractional DNA (subG0/G1) substantially decreased compared to negative control with 1% dimethyl sulfoxide: 4.49 ± 0.87 vs. 15.18 ± 2.17, $p < 0.05$ (Figure 9d–f,h,j).

3.4.7. Principal Component Analysis

Principal component analysis (PCA) was performed for UBA-loaded mucoadhesive oral patches and both controls (C1-DMSO and C2UA) and variable parameters determined in both cell types (blood cells and CLS-354 tumor cells) according to the correlation matrix and the PCA–correlation circle in the Supplementary Material.

Two principal components explained the total data variance, with 69.38% attributed to the first (PC1) and 30.62% to the second (PC2). PC1 is associated with controls (C1-DMSO and C2UA), caspase 3/7 activity in both cell types (blood cells and CLS-354 tumor cells), and ROS levels in CLS-354 cells. At the same time, PC2 related to F-UBA mucoadhesive oral films and ROS levels in normal blood cells (Figure 10).

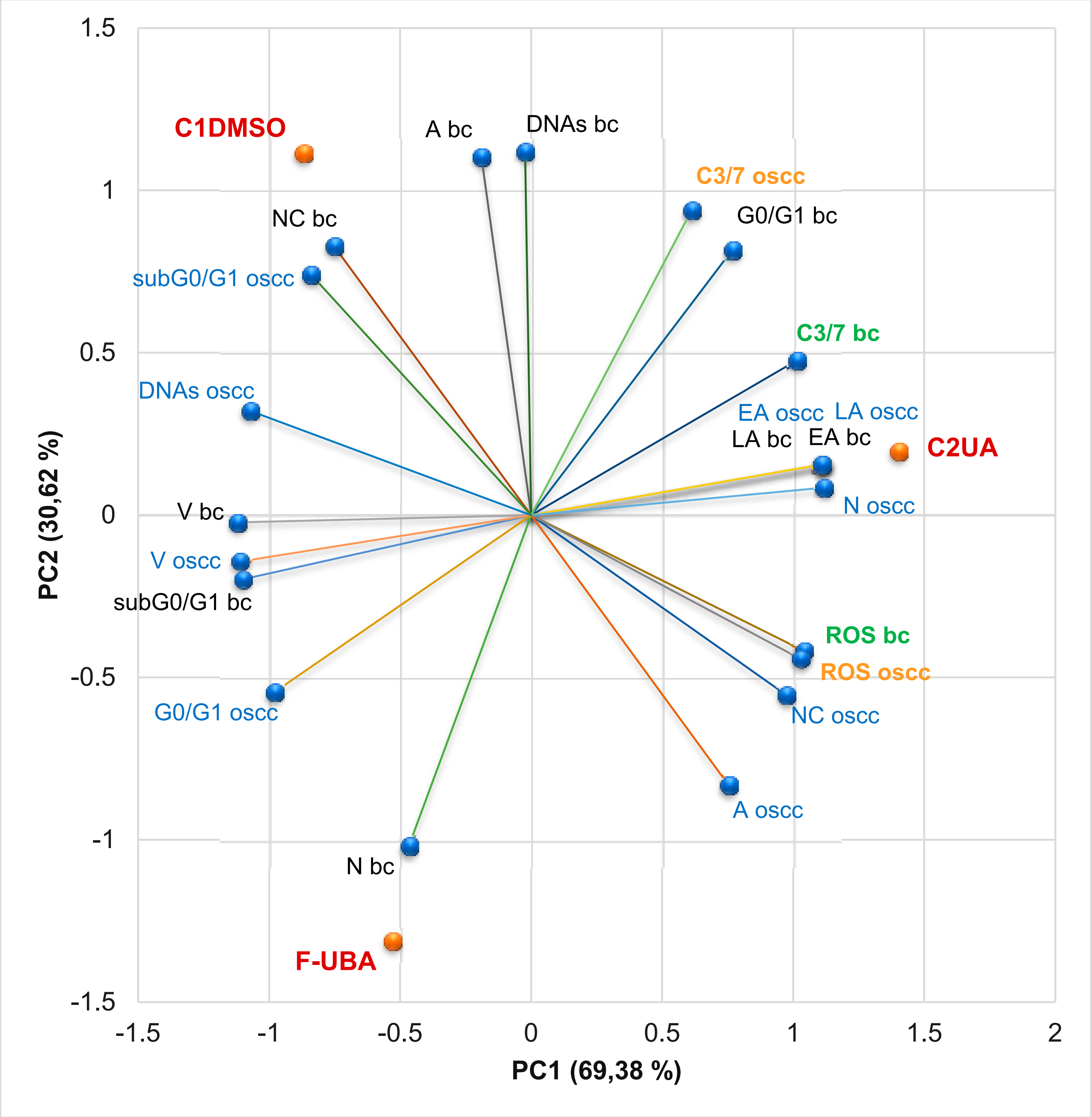

Figure 10. PCA-Correlation biplot between mechanisms (caspase 3/7 activity and cellular oxidative stress) and processes induced by F-UBA and both controls (C1-DMSO and C2UA) in blood cells (bc) and CLS-354 tumor cells (oscc). V—viability, EA—early apoptosis, LA—late apoptosis, N—necrosis, NC—nuclear condensation, A—autophagy, DNAs—DNA synthesis, G0/G1—cell cycle arrest in G0/G1, ROS—oxidative stress, C3/7—caspase 3/7 activity, F-UBA—UBA-loaded mucoadhesive oral films.

Figure 10 shows that in normal blood cells, caspase 3/7 activation (C3/7) highly positively correlates with early and late apoptosis ($r = 0.955$, $p > 0.05$) and cell cycle arrest in G0/G1 ($r = 0.930$, $p > 0.05$). C3/7 is also moderately correlated with oxidative stress ($r = 0.681$, $p > 0.05$). It shows a strong negative correlation with subG0/G1 ($r = -0.966$, $p > 0.05$) and a moderate one with necrosis ($r = -0.764$, $p > 0.05$). Oxidative stress in normal cells is considerably positively correlated with EA and LA ($r = 0.867$, $p > 0.05$) and negatively correlated with nuclear condensation and subG0/G1 ($r = -0.900$ and -0.848, $p > 0.05$).

In CLS-354 tumor cells, ROS level is substantially positively correlated with nuclear condensation, autophagy, necrosis, and early and late apoptosis ($r = 0.994$, 0.919, 0.886, and 0.854, $p > 0.05$), and negatively correlated with DNA synthesis and subG0/G1 ($r = -0.993$ and -0.951, $p > 0.05$). It shows a moderate negative correlation with cell cycle arrest in G0/G1 ($r = -0.610$, $p > 0.05$) and a minimal positive one with C3/7 ($r = 0.170$, $p > 0.05$). Caspase 3/7 activity is highly negatively correlated with cell cycle arrest in G0/G1 ($r = -0.884$, $p > 0.05$) and moderately positively correlated with necrosis and early and late apoptosis ($r = 0.608$ and 0.658, $p > 0.05$).

Therefore, the placement of F-UBA and both controls (C1-DMSO and C2UA) in the PCA-biplot (Figure 10) was explained, highlighting the corresponding processes triggered in the CLS-354 cancer cell line and normal blood cell cultures.

3.5. Antimicrobial Activity

Minimum inhibitory concentrations (MICs) are defined as the lowest concentration of an antimicrobial that will inhibit the visible growth of a microorganism after overnight incubation [71]. According to Phe et al. [72], regarding *S. aureus*, MIC of CTR is 4–8 µg/mL. On *P. aeruginosa*, MIC is substantially higher, varying from 16 µg/mL to over 256 µg/mL (for the highest resistant strains) [73].

The results are displayed in Table 2.

The first data from Table 2 show the standard antibiotic (CTR), antifungal drug (TRF), and F-UBA microdilutions used.

The following data from Table 2 show that the colors of standard antibiotics correlate with their inhibiting power and are directly proportional to their concentration. We can observe that CTR microdilutions are over MIC for both tested bacteria. However, S. aureus sensibility at CTR is higher than P. aeruginosa.

The inhibitory activity of UBA-loaded mucoadhesive oral films is higher on *P. aeruginosa* than on *S. aureus.* Therefore, the inhibitory activity of F-UBA of [3.497–0.055] mg/mL against *S. aureus* is similar to CTR of [0.755–0.023] mg/mL. On *P. aeruginosa*, F-UBA of 3.487 mg/mL acts similarly with CTR of 1.603 mg/mL; lower film concentrations of [1.749–0.055] mg/mL have similar effects with CTR of [1.511–0.023] mg/mL.

Data from Table 2 show TRF fungicidal effect on both *Candida* sp. [63] in the entire microdilutions domain.

The F-UBA acts similarly on both *Candida* sp. in a dose-dependent manner. After 24 h incubation with 3.497 mg/mL F-UBA, both *Candida* sp. strains are partially dead [63]. After contact with 1.749 mg/mL F-UBA both fungal strains are alive but do not proliferate. The following F-UBA concentrations [0.874–0.055] mg/mL induced low to moderate proliferation in both *Candida* sp. (Table 2).

Table 2. Initial concentrations and microdilutions of standard antibacterial and antifungal drugs and sample (F-UBA) and antimicrobial activity of UBA-loaded mucoadhesive oral films.

Micro-Dilution	**CTR (mg/mL)** **30.230 ± 0.630**	**CTR (mg/mL)** **122.330 ± 0.850**	**TRF (mg/mL)** **10.050 ± 0.180**	**F-UBA (mg/mL)** **70 ± 3.540**
1	1.511 ± 0.043	6.117 ± 0.042	0.500 ± 0.009	3.497 ± 0.172
2	0.755 ± 0.022	4.893 ± 0.034	0.250 ± 0.004	1.749 ± 0.086
3	0.377 ± 0.011	3.914 ± 0.027	0.125 ± 0.002	0.874 ± 0.043
4	0.188 ± 0.005	3.131 ± 0.021	0.061 ± 0.001	0.438 ± 0.022
5	0.094 ± 0.002	2.505 ± 0.017	0.031 ± 0.001	0.219 ± 0.011
6	0.047 ± 0.002	2.004 ± 0.014	0.015 ± 0.001	0.110 ± 0.006
7	0.023 ± 0.001	1.603 ± 0.011	0.007 ± 0.001	0.055 ± 0.003

S. aureus				*P. aeruginosa*			
F-UBA		**CTR**		**F-UBA**		**CTR**	
A *	**B ****	**A ***	**B ****	**A ***	**B ****	**A ***	**B ****

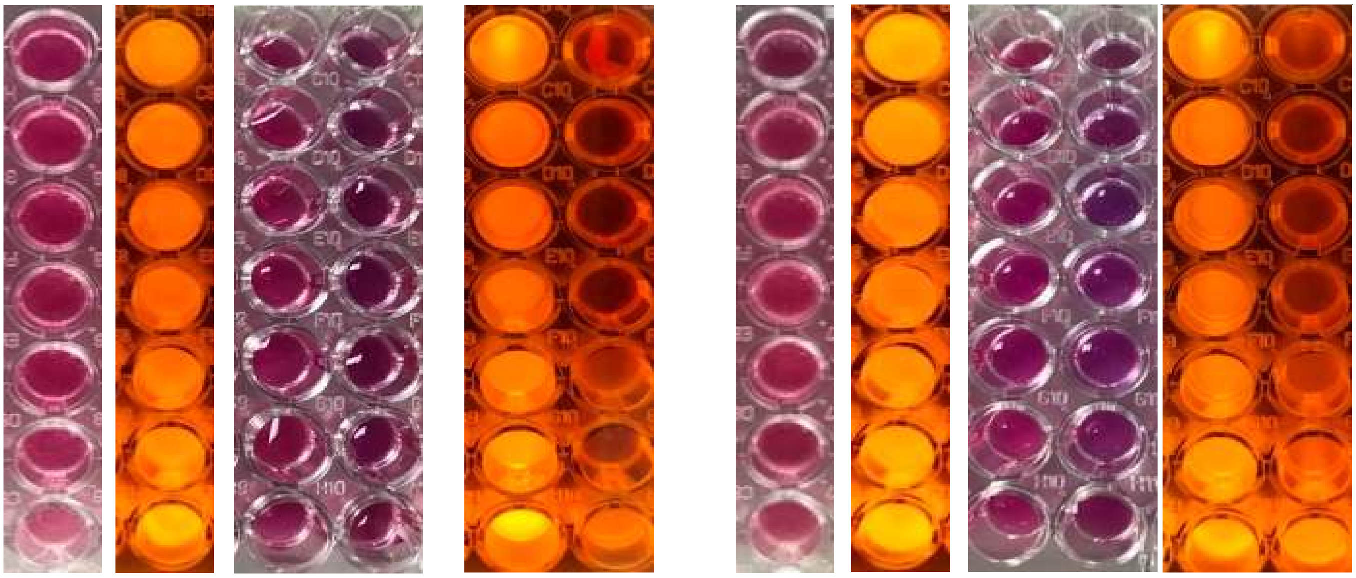

🟦 🟦 🟪 🟪 🟥 🟥 ⬜ *

C. albicans TRF	*C. albicans* F-UBA	*C. parapsilosis* TRF	*C. parapsilosis* F-UBA	Color ***	Score ***	Signification ***
				■	0	Blue— cells are dead
				■	1	Violet-blue— cells are partially dead
				■	2	Violet— cells are alive; no proliferation
				■	3	Light-violet— low proliferation
				■	4	Dark pink— moderate proliferation
				■	5	Pink— fast proliferation
				■	6	Light pink— very fast proliferation

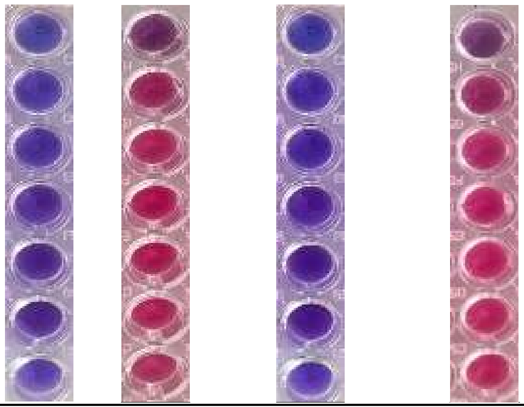

* Interpretation of obtained results adapted from Madushan et al. [61] (A); blue: excellent; light blue—very good, violet—good, purple pink—moderate, light pink—low, pink—very low, white—no effect; CTR—Ceftriaxone, F-UBA—Mucoadhesive film with *U. barbata* dry extract in acetone. ** Well plates examined at a wavelength of 470 nm (B). *** Results interpreting adapted from Bitacura et al. [63]. TRF—Terbinafine.

4. Discussion

In the plant kingdom, lichens are promising sources of antimicrobial and anticancer drugs [74], and *Usnea* sp. is one of the most known representatives as a potent phytomedicine [75]. For almost 6 years, our team studied *U. barbata* from the Călimani mountains. Obtaining various *U. barbata* extracts, quantifying their secondary metabolites, and investigating their pharmacological potential, we aimed to select suitable ones for pharmaceutical formulations. HPLC-DAD analysis of *U. barbata* dry acetone extract (obtained with a yield of 6.36%) shows 282.78 µg/g of usnic acid from a total phenolic content of 862.843 µg/g. Using a complex UHPLC-ESI-OT-MS-MS analysis, Salgado et al. [76] identified other phenolic secondary metabolites which would be extracted in acetone: depsides (e.q., atranorin, lecanoric acid, barbatolic acid) and depsidones (e.q., salazinic acid, norstictic acid). Due to its phenolic constituents, UBA has significant antiradical properties [34,77]. The pharmacological potential of *U. barbata* dry acetone extract was investigated first on *A. salina* larvae as cytotoxicity prescreen and then on the tongue squamous cell carcinoma (CAL-27 cell line) [24,25,77]. Compared to normal fibroblasts (V-79 cell line) [25], UBA cytotoxic effects quantified by MTT assay were higher on CAL-27 tumor cells. The wound healing action was noticeable on tumor cells and minimal on normal cells; the colony formation was substantially inhibited in tumor cells and considerably induced in normal ones. The dry acetone extract acted as a pro-oxidant, causing intense ROS production, and thus stimulating the enzymatic activity of SOD, CAT, and GPx in CAL-27 tumor cells. On V-79 fibroblasts, it acted as an antioxidant, diminishing the levels of antioxidant defense (SOD and CAT) and lipid peroxidation (expressed as MDA levels) [25]. Numerous studies from the scientific literature described in vitro and in vivo studies on liver cells, highlighting the usnic acid hepatotoxicity; therefore, we examined the UBA effects on blood cell cultures due to their various cell types, nucleate white blood cells (WBC), and nucleus-free platelets and red blood cells (RBC) containing neither mitochondria nor nucleus. The *U. barbata* dry acetone extract displayed dose-dependent cytotoxicity; high doses promoted apoptosis and DNA damage in human blood cells by enhancing ROS levels [53]. Only WBC are related to DNA damage.

Moreover, we evaluated the UBA antimicrobial potential on bacterial and fungal strains responsible for opportunistic oral cavity infections in elderly and/or immunocompromised patients [78–80]: *S. aureus*, *S. pneumoniae*, *S. pyogenes*, *Enterococcus* sp., other Gram-positive bacteria isolated from oral cavity and pharynx (*S. epidermidis*, *S. oralis*, *S. intermedius*) and *P. aeruginosa* [34,81–83]. It was also tested on *C. albicans and C. parapsilosis* [83]. Usnic acid and all phenolic compounds extracted in acetone have antibacterial and antifungal properties and could act synergistically in UBA, and its inhibitory effects are dose-dependent.

All UBA pharmacological activities could have promising applications in oral medicine; therefore, it was incorporated into mucoadhesive oral films. Through physico-chemical and pharmacotechnical analyses, F-UBA properties were compared with reference ones to evaluate their suitability for application to the oral mucosa. A slight weight difference was observed due to the UBA load in the R formulation, and an appropriate uniformity of the films belonging to the same batch was registered, proving that a homogenous drug loading was achieved. The F-UBA thickness allows application on the oral mucosa, being easily acceptable by patients, and its values are included in the optimal range of 0.005–0.200 mm [84]. This property correlates to UBA loaded and is influenced by the type and amount of plasticizer used because the polymer can occasionally increase the film thickness [85]. The folding endurance (expressed as the number of folds needed to break the films or develop visible cracks) is a brittleness indicator [86]. The obtained values over 300 evidence excellent flexibility and hardness due to PEG 400 and HPMC used in the formulations, confirming that UBA incorporation did not modify the film resistance. Pandey and Chauhan [87] developed fast-dissolving sublingual films with Zolmitriptan, and Winarty et al. [88] optimized buccal films with Diltiazem with a similar folding endurance. Tensile strength is the force required to break the oral films [89], while elongation is the film length maximal deformation without damaging it [90]. The mean tensile strength and elongation are also very close between the F-UBA and R, indicating that mucoadhesive oral films exhibit good elastic properties due to HPMC as a matrix-former. The plasticizer increases the flexibility of polymer macromolecules (or macromolecular segments) by loosening the strength of intermolecular tensions [91,92]. Both F-UBA parameters are included in the range of 2.27–4.59 kg/mm^2 tensile strength and 31.85–54.64% elongation, reported by Kraisit et al. [93] for their buccal films with propranolol nanoparticles, displaying a solid film structure associated with substantial mechanical resistance and flexibility.

The efficiency of a plasticizer agent in mucoadhesive film formulations is primarily determined by the amount used and the polymer–plasticizer interaction. When it comes to an aqueous dispersion, the proportion and amount of partition are influenced by the plasticizer's solubility in water and its affinity for the polymer. The moisture content affects the mucoadhesive film's physical stability, preventing them from being brittle. The film has retained water due to the plasticizer hygroscopic attributes, and less than 5% moisture loss is required for better physical strength [94]. As expected, UBA inclusion in the polymer matrix does not considerably change the humidity content of the film.

The neutral pH confirms that mucoadhesive oral films should not irritate the oral mucosa [95]. In addition, a fast disintegration performance was registered for both formulations, resulting from the intense hydrophilicity of HPMC used as a film-forming polymer. The presence of UBA in the film's structure delayed the disintegration time by only 8 s compared to the References. The measured swelling rate agreed with the expectations, and no significant difference between both films was assessed. Hashemi et al. [31] optimized oral mucoadhesive patches containing *M. communis* had a disintegration time from 3 h to over 24 h and a swelling ratio between 136–272%.

The presence of hydroxyl groups in the HPMC molecule ensures the matrix stability of the swollen hydrophilic polymer [96]. Soon after swelling starts, the bioadhesion occurs, but the link created is not very strong. Optimal swelling and mucoadhesion only happen at the polymer's specific hydration level [97,98] and the amount of film-forming polymer and plasticizer strongly influences the retention time over mucosa [99]. It rises with the hydration degree [100], but overhydration causes a rapid decline of mucoadhesive strength due to disentanglement at the polymer/tissue interface. Vasantha et al. [101] developed Eudragit-based mucoadhesive buccal patches of salbutamol sulfate with a mucoadhesion time of 101–110 min.

All pharmacotechnical parameters indicated no substantial differences between F-UBA and R, confirming that UBA-loaded mucoadhesive oral films are suitable for application to the oral mucosa.

Numerous authors, knowing the bioactivities of plant extracts incorporated in various polymeric films, described only their physico-chemical and pharmacotechnical properties [29,31,102].

In our study, UBA-loaded mucoadhesive oral films have neutral pH, and fast disintegration permitted pharmacological potential evaluation through in vivo and in vitro studies.

The F-UBA investigation was performed using similar studies evaluating *U. barbata* dry acetone extract. Thus, the cytotoxicity prescreen was performed on A. salina larvae. Anticancer activity was assessed on a similar OSCC cell line (CLS-354, mouth epithelial squamous cell carcinoma). Blood cell cultures were used as normal cells because buccal mucosa has a substantial blood supply and is permeable for most blood cells [103]. The two structural layers of the oral mucosa are the outer epithelium and the underlying lamina propria (LP). The buccal epithelium is a physical and chemical barrier, but WBCs pass through the epithelium to LP, constituting the immunological defense of the oral cavity. Conventionally, resident cells in the oral mucosa are the ones of stromal origin, such as gingival keratinocytes, fibroblasts, and periodontal ligament cells [104]. Migratory cells are lymphocytes (with T cells) and segmented cells (polymorphonuclear, including neutrophils and eosinophils). In oral cancer, the lymphocytes number decreases [105].

In addition, various substances go through the oral mucosa by simple diffusion, reaching the capillary area under normal conditions. The UBA-loaded mucoadhesive films are projected to remain on oral mucosa different lesions for 85 min. Therefore, it is essential to know their effects on blood cells because sensitization and bleeding are much more frequent in the buccal mucosa. The blood samples were collected from a single donor (the same as previously described in UBA biological studies).

The UBA has a considerable UA content, and F-UBA action is expected to be similar to that of the positive control (C2UA). Data analysis shows that F-UBA selectively affected tumor cells. Compared with C1DMSO negative control, it increased ROS levels, nuclear condensation, autophagy, and cell cycle arrest in G0/G1 and diminished DNA synthesis in the CLS-354 (oral epithelial squamous cell carcinoma) tumor cell line. Inducing high oxidative stress, F-UBA triggered the previously mentioned processes that lead to CLS-354 cancer cells' death. The F-UBA exhibited a protective effect on normal blood cells, diminishing the apoptotic processes due to 1% DMSO: caspase 3/7 activation, cell cycle arrest in G0/G1, nuclear condensation, and autophagy.

Usnic acid, the main bioactive metabolite in the *Usnea* lichens, is soluble in acetone and is found in a significant amount in the *U. barbata* dry acetone extract [34]. Assessing the effects of UA (100–300) mg/kg on adult male rats, Alahmadi et al. [106] reported that hepatocytes had an increased lipid droplet, swollen mitochondria, and fragmented rough endoplasmic reticulum and cell membrane damage. These harmful effects induced by UA on the cellular level are similar to the present study's results on *A. salina* larvae, used as an animal model. After 24 h of exposure to F-UBA, the lipids accumulation in the digestive tube and their progressive penetration in neighboring tissues lead to massive cellular damage and brine shrimp larvae death after 48 h.

Nevertheless, UA exhibits beneficial bioactivities (antimicrobial, anticancer, antioxidant), displaying a dual redox behavior (pro-oxidant in tumor cells and antioxidant, protective, in normal cells [107], and the present results confirmed it. Andania et al. also proved the usnic acid antitumor effect on the OSCC cell line (HSC-3). In *Usnea* sp. extracts, the primary quantified metabolite is usnic acid; the others are not commonly determined individually and are quantified as total phenolic content. The dry acetone extract loaded in F-UBA contains total phenolic compounds of 862.84 mg PyE/g, from which 241.83 mg/g is usnic acid [34]. The action of F-UBA on CLS-354 tumor cells through high cellular oxidative stress was similar to usnic acid of 125 mg/mL; it had a lower intensity due to the significant difference in UA content. The usnic acid phenolic structure is responsible for all bioactivities at the cellular level [108–110].

The antimicrobial activity of oral films containing plant extracts is evaluated through various methods. For example, Gajdziok et al. [111] applied a microbial suspension (*S. aureus* and *C. albicans*) on the surface of their mucoadhesive oral patches. After incubation, the patches were examined by direct imprinting on a solid culture medium; the growth of bacteria and yeast strains was observed and expressed as the number of colony-forming units (CFU) on the surface of the imprint. Chiaoprakobkij et al. [33] performed antibacterial studies on *S. aureus* and *E. coli*, counting the living bacterial cells on the films loaded with *Garcinia mangostana* L. extract. Other authors also selected *S. aureus* and *E. coli* for antibacterial activity evaluation of their poly(vinyl alcohol)/plant extracts films [112]. They measured the inhibition zone diameter (IZD), and the interpretation of the results used Poly (vinil alcohol) as a reference. It had no inhibitory activity (IZD = 0 cm) and was noted with (−)—no action. The highest values were registered as (++++ and +++)—Very good activity, followed, in decreasing order, by (++)—good activity and (+)—weak activity. The appreciation of their inhibitory activity was the most part, proving in qualitative mode this property of the films with plant extracts without using a standard antibiotic drug [112].

In a great measure, these qualificatives are similar to the resazurin dye chart for a rapid evaluation of antibacterial [61] and antifungal [63] activities. Our study examined the F-UBA inhibitory effects against the most common bacterial and fungal species implicated in oral infections in immunocompromised patients.

Directly applied to the oral malignant lesion, the UBA-loaded mucoadhesive oral films could exert a topical anticancer effect, reducing the progression of oral squamous cell carcinoma. This formulation could also help through other mechanisms [113]. Because OSCC decreases immune defense, the oral cavity becomes more susceptible to bacterial and fungal infections. Therefore, UBA-loaded mucoadhesive oral films could inhibit *S. aureus*, *P. aeruginosa*, and *Candida* sp., which are responsible for opportunistic oral infectious diseases in immunocompromised patients [78,79]. These results proved the chemotherapeutic effect of UBA-loaded mucoadhesive oral films. F-UBA could also display a chemopreventive action. Due to their cytoprotective effect and inhibitory activity against *C. albicans*, F-UBA can maintain a low risk because this fungal species is implied in OSCC generation, according to Prakash et al. [14]. The third condition, sensitizing in multidrug resistance, according to Dehelean et al. [13], could be supported by usnic acid's powerful effect-enhancing and toxicity-reducing in ascitic tumor-bearing mice treated with bleomycin [114]; usnic acid inhibits angiogenesis in vascular endothelial growth factor (VEGF) model and chick embryo [115]. Dar et al. [82] consider combination therapy in cancer essential for declining drug resistance, reducing tumor development, blocking mitotic cells, and inducing apoptosis. At the same time, the toxicity of monotherapy could be minimized. The results suggest that UBA-loaded in mucoadhesive oral films could be considered a combination in oral squamous cell carcinoma therapy due to the synergic action of usnic acid and other secondary phenolic metabolites.

None of the numerous analyzed mucoadhesive film compositions included lichen extracts, even though lichens are known for their antitumor, antibacterial, antifungal, antiviral, and enzyme inhibitory properties. Recognized in Traditional Chinese Medicine (TCM) as "Song Lo," *Usnea* lichens were consumed as tea or decoction for liver detoxification [116]. The typical TCM dosages are 6–9 g of dried lichen, corresponding to approximately 60–120 mg of usnic acid per day. Usnic acid was included in fat-burning products such as UCP-1 (BDC Nutrition, Richmond, Kentucky, which contains usnic acid, L-carnitine, and calcium pyruvate) and Lipo Kinetix (Syntrax Innovations Inc., Cape Girardeau, Missouri, containing norephedrine hydrochloride, sodium usniate, 3,5-diiodothyronine, yohimbine hydrochloride, and caffeine) [117] and associated with severe hepatotoxicity. In the present study, each F-UBA evaluated for potential therapeutic application contains 175 µg UBA, corresponding to a usnic acid content of 42.32 µg, a value more than 1400 times lower than the minimal dose allowed by TCP.

5. Conclusions

In this study, mucoadhesive oral films containing *U. barbata* dry acetone extract were manufactured using HPMC K100 as a polymer matrix and PEG 400 as a plasticizer. Complex physico-chemical and pharmacotechnical analyses proved their suitability for oral administration.

The pharmacological evaluation confirmed F-UBA in vitro anticancer activity on oral squamous cell carcinoma based on high oxidative stress induced in CLS-354 cells. The results also revealed F-UBA cytoprotective action on normal cells and the dose-dependent growth inhibition of bacterial and fungal pathogens involved in immunosuppressed patients' oral infections.

Therefore, the present study suggests that UBA-loaded mucoadhesive oral films could be a helpful phytotherapeutic formulation in the complementary treatment of oral squamous cell carcinoma. Further in vivo and clinical research could be following steps in the F-UBA analysis, aiming to confirm their medical benefits.

Supplementary Materials: The following supporting information can be downloaded at: https://www.mdpi.com/article/10.3390/antiox11101934/s1, Figure S1. Bioadhesive films: (a) Loaded with UBA (F-UBA); (b) References (R).

Author Contributions: Conceptualization, V.P., E.M., G.C.C., C.E.G., L.B., V.S. and E.A.O.; methodology, E.M., G.C.C., L.B., V.S., E.A.O., A.M.M., D.L. and M.A.(Mariana Aschie); software, V.P., E.M.,

V.S., E.A.O. and M.A.M.; validation, E.M., G.C.C., L.B., C.E.G., E.A.O., A.M.M. and V.B.; formal analysis, A.M.M., S.P., I.A., A.R., R.-A.M. and M.A. (Mihai Anastasescu); investigation, C.E.G., A.M.M., M.A.M., S.P., I.A., A.R. and R.-A.M.; resources, V.P., L.B., V.S., D.L. and M.A. (Mariana Aschie;) data curation, G.C.C., A.M.M. and M.A.M.; writing—original draft preparation, V.P., E.M., E.A.O., V.S. and A.M.M.; writing—review and editing, V.P., E.M., E.A.O. and A.M.M.; visualization, G.C.C., L.B., C.E.G., D.L., M.A. (Mariana Aschie) A.C. and V.B.; supervision, G.C.C., L.B., C.E.G., D.L., M.A. (Mariana Aschie), and V.B.; project administration, V.B.; funding acquisition, V.P. and M.A.M. All authors have read and agreed to the published version of the manuscript.

Funding: This research was supported by the project ANTREPRENORDOC, in the framework of Human Resources Development Operational Programme 2014–2020, financed from the European Social Fund under the contract number 36355/23.05.2019 HRD OP/380/6/13—SMIS Code: 123847. The APC was funded by Carol Davila University of Medicine and Pharmacy, Bucharest, Romania.

Institutional Review Board Statement: The study was conducted according to the Declaration of Helsinki and approved by the Institutional Ethics Committee of Ovidius University of Constanta, code 7080/10 June 2021 for studies involving humans.

Informed Consent Statement: Written informed consent has been obtained from the blood donor to publish this paper, code 39/30 June 2021.

Data Availability Statement: Data are contained within the manuscript.

Acknowledgments: This project was performed in collaboration with the Department of Pharmaceutical Technology and Biopharmacy, and the Department of Pharmacognosy, Phytochemistry, and Phytotherapy, Faculty of Pharmacy, Carol Davila University of Medicine and Pharmacy, 6 Traian Vuia Street, 020956 Bucharest, Romania, the Institute of Physical Chemistry “Ilie Murgulescu”, 202 Splaiul Independentei Street, 060021. Bucharest, Romania, and the Center for Research and Development of the Morphological and Genetic Studies of Malignant Pathology, Ovidius University of Constanta, CEDMOG, 145 Tomis Blvd., 900591 Constanta, Romania.

Conflicts of Interest: The authors declare no conflict of interest.

References

1. Kumar, M.; Nanavati, R.; Modi, T.; Dobariya, C. Oral cancer: Etiology and risk factors: A review. *J. Cancer Res. Ther.* **2016**, *12*, 458–463. [CrossRef] [PubMed]
2. Proia, N.K.; Paszkiewicz, G.M.; Nasca, M.A.S.; Franke, G.E.; Pauly, J.L. Smoking and smokeless tobacco-associated human buccal cell mutations and their association with oral cancer-A review. *Cancer Epidemiol. Biomark. Prev.* **2006**, *15*, 1061–1077. [CrossRef] [PubMed]
3. Madathil, S.A.; Rousseau, M.C.; Wynant, W.; Schlecht, N.F.; Netuveli, G.; Franco, E.L.; Nicolau, B. Nonlinear association between betel quid chewing and oral cancer: Implications for prevention. *Oral Oncol.* **2016**, *60*, 25–31. [CrossRef] [PubMed]
4. Warnakulasuriya, S. Living with oral cancer: Epidemiology with particular reference to prevalence and life-style changes that influence survival. *Oral Oncol.* **2010**, *46*, 407–410. [CrossRef]
5. Lee, Y.C.A.; Li, S.; Chen, Y.; Li, Q.; Chen, C.J.; Hsu, W.L.; Lou, P.J.; Zhu, C.; Pan, J.; Shen, H.; et al. Tobacco smoking, alcohol drinking, betel quid chewing, and the risk of head and neck cancer in an East Asian population. *Head Neck* **2019**, *41*, 92–102. [CrossRef]
6. Irani, S. Soussan Irani New Insights into Oral Cancer—Risk Factors and Prevention: A Review of Literature. *Int. J. Prev. Med.* **2020**, *11*, 202. [CrossRef]
7. Migueláñez-Medrán, B.D.C.; Pozo-Kreilinger, J.J.; Cebrián-Carretero, J.L.; Martínez-García, M.Á.; López-Sánchez, A.F. Oral squamous cell carcinoma of tongue: Histological risk assessment. A pilot study. *Med. Oral Patol. Oral Cir. Bucal* **2019**, *24*, e603–e609. [CrossRef]
8. Lin, N.C.; Hsien, S.I.; Hsu, J.T.; Chen, M.Y.C. Impact on patients with oral squamous cell carcinoma in different anatomical subsites: A single-center study in Taiwan. *Sci. Rep.* **2021**, *11*, 15446. [CrossRef]
9. Russo, D.; Mariani, P.; Caponio, V.C.A.; Lo Russo, L.; Fiorillo, L.; Zhurakivska, K.; Lo Muzio, L.; Laino, L.; Troiano, G. Development and validation of prognostic models for oral squamous cell carcinoma: A systematic review and appraisal of the literature. *Cancers* **2021**, *13*, 5755. [CrossRef]
10. PDQ®Supportive and Palliative Care Editorial Board. PDQ Oral Complications of Chemotherapy and Head/Neck Radiation. Bethesda, MD: National Cancer Institute. Updated 2022. Available online: https://www.cancer.gov/about-cancer/treatment/side-effects/mouth-throat/oral-complications-hp-pdq (accessed on 6 September 2022).

11. PDQ®Adult Treatment Editorial Board. PDQ Lip and Oral Cavity Cancer Treatment (Adult). Bethesda, MD: National Cancer Institute. Updated 2022. Available online: https://www.cancer.gov/types/head-and-neck/hp/adult/lip-mouth-treatment-pdq (accessed on 6 September 2022)
12. Morioka, R.; Matsuda, Y.; Kato, A.; Okui, T.; Okuma, S.; Tatsumi, H. Oral functional impairment may cause malnutrition following oral cancer treatment in a single - center cross - sectional study. *Sci. Rep.* **2022**, *12*, 14787. [CrossRef]
13. Dehelean, C.A.; Marcovici, I.; Soica, C.; Mioc, M.; Coricovac, D.; Iurciuc, S.; Cretu, O.M.; Pinzaru, I. Plant-Derived Anticancer Compounds as New Perspectives in Drug Discovery and Alternative Therapy. *Molecules* **2021**, *26*, 1109. [CrossRef] [PubMed]
14. Prakash, S.; Kumar, M.; Kumari, N.; Thakur, M.; Rathour, S.; Pundir, A.; Sharma, A.K.; Bangar, S.P.; Dhumal, S.; Singh, S.; et al. Plant-based antioxidant extracts and compounds in the management of oral cancer. *Antioxidants* **2021**, *10*, 1358. [CrossRef] [PubMed]
15. Guran, K.; Buzatu, R.; Pinzaru, I.; Boruga, M.; Marcovici, I.; Coricovac, D.; Avram, S.; Poenaru, M.; Susan, M.; Susan, R.; et al. In vitro pharmaco-toxicological characterization of melissa officinalis total extract using oral, pharynx and colorectal carcinoma cell lines. *Processes* **2021**, *9*, 850. [CrossRef]
16. Yeh, C.C.; Yang, J.I.; Lee, J.C.; Tseng, C.N.; Chan, Y.C.; Hseu, Y.C.; Tang, J.Y.; Chuang, L.Y.; Huang, H.W.; Chang, F.R.; et al. Anti-proliferative effect of methanolic extract of Gracilaria tenuistipitata on oral cancer cells involves apoptosis, DNA damage, and oxidative stress. *BMC Complement. Altern. Med.* **2012**, *12*, 142. [CrossRef]
17. Hassabou, N.F.; Farag, A.F. Anticancer effects induced by artichoke extract in oral squamous carcinoma cell lines. *J. Egypt. Natl. Canc. Inst.* **2020**, *32*, 17. [CrossRef]
18. Keshava, R.; Muniyappa, N.; Gope, R.; Ramaswamaiah, A.S. Anti-cancer effects of Imperata cylindrica leaf extract on human oral squamous carcinoma cell line SCC-9 in vitro. *Asian Pac. J. Cancer Prev.* **2016**, *17*, 1891–1898. [CrossRef]
19. KIM, J.H.; Hyun, J.W.; Kim, Y.G. Anticancer Effects of Natural Medicinal Plant Extracts on Oral Carcinoma Cells. *Biomol. Ther.* **1999**, *7*, 153–157.
20. Joo, M.; Heo, J.B.; Kim, S.; Kim, N.; Jeon, H.J.; An, Y.; Song, G.Y.; Kim, J.M.; Lee, H.J. Decursin inhibits tumor progression in head and neck squamous cell carcinoma by downregulating CXCR7 expression in vitro. *Oncol. Rep.* **2022**, *47*, 39. [CrossRef]
21. Di Prima, G.; Conigliaro, A.; De Caro, V. Mucoadhesive Polymeric Films to Enhance Barbaloin Penetration into Buccal Mucosa: A Novel Approach to Chemoprevention. *AAPS PharmSciTech* **2019**, *20*, 1–12. [CrossRef]
22. Zhang, Q.; Alyami, N.M.; Alyami, H.M. Influence of Padina gymnospora on Apoptotic Proteins of Oral Cancer Cells—A Proteome - Wide Analysis. *Appl. Biochem. Biotechnol.* **2022**, 1–18. [CrossRef]
23. Tang, J.Y.; Wu, K.H.; Wang, Y.Y.; Farooqi, A.A.; Huang, H.W.; Yuan, S.S.F.; Jian, R.I.; Tsao, L.Y.; Chen, P.A.; Chang, F.R.; et al. Methanol extract of usnea barbata induces cell killing, apoptosis, and dna damage against oral cancer cells through oxidative stress. *Antioxidants* **2020**, *9*, 694. [CrossRef] [PubMed]
24. Popovici, V.; Bucur, L.A.; Schröder, V.; Gherghel, D.; Mihai, C.T.; Caraiane, A.; Badea, F.C.; Vochița, G.; Badea, V. Evaluation of the cytotoxic activity of the Usnea barbata (L.) F. H. Wigg dry extract. *Molecules* **2020**, *25*, 1865. [CrossRef]
25. Popovici, V.; Bucur, L.; Vochita, G.; Gherghel, D.; Mihai, C.T.; Rambu, D.; Calcan, S.I.; Costache, T.; Cucolea, I.E.; Matei, E.; et al. In vitro anticancer activity and oxidative stress biomarkers status determined by usnea barbata (L.) f.h. wigg. dry extracts. *Antioxidants* **2021**, *10*, 1141. [CrossRef] [PubMed]
26. Pérez Zamora, C.M.; Michaluk, A.G.; Chiappetta, D.A.; Nuñez, M.B. Herbal buccal films with in vitro antibacterial and anti-inflammatory effects. *J. Herb. Med.* **2022**, *31*, 100527. [CrossRef]
27. Pagano, C.; Luzi, F.; Ricci, M.; Di Michele, A.; Puglia, D.; Ceccarini, M.R.; Beccari, T.; Blasi, F.; Cossignani, L.; Schoubben, A.; et al. Wound Dressing: Combination of Acacia Gum/PVP/Cyclic Dextrin in Bioadhesive Patches Loaded with Grape Seed Extract. *Pharmaceutics* **2022**, *14*, 485. [CrossRef] [PubMed]
28. Utama-ang, N.; Sida, S.; Wanachantararak, P.; Kawee-ai, A. Development of edible Thai rice film fortified with ginger extract using microwave-assisted extraction for oral antimicrobial properties. *Sci. Rep.* **2021**, *11*, 1–10.
29. Manikiran, S.S.; Priya, N.S.; Molly, B.A.; Nori, L.P. Fabrication and characterization of fast dissolving films of eclipta prostrate leaves extract to treat mouth ulcers. *Int. J. Appl. Pharm.* **2021**, *13*, 263–271.
30. Burgess, J.; Van Der Ven, P.D.; Martin, M.; Sherman, J.; Haley, J. Review of over-the-counter treatments for aphthous ulceration and results from use of a dissolving oral patch containing glycyrrhiza complex herbal extract. *J. Contemp. Dent. Pract.* **2008**, *9*, 088–098. [CrossRef]
31. Hashemi, M.; Ramezani, V.; Seyedabadi, M.; Ranjbar, A.M.; Jafari, H.; Honarvar, M.; Fanaei, H. Formulation and optimization of oral mucoadhesive patches of myrtus communis by box behnken design. *Adv. Pharm. Bull.* **2017**, *7*, 441–450. [CrossRef]
32. Nam, S.; Lee, J.J.; Lee, S.Y.; Jeong, J.Y.; Kang, W.S.; Cho, H.J. Angelica gigas Nakai extract-loaded fast-dissolving nanofiber based on poly(vinyl alcohol) and Soluplus for oral cancer therapy. *Int. J. Pharm.* **2017**, *526*, 225–234. [CrossRef]
33. Chiaoprakobkij, N.; Seetabhawang, S.; Okhawilai, M. Multifunctional bacterial cellulose - gelatin containing mangosteen extract films with improved antibacterial and anticancer properties. *Cellulose* **2022**, *29*, 6811–6830. [CrossRef]
34. Popovici, V.; Bucur, L.; Gîrd, C.E.; Popescu, A.; Matei, E.; Caraiane, A.; Botnarciuc, M. Phenolic Secondary Metabolites and Antiradical and Antibacterial Activities of Different Extracts of Usnea barbata (L.) Weber ex F.H. Wigg from C ă limani Mountains, Romania. *Pharmaceuticals* **2022**, *15*, 829. [CrossRef] [PubMed]

35. Pop, A.L.; Musuc, A.M.; Nicoară, A.C.; Ozon, E.A.; Crisan, S.; Penes, O.N.; Nasui, B.A.; Lupuliasa, D.; Secăreanu, A.A. Optimization of the Preformulation and Formulation Parameters in the Development of New Extended-Release Tablets Containing Felodipine. *Appl. Sci.* **2022**, *12*, 5333. [CrossRef]
36. Ding, C.; Zhang, M.; Li, G. Preparation and characterization of collagen/hydroxypropyl methylcellulose (HPMC) blend film. *Carbohydr. Polym.* **2015**, *119*, 194–201. [CrossRef]
37. Gavriloaia, M.R.; Budura, E.A.; Toma, C.C.; Mitu, M.A.; Karampelas, O.; Arama, C.; Lupuleasa, D. In vitro evaluation of diffusion and rheological profiles for dexamethasone inclusion complexes with β-cyclodextrin or hydroxypropyl β-cyclodextrin. *Farmacia* **2012**, *60*, 895–904.
38. Oana, M.; Simona, M.D.; Dumitru, L.; Adriana, M.M.; Svetlana, G.K.; Ştefan, R.F. The influence of structural characteristics on the in vitro drug release rate of terbinafine from topical gels. *Farmacia* **2012**, *60*, 325–333.
39. Domján, A.; Bajdik, J.; Pintye-Hódi, K. Understanding of the plasticizing effects of glycerol and PEG 400 on chitosan films using solid-state NMR spectroscopy. *Macromolecules* **2009**, *42*, 4667–4673. [CrossRef]
40. Guo, R.; Du, X.; Zhang, R.; Deng, L.; Dong, A.; Zhang, J. Bioadhesive film formed from a novel organic-inorganic hybrid gel for transdermal drug delivery system. *Eur. J. Pharm. Biopharm.* **2011**, *79*, 574–583. [CrossRef]
41. Nafee, N.A.; Ismail, F.A.; Boraie, N.A.; Mortada, L.M. Mucoadhesive buccal patches of miconazole nitrate: In vitro/in vivo performance and effect of ageing. *Int. J. Pharm.* **2003**, *264*, 1–14. [CrossRef]
42. Balaci, T.; Velescu, B.; Karampelas, O.; Musuc, A.M.; Nițulescu, G.M.; Ozon, E.A.; Nițulescu, G.; Gîrd, C.E.; Fița, C.; Lupuliasa, D. Physico-chemical and pharmaco-technical characterization of inclusion complexes formed by rutoside with β-cyclodextrin and hydroxypropyl-β-cyclodextrin used to develop solid dosage forms. *Processes* **2021**, *9*, 26. [CrossRef]
43. Musuc, A.M.; Anuta, V.; Atkinson, I.; Sarbu, I.; Popa, V.T.; Munteanu, C.; Mircioiu, C.; Ozon, E.A.; Nitulescu, G.M.; Mitu, M.A. Formulation of chewable tablets containing carbamazepine-β-cyclodextrin inclusion complex and f-melt disintegration excipient. The mathematical modeling of the release kinetics of carbamazepine. *Pharmaceutics* **2021**, *13*, 915. [CrossRef] [PubMed]
44. Perioli, L.; Ambrogi, V.; Angelici, F.; Ricci, M.; Giovagnoli, S.; Capuccella, M.; Rossi, C. Development of mucoadhesive patches for buccal administration of ibuprofen. *J. Control. Release* **2004**, *99*, 73–82. [CrossRef] [PubMed]
45. Derle, D.; Joshi, O.; Pawar, A.; Patel, J.; Perdeshi, V. Effect of tablet excipients on mucoadhesive properties of polyoxyethylene and Carbopol 971P. *Int. J. Pharm. Pharm. Sci.* **2009**, *1*, 198–205.
46. Don, T.M.; Huang, M.L.; Chiu, A.C.; Kuo, K.H.; Chiu, W.Y.; Chiu, L.H. Preparation of thermo-responsive acrylic hydrogels useful for the application in transdermal drug delivery systems. *Mater. Chem. Phys.* **2008**, *107*, 266–273. [CrossRef]
47. Gupta, A.; Garg, S.; Khar, R.K. Measurement of bioadhesive strength of mucoadhesive buccal tablets: Design of an in-vitro assembly. *Indian Drugs* **1993**, *30*, 1–6.
48. Nazir, S.; Ansari, F.L.; Hussain, T.; Mazhar, K.; Muazzam, A.G.; Qasmi, Z.U.H.; Makhmoor, T.; Noureen, H.; Mirza, B. Brine shrimp lethality assay "an effective prescreen": Microwave-assisted synthesis, BSL toxicity and 3DQSAR studies-based designing, docking and antitumor evaluation of potent chalcones. *Pharm. Biol.* **2013**, *51*, 1091–1103. [CrossRef]
49. Popovici, V.; Bucur, L.; Gîrd, C.E.; Rambu, D.; Calcan, S.I.; Cucolea, E.I.; Costache, T.; Ungureanu-Iuga, M.; Oroian, M.; Mironeasa, S.; et al. Antioxidant, Cytotoxic, and Rheological Properties of Canola Oil Extract of Usnea barbata (L.) Weber ex F.H. Wigg from Călimani Mountains, Romania. *Plants* **2022**, *11*, 854. [CrossRef]
50. Schröder, V.; Arcus, M.; Anghel, A.H.; Busuricu, F.; Lepadatu, A.C. Cell differentiation process of Artemia sp. *larvae tools for natural products testing.* **2019**, *LXII*, 149–153.
51. Iancu, I.M.; Bucur, L.A.; Schroder, V.; Mireșan, H.; Sebastian, M.; Iancu, V.; Badea, V. Phytochemical evaluation and cytotoxicity assay of lythri herba extracts. *Farmacia* **2021**, *69*, 51–58. [CrossRef]
52. Popovici, V.; Bucur, L.; Gîrd, C.E.; Calcan, S.I.; Cucolea, E.I.; Costache, T.; Rambu, D.; Oroian, M.; Mironeasa, S.; Schröder, V.; et al. Advances in the Characterization of Usnea barbata (L.) Weber ex F.H. Wigg from Călimani Mountains, Romania. *Appl. Sci.* **2022**, *12*, 4234. [CrossRef]
53. Popovici, V.; Matei, E.; Cozaru, G.C.; Aschie, M.; Bucur, L.; Rambu, D.; Costache, T.; Cucolea, I.E.; Vochita, G.; Gherghel, D.; et al. Usnic acid and usnea barbata (L.) F.H. wigg. dry extracts promote apoptosis and DNA damage in human blood cells through enhancing ROS levels. *Antioxidants* **2021**, *10*, 1171. [CrossRef]
54. Matei, E.; Aschie, M.; Mitroi, A.F.; Ghinea, M.M.; Gheorghe, E.; Petcu, L.; Dobrin, N.; Chisoi, A.; Mihaela, M. Biomarkers involved in evaluation of platelets function in South-Eastern Romanian patients with hematological malignancies subtypes. *Medicine* **2021**, *100*, e25944. [CrossRef] [PubMed]
55. Chunglok, W.; Utaipan, T.; Somchit, N.; Lertcanawanichakul, M.; Sudjaroen, Y. Antioxidant and antiproliferative activities of non-edible parts of selected tropical fruits. *Sains Malays.* **2014**, *43*, 689–696.
56. Varghese, J.; Radhika, G.; Sarin, A. The role of calpain in caspase activation during etoposide induced apoptosis in T cells. *Eur. J. Immunol.* **2001**, *31*, 2035–2041. [CrossRef]
57. Indurkar, A.; Bangde, P.; Gore, M.; Reddy, P.; Jain, R.; Dandekar, P. Optimization of guar gum-gelatin bioink for 3D printing of mammalian cells. *Bioprinting* **2020**, *20*, e00101. [CrossRef]
58. Thomé, M.P.; Filippi-Chiela, E.C.; Villodre, E.S.; Migliavaca, C.B.; Onzi, G.R.; Felipe, K.B.; Lenz, G. Ratiometric analysis of Acridine Orange staining in the study of acidic organelles and autophagy. *J. Cell Sci.* **2016**, *129*, 4622–4632. [CrossRef]
59. Fathi, F.; Ghobeh, M.; Tabarzad, M. Anti-Microbial Peptides: Strategies of Design and Development and Their Promising Wound-Healing Activities. *Mol. Biol. Rep.* **2022**, *8*, 1–12. [CrossRef]

60. Elshikh, M.; Ahmed, S.; Funston, S.; Dunlop, P.; McGaw, M.; Marchant, R.; Banat, I.M. Resazurin-based 96-well plate microdilution method for the determination of minimum inhibitory concentration of biosurfactants. *Biotechnol. Lett.* **2016**, *38*, 1015–1019. [CrossRef]
61. Madushan, R.; Vidanarachchi, J.K.; Prasanna, P.H.P.; Werellagama, S.; Priyashantha, H. Use of natural plant extracts as a novel microbiological quality indicator in raw milk: An alternative for resazurin dye reduction method. *LWT* **2021**, *144*, 111221. [CrossRef]
62. Cox, K.D.; Quello, K.; Deford, R.J.; Beckerman, J.L. A rapid method to quantify fungicide sensitivity in the brown rot pathogen Monilinia fructicola. *Plant Dis.* **2009**, *93*, 328–331. [CrossRef]
63. Bitacura, J.G. The Use of Baker's Yeast in the Resazurin Reduction Test: A Simple, Low-Cost Method for Determining Cell Viability in Proliferation and Cytotoxicity Assays. *J. Microbiol. Biol. Educ.* **2018**, *19*, jmbe-19-87. [CrossRef] [PubMed]
64. Li, J.; Xu, Z.; Wu, W.; Jing, Y.; Dai, H.; Fang, G. Nanocellulose/Poly(2-(dimethylamino)ethyl methacrylate)Interpenetrating polymer network hydrogels for removal of Pb(II) and Cu(II) ions. *Colloids Surf. A Physicochem. Eng. Asp.* **2018**, *538*, 474–480. [CrossRef]
65. Wang, D.; Yu, H.; Fan, X.; Gu, J.; Ye, S.; Yao, J.; Ni, Q. High Aspect Ratio Carboxylated Cellulose Nanofibers Cross-linked to Robust Aerogels for Superabsorption-Flocculants: Paving Way from Nanoscale to Macroscale. *ACS Appl. Mater. Interfaces* **2018**, *10*, 20755–20766. [CrossRef] [PubMed]
66. Li, Y.; Liu, Y.; Liu, Y.; Lai, W.; Huang, F.; Ou, A.; Qin, R.; Liu, X.; Wang, X. Ester Crosslinking Enhanced Hydrophilic Cellulose Nanofibrils Aerogel. *ACS Sustain. Chem. Eng.* **2018**, *6*, 11979–11988. [CrossRef]
67. Chelu, M.; Calderon Moreno, J.; Atkinson, I.; Pandele Cusu, J.; Rusu, A.; Bratan, V.; Aricov, L.; Anastasescu, M.; Seciu-Grama, A.M.; Musuc, A.M. Green synthesis of bioinspired chitosan-ZnO-based polysaccharide gums hydrogels with propolis extract as novel functional natural biomaterials. *Int. J. Biol. Macromol.* **2022**, *211*, 410–424. [CrossRef]
68. George, J.; Kumar, R.; Sajeevkumar, V.A.; Ramana, K.V.; Rajamanickam, R.; Abhishek, V.; Nadanasabapathy, S. Siddaramaiah Hybrid HPMC nanocomposites containing bacterial cellulose nanocrystals and silver nanoparticles. *Carbohydr. Polym.* **2014**, *105*, 285–292. [CrossRef]
69. Wang, T.; Chen, L.; Shen, T.; Wu, D. Preparation and properties of a novel thermo-sensitive hydrogel based on chitosan/hydroxypropyl methylcellulose/glycerol. *Int. J. Biol. Macromol.* **2016**, *93*, 775–782. [CrossRef]
70. Marques, N.d.N.; Balaban, R.d.C.; Halila, S.; Borsali, R. Synthesis and characterization of carboxymethylcellulose grafted with thermoresponsive side chains of high LCST: The high temperature and high salinity self-assembly dependence. *Carbohydr. Polym.* **2018**, *184*, 108–117. [CrossRef]
71. Andrews, J.M. Determination of minimum inhibitory concentrations. *J. Antimicrob. Chemother.* **2001**, *48*, 5–16. [CrossRef]
72. Phe, K.; Dao, D.; Palmer, H.R.; Tama, V.H. In vitro ceftriaxone susceptibility in methicillin-susceptible staphylococcus aureus. *Antimicrob. Agents Chemother.* **2015**, *59*, 1370. [CrossRef]
73. Ochoa, S.A.; Cruz-Córdova, A.; Rodea, G.E.; Cázares-Domínguez, V.; Escalona, G.; Arellano-Galindo, J.; Hernández-Castro, R.; Reyes-López, A.; Xicohtencatl-Cortes, J. Phenotypic characterization of multidrug-resistant Pseudomonas aeruginosa strains isolated from pediatric patients associated to biofilm formation. *Microbiol. Res.* **2015**, *172*, 68–78. [CrossRef] [PubMed]
74. Shrestha, G.; St. Clair, L.L. Lichens: A promising source of antibiotic and anticancer drugs. *Phytochem. Rev.* **2013**, *12*, 229–244. [CrossRef]
75. Paliya, B.S.; Bajpai, R.; Jadaun, V.; Kumar, J.; Kumar, S.; Upreti, D.K.; Singh, B.R.; Nayaka, S.; Joshi, Y.; Singh, B.N. The genus Usnea: A potent phytomedicine with multifarious ethnobotany, phytochemistry and pharmacology. *RSC Adv.* **2016**, *6*, 21672–21696.
76. Salgado, F.; Albornoz, L.; Cortéz, C.; Stashenko, E.; Urrea-Vallejo, K.; Nagles, E.; Galicia-Virviescas, C.; Cornejo, A.; Ardiles, A.; Simirgiotis, M.; et al. Secondary metabolite profiling of species of the genus usnea by UHPLC-ESI-OT-MS-MS. *Molecules* **2018**, *23*, 54. [CrossRef]
77. Popovici, V.; Bucur, L.; Popescu, A.; Schröder, V.; Costache, T.; Rambu, D.; Cucolea, I.E.; Gîrd, C.E.; Caraiane, A.; Gherghel, D.; et al. Antioxidant and cytotoxic activities of usnea barbata (L.) f.h. wigg. dry extracts in different solvents. *Plants* **2021**, *10*, 909. [CrossRef]
78. Jardón-Romero, E.A.; Lara-Carrillo, E.; González-Pedroza, M.G.; Sánchez-Mendieta, V.; Salmerón-Valdés, E.N.; Toral-Rizo, V.H.; Olea-Mejía, O.F.; López-González, S.; Morales-Luckie, R.A. Antimicrobial Activity of Biogenic Silver Nanoparticles from Syzygium aromaticum against the Five Most Common Microorganisms in the Oral Cavity. *Antibiotics* **2022**, *11*, 834. [CrossRef]
79. Rafey, A.; Amin, A.; Kamran, M.; Haroon, U.; Farooq, K.; Foubert, K.; Pieters, L. Analysis of plant origin antibiotics against oral bacterial infections using in vitro and in silico techniques and characterization of active constituents. *Antibiotics* **2021**, *10*, 1504. [CrossRef]
80. Thiyahuddin, N.M.; Lamping, E.; Rich, A.M.; Cannon, R.D. Yeast species in the oral cavities of older people: A comparison between people living in their own homes and those in rest homes. *J. Fungi* **2019**, *5*, 30. [CrossRef]
81. Popovici, V.; Bucur, L.; Popescu, A.; Caraiane, A.; Badea, V. Evaluation of the Antibacterial Action of the *Usnea barbata* L. Extracts on Streptococcus Species from the Oro-Dental Cavity. In Proceedings of the Romanian National Congress of Pharmacy, Bucharest, Romania, 26–29 September 2018. 17th ed..
82. Popovici, V.; Bucur, L.; Popescu, A.; Caraiane, A.; Badea, V. Comparative study regarding antibacterial action if the *Usnea barbata* L. In extracts on Gram-positive bacteria from the oro-dental cavity. In Proceedings of the 5th SGEM International Multidisciplinary Scientific Conferences on Social Sciences and Arts, Albena, Bulgaria, 24 August–2 September 2018.

83. Popovici, V.; Bucur, L.; Calcan, S.I.; Cucolea, E.I.; Costache, T.; Rambu, D.; Schröder, V.; Gîrd, C.E.; Gherghel, D.; Vochita, G.; et al. Elemental Analysis and In Vitro Evaluation of Antibacterial and Antifungal Activities of Usnea barbata (L.) Weber ex F.H. Wigg from C ă limani Mountains, Romania. *Plants* **2022**, *11*, 32. [CrossRef]
84. Rajaram, D.M.; Laxman, S.D. Buccal mucoadhesive films: A review. *Syst. Rev. Pharm.* **2016**, *8*, 31–38. [CrossRef]
85. Gayathri, D.; Jayakumari, L.S. Evaluation of commercial arrowroot starch/CMC film for buccal drug delivery of glipizide. *Polimeros* **2019**, *29*, e2019047. [CrossRef]
86. Saini, S.; Nanda, A.; Dhari, J. Formulation, development & evaluation of oral fast dissolving anti-allergic film of levocetrizine dihydrochloride. *J. Pharm. Sci. Res.* **2011**, *3*, 1322–1325.
87. Pandey, P.; Chauhan, S. Fast dissolving sublingual films of Zolmitriptan: A novel treatment approach for migraine attacks. *Indian J. Pharm. Educ. Res.* **2014**, *48*, 67–72. [CrossRef]
88. Winarti, L.; Laksono, B.T.; Oktora, L.; Sari, R.K. Optimization of hydroxy propyl methyl cellulose and carbomer in diltiazem hydrochloride mucoadhesive buccal film. *Indones. J. Pharm.* **2021**, *32*, 43–51. [CrossRef]
89. Elshafeey, A.H.; El-Dahmy, R.M. Formulation and development of oral fast-dissolving films loaded with nanosuspension to augment paroxetine bioavailability: In vitro characterization, ex vivo permeation, and pharmacokinetic evaluation in healthy human volunteers. *Pharmaceutics* **2021**, *13*, 1869. [CrossRef]
90. Salehi, S.; Boddohi, S. New formulation and approach for mucoadhesive buccal film of rizatriptan benzoate. *Prog. Biomater.* **2017**, *6*, 175–187. [CrossRef]
91. Bergo, P.; Sobral, P.J.A. Effects of plasticizer on physical properties of pigskin gelatin films. *Food Hydrocoll.* **2007**, *21*, 1285–1289. [CrossRef]
92. Meier-Haack, J.; Müller, M.; Lunkwitz, K. *Polymers-Opportunities and Risks II: Sustainability, Product Design and Processing*, 12th ed.; Eyerer, P., Weller, M., Hübner, C., Eds.; Springer: Berlin/Heidelberg, Germany, 2010; pp. 281–297.
93. Kraisit, P.; Limmatvapirat, S.; Luangtana-Anan, M.; Sriamornsak, P. Buccal administration of mucoadhesive blend films saturated with propranolol loaded nanoparticles. *Asian J. Pharm. Sci.* **2018**, *13*, 34–43. [CrossRef]
94. Pilicheva, B.; Uzunova, Y.; Marudova, M. Polyelectrolyte Multilayer Films as a Potential Buccal Platform for Drug Delivery. *Polymers* **2022**, *14*, 734. [CrossRef]
95. Aframian, D.J.; Davidowitz, T.; Benoliel, R. The distribution of oral mucosal pH values in healthy saliva secretors. *Oral Dis.* **2006**, *12*, 420–423. [CrossRef]
96. Muzib, Y.i.; Kumari, K.s. Mucoadhesive buccal films of glibenclamide: Development and evaluation. *Int. J. Pharm. Investig.* **2011**, *1*, 42. [CrossRef] [PubMed]
97. Lindert, S.; Breitkreutz, J. Oromucosal multilayer films for tailor-made, controlled drug delivery. *Expert Opin. Drug Deliv.* **2017**, *14*, 1265–1279. [CrossRef] [PubMed]
98. Garipova, V.R.; Gennari, C.G.M.; Selmin, F.; Cilurzo, F.; Moustafine, R.I. Mucoadhesive interpolyelectrolyte complexes for the buccal delivery of clobetasol. *Polymers* **2018**, *10*, 85. [CrossRef] [PubMed]
99. Dobaria, N.B.; Badhan, A.C.; Mashru, R.C. A novel itraconazole bioadhesive film for vaginal delivery: Design, optimization, and physicodynamic characterization. *AAPS PharmSciTech* **2009**, *10*, 951–959. [CrossRef] [PubMed]
100. Peh, K.K.; Wong, C.F. Polymeric films as vehicle for buccal delivery: Swelling, mechanical, and bioadhesive properties. *J. Pharm. Pharm. Sci.* **1999**, *2*, 53–61.
101. Vasantha, P.V.; Puratchikody, A.; Mathew, S.T.; Balaraman, A.K. Development and characterization of Eudragit based mucoadhesive buccal patches of salbutamol sulfate. *Saudi Pharm. J.* **2011**, *19*, 207–214. [CrossRef]
102. Caro, V.D.; Murgia, D.; Seidita, F.; Bologna, E.; Alotta, G.; Zingales, M.; Campisi, G. Enhanced in situ availability of Aphanizomenon Flos-Aquae constituents entrapped in buccal films for the treatment of oxidative stress-related oral diseases: Biomechanical characterization and in vitro/ex vivo evaluation. *Pharmaceutics* **2019**, *11*, 35. [CrossRef]
103. Theda, C.; Hwang, S.H.; Czajko, A.; Loke, Y.J.; Leong, P.; Craig, J.M. Quantitation of the cellular content of saliva and buccal swab samples. *Sci. Rep.* **2018**, *8*, 4–11. [CrossRef]
104. Park, J.Y.; Chung, H.; Choi, Y.; Park, J.H. Phenotype and tissue residency of lymphocytes in the murine oral mucosa. *Front. Immunol.* **2017**, *8*, 250. [CrossRef]
105. Düzlü, M.; Karamert, R.; Tutar, H.; Şahin, M.; Türkcan, A.; Yilmaz, M. Diagnostic role of neutrophil-lymphocyte ratio in oral cavity cancers. *Niger. J. Clin. Pract.* **2018**, *21*, 49–53.
106. Al-Ahmadi, A.A.; Ayuob, N.N.; Ali, S.S.; Al-Robai, A.A.; Abo-Khatwa, N.A. Effect of (+)-usnic acid as a fat burner on the rat hepatocyte; Correlated histological and biochemical in vivo study. *J. Anim. Vet. Adv.* **2012**, *11*, 1368–1377.
107. Rabelo, T.K.; Zeidán-Chuliá, F.; Vasques, L.M.; dos Santos, J.P.A.; da Rocha, R.F.; Pasquali, M.A.d.B.; Rybarczyk-Filho, J.L.; Araújo, A.A.S.; Moreira, J.C.F.; Gelain, D.P. Redox characterization of usnic acid and its cytotoxic effect on human neuron-like cells (SH-SY5Y). *Toxicol. Vitr.* **2012**, *26*, 304–314. [CrossRef] [PubMed]
108. Antonenko, Y.N.; Khailova, L.S.; Rokitskaya, T.I.; Nosikova, E.S.; Nazarov, P.A.; Luzina, O.A.; Salakhutdinov, N.F.; Kotova, E.A. Mechanism of action of an old antibiotic revisited: Role of calcium ions in protonophoric activity of usnic acid. *Biochim. Biophys. Acta-Bioenerg.* **2019**, *1860*, 310–316. [CrossRef]
109. Chelombitko, M.A.; Firsov, A.M.; Kotova, E.A.; Rokitskaya, T.I.; Khailova, L.S.; Popova, L.B.; Chernyak, B.V.; Antonenko, Y.N. Usnic acid as calcium ionophore and mast cells stimulator. *Biochim. Biophys. Acta-Biomembr.* **2020**, *1862*, 183303. [CrossRef] [PubMed]

110. Alahmadi, A.A. Usnic acid biological activity: History, evaluation and usage. *Int. J. Basic Clin. Pharmacol.* **2017**, *6*, 2752. [CrossRef]
111. Gajdziok, J.; Holešová, S.; Štembírek, J.; Pazdziora, E.; Landová, H.; Doležel, P.; Vetchý, D.; Pillay, V. Carmellose mucoadhesive oral films containing vermiculite/chlorhexidine nanocomposites as innovative biomaterials for treatment of oral infections. *Biomed Res. Int.* **2015**, *2015*, 580146. [CrossRef]
112. Barbălată-Mândru, M.; Serbezeanu, D.; Butnaru, M.; Rîmbu, C.M.; Enache, A.A.; Aflori, M. Poly(vinyl alcohol)/Plant Extracts Films: Preparation, Surface Characterization and Antibacterial Studies against Gram Positive and Gram Negative Bacteria. *Materials* **2022**, *15*, 2493. [CrossRef]
113. Basilicata, M.; Lauro, M.D.; Campolattano, V.; Marrone, G.; Celotto, R.; Mitterhofer, A.P.; Bollero, P.; Daniele, N.D.; Noce, A. Natural Bioactive Compounds in the Management of Oral Diseases in Nephropathic Patients. *Int. J. Environ. Res. Public Health* **2022**, *19*, 1665. [CrossRef]
114. Su, Z.Q.; Liu, Y.H.; Guo, H.Z.; Sun, C.Y.; Xie, J.H.; Li, Y.C.; Chen, J.N.; Lai, X.P.; Su, Z.R.; Chen, H.M. Effect-enhancing and toxicity-reducing activity of usnic acid in ascitic tumor-bearing mice treated with bleomycin. *Int. Immunopharmacol.* **2017**, *46*, 146–155. [CrossRef]
115. Dar, T.U.H.; Dar, S.A.; Islam, S.U.; Mangral, Z.A.; Dar, R.; Singh, B.P.; Verma, P.; Haque, S. Lichens as a repository of bioactive compounds: An open window for green therapy against diverse cancers. *Semin. Cancer Biol.* **2021**, *44*, 259–267. [CrossRef]
116. Guo, L.; Shi, Q.; Fang, J.L.; Mei, N.; Ali, A.A.; Lewis, S.M.; Leakey, J.E.A.; Frankos, V.H. Review of usnic acid and Usnea barbata toxicity. *J. Environ. Sci. Health-Part C Environ. Carcinog. Ecotoxicol. Rev.* **2008**, *26*, 317–338. [CrossRef] [PubMed]
117. Sanchez, W.; Maple, J.T.; Burgart, L.J.; Kamath, P.S. Severe hepatotoxicity associated with use of a dietary supplement containing usnic acid. *Mayo Clin. Proc.* **2006**, *81*, 541–544. [CrossRef] [PubMed]

antioxidants

Article

Design, Characterization, and Anticancer and Antimicrobial Activities of Mucoadhesive Oral Patches Loaded with *Usnea barbata* (L.) F. H. Wigg Ethanol Extract F-UBE-HPMC

Violeta Popovici [1,†], Elena Matei [2,*], Georgeta Camelia Cozaru [2,3,†], Laura Bucur [4,†], Cerasela Elena Gîrd [5,†], Verginica Schröder [6,*], Emma Adriana Ozon [7,*], Mirela Adriana Mitu [7,*], Adina Magdalena Musuc [8,*], Simona Petrescu [8,*], Irina Atkinson [8], Adriana Rusu [8], Raul-Augustin Mitran [8], Mihai Anastasescu [8], Aureliana Caraiane [9], Dumitru Lupuliasa [7,‡], Mariana Aschie [2,3,‡], Eugen Dumitru [2,10,‡] and Victoria Badea [1,‡]

[1] Department of Microbiology and Immunology, Faculty of Dental Medicine, Ovidius University of Constanta, 7 Ilarie Voronca Street, 900684 Constanta, Romania
[2] Center for Research and Development of the Morphological and Genetic Studies of Malignant Pathology, Ovidius University of Constanta, CEDMOG, 145 Tomis Blvd., 900591 Constanta, Romania
[3] Clinical Service of Pathology, Sf. Apostol Andrei Emergency County Hospital, 145 Tomis Blvd., 900591 Constanta, Romania
[4] Department of Pharmacognosy, Faculty of Pharmacy, Ovidius University of Constanta, 6 Capitan Al. Serbanescu Street, 900001 Constanta, Romania
[5] Department of Pharmacognosy, Phytochemistry, and Phytotherapy, Faculty of Pharmacy, Carol Davila University of Medicine and Pharmacy, 6 Traian Vuia Street, 020956 Bucharest, Romania
[6] Department of Cellular and Molecular Biology, Faculty of Pharmacy, Ovidius University of Constanta, 6 Capitan Al. Serbanescu Street, 900001 Constanta, Romania
[7] Department of Pharmaceutical Technology and Biopharmacy, Faculty of Pharmacy, Carol Davila University of Medicine and Pharmacy, 6 Traian Vuia Street, 020956 Bucharest, Romania
[8] Ilie Murgulescu Institute of Physical Chemistry, Romanian Academy, 202 Spl. Independentei, 060021 Bucharest, Romania
[9] Department of Oral Rehabilitation, Faculty of Dental Medicine, Ovidius University of Constanta, 7 Ilarie Voronca Street, 900684 Constanta, Romania
[10] Department of Gastroenterology, Emergency Hospital of Constanța, 145 Tomis Blvd., 900591 Constanta, Romania
* Correspondence: sogorescuelena@gmail.com (E.M.); verginica.schroder@univ-ovidius.ro (V.S.); emma.budura@umfcd.ro (E.A.O.); mirela.mitu@umfcd.ro (M.A.M.); amusuc@icf.ro (A.M.M.); simon_pet@icf.ro (S.P.)
† These authors contributed equally to this work.
‡ These authors contributed equally to this work.

Citation: Popovici, V.; Matei, E.; Cozaru, G.C.; Bucur, L.; Gîrd, C.E.; Schröder, V.; Ozon, E.A.; Mitu, M.A.; Musuc, A.M.; Petrescu, S.; et al. Design, Characterization, and Anticancer and Antimicrobial Activities of Mucoadhesive Oral Patches Loaded with *Usnea barbata* (L.) F. H. Wigg Ethanol Extract F-UBE-HPMC. *Antioxidants* **2022**, *11*, 1801. https://doi.org/10.3390/antiox11091801

Academic Editors: Christof E. Dörfer, Mohamed Mekhemar and Manoj Kumar

Received: 16 July 2022
Accepted: 7 September 2022
Published: 13 September 2022

Abstract: The oral cavity's common pathologies are tooth decay, periodontal disease, and oral cancer; oral squamous cell carcinoma (OSCC) is the most frequent oral malignancy, with a high mortality rate. Our study aims to formulate, develop, characterize, and pharmacologically investigate the oral mucoadhesive patches (F-UBE-HPMC) loaded with *Usnea barbata* (L.) F.H. Wigg dry ethanol extract (UBE), using HPMC K100 as a film-forming polymer. Each patch contains 312 µg UBE, with a total phenolic content (TPC) of 178.849 µg and 33.924 µg usnic acid. Scanning electron microscopy (SEM) and atomic force microscopy (AFM) were performed for their morphological characterization, followed by Fourier transform infrared spectroscopy (FTIR), X-ray diffraction (XRD), and thermogravimetric analysis (TGA). Pharmacotechnical evaluation involved the measurement of the specific parameters for mucoadhesive oral patches as follows: weight uniformity, thickness, folding endurance, tensile strength, elongation, moisture content, pH, disintegration time, swelling rate, and ex vivo mucoadhesion time. Thus, each F-UBE-HPMC has 104 ± 4.31 mg, a pH = 7.05 ± 0.04, a disintegration time of 130 ± 4.14 s, a swelling ratio of 272 ± 6.31% after 6 h, and a mucoadhesion time of 102 ± 3.22 min. Then, F-UBE-HPMCs pharmacological effects were investigated using brine shrimp lethality assay (BSL assay) as a cytotoxicity prescreening test, followed by complex flow cytometry analyses on blood cell cultures and oral epithelial squamous cell carcinoma CLS-354 cell line. The results revealed significant anticancer effects by considerably increasing oxidative stress and blocking DNA synthesis in CLS-354 cancer cells. The antimicrobial potential against

Staphylococcus aureus ATCC 25923, *Pseudomonas aeruginosa* ATCC 27353, *Candida albicans* ATCC 10231, and *Candida parapsilosis* ATCC 22019 was assessed by a Resazurin-based 96-well plate microdilution method. The patches moderately inhibited both bacteria strains growing and displayed a significant antifungal effect, higher on *C. albicans* than on *C. parapsilosis*. All these properties lead to considering F-UBE-HPMC suitable for oral disease prevention and therapy.

Keywords: *Usnea barbata* dry ethanol extract; oral mucoadhesive patches; physico-chemical properties; pharmacotechnical properties; oral health; oral cancer; anticancer activity; ROS; antimicrobial activity

---

1. Introduction

Oral health consists of the health of the oral mucosa, gums, teeth, and the whole system that allows us to speak, chew, taste, swallow, smile, and communicate with confidence various emotions through facial expressions. It is an essential component of general health, implying physiological, social, and psychological attributes fundamental to the quality of life [1]. The oral cavity's common pathologies group includes dental decays, gums and periodontia diseases, and oral cancer; oral squamous cell carcinoma (OSCC) is a substantially frequent oral malignancy (over 80–90% of all oral cavity's neoplasms) [2].

Oral diseases are caused by different infectious pathogens [3,4] and modifiable risk factors, including poor hygiene, sugar consumption, tobacco use, alcohol use, and other damaging habits [5]; various social and commercial determinants influence their impact. According to a World Health Organization (WHO) resolution [6], numerous oral health conditions could be preventable or treated in the early stages. In addition to conventional therapy, many phytotherapeutic products are made, especially for prophylaxis and early treatment of oral cavity diseases [7]. These products have various pharmaceutical formulations, as follows: concentrated mouthwashes, sprays, badinages, and mucoadhesive patches with antimicrobial and anti-inflammatory activities. Recently, Kumar et al. [8] detailed the benefits of apitherapy in periodontal diseases based on in vitro, in vivo, and clinical studies. They also profoundly analyzed the significant role of plant secondary metabolites with antioxidant potential in maintaining oral health [9]. Prakash et al. [10] extensively reviewed plant-based antioxidant extracts and compounds to manage oral cancer.

In the plant world, lichens represent a promising source of anticancer and antibiotic drugs [11]. Numerous studies have analyzed the cytotoxic and anticancer properties of *Usnea* sp. extracts [12–20], isolated metabolites, and their derivatives [21–28]. Some authors explored the potential pharmaceutical applications of usnic acid as an anticancer drug, aiming to increase its biodisponibility and simultaneously diminish its most known toxicity [29]. The usnic acid medicinal application limits, such as low solubility in water, hepatotoxicity, and reduced therapeutical index, have led to innovative pharmaceutical formulations [30] with antitumor effects. Thus, Alpsoy et al. [31] developed stable usnic acid (UA)-conjugated superparamagnetic iron oxide nanoparticles (SPIONs) as a potential drug carrier for in vitro analysis of MCF-7 (breast cancer), HeLa (cervix cancer), L-929 (mouse fibroblast), U-87 (glioblastoma), and A-549 (human lung cancer) cell lines. Pereira da Silva Santos et al. [32] investigated the antitumor activity of usnic acid encapsulated into nanocapsules prepared with lactic-co-glycolic acid polymer. Garg et al. [33] formulated usnic acid (UA) loaded heparin-modified gellan gum (HAG) nanoparticles (NPs), proving their substantial antitumor potential on A-549 cancer cells. However, data regarding the anticancer activity of different pharmaceutical formulations with *Usnea* sp extracts found in the accessed scientific literature are very rare; Isik et al. reported the anticancer activity of *Usnea* sp. extract-based synthesized Ag@ZnO bimetallic nanocomposite on the H-SY5Y human neuroblastoma cell line [34].

Most lichen-based nanoparticles (NPs) have antibacterial effects [35]. Few researchers designed different pharmaceutical formulations with *Usnea* lichens and evaluated their antibacterial effects. Thus, Siddiqi et al. [36] described the biogenic fabrication and characterization of silver nanoparticles using *U. longissima* aqueous-ethanolic extract and analyzed their antibacterial activity. They reported the nanoparticles' inhibitory effect on *S. aureus*, *P. aeruginosa*, and other Gram-positive and Gram-negative bacteria due to silver ions released from Ag NPs. Moreover, they suggested the following four possible bactericidal mechanisms: interference during cell wall synthesis, protein biosynthesis suppression, disruption of the transcription processes, and major metabolic pathways. Abdolmaleki et al. [37] obtained silver nanoparticles from two lichens (*U. articulata* and *R. sinensis*) with effective antibacterial activity against *S. aureus* and *P. aeruginosa.* Balaz et al. [38] recently proposed a bio-mechanochemical synthesis of silver nanoparticles using *U. antarctica* and other lichen species. Using $AgNO_3$ (as a silver precursor) and lichens (as reduction agents), they performed techniques of mechanochemistry (ball milling) and obtained nanoparticles with an intense antibacterial effect against *S. aureus*. This described procedure overcomes the lichen secondary metabolites' low solubility in water [38].

Tadic et al. [39] performed an oral product formulated as compressed tablets based on plant extracts/essential oils. It contains *U. barbata* supercritical CO_2 extract, *O. heracleoticum* L. and *Sideritis scardica* L. water-alcohol extracts, and *Satureja montana* L. essential oil. The stated oral formulation is intended for topical application (local treatment of the inflammation of oropharyngeal mucosa), comprising a combination of herbal preparations with antimicrobial activity against causative agents. We aim to formulate and develop mucoadhesive oral patches loaded with *Usnea barbata* (L.) F. H. Wigg dry ethanol extract and evaluate their cytotoxicity and in vitro anticancer and antimicrobial activities. Our results suggest that this lichen-based pharmaceutical formulation is suitable for potential use in various oral disease therapies.

2. Materials and Methods

2.1. Materials

Our study's chemicals, standards, and reagents were of analytical grade. Usnic acid standard 98.1% purity, Propidium Iodide (PI) 1.0 mg/mL, Dimethyl sulfoxide (DMSO), Polyethylene Glycol 400 (PEG 400), and Hydroxypropyl methylcellulose (HPMC) and Antibiotics mix solution—100 µL/mL with 10 mg Streptomycin, 10,000 U Penicillin, 25 µg Amphotericin B per 1 mL—were provided by Sigma-Aldrich Chemie GmbH (Taufkirchen, Germany). Annexin V Apoptosis Detection Kit and flow cytometry staining buffer (FCB) were purchased from eBioscience^{TM} (Frankfurt am Main, Germany) and RNase A 4 mg/mL from Promega (Madison, WI, USA). Magic Red® Caspase-3/7 Assay Kit, Reactive Oxygen Species (ROS) Detection Assay Kit, and EdU i-Fluor 488 Kit were supplied by Abcam (Cambridge, UK).

The OSCC cell line (CLS-354) and the culture medium—Dulbecco's Modified Eagle's Medium (DMEM) High Glucose, basic supplemented with 4.5 g/L glucose, L-glutamine and 10% Fetal Bovine Serum (FBS) were provided by CLS Cell Lines Service GmbH (Eppelheim, Germany). Trypsin-ethylenediamine tetra acetic acid (Trypsin EDTA) and the media for blood cells—Dulbecco's phosphate-buffered saline with $MgCl_2$ and $CaCl_2$, FBS and L-Glutamine (200 mM) solution—were purchased from Gibco^{TM} Inc (Billings, MT, USA).

From a non-smoker healthy donor (BIII, Rh+), the blood samples were collected according to Ethical approval code 7080/10.06.2021 from Ovidius University of Constanta and Donor Consent code 39/30.06.2021.

U. barbata was harvested in March 2021 from the forest in the Călimani Mountains (47°29′ N, 25°12′ E, and 900 m altitude) and identified by the Department of Pharmaceutical Botany of the Faculty of Pharmacy, Ovidius University of Constanta, using standard methods. A voucher specimen is deposited in the Herbarium of Pharmacognosy Department, Faculty of Pharmacy, Ovidius University of Constanta (Popovici 3/2021, Ph-UOC). The 96% ethanol for *U. barbata* dry extract preparation was provided by Chimreactiv SRL Bucharest, Romania.

Artemia salina eggs and *Artemia* salt (Dohse Aquaristik GmbH & Co. Gelsdorf, Germany) were purchased online from https://www.aquaristikshop.com/ (accessed on 5 May 2022).

Bacterial and fungal cell lines (*S. aureus* ATCC 25923, *P. aeruginosa* ATCC 27353, *C. albicans* ATCC 10231, and *C. parapsilosis* ATCC 22019) for antimicrobial activity evaluation were obtained from Microbiology Department, S.C. Synevo Romania S.R.L., Constanta Laboratory according to agreement of partnership No 1060/25.01.2018 with the Faculty of Pharmacy, Ovidius University of Constanta. Thermo Fisher Scientific (GmbH, Dreieich, Germany) provided culture medium Mueller-Hinton agar (MHA); Resazurin solution (from in vitro Toxicology Assay Kit, TOX8-1KT, Resazurin based), and RPMI 1640 Medium were purchased from Sigma-Aldrich Chemie GmbH (Taufkirchen, Germany).

2.2. Formulation and Development of Mucoadhesive Oral Patches

The *U. barbata* dry extract in ethanol (UBE) was obtained through a method described in a previous study [40]. The dried lichen was ground in a laboratory mill, LM 120 (Perkin Elmer, Waltham, MA, USA) [41], and extracted for eight hours with 96% ethanol in a Soxhlet continuous reflux system. The Soxhlet extraction was performed at the ethanol boiling point (65–70 °C). The rotary evaporator TURBOVAP 500 Caliper was used for solvent evaporation. Next, the extract was kept for 16 h in a chemical exhaust hood for optimal solvent evaporation. The obtained dry extract was transferred to a sealed glass bottle and stored in the freezer (Sirge FREEZER) at −24 °C until processing [40].

To develop the mucoadhesive oral patches containing *U. barbata* dry extract in 96% ethanol (F-UBE-HPMC), we used HPMC K100 with a viscosity of 100 mPa as a film-forming polymer and PEG 400 as an external plasticizer for its high hydrophilic character and non-toxicity [42].

To prove the UBE activity and influence on the F-UBE-HPMC patches' pharmaceutical characteristics, we prepared mucoadhesive oral patches containing suitable excipients but no active ingredient load. We used them as References (R).

The UBE amount was selected to achieve a suitable dosage between the formulations. HPMC was weighed using a Mettler Toledo AT261 balance (Marshall Scientific, Hampton, NH, USA) with 0.01 mg sensitivity for the polymeric matrix system. Then, it was dispersed in water by stirring at 700 rpm and room temperature, using an MR 3001K magnetic stirrer (Heidolph Instruments GmbH & Co. KG, Schwabach, Germany); PEG 400 was added and mixed. UBE was dissolved in ethanol, and the solution was slowly added to the previously prepared matrix and stirred in the same conditions. Reference products were realized by mixing the 96% ethanol with the base system.

The formed gels were left overnight at room temperature for deaeration. The viscous dispersions were poured in a thin layer into Petri glass plates and dried in ambient conditions for 24 h. Finally, the dried patches were peeled off the plate surface and cut into (1.5 × 2) cm patches.

2.3. Physico-Chemical Analysis of Mucoadhesive Oral Patches

2.3.1. SEM Morphology

The mucoadhesive patches morphology was investigated by scanning electron microscopy (SEM) in a high-resolution scanning electron microscope Quanta3D FEG (Thermo Fisher Scientific, GmbH, Dreieich, Germany).

2.3.2. Atomic Force Microscopy

The atomic force microscopy (AFM) measurements were carried out with AFM XE-100 (Park Systems Corporate, Suwon, Korea). AFM images were obtained in non-contact mode to minimize the tip-sample interaction; the microscope was equipped with flexure-guided, crosstalk-eliminated scanners. They were registered with sharp tips (PPP-NCLR, from NANOSENSORS™, Neuchatel, Switzerland) with less than 10-nm radius of curvature, 225 mm mean length, 38 mm mean width, ~48 N/m force constant, and a resonance frequency of 190 kHz. The AFM image processing was performed with an XEI program (v 1.8.0—Park Systems Corporate, Suwon, Korea) to display purpose and to evaluate roughness. Representative line scans are presented below the images in so-called "enhanced contrast" mode, showing the surface profile of the scanned samples (the dimensions of the selected particles are indicated with red arrows along the fixed line).

2.3.3. Fourier Transform Infrared Spectroscopy

Fourier transform infrared (FTIR) spectra of both patches were recorded using a Nicolet Spectrometer 6700 FTIR (Thermo Electron Corporation, Waltham, MA, USA) apparatus with a Smart DuraSamplIR HATR (Horizontal Attenuated Total Reflectance) accessory and a laminated–diamond crystal in the range of 400–4000 cm^{-1}, in transmittance mode.

2.3.4. X-ray Diffraction

X-ray Diffraction (XRD) patterns were registered using a Rigaku Ultima IV diffractometer (Rigaku Corporation, Tokyo, Japan) in parallel beam geometry with a step size of 0.02 and a speed of 2° (2θ)/min over a range of 5–60°. A CuKα tube (λ = 1.54056 Å) operating at 40 kV and 30 mA was the source of the X-rays.

2.3.5. Thermogravimetric Analysis

Thermogravimetric analysis (TGA) coupled with differential thermal analyses (DTA) was performed using a Mettler Toledo TGA/SDTA851e thermogravimetric analyzer (Mettler-Toledo GmbH, Greifensee, Switzerland), at a heating rate of 10 °C min^{-1}, under 80 mL min^{-1} synthetic air atmosphere.

2.4. Pharmacotechnical Analysis of Mucoadhesive Oral Patches

2.4.1. Weight Uniformity

The weight uniformity was evaluated on 20 patches of both formulations (F-UBE-HPMC and Reference). They were individually weighed, and the average weight was determined.

2.4.2. Thickness

This parameter was also measured on 20 patches of each formulation (F-UBE-HPMC and Reference) using a Yato digital micrometer (Yato China Trading Co., Ltd., Shanghai, China) with a 0–25 mm measuring range and 0.001 mm resolution. The mean value was calculated.

2.4.3. Folding Endurance

The F-UBE-HPMC patches were repeatedly folded and rolled until they broke, or up to 300× [43]. The folding times were registered and expressed as folding endurance values.

2.4.4. Tensile Strength and Elongation Ability

The tensile strength and elongation ability were determined using an LR 10K Plus digital tensile force tester for universal materials (Lloyd Instruments Ltd., West Sussex, UK). The analysis was performed from a 30 mm distance with a speed of 30 mm/min. The patch was placed vertically between the two braces, and the breakage force was registered. The measurement was executed in triplicate.

The following equations (Equations (1) and (2)) were used to calculate the tensile strength and the elongation at break:

$$\text{Tensile strength}\left(\text{kg/mm}^2\right) = \frac{\text{Force at breakage (kg)}}{\text{Patch thickness (mm)} \times \text{ Patch width (mm)}} \tag{1}$$

$$\text{Elongation \%} = \frac{\text{Increase in patch length (cm)}}{\text{Initial patch length (cm)}} \times 100 \tag{2}$$

2.4.5. Moisture Content

The moisture content was assessed as the loss on drying by the thermogravimetric method using an HR 73 halogen humidity analyzer (Mettler-Toledo GmbH, Greifensee, Switzerland) [6]. Five patches of each formulation were analyzed.

2.4.6. Surface pH

Five patches of each formulation were moistened with 1 mL of distilled water (pH 6.5 ± 0.5) for 5 min at room temperature. The pH value was determined by touching the electrode of the CONSORT P601 pH-meter (Consort bvba, Turnhout, Belgium) with the patch surface.

2.4.7. In Vitro Disintegration Time

The time required to disintegrate the patches, with no residual mass thoroughly, was measured in simulated saliva phosphate buffer pH of 6.8 at 37 ± 2 °C, using an Erweka DT 3 apparatus (Erweka® GmbH, Langen, Germany) [44].

2.4.8. Swelling Ratio

Six patches of each formulation were placed on 1.5% agar gel in Petri plates and incubated at 37 ± 1 °C. Every 30 min, for 6 h, the patches were weighed. The swelling ratio was calculated according to Equation (3) as follows:

$$\text{Swelling ratio} = \frac{\text{Wt} - \text{Wi}}{\text{Wi}} \times 100 \tag{3}$$

Wt—the patch's weight at "t" time after incubation and Wi—the initial weight [43,45–47].

2.4.9. Ex Vivo Mucoadhesion Time

The study was performed by the method described by Gupta et al. [48] on a detached porcine buccal mucosa; then, the fat layer and any tissue residue were removed. The membrane was washed with ultrapure water and a phosphate buffer pH 6.8 at 37 °C, then fixed on a glass plate. Each F-UBE-HPMC patch was hydrated in the center with 15 µL phosphate buffer and brought to the mucosa surface by pressing it for 30 s. The glass plate was placed in 200 mL phosphate buffer pH 6.8 and maintained at 37 °C for 2 min. A paddle with a stirring rate of 28 rpm was operated to ensure the appropriate simulation of the oral cavity conditions.

The mucoadhesion time was expressed as the time needed by each patch to detach over the oral mucosa. All tests were realized in triplicate.

2.5. Evaluation of the Cytotoxic Activity of Mucoadhesive Oral Patches on A. salina Larvae

2.5.1. Sample Preparation

F-UBE-HPMC was placed in a diluted buffer (1 mL) and incubated for 15 min at 37 °C; then, its homogenous dispersion in the buffer solution was observed.

2.5.2. BSL Assay

Artemia salina (brine shrimp) was used as an animal model for the F-UBE-HPMC cytotoxicity investigation, adapted from Nazir et al. [49]. The *A. salina* larvae were obtained under continuous light and aeration conditions at a temperature of 20 °C by introducing the cysts for 24–48 h in a saline solution of 0.35%. The brine shrimp larvae in the first stage (instar I) were introduced in 0.3% saline solution into experimental pots (with a volume of 1 mL) [50]. The analysis was compared to a blank (untreated nauplii) to obtain accurate results regarding the F-UBE-HPMC cytotoxic effect. The nauplii were not fed during the test to not interfere with the tested extracts. Their evolution was evaluated after 24 h and 48 h; the larvae had embryonic energy reserves as lipids throughout this period.

2.5.3. Fluorescent Microscopy

The brine shrimp larvae were stained with 3% acridine orange (Merck Millipore, Burlington, MA, USA) for 5 min. The samples were subjected to drying for 15 min in darkness and placed on the microscope slides.

2.5.4. Data Processing

The microscopic images were achieved using a VWR microscope VisiScope 300D (VWR International, Radnor, PA, USA) with a Visicam X3 camera (VWR International Radnor, PA, USA) at 40×, 100×, and 400× magnifications and processed with VisiCam Image Analyzer 2.13.

Fluorescent microscopy images were obtained using an OPTIKA B-350 microscope (Ponteranica, BG, Italy) blue filter (λex = 450–490 nm; λem = 515–520 nm) and green filter (λex = 510–550 nm; λem = 590 nm) [41]. The FM images at 100× and 400× magnification were processed with Optikam Pro 3 Software (OPTIKA S.R.L., Ponteranica, BG, Italy).

All observations were performed in triplicate.

2.6. In Vitro Analysis of the Biological Effects of Mucoadhesive Oral Patches on Human Blood Cell Cultures and Oral Cancer Cell Line CLS-354

2.6.1. Equipment

Our study platform for in vitro cytotoxicity analysis of F-UBE-HPMC was the Attune Acoustic focusing cytometer (Applied Biosystems, Bedford, MA, USA). Before cell analysis, the flow cytometer was first set by using fluorescent beads—Attune performance tracking beads, labeling, and detection (Life Technologies, Europe BV, Bleiswijk, The Netherlands) [51], with a standard size (four intensity levels of beads population). The cell number was established by enumerating cells below 1 µm [52]. Using Forward Scatter (FSC) and Side Scatter (SSC), more than 10,000 cells per sample for each analysis were gated.

2.6.2. Data Processing

Flow cytometry data were achieved using Attune Cytometric Software v.1.2.5, Applied Biosystems 2010 (Bedford, MA, USA).

2.6.3. Human Blood Cells Cultures

The blood sample was collected into heparin vacutainers. The heparinized blood (1.0 mL) was added to untreated Nunclon Vita Cell culture 6-well plates (Kisker Biotech GmbH & Co.KG, Steinfurt, Germany), together with 6.0 mL of Dulbecco's phosphate-buffered saline with $MgCl_2$ and $CaCl_2$ medium supplemented with 10% bovine fetal serum, L-glutamine, and antibiotic mix solution. They were incubated in a Steri-Cycle™ i160 CO_2 Incubator (Thermo Fisher Scientific Inc, Waltham, MA, USA) with 5% CO_2 at 37 °C. After 72 h, the blood cell cultures were treated with the samples and controls. Then, the cells were subjected to 24 h of incubation under the same conditions [51]. All flow cytometry analyses were performed after this incubation time.

2.6.4. CLS-354 Cell Line, Cells Culture

The CLS-354 tumor cells were cultured in DMEM High Glucose with 10% FBS supplemented with antibiotic mix solution in humidity conditions of 5% CO_2 at 37 °C for 7 days [53]. Then, the cells were dissociated with Trypsin-EDTA and centrifugated at 3000 rpm for 10 min in a Fisher Scientific GT1 Centrifuge (Thermo Fisher Scintific Inc, Waltham, MA, USA). Then, the cells were distributed in Millicell™ 24-Well Cell Culture Microplates (Termo Fisher Scientific Inc, Waltham, MA, USA). After treatment, the cells were incubated for 24 hours in the same conditions [54]. All the flow-cytometry analyses were performed after this incubation period.

2.6.5. Samples and Control Solutions

The F-UBE-HPMC were dissolved in the suitable culture media for both types of cells with 1% DMSO. As a positive control, usnic acid (125 µg/mL in 1% DMSO) was selected, and the negative control was 1% DMSO.

2.7. Evaluation of Total ROS Activity

In total, 100 µL of ROS Assay Stain solution was added to each 1 mL of cell culture in flow cytometry tubes and well mixed. Then, the cells were incubated in a 5% CO_2 atmosphere at 37 °C for 60 min. After this process, the cells were analyzed by flow cytometry, using a 488 nm excitation and green emission for ROS (BL1 channel).

2.8. Evaluation of Caspase 3/7 Activity

In total, 300 µL of both cell cultures were transferred in flow cytometry tubes; then, 20 µL of a Magic Red® Caspase-3/7 Substrate—MR-$(DEVD)_2$—solution was well-mixed with the cells. Next, 20 µL of PI was added. After incubation, 1 mL FCB was added. Then, the early stages of cell apoptosis by activating caspases 3/7 (DEVD-ases) [55,56] were analyzed through flow cytometry using a 488 nm excitation, red emission for MR-$(DEVD)_2$—BL3 channel, and orange emission for PI—BL2 channel.

2.9. Cell Cycle Analysis

A cell culture volume of 1 mL was washed in FCB, introduced into flow cytometry tubes, and fixed with 50 µL ethanol for 30 min [51]. Next, the cells were treated with PI (20 µg/mL) and RNase A (30 µg/mL) and incubated at room temperature, in darkness, for 30 min [51]. Then, 1 mL FCB was added, and the cell cycle distribution was detected at the flow cytometer in the following conditions: a 488 nm excitation and orange emission for PI (BL2 channel) [51].

2.10. Evaluation of Nuclear Condensation and Lysosomal Activity

Magic Red® Caspase-3/7 Assay Kit contains Hoechst 33342 stain (200 µg/mL) and acridine orange (AO, 1.0 µM). Hoechst 33342 is a cell-permeant nuclear stain [57]; when it is linked to double chain DNA, it emits blue fluorescence, highlighting condensed nuclei in apoptotic cells. Acridine orange is a chelating dye that can be used to reveal lysosomal activity [58,59]. Therefore, 300 µL of each cell culture was introduced in flow cytometry tubes; then, 2 µL of Hoechst 33342 stain was added, and the cells were mixed well [51]. After these operations, 50 µL of AO (1.0 µM) was added; the cells were incubated at room temperature in darkness for 30 min. After incubation, 1 mL FCB was added; the cells were examined at the flow cytometer under the following conditions: an excitation of 488 nm, the UV excitation, and blue emission for Hoechst 33342 (VL2), and green emission acridine orange (BL1 channel) [51].

2.11. Annexin V-FITC Apoptosis Assay

The normal blood cells and CLS-354 tumor cells were incubated in flow cytometry tubes with 2 µL Annexin V-FITC and 2 µL PI (20 µg/mL) for 30 min, at room temperature, in darkness. After incubation, 1 mL of FCB was added. All viable cells, early apoptotic cells, late apoptotic cells, and necrotic cells were examined at a flow cytometer using the following conditions: an excitation of 488 nm and the following two emission types: green—for Annexin V-FITC (BL1 channel) and orange—for PI (BL2 channel) [51].

2.12. Evaluation of Cell Proliferation

Volumes of 1 mL of both cell cultures were incubated with 50 µM EdU (500 µL) at 37 °C for 2 h. Then, both cell types were fixed with 4% paraformaldehyde in PBS (100 µL) and permeabilized with Triton X-100 (100 µL). After washing in 3% buffer sodium azide (BSA) and centrifuging at 300 rpm for 5 min at 4 °C, the cells were incubated with a reaction mix (500 µL) for 30 min at room temperature in darkness. Then, they were washed in permeabilization buffer and centrifuged at 300 rpm for 5 min at 4 °C. After these procedures, 1 mL FCB was added, and the cells were examined by flow cytometry, using a 488 nm excitation and green emission for EdU-iFluor 488 (BL1).

2.13. Antimicrobial Activity Evaluation by Resazurin-Based 96-Well Plate Microdilution Method

2.13.1. Inoculum Preparation

The direct colony suspension method (CLSI) was used for preparing the bacterial inoculum. Thus, bacterial colonies selected from a 24 h agar plate were suspended in an MHA medium. The bacterial inoculum was accorded to the 0.5 McFarland standard, measured at Densimat Densitometer (Biomerieux, Marcy-l'Étoile, France) with around 10^8 CFU/mL (CFU = colony-forming unit). The fungal inoculum was prepared using the same method, adjusting the RPMI 1640 with fungal colonies to the 1.0 McFarland standard, with 10^6 CFU/mL.

2.13.2. Samples and Standards

F-UBE-HPMC was dissolved in 1 mL of diluted phosphate buffer. As standards, Ceftriaxone (Cefort 1g Antibiotice SA, Iasi, Romania) solutions 30 mg/mL and 122 mg/mL in distilled water were used for bacteria. The Cefort powder was weighted at Partner Analytical balance (Fink & Partner GmbH, Goch, Germany) and dissolved in distilled water. Terbinafine solution 10.1 mg/mL (Rompharm Company S.R.L., Otopeni, România) was selected as standard for *Candida* sp2.13.3. Resazurin-Based 96-Well Plate Microdilution Method.

All successive steps were performed in an Aslair Vertical 700, laminar flow, microbiological protection cabinet (Asal Srl, Cernusco, MI, Italy). In four 96-well plates, we performed seven serial dilutions, adapting the protocol described by Fathi et al. [60] and Elshikh et al. [61].

The 96-well plates were incubated for 24 h at 37 °C for bacteria and 35 °C for yeasts in a My Temp mini Z763322 Digital Incubator (Benchmark Scientific Inc., Sayreville, NJ, USA).

2.13.3. Reading and Interpreting

After 24 h incubation, the colors that appeared in 96-well plates were examined to see the differences between the standard and samples [62]. Moreover, they were examined at the Smart LED Illuminator (Kaneka Eurogentec S.A., Seraing, Belgium) at 470 nm in blue light. The sample's active concentrations were compared with the standard antibiotic ones. For yeasts, the color chart of the Resazurin dye reduction method was used [63,64].

2.14. Data Analysis

All analyses were performed in triplicate, and the obtained results were presented as means values ± standard deviation (SD). Our results are presented as percent (%) of cell and nuclear apoptosis, caspase 3/7 activity, autophagy, cell cycle, DNA synthesis, and count ($\times 10^4$) of oxidative cellular stress after flow cytometry analyses were performed with SPSS v. 23 software, 2015 (IBM, Armonk, NY, USA). The Levene test was analyzed for homogeneity of variances of samples. Paired t-test was used to establish the differences between samples and controls, and $p < 0.05$ was considered statistically significant. The principal component analysis (PCA) was performed using XLSTAT 2022.2.1. by Addinsoft (New York, NY, USA) [65].

3. Results

3.1. Organoleptic Characteristics of Mucoadhesive Oral Patches

The composition and properties of the developed F-UBE-HPMC and R mucoadhesive oral patches are displayed in Table 1.

Table 1. Composition and properties of mucoadhesive oral patches loaded with *U. barbata* dry extract in 96% ethanol (F-UBE-HPMC) versus References (R).

Variable	F-UBE-HPMC	R
Ingredients		
UBE (g)	0.30	-
Ethyl alcohol 96% (*v*/*v*) (g)	10.00	10.00
PEG 400 (g)	5.00	5.00
HPMC 15% water dispersion (*w*/*w*) (g)	84.70	85.00
Thermal parameters		
Solvent Mass Loss (%)	2.4	1.8
T (°C)/Mass Loss 1st Decomposition Step (%)	351.7 °C/84.2	466.2 °C/13.4
T (°C)/Mass Loss 2nd Decomposition Step (%)	352.3 °C/85.2	456.8 °C/13.0
*Pharmacotechnical Parameters **		
Weight uniformity (mg)	104 ± 4.31	102 ± 2.55
Thickness (mm)	0.082 ± 0.003	0.081 ± 0.002
Folding endurance value	>300	>300
Tensile strength (kg/mm^2)	2.55 ± 1.31	2.83 ± 1.25
Elongation %	51.26 ± 1.77	49.47 ± 2.13
Moisture content % (*w*/*w*)	6.24 ± 0.26	6.02 ± 0.14
pH	7.05 ± 0.04	7.03 ± 0.02
Disintegration time (seconds)	130 ± 4.14	131 ± 3.27
Swelling ratio (% after 6 h)	272 ± 6.31	286 ± 4.93
Ex vivo mucoadhesion time (minutes)	102 ± 3.22	106 ± 3.35

UBE—*U. barbata* dry ethanol extract, F-UBE-HPMC—mucoadhesive oral patches with *U. barbata* dry ethanol extract; R—Reference (mucoadhesive oral patches containing the suitable excipients, without UBE); PEG—polyethylene glycol; HPMC—hydroxypropyl methylcellulose; T—temperature; * Expressed as mean value ± SD.

The manufacturing process led to defined concentrations of UBE in mucoadhesive oral patches formulation, each F-UBE-HPMC enclosing 312 µg UBE, with total phenols content of 178.849 µg and 33.924 µg usnic acid.

Both formulations lead to a homogenous, thin, easy-to-peel, with a uniform, smooth, and glossy surface patch (Figure S1, Supplementary Material).

The Reference (R, Figure S1a) are colorless; F-UBE-HPMC has a green-faint brown color (Figure S1b); both R and F-UBE-HPMC are transparent (Figure S1a,b).

The patches' organoleptic characteristics are highly dependent on the active ingredient state. F-UBE-HPMC maintains the characteristic color of UBE and withstands normal handling and cutting processes without air bubbles, cracks, or imperfections.

3.2. Physico-Chemical Analysis of the Mucoadhesive Oral Patches

3.2.1. SEM Morphology

Scanning electron microscopy (SEM) was performed to achieve the patch morphology. Figure 1 shows their surface morphology. The R surface is denser, containing a few small elongated-shaped protrusions (Figure 1a), and the F-UBE-HPMC one is relatively smooth (Figure 1b).

3.2.2. Atomic Force Microscopy

The AFM images are displayed in Figure 1c,d.

The Reference (R) is flat and uniform (repetitive surface features), as pointed out by the arbitrary line scan (surface profile line) depicted below the AFM image (Figure 1c) with a vertical height of ~10 nm (see the *Y*-axis of the line scan from −5 to 5 nm). Due to the presence of small agglomerations (in the form of "hills"-see the black arrows in Figure 1e), not exceeding 70 nm in the vertical direction, the peak-to-valley parameter (Rpv) is 86.5 nm (Figure 1c,f). In comparison, the global root mean square (RMS) roughness of the same area is 3.2 nm (Figure 1e). Random superficial nanometric-sized pores, visible as dark blue spots, are also seen in Figure 1c.

The UBE incorporation changes the Reference morphology (Figure 1d). The F-UBE-HPMC surface becomes more compact; the superficial pores are covered at the nanometric scale. Instead, a few larger pits (see the red arrows in Figure 1d) appeared on the surface, with more than 100 nm in diameter. The RMS roughness of the image from Figure 1d,e is 20.2 nm, while the peak-to-valley global parameter is 240.3 nm, three times more than Reference (Figure 1f). The Rpv and RMS roughness along the line scans are illustrated in Figure 1g,h.

3.2.3. FTIR Spectra

The FTIR spectra for both mucoadhesive oral films (Reference and F-UBE-HPMC) are displayed in Figure 2a,b.

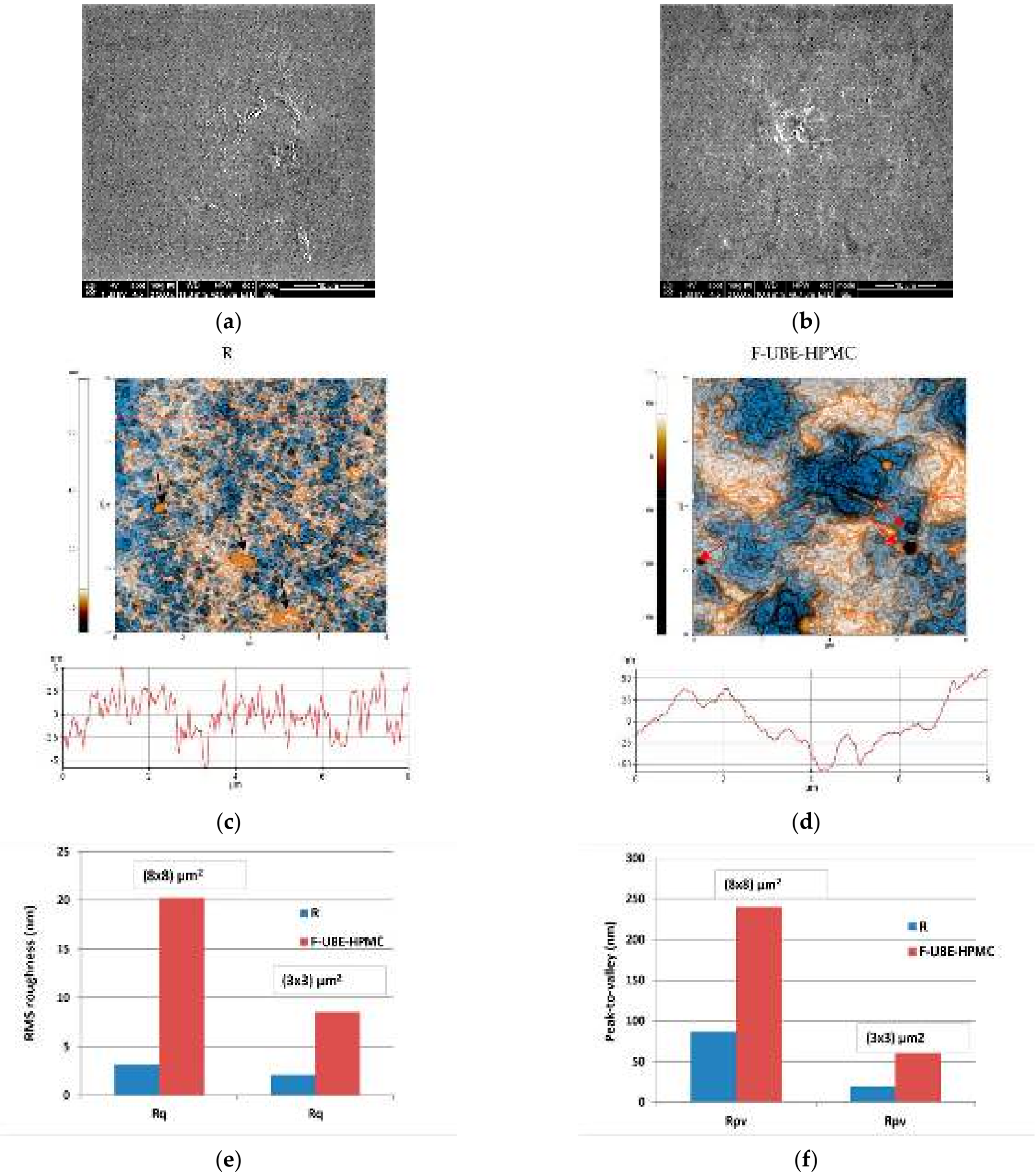

(**a**) (**b**)

(**c**) (**d**)

(**e**) (**f**)

Figure 1. *Cont.*

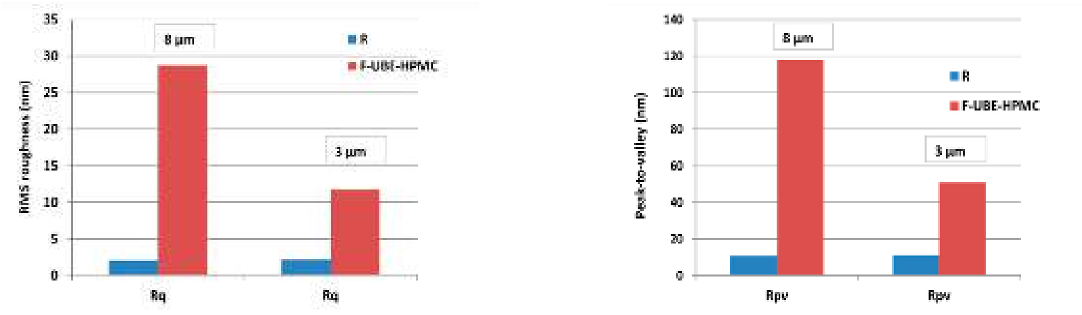

(**g**) (**h**)

Figure 1. SEM images of R (**a**) and F-UBE-HPMC (**b**); 2D-AFM images (enhanced contrast view) at the scale of (8 × 8) μm^2 together with representative line scans for R (**c**) and F-UBE-HPMC (**d**). Roughness (Rq) and peak-to-valley (Rpv) parameters for the whole scanned areas at (8 × 8) μm^2 and (3 × 3) μm^2 (**e**,**f**) and along the line scans over 8 μm and 3 μm (**g**,**h**). F-UBE-HPMC—mucoadhesive oral patches loaded with UBE; UBE—*U. barbata* dry ethanol extract; R—Reference (mucoadhesive oral patches without UBE).

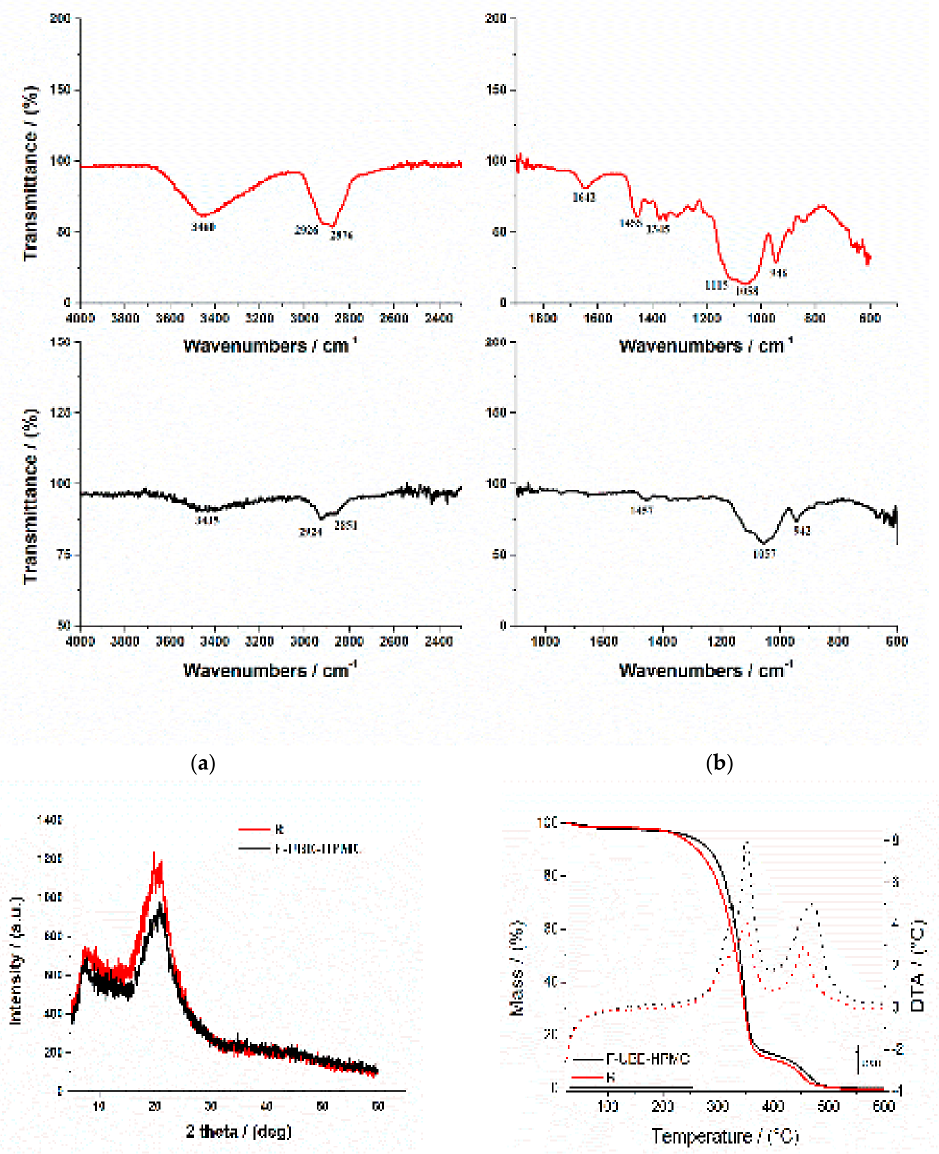

(**a**) (**b**)

(**c**) (**d**)

Figure 2. *Cont*.

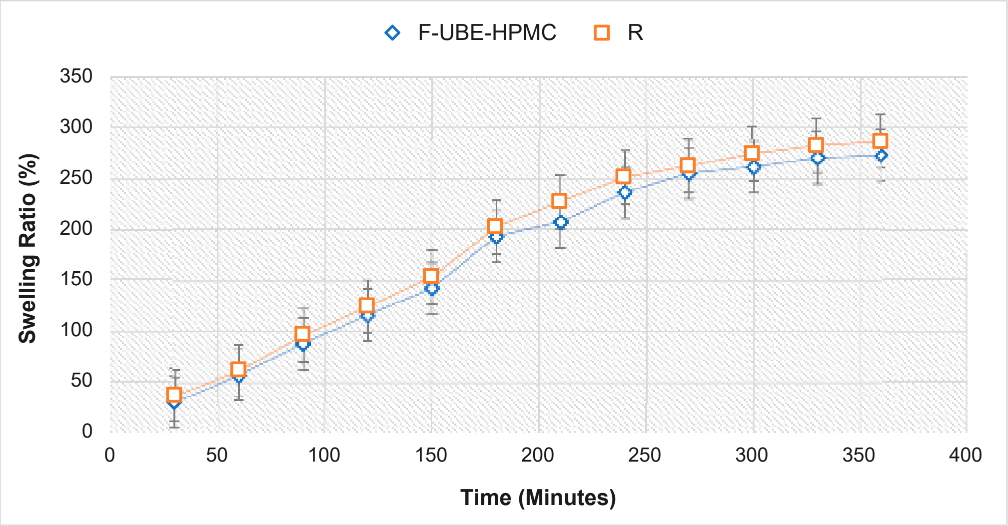

(**e**)

Figure 2. FTIR Spectra of mucoadhesive oral patches (**a**,**b**): Reference (red line) and F-UBE-HPMC (black line) in the range 4000–2200 cm^{-1} (**a**) and 2000–400 cm^{-1} (**b**); X-ray Diffractograms of Reference and F-UBE-HPMC oral mucoadhesive patches (**c**); Thermogravimetric analysis coupled with differential thermal analysis of the mucoadhesive oral patches (**d**). Swelling rate% over 6 h of F-UBE-HPMC versus R (**e**). R—Reference (patch without UBE); F-UBE-HPMC—mucoadhesive oral patches loaded with UBE; UBE—*U. barbata* dry ethanol extract.

In Figure 2a, the R spectrum shows an absorption band at 3460 cm^{-1} assigned to the stretching frequency of the HPMC's hydroxyl (-OH) group. Another band at 1345 cm^{-1} is due to the bending vibration of -OH. Other stretching vibration bands related to C-H and C-O were observed at 2926 cm^{-1} and 1058 cm^{-1}, respectively. The characteristic vibration peaks associated with HPMC appeared at 1455 cm^{-1} related to the methoxy (-OCH_3) group and at 946 cm^{-1}, corresponding to the pyranose ring [66].

On the other hand, the FTIR spectrum of the F-UBE-HPMC (Figure 2b) shows some peaks found in Reference one, with lower intensities. The peaks are shifted to a lower frequency due to UBE interaction with the polymer matrix.

3.2.4. X-ray Diffractograms

The X-ray diffractograms of R and F-UBE-HPMC are presented in Figure 2c. The X-ray diffraction patterns of the Reference and F-UBE-HPMC (Figure 2c) show that both mucoadhesive oral patches exhibited the characteristic diffraction peaks of HPMC at $2\theta = 8°$ and $2\theta = 20°$ [67]. A careful analysis of their XRD patterns indicates that the amorphous region peak ($2\theta = 8°$) and crystalline region ($2\theta = 20°$) decrease in their intensities due to the UBE blending in the polymer matrix in the case of F-UBE-HPMC (Figure 2c).

3.2.5. Thermogravimetric Analysis

Thermogravimetric and differential thermal analysis aimed to characterize the patch's thermal behavior and stability. Both patches (Reference and F-UBE-HPMC) exhibit a similar behavior upon heating from 25 to 600 °C (Figure 2d). A 0.8–2.5% weight mass loss occurs on heating up to ~100 °C, which can be associated with the loss of residual solvent and physisorbed water. The decomposition process of the organic compounds occurs in two distinct steps, between 200–400 °C and 400–550 °C. Each decomposition step is accompanied by an exothermic thermal effect (Figure 2d). The mass losses associated with the solvent loss and first and second organic decomposition steps are presented in Table 1 (thermal parameters).

Figure 2d and Table 1 (thermal parameters) indicate that the first stage of both R and F-UBE-HPMC starts at a temperature below 100 °C and is due to the loss of solvent and adsorbed water. The second stage begins from 220 °C to 390 °C, and this stage corresponds to ~85% for R and ~84% for F-UBE-HPMC patches' weight loss. The third stage, with a maximum at $T_{\max}$ = 456.8 °C for R and $T_{\max}$ = 466.2 °C for F-UBE-HPMC, was due to the decomposition of the different organic components. The F-UBE-HPMC thermal stability is higher than the Reference one.

3.3. Pharmacotechnical Evaluation of Mucoadhesive Oral Patches

The results of the pharmacotechnical evaluation of F-UBE-HPMC and Reference are presented in Table 1 (pharmacotechnical properties).

The mucoadhesive oral patches' weight varies depending on the state of the active ingredient and its dispersion method. No significant differences were registered between F-UBE-HPMC and R. Moreover, considering the variability between the patches of the same series, a remarkable uniformity is noticed.

The F-UBE-HPMC thickness (mm) is similar to Reference one: 0.082 ± 0.003 vs. 0.081 ± 0.002, $p > 0.05$. Low SDs in thickness indicate no significant differences within each patch type.

Both formulations exhibited a great folding endurance, with values above 300, proving suitable flexibility. Their flexibility is induced by the plasticizer used in the formulation and the patch-forming polymer [68].

Regarding the mechanical properties of the F-UBE-HPMC and Reference, it can be noticed that the differences between the formulations are not so significant; this could be predictable as they contain identical amounts of HPMC and PEG 400. Also, it is remarked that the UBE-loaded mucoadhesive oral patches display a higher elongation (51.26%) and a lower tensile strength (2.55 kg/mm^2) than their References (49.47%, respectively 2.83 kg/mm^2), proving the influence of the active ingredients on their resistance and elasticity. F-UBE-HPMC elongation and tensile strength are adequate to resist during handling [69].

The F-UBE-HPMC moisture content was 6.24%, with minor differences compared to Reference (6.02%). Both patches present suitable humidity. The moisture is due to the solvent system used in the formulation or to the ingredients' hygroscopic properties, especially the plasticizer [70]. A moderate amount of moisture is needed in mucoadhesive oral patches to ensure their elasticity and protection from being brittle, dry, and easy to break [71].

F-UBE-HPMC has a neutral pH value close to the oral cavity, ensuring good tolerability with no possible irritation of the buccal mucosa. It can be noticed that the active ingredients did not modify the pH of the matrix system, as the tested UBE-loaded formulation displayed a similar pH value to the Reference one.

F-UBE-HPMC reveals an in vitro disintegration time in a simulated saliva medium of 130 s. There are no differences between F-UBE-HPMC and R, suggesting that the UBE load does not influence the patches' disintegration performance. However, these results offer only orientation data considering that when applied to the oral mucosa, the patches are immobilized, and the fluid medium is secreted in low quantity.

The swelling rate over the 6 h of the study is presented in Figure 2e.

No significant differences between the UBE-loaded patch and Reference are revealed regarding the swelling ratio. The F-UBE-HPMC (272%) displays a lower swelling behavior than R (286%); the UBE state and dispersion determine it. We can observe that the swelling index increases more in the first 4 h, then the growth is slower, the differences between 330 and 360 min being insignificant. It is noticeable that the swelling rate increases linearly in the first 4 h, with around 20% every 30 min. The equilibrium state of swelling was reached at 240 min, and then the swelling was minor. The use of UBE does not considerably influence the swelling ability. No patch eroded after 6 h, and no swelling could be detected after this time.

Regarding the mucoadhesion time, F-UBE-HPMC has a retention time of 102 min on the oral mucosa, the Reference one being 106 min. Generally, the active ingredient dispersion in the polymer base significantly influences the bioadhesive behavior. The retention time depends on the film-forming polymer's and the plasticizer's retention properties; it is also highly controlled by the ratio between them [72].

3.4. BSL Assay

After 24 h, all the larvae were alive, swimming, and showing normally visible movements. After 48 h, 35.89% of larvae were active, and 12.82% were in the sublethal stage; the registered mortality was 51.28%. We investigated them under a microscope to observe the changes after 24 and 48 h of exposure. All these microscopic images are presented in Figure 3a–p.

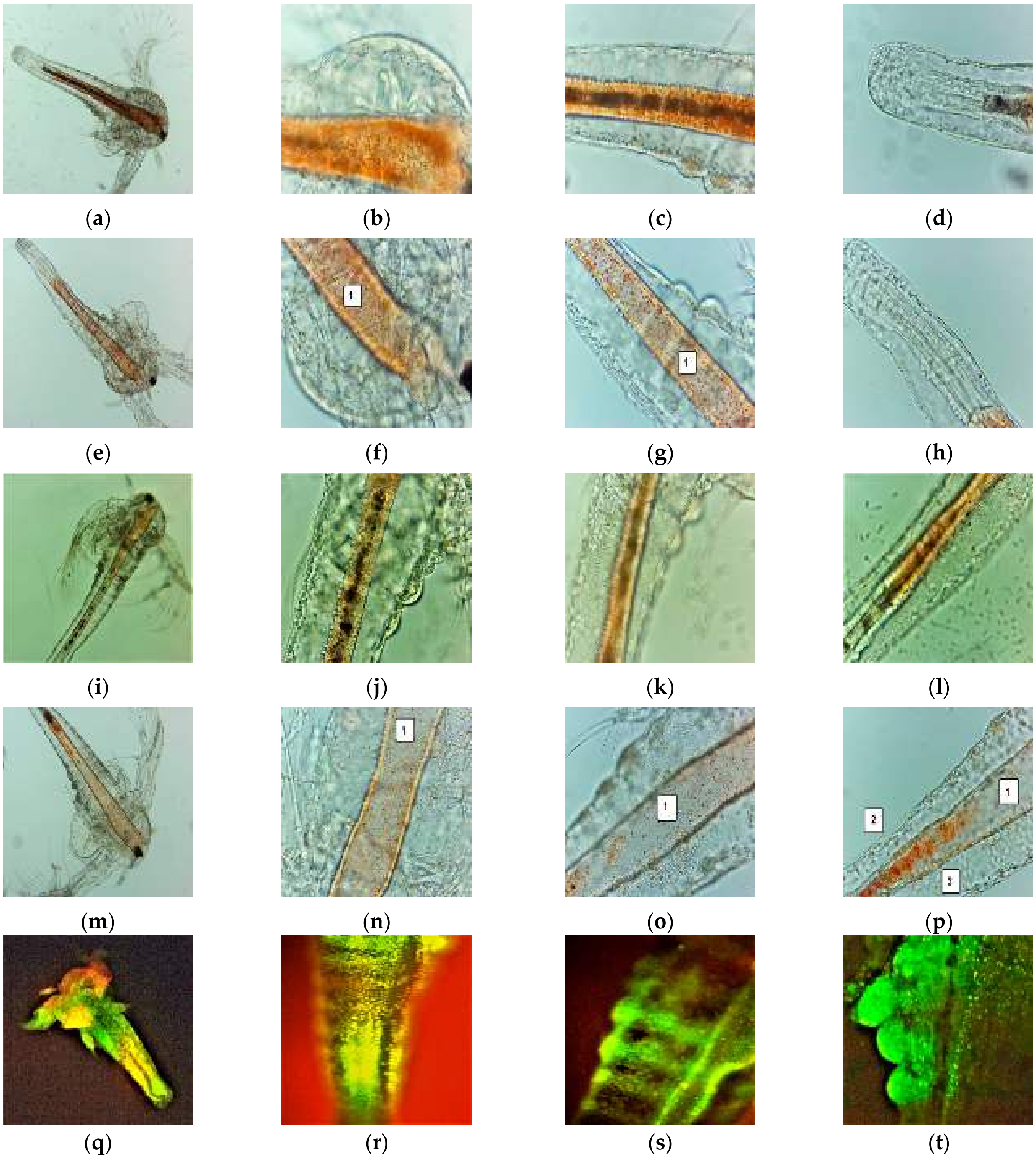

(**a**) (**b**) (**c**) (**d**)
(**e**) (**f**) (**g**) (**h**)
(**i**) (**j**) (**k**) (**l**)
(**m**) (**n**) (**o**) (**p**)
(**q**) (**r**) (**s**) (**t**)

Figure 3. *Cont.*

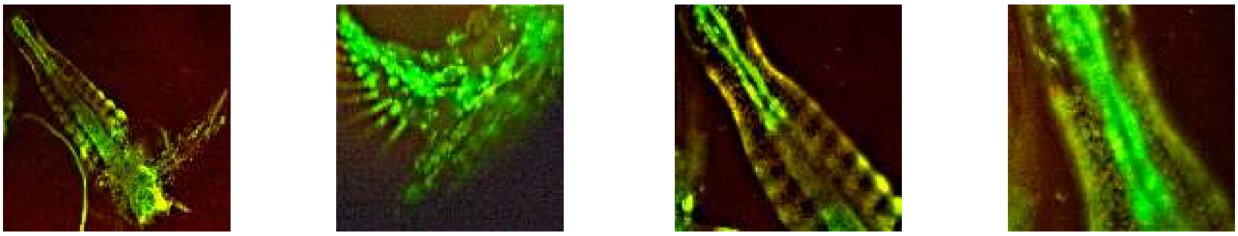

(**u**) (**v**) (**w**) (**x**)

Figure 3. *A. salina* larvae after the exposure to F-UBE-HPMC (**a**–**p**)—microscopic images at 100× (**a**,**e**,**i**,**m**) and 400× (**b**–**d**,**f**–**h**,**j**–**l**,**n**–**p**). After 24 h: blank (**a**–**d**) and F-UBE-HPMC (**e**–**g**); after 48 h: blank (**i**–**l**) and F-UBE-HPMC (**m**–**p**). The following changes can be observed compared to blank: (**f**–**g**,**n**–**p**) a low quantity of food in the digestive tract (1), (**p**) a low detachment of the cuticle from larval tissues (2), the cell damage with large intercellular spaces (3). FM images of *A. salina* larvae after 48 h of exposure at F-UBE-HPMC (**q**–**x**) stained with acridine orange 100× (**q**,**u**) 200× (**r**–**t**,**w**,**x**) and 400× (**f**). (**q**–**t**)—blank; (**u**–**x**)—F-UBE-HPMC. Intracellular lysosomes activated in cell death processes were revealed by the red fluorescence (**w**,**x**). F-UBE-HPMC—mucoadhesive oral patches loaded with *U. barbata* dry ethanol extract.

The brine shrimp larvae could not feed; after exposure for 24 h to F-UBE-HPMC they have a lower amount of food in the digestive tract (Figure 3e–h) than the negative control (Figure 3a–d). Because of this, they have not even passed to a higher larval stage. After 48 h, the high mortality rate recorded is due to starvation. Compared to blank (Figure 3i–l), the exposed larvae have an empty digestive tract (Figure 3m–p). The lack of nutrients leads to cell and tissue destruction, finalized with the death of *Artemia* nauplii.

In addition, at the intracellular level, FM images (Figure 3q–x) show activated lysosomes in cell death processes (Figure 3w,x).

3.5. In Vitro Analysis of the Biological Effects of Mucoadhesive Patches on Human Blood Cell Cultures and Oral Cancer Cell Line CLS-354

Our work continues the preliminary studies of *U. barbata* (L) dry extracts on normal and tumor cells [51,54]. In the present study, *U. barbata* dry extract in 96% ethanol was loaded into mucoadhesive patches (F-UBE-HPMC). Thus, we aim to explore the F-UBE-HPMC biological mechanisms implied in oxidative stress, caspase 3/7 activity, cell cycle, nuclear shrinkage, autophagy, apoptosis, and DNA synthesis in blood cells and CLS-354 tumor cells.

3.5.1. Evaluation of Total ROS Activity

F-UBE-HPMC induced oxidative cellular stress (expressed as total ROS) in blood cell cultures and CLS-354 tumor cell lines (Figure 4).

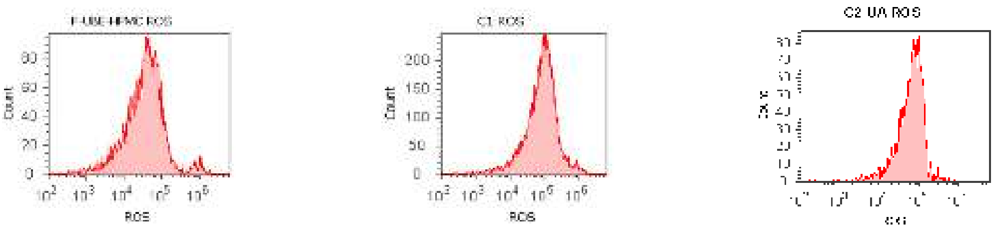

(**a**) (**b**) (**c**)

Figure 4. *Cont.*

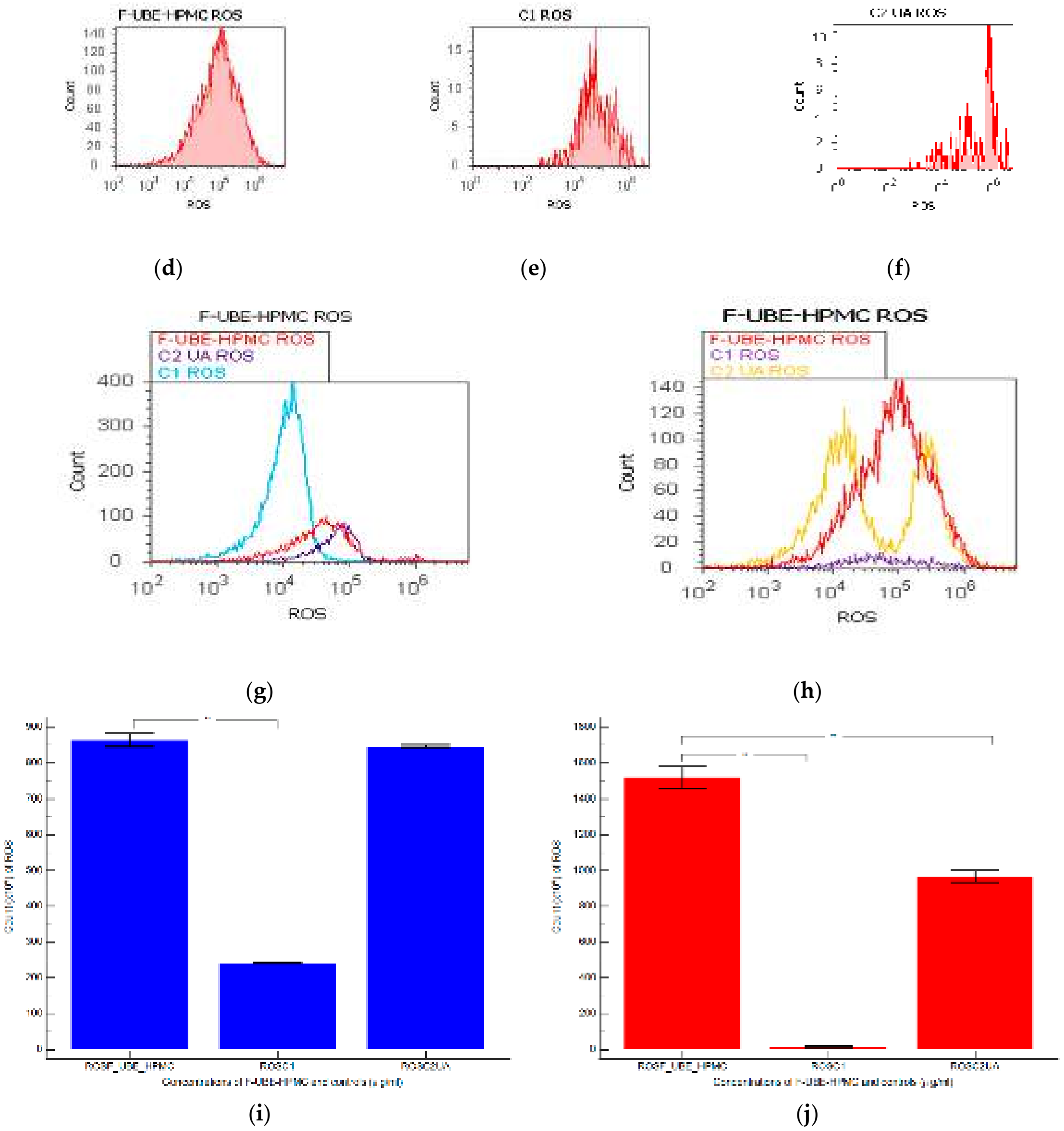

Figure 4. Reactive oxygen species (ROS) levels models in normal blood cells (**a**–**c**) and CLS-354 tumor cells (**d**–**f**) after 24 h treatment with F-UBE-HPMC. UBE-loaded mucoadhesive patches and controls extrapolated on ROS axis (**g**,**h**) in blood cells (**g**) and CLS-354 tumor cells (**h**); F-UBE-HPMC—mucoadhesive oral patch loaded with *U. barbata* dry ethanol extract (**a**,**d**); C1—1% DMSO negative control (**b**,**e**); C2—125 µg/mL UA-positive control (**c**,**f**). Statistical analysis of reactive oxygen species (ROS) in normal blood cells (**i**) and CLS-354 tumor cells (**j**). ** $p < 0.01$ evidence of significant statistical differences between controls and F-UBE-HPMC made by paired samples *t*-test; F-UBE-HPMC—mucoadhesive oral patches loaded with *U. barbata* (L.) dry ethanol extract; C1—negative control with 1% dimethyl sulfoxide (DMSO); C2UA—positive control with 125 µg/mL usnic acid (UA).

Significant elevations of ROS levels were reported in the blood cells treated with F-UBE-HPMC compared to both controls as follows: $863.33 \times 10^4 \pm 32.14$; vs. C1: $242.00 \times 10^4 \pm 2.00$; $p < 0.01$; C2UA: $846.66 \times 10^4 \pm 5.77$, $p \geq 0.05$ (Figure 4a–c,g,i).

The F-UBE-HPMC induced an intense ROS production in OSCC cells, compared to 1% DMSO and 125 µg/mL UA as follows: $1516.66 \times 10^4 \pm 105.98$; vs. $15.66 \times 10^4 \pm 4.04$; $966.66 \times 10^4 \pm 57.73$, $p < 0.01$ (Figure 4d–f,h,j).

3.5.2. Evaluation of Caspases 3/7 Activity

Caspase 3 controls DNA fragmentation and morphological changes in apoptosis. In contrast, caspase 7 appears to be more important to the loss of cellular viability. Thus, the combined role of both caspases is essential in mitochondrial apoptotic events [73]. To examine the pro-apoptotic effects of F-UBE-HPMC through the caspase 3/7 signaling pathway in normal blood cells and CLS-354 tumor cells, we have determined the enzymatic activity of caspase 3/7 by flow cytometry (Figure 5).

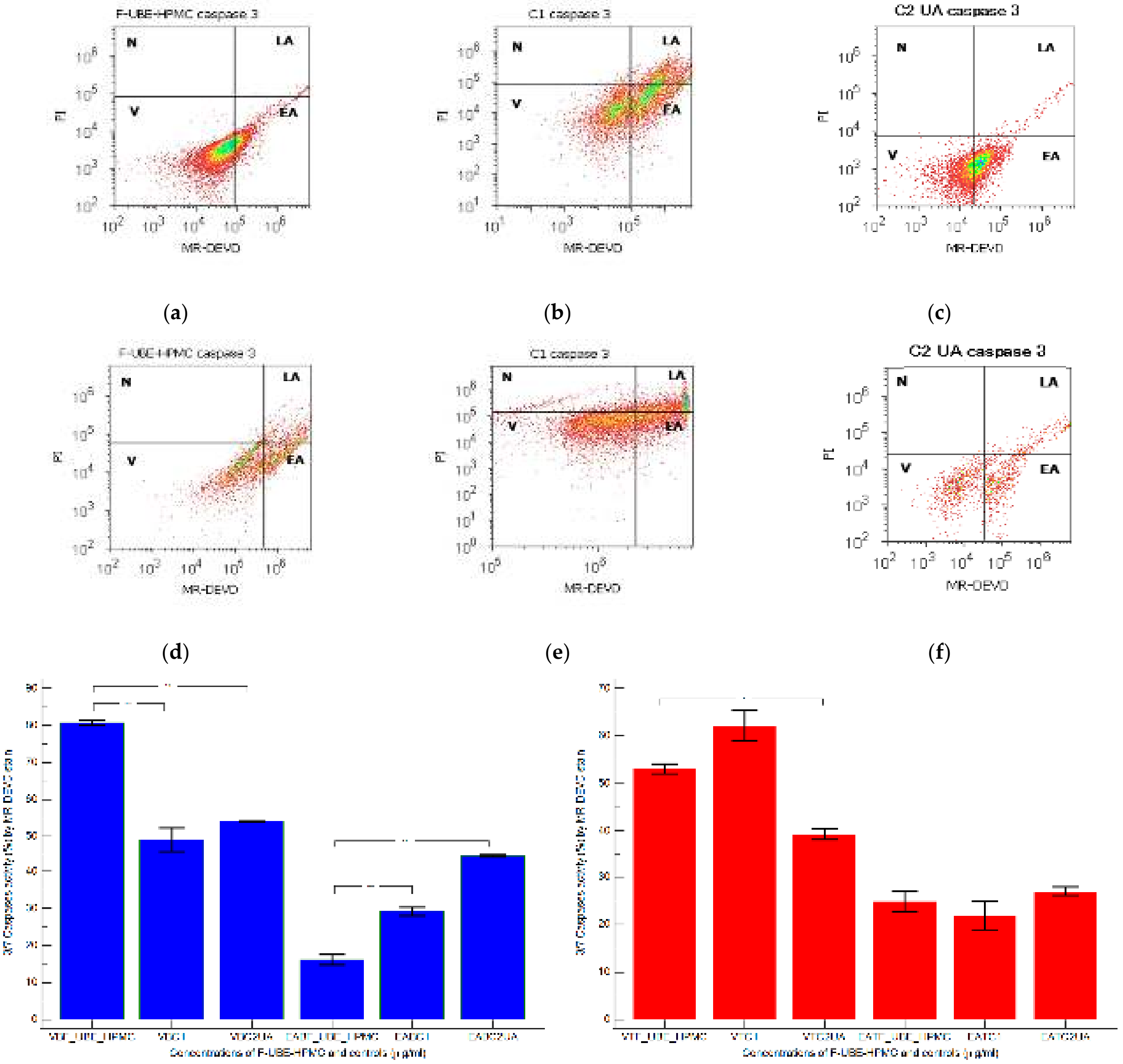

(**a**) (**b**) (**c**)

(**d**) (**e**) (**f**)

(**g**) (**h**)

Figure 5. Caspases 3/7 activity models in normal blood cells (**a**–**c**) and CLS-354 tumor cells (**d**–**f**) after 24 h treatment with F-UBE-HPMC. MR-DEVD patterns of F-UBE-HPMC (**a**,**d**), 1% DMSO negative control (**b**,**e**), and 125 µg/mL UA-positive control (**c**,**f**); Statistical analysis of 3/7 caspases activity in normal blood cells (**g**) and CLS-354 tumor cells (**h**). * $p < 0.05$ and ** $p < 0.01$ evidence significant statistical differences between controls and F-UBE-HPMC made by paired samples *t*-test; V—viability; EA—early apoptosis; F-UBE-HPMC—mucoadhesive oral patches loaded with *U. barbata* (L.) dry ethanol extract; C1—negative control with 1% dimethyl sulfoxide (DMSO); C2UA—positive control with 125 µg/mL usnic acid (UA).

Caspase 3/7 activity in blood cell cultures after 24 h of treatment with F-UBE-HPMC reported significantly lower values compared to both controls: 16.16 ± 2.40 vs. C1: 29.26 ± 1.97; C2UA: 44.74 ± 0.41, $p < 0.01$ (Figure 5a–c,g).

In CLS-354 tumor cells, the biochemical cascade of reactions implied in the proapoptotic signal induced by F-UBE-HPMC is slowly higher than the negative control and lower than positive control: 24.84 ± 3.65; vs. 21.88 ± 5.09; 27.02 ± 1.64, $p \geq 0.05$ (Figure 5d–f,h).

3.5.3. Cell Cycle Analysis

Using propidium iodide/RNase stain for DNA content allowed us to explore the effects of F-UBE-HPMC on cell cycle distribution in normal blood cells and CLS-354 tumor cells (Figure 6).

The F-UBE-HPMC induced a cell cycle arrest in the G1/G0 phase (90.60 ± 0.79) compared to negative control (88.52 ± 0.54, $p < 0.05$) and decreased DNA synthesis (1.91 ± 0.65 vs. 4.76 ± 0.68, $p < 0.01$) in normal blood cells (Figure 6a–c,g,i).

In CLS-354 tumor cells, F-UBE-HPMC determined a higher cell cycle arrest in the G0/G1 phase than the positive control: 93.03 ± 3.13 vs. 90.05 ± 3.45, $p < 0.01$ (Figure 6d–f,h,j). Significantly lower values of DNA synthesis were registered in CLS-354 tumor cells after treatment with F-UBE-HPMC compared to 1% DMSO: 3.58 ± 0.80 vs. 5.47 ± 0.83, $p < 0.01$ (Figure 6d,e,h,j).

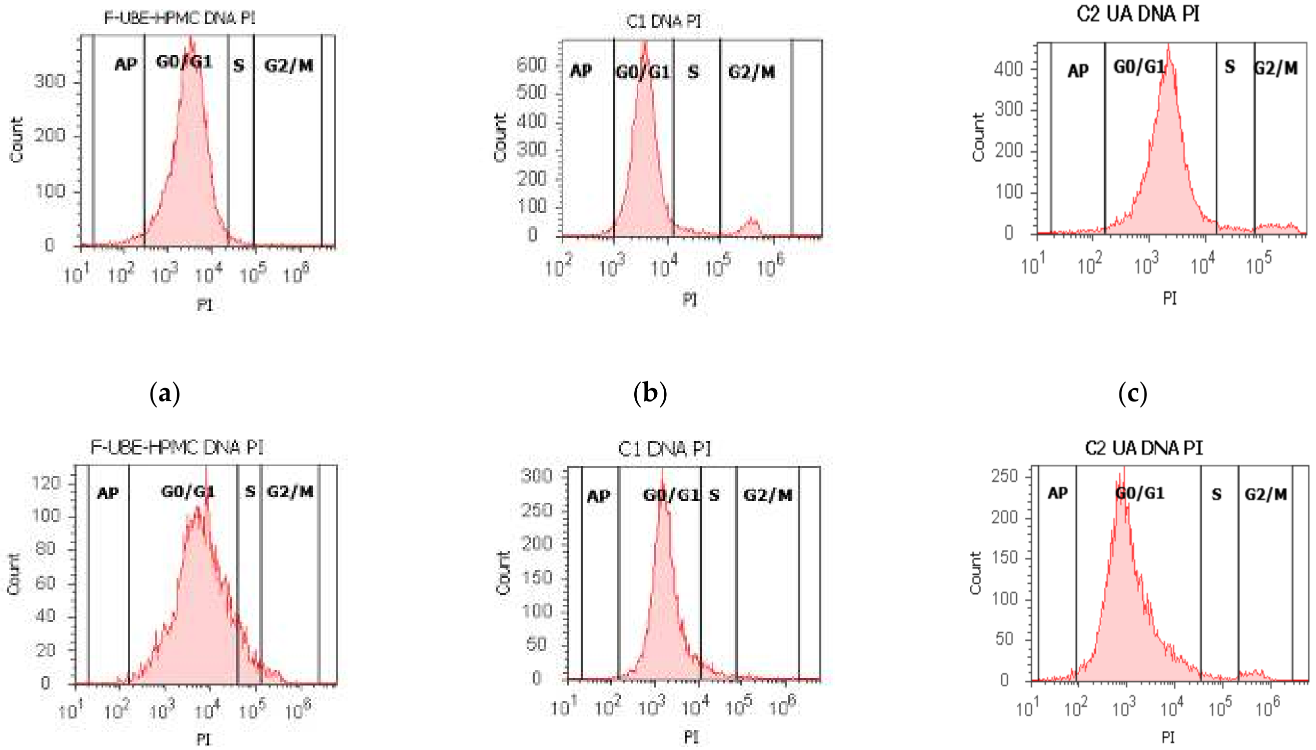

(**a**) (**b**) (**c**)

(**d**) (**e**) (**f**)

Figure 6. *Cont.*

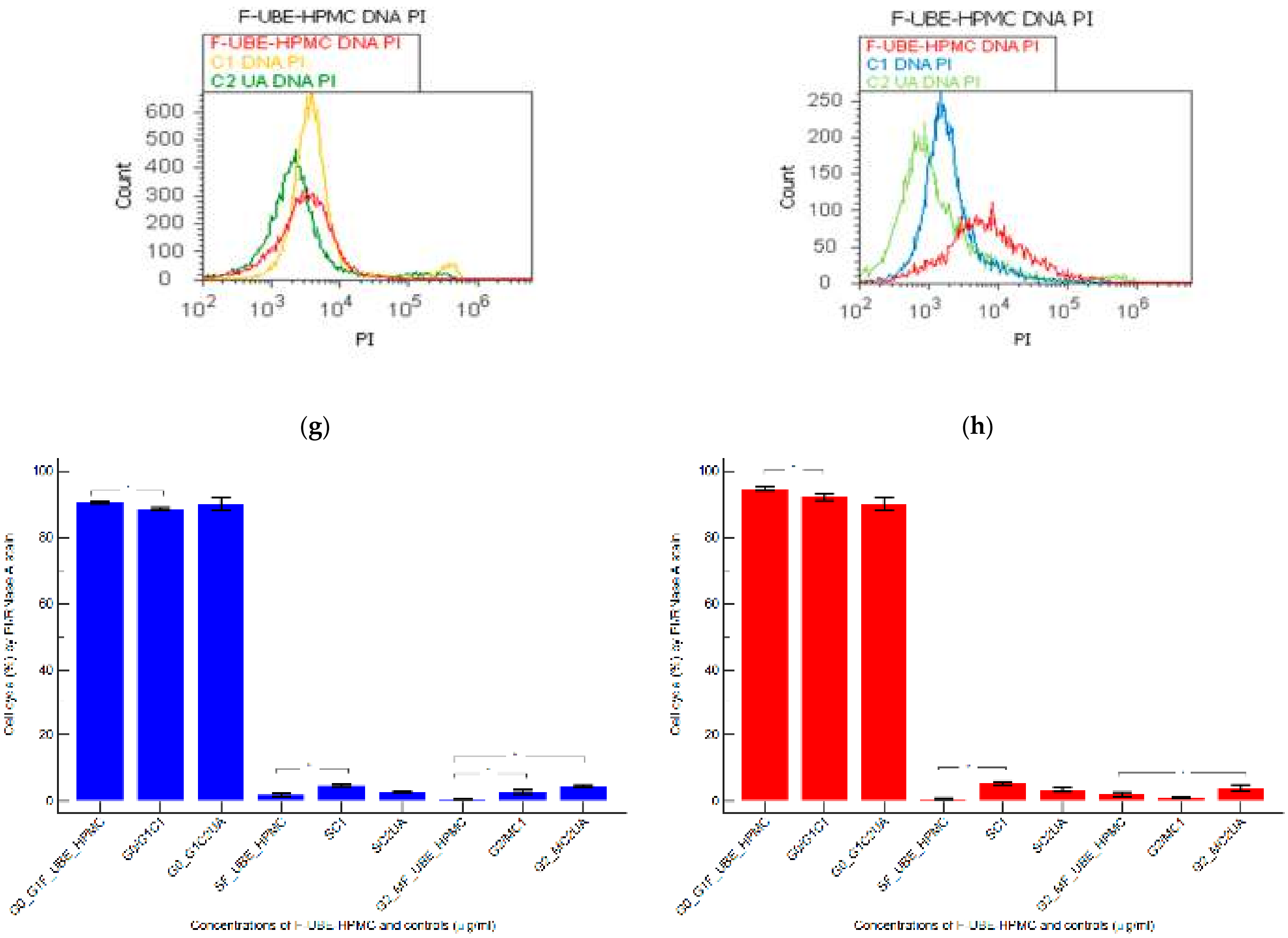

(**g**) (**h**)

(**i**) (**j**)

Figure 6. Cell cycle analysis in normal blood cells (**a**–**c**) and CLS-354 tumor cells (**d**–**f**) after 24 h treatment with F-UBE-HPMC. PI/RNase patterns of F-UBE-HPMC (**a**,**d**); 1% DMSO negative control (**b**,**e**); 125 µg/mL UA-positive control (**c**,**f**); F-UBE-HPMC and controls extrapolated on PI axis (**g**,**h**); AP—apoptosis (sub G0/G1); Statistical analysis (**i**,**j**) of G0/G1, synthesis (S), and G2/M phases of the cell cycle in normal blood cells (**i**) and CLS-354 tumor cells (**j**). * $p < 0.05$ and ** $p < 0.01$ represents significant statistical differences between controls and F-UBE-HPMC made by paired samples *t*-test; F-UBE-HPMC—mucoadhesive oral patches loaded with *U. barbata* (L.) dry ethanol extract; C1—negative control with 1% dimethyl sulfoxide (DMSO); C2UA—positive control with 125 µg/mL usnic acid (UA).PI–propidium iodide; S-synthesis of cell cycle phases; F-UBE-HPMC—mucoadhesive oral patches loaded with *U. barbata* (L.) dry ethanol extract.

3.5.4. Nuclear Condensation and Lysosomal Activity

Apoptotic cells display highly condensed pyknotic nuclei, stained with Hoechst 33342. Acridine orange highlighted the lysosomal activity after F-UBE-HPMC treatment on normal blood cells and CLS-354 tumor cells, as shown in Figure 7.

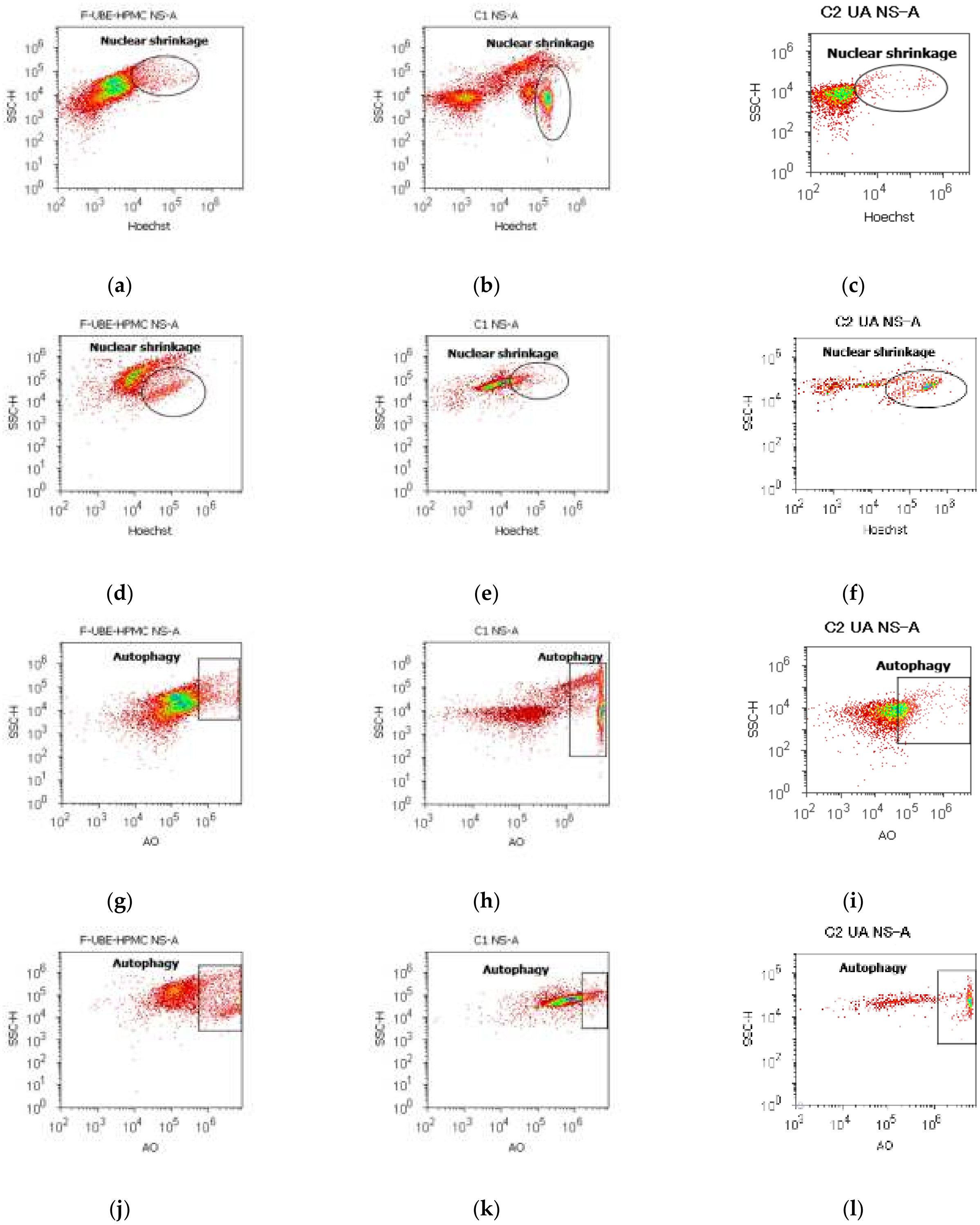

Figure 7. *Cont.*

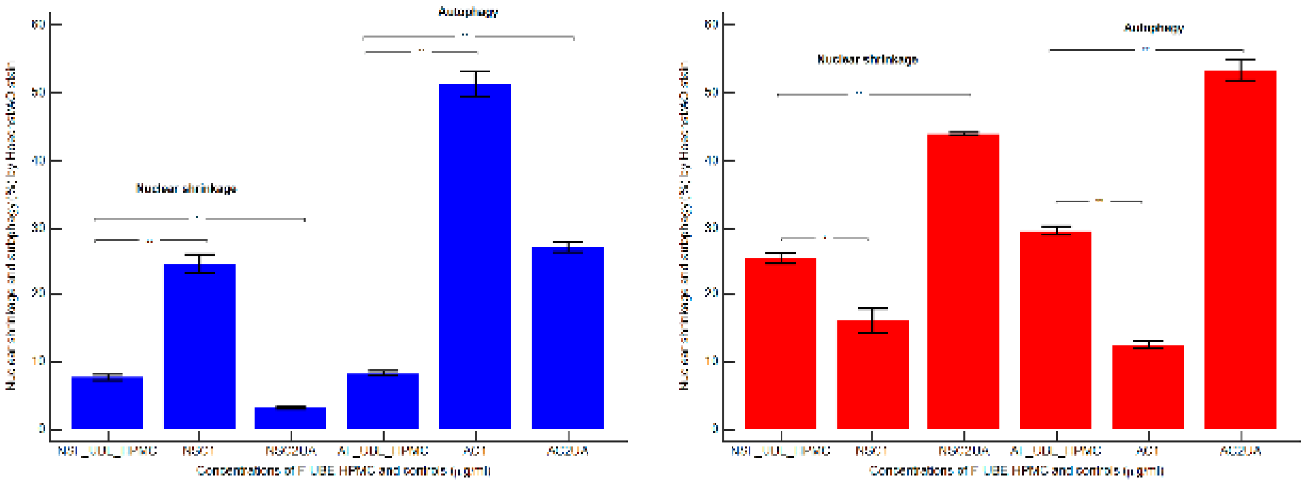

(**m**) (**n**)

Figure 7. Nuclear shrinkage models (**a**–**f**) in normal blood cells (**a**–**c**) and CLS-354 tumor cells (**d**–**f**), after 24 h treatment with F-UBE-HPMC. Hoechst patterns of F-UBE-HPMC (**a**,**d**); 1% DMSO negative control (**b**,**e**); 125 µg/mL UA-positive control (**c**,**f**); Lysosomal Activity (**g-l**) in normal blood cells (**g**–**i**) and CLS-354 tumor cells (**j**–**l**). Acridine orange patterns of F-UBE-HPMC (**g**,**j**); 1% DMSO negative control (**h**,**k**); 125 µg/mL UA-positive control (**i**,**l**); Statistical analysis of nuclear shrinkage and lysosomal activity (**m**,**n**) in normal blood cells (**m**) and CLS-354 tumor cells (**n**). * $p < 0.05$ and ** $p \leq 0.01$ reveal significant statistical differences between controls and F-UBE-HPMC made by paired samples *t*-test; NS—nuclear shrinkage; A—autophagy; F-UBE-HPMC—mucoadhesive oral patches loaded with *U. barbata* (L.) dry ethanol extract; C1—negative control with 1% dimethyl sulfoxide (DMSO); C2UA—positive control with 125 µg/mL usnic acid (UA).

After 24 h of treatment, the influence of the F-UBE-HPMC on nuclear shrinkage in normal blood cells was substantially lower (7.70 ± 0.80) reported to 1% DMSO: 24.50 ± 2.21, $p < 0.01$ (Figure 7a,b,m). However, they are significantly higher than the 125 µg/mL UA: 3.19 ± 0.30, $p < 0.05$ (Figure 7a,c,m).

The F-UBE-HPMC-induced autophagy had considerably diminished values in normal blood cells, compared to controls: 8.32 ± 0.61; vs. C1: 51.30 ± 3.25; C2UA: 27.05 ± 1.52, $p < 0.01$ (Figure 7g–i,m).

By flow cytometry examination, Hoechst 33342/acridine orange dual stained cells revealed chromatin condensation (NS) and autophagy (A) in OSCC cell lines exposed to F-UBE-HPMC for 24 h. Both processes were significantly intensified compared to 1% DMSO. The NS values were 25.29 ± 1.35 vs. 16.11 ± 3.11, $p < 0.05$ (Figure 7d,e,n) and A levels of 29.75 ± 1.12 vs. 12.57 ± 0.92, $p < 0.01$ (Figure 7j,k,n).

However, F-UBE-HPMC had significantly lower effects on nuclear shrinkage and lysosomal activity than 125 µg/mL UA: NS: 25.29 ± 1.35 vs. 44.03 ± 0.36, $p < 0.01$; A: 29.75 ± 1.12 vs. 53.35 ± 2.63, $p < 0.01$ (Figure 7d,f,j,l,n).

3.5.5. Annexin V-FITC Apoptosis Assay

Cell apoptosis by externalizing phosphatidyl serine—as evidenced by annexin V-FITC/PI stain—triggered by F-UBE-HPMC was determined by flow cytometry based on morphology and cell membrane integrity in normal blood cells and CLS-354 tumor cells (Figure 8).

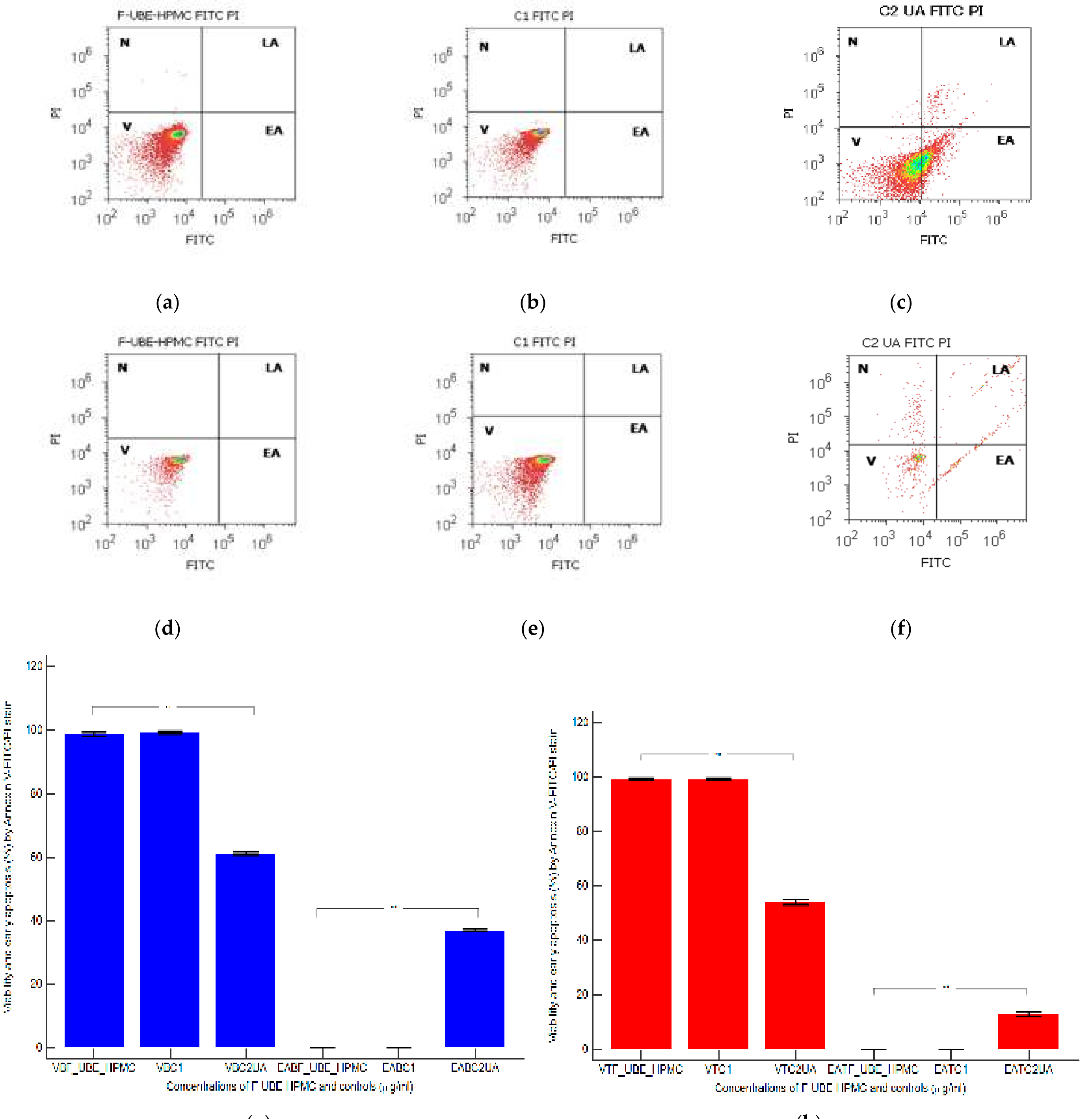

(**a**) (**b**) (**c**)

(**d**) (**e**) (**f**)

(**g**) (**h**)

Figure 8. Cell apoptosis models in normal blood cells (**a**–**c**) and CLS-354 tumor cells (**d**–**f**) after 24 h treatment with F-UBE-HPMC. Annexin V-FITC/PI patterns of F-UBE-HPMC (**a**,**d**); 1% DMSO negative control (**b**,**e**); 125 µg/mL UA-positive control (**c**,**f**); F-UBE-HPMC—mucoadhesive oral patches loaded with *U. barbata* (L.) dry ethanol extract. Statistical analysis of cell apoptosis in normal blood cell cultures (**g**) and CLS-354 tumor cell lines (**h**). ** $p < 0.01$ highlights significant statistical differences between controls and F-UBE-HPMC made by paired samples *t*-test; V—viability; EA—early apoptosis; F-UBE-HPMC—mucoadhesive oral patches loaded with *U. barbata* (L.) dry ethanol extract; C1—negative control with 1% dimethyl sulfoxide (DMSO); C2UA—positive control with 125 µg/mL usnic acid (UA).

After 24 h of treatment, in normal blood cells, F-UBE-HPMC did not induce early cell apoptosis (EA); the cell viability (V) had significant differences compared to C2UA. The following values were registered: EA—0.00 ± 0.00 vs. 37.04 ± 0.66, $p < 0.01$; V—98.76 ± 1.13 vs. 61.43 ± 0.88, $p < 0.01$ (Figure 8a,c,g).

Similar results were obtained at F-UBE-HPMC compared to 125 µg/mL UA regarding EA of tumor cells: 0.00 ± 0.00 vs. 12.92 ± 1.35, $p < 0.01$. Only UA induced EA in OSCC cells. Generally, the viability of tumor cells exposed to F-UBE-HPMC had considerably higher values than positive control: 99.36 ± 0.61 vs. 54.05 ± 1.35, $p < 0.01$ (Figure 8d,f,h).

3.5.6. Cell Proliferation

EdU (5-ethynyl-2′-deoxyuridine) directly measured DNA synthesis in normal blood cells and CLS-354 tumor cells treated with F-UBE-HPMC. Simultaneously, this test permitted the evaluation of DNA fragmentation as a sub G0/G1 phase corresponding to apoptotic cell fraction [74]. The obtained results are presented in Figure 9.

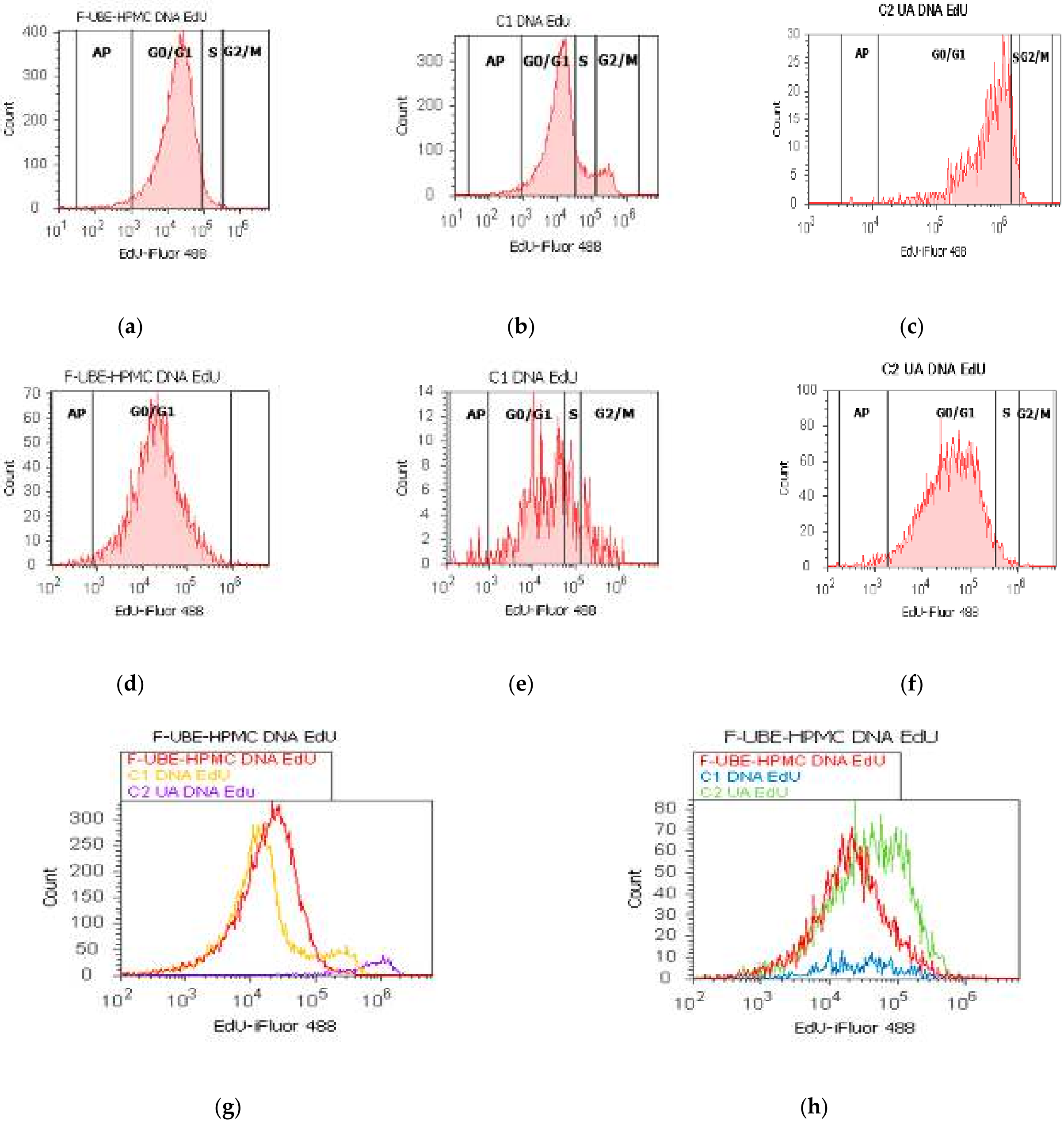

(a) (b) (c)

(d) (e) (f)

(g) (h)

Figure 9. *Cont.*

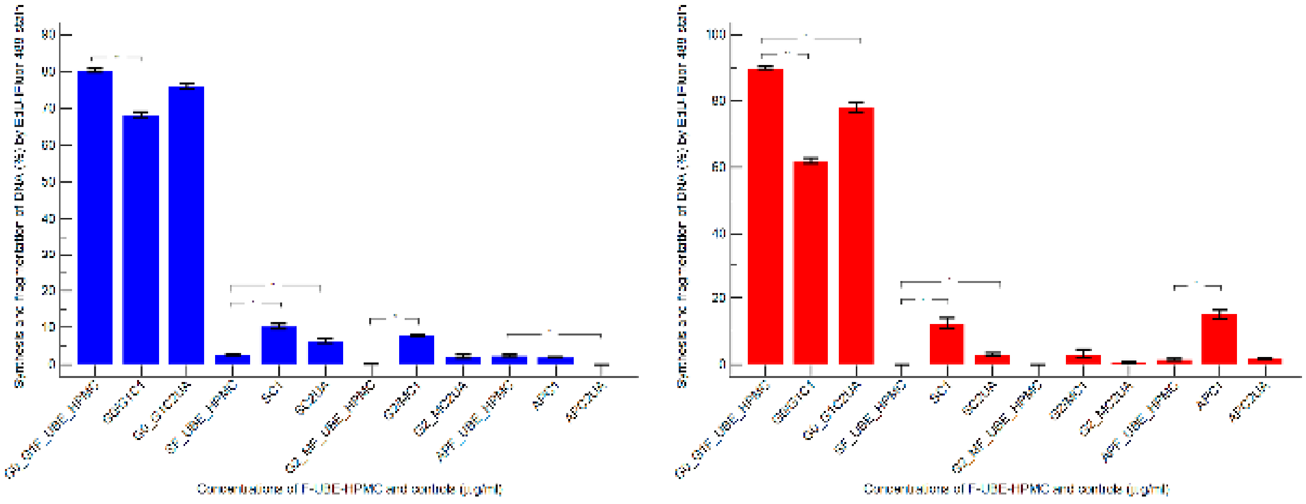

(i) **(j)**

Figure 9. Synthesis (S) and fragmentation of DNA models in normal blood cells (**a**–**c**) and CLS-354 tumor cells (**d**–**f**) after 24 h treatment with F-UBE-HPMC. EdU-iFluor 488 patterns of F-UBE-HPMC (**a**,**d**); 1% DMSO negative control (**b**,**e**); 125μg/mL UA-positive control (**c**,**f**). F-UBE-HPMC and controls extrapolated on EdU-iFluor 488 axis (**g**,**h**); AP—apoptotic cell fraction (sub G0/G1); F-UBE-HPMC—mucoadhesive oral patches loaded with *U. barbata* (L.) dry ethanol extract. Statistical analysis (**i**,**j**) of DNA synthesis (S) and fragmentation (AP—apoptotic cell fraction, sub G0/G1 phase) in normal blood cell cultures (**i**) and CLS-354 tumor cell lines (**j**). * $p < 0.05$ and ** $p < 0.01$ underlines significant statistical differences between both controls and F-UBE-HPMC made by paired samples *t*-test; F-UBE-HPMC—mucoadhesive oral patches loaded with *U. barbata* (L.) dry ethanol extract; C1—negative control with 1% dimethyl sulfoxide (DMSO); C2UA—positive control with 125 μg/mL usnic acid (UA).

In normal blood cells, F-UBE-HPMC considerably diminished DNA synthesis compared with both controls as follows: 2.75 ± 0.21 vs. 10.36 ± 1.21 (C1) and 6.49 ± 1.25 (C2UA), $p < 0.05$. DNA fragmentation implied in apoptosis significantly increased compared to 125 μg/mL UA: 2.49 ± 0.50 vs. 0.00 ± 0.00, $p < 0.05$ (Figure 9a–c,g,i).

On the other hand, in CLS-354 tumor cells, F-UBE-HPMC blocked DNA synthesis compared to both controls as follows: 0.00 ± 0.00 vs. 12.44 ± 2.80 (C1) and 3.14 ± 0.50 (C2UA), $p < 0.05$. However, the apoptotic cell fraction represented by fractional DNA (sub G0/G1 phase) [74] had lower values reported to 1% DMSO: 1.54 ± 0.70 vs. 15.18 ± 2.17, $p < 0.05$ (Figure 9d–f,h,j).

3.5.7. Principal Component Analysis

The principal component analysis (PCA) [75] was realized for F-UBE-HPMC and both controls (C1-DMSO and C2UA) and variable parameters measured in normal blood cells and CLS-354 OSCC tumor cells, according to the correlation matrix and PCA-correlation circle from Supplementary Material.

The PCA results are illustrated in Figure 10.

The two principal components explained the total data variance, with 64.26% attributed to the first (PC1) and 35.74% to the second (PC2). The PC1 was associated with controls (C1-DMSO and C2UA), caspase 3/7 activity in CLS-354 tumor cells, and ROS levels in normal blood cells. PC2 was related to F-UBE-HPMC mucoadhesive oral patches, ROS levels in CLS-354 tumor cells, and caspase 3/7 activity in normal blood cells.

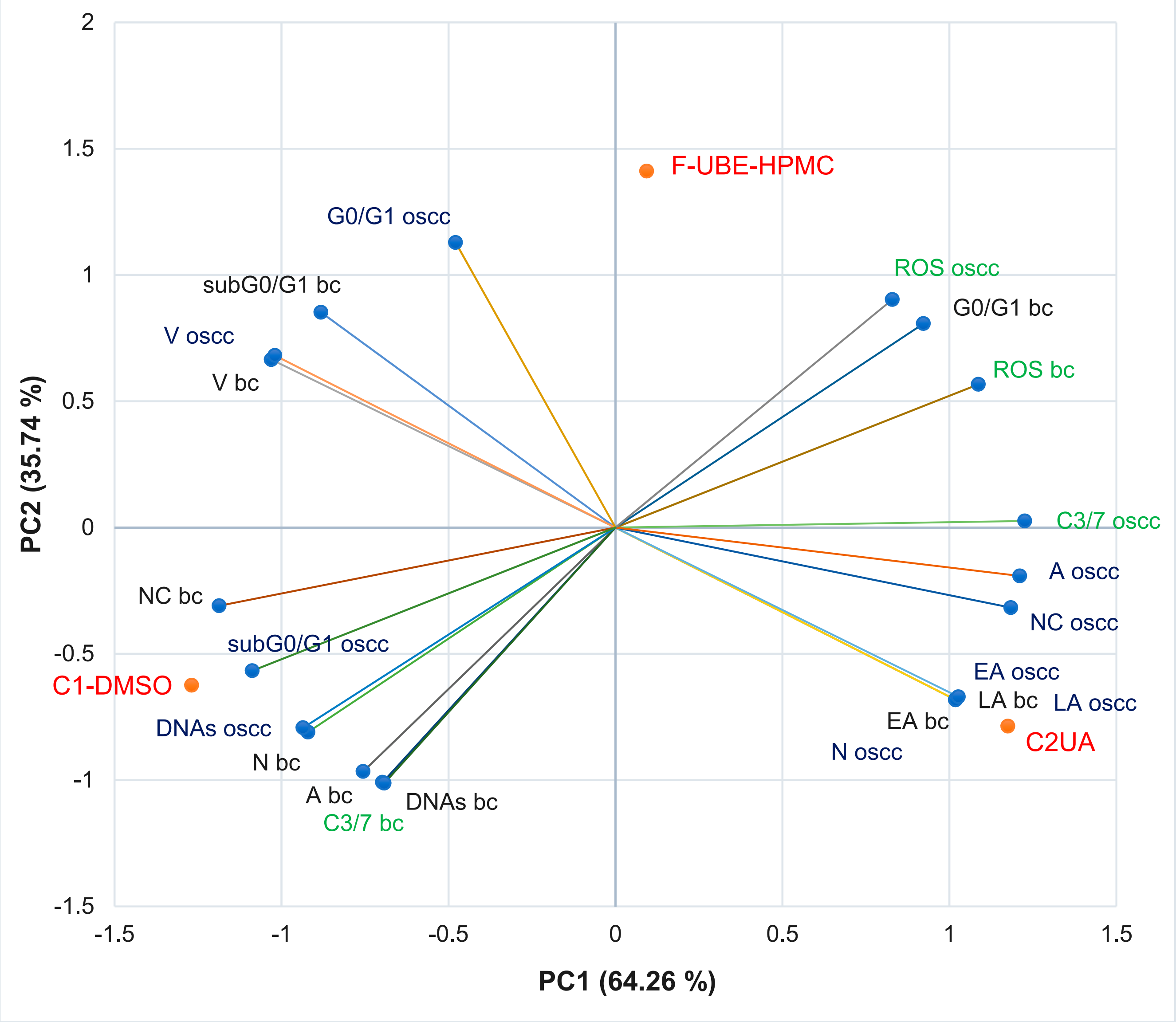

Figure 10. PCA-Correlation biplot between mechanisms (caspase 3/7 activity and cellular oxidative stress) and processes induced by F-UBE-HPMC and both controls (C1-DMSO and C2UA) in normal blood cells (bc) and CLS-354 tumor cells (oscc). F-UBE-HPMC—mucoadhesive oral patches loaded with *U. barbata* (L.) dry ethanol extract; V—viability, EA—early apoptosis, LA—late apoptosis, N—necrosis, NC—nuclear condensation, A—autophagy, DNAs—DNA synthesis, sub G0/G1—apoptotic cell fraction G0/G1—cell cycle arrest in G0/G1 phase, ROS—oxidative stress, C3/7—caspase 3/7 activity.

In normal blood cells, caspase 3/7 activity shows a high positive correlation with autophagy ($r = 0.998$, $p < 0.05$), DNA synthesis ($r = 0.999$, $p < 0.05$) and necrosis ($r = 0.970$, $p > 0.05$) and a moderate one with nuclear condensation ($r = 0.758$, $p > 0.05$). This pathway is highly negatively correlated with oxidative stress and cell cycle arrest in G0/G1 ($r = -0.885$, respectively $r = -0.970$, $p > 0.05$). Figure 10 also indicates that ROS level highly positively correlates with cell cycle arrest in G0/G1 ($r = 0.972$, $p > 0.05$); it reports a low correlation with ($r = 0.479$, $p > 0.05$). Oxidative stress shows a high negative correlation with DNA synthesis ($r = -0.882$, $p > 0.05$), necrosis ($r = -0.971$, $p > 0.05$), nuclear condensation ($r = -0.975$, $p > 0.05$), and autophagy ($r = -0.911$, $p > 0.05$).

In CLS-354 tumor cells, the effector caspase 3/7 activity is substantially positively correlated with autophagy ($r = 0.984$, $p > 0.05$), nuclear condensation ($r = 0.960$, $p > 0.05$), early apoptosis ($r = 0.819$, $p > 0.05$), late apoptosis ($r = 0.819$, $p > 0.05$) and necrosis ($r = 0.826$,

$p > 0.05$) and moderately correlated with ROS levels ($r = 0.692$, $p > 0.05$). This previously mentioned mechanism negatively correlates with DNA fragmentation in the sub G0/G1 phase (high, $r = -0.896$, $p > 0.05$), DNA synthesis (moderate, $r = -0.776$, $p > 0.05$), and cell cycle arrest in G0/G1 (low, $r = -0.371$, $p > 0.05$). The oxidative stress is considerably negatively correlated with DNA synthesis ($r = -0.992$, $p > 0.05$) and sub G0/G1 phase ($r = -0.940$, $p > 0.05$), and low positively correlated with early and late apoptosis, necrosis, nuclear condensation, and autophagy ($r = 0.152$–0.553, $p > 0.05$).

A general data analysis for the good visualization of F-UBE-HPMC and controls activity on normal and tumor cells is illustrated in Figure S2, Supplementary Material. Figure S2 shows that F-UBE-HPMC and the positive control (UA of 125 µg/mL) exhibit a higher activity on tumor cells than on normal blood cells (Figure S2A,C–E). The UBE-loaded mucoadhesive oral patches and UA diminish the blood cell damage induced by 1% DMSO through caspase 3/7 activity, nuclear condensation, and autophagy which trigger necrotic processes (Figure S2D). Moreover, F-UBE-HPMC has a higher protective action on normal cells than UA. On CLS-354 tumor cells, the UBE-loaded mucoadhesive patches induced the most elevated oxidative stress and complete inhibition of DNA synthesis (Figure S2A,E). Usnic acid, the main phenolic secondary metabolite of *Usnea* sp., exhibited the highest antitumor activity. These data correlation and interpretation established the places of F-UBE-HPMC and both controls (C1-DMSO and C2UA) in the PCA-biplot (Figure 10), highlighting the corresponding processes triggered in CLS-354 cancer cells and normal blood cells.

3.6. Antimicrobial Activity

Data registered in Table 2 display the used in microdilutions of standard antibiotic (CTR) and antifungal (TRF) drugs and F-UBE-HPMC. Data from Table 2 show that the colors of standard antibiotics correlate with their inhibiting power and are directly proportional to their concentration. We can observe CTR dose-dependent inhibitory activity on both tested bacteria. However, *S. aureus* sensibility at CTR is higher than *P. aeruginosa.*

Contrariwise, the inhibitory activity of F-UBE-HPMC is higher on *P. aeruginosa* than on *S. aureus.* Therefore, the inhibitory activity of F-UBE-HPMC of [5.2–0.65] mg/mL against *S. aureus* is similar to CTR of [0.75–0.093] mg/mL. On *P. aeruginosa,* F-UBE-HPMC of [5.2–0.325] mg/mL acts similarly with CTR of [1.998–1.599] mg/mL; lower concentrations of [0.162–0.081] mg/mL have a similar effect with CTR of [0.093–0.046] mg/mL.

Data from Table 2 shows that TRF had a fungicidal effect on both *Candida* sp. [64] and in the entire microdilutions domain.

On *C. albicans*, the F-UBE-HPMC of [5.2–0.65] mg/mL acts similarly to TRF. The lower dilutions of [0.325–0.081] mg/mL exhibit a significantly diminished effect, inducing a moderate to fast proliferation of *C. albicans* colonies (Table 2).

After 24 h of incubation with the first two dilutions of F-UBE-HPMC [5.2–2.6] mg/mL, *C. parapsillosis* fungal cells were partially dead [64]. The following F-UBE-HPMC concentrations of [1.3–0.081] mg/mL progressively induced low to moderate cell proliferation.

Table 2. Antibacterial and antifungal activity of UBE-loaded mucoadhesive oral patches.

	Microdilutions			
Microdilution	**CTR**		**TRF**	**F-UBE-HPMC**
	30 mg/mL	**122 mg/mL**	**10.1 mg/mL**	**104 mg/mL**
1	1.5	6.1	0.5	5.2
2	0.75	4.88	0.25	2.6
3	0.375	3.904	0.125	1.3
4	0.187	3.123	0.062	0.65
5	0.093	2.498	0.031	0.325
6	0.046	1.998	0.015	0.162
7	0.023	1.599	0.007	0.081

Table 2. *Cont.*

	Antibacterial activity							
	S. aureus				***P. aeruginosa***			
Dil.	**CTR**		**F-UBE-HPMC**		**CTR**		**F-UBE-HPMC**	
	A	**B**	**A**	**B**	**A**	**B**	**A**	**B**
1		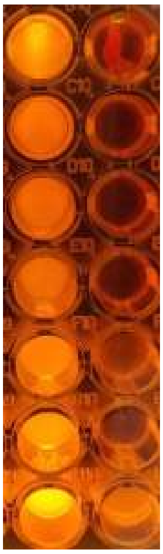	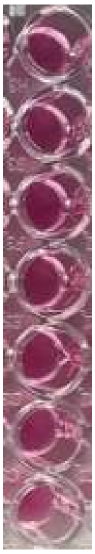	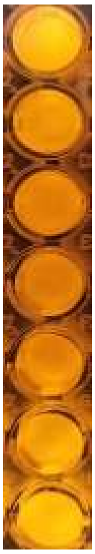				
2								
3								
4								
5								
6								
7								
	🟦	🟦	🟪	🟪	🟥	🟥	⬜ *	

	Antifungal activity										
	C. albicans				***C. parapsilosis***						
Dil.	**TRF**		**F-UBE-HPMC**		**TRF**		**F-UBE-HPMC**		**Color ****	**Score ****	**Signification ****
	A	**B**	**A**	**B**	**A**	**B**	**A**	**B**			
1									🟦	0	Blue—cells are death
2									🟪	1	Violet-blue—cells are partially dead
3									🟪	2	Violet—cells are alive; no proliferation
4									🟪	3	Light-violet—low proliferation
5									🟪	4	Dark pink—mode-rate proliferation
6									🟪	5	Pink—fast proliferation
7									⬜	6	Light pink—very fast proliferation

CTR—ceftriaxone; TRF—Terbinafine; F-UBE-HPMC—mucoadhesive oral patch loaded with UBE; UBE—*U. barbata* dry ethanol extract; * Resazurin dye chart adapted from Madushan et al. [62] as follows: blue—"excellent"; light blue—"very good"; violet—"good"; purple-pink—"moderate"; light pink—"low"; pink—"very low"; white—"no effect"; A. well plates examined by using Resazurin dye chart; B. well plates examined at a wavelength of 470 nm; ** Results interpreting adapted from Bitacura et al. [64]. TRF—Terbinafine, F-UBE-HPMC—mucoadhesive oral patches loaded with UBE (*U. barbata* dry ethanol extract), A—well plates examined through Resazurin color; B—well plates read at a wavelength of 470 nm.

4. Discussion

Until the pharmaceutical formulation, our team studied *U. barbata* from the Calimani mountains for almost 6 years, according to current medicinal plant legislation [76–78]. In the present work, mucoadhesive oral patches containing *U. barbata* dry ethanol extract were manufactured and analyzed, compared to References (the same formulation without UBE). HPMC in a 15% aqueous dispersion ensured suitable patch toughness. PEG 400—in a 5% concentration of the patch mass—provided an elegant, glossy, smooth appearance and high flexibility. The F-UBE-HPMC homogeneity proved that the active ingredient was adequately incorporated into the polymer matrix due to the miscibility of the vehicles.

Weight and thickness low variations guarantee the efficiency of the formulation and applied method and provide a certain content uniformity. F-UBE-HPMCs have suitable weight and thickness for application to the oral mucosa [45,79,80], and our results are similar to other developed studies on HPMC patches [79].

The patches' flexibility is essential for easy handling and administration. Semalty et al. [81] proved that mixing HPMC with PEG in 30% of the polymer weight leads to low folding endurance. Thus, PEG used in low concentrations represents the optimal plasticizer. In the present study, PEG 400 in a 5% proportion confirms the excellent flexibility of both patches. The plasticizer reduces patch rigidity by minimizing intermolecular forces [82]. High amounts of plasticizer, due to over-hydration, might diminish the patches' mucoadhesive properties [83].

In F-UBE-HPMC, UBE is dissolved in the base, thus maintaining its natural structure. The polymer molecular chain disruption induces higher chain mobility, increasing flexibility, and decreased rigidity. Maher et al. [84] proved the influence of the polymer type on the patch tensile strength. Also, it was confirmed that the tensile strength increases with the film-forming polymer concentration. The HPMC 15% dispersed in water leads to developing a strong matrix with a suitable network density. The results show the film-forming agent and the plasticizer's substantial influence on the patches' mechanical properties. Their strength is affected by the active ingredient's nature, concentration, and dispersion type.

The amount of moisture influences the patches' friability; as proven, both ones display good resistance. Thus, the contained humidity could offer suitable mechanical properties. PEG 400 highlights a substantial hygroscopicity due to its hydrophilic hydroxyl groups interacting with water [35], providing numerous sites for interactions and leading to the patches' moisture retention. However, HPMC has hydrophilic hydroxypropyl substituents but contains hydrophobic methoxyl groups and does not maintain excessive moisture [85].

All the ingredients influence the patches' pH values. We aimed to properly select them to obtain a surface pH similar to the buccal one, and F-UBE-HPMCs are biocompatible with the oral mucosa, having a neutral pH.

The disintegration time displayed by both patches intensely depends on the polymer matrix. Shen et al. [86] demonstrated that the patch disintegration time rises with increasing HPMC concentration. The patches' in vitro behavior was typical for rapid disintegration systems, allowing a fast release of the active ingredient.

The swelling properties are essential for patches' mucoadhesion. They considerably depend on the diffusivity of water into the polymer [87]. Therefore, it was proven that the disturbance of the polymer chains by including active ingredients in the matrix decreases the water content [88].

The values registered for ex vivo retention time help predict the patches' in vivo mucoadhesive performance. The obtained results proved to be satisfactory for the studied formulations. Adhesion is enhanced with the hydration increase until an optimal point; overhydration determines the polymer/tissue interface damage and diminishes the bioadhesive force.

The neutral pH and rapid disintegration of F-UBE-HPMC permitted in vitro and in vivo investigation. The *U. barbata* dry ethanol extract was previously studied and proved to have significant pharmacological potential. Its secondary phenolic metabolites were quantified through HPLC-DAD; UBE has a total phenolic content of 573.234 ± 42.308 mg PyE/g, of which 108.742 ± 0.703 mg/g usnic acid, 0.605 ± 0.007 mg/g ellagic acid, and 0.870 ± 0.008 mg/g gallic acid [65]. Moreover, using UHPLC/ESI/MS/MS in negative mode, Salgado et al. [89] identified other secondary metabolites with phenolic structures (depsides, depsidones, diphenyl ethers). We investigated the cytotoxic activity of UBE on brine shrimp larvae [40], normal blood cells [51], and OSCC cancer cells CAL-27 [54], and its antimicrobial activity on various bacterial and fungal strains [90–92].

To compare the F-UBE-HPMC bioactivities with the UBE ones, we opted for similar studies: BSL assay for cytotoxicity prescreening, blood cell cultures from the same donor (a member of our research team), and another OSCC cell line (CLS-354).

The brine shrimp lethality assay is a significant and low-cost antitumor prescreening in anticancer drug discovery [49]. The effects of F-UBE-HPMC on *A. salina* nauplii can be extrapolated to the analysis of their activity on tumor cells [93]. After 24 h of exposure, the brine shrimp larvae were alive with normal movements. However, the microscopic examination of *A salina* nauplii showed that they could not feed. Compared to the control, there is a low food amount in the digestive tract of the exposed larvae for 24 h to the F-UBE-HPMC; therefore, they have not even passed to a higher larval stage. After 48 h, a high level of larvae mortality was registered; it could be extrapolated to tumor cells as a blockage of DNA synthesis and cell cycle arrest in G0/G1 [93,94].

After 24 h of F-UBE-HPMC treatment, the viability of tumor cells was over 99%, similar to BSL assay results. However, the flow-cytometry analyses have shown that UBE-loaded mucoadhesive oral patches trigger apoptotic mechanisms in OSCC cells by a massive increase in ROS level and stimulation of effector caspases 3/7 enzymatic activity. Both mechanisms lead to DNA synthesis blockage, cell cycle arrest in G0/G1, nuclear condensation, and autophagy. Through the pro-oxidant activity, f-UBE-HPMC exhibits a higher activity on tumor cells than on normal blood cells. In normal blood cells, the patches highlighted a substantially lower ROS production. Their protective effects on normal cells diminish the blood cell damage induced by 1% DMSO through necrotic processes and reduce caspase 3/7 enzymatic activity, nuclear condensation, and autophagy. All these results could be explained by the dual redox behavior of usnic acid and other phenolic secondary metabolites (pro-oxidant in tumor cells and antioxidant in normal cells), as proved by numerous studies from the scientific literature [54,95–103]. Compared to the patches, the UBE effects were faster, with the larvae and cell viability diminished after 24 h [40,51,54]. Moreover, its activity on tumor cells was noticeable. UBE also proved an effective in vitro wound-healing potential, higher on normal cells than tumor ones [54].

In their previous studies, Jardón-Romero et al. [104], Rafey et al. [105], and Thiyahuddin et al. [106] considered *S. aureus, P. aeruginosa, C. albicans,* and *C. parapsillosis* as the most frequent pathogens responsible for opportunistic oral cavity infections in immunocompromised and older people; we previously examined UBE inhibitory activity against these microbial species [90]. Our results showed that oral mucoadhesive patches loaded with *U. barbata* dry ethanol extract have a dose-dependent inhibitory activity against these microorganisms. Usnic acid and other phenolic constituents from UBE underlie these antimicrobial effects through various mechanisms, acting on many sites at the cellular level [107–109]. The results of the F-UBE-HPMC pharmacological potential investigation proved that this pharmaceutical formulation preserved all the properties of UBE as an active ingredient. Moreover, the manufacturing process and polymers used for obtaining UBE-loaded mucoadhesive oral patches did not affect the bioactive secondary metabolites of *U. barbata* dry ethanol extract, being optimal for its therapeutic purposes.

It is known that usnic acid, the main secondary metabolite of *Usnea* sp., displays severe hepatotoxicity. It caused fulminant liver failure when it was used as a fat burner in a complex dietary supplement (LipoKinetix, Syntrax, Cape Girardeau, MO, USA) [110], associated with a recommended daily dose of 300–600 mg. *Usnea* sp is also known in Traditional Chinese Medicine as a liver detoxifier. The common TCM dosages were 6–9 g of dried lichen, corresponding to around 60–120 mg of usnic acid per day [111]; thus, 1768 patches cover the minimal used daily dose.

5. Conclusions

In this study, the mucoadhesive oral patches loaded with *U. barbata* dry ethanol extract were prepared using HPMC and PEG 400 for their formulation. The F-UBE-HPMCs were compared to References (the same patches without active lichen extract) through complex physico-chemical and pharmacotechnical procedures, proving their suitability for oral topical administration.

Moreover, F-UBE-HPMC pharmacological potential investigation confirmed an in vitro anticancer activity on oral squamous cell carcinoma and dose-dependent inhibitory effects against the most common bacterial and fungal pathogens implicated in immunosuppressed patients' oral infections.

The results suggest that the mucoadhesive oral patches loaded with *U. barbata* dry ethanol extract could be a promising phytotherapeutic formulation with potential application in oral medicine.

Supplementary Materials: The following supporting information can be downloaded at: https://www.mdpi.com/article/10.3390/antiox11091801/s1, Figure S1. Mucoadhesive oral patches: (a) Reference, (b) F-UBE-HPMC; Figure S2. Comparative activity on normal blood cells and CLS-354 tumor cells of F-UBE-HPMC and both controls. A. F-UBE-HPMC; B. 1% DMSO (negative control); C. UA of 125 µg/mL (positive control); D,E. An overview of F-UBE-HPMC films' activity and controls on normal blood cells (D) and OSCC tumor cells (E). V—viability, EA—early apoptosis, LA—late apoptosis, N—necrosis, NC—nuclear condensation, A—autophagy, DNAs—DNA synthesis, sub G0/G1—apoptotic cell fraction, G0/G1—cell cycle arrest in G0/G1 gap, ROS—oxidative stress, C3/7—caspase 3/7 activity. File S1: Principal component analysis processes induced by F-UBE-HPMC and both controls (C1-DMSO and C2UA) in normal blood cells (bc) and CLS-354 tumor cells (oscc).

Author Contributions: Conceptualization, V.P., E.M., G.C.C., L.B., C.E.G., V.S. and E.A.O.; methodology, E.M., G.C.C., L.B., V.S., E.A.O., A.M.M., D.L., M.A. (Mariana Aschie) and E.D.; software, V.P., E.M., V.S., E.A.O., M.A.M. and S.P.; validation, E.M., G.C.C., L.B., C.E.G., E.A.O., M.A.M., A.M.M. and V.B.; formal analysis, A.M.M., S.P., I.A., A.R., R.-A.M. and M.A. (Mihai Anastasescu); investigation, C.E.G., M.A.M., A.M.M., S.P., I.A., A.R. and R.-A.M.; resources, V.P., L.B., V.S., D.L., M.A. (Mariana Aschie) and E.D.; data curation, G.C.C., M.A.M. and A.M.M.; writing—original draft preparation, V.P., E.M., E.A.O., V.S. and A.M.M.; writing—review and editing, V.P., E.M., E.A.O. and A.M.M.; visualization, G.C.C., L.B., C.E.G., A.C., D.L., M.A. (Mariana Aschie), E.D. and V.B.; supervision, G.C.C., L.B., C.E.G., D.L., M.A. (Mariana Aschie), E.D. and V.B.; project administration, V.B.; funding acquisition, V.P. All authors have read and agreed to the published version of the manuscript.

Funding: This project was supported by the project ANTREPRENORDOC, in the framework of Human Resources Development Operational Programme 2014–2020, financed from the European Social Fund under the contract number 36355/23.05.2019 HRD OP/380/6/13—SMIS Code: 123847.

Institutional Review Board Statement: The study was conducted according to the Declaration of Helsinki and approved by the Institutional Ethics Committee of Ovidius University of Constanta, code 7080/10.06.2021 for studies involving humans.

Informed Consent Statement: Written informed consent has been obtained from the blood donor to publish this paper, code 39/30.06.2021.

Data Availability Statement: Data are available in this manuscript.

Acknowledgments: This project was performed in collaboration with the Department of Pharmaceutical Technology and Biopharmacy, and Department of Pharmacognosy, Phytochemistry, and Phytotherapy, Faculty of Pharmacy, Carol Davila University of Medicine and Pharmacy, 6 Traian Vuia Street, 020956 Bucharest, Romania, the Institute of Physical Chemistry "Ilie Murgulescu", 202 Splaiul Independentei Street, 060021. Bucharest, Romania, and the Center for Research and Development of the Morphological and Genetic Studies of Malignant Pathology, Ovidius University of Constanta, CEDMOG, 145 Tomis Blvd., 900591 Constanta, Romania.

Conflicts of Interest: The authors declare no conflict of interest.

References

1. Glick, M.; Williams, D.M.; Kleinman, D.V.; Vujicic, M.; Watt, R.G.; Weyant, R.J. A new definition for oral health developed by the FDI World Dental Federation opens the door to a universal definition of oral health. *Int. Dent. J.* **2016**, *66*, 322–324. [CrossRef] [PubMed]
2. Pires, F.R.; Ramos, A.B.; de Oliveira, J.B.C.; Tavares, A.S.; de Luz, P.S.R.; dos Santos, T.C.R.B. Oral squamous cell carcinoma: Clinicopathological features from 346 cases from a single oral pathology service during an 8-year period. *J. Appl. Oral Sci.* **2013**, *21*, 460–467. [CrossRef] [PubMed]
3. Sathish, N.; Wang, X.; Yuan, Y. Human Papillomavirus (HPV)-associated Oral Cancers and Treatment Strategies. *J. Dent. Res.* **2014**, *93*, 29–36. [CrossRef]
4. Di Stefano, M.; Polizzi, A.; Santonocito, S.; Romano, A.; Lombardi, T.; Isola, G. Impact of Oral Microbiome in Periodontal Health and Periodontitis: A Critical Review on Prevention and Treatment. *Int. J. Mol. Sci.* **2022**, *23*, 5142. [CrossRef] [PubMed]
5. Zhang, Y.; He, J.; He, B.; Huang, R.; Li, M. Effect of tobacco on periodontal disease and oral cancer. *Tob. Induc. Dis.* **2019**, *17*, 40. [CrossRef]
6. Lamster, I.B. The 2021 WHO Resolution on Oral Health. *Int. Dent. J.* **2021**, *71*, 279–280. [CrossRef] [PubMed]
7. Moghadam, E.T.; Yazdanian, M.; Tahmasebi, E.; Tebyanian, H.; Ranjbar, R.; Yazdanian, A.; Seifalian, A.; Tafazoli, A. Current herbal medicine as an alternative treatment in dentistry: *In vitro, in vivo* and clinical studies. *Eur. J. Pharmacol.* **2020**, *889*, 173665. [CrossRef]
8. Kumar, M.; Prakash, S.; Lorenzo, J.M.; Chandran, D.; Dhumal, S.; Dey, A.; Senapathy, M.; Rais, N.; Singh, S.; Kalkreuter, P.; et al. Apitherapy and Periodontal Disease: Insights into In Vitro, In Vivo, and Clinical Studies. *Antioxidants* **2022**, *11*, 823. [CrossRef]
9. Kumar, M.; Prakash, S.; Kumari, N.; Pundir, A.; Punia, S.; Saurabh, V.; Choudhary, P.; Changan, S.; Dhumal, S.; Pradhan, P.C.; et al. Beneficial role of antioxidant secondary metabolites from medicinal plants in maintaining oral health. *Antioxidants* **2021**, *10*, 1061. [CrossRef]
10. Prakash, S.; Kumar, M.; Kumari, N.; Thakur, M.; Rathour, S.; Pundir, A.; Sharma, A.K.; Bangar, S.P.; Dhumal, S.; Singh, S.; et al. Plant-based antioxidant extracts and compounds in the management of oral cancer. *Antioxidants* **2021**, *10*, 1358. [CrossRef]
11. Shrestha, G.; St. Clair, L.L. Lichens: A promising source of antibiotic and anticancer drugs. *Phytochem. Rev.* **2013**, *12*, 229–244. [CrossRef]
12. Tang, J.Y.; Wu, K.H.; Wang, Y.Y.; Farooqi, A.A.; Huang, H.W.; Yuan, S.S.F.; Jian, R.I.; Tsao, L.Y.; Chen, P.A.; Chang, F.R.; et al. Methanol extract of *Usnea barbata* induces cell killing, apoptosis, and dna damage against oral cancer cells through oxidative stress. *Antioxidants* **2020**, *9*, 694. [CrossRef] [PubMed]
13. Mammadov, R.; Suleyman, B.; Altuner, D.; Demirci, E.; Cetin, N.; Yilmaz, A.; Baykal, H.; Alpcan, H.; Turumtay, E.A.; Suleyman, H. Effect of ethyl acetate extract of *Usnea longissima* o esophagogastric adenocarcinoma in rats. *Acta Cir. Bras.* **2019**, *34*, e201900305. [CrossRef] [PubMed]
14. Emsen, B.; Ozdemir, O.; Engin, T.; Togar, B.; Cavusoglu, S.; Turkez, H. Inhibition of growth of U87MG human glioblastoma cells by *Usnea longissima* ach. *An. Acad. Bras. Cienc.* **2019**, *91*, 1–14. [CrossRef]
15. Disoma, C.; Erkisa, M.; Oran, S.; Aloglou, I.; Ulkaya, E.; Ari, F. Usnea filipendula Induces Apoptosis in Human Colon Cancer Cell Lines. *Indian J. Pharm. Sci.* **2018**, *80*, 1078–1085. [CrossRef]
16. Ozturk, S.; Erkisa, M.; Oran, S.; Ulukaya, E.; Celikler, S.; Ari, F. Lichens exerts an anti-proliferative effect on human breast and lung cancer cells through induction of apoptosis. *Drug Chem. Toxicol.* **2021**, *44*, 259–267. [CrossRef]
17. Londoñe-Bailon, P.; Sánchez-Robinet, C.; Alvarez-Guzman, G. In vitro antibacterial, antioxidant and cytotoxic activity of methanol-acetone extracts from Antarctic lichens (*Usnea antarctica* and *Usnea aurantiaco-atra*). *Polar Science* **2019**, *22*, 100477. [CrossRef]
18. Basiouni, S.; Fayed, M.A.A.; Tarabees, R.; El-Sayed, M.; Elkhatam, A.; Töllner, K.R.; Hessel, M.; Geisberger, T.; Huber, C.; Eisenreich, W.; et al. Characterization of sunflower oil extracts from the lichen *Usnea barbata*. *Metabolites* **2020**, *10*, 353. [CrossRef]
19. Zugic, A.; Jeremic, I.; Isakovic, A.; Arsic, I.; Savic, S.; Tadic, V. Evaluation of anticancer and antioxidant activity of a commercially available CO2 supercritical extract of old man's beard (*Usnea barbata*). *PLoS ONE* **2016**, *11*, e0146342. [CrossRef]
20. Tram, N.T.T.; Anh, D.H.; Thuc, H.H.; Tuan, N.T. Investigation of chemical constituents and cytotoxic activity of the lichen *Usnea undulata*. *Vietnam J. Chem.* **2020**, *58*, 63–66. [CrossRef]
21. Kwong, S.P.; Wang, C. Review: Usnic acid-induced hepatotoxicity and cell death. *Environ. Toxicol. Pharmacol.* **2020**, *80*, 103493. [CrossRef] [PubMed]
22. Kumari, M.; Kamat, S.; Jayabaskaran, C. Usnic acid induced changes in biomolecules and their association with apoptosis in squamous carcinoma (A-431) cells: A flow cytometry, FTIR and DLS spectroscopic study. *Spectrochim. Acta Part A Mol. Biomol. Spectrosc.* **2022**, *274*, 121098. [CrossRef] [PubMed]
23. Chae, H.J.; Kim, G.J.; Deshar, B.; Kim, H.J.; Shin, M.J.; Kwon, H.; Youn, U.J.; Nam, J.W.; Kim, S.H.; Choi, H.; et al. Anticancer activity of 2-o-caffeoyl alphitolic acid extracted from the lichen, *Usnea barbata* 2017-kl-10. *Molecules* **2021**, *26*, 3937. [CrossRef] [PubMed]
24. Brisdelli, F.; Perilli, M.; Sellitri, D.; Piovano, M.; Garbarino, J.A.; Nicoletti, M.; Bozzi, A.; Amicosante, G.; Celenza, G. Cytotoxic activity and antioxidant capacity of purified lichen metabolites: An in vitro study. *Phyther. Res.* **2013**, *27*, 431–437. [CrossRef]

25. Qi, W.; Lu, C.; Huang, H.; Zhang, W.; Song, S.; Liu, B. (+)-Usnic Acid Induces ROS-dependent Apoptosis via Inhibition of Mitochondria Respiratory Chain Complexes and Nrf2 Expression in Lung Squamous Cell Carcinoma. *Int. J. Mol. Sci.* **2020**, *21*, 876. [CrossRef] [PubMed]
26. Wang, S.; Zang, J.; Huang, M.; Guan, L.; Xing, K.; Zhang, J.; Liu, D.; Zhao, L. Discovery of novel (+)-Usnic acid derivatives as potential anti-leukemia agents with pan-Pim kinases inhibitory activity. *Bioorg. Chem.* **2019**, *89*, 102971. [CrossRef]
27. Nguyen, V.K.; Sichaem, J.; Nguyen, H.H.; Nguyen, X.H.; Huynh, T.T.L.; Nguyen, T.P.; Niamnont, N.; Mac, D.H.; Pham, D.D.; Chavasiri, W.; et al. Synthesis and cytotoxic evaluation of usnic acid benzylidene derivatives as potential anticancer agents. *Nat. Prod. Res.* **2021**, *35*, 1097–1106. [CrossRef]
28. Kumar, K.; Mishra, J.P.N.; Singh, R.P. Usnic acid induces apoptosis in human gastric cancer cells through ROS generation and DNA damage and causes up-regulation of DNA-PKcs and γ-H2A.X phosphorylation. *Chem. Biol. Interact.* **2020**, *315*, 108898. [CrossRef]
29. Zugic, A.; Tadic, V.; Savic, S. Nano-and microcarriers as drug delivery systems for usnic acid: Review of literature. *Pharmaceutics* **2020**, *12*, 156. [CrossRef]
30. Macedo, D.C.S.; Almeida, F.J.F.; Wanderley, M.S.O.; Ferraz, M.S.; Santos, N.P.S.; López, A.M.Q.; Santos-Magalhães, N.S.; Lira-Nogueira, M.C.B. Usnic acid: From an ancient lichen derivative to promising biological and nanotechnology applications. *Phytochem. Rev.* **2021**, *20*, 609–630. [CrossRef]
31. Alpsoy, L.; Baykal, A.; Amir, M.; Ülker, Z.; Nawaz, M. SPION@APTES@FA-PEG@Usnic Acid Bionanodrug for Cancer Therapy. *J. Supercond. Nov. Magn.* **2018**, *31*, 1395–1401. [CrossRef]
32. Da Silva Santos, N.P.; Nascimento, S.C.; Wanderley, M.S.O.; Pontes-Filho, N.T.; da Silva, J.F.; de Castro, C.M.M.B.; Pereira, E.C.; da Silva, N.H.; Honda, N.K.; Santos-Magalhães, N.S. Nanoencapsulation of usnic acid: An attempt to improve antitumour activity and reduce hepatotoxicity. *Eur. J. Pharm. Biopharm.* **2006**, *64*, 154–160. [CrossRef] [PubMed]
33. Garg, A.; Garg, S.; Sahu, N.K.; Rani, S.; Gupta, U.; Yadav, A.K. Heparin appended ADH-anionic polysaccharide nanoparticles for site-specific delivery of usnic acid. *Int. J. Pharm.* **2019**, *557*, 238–253. [CrossRef] [PubMed]
34. Isik, Y.; Unal, G.; Koca, F.D.; Halici, M.G. Anticancer Activity of Lichen Extract (*Usnea* sp.) Based Synthesized Ag@ZnO Bimetallic Nanocomposite. *Proceedings* **2019**, *40*, 51.
35. Hamida, R.S.; Ali, M.A.; Abdelmeguid, N.E.; Al-Zaban, M.I.; Baz, L.; Bin-Meferij, M.M. Lichens—A potential source for nanoparticles fabrication: A review on nanoparticles biosynthesis and their prospective applications. *J. Fungi* **2021**, *7*, 291. [CrossRef] [PubMed]
36. Siddiqi, K.S.; Rashid, M.; Rahman, A.; Husen, A.; Rehman, S. Biogenic fabrication and characterization of silver nanoparticles using aqueous-ethanolic extract of lichen (*Usnea longissima*) and their antimicrobial activity. *Biomater. Res.* **2018**, *22*, 23. [CrossRef]
37. Abdolmaleki, H.; Purali, P.; Sohrabi, M. Biosynthesis of silver nanoparticles by two lichens of "*Usnea articulata*" and "*Ramalina sinensis*" and investigation of their antibacterial activity against some pathogenic bacteria. *EBNESINA* **2016**, *17*, 33–42.
38. Baláž, M.; Goga, M.; Hegedüs, M.; Daneu, N.; Kováčová, M.; Tkáčiková, L.; Balážová, L.; Bačkor, M. Biomechanochemical Solid-State Synthesis of Silver Nanoparticles with Antibacterial Activity Using Lichens. *ACS Sustain. Chem. Eng.* **2020**, *8*, 13945–13955. [CrossRef]
39. Tadić, V.; Žugić, A.; Đorđević, S.; Žižović, I.; Homšek, I.; Mišić, D.; Nešić, I. The RP-HPLC method for analysis of usnic acid as potential marker of herbal drugs-based formulations containing *Usnea barbata*. *J. Serb. Chem. Soc.* **2022**, *71*, 45. [CrossRef]
40. Popovici, V.; Bucur, L.; Popescu, A.; Schröder, V.; Costache, T.; Rambu, D.; Cucolea, I.E.; Gîrd, C.E.; Caraiane, A.; Gherghel, D.; et al. Antioxidant and cytotoxic activities of *Usnea barbata* (L.) f.h. wigg. dry extracts in different solvents. *Plants* **2021**, *10*, 909. [CrossRef]
41. Popovici, V.; Bucur, L.; Gîrd, C.E.; Calcan, S.I.; Cucolea, E.I.; Costache, T.; Rambu, D.; Oroian, M.; Mironeasa, S.; Schröder, V.; et al. Advances in the Characterization of *Usnea barbata* (L.) Weber ex F.H. Wigg from Călimani Mountains, Romania. *Appl. Sci.* **2022**, *12*, 4234. [CrossRef]
42. Domján, A.; Bajdik, J.; Pintye-Hódi, K. Understanding of the plasticizing effects of glycerol and PEG 400 on chitosan films using solid-state NMR spectroscopy. *Macromolecules* **2009**, *42*, 4667–4673. [CrossRef]
43. Nafee, N.A.; Ismail, F.A.; Boraie, N.A.; Mortada, L.M. Mucoadhesive buccal patches of miconazole nitrate: In vitro/in vivo performance and effect of ageing. *Int. J. Pharm.* **2003**, *264*, 1–14. [CrossRef]
44. Musuc, A.M.; Anuta, V.; Atkinson, I.; Sarbu, I.; Popa, V.T.; Munteanu, C.; Mircioiu, C.; Ozon, E.A.; Nitulescu, G.M.; Mitu, M.A. Formulation of chewable tablets containing carbamazepine-β-cyclodextrin inclusion complex and f-melt disintegration excipient. The mathematical modeling of the release kinetics of carbamazepine. *Pharmaceutics* **2021**, *13*, 915. [CrossRef] [PubMed]
45. Perioli, L.; Ambrogi, V.; Angelici, F.; Ricci, M.; Giovagnoli, S.; Capuccella, M.; Rossi, C. Development of mucoadhesive patches for buccal administration of ibuprofen. *J. Control. Release* **2004**, *99*, 73–82. [CrossRef] [PubMed]
46. Don, T.M.; Huang, M.L.; Chiu, A.C.; Kuo, K.H.; Chiu, W.Y.; Chiu, L.H. Preparation of thermo-responsive acrylic hydrogels useful for the application in transdermal drug delivery systems. *Mater. Chem. Phys.* **2008**, *107*, 266–273. [CrossRef]
47. Derle, D.; Joshi, O.; Pawar, A.; Patel, J.; Perdeshi, V. Effect of tablet excipients on mucoadhesive properties of polyoxyethylene and Carbopol 971P. *Int. J. Pharm. Pharm. Sci.* **2009**, *1*, 198–205.
48. Gupta, A.; Garg, S.; Khar, R.K. Measurement of bioadhesive strength of mucoadhesive buccal tablets: Design of an in-vitro assembly. *Indian Drugs* **1993**, *30*, 1–6.

49. Nazir, S.; Ansari, F.L.; Hussain, T.; Mazhar, K.; Muazzam, A.G.; Qasmi, Z.U.H.; Makhmoor, T.; Noureen, H.; Mirza, B. Brine shrimp lethality assay "an effective prescreen": Microwave-assisted synthesis, BSL toxicity and 3DQSAR studies-based designing, docking and antitumor evaluation of potent chalcones. *Pharm. Biol.* **2013**, *51*, 1091–1103. [CrossRef]
50. Popovici, V.; Bucur, L.; Gîrd, C.E.; Rambu, D.; Calcan, S.I.; Cucolea, E.I.; Costache, T.; Ungureanu-Iuga, M.; Oroian, M.; Mironeasa, S.; et al. Antioxidant, Cytotoxic, and Rheological Properties of Canola Oil Extract of *Usnea barbata* (L.) Weber ex F. H. Wigg from Călimani Mountains, Romania. *Plants* **2022**, *11*, 854. [CrossRef]
51. Popovici, V.; Matei, E.; Cozaru, G.C.; Aschie, M.; Bucur, L.; Rambu, D.; Costache, T.; Cucolea, I.E.; Vochita, G.; Gherghel, D.; et al. Usnic acid and *Usnea barbata* (L.) F.H. wigg. dry extracts promote apoptosis and DNA damage in human blood cells through enhancing ROS levels. *Antioxidants* **2021**, *10*, 1171. [CrossRef] [PubMed]
52. Matei, E.; Aschie, M.; Mitroi, A.F.; Ghinea, M.M.; Gheorghe, E.; Petcu, L.; Dobrin, N.; Chisoi, A.; Mihaela, M. Biomarkers involved in evaluation of platelets function in South-Eastern Romanian patients with hematological malignancies subtypes. *Medicine* **2021**, *100*, e25944. [CrossRef] [PubMed]
53. Utaipan, T.; Athipornchai, A.; Suksamrarn, A.; Jirachotikoon, C.; Yuan, X.; Lertcanawanichakul, M.; Chunglok, W. Carbazole alkaloids from Murraya koenigii trigger apoptosis and autophagic flux inhibition in human oral squamous cell carcinoma cells. *J. Nat. Med.* **2017**, *71*, 158–169. [CrossRef] [PubMed]
54. Popovici, V.; Bucur, L.; Vochita, G.; Gherghel, D.; Mihai, C.T.; Rambu, D.; Calcan, S.I.; Costache, T.; Cucolea, I.E.; Matei, E.; et al. In vitro anticancer activity and oxidative stress biomarkers status determined by *Usnea barbata* (L.) f.h. wigg. dry extracts. *Antioxidants* **2021**, *10*, 1141. [CrossRef]
55. Chen, Q.M.; Tu, V.C.; Wu, Y.; Bahl, J.J. Hydrogen peroxide dose dependent induction of cell death or hypertrophy in cardiomyocytes. *Arch. Biochem. Biophys.* **2000**, *373*, 242–248. [CrossRef]
56. Zhang, J.; Wang, X.; Cui, W.; Wang, W.; Zhang, H.; Liu, L.; Zhang, Z.; Li, Z.; Ying, G.; Zhang, N.; et al. Visualization of caspase-3-like activity in cells using a genetically encoded fluorescent biosensor activated by protein cleavage. *Nat. Commun.* **2013**, *4*, 2157. [CrossRef]
57. Bucevičius, J.; Lukinavičius, G.; Gerasimaite, R. The use of hoechst dyes for DNA staining and beyond. *Chemosensors* **2018**, *6*, 18. [CrossRef]
58. Jonhede, S.; Petersen, A.; Zetterberg, M.; Karlsson, J.O. Acute effects of the sigma-2 receptor agonist siramesine on lysosomal and extra-lysosomal proteolytic systems in lens epithelial cells. *Mol. Vis.* **2010**, *16*, 819–827.
59. Dyshlovoy, S.A.; Hauschild, J.; Amann, K.; Tabakmakher, K.M.; Venz, S.; Walther, R.; Guzii, A.G.; Makarieva, T.N.; Shubina, L.K.; Fedorov, S.N.; et al. Marine alkaloid Monanchocidin a overcomes drug resistance by induction of autophagy and lysosomal membrane permeabilization. *Oncotarget* **2015**, *6*, 17328–17341. [CrossRef]
60. Fathi, F.; Ghobeh, M.; Tabarzad, M. Anti-Microbial Peptides: Strategies of Design and Development and Their Promising Wound-Healing Activities. *Mol. Biol. Rep.* **2022**, *8*, 9001–9012. [CrossRef]
61. Elshikh, M.; Ahmed, S.; Funston, S.; Dunlop, P.; McGaw, M.; Marchant, R.; Banat, I.M. Resazurin-based 96-well plate microdilution method for the determination of minimum inhibitory concentration of biosurfactants. *Biotechnol. Lett.* **2016**, *38*, 1015–1019. [CrossRef] [PubMed]
62. Madushan, R.; Vidanarachchi, J.K.; Prasanna, P.H.P.; Werellagama, S.; Priyashantha, H. Use of natural plant extracts as a novel microbiological quality indicator in raw milk: An alternative for resazurin dye reduction method. *LWT* **2021**, *144*, 111221. [CrossRef]
63. Cox, K.D.; Quello, K.; Deford, R.J.; Beckerman, J.L. A rapid method to quantify fungicide sensitivity in the brown rot pathogen Monilinia fructicola. *Plant Dis.* **2009**, *93*, 328–331. [CrossRef] [PubMed]
64. Bitacura, J.G. The Use of Baker's Yeast in the Resazurin Reduction Test: A Simple, Low-Cost Method for Determining Cell Viability in Proliferation and Cytotoxicity Assays. *J. Microbiol. Biol. Educ.* **2018**, *19*, 19–87. [CrossRef] [PubMed]
65. Popovici, V.; Bucur, L.; Gîrd, C.E.; Popescu, A.; Matei, E.; Caraiane, A.; Botnarciuc, M. Phenolic Secondary Metabolites and Antiradical and Antibacterial Activities of Different Extracts of *Usnea barbata* (L.) Weber ex F. H. Wigg from Călimani Mountains, Romania. *Pharmaceuticals* **2022**, *15*, 829. [CrossRef]
66. Feroz, S.; Dias, G. Hydroxypropylmethyl Cellulose (Hpmc) Crosslinked Keratin/Hydroxyapatite (Ha) Scaffold Fabrication, Characterization And in vitro Biocompatibility Assessment as A Bone Graft for Alveolar Bone Regeneration. *Heliyon* **2021**, *7*, e08294. [CrossRef]
67. Jillani, U.; Mudassir, J.; Ijaz, Q.A.; Latif, S.; Qamar, N.; Aleem, A.; Ali, E.; Abbas, K.; Wazir, M.A.; Hussain, A.; et al. Design and Characterization of Agarose/HPMC Buccal Films Bearing Ondansetron HCl in vitro and *in Vivo*: Enhancement Using Iontophoretic and Chemical Approaches. *Biomed. Res. Int.* **2022**, *2022*, 1662194. [CrossRef]
68. Peh, K.; Khan, T.; Ch'ng, H. Mechanical, bioadhesive strength and biological evaluations of chitosan films for wound dressing. *J. Pharm. Pharm. Sci.* **2000**, *3*, 303–311.
69. Mandal, U.K.; Chatterjee, B.; Senjoti, F.G.; Adebisi, A.O.; Laity, P.R.; Conway, B.R.; Rajab, M.; Jouma, M.; Neubert, R.H.H.; Dittgen, M.; et al. A Review on Buccal Mucoadhesive Drug Delivery Systems. *AAPS PharmSciTech* **2006**, *7*, 197–208.
70. Elshafeey, A.H.; El-Dahmy, R.M. Formulation and development of oral fast-dissolving films loaded with nanosuspension to augment paroxetine bioavailability: In vitro characterization, ex vivo permeation, and pharmacokinetic evaluation in healthy human volunteers. *Pharmaceutics* **2021**, *13*, 1869. [CrossRef]

71. Londhe, V.; Shirsat, R. Formulation and Characterization of Fast-Dissolving Sublingual Film of Iloperidone Using Box–Behnken Design for Enhancement of Oral Bioavailability. *AAPS PharmSciTech* **2018**, *19*, 1392–1400. [CrossRef] [PubMed]
72. Castán, H.; Ruiz, M.A.; Clares, B.; Morales, M.E. Design, development and characterization of buccal bioadhesive films of Doxepin for treatment of odontalgia. *Drug Deliv.* **2015**, *22*, 869–876. [CrossRef] [PubMed]
73. Lakhani, S.A.; Masud, A.; Kuida, K.; Porter, G.A.; Booth, C.J.; Mehal, W.Z.; Inayat, I.; Flavell, R.A. Caspases 3 and 7: Key mediators of mitochondrial events of apoptosis. *Science* **2006**, *311*, 847–851. [CrossRef] [PubMed]
74. Agustini, K.; Churiyah, C.; Wibowo, A.E. Cytotoxic and Apoptotic Activity on Mcf7 Cell from Ethanolic Extract of Trigonella foenum-graecum L., Aglaia elliptica Blume. and Foeniculum vulgare Mill. *Indones. J. Cancer Chemoprev.* **2017**, *6*, 78. [CrossRef]
75. Popovici, V.; Matei, E.; Cozaru, G.C.; Bucur, L.; Gîrd, C.E.; Schröder, V.; Ozon, E.A.; Karampelas, O.; Musuc, A.M.; Atkinson, I.; et al. Evaluation of *Usnea barbata* (L.) Weber ex F. H. Wigg Extract in Canola Oil Loaded in Bioadhesive Oral Films for Potential Applications in Oral Cavity Infections and Malignancy. *Antioxidants* **2022**, *11*, 1601. [CrossRef]
76. World Health Organization. *WHO Quality Control Methods for Medicinal Plant Materials*; World Health Organization: Geneva, Switzerland, 1998; Available online: https://www.gmp-compliance.org/files/guidemgr/WHO_9241545100.pdf (accessed on 1 September 2022).
77. World Health Organization. *WHO Guidelines on Good Manufacturing Practices (GMP) for Herbal Medicines 2007*; IRIS (Institutional Repository for Information Sharing); World Health Organization: Geneva, Switzerland, 2007; Available online: https://apps.who.int/iris/handle/10665/43672 (accessed on 20 May 2022).
78. Popovici, V.; Matei, E.; Cozaru, G.; Bucur, L.; Gîrd, C.E.; Schröder, V.; Ozon, E.A.; Sarbu, I.; Musuc, A.M.; Atkinson, I.; et al. Formulation and Development of Bioadhesive Oral Films Containing *Usnea barbata* (L.) F. H. Wigg Dry Ethanol Extract (F-UBE-HPC) with Antimicrobial and Anticancer Properties for Potential Use in Oral Cancer Complementary Therapy. *Pharmaceutics* **2022**, *14*, 1808. [CrossRef]
79. Priya, S.; Rathnanand, M.; Nayanabhirama, U.; Ongole, R.; Sumanth, K.N.; Joshi, U. Preparation and evaluation of buccal mucoadhesive patch of betamethasone sodium phosphate for the treatment of Oral submucous fibrosis. *J. Chem. Pharm. Res.* **2011**, *3*, 56–65.
80. Cao, N.; Yang, X.; Fu, Y. Effects of various plasticizers on mechanical and water vapor barrier properties of gelatin films. *Food Hydrocoll.* **2009**, *23*, 729–735. [CrossRef]
81. Semalty, M.; Semalty, A.; Kumar, G. Formulation and characterization of mucoadhesive buccal films of glipizide. *Indian J. Pharm. Sci.* **2008**, *70*, 43–48. [CrossRef]
82. Karki, S.; Kim, H.; Na, S.J.; Shin, D.; Jo, K.; Lee, J. Thin films as an emerging platform for drug delivery. *Asian J. Pharm. Sci.* **2016**, *11*, 559–574. [CrossRef]
83. Kaur, G.; Singh, D.; Brar, V. Bioadhesive okra polymer based buccal patches as platform for controlled drug delivery. *Int. J. Biol. Macromol.* **2014**, *70*, 408–419. [CrossRef] [PubMed]
84. Maher, E.M.; Ali, A.M.A.; Salem, H.F.; Abdelrahman, A.A. In vitro/in vivo evaluation of an optimized fast dissolving oral film containing olanzapine co-amorphous dispersion with selected carboxylic acids. *Drug Deliv.* **2016**, *23*, 3088–3100. [CrossRef] [PubMed]
85. Mali, S.; Sakanaka, L.S.; Yamashita, F.; Grossmann, M.V.E. Water sorption and mechanical properties of cassava starch films and their relation to plasticizing effect. *Carbohydr. Polym.* **2005**, *60*, 283–289. [CrossRef]
86. Shen, C.; Shen, B.; Xu, H.; Bai, J.; Dai, L.; Lv, Q.; Han, J.; Yuan, H. Formulation and optimization of a novel oral fast dissolving film containing drug nanoparticles by Box-Behnken design-response surface methodology. *Drug Dev. Ind. Pharm.* **2014**, *40*, 649–656. [CrossRef]
87. Singh, S.; Jain, S.; Muthu, M.S.; Tiwari, S.; Tilak, R. Preparation and evaluation of buccal bioadhesive films containing clotrimazole. *AAPS PharmSciTech* **2008**, *9*, 660–667. [CrossRef]
88. Pagano, C.; Puglia, D.; Luzi, F.; di Michele, A.; Scuota, S.; Primavilla, S.; Ceccarini, M.R.; Beccari, T.; Iborra, C.A.V.; Ramella, D.; et al. Development and characterization of xanthan gum and alginate based bioadhesive film for pycnogenol topical use in wound treatment. *Pharmaceutics* **2021**, *13*, 324. [CrossRef]
89. Salgado, F.; Albornoz, L.; Cortéz, C.; Stashenko, E.; Urrea-Vallejo, K.; Nagles, E.; Galicia-Virviescas, C.; Cornejo, A.; Ardiles, A.; Simirgiotis, M.; et al. Secondary metabolite profiling of species of the genus usnea by UHPLC-ESI-OT-MS-MS. *Molecules* **2018**, *23*, 54. [CrossRef]
90. Popovici, V.; Bucur, L.; Calcan, S.I.; Cucolea, E.I.; Costache, T.; Rambu, D.; Schröder, V.; Gîrd, C.E.; Gherghel, D.; Vochita, G.; et al. Elemental Analysis and in vitro Evaluation of Antibacterial and Antifungal Activities of *Usnea barbata* (L.) Weber ex F.H. Wigg from Călimani Mountains, Romania. *Plants* **2022**, *11*, 32. [CrossRef]
91. Popovici, V.; Bucur, L.; Popescu, A.; Caraiane, A.; Badea, V. Comparative study regarding antibacterial action if the *Usnea barbata* L. extracts on Gram-positive bacteria from the oro-dental cavity. In Proceedings of the 5th SGEM International Multidisciplinary Scientific Conferences on Social Sciences and Arts, Albena, Bulgaria, 24 August–2 September 2018.
92. Popovici, V.; Bucur, L.; Popescu, A.; Caraiane, A.; Badea, V. Evaluation of the Antibacterial Action of the *Usnea barbata* L. Extracts on Streptococcus Species from the Oro-Dental Cavity. In Proceedings of the 17th Romanian National Congress of Pharmacy, Bucharest, Romania, 26–29 September 2018.
93. Schröder, V.; Arcus, M.; Anghel, A.H.; Busuricu, F.; Lepadatu, A.C. Cell differentiation process of *Artemia* sp. larvae tools for natural products testing. *Sci. Pap. Ser. D Anim. Sci.* **2019**, *LXII*, 149–153.

94. Iancu, I.M.; Bucur, L.A.; Schroder, V.; Mireșan, H.; Sebastian, M.; Iancu, V.; Badea, V. Phytochemical evaluation and cytotoxicity assay of *Lythri herba* extracts. *Farmacia* **2021**, *69*, 51–58. [CrossRef]
95. Rabelo, T.K.; Zeidán-Chuliá, F.; Vasques, L.M.; dos Santos, J.P.A.; da Rocha, R.F.; de Pasquali, M.A.B.; Rybarczyk-Filho, J.L.; Araújo, A.A.S.; Moreira, J.C.F.; Gelain, D.P. Redox characterization of usnic acid and its cytotoxic effect on human neuron-like cells (SH-SY5Y). *Toxicol. In Vitro* **2012**, *26*, 304–314. [CrossRef] [PubMed]
96. Studzinska-Sroka, E.; Galanty, A.; Bylka, W. Atranorin—An Interesting Lichen Secondary Metabolite. *Mini Rev. Med. Chem.* **2017**, *17*, 1633–1645. [CrossRef] [PubMed]
97. Kahkeshani, N.; Farzaei, F.; Fotouhi, M.; Alavi, S.S.; Bahramsoltani, R.; Naseri, R.; Momtaz, S.; Abbasabadi, Z.; Rahimi, R.; Farzaei, M.H.; et al. Pharmacological effects of gallic acid in health and disease: A mechanistic review. *Iran. J. Basic Med. Sci.* **2019**, *22*, 225–237. [PubMed]
98. Maurya, D.K.; Nandakumar, N.; Devasagayam, T.P.A. Anticancer property of gallic acid in A549, a human lung adenocarcinoma cell line, and possible mechanisms. *J. Clin. Biochem. Nutr.* **2011**, *48*, 85–90. [CrossRef] [PubMed]
99. Fernández-Moriano, C.; Gómez-Serranillos, M.P.; Crespo, A. Antioxidant potential of lichen species and their secondary metabolites. A systematic review. *Pharm. Biol.* **2016**, *54*, 1–17. [CrossRef] [PubMed]
100. Yoganathan, S.; Alagaratnam, A.; Acharekar, N.; Kong, J. Ellagic acid and schisandrins: Natural biaryl polyphenols with therapeutic potential to overcome multidrug resistance in cancer. *Cells* **2021**, *10*, 458. [CrossRef]
101. White, P.A.S.; Oliveira, R.C.M.; Oliveira, A.P.; Serafini, M.R.; Araújo, A.A.S.; Gelain, D.P.; Moreira, J.C.F.; Almeida, J.R.G.S.; Quintans, J.S.S.; Quintans-Junior, L.J.; et al. Antioxidant activity and mechanisms of action of natural compounds isolated from lichens: A systematic review. *Molecules* **2014**, *19*, 14496–14527. [CrossRef]
102. Rice-Evans, C.A.; Miller, N.J.; Paganga, G. Antioxidant properties of phenolic compounds. *Trends Plant Sci.* **1997**, *2*, 152–159. [CrossRef]
103. Di Lorenzo, C.; Colombo, F.; Biella, S.; Stockley, C.; Restani, P. Polyphenols and human health: The role of bioavailability. *Nutrients* **2021**, *13*, 273. [CrossRef]
104. Jardón-Romero, E.A.; Lara-Carrillo, E.; González-Pedroza, M.G.; Sánchez-Mendieta, V.; Salmerón-Valdés, E.N.; Toral-Rizo, V.H.; Olea-Mejía, O.F.; López-González, S.; Morales-Luckie, R.A. Antimicrobial Activity of Biogenic Silver Nanoparticles from Syzygium aromaticum against the Five Most Common Microorganisms in the Oral Cavity. *Antibiotics* **2022**, *11*, 834. [CrossRef]
105. Rafey, A.; Amin, A.; Kamran, M.; Haroon, U.; Farooq, K.; Foubert, K.; Pieters, L. Analysis of plant origin antibiotics against oral bacterial infections using in vitro and *in silico* techniques and characterization of active constituents. *Antibiotics* **2021**, *10*, 1504. [CrossRef] [PubMed]
106. Thiyahuddin, N.M.; Lamping, E.; Rich, A.M.; Cannon, R.D. Yeast species in the oral cavities of older people: A comparison between people living in their own homes and those in rest homes. *J. Fungi* **2019**, *5*, 30. [CrossRef] [PubMed]
107. Antonenko, Y.N.; Khailova, L.S.; Rokitskaya, T.I.; Nosikova, E.S.; Nazarov, P.A.; Luzina, O.A.; Salakhutdinov, N.F.; Kotova, E.A. Mechanism of action of an old antibiotic revisited: Role of calcium ions in protonophoric activity of usnic acid. *Biochim. Biophys. Acta Bioenerg.* **2019**, *1860*, 310–316. [CrossRef]
108. Sikkema, J.; De Bont, J.A.M.; Poolman, B. Mechanisms of membrane toxicity of hydrocarbons. *Microbiol. Rev.* **1995**, *59*, 201–222. [CrossRef] [PubMed]
109. Bouarab-Chibane, L.; Forquet, V.; Lantéri, P.; Clément, Y.; Léonard-Akkari, L.; Oulahal, N.; Degraeve, P.; Bordes, C. Antibacterial properties of polyphenols: Characterization and QSAR (Quantitative structure-activity relationship) models. *Front. Microbiol.* **2019**, *10*, 829. [CrossRef] [PubMed]
110. Favreau, J.T.; Ryu, M.L.; Braunstein, G.; Orshansky, G.; Park, S.S.; Coody, G.L.; Love, L.A.; Fong, T.L. Severe hepatotoxicity associated with the dietary supplement LipoKinetix. *Ann. Intern. Med.* **2002**, *136*, 590–595. [CrossRef] [PubMed]
111. Food and Drug Administration, Division of Dietary Supplement Programs. *NTP Nomination for Usnic Acid and Usnea barbata Herb*; FDA: Silver Spring, MD, USA, 2005. Available online: https://ntp.niehs.nih.gov/ntp/htdocs/chem_background/exsumpdf/usnicacid_508.pdf (accessed on 1 September 2022).

pharmaceutics

MDPI

Article

Formulation and Development of Bioadhesive Oral Films Containing *Usnea barbata* (L.) F.H.Wigg Dry Ethanol Extract (F-UBE-HPC) with Antimicrobial and Anticancer Properties for Potential Use in Oral Cancer Complementary Therapy

Violeta Popovici [1,†], Elena Matei [2,*], Georgeta-Camelia Cozaru [2,3,†], Laura Bucur [4,†], Cerasela Elena Gîrd [5,†], Verginica Schröder [6,*], Emma Adriana Ozon [7,*], Iulian Sarbu [8,*], Adina Magdalena Musuc [9,*], Irina Atkinson [9], Adriana Rusu [9], Simona Petrescu [9], Raul-Augustin Mitran [9], Mihai Anastasescu [9], Aureliana Caraiane [10], Dumitru Lupuliasa [7,‡], Mariana Aschie [2,3,‡] and Victoria Badea [1,‡]

[1] Department of Microbiology and Immunology, Faculty of Dental Medicine, Ovidius University of Constanta, 7 Ilarie Voronca Street, 900684 Constanta, Romania
[2] Center for Research and Development of the Morphological and Genetic Studies of Malignant Pathology, Ovidius University of Constanta, CEDMOG, 145 Tomis Blvd., 900591 Constanta, Romania
[3] Clinical Service of Pathology, Sf. Apostol Andrei Emergency County Hospital, 145 Tomis Blvd., 900591 Constanta, Romania
[4] Department of Pharmacognosy, Faculty of Pharmacy, Ovidius University of Constanta, 6 Capitan Al. Serbanescu Street, 900001 Constanta, Romania
[5] Department of Pharmacognosy, Phytochemistry, and Phytotherapy, Faculty of Pharmacy, Carol Davila University of Medicine and Pharmacy, 6 Traian Vuia Street, 020956 Bucharest, Romania
[6] Department of Cellular and Molecular Biology, Faculty of Pharmacy, Ovidius University of Constanta, 6 Capitan Al. Serbanescu Street, 900001 Constanta, Romania
[7] Department of Pharmaceutical Technology and Biopharmacy, Faculty of Pharmacy, Carol Davila University of Medicine and Pharmacy, 6 Traian Vuia Street, 020956 Bucharest, Romania
[8] Department of Pharmaceutical Physics and Biophysics, Drug Industry and Pharmaceutical Biotechnologies, Faculty of Pharmacy, "Titu Maiorescu" University, 004051 Bucharest, Romania
[9] "Ilie Murgulescu" Institute of Physical Chemistry, Romanian Academy, 202 Spl. Independentei, 060021 Bucharest, Romania
[10] Department of Oral Rehabilitation, Faculty of Dental Medicine, Ovidius University of Constanta, 7 Ilarie Voronca Street, 900684 Constanta, Romania
* Correspondence: sogorescuelena@gmail.com (E.M.); verginica.schroder@univ-ovidius.ro (V.S.); emma.budura@umfcd.ro (E.A.O.); iulian.sarbu@prof.utm.ro (I.S.); amusuc@icf.ro (A.M.M.)
† These authors contributed equally to this work.
‡ These authors contributed equally to this work.

check for updates

Citation: Popovici, V.; Matei, E.; Cozaru, G.-C.; Bucur, L.; Gîrd, C.E.; Schröder, V.; Ozon, E.A.; Sarbu, I.; Musuc, A.M.; Atkinson, I.; et al. Formulation and Development of Bioadhesive Oral Films Containing *Usnea barbata* (L.) F.H.Wigg Dry Ethanol Extract (F-UBE-HPC) with Antimicrobial and Anticancer Properties for Potential Use in Oral Cancer Complementary Therapy. *Pharmaceutics* **2022**, *14*, 1808. https://doi.org/10.3390/pharmaceutics14091808

Academic Editors: Mihaela Silion, Anca Roxana Petrovici and Natalia Simionescu

Received: 2 August 2022
Accepted: 25 August 2022
Published: 28 August 2022

Abstract: Medical research explores plant extracts' properties to obtain potential anticancer drugs. The present study aims to formulate, develop, and characterize the bioadhesive oral films containing *Usnea barbata* (L.) dry ethanol extract (F-UBE-HPC) and to investigate their anticancer potential for possible use in oral cancer therapy. The physicochemical and morphological properties of the bioadhesive oral films were analyzed through Fourier transform infrared spectroscopy (FTIR), scanning electron microscopy (SEM), Atomic Force Microscopy (AFM), thermogravimetric analysis (TG), and X-ray diffraction techniques. Pharmacotechnical evaluation (consisting of the measurement of the specific parameters: weight uniformity, thickness, folding endurance, tensile strength, elongation, moisture content, pH, disintegration time, swelling rate, and ex vivo mucoadhesion time) completed the bioadhesive films' analysis. Next, oxidative stress, caspase 3/7 activity, nuclear condensation, lysosomal activity, and DNA synthesis induced by F-UBE-HPC in normal blood cell cultures and oral epithelial squamous cell carcinoma (CLS-354) cell line and its influence on both cell types' division and proliferation was evaluated. The results reveal that each F-UBE-HPC contains 0.330 mg dry extract with a usnic acid (UA) content of 0.036 mg. The bioadhesive oral films are thin (0.093 ± 0.002 mm), reveal a neutral pH (7.10 ± 0.02), a disintegration time of 118 ± 3.16 s, an ex vivo bioadhesion time of 98 ± 3.58 min, and show a swelling ratio after 6 h of 289 ± 5.82%, being suitable for application on the oral mucosa. They displayed in vitro anticancer activity on CLS-354 tumor cells. By considerably increasing cellular oxidative stress and caspase 3/7 activity, they triggered apoptotic processes in oral cancer cells, inducing high levels of nuclear condensation and lysosomal activity, cell cycle arrest in G0/G1, and blocking DNA synthesis. All these properties lead to considering the UBE-loaded bioadhesive oral films suitable for potential application as a complementary therapy in oral cancer.

Keywords: *Usnea barbata* (L.) F. H. Wigg dry ethanol extract; oral squamous cell carcinoma; bioadhesive oral films; usnic acid; antimicrobial activity; CLS-354 cell line; blood cell cultures; oxidative stress; anticancer potential

---

1. Introduction

Oral cancer belongs to the head and neck cancers group, which includes the larynx, throat, lips, mouth, nose, and salivary glands malignancies [1]. It is the sixth most common neoplastic disease worldwide [2]. Tobacco or/and alcohol use, betel-quid chewing, and human papillomavirus (HPV) infection are adequately evidenced as risk factors associated with oral cancer [3]. These confirmed factors, associated with pollution, diet and nutrition, poor oral hygiene, chronic inflammation, infectious diseases (i.e., with *C. albicans* [4]), and a hereditary predisposition, have contributed to the increased risk of developing oral cavity malignancies [5]. The conventional treatment of oral cancer consists of surgical intervention and radiotherapy; in an advanced stage, they could be combined with chemotherapy after clinical trials. Radiation exposure makes oral tissues more easily damaged, and physiological repair mechanisms are compromised due to permanent cellular damage [6]; thus, radiotherapy-induced oral complications occur (i.e., oral mucositis, bacterial and fungal infections, saliva change, mucosal fibrosis, sensory dysfunctions, dental caries, periodontal disease, and osteoradionecrosis) [6,7]. The optimal combination with high benefits for oral cancer patients is still unknown, and 5-year survival is around 52% [3] due to its invasive character and late diagnosis.

The National Cancer Institute also accepts non-conventional products and practices of Complementary and Alternative Medicine (CAM) https://www.cancer.gov/about-cancer/treatment/cam/patient (accessed on 30 July 2022). Numerous conventional medical care practitioners are also CAM ones [8] and support global research investigating plant extracts' properties to obtain potential anticancer drugs. The rate of patients using CAM in addition to the standard therapy regime is 40–90% [9], and plant-based products could help them to prevent and recover from oral complications.

Many in vitro, in vivo, and clinical studies proved the benefits of various plant-based formulations for oral cancer patients. Thus, a recently published review highlights the promising effects of milk thistle extracts in oral pathology, i.e., oral cancer, oral mucositis (OM), periodontal disease, dental caries, and oral candidiasis [10]. Other authors evidenced topically applied chamomile's effectiveness in OM—the most painful acute oral complication of radio and chemotherapy [11,12]. A previous clinical study revealed the benefits of SAMITAL$^{®}$ (Indena S.p.A.), a phytopharmaceutical combination of three highly standardized botanical drug extracts (*Vaccinium myrtillus* fruits, *Macleaya cordata* fruits, and *Echinacea angustifolia* roots) in OM treatment [13].

Choi et al. [14] recommend the mixture of *Momordica charantia* Linn., *Pistacia lentiscus*, and *Commiphora myrrha* supercritical extracts as a preventive and therapeutic agent for oral mucosa inflammation and oral cancer, supported by an in vitro and in vivo evaluation. The present study suggests *U. barbata* dry ethanol extract for the previously mentioned applications, based on animal model cytotoxicity prescreen and in vitro studies. Moreover, recent studies proposed pyroligneous extracts films of *Eucalyptus grandis* and chitosan [15] and mucoadhesive buccal films with *Aloe barbadensis* dry extract [16] for oral cancer prevention and treatment. In this work, *U. barbata* (L.) F.H. Wigg dry ethanol extract (UBE) was incorporated in bioadhesive oral films. Then, UBE-loaded films were analyzed through complex physicochemical, pharmacotechnical, and biological studies, aiming to investigate their suitability for oral administration and pharmacological activities for potential application as a complementary therapy in oral cancer.

2. Materials and Methods

2.1. Materials

This study's chemicals, reagents, and standards were of analytical grade. Usnic acid standard 98.1% purity, Propidium Iodide (PI) 1.0 mg/mL, Dimethyl sulfoxide (DMSO), Polyethylene Glycol 400 (PEG 400), and Hydroxypropyl cellulose (HPC) and Antibiotics mix solution—100 µL/mL with 10 mg Streptomycin, 10,000 U Penicillin, 25 µg Amphotericin B per 1 mL—were provided by Sigma-Aldrich Chemie GmbH (Taufkirchen, Germany). Annexin V Apoptosis Detection Kit and flow cytometry staining buffer (FCB) were purchased from eBioscience^{TM} (Frankfurt am Main, Germany) and RNase A 4 mg/mL from Promega (Madison, WI, USA). Magic Red$^{®}$ Caspase-3/7 Assay Kit, Reactive Oxygen Species (ROS) Detection Assay Kit, and EdU i-Fluor 488 Kit were supplied by Abcam (Cambridge, UK).

The OSCC cell line (CLS-354) and the culture medium—Dulbecco's Modified Eagle's Medium (DMEM) High Glucose, basic supplemented with 4.5 g/L glucose, L-glutamine, and 10% Fetal Bovine Serum (FBS) were provided by CLS Cell Lines Service GmbH (Eppelheim, Germany). Trypsin–ethylenediamine tetra acetic acid (Trypsin EDTA) and the media for blood cells—Dulbecco's phosphate-buffered saline with $MgCl_2$ and $CaCl_2$, FBS, and L-Glutamine (200 mM) solution—were purchased from Gibco^{TM} Inc. (Billings, MT, USA).

The blood samples were collected from a non-smoker healthy donor (B Rh+ blood type), according to Ovidius University of Constanta Ethical approval code 7080/10.06.2021 and Donor Consent code 39/30.06.2021.

U. barbata lichen was harvested in March 2021 from the branches of conifers in the forest localized in the Călimani Mountains (47°29′ N, 25°12′ E, and 900 m altitude). It was identified by the Department of Pharmaceutical Botany of the Faculty of Pharmacy, Ovidius University of Constanta, using standard methods. A voucher specimen is deposited in the Herbarium of Pharmacognosy Department, Faculty of Pharmacy, Ovidius University of Constanta (Popovici 3/2021, Ph-UOC). The 96% ethanol for *U. barbata* dry extract preparation was provided by Chimreactiv SRL Bucharest, Romania.

Artemia salina eggs and *Artemia* salt (Dohse Aquaristik GmbH & Co., Gelsdorf, Germany) were purchased online from https://www.aquaristikshop.com/ (accessed on 5 May 2022).

Bacterial and fungal cell lines (*S. aureus* ATCC 25923, *P. aeruginosa* ATCC 27353, *C. albicans* ATCC 10231, and *C. parapsilosis* ATCC 22019) for antimicrobial activity evaluation were obtained from Microbiology Department, S.C. Synevo Romania S.R.L., Constanta Laboratory, in partnership agreement No 1060/25.01.2018 with the Faculty of Pharmacy, Ovidius University of Constanta. Culture medium Mueller-Hinton agar (MHA) was supplied by Thermo Fisher Scientific, GmbH, Dreieich, Germany; RPMI 1640 Medium and Resazurin solution (from In Vitro Toxicology Assay Kit, TOX8-1KT, Resazurin based) were purchased from Sigma-Aldrich Chemie GmbH (Taufkirchen, Germany).

2.2. The Development of UBE-Loaded Bioadhesive Oral Films

Bioadhesive films with the same excipients but no active ingredient load were obtained and utilized as References to show the lichen extract's efficacy and influence on the pharmacotechnical properties.

The composition of the developed bioadhesive films is displayed in Table 1.

The UBE dosage was established considering its solubility in ethanol (3% *w*/*w*). HPC was dispersed in water using a Heidolph MR 3001K magnetic stirrer at 750 rpm and room temperature; then, PEG 400 was added and blended. UBE was dissolved in ethanol, and the obtained solution was slowly poured into the polymer matrix while stirring under the same conditions. The final hydrogels were left overnight at room temperature for deaeration, then poured into Petri glass plates in a thin layer and let to dry for 24 h at ambient temperature. Dry films were peeled away from the plate surface and cut into 1.5 cm × 2 cm patches.

Table 1. Bioadhesive oral film formulations.

Ingredients	Quantity (g)	
	F-UBE-HPC	**R**
UBE	0.30	-
Ethyl alcohol 96% (*v*/*v*)	10.00	10.00
PEG 400	5.00	5.00
HPC 20% water dispersion (*w*/*w*)	84.70	85.00

F-UBE-HPC—bioadhesive oral film loaded with *U. barbata* dry ethanol extract; R—bioadhesive oral film without active lichen extract.

2.3. Physico-Chemical Characterization of the UBE-Loaded Bioadhesive Oral Films

2.3.1. SEM Analysis

A high-resolution scanning electron microscope Quanta3D FEG (Thermo Fisher Scientific, GmbH, Dreieich, Germany) was used to evaluate both films (R and F-UBE-HPC) morphology.

2.3.2. Atomic Force Microscopy (AFM)

AFM investigations were performed in non-contact mode, using decoupled, flexure-guided crosstalk eliminated scanners with an XE-100 microscope from Park Systems. In all AFM measurements, sharp tips were used, NCHR from Nanosensors$^{\text{TM}}$, with typically ~8 nm radius of curvature, ~125 μm mean length, 30 μm mean width, ~42 N/m force constant, and ~330 kHz resonance frequency. XEI program (v 1.8.0) from Park Systems was used for image processing and roughness evaluation. Below the AFM images, presented as "enhanced contrast" view mode, representative line scans are plotted, showing in detail the surface profile of the scanned samples.

2.3.3. Fourier Transform Infrared Spectroscopy (FTIR)

Bioadhesive oral films were characterized by Fourier Transform Infrared (FTIR) using a Nicolet Spectrometer 6700 FTIR and a Smart DuraSamplIR HATR (Horizontal Attenuated Total Reflectance) accessory with a laminated–diamond crystal (Thermo Electron Corporation, Waltham, MA, USA). FTIR spectra were achieved in the spectral range from 4000 to 400 cm^{-1}, using a DTGS KBr detector, in transmittance mode. The spectra were the average of 32 scans recorded at 4 cm^{-1} resolution.

2.3.4. Powder X-ray Diffractometry

The powder X-ray diffractometry (XRD) patterns were recorded using a Rigaku Ultima IV diffractometer (Rigaku Corporation, Tokyo, Japan) in parallel beam geometry. A Cu tube (λ = 1.54056 Å) operating at 40 kV voltage and 30 mA current was used. The scanning rate employed was 2°/min over a diffraction angle of 2θ, with a step size of 0.02 and a range of 5–60°.

2.3.5. Thermogravimetric Analysis

The thermal curves of both bioadhesive oral films were recorded using a Mettler Toledo TGA/SDTA 851^{e} thermogravimetric analyzer (Mettler-Toledo GmbH, Greifensee, Switzerland). All experiments were conducted in a synthetic air atmosphere with a heating rate of 10 °C min^{-1} and a flow rate of 80 mL min^{-1}.

2.4. Pharmacotechnical Properties of the UBE-Loaded Bioadhesive Oral Films

2.4.1. Weight Uniformity

Twenty films from each series (F-UBE-HPC and R) were separately weighed, and the mean weight was calculated.

2.4.2. Thickness

Thickness was measured on 20 films of each batch using a digital micrometer (Yato Trading CO., LTD, Shanghai, China) with a 0–25 mm measurement range and 0.001 mm resolution. The average values were calculated for both films.

2.4.3. Folding Endurance

The films were folded and rolled repeatedly, at the same place, until they broke, or up to 300 times [17]. The folding times were recorded and reported as folding endurance values.

2.4.4. Tensile Strength and Elongation Ability

A digital tensile force tester for universal materials was used to determine the tensile strength and elongation behavior of a Lloyd Instruments Ltd., LR 10K Plus, West Sussex, United Kingdom digital tensile force tester for universal materials. The analysis was carried out at a speed of 30 mm/min from a distance of 30 mm. The breaking force was measured by placing the patch in a vertical position between the two bracing. The tests were performed on five patches of each batch.

The tensile strength and elongation at break were calculated using the following equations:

$$\text{Tensile strength}\left(\text{kg}/\text{mm}^2\right) = \frac{\text{Force at breakage (kg)}}{\text{Film thickness (mm)} \times \text{Film width (mm)}} \tag{1}$$

$$\text{Elongation \%} = \frac{\text{Increase in film length}}{\text{Inital film length}} \times 100 \tag{2}$$

2.4.5. Moisture Content

A thermogravimetric method was used to determine the drying loss using an HR 73 Mettler Toledo halogen humidity (Mettler-Toledo GmbH, Greifensee, Switzerland) [18]. Five films of each formulation were tested.

2.4.6. Surface pH

Five films of each formulation were moistened for 5 min at room temperature with 1 mL distilled water (pH 6.5 ± 0.5). The pH value was registered by touching the film surface with the electrode of a CONSORT P601 pH-meter (Consort bvba, Turnhout, Belgium).

2.4.7. In Vitro Disintegration Time

Using an Erweka DT 3 apparatus (Erweka® GmbH, Langen, Germany), the time necessary for both films' disintegration was determined in a simulated saliva phosphate buffer with a pH of 6.8 at 37 ± 2 °C [19].

2.4.8. Swelling Ratio

Six films of each series were placed in Petri plates on a 1.5% agar gel and incubated at 37 ± 1 °C. The films were weighed every 30 min for 6 h. The swelling ratio is calculated through the following equation:

$$\text{Swelling ratio} = \frac{\text{Wt} - \text{Wi}}{\text{Wi}} \times 100 \tag{3}$$

Wt is the patch weight at time t after the incubation, and Wi is the initial weight [20–22].

2.4.9. Ex Vivo Bioadhesion Time

This determination was assessed using the technique described by Gupta et al. [23] on a detached porcine oral mucosa. The fat layer and any tissue residue were removed from the membrane surface; then, it was fixed on a glass plate after being rinsed with distilled water and a phosphate buffer pH of 6.8 at 37 °C. Each film was hydrated in the center with 15 µL phosphate buffer and pressed onto the mucosa surface for 30 s. The glass plate was submerged in 200 mL phosphate buffer (pH 6.8) and kept at 37 °C for 2 min. A paddle set at a 28 rpm stirring rate simulated the oral cavity conditions, and the time requested for each film to detach from the oral mucosa was measured. This registered time is known as residence time or bioadhesion time. All tests were carried out in triplicate.

2.5. Antimicrobial Activity

2.5.1. Inoculum Preparation

The direct colony suspension method (CLSI) was used to prepare the bacterial inoculum. Thus, bacterial colonies selected from a 24 h agar plate were suspended in M.H.A. medium, according to the 0.5 McFarland standard, measured at Densimat Densitometer (Biomerieux, Marcy-l'Étoile, France) with around 108 CFU/mL (CFU = colony-forming unit). The yeast inoculum was achieved using the same method, adjusting the RPMI 1640 with fungal colonies to the 1.0 McFarland standard, with 10^6 CFU/mL.

2.5.2. Samples and Standards

F-UBE-HPC was dissolved in 1 mL of diluted phosphate buffer. As standards, Ceftriaxone (Cefort 1g Antibiotice SA, Iași, Romania) solutions 30 mg/mL and 150 mg/mL in distilled water were used for bacteria. The Cefort powder was weighted at Partner Analytical balance (Fink & Partner GmbH, Goch, Germany) and dissolved in distilled water. Terbinafine solution 10.1 mg/mL (Rompharm Company S.R.L., Otopeni, România) was selected as standard for *Candida* sp.

2.5.3. Microdilution Method

All successive steps were performed in an Aslair Vertical 700, laminar flow, microbiological protection cabinet (Asal Srl, Cernusco (MI) Italy). In four 96-well plates, we performed seven serial dilutions, adapting the protocol described by Fathi et al. [24].

All 96-well plates were incubated for 24 h at 37 °C for bacteria and 35 °C for yeasts in My Temp mini Z763322 Digital Incubator (Benchmark Scientific Inc., Sayreville, NJ, USA).

2.5.4. Reading and Interpreting

The 96-well plates were examined with a free eye to see the color differences between standard and samples after 24 h incubation [25]. The corresponding sample concentration activities were compared with the standard antibiotic ones. For yeasts, the color chart of the resazurin dye reduction method was used [26,27].

2.6. Cytotoxic Activity of UBE-Loaded Bioadhesive Oral Films on A. salina Larvae

F-UBE-HPC was placed in 1 mL of diluted buffer and left to incubate for 15 min at 37 °C; after this time, its homogenous dispersion in the buffer solution was used as a treatment for *A. salina* larvae.

Brine shrimp larvae were achieved by placing the *A. salina* cysts in a saline solution of 0.35%, for 24–48 h, under continuous aeration and light, at room temperature. (20–22 °C). At the first larval stage, they were separated and introduced into experimental well plates (with a volume of 1 mL) in 0.3% saline solutions [28]. The prescreen was compared with a blank (untreated brine shrimp nauplii) to obtain accurate results regarding the F3 patch cytotoxic effect. During the test period, *A. salina* larvae were not fed to not interfere with the tested extracts. Their evolution was investigated after 24 h and 48 h, during which the larvae had embryonic energy reserves as lipids [29].

2.6.1. Fluorescent Microscopy

The brine shrimp larvae were stained with 3% acridine orange (Merck Millipore, Burlington, MA, USA) for 5 min. The samples were dried in darkness for 15 min and placed on the microscope slides.

2.6.2. Data Processing

The microscopic images were achieved using a VWR microscope VisiScope 300D (VWR International, Radnor, PA, USA) with a Visicam X3 camera (VWR International, Hilden, Germany) at 40×, 100×, and 400× magnifications and processed with VisiCam Image Analyzer 2.13.

Fluorescent microscopy (FM) images were achieved using an OPTIKA B-350 microscope (Ponteranica, BG, Italy) blue filter (λex = 450–490 nm; λem = 515–520 nm) and green filter (λex = 510–550 nm; λem = 590 nm). These images were obtained at 100×, 200×, and 400× magnification and processed with Optikam Pro 3 Software (OPTIKA S.R.L., Ponteranica, BG, Italy) [30]. All observations were performed in triplicate.

2.7. In Vitro Analysis of the Biological Effects of UBE-Loaded Bioadhesive Oral Films on Human Blood Cell Cultures and CLS-354 Tumor Cell Line

2.7.1. Equipment

The study platform for in vitro cytotoxicity analysis was the Attune Acoustic focusing cytometer (Applied Biosystems, Bedford, MA, USA). Before cell analysis, the flow cytometer was first set using fluorescent beads (Attune performance tracking beads, labeling, and detection, Life Technologies, Europe BV, Bleiswijk, Netherlands [31], with standard size (four intensity levels of beads population). The cell quantity was established by countering the cells below 1 µm. Over 10,000 cells per sample were gated by Forward Scatter (FSC) and Side Scatter (SSC) for each analysis.

2.7.2. Data Processing

Flow cytometry results were collected using Attune Cytometric Software v.1.2.5, Applied Biosystems, 2010 (Bedford, MA, USA).

2.7.3. Human Blood Cells Cultures

Blood samples were collected into heparinized vacutainers and used throughout the experiment. The blood (1.0 mL) was introduced in 6.0 mL of Dulbecco's phosphate buffered saline (with $MgCl_2$ and $CaCl_2$) medium, supplemented with 10% bovine fetal serum, L-glutamine, and antibiotics mix solution. The mixture was placed in untreated Nunclon Vita Cell culture 6-well plates (Kisker Biotech GmbH & Co.KG, Steinfurt, Germany) were incubated in a Steri-Cycle™ i160 CO_2 Incubator (Thermo Fisher Scientific Inc., Waltham, MA, USA), with 5% CO_2, at 37 °C for 72 h. Next, blood cell cultures were treated with the samples and controls and incubated for 24 h in the same conditions. All the flow-cytometry analyses were performed after this incubation time.

2.7.4. CLS-354 Cell Line, Cell Culture

The CLS-354 cells were cultured for 7 days in DMEM High Glucose with 10% FBS supplemented with antibiotic mix solution in a 5% CO_2 humidified atmosphere at 37 °C, according to https://www.clsgmbh.de/pdf/cls-354.pdf (accessed on 5 March 2022). Then, the cells were dissociated with Trypsin-EDTA and centrifugated at 3000 rpm for 10 min in a Fisher Scientific GT1 Centrifuge (Thermo Fisher Scintific Inc., Waltham, MA, USA). Then, the cells were distributed in Millicell™ 24-Well Cell Culture Microplates (Termo Fisher Scientific Inc., Waltham, MA, USA). After treatment, the cells were incubated for 24 h in the same conditions. All the flow-cytometry analyses were performed after this incubation period.

2.7.5. Samples and Control Solutions

F-UBE-HPC was dispersed in 1 mL of suitable culture media for both types of cells with 1% DMSO and incubated at 37 °C for 24 h. Usnic acid of 125 µg/mL in 1% DMSO was selected as positive control; 1%DMSO was also the negative control.

2.7.6. Annexin V-FITC Apoptosis Assay

The cells were placed in flow-cytometry tubes (with 2 µL Annexin V-FITC and 2 µL PI of 20 µg/mL) and incubated at room temperature, in darkness, for 30 min. Then, 1 mL of FCB was added, and viable cells, early apoptotic cells, late apoptotic cells, and necrotic cells were examined with a flow cytometer using a 488 nm excitation, green emission for Annexin V-FITC (BL1 channel), and orange emission for PI (BL2 channel).

2.7.7. Evaluation of Caspase 3/7 Activity

A total of 300 µL of cell cultures was transferred in flow-cytometry tubes; then, 20 µL of Magic Red® Caspase-3/7 Substrate-MR-(DEVD)$_2$-solution was added and well-mixed with the cells. Next, 20 µL of PI was added. After incubation, 1 mL FCB was added. Then, the early stages of cell apoptosis by activating caspases 3/7 (DEVD-ases, according to https://www.abcam.com/caspase-37-assay-kit-magic-red-ab270771.html (accessed on 3 April 2022) were analyzed through flow cytometry using a 488 nm excitation, red emission for MR-(DEVD)$_2$-BL3 channel, and orange emission for PI-BL2 channel.

2.7.8. Evaluation of Nuclear Condensation and Lysosomal Activity

A Magic Red® Caspase-3/7 Assay Kit containing Hoechst 33,342 stain (200 µg/mL) and acridine orange (AO, 1.0 µM) was used. Hoechst 33,342 is a cell-permeant nuclear stain; when it is linked to double chain DNA, it emits blue fluorescence, highlighting condensed nuclei in apoptotic cells.

Acridine orange is a chelating dye that can be used to reveal lysosomal activity-https://www.abcam.com/caspase-37-assay-kit-magic-red-ab270771.html (accessed on 3 April 2022). Therefore, 300 µL of cell culture was introduced in flow-cytometry tubes; then, 2 µL of Hoechst 33,342 stain was added, and the cells were well-mixed. Then, 50 µL of acridine orange 1.0 µM was added, and the cells were incubated in darkness, at room temperature, for 30 min. Finally, 1 mL FCB was added, permitting the examination of the cells at the flow cytometer. UV excitation and blue emission for Hoechst 33,342 (VL2) at 488 nm and green emission acridine orange (BL1 channel) were used for examination.

2.7.9. Evaluation of Total ROS Activity

A total of 100 µL of stain solution from ROS Assay was added to each 1 mL of cell culture in flow-cytometry tubes and well-mixed. After incubation at 37 °C, in 5% CO_2, for 60 min, the cells were examined with a flow cytometer using a 488 nm excitation and green emission for ROS (BL1 channel).

2.7.10. Cell Cycle Analysis

A total of 1 mL of cell culture was washed in FCB and fixed for 10 min with 50 µL ethanol. Next, the cells were treated with PI (20 µg/mL) and RNase A (30 µg/mL) and incubated at room temperature, in darkness, for 30 min. Then, 1 mL FCB was added, and the cell cycle distribution was examined by flow cytometry using a 488 nm excitation and orange emission for PI (BL2 channel).

2.7.11. Evaluation of Cell Proliferation

Volumes of 1 mL of cell cultures were incubated with 50 µM EdU (500 µL) at 37 °C for 2 h. Then, the cells were fixed (with 100 µL 4% paraformaldehyde in PBS) and permeabilized (with 100 µL Triton X-100). After washing in 3% buffer sodium azide (BSA) and centrifuging at 300 rpm for 5 min, at 4 °C, the cells were incubated with a reaction mix (500 µL) for 30 min at room temperature, in darkness. Then, they were washed in permeabilization buffer and centrifuged at 300 rpm for 5 min, at 4 °C. After these procedures, 1 mL FCB was added, and the cells were examined by flow cytometry using a 488 nm excitation and green emission for EdU-iFluor 488 (BL1).

2.8. Data Analysis

All analyses were performed in triplicate, and the results were presented as means values ± standard deviation (SD). The results are presented as percent (%) of cell and nuclear apoptosis, caspase 3/7 activity, autophagy, cell cycle, DNA synthesis, and count ($\times 10^4$) of oxidative cellular stress after flow-cytometry analyses were performed with SPSS v. 23 software, IBM, Armonk, NY, USA, 2015. The Levene test was analyzed for homogeneity of variances of samples. At the same time, a paired *t*-test was used to evidence the differences between sample and controls; $p < 0.05$ was established as statistically significant. The Principal Component Analysis was achieved with XLSTAT v. 2022.2.1. by Addinsoft (New York, NY, USA).

3. Results

3.1. Development of the Bioadhesive Oral Films

Both films are transparent, flexible, and homogenous with smooth surfaces (Figure S1, Supplementary Material). F-UBE-HPC (Figure S1a) has a yellowish-green, faint-brown color, while R is colorless. (Figure S1b). The patches peeling and cutting processes occurred without forming air bubbles, cracks, or other defects.

Each UBE-loaded bioadhesive oral film has 0.330 mg UBE, with a total phenolic content (TPC) of 573.234 mg/g (one film has a TPC of 0.189 mg) and 108.742 mg/g usnic acid (one film contains 0.036 mg UA).

3.2. Physico-Chemical Characterization of the Bioadhesive Films

3.2.1. SEM Analysis

Figure 1 shows the SEM images of Reference (R) and F-UBE-HPC. A clear difference can be noticed between their aspect. Thus, R has a rough surface (Figure 1a), while F-UBE-HPC shows an almost entirely smooth one (Figure 1b).

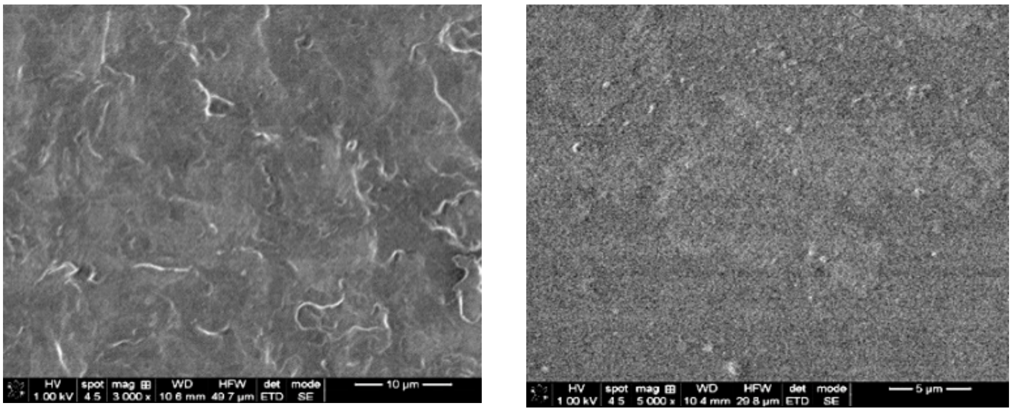

(a) **(b)**

Figure 1. SEM images of (**a**) Reference (R); (**b**) F-UBE-HPC; R—bioadhesive oral film without active lichen extract; F-UBE-HPC—bioadhesive oral film loaded with *U. barbata* dry ethanol extract.

3.2.2. AFM Analysis

The AFM 2D images at the scale of (8 × 8) μm^2 in the so-called "enhanced contrast" view mode are presented in Figure 2a,b.

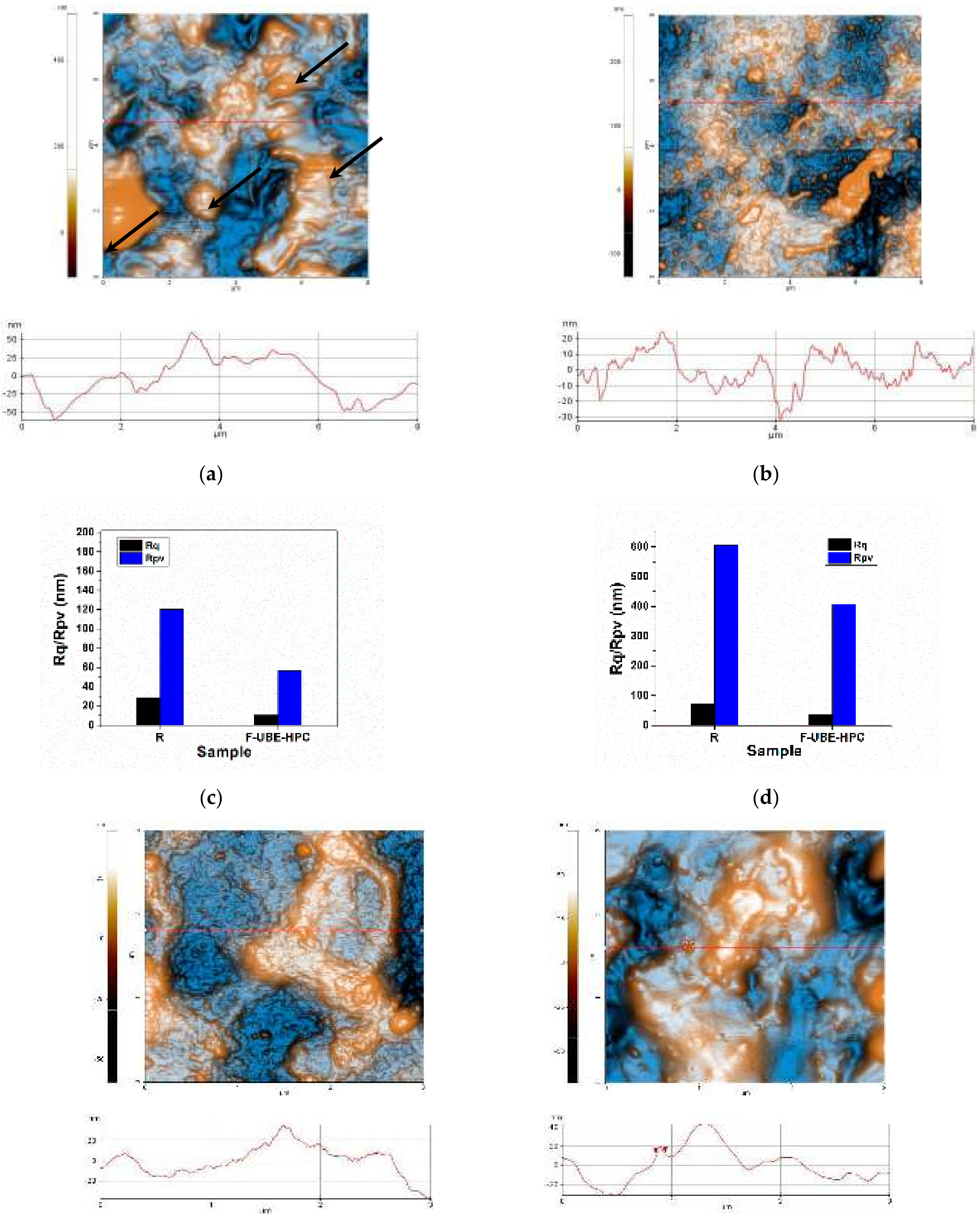

(**a**) (**b**)

(**c**) (**d**)

(e) (f)

Figure 2. The 2D AFM images (enhanced contrast view) at the scale of (8 × 8) μm^2 together with representative line-scans for bioadhesive films: (**a**) R, (**b**) F-UBE-HPC; roughness (Rq) and peak-to-valley (Rpv) parameters (**c**) along the line scans and (**d**) for the whole scanned areas; 2D AFM images (enhanced contrast view) at the scale of (3 × 3) μm^2 together with representative line-scans for the films (**e**) R and (**f**) F-UBE-HPC; R—bioadhesive oral film without active lichen extract; F-UBE-HPC—bioadhesive oral film loaded with *U. barbata* dry ethanol extract.

The first row shows the Reference (R) (Figure 2a). Some differences in the morphology of the parental patch can be noticed as the sample R appears more compact with local accumulations of material (as indicated with a few arrows in Figure 2a). Some large pits (surface cavities) are also observed on the R surface. The arbitrary lines plotted below the AFM images of R suggest a similar z-scale (level oscillations) of about 120 nm (the vertical scale of the plotted line scans in Figure 2a).

The morphology of F-UBE-HPC (Figure 2b) is much more uniform compared with the parental sample, exhibiting small protuberances. There is a decrease in roughness (Rq), as also observed in the line scan from Figure 2b, where a vertical scale of ~50 nm can be observed (from −30 to +20 nm). Moreover, the peak-to-valley (Rpv) parameter decreases after "functionalization" (from R to F-UBE-HPC), as visible in Figure 2c. The histograms of the roughness (Rq) and peak-to-valley (Rpv) (Figure 2c) were plotted for all the line scans, indicated by red horizontal lines in the AFM images. When the corrugation parameters are calculated for the whole scanned area (i.e., (8 × 8) μm^2), as displayed in Figure 2d, it was observed that the R and F-UBE-HPC samples are roughed.

Relevant images of both films' morphology are presented in Figure 2e,f at the scale of (3 × 3) μm^2, choosing some areas as flat as possible. In this case, it is evident that locally, meaning in small areas, the films are relatively uniform regarding the morphological characteristics but maintain the same trend regarding their roughness.

3.2.3. FTIR Analysis

FTIR spectroscopy was used to study the formation of bioadhesive films. The FTIR spectra of both films (R and F-UBE-HPC) are shown in Figure 3.

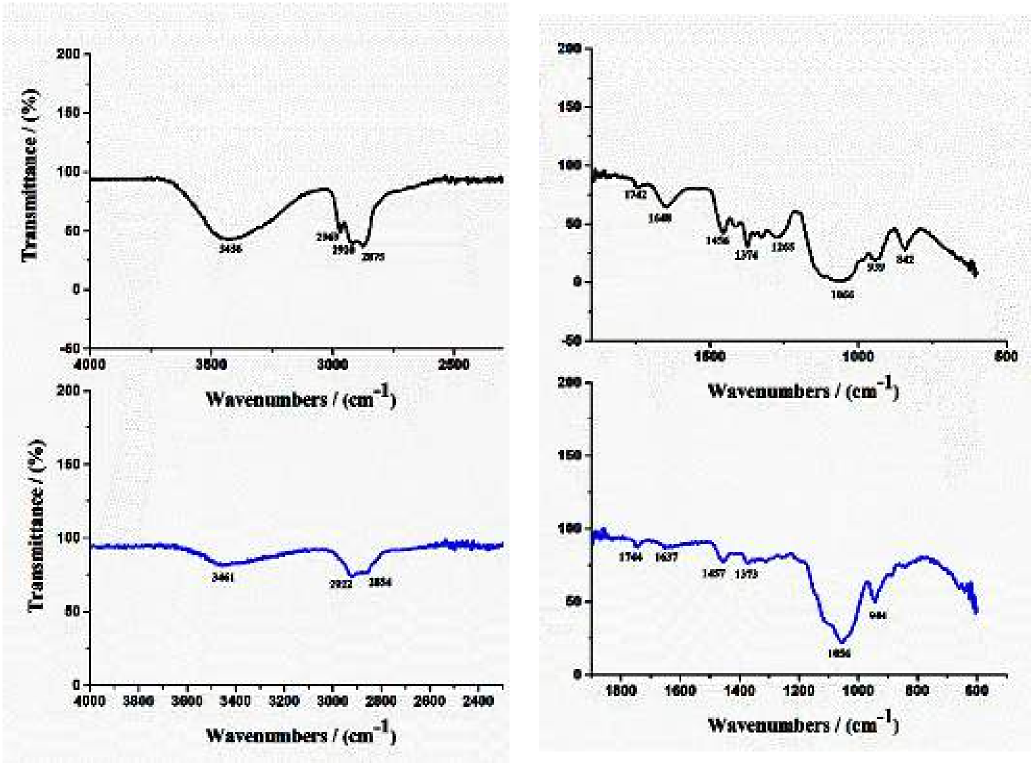

(**a**) (**b**)

Figure 3. FTIR spectra of R (black line) and F-UBE-HPC (blue line), in the range of 4000–2000 cm $^{-1}$ (**a**) and 2000–400 cm^{-1} (**b**). R—bioadhesive oral film without active lichen extract; F-UBE-HPC—bioadhesive oral film loaded with *U. barbata* dry ethanol extract.

In Figure 3, for the peak's optimal visualization, evidencing the differences between both films, the spectral range was divided into two parts: 4000–2000 cm^{-1} (a) and 2000–400 cm^{-1} (b); moreover, R was marked with black color and F-UBE-HPC with blue.

The FTIR spectrum of pure HPC shows absorption bands at 3431 cm^{-1} due to the OH group from the pyranose unit, at 2967 cm^{-1} and 2932 cm^{-1} due to CH2 and CH stretching vibrations, at 1533 cm^{-1} due to C=C stretching vibration, and at 1079 cm^{-1} due to C-O-C stretching vibration [32].

The FTIR spectrum of PEG shows a broad band around 3500 cm^{-1} due to the OH group forming hydrogen bonds with other polymers. The characteristic bands appearing at 1724 cm^{-1} and 1633 cm^{-1} are attributed to the carbonyl group (C=O) and stretching vibrations of CH, CH2, and CH3 groups. The bands at 1464 and 1343 cm^{-1} are associated with the C-H bending. The stretching vibrations of the C-C-O group appear at 1280 and 1100 cm^{-1}. At around 950 and 840 cm^{-1}, the harmonic bands of the C-C-O group appear [33].

The FTIR spectra of R and F-UBE-HPC bioadhesive films show almost the same peaks as in the pure polymers but with some displacement. This aspect proves that between the two polymers exists a strong interaction. The UBE presence reduces the FTIR peak intensity compared with R (Figure 3—blue line), evidencing its complete dispersion in the polymer matrix.

3.2.4. XRD Analysis

Figure 4a shows the XRD patterns of the reference R and F-UBE-HPC films. According to Ishii et al. [34], the XRD pattern of HPC showed an amorphous characteristic, with a broad peak at $2\theta^\circ = 9^\circ$ and 20°.

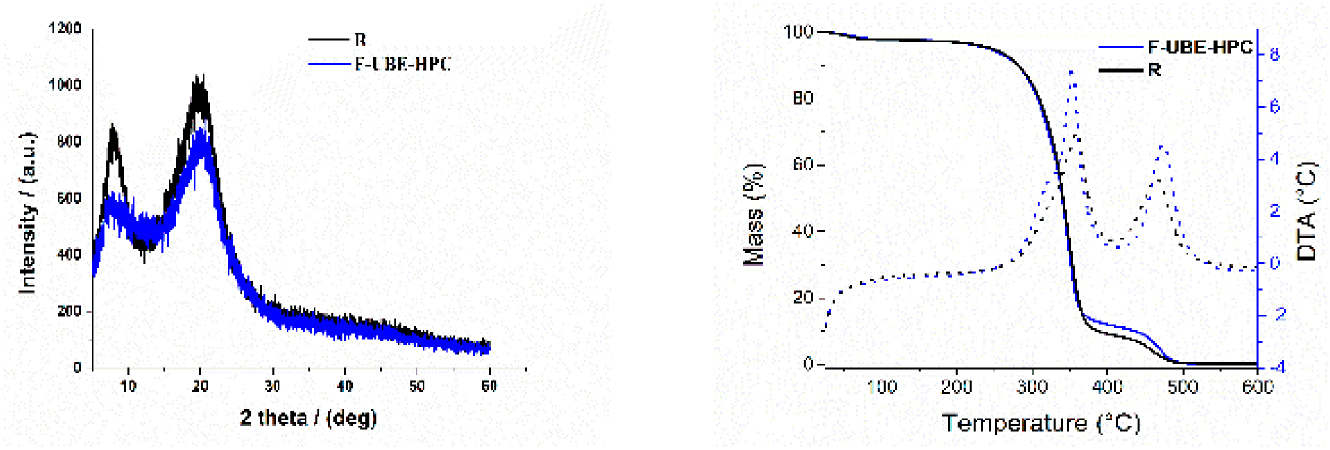

(**a**) (**b**)

Figure 4. (**a**) XRD pattern and (**b**) TG/DTA curves of bioadhesive oral films: R (black line) and F-UBE-HPC (blue line). R—bioadhesive oral film without active lichen extract; F-UBE-HPC—bioadhesive oral film loaded with *U. barbata* dry ethanol extract.

In the XRD pattern of R, the amorphous character was observed with the two broader peaks characteristic of the HPC compound. The amorphous aspect is maintained when UBE is loaded, but the peak intensities are reduced, thus proving that UBE was successfully dispersed in the polymer matrix.

3.2.5. TG Analysis

Thermogravimetric and differential thermal analyses were performed to assess the bioadhesive films' thermal behavior and stability. Reference (R) and F-UBE-HPC exhibited similar behavior when a heating program from 25 to 600 °C (Figure 4b) was performed.

In the first step (between 25 and 100 °C), the films' mass loss (of 2.4% for R and 2.3% for F-UBE-HPC) can be associated with the loss of residual solvent and physisorbed water.

The decomposition process of the organic compounds occurs in two distinct steps, between 190–380 °C and 380–550 °C. The mass losses and maximum decomposition temperatures obtained from DTA curves associated with the three steps are presented in Table 2.

Table 2. Thermal data of the studied samples.

Film	**1st Step (%)**	**2nd Step (%)**	**3rd Step (%)**
	TG (%)	**TG(%)/T_{max} (°C)**	**TG(%)/T_{max} (°C)**
R	2.4%	88.4%/357.6 °C	9.2%/468.3 °C
F-UBE-HPC	2.3%	85.6%/352.3 °C	12.1%/471.8 °C

R—bioadhesive oral film without active lichen extract; F-UBE-HPC—bioadhesive oral film loaded with *U. barbata* dry ethanol extract.

3.3. Pharmacotechnical Properties of the Bioadhesive Oral Films

The pharmacotechnical properties evaluated in this study are displayed in Table 3. Data from Table 3 show that the F-UBE-HPC average weight reported no significant difference compared with R (110 ± 4.77 vs. 107 ± 5.25, $p > 0.05$). Both films have a thickness of 0.093 mm, with minimal differences in standard deviation (SD) values between F-UBE-HPC and R (0.003 vs. 0.002).

Table 3. Bioadhesive oral films' pharmacotechnical characteristics.

Parameter *	**Formulation Code**	
	F-UBE-HPC	**R**
Weight uniformity (mg)	110 ± 4.77	107 ± 5.25
Thickness (mm)	0.093 ± 0.002	0.093 ± 0.003
Folding endurance value	>300	>300
Tensile strength (kg/mm^2)	2.48 ± 1.58	2.57 ± 1.71
Elongation %	63.14 ± 1.94	62.75 ± 1.52
Moisture content % (*w*/*w*)	6.58 ± 0.44	6.23 ± 0.56
pH	7.10 ± 0.02	7.07 ± 0.01
Disintegration time (seconds)	118 ± 3.16	115 ± 4.19
Swelling ratio (% after 6 h)	289 ± 5.82	288 ± 6.13
Ex vivo biooadhesion time (minutes)	98 ± 3.58	98 ± 4.17

* Expressed as mean value ± SD; F-UBE-HPC—bioadhesive oral film loaded with *U. barbata* dry ethanol extract; R—bioadhesive oral film without active lichen extract.

Both developed films displayed a high folding endurance, above 300. Moreover, tensile strength and elongation did not show significant differences between F-UBE-HPC and R (2.48 ± 1.58 vs. 2.57 ± 1.71 and 63.14 ± 1.94 vs. 62.75 ± 1.52, $p > 0.05$). F-UBE-HPC's moisture content was similar to the R one (6.58 ± 0.44 vs. 6.23 ± 0.56, $p > 0.05$). Both bioadhesive films have a neutral pH, without noticeable differences between F-UBE-HPC and R (7.10 ± 0.02 vs. 7.07 ± 0.01, $p > 0.05$). The films displayed a fast disintegration time of 118 ± 3.16 (F-UBE-HPC) vs. 115 ± 4.19 (R).

The swelling rate over the 6 h of study is presented in Figure 5.

Table 3 and Figure 5 show that F-UBE-HPC and R have the same swelling performance after 6 h (289 ± 5.82 vs. 288 ± 6.13, $p > 0.05$).

Regarding the ex vivo bioadhesion time, both oral films (F-UBE-HPC and R) show similar values: 98 ± 3.58 vs. 98 ± 4.17, $p > 0.05$ (Table 3).

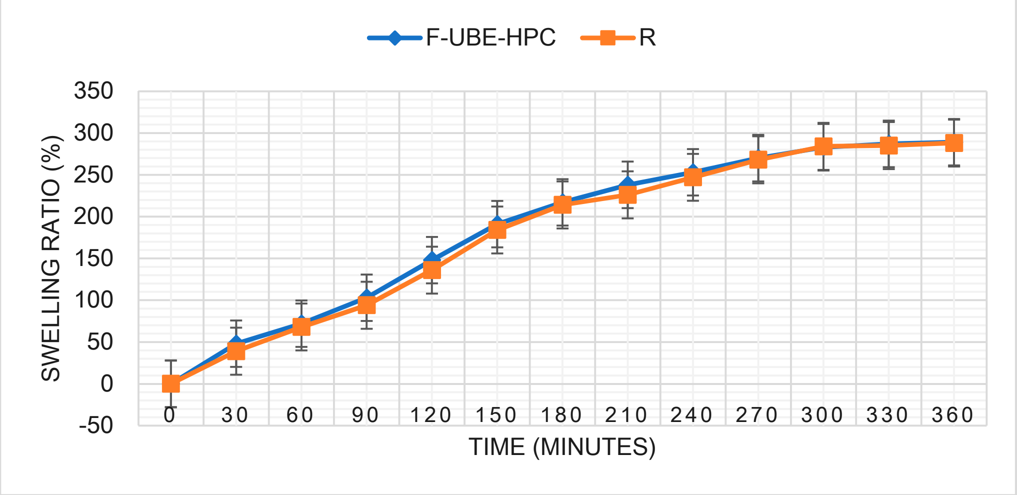

Figure 5. Swelling rate over 6 h for F-UBE-HPC and R; F-UBE-HPC—bioadhesive oral film loaded with *U. barbata* dry ethanol extract; R—bioadhesive oral film without active lichen extract.

3.4. Antimicrobial Activity

The standard drugs and F-UBE-HPC microdilutions used in antimicrobial activity evaluation are registered in Table 4.

Table 4. Microdilutions of Ceftriaxone, Terbinafine, and F-UBE-HPC films.

Microdilution	CTR		TRF	F-UBE-HPC
	30 mg/mL	122 mg/mL	10.1 mg/mL	110 mg/mL
1	1.5	6.10	0.5	5.5
2	0.75	4.88	0.25	2.75
3	0.375	3.904	0.125	1.375
4	0.187	3.123	0.062	0.685
5	0.093	2.498	0.031	0.342
6	0.046	1.998	0.015	0.171
7	0.024	1599	0.007	0.085

CTR—Ceftriaxone, TRF—Terbinafine http://allie.dbcls.jp/pair/TRF;terbinafine.html (accessed on 5 July 2022), and F-UBE-HPC—bioadhesive oral film loaded with *U. barbata* dry ethanol extract.

F-UBE-HPC inhibitory activity on both bacterial and fungal strains was dose-dependent, and the obtained data are displayed in Table 5 and Figure 6.

Table 5 shows that F-UBE-HPC of [5.5–0.085] mg/mL concentration act on *S. aureus* similar to CTR of [1.5–0.024] mg/mL (Table 5). On *P. aeruginosa,* their inhibitory activity is higher: in the range of [5.5–0.685] mg/mL and act similarly to CTR of [2.498–0.187] mg/mL. The final F-UBE-HPC concentration range of [0.342–0.085] mg/mL inhibits bacterial colonies proliferation such as a CTR of [0.093–0.024] mg/mL.

Figure 6 shows that F-UBE-HPC of [5.5–2.75] mg/mL induces *C. albicans* partial death and a low proliferation of *C. parapsilosis.* At the following concentration range [1.375–0.171] mg/mL, it similarly acts on both *Candida* sp., determining a moderate proliferation. The final concentration (0.085 mg/mL) leads to *C. albicans* fast proliferation and *C. parapsilosis* moderate.

Table 5. Inhibitory activity of F-UBE-HPC on *S. aureus* and *P. aeruginosa*.

Dil.	***S. aureus***				***P. aeruginosa***			
	CTR F-UBE		**F-UBE-HPC**		**CTR**		**F-UBE-HPC**	
	A	**B**	**C**	**D**	**E**	**F**	**G**	**H**
1								
2								
3								
4								
5								
6								
7								

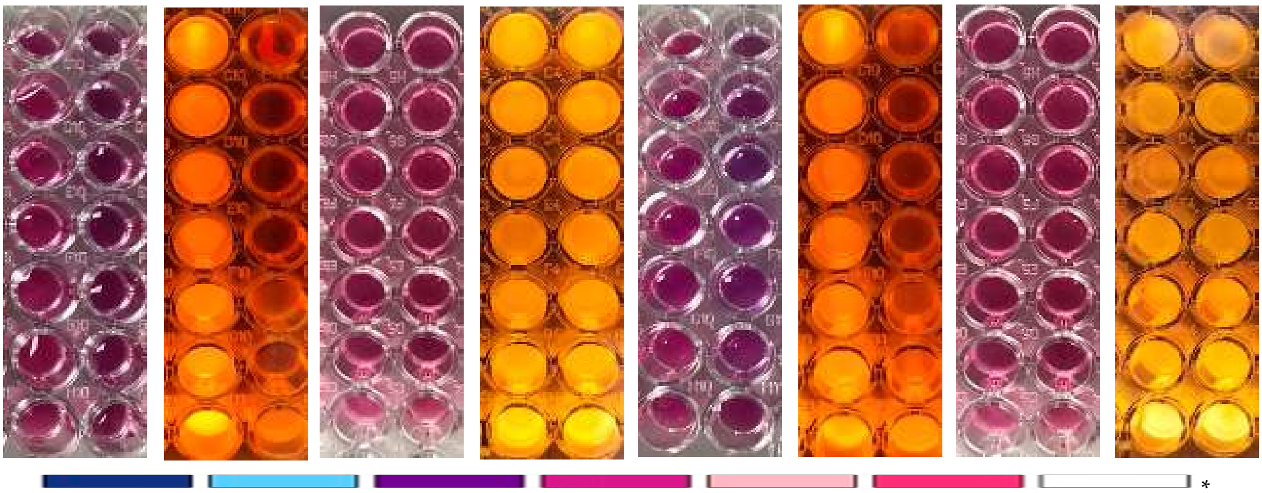
*

* Interpreting obtained results adapted from Madushan et al. [25] as blue—excellent; light blue—very good; violet—good; purple pink—moderate; light pink—low; pink—very low; white—no effect. CTR—Ceftriaxone and F-UBE-HPC—Bioadhesive film loaded with *U. barbata* dry ethanol extract; a,c,e,g well plates examined with a free eye; b,d,f,h well plates analyzed at 470 nm.

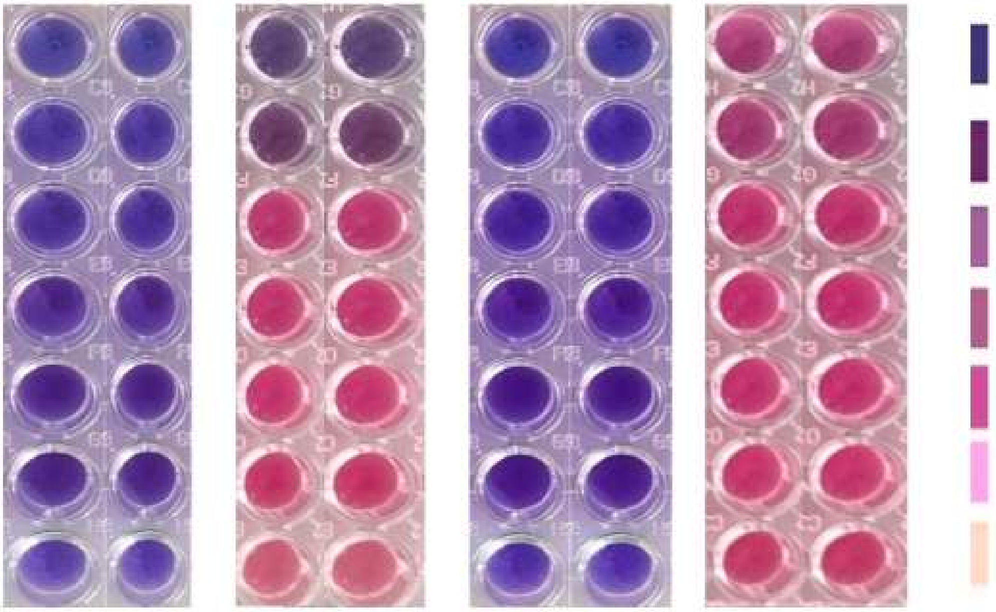
(**a**) (**b**) (**c**) (**d**) (**e**)

Figure 6. Inhibitory activity of F-UBE-HPC (**b**,**d**) on *C. albicans* (**a**,**b**) and *C. parapsilosis* (**c**,**d**). The results were compared with Terbinafine (**a**,**c**) as an antifungal drug. (**e**) Results interpretation adapted from Bitacura et al. [27], as follows: blue—cells are dead; violet–blue—cells are partially dead; violet—cells are alive, no proliferation; light-violet—low proliferation; dark pink—moderate proliferation; pink—fast proliferation; light pink—very fast proliferation. F-UBE-HPC—bioadhesive oral film loaded with *U. barbata* dry ethanol extract.

3.5. Cytotoxic Activity on *A. salina* Larvae

After 24 h, the larvae were alive, swimming, and showing normally visible movements. We investigated them under a microscope to observe the changes after 24 and 48 h of exposure. All these microscopic images are presented in Figures 7 and 8.

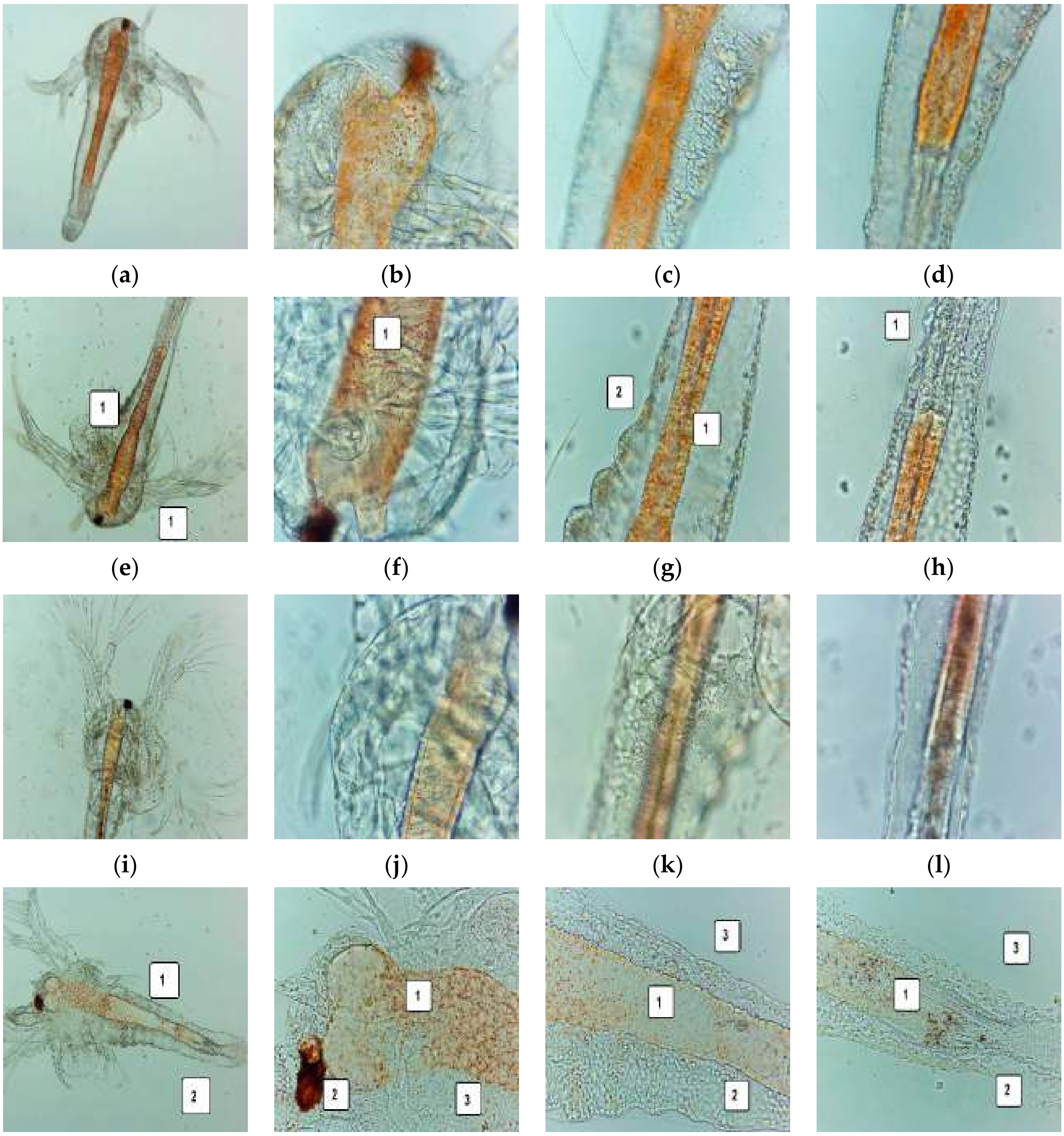

(**a**) (**b**) (**c**) (**d**)

(**e**) (**f**) (**g**) (**h**)

(**i**) (**j**) (**k**) (**l**)

(**m**) (**n**) (**o**) (**p**)

Figure 7. *A. salina* larvae after 24 and 48 h exposure to F-UBE-HPC—microscopic images at 100× (**a**,**e**,**i**,**m**) and 400× (**b**–**d**,**f**–**h**,**j**–**l**,**n**–**p**). After 24 h: blank (**a**–**d**) and sample (**e**–**h**); after 48 h: blank (**i**–**l**) and sample (**m**–**p**). (**e**) contraction of the digestive tube in the upper and middle portion (1); (**f**) reduced amount of food in the upper digestive tube (1); (**g**) early digestive blockage (1), low detachment of the cuticle from larval tissue (2); (**h**) low detachment of cuticle from the peripheral larval tissues (1); (**m**) dead larvae with massive digestive blockage (1) and tissue destruction (2); (**n**) digestive blockage (1) and massive tissue damage (2,3); (**o**,**p**) low quantity of foods in the digestive tube (1), massive tissue destruction (2) and high detachment of the cuticle from larval tissues (3); F-UBE-HPC—bioadhesive oral film loaded with *U. barbata* dry ethanol extract.

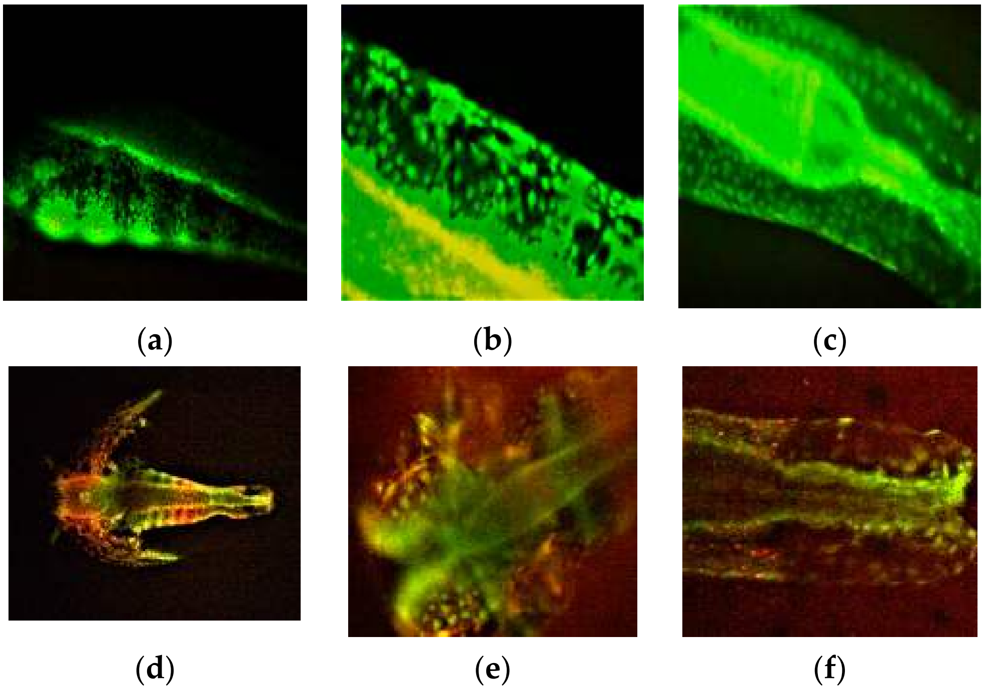

Figure 8. *A. salina* larvae after 48 h of exposure to F-UBE-HPC stained with acridine orange 100× (**d**), 200× (**b**,**c**,**e**,**f**), and 400× (**a**). (**a**–**c**)—blank; (**d**–**f**)—samples. The red fluorescence shows intracellular lysosomes activated in cell death processes (**e**,**f**); F-UBE-HPC—bioadhesive oral film loaded with *U. barbata* dry ethanol extract.

After 24 h of exposure, *A. salina* larvae showed an early digestive blockage, with contraction of the digestive tube, a low amount of food in the upper digestive part, and a low detachment of cuticle from peripheral tissues (Figure 7e–h). After 48 h, 35.82% of larvae were alive, and 8.95% were in a sublethal stage. The registered mortality was 55.22% due to massive digestive blockage and tissue destruction (Figure 7m–p).

The FM images show *A. salina* larvae after 48 h exposure at F-UBE-HPC (Figure 8d–f) compared with blank (Figure 8a–c). Figure 8e,f shows intracellular lysosomes activated in the cell death process, evidenced by red fluorescence.

3.6. In Vitro Analysis of the Biological Effects of UBE-Loaded Mucoadhesive Oral Films on Human Blood Cell Cultures and CLS-354 Cancer Cell Line

The effects of F-UBE-HPC on blood cell cultures and CLS-354 tumor cell line were studied by highlighting the biological mechanisms implied in caspases 3/7 activity, nuclear shrinkage, autophagy, oxidative stress, cell cycle, apoptosis, and DNA synthesis and fragmentation, following previous preliminary studies with *U. barbata* dry ethanol extract [35,36].

3.6.1. Caspase 3/7 Activity

To prove that F-UBE-HPC causes cell apoptosis in normal blood cells and OSCC tumor cells, the effector caspase 3/7 intracellular activity was determined by flow cytometry. The results are illustrated in Figure 9.

After 24 h of treatment, the caspase-3/7 activation mechanisms present significantly more decreased values than the negative and positive controls (13.56 ± 3.13 vs. C1: 29.26 ± 1.97, $p < 0.05$; C2UA: 44.74 ± 0.41, $p < 0.01$, Figure 9A–C,G).

The biochemical cascade of reactions implied in the proapoptotic signal after F-UBE-HPC treatment in the CLS-354 tumor cell line registers a considerable augmentation reported to 1% DMSO negative control and 125 µg/mL UA positive control (53.42 ± 3.16; vs. 21.88 ± 5.09; 27.02 ± 1.64, $p < 0.01$, Figure 9D–F,H).

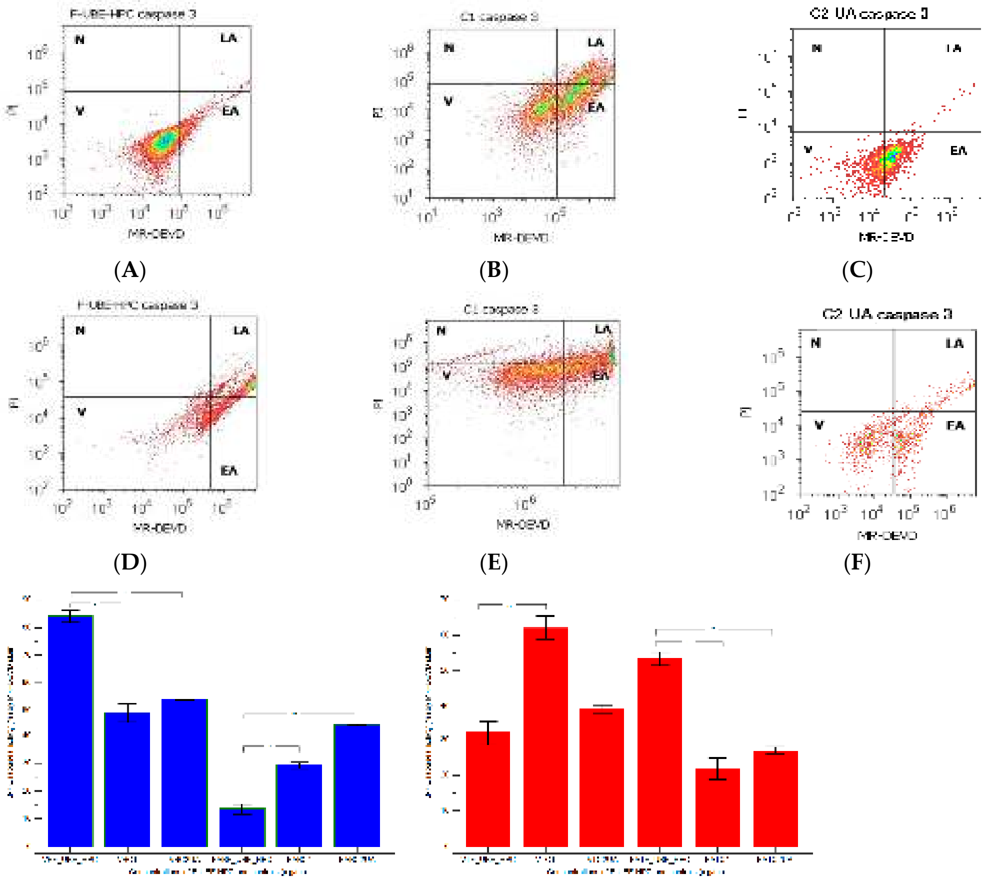

(**A**) (**B**) (**C**)

(**D**) (**E**) (**F**)

(G) (H)

Figure 9. The activity of 3/7 effector caspases in normal blood cells (**A**–**C**) and CLS-354 tumor cells (**D**–**F**) after 24 h treatment with F-UBE-HPC; MR-DEVD patterns of F-UBE-HPC (**A**,**D**), 1% DMSO negative control (**B**,**E**); 125 µg/mL UA positive control (**C**,**F**). Statistical analysis of 3/7 caspases activity (**G**,**H**) in normal blood cell cultures (**G**) and CLS-354 tumor cell line (**H**), * $p < 0.05$ and ** $p < 0.01$ represent significant statistical differences between controls and sample made by paired samples *t*-test; V—viability; EA—early apoptosis; C1—negative control with 1% dimethyl sulfoxide (DMSO); C2UA—positive control with 125 µg/mL usnic acid (UA); F-UBE-HPC—bioadhesive oral film loaded with *U. barbata* dry ethanol extract.

3.6.2. Nuclear Condensation and Lysosomal Activity

After 24 h of F-UBE-HPC treatment in normal blood cells and CLS-354 tumor cells, the presence of pyknotic nuclei (stained with Hoechst 33342) and the lysosomal activity (evidenced by acridine orange) are displayed in Figure 10.

Nuclear shrinkage, after 24 h treatment with F-UBE-HPC in normal blood cell cultures had significantly lower values (4.23 ± 0.58) than 1% DMSO negative control: 24.50 ± 2.21, $p < 0.01$ (Figure 10A,B,M), and appreciably higher than 125 µg/mL UA positive control: 3.19 ± 0.30, $p < 0.05$ (Figure 10A,C,M). The autophagy levels strongly decreased compared with both controls: 5.36 ± 0.65; vs. C1: 51.30 ± 3.25; C2UA: 27.05 ± 1.52, $p < 0.01$ (Figure 10G–I,M).

Flow-cytometry examination by Hoechst 33342/acridine orange dual stain of tumor cells after F-UBE-HPC treatment showed chromatin condensation (NS) and autophagy (A) significant elevation compared with 1% DMSO negative control: NS: 35.36 ± 2.28 vs. 16.11 ± 3.11; A: 71.81 ± 1.47 vs. 12.57 ± 0.92, $p < 0.01$; Figure 10D,E,J,K,M).

As shown in Figure 10D,F,J,L,N, F-UBE-HPC displays significantly lower values of nuclear shrinkage (NS) and appreciably higher autophagy (A) levels reported to positive control with 125 µg/mL UA (NS: 35.36 ± 2.28 vs. 44.03 ± 0.36; A: 71.81 ± 1.47 vs. 53.35 ± 2.63, $p < 0.05$).

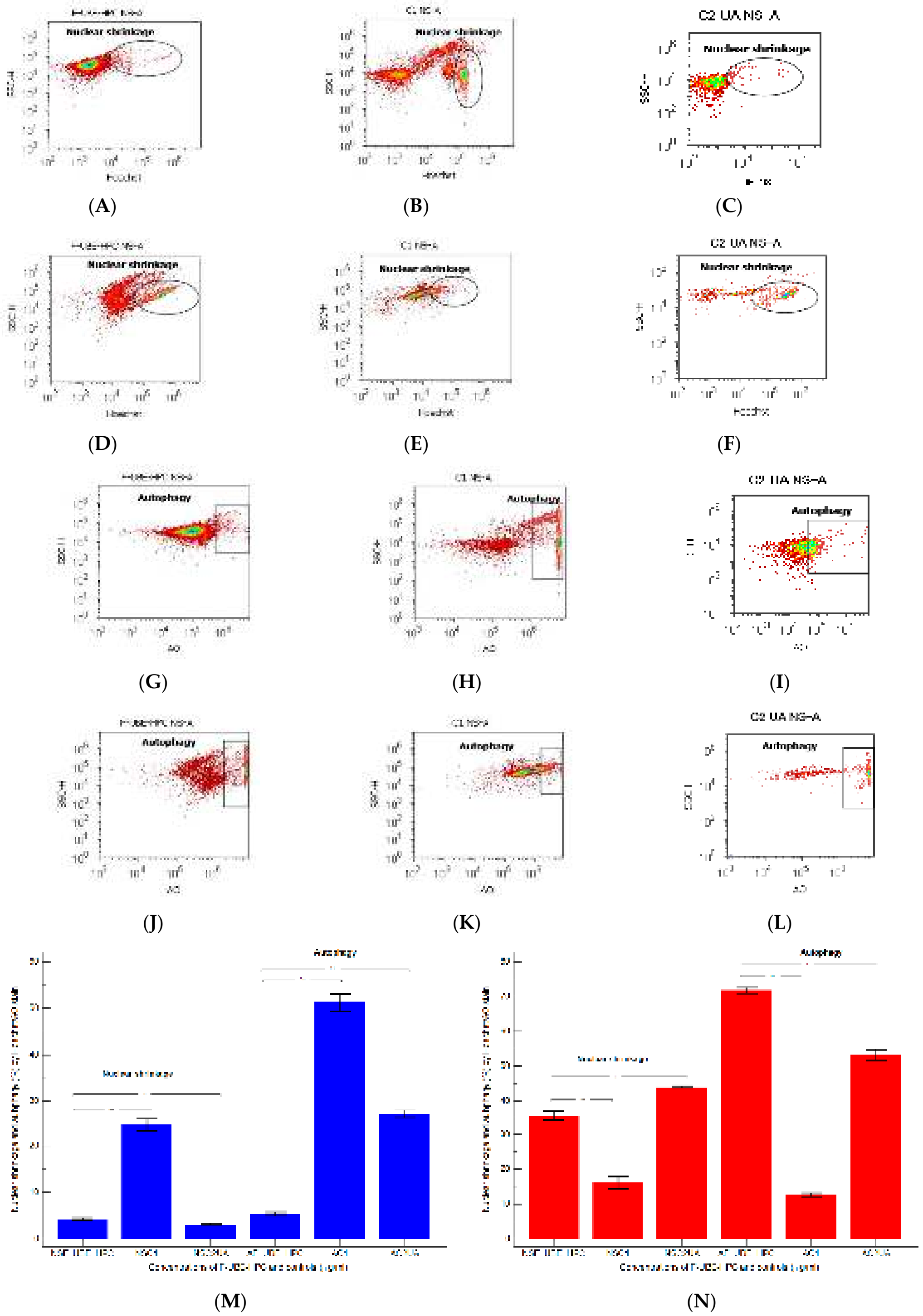

(A) (B) (C)

(D) (E) (F)

(G) (H) (I)

(J) (K) (L)

(M) (N)

Figure 10. Nuclear shrinkage (**A**–**F**) and Lysosomal activity (**G**–**L**) after 24 h treatment with F-UBE-HPC in normal blood cells (**A**–**C**,**G**–**I**) and CLS-354 tumor cells (**D**–**F**,**J**–**L**). Hoechst patterns of F-UBE-HPC (**A**,**D**); 1% DMSO negative control (B, E); 125 µg/mL UA positive control (**C**,**F**); acridine orange patterns of F-UBE-HPC (**G**,**J**); 1% DMSO negative control (**H**,**K**); 125 µg/mL UA positive control (**I**,**L**). Statistical analysis of nuclear shrinkage and autophagy (**M**,**N**) in normal blood cell cultures (**M**) and CLS-354 tumor cell line (**N**). * $p < 0.05$ and ** $p < 0.01$ represent significant statistical differences between controls and sample made by paired samples *t*-test; NS—nuclear shrinkage; A—autophagy; C1—negative control with 1% dimethyl sulfoxide (DMSO); C2UA—positive control with 125 µg/mL usnic acid (UA); F-UBE-HPC—bioadhesive oral film loaded with *U. barbata* dry ethanol extract.

3.6.3. ROS Levels

In blood cell cultures and CLS-354 tumor cell line, F-UBE-HPC induced powerful oxidative stress expressed as total ROS level measured through flow cytometry. The obtained results are indicated in Figure 11.

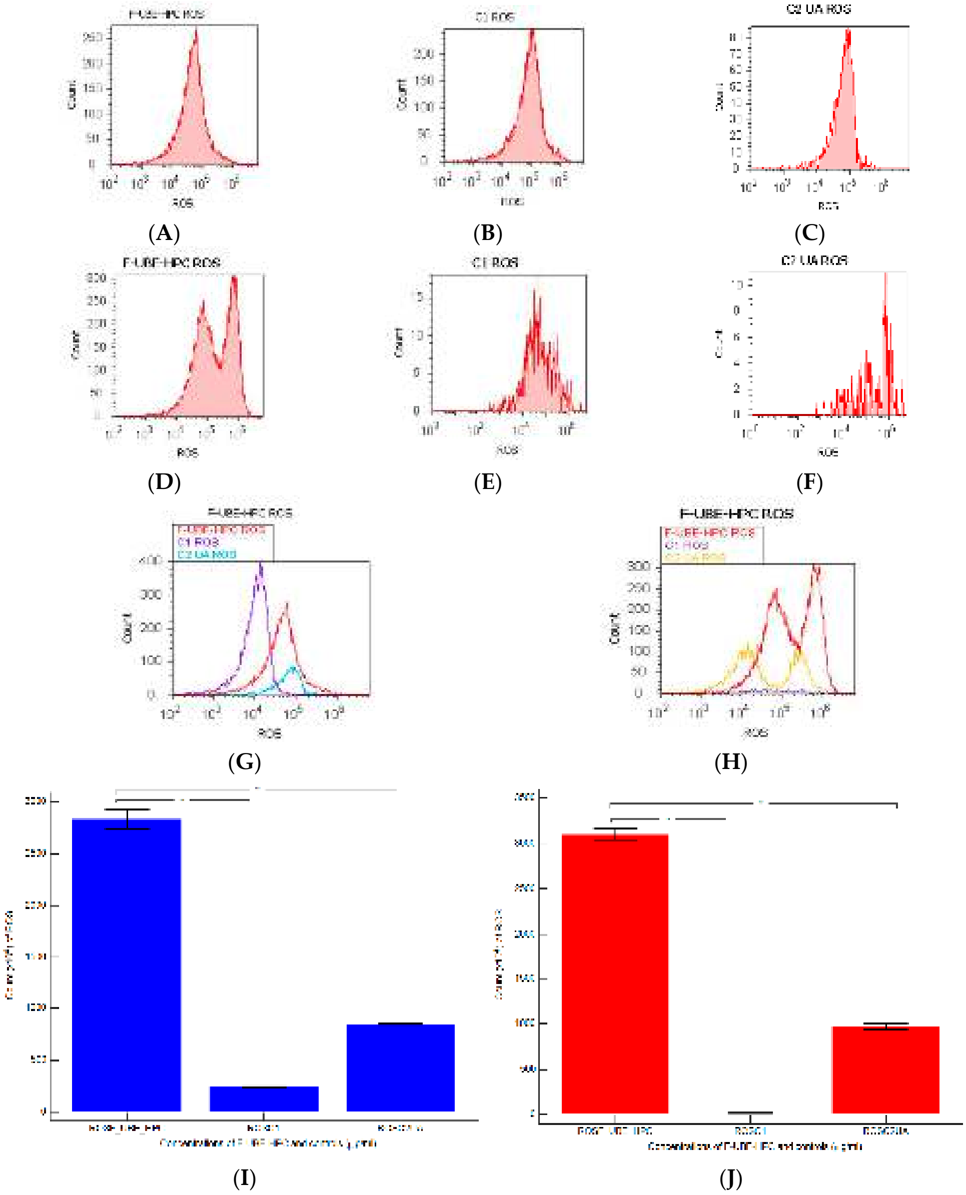

(A) (B) (C)

(D) (E) (F)

(G) (H)

(I) (J)

Figure 11. Reactive oxygen species (ROS) after 24 h treatment with F-UBE-HPC applied to normal blood cells (**A**–**C**) and CLS-354 tumor cells (**D**–**F**); 1% DMSO negative control (**B**,**E**); 125 µg/mL UA positive control (**C**,**F**); F-UBE-HPC and controls extrapolated on ROS axis (**G**,**H**); statistical analysis of ROS (**I**,**J**) in normal blood cell cultures (**I**); CLS-354 tumor cell line (**J**). ** $p < 0.01$ represents significant statistical differences between controls and samples made by paired samples *t*-test; C1—negative control with 1% dimethyl sulfoxide (DMSO); C2UA—positive control with 125 µg/mL usnic acid (UA); F-UBE-HPC—bioadhesive oral film loaded with *U. barbata* dry ethanol extract.

ROS levels substantially increased in the blood cells treated with F-UBE-HPC compared with the 1% DMSO negative control and positive control of 125 µg/mL of UA (2833.33 × 104 ± 152.75; vs. 242.00 × 104 ± 2.00; 846.66 × 104 ± 5.77; $p < 0.01$, Figure 11A–C,G,I).

Oxidative stress was strongly augmented in the OSCC cell line after 24 h contact with F-UBE-HPC compared with the 1% DMSO negative control and 125 µg/mL of UA positive control: 3100.00 × 104 ± 100.00; vs. 15.66 × 104 ± 4.04; 966.66 × 104 ± 57.73, $p < 0.01$ (Figure 11D–F,H,J).

3.6.4. Cell Cycle Analysis

Human blood consists of leukocytes (white blood cells, WBC), thrombocytes (platelets), and erythrocytes (red blood cells, RBW). Only leukocytes contain a cell nucleus, essential when estimating the amount of DNA in human blood cell cultures [37].

DNA content was performed by propidium iodide/RNase stain to explore the effects of F-UBE-HPC in normal blood cells and CLS-354 tumor cells (Figure 12).

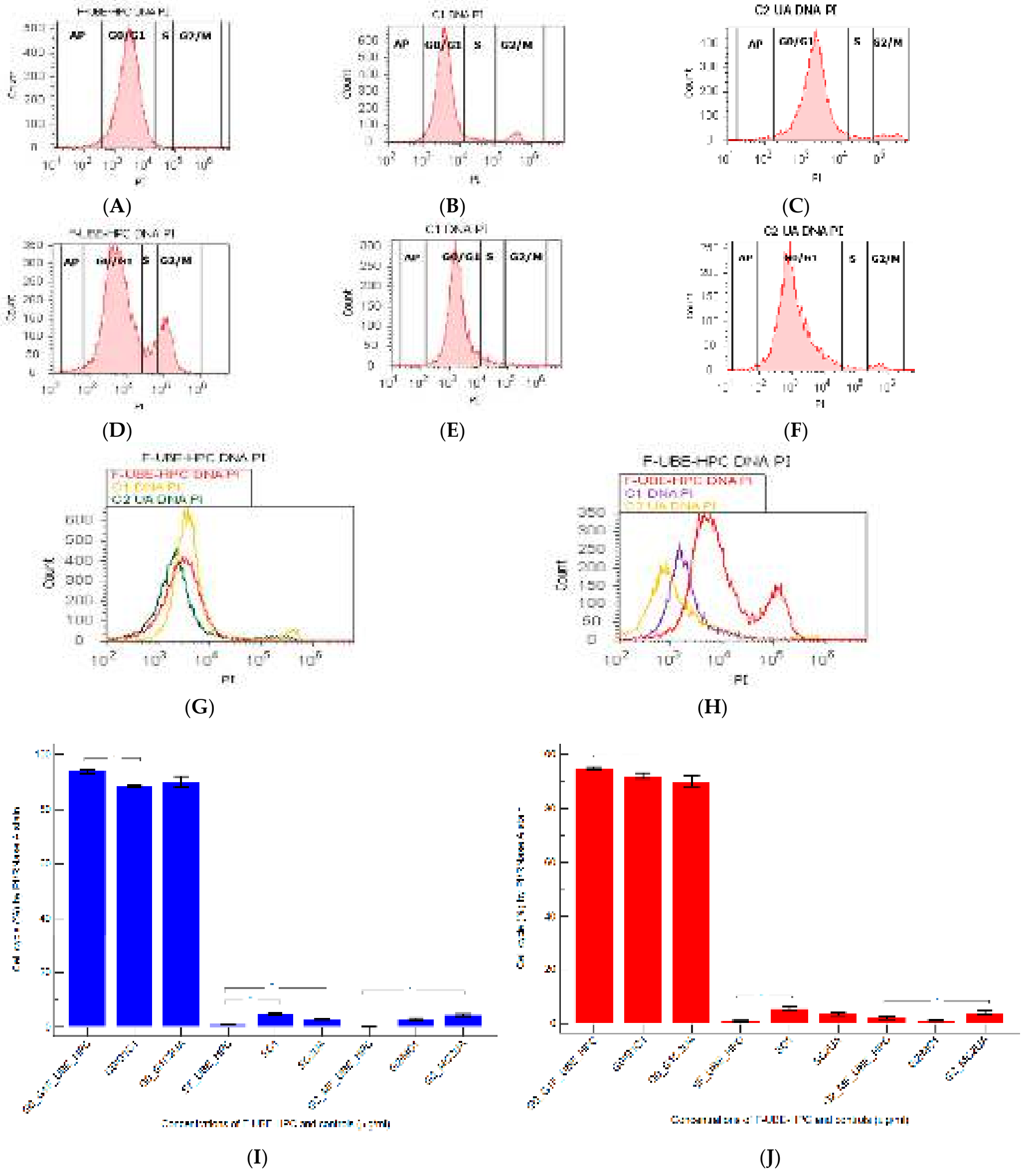

(A) (B) (C)

(D) (E) (F)

(G) (H)

(I) (J)

Figure 12. Cell cycle after 24 h treatment with F-UBE-HPC in normal blood cells (**A**–**C**) and CLS-354 tumor cells (**D**–**F**); PI/RNase patterns of F-UBE-HPC (**A**,**D**); 1%DMSO negative control (**B**,**E**); 125 µg/mL UA positive control (**C**,**F**); F-UBE-HPC and controls extrapolated on PI axis (**G**,**H**); statistical analysis of G0/G1, synthesis (S), and G2/M phases of the cell cycle (**I**,**J**) in normal blood cell cultures (**I**) and CLS-354 tumor cell line (**J**).* $p < 0.05$ and ** $p < 0.01$ represent significant statistical differences between controls and sample made by paired samples t-test; PI—propidium iodide; C1—negative control with 1% dimethyl sulfoxide (DMSO); C2UA—positive control with 125 µg/mL usnic acid (UA); F-UBE-HPC—bioadhesive oral film loaded with *U. barbata* dry ethanol extract; AP—apoptotic cell fraction (subG0/G1); S—synthesis of cell cycle phases.

As shown in Figure 12A,B,G,I, in normal blood cell cultures, F-UBE-HPC induces a higher cell cycle arrest in G1/G0 phase (93.91 ± 1.41) than the negative control (88.52 ± 0.54, $p < 0.05$). DNA synthesis phase of the cell cycle presented significantly more decreased values than both controls: 0.99 ± 0.24 vs. C1: 4.76 ± 0.68, C2UA: 2.86 ± 0.23; $p < 0.01$ (Figure 12A–C,G,I).

CLS-354 tumor cells were treated for 24 h with F-UBE-HPC to understand whether cell growth inhibition was due to cell cycle arrest. The results show a significant G0/G1 phase increase compared with the 1%DMSO negative control (94.66 ± 1.01 vs. 92.13 ± 1.61, $p < 0.05$ (Figure 12D,E,H,J). DNA synthesis reported considerably lower values reported to 1% DMSO negative control: 0.73 ± 0.43 vs. 5.47 ± 0.83, $p < 0.01$ (Figure 12D,E,H,J).

3.6.5. Apoptosis

The effects of F-UBE-HPC treatment in normal blood cells and CLS-354 tumor cells were achieved by examining morphology and cell membrane integrity with annexin V-FITC/PI stain (Figure 13).

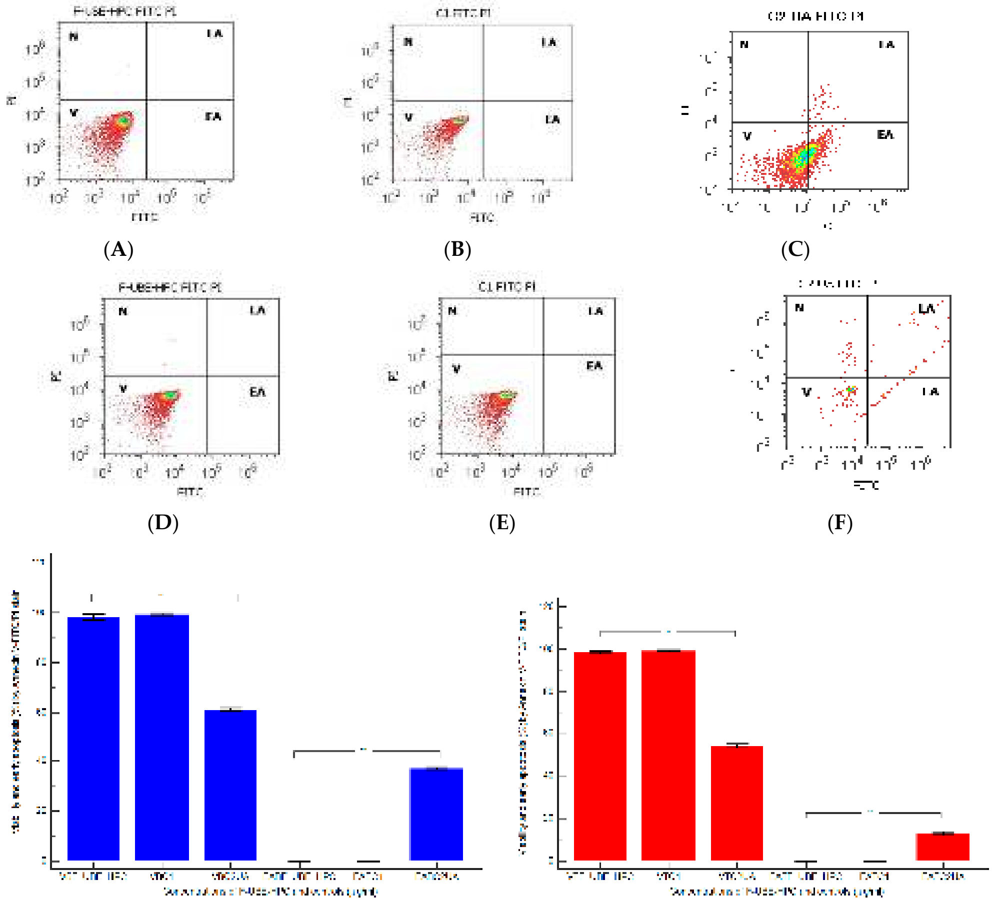

(A) (B) (C)

(D) (E) (F)

(G) (H)

Figure 13. Cell apoptosis after 24 h treatment with F-UBE-HPC in normal blood cells (**A**–**C**) and CLS-354 tumor cells (**D**–**F**); annexin V-FITC/PI patterns of F-UBE-HPC (**A**,**D**); 1%DMSO negative control (**B**,**E**); 125 µg/mL UA positive control (**C**,**F**); statistical analysis of cell apoptosis (**G**,**H**) in normal blood cell cultures and (**B**) CLS-354 tumor cell line (**H**), ** $p < 0.01$ represents significant statistical differences between controls and sample made by paired samples *t*-test; V—viability; EA—early apoptosis; C1—negative control with 1% dimethyl sulfoxide (DMSO); C2UA—positive control with 125 µg/mL usnic acid (UA); F-UBE-HPC—bioadhesive oral film loaded with *U. barbata* dry ethanol extract.

In normal blood cells, after 24 h, F-UBE-HPC did not induce early cell apoptosis (0.00 ± 0.00), reporting significant differences compared with the positive control (C2UA: 37.04 ± 0.66, $p < 0.01$). Consequently, cell viability shows appreciably elevated values: 98.35 ± 1.87 vs. 61.43 ± 0.88, $p < 0.01$, Figure 13A,C,G).

In the CLS-354 tumor cell line, similar results were obtained after treatment for 24 h with F-UBE-HPC compared with C2UA (EA: 0.00 ± 0.00 vs. 12.92 ± 1.35, $p < 0.01$ and V: 99.79 ± 1.12 vs. 54.05 ± 1.68, $p < 0.01$) as shown in Figure 13D,F,H).

3.6.6. Cell Proliferation

DNA synthesis (S) and fragmentation (subG0/G1) by EdU incorporation in both cell types were examined to observe the effects of 24 h treatment with F-UBE-HPC (Figure 14).

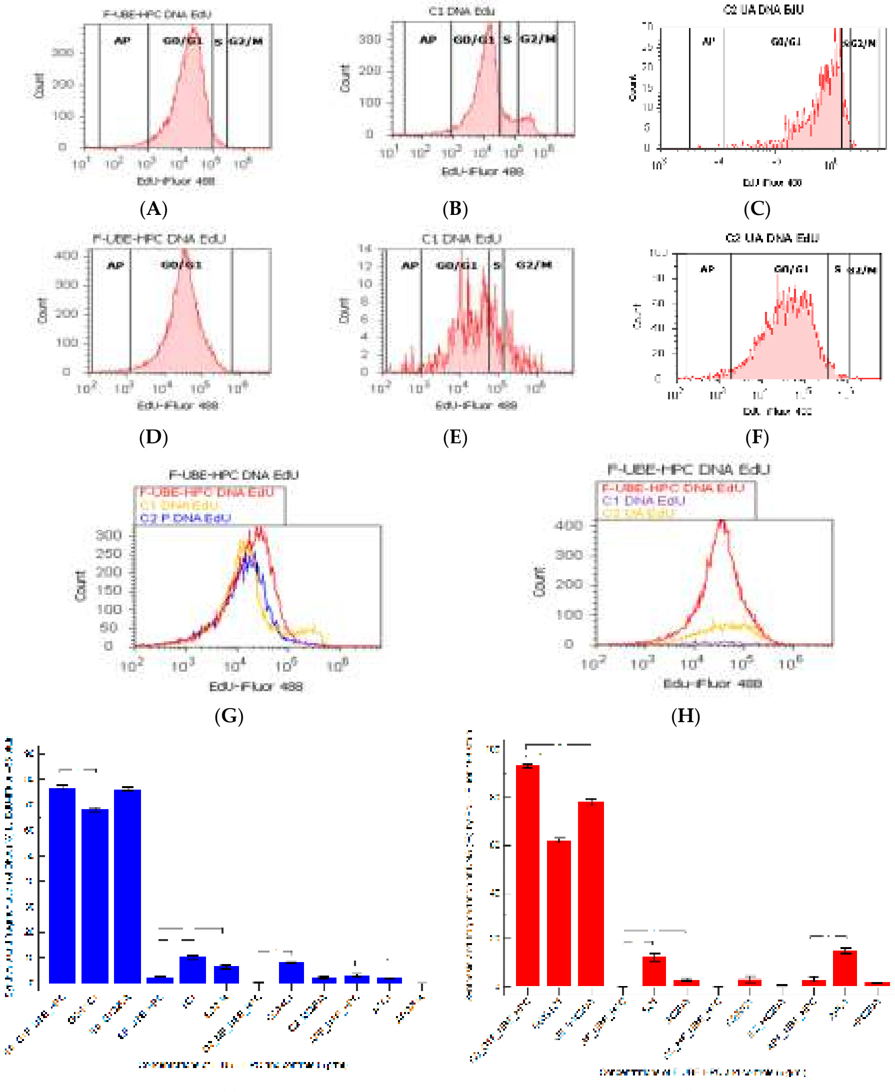

(A) (B) (C)

(D) (E) (F)

(G) (H)

(I) (J)

Figure 14. DNA synthesis (S) and DNA fragmentation (subG0/G1) after 24 h treatment with F-UBE-HPC in normal blood cell cultures (**A**–**C**) and CLS-354 tumor cells (**D**–**F**); EdU-iFluor 488 patterns of F-UBE-HPC (**A**,**D**); 1%DMSO negative control (**B**,**E**); 125 µg/mL UA positive control (**C**,**F**). F-UBE-HPC and controls extrapolated on EdU-iFluor 488 axis (**G**,**H**); statistical analysis of cell proliferation (**I**,**J**) in normal blood cell cultures and (**I**) CLS-354 tumor cell line (**J**). * $p < 0.05$ and ** $p < 0.01$ represent significant statistical differences between controls and sample made by paired samples *t*-test; C1—negative control with 1% dimethyl sulfoxide (DMSO); C2UA—positive control with 125 µg/mL usnic acid (UA). AP—apoptosis (subG0/G1); F-UBE-HPC—bioadhesive oral film loaded with *U. barbata* dry ethanol extract.

In normal blood cell cultures, F-UBE-HPC determined considerably lower levels of DNA synthesis than the negative and positive controls (2.44 ± 0.40 vs. C1:10.36 ± 1.21; $p < 0.01$; C2UA: 6.49 ± 1.25, $p < 0.05$). However, DNA fragmentation (implied in apoptosis) significantly increased compared with the 125 µg/mL UA positive control (3.13 ± 1.03 vs. 0.00 ± 0.00, $p < 0.05$, Figure 14A–C,G,I).

On the other hand, in CLS-354 tumor cells, F-UBE-HPC blocked DNA synthesis: (0.00 ± 0.00 vs. C1: 12.44 ± 2.80, and C2UA: 3.14 ± 0.50, $p < 0.05$), while the apoptosis represented by fractional DNA (subG0/G1 phase) decreased compared with the 1% DMSO negative control: 3.19 ± 1.86 vs. 15.18 ± 2.17, $p < 0.05$ (Figure 14D–F,H,J).

3.6.7. Principal Component Analysis

The Principal Component Analysis (PCA) was performed for F-UBE-HPMC oral mucoadhesive patches and both controls (C1-DMSO and C2UA) and variable parameters determined in both cell types (normal blood cells and CLS-354 tumor cells) according to the correlation matrix and PCA-Correlation circle from the Supplementary Material. The results are displayed in Figure 15.

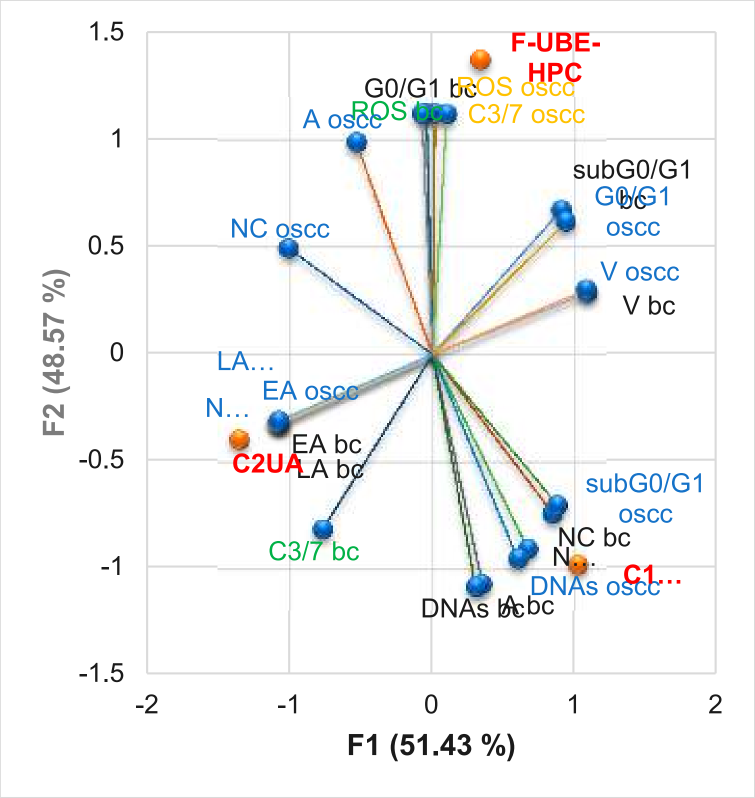

Figure 15. PCA-Correlation biplot between mechanisms (caspase 3/7 activity and cellular oxidative stress) and processes induced by F-UBE-HPC and both controls (C1-DMSO and C2UA) in normal blood cells (bc) and CLS-354 tumor cells (oscc). V—viability; EA—early apoptosis; LA—late apoptosis; N—necrosis; NC—nuclear condensation; A—autophagy; DNAs—DNA synthesis; subG0/G1—apoptotic cell fraction http://www.icms.qmul.ac.uk/flowcytometry/uses/apoptosis/dnafragmentation/ (accessed on 11 July 2022); G0/G1—cell cycle arrest in G0/G1; ROS—oxidative stress; C3/7—caspase 3/7 activity; F-UBE-HPC—bioadhesive oral film loaded with *U. barbata* dry ethanol extract.

The two principal components explained the total data variance, with 51.43% attributed to the first (PC1) and 48.57% to the second (PC2). The PC1 was associated with both controls (C1-DMSO and C2UA), viability, early and late apoptosis, nuclear condensation, and DNA fragmentation (subG0/G1) in both cell types and cell cycle arrest in G0/G1 and necrosis in CLS-354 tumor cells. The PC2 was related to F-UBE-HPC, ROS, and caspase 3/7 activity, DNA synthesis and autophagy in both cell types, and cell cycle arrest in G0/G1 and necrosis in normal blood cells.

In normal blood cells, caspase 3/7 activity has a high positive correlation with early and late apoptosis ($r = 0.864$, $p > 0.05$) and a low one with DNA synthesis and autophagy ($r = 0.514$ and 0.475, $p > 0.05$). It moderate negatively correlates with ROS ($r = -0.735$, $p > 0.05$) and cell cycle arrest in G0/G1 ($r = -0.698$, $p > 0.05$). Cellular oxidative stress (ROS) shows a strong positive correlation with subG0/G1 ($r = 0.999$, $p < 0.05$). It highly negatively correlates with DNA synthesis and autophagy ($r = -0.959$ and 0.946, $p > 0.05$) and moderately with necrosis and nuclear condensation ($r = -0.796$ and 0.648, $p > 0.05$).

In CLS-354 tumor cells, ROS levels are considerably correlated with caspase 3/7 activation ($r = 0.988$, $p > 0.05$) and autophagy ($r = 0.908$, $p > 0.05$). Caspase 3/7 activity also highly correlates with autophagy, but the r value is slightly lower compared to ROS ($r = 0.834$, $p > 0.05$). Oxidative stress reports a high negative correlation with DNA synthesis ($r = -0.880$, $p > 0.05$) and a moderate one with subG0/G1 ($r = -0.675$, $p > 0.05$). Caspase 3/7 activity is also negatively correlated with both processes, but the r values are lower than ROS ones ($r = -0.797$ and -0.554, $p > 0.05$). Moreover, caspase 3/7 activity moderately correlates with cell cycle arrest in G0/G1 ($r = 0.621$, $p > 0.05$).

By correlating and interpreting these data, the places of F-UBE-HPC patches and both controls (C1-DMSO and C2UA) in the PCA-correlation biplot (Figure 15) were explained, highlighting the corresponding processes triggered in CLS-354 cancer cells and normal blood cells and their complementary mechanisms.

4. Discussion

Until the preparation of UBE-loaded bioadhesive oral films analyzed in the present work for potential applications in oral cancer treatment, *U. barbata* lichen was thoroughly studied for almost six years.

First, it is essential to mention that this lichen was harvested from a coniferous forest in the same area (47°28′ N, 25°12′ E, and 900 m altitude), belonging to the highest Romanian volcanic mountains (Calimani mountains) [30,38]. Coniferous forest soil is adjacent to the Tinovul Mare Poiana Stampei peat bog with a natural origin, its accumulation beginning in the post-glacial period [39]. The specific conditions of the *U. barbata* native zone consist of seasonal water-level fluctuations with thermic variations between −1 °C and 14 °C, with a precipitation range of 600–800 mL [39]. The soil has pH values between 4.09 and 5.89 and contains several trace/heavy metals under the alert threshold from national protocols [39].

A detailed elemental analysis was performed on dried lichen harvested in 2020 [30,38]. Twenty-three metals were investigated by inductively coupled plasma mass spectrometry (ICP-MS) [38]. The heavy metal concentrations were associated with those reported by Cazacu et al. [39] in the forest soil, and the results reveal that autochthonous *U. barbata* contains all, in lower amounts than the permissible limits for medicinal plants. However, the mercury content (0.671 ± 0.020 μg/g) was lower than the WHO's and FDA's approvable limit (1 μg/g) and over the one mentioned in the European Pharmacopoeia (0.1 μg/g) [38]. The metal concentrations were compared with those reported in the scientific literature regarding *U. barbata* from unpolluted zones (Mountain Natural Park in Bulgaria [40], Sri Lanka rain forest [41] and central and southern Tierra del Fuego, Patagonia, Argentina [42]). Thus, the data obtained confirmed the autochthonous lichen's suitability for pharmaceutical use [30], according to regulatory agencies [43], which restrict the harvesting area for accurate results in human-safe formulations.

The loss of drying of the dried lichen was determined [44], and bioactive secondary metabolites were identified and quantified [45]. The research on *U. barbata* from the Calimani mountains continued with the preparation of various extracts in different solvents through low-cost and easy-to-use conventional processes [38,44,46], investigating the suitable solvents and extraction conditions to obtain *U. barbata* extracts with pharmacological potential. All extracts were comparatively analyzed, quantifying their metabolites through

HPLC-DAD [45,47] and evaluating their antioxidant, antimicrobial, and cytotoxic potential. The cytotoxicity prescreen was performed using *A. salina* as an animal model [44], continuing with complex studies on normal and tumor cells [35,36].

This previously described interdisciplinary research on *U. barbata* from the Calimani mountains led to selecting the most appropriate extracts for bioadhesive oral film formulation, including the dry ethanol extract. UBE contains usnic acid and other various phenolic compounds [48–50], including common polyphenols (ellagic acid and gallic acid) with high pharmacological potential [51]. Thus, *U. barbata* ethanol extract shows a dose-dependent inhibitory activity on the most known bacteria responsible for oral infectious disease [52] in immunocompromised patients: *S. aureus, S. pneumoniae, S. pyogenes, Enterococcus* sp., other Gram-positive bacteria isolated from oral cavity and pharynx *(S. epidermidis, S. oralis, S. intermedius)*, and *P. aeruginosa* [38,51,53,54]. It also reported inhibitory effects on *C. albicans* [38]. Phenolic compounds extracted in ethanol have antibacterial and antifungal properties and could act synergistically in UBE. Moreover, inhibitory activity on bacterial strains varies in direct proportion to antioxidant potential [55], and UBE exhibits an intense antioxidant activity [51]. In normal cells, it shows antioxidant and protective effects, neutralizing a part of the free radicals generated by 0.2%DMSO, thus reducing the lipids peroxidation [56] and activity of antioxidant enzymes Superoxide dismutase (SOD) and Catalase (CAT) induced by cellular oxidative stress [36]. Contrarily, UBE demonstrated an in vitro anticancer effect on CAL-27 tumor cell line, triggering cell death processes. It acts as a prooxidant, increasing the oxidative stress induced by 0.2% DMSO and thus stimulating cellular antioxidant defense—Glutathione peroxidase (GPx) and SOD—and augmenting the malondialdehyde (MDA) levels [36,57].

Knowing the UBE bioactive metabolites' content and its pharmacological potential, the present work aimed to study a pharmaceutical formulation containing this *U. barbata* dry extract. Thus, UBE-loaded bioadhesive oral films were prepared and analyzed, their properties being compared with References (films without UBE). As a film-forming polymer, HPC was selected due to its non-ionic character and water solubility. In addition, it proved to be physiologically inert, non-irritating, bioadhesive, and biodegradable [58–61]. PEG 400 was used as a plasticizer in a 5% (w/w) amount to improve the film flexibility and obtain suitable mechanical properties [62,63]. Both films are transparent, flexible, and homogenous. The yellowish-green, faint-brown color of F-UBE-HPC is due to lichen dry ethanol extract, and its morphology shows a smooth surface.

The physical and chemical investigation of the bioadhesive oral films containing *Usnea barbata* dry ethanol extract demonstrated the successful incorporation of the UBE in the polymer matrix. The pharmacotechnical analysis of F-UBE-HPC was realized according to other previously published studies on bioadhesive films containing plant extracts [64,65].

Therefore, both films' thickness values show that UBE does not influence their dimensions. Because the films' thickness is directly connected to active ingredient concentration and the polymer's mucoadhesive function, uniformity is required. The selected plasticizer type and amount also influence the film thickness. Generally, the suitable thickness for bioadhesive oral films is 0.05–1.0 mm [66–68], and the UBE-loaded formulation belongs to this. The film's considerable folding endurance highlights appreciable flexibility and mechanical resistance provided by PEG 400 (used as a plasticizer in a 5% amount). The plasticizer's role is to modify the viscoelastic properties of the polymer, which will subsequently influence the adhesion ability and release behavior. Moreover, the UBE load did not change the films' mechanical properties.

The bioadhesive films' elongation evidenced their remarkable flexibility. The tensile strength indicates the films' high resistance, suitable to withstand the mechanical stress that occurs during unpacking and appliance on the oral mucosa. The films' hardness depends on the type and amount of polymer and plasticizer used. The obtained results prove the accurate selection of the excipients appropriate to incorporate UBE as an active ingredient in achieving high-quality bioadhesive films. Moreover, the films' flexibility is essential in aiding the penetration of active ingredients and attachment to the oral mucosa.

Bharkatiya et al. [69] stated that low tensile strength and elongation characterize a soft and weak polymer. In contrast, moderate tensile strength and low elongation are typical for a hard and brittle polymer. Furthermore, high tensile strength and elongation describe a soft and tough polymer, as in the studied formulations.

The flexibility of the chains diminishes as the crosslinking density in water-soluble polymers increases, thus protecting against overhydration. The bound water can build H-links with the HPC's accessible chains, allowing them to move more freely [70,71]. Repka et al. [72] stated that HPC has less water affinity. The obtained values also indicate a certain amount of moisture content in the films' structure, but it is well-known that humidity is needed to ensure bioadhesion. Moreover, bioadhesion is improved by functional groups that can create hydrogen bonds.

Both films' neutral pH ensures their tolerability and biocompatibility with oral mucosa. This property confirms that UBE inclusion in the polymer matrix does not affect the base films' pharmacotechnical properties; they exclusively depend on the selected excipients. In addition, pH value can influence the polymer's bioadhesive properties, and a neutral value is optimal for mucoadhesion [73,74]. HPC used as polymer film-forming is responsible for rapid disintegration, and the plasticizer also significantly influences this property. Another essential factor is the manner of active ingredient dispersion in the matrix base. In the studied formulation, UBE was solubilized and mixed with the polymer matrix, thus diminishing the disintegration time.

The swelling index plays an essential role in regulating the release rate of the active ingredient. The diffusion of water molecules into the hydrated decreases the number of hydrogen bonds and increases the strength between the polymers. Panomsuk et al. [75] proved that a polymer chain with a low ability to make hydrogen bonds cannot build a strong matrix structure, and water penetration would be difficult. The polymeric matrix swelling ability depends on its resistance to the migration of the water molecules, and the hydroxyl group is essential for hydrophilic cellulose polymers' matrix integrity [37]. Moreover, the polymer's substituted groups significantly limit the active ingredients' influence on the swelling properties. Hence, the similar swelling ratio of F-UBE-HPC and R demonstrates the impact of the active ingredient dispersion on the swelling degree because UBE incorporated as a solution in F-UBE-HPC did not change the polymer properties.

The swelling behavior also has an impact on the film's bioadhesive performance. The increased residence time is the result of the elastic behavior induced by the used plasticizer. The interaction between free polymer chains and mucin is essential; the active ingredients loaded into the matrix could occupy the chains [76], proving that their dispersion directly impacts the adhesion performance. The obtained data show that both oral films have the same bioadhesion time, demonstrating that UBE load did not influence the matrix adhesivity.

The F-UBE-HPC rapid disintegration and neutral pH were essential for accurately evaluating their pharmacological potential because the afferent studies were conducted in vitro (using bacterial, blood, and tumor cell cultures) and in vivo (on *A. salina* larvae used as an animal model) [77]. These previously mentioned analyses were performed with homogenous dispersions of UBE-loaded films in different culture media and, respectively, in phosphate buffer. On the other hand, the tested cultured cells and *A. salina* larvae are strongly affected by pH variation; thus, the films' neutral pH was requested to obtain accurate results.

For optimal evaluation, the studies used for the UBE-loaded films had a similar trend to previous ones for UBE investigation. Thus, the F-UBE-HPC antimicrobial effects were examined on similar bacterial and fungal species, and a cytotoxicity prescreen was performed on *A. salina* larvae. Anticancer activity was evaluated on a similar OSCC cell line (CLS-354, mouth epithelial squamous cell carcinoma). As normal cells, blood cell cultures were used from a single donor (the same as previously described in UBE's biological studies) because buccal mucosa has a substantial blood supply and is permeable for most blood cells. Therefore, the most common types of WBC in blood—lymphocytes (with T cells) and segmented cells (polymorphonuclear, including neutrophils and eosinophils)—are the predominant leukocytes mixed with various endothelial cell types in the oral mucosa. No significant differences in the proportions of these cells between healthy children and adults indicate that both innate and adaptive immune systems function in the oral cavity [78]. All selected studies reproduced, in a certain measure, the conditions of the previous UBE pharmacological evaluation, aiming to know whether the UBE-loaded films' activities are similar to the UBE ones.

The results show that F-UBE-HPC displayed dose-dependent inhibitory effects against *S. aureus, P. aeruginosa,* and both *Candida* sp. through various mechanisms belonging to UBE's phenolic secondary metabolites: inhibiting protein, DNA, and cell wall synthesis, permeabilizing the cell wall and chelating various microbial micronutrients and reducing their disponibility for cell growth [79]. These microbial species are frequently implied in immunocompromised patients' oral cavity infections. UBE-loaded bioadhesive films could protect them, facilitate their recovery after radiotherapy, and generally increase their life quality. Moreover, the significant inhibitory action against *C. albicans* could also be helpful in oral cancer prevention [80,81].

The BSL assay was used as cytotoxicity prescreen because it is a low-cost, fast, and effective analysis due to *A. salina* larvae sensitivity. It can be adapted to various applications [82–84]. The brine shrimp larvae used as biotester have a rapid growth rate and, in 24 h, pass to another developing stage (i.e., nauplii). Their mortality could be associated with blocking DNA synthesis or cell cycle arrest [29]. The movements of larvae and different morphological changes (visualized due to the larvae's transparency) could be associated with various cytotoxic mechanisms [28,82,85]. Previous studies consider that BSL assay results could predict the antitumor activity of tested products [86,87]. Thus, morphological changes induced by F-UBE-HPC on *A. salina* larvae and intracellular lysosomes activated in cell death processes (evidenced in FM images) anticipate the previously described in vitro anticancer effects on oral epithelial squamous cell carcinoma [86]. The brine shrimp larvae mortality could be associated with the blockage of DNA synthesis and cell cycle arrest in G0/G1 and intracellular lysosomes from FM images with autophagy.

All previously mentioned factors implied in oral cancer development produce oxidative stress (an imbalance between ROS generation and antioxidant defense, leading to high intracellular ROS levels) [88]. Excessive ROS causes oxidative damage to cellular constituents (lipids, proteins, and DNA), hardly affecting normal cells and then contributing to carcinogenesis [89,90]. ROS are also essential in cell signaling, modulating the most significant cell death pathways (mediated by mitochondria, endoplasmic reticulum, and death receptors) [91]. ROS in high concentration could induce caspase 3/7 activation, triggering cellular processes associated with cell death (DNA damage with cell cycle arrest in different phases [92], nuclear condensation [93], blockage of DNA synthesis, and autophagy [88]).

Generally, cancer cells (due to mitochondrial abnormalities) have higher ROS levels compared with normal cells [94]. Therefore, an overproduction of ROS in cancer cells may offer a cancer-specific therapy [95]. F-UBE-HPC acts on CLS-354 cancer cells, considerably increasing cellular oxidative stress and caspase 3/7 activity, triggering nuclear condensation and autophagy, inducing cell cycle arrest in G0/G1, and blocking DNA synthesis. Compared with UA 125 μg/mL, F-UBE-HPC generates an ROS level 3 × higher; the caspase activity level is double that of UA. Moreover, DNA synthesis is completely stopped, and lysosomal activity is substantially increased compared with UA. Even though CLS-354 tumor cell viability is slowly diminished after 24 h, all intracellular and molecular processes leading to tumor cell death are triggered at a significant level.

On the other hand, in normal blood cells, the basal ROS level is lower than the one in the cancer cell line. A moderate ROS level is essential to promote cell proliferation and survival. In blood cell cultures, oxidative stress induced by UBE-loaded films is lower than in the CLS-354 tumor cell line; their viability after 24 h is over 98%. Compared with cancer cells, it could be considered that F-UBE-HPC displays a protective role in blood cell cultures, remarkably diminishing caspase 3/7 activity, nuclear condensation, and lysosomal activity triggered by 1% DMSO.

If any concerns regarding the F-UBE-HPC safety for human health [96] in relationship with usnic acid hepatotoxicity still exist, the following data could be significant. LipoKinetix (Syntrax, Cape Girardeau, MO), the fat-burning diet supplement [97], was a multi-ingredient product, including 100 mg usnic acid per capsule, together with 25 mg of norephedrine hydrochloride, 100 µg of 3,5-diiodothyronine, 3 mg of yohimbine hydrochloride, and 100 mg of caffeine [98]. The recommended daily dose associated with severe liver failure was 3–6 capsules, corresponding to 300–600 mg of usnic acid [99]. One UBE-loaded bioadhesive oral film contains 0.330 mg UBE, corresponding to 0.036 mg UA; hence, over 2700 films should be necessary to ensure the usnic acid content of 100 mg from a single capsule of LipoKinetix.

5. Conclusions

In the present study, bioadhesive oral films loaded with *U. barbata* dry ethanol extract were formulated and manufactured using HPC as a polymer matrix and PEG 400 as a plasticizer.

F-UBE-HPCs and References (the same formulation without UBE) were investigated through physicochemical and pharmacotechnical analyses, and the obtained data reported no significant differences, proving the active ingredient's consistent incorporation.

The F-UBE-HPC properties are optimal for accurately maintaining the lichen extract's pharmacological potential. The results prove it, recommending UBE-loaded bioadhesive oral films for possible application in oral cancer treatment and prevention. Additional research will optimize the bioadhesive oral film formulation, performing drug release in vivo and clinical studies, aiming to complete this interdisciplinary work and confirm their therapeutical benefits.

Supplementary Materials: The following supporting information can be downloaded at: https://www.mdpi.com/article/10.3390/pharmaceutics14091808/s1. Principal Component Analysis and Figure S1: Bioadhesive oral films F-UBE-HPC (a) and Reference (b); R—bioadhesive oral films without active lichen extract; F-UBE-HPC—bioadhesive oral film loaded with *U. barbata* dry ethanol extract. File S1: PCA F-UBE-HPC.

Author Contributions: Conceptualization, V.P., E.M., G.-C.C., C.E.G., L.B., V.S. and E.A.O.; methodology, E.M., G.-C.C., L.B., V.S., E.A.O., A.M.M., D.L. and M.A. (Mariana Aschie); software, V.P., E.M., V.S. and I.S.; validation, E.M., G.-C.C., L.B., C.E.G., E.A.O., A.M.M. and V.B.; formal analysis, A.M.M., S.P., I.A., A.R., R.-A.M. and M.A. (Mihai Anastasescu); investigation, C.E.G., A.M.M., I.S., S.P., I.A., A.R. and R.-A.M.; resources, V.P., L.B., V.S., D.L. and M.A. (Mariana Aschie); data curation, G.-C.C., A.M.M. and I.S.; writing—original draft preparation, V.P., E.M., E.A.O., V.S. and A.M.M.; writing—review and editing, V.P., E.M., E.A.O. and A.M.M.; visualization, G.-C.C., L.B., C.E.G., D.L., M.A. (Mariana Aschie), A.C. and V.B.; supervision, G.-C.C., L.B., C.E.G., D.L., M.A. (Mariana Aschie) and V.B.; project administration, V.B.; funding acquisition, V.P. and E.A.O. All authors have read and agreed to the published version of the manuscript.

Funding: This research was supported by the project ANTREPRENORDOC, in the framework of Human Resources Development Operational Programme 2014–2020, financed from the European Social Fund under the contract number 36355/23.05.2019 HRD OP/380/6/13—SMIS Code: 123847. The APC was funded by "Carol Davila" University of Medicine and Pharmacy, Bucharest, Romania.

Institutional Review Board Statement: The study was conducted in accordance with the Declaration of Helsinki and approved by the Institutional Ethics Committee of Ovidius University of Constanta, code 7080/10 June 2021 for studies involving humans.

Informed Consent Statement: Written informed consent has been obtained from the blood donor to publish this paper, code 39/30 June 2021.

Data Availability Statement: All data are available in the manuscript.

Acknowledgments: This project was performed in collaboration with the Department of Pharmaceutical Technology and Biopharmacy and the Department of Pharmacognosy, Phytochemistry, and Phytotherapy, Faculty of Pharmacy, Carol Davila University of Medicine and Pharmacy, 6 Traian Vuia Street, 020956 Bucharest, Romania, the Institute of Physical Chemistry "Ilie Murgulescu," 202 Splaiul Independentei Street, 060021. Bucharest, Romania, and the Center for Research and Development of the Morphological and Genetic Studies of Malignant Pathology, Ovidius University of Constanta, CEDMOG, 145 Tomis Blvd., 900591 Constanta, Romania.

Conflicts of Interest: The authors declare no conflict of interest.

References

1. PDQ® Screening and Prevention Editorial Board. *PDQ Oral Cavity, Oropharyngeal, Hypopharyngeal, and Laryngeal Cancers Prevention*; National Cancer Institute: Bethesda, MD, USA, 2022. Available online: https://www.cancer.gov/types/head-and-neck/hp/oral-prevention-pdq (accessed on 30 July 2022).
2. Gupta, N.; Gupta, R.; Acharya, A.K.; Patthi, B.; Goud, V.; Reddy, S.; Garg, A.; Singla, A. Changing Trends in oral cancer—A global scenario. *Nepal J. Epidemiol.* **2017**, *6*, 613–619. [CrossRef]
3. PDQ® Adult Treatment Editorial Board. *PDQ Lip and Oral Cavity Cancer Treatment (Adult)*; National Cancer Institute: Bethesda, MD, USA, 2022. Available online: https://www.cancer.gov/types/head-and-neck/hp/adult/lip-mouth-treatment-pdq (accessed on 30 July 2022).
4. Mäkinen, A.; Nawaz, A.; Mäkitie, A.; Meurman, J.H. Role of Non-Albicans *Candida* and *Candida albicans* in Oral Squamous Cell Cancer Patients. *J. Oral Maxillofac. Surg.* **2018**, *76*, 2564–2571. [CrossRef]
5. Soussan Irani New Insights into Oral Cancer—Risk Factors and Prevention: A Review of Literature. *Int. J. Prev. Med.* **2020**, *11*, 202. [CrossRef]
6. PDQ® Supportive and Palliative Care Editorial Board. *PDQ Oral Complications of Chemotherapy and Head/Neck Radiation*; National Cancer Institute: Bethesda, MD, USA, 2022. Available online: https://www.cancer.gov/about-cancer/treatment/side-effects/mouth-throat/oral-complications-hp-pdq (accessed on 30 July 2022).
7. Sroussi, H.Y.; Epstein, J.B.; Bensadoun, R.J.; Saunders, D.P.; Lalla, R.V.; Migliorati, C.A.; Heaivilin, N.; Zumsteg, Z.S. Common oral complications of head and neck cancer radiation therapy: Mucositis, infections, saliva change, fibrosis, sensory dysfunctions, dental caries, periodontal disease, and osteoradionecrosis. *Cancer Med.* **2017**, *6*, 2918–2931. [CrossRef]
8. Huebner, J.; Follmann, M. Complementary medicine in guidelines of the German Guideline Program in Oncology: Comparison of the evidence base between complementary and conventional therapy. *J. Cancer Res. Clin. Oncol.* **2013**, *139*, 1481–1488. [CrossRef]
9. Chong, W.Q.; Mogro, M.J.; Arsad, A.; Tai, B.C.; Lee, S.C. Use of decision aid to improve informed decision-making and communication with physicians on the use of oral complementary and alternative medicine (CAM) among cancer patients on chemotherapy treatment: A randomised controlled trial. *Support. Care Cancer* **2021**, *29*, 3689–3696. [CrossRef]
10. Eita, A.A.B. Milk thistle (*Silybum marianum* (L.)Gaertn.): An overview about its pharmacology and medicinal uses with an emphasis on oral diseases. *J. Oral Biosci.* **2022**, *64*, 71–76. [CrossRef]
11. da Silva, A.C.A.; Ramos, A.I.; Schirmer, E.M.; Massaroli, A.; Araújo, J.S.; da Conceição, V.M. Effect of Chamomilla Recutita in the oncology patient with oral mucositis: A systematic review. *Enferm. Glob.* **2021**, *20*, 640–652. [CrossRef]
12. Santos, H.T.C.; Coimbra, M.C.; Meri Junior, A.E.; Gomes, A.J.P.S. Effectiveness of topically applied chamomile in the treatment of oral mucositis: A literature review. *Res. Soc. Dev.* **2021**, *10*, e433101422081. [CrossRef]
13. Pawar, D.; Neve, R.S.; Kalgane, S.; Riva, A.; Bombardelli, E.; Ronchi, M.; Petrangolini, G.; Morazzoni, P. SAMITAL® improves chemo/radiotherapy-induced oral mucositis in patients with head and neck cancer: Results of a randomized, placebo-controlled, single-blind Phase II study. *Support. Care Cancer* **2013**, *21*, 827–834. [CrossRef]
14. Choi, M.J.; Yoo, H.S.; Park, S.J. The Effects of the Supercritical Extracts of *Momordica charantia* Linn., *Pistacia lentiscus*, and *Commiphora myrrha* on Oral Inflammation and Oral Cancer. *Sustainability* **2022**, *14*, 2458. [CrossRef]
15. de Souza, J.L.S.; Alves, T.; Camerini, L.; Nedel, F.; Campos, A.D.; Lund, R.G. Antimicrobial and cytotoxic capacity of pyroligneous extracts films of *Eucalyptus grandis* and chitosan for oral applications. *Sci. Rep.* **2021**, *11*, 21531. [CrossRef] [PubMed]
16. Di Prima, G.; Conigliaro, A.; De Caro, V. Mucoadhesive Polymeric Films to Enhance Barbaloin Penetration into Buccal Mucosa: A Novel Approach to Chemoprevention. *AAPS Pharm. Sci. Tech.* **2019**, *20*, 1–12. [CrossRef] [PubMed]
17. Nafee, N.A.; Ismail, F.A.; Boraie, N.A.; Mortada, L.M. Mucoadhesive buccal patches of miconazole nitrate: In vitro/in vivo performance and effect of ageing. *Int. J. Pharm.* **2003**, *264*, 1–14. [CrossRef]
18. Balaci, T.; Velescu, B.; Karampelas, O.; Musuc, A.M.; Nițulescu, G.M.; Ozon, E.A.; Nițulescu, G.; Gîrd, C.E.; Fița, C.; Lupuliasa, D. Physico-chemical and pharmaco-technical characterization of inclusion complexes formed by rutoside with β-cyclodextrin and hydroxypropyl-β-cyclodextrin used to develop solid dosage forms. *Processes* **2021**, *9*, 26. [CrossRef]
19. Musuc, A.M.; Anuta, V.; Atkinson, I.; Sarbu, I.; Popa, V.T.; Munteanu, C.; Mircioiu, C.; Ozon, E.A.; Nitulescu, G.M.; Mitu, M.A. Formulation of chewable tablets containing carbamazepine-β-cyclodextrin inclusion complex and f-melt disintegration excipient. The mathematical modeling of the release kinetics of carbamazepine. *Pharmaceutics* **2021**, *13*, 915. [CrossRef]
20. Perioli, L.; Ambrogi, V.; Angelici, F.; Ricci, M.; Giovagnoli, S.; Capuccella, M.; Rossi, C. Development of mucoadhesive patches for buccal administration of ibuprofen. *J. Control. Release* **2004**, *99*, 73–82. [CrossRef]

21. Don, T.M.; Huang, M.L.; Chiu, A.C.; Kuo, K.H.; Chiu, W.Y.; Chiu, L.H. Preparation of thermo-responsive acrylic hydrogels useful for the application in transdermal drug delivery systems. *Mater. Chem. Phys.* **2008**, *107*, 266–273. [CrossRef]
22. Derle, D.; Joshi, O.; Pawar, A.; Patel, J.; Perdeshi, V. Effect of tablet excipients on mucoadhesive properties of polyoxyethylene and Carbopol 971P. *Int. J. Pharm. Pharm. Sci.* **2009**, *1*, 198–205.
23. Gupta, A.; Garg, S.; Khar, R.K. Measurement of bioadhesive strength of mucoadhesive buccal tablets: Design of an in-vitro assembly. *Indian Drugs* **1993**, *30*, 1–6.
24. Fathi, F.; Ghobeh, M.; Tabarzad, M. Anti-Microbial Peptides: Strategies of Design and Development and Their Promising Wound-Healing Activities. *Mol. Biol. Rep.* **2022**, *8*, 1–12. [CrossRef]
25. Madushan, R.; Vidanarachchi, J.K.; Prasanna, P.H.P.; Werellagama, S.; Priyashantha, H. Use of natural plant extracts as a novel microbiological quality indicator in raw milk: An alternative for resazurin dye reduction method. *LWT* **2021**, *144*, 111221. [CrossRef]
26. Cox, K.D.; Quello, K.; Deford, R.J.; Beckerman, J.L. A rapid method to quantify fungicide sensitivity in the brown rot pathogen Monilinia fructicola. *Plant Dis.* **2009**, *93*, 328–331. [CrossRef]
27. Bitacura, J.G. The Use of Baker's Yeast in the Resazurin Reduction Test: A Simple, Low-Cost Method for Determining Cell Viability in Proliferation and Cytotoxicity Assays. *J. Microbiol. Biol. Educ.* **2018**, *19*, jmbe-19–87. [CrossRef]
28. Popovici, V.; Bucur, L.; Gîrd, C.E.; Rambu, D.; Calcan, S.I.; Cucolea, E.I.; Costache, T.; Ungureanu-Iuga, M.; Oroian, M.; Mironeasa, S.; et al. Antioxidant, Cytotoxic, and Rheological Properties of Canola Oil Extract of *Usnea barbata* (L.) Weber ex F.H. Wigg from Călimani Mountains, Romania. *Plants* **2022**, *11*, 854. [CrossRef]
29. Schröder, V.; Arcus, M.; Anghel, A.H.; Busuricu, F.; Lepadatu, A.C. Cell differentiation process of *Artemia* sp. larvae tools for natural products testing. *Anim. Sci.* **2019**, *62*, 149–153.
30. Popovici, V.; Bucur, L.; Gîrd, C.E.; Calcan, S.I.; Cucolea, E.I.; Costache, T.; Rambu, D.; Oroian, M.; Mironeasa, S.; Schröder, V.; et al. Advances in the Characterization of *Usnea barbata* (L.) Weber ex F.H. Wigg from Călimani Mountains, Romania. *Appl. Sci.* **2022**, *12*, 4234. [CrossRef]
31. Ionescu, C.; Aschie, M.; Matei, E.; Cozaru, G.-C.; Deacu, M.; Mitroi, A.F.; Baltatescu, G.I.; Nicolau, A.; Mazilu, L.; Tuta, L.A.; et al. Characterization of the Tumor Microenvironment and the Biological Processes with a Role in Prostatic Tumorigenesis. *Biomedicines* **2022**, *10*, 1672. [CrossRef]
32. Eguchi, N.; Kawabata, K.; Goto, H. Electrochemical Polymerization of 4,4-Dimethyl-2,2′-Bithiophene in Concentrated Polymer Liquid Crystal Solution. *J. Mater. Sci. Chem. Eng.* **2017**, *05*, 64–70. [CrossRef]
33. Askari, F.; Zandi, M.; Shokrolahi, P.; Tabatabaei, M.H.; Hajirasoliha, E. Reduction in protein absorption on ophthalmic lenses by PEGDA bulk modification of silicone acrylate-based formulation. *Prog. Biomater.* **2019**, *8*, 169–183. [CrossRef]
34. Ishii, N.; Mizobuchi, S.; Kawano, Y.; Hanawa, T. Preparation and evaluation of a powdered rebamipide mouthwash as in-hospital formulation: Considering dispersion before use in patients. *Pharmaceutics* **2021**, *13*, 1848. [CrossRef] [PubMed]
35. Popovici, V.; Matei, E.; Cozaru, G.-C.; Aschie, M.; Bucur, L.; Rambu, D.; Costache, T.; Cucolea, I.E.; Vochita, G.; Gherghel, D.; et al. Usnic acid and *Usnea barbata* (L.) F.H. wigg. dry extracts promote apoptosis and DNA damage in human blood cells through enhancing ROS levels. *Antioxidants* **2021**, *10*, 1171. [CrossRef] [PubMed]
36. Popovici, V.; Bucur, L.; Vochita, G.; Gherghel, D.; Mihai, C.T.; Rambu, D.; Calcan, S.I.; Costache, T.; Cucolea, I.E.; Matei, E.; et al. In vitro anticancer activity and oxidative stress biomarkers status determined by *Usnea barbata* (L.) f.h. wigg. dry extracts. *Antioxidants* **2021**, *10*, 1141. [CrossRef] [PubMed]
37. Spisák, S.; Solymosi, N.; Ittzés, P.; Bodor, A.; Kondor, D.; Vattay, G.; Barták, B.K.; Sipos, F.; Galamb, O.; Tulassay, Z.; et al. Complete Genes May Pass from Food to Human Blood. *PLoS ONE* **2013**, *8*, e69805. [CrossRef] [PubMed]
38. Popovici, V.; Bucur, L.; Calcan, S.I.; Cucolea, E.I.; Costache, T.; Rambu, D.; Schröder, V.; Gîrd, C.E.; Gherghel, D.; Vochita, G.; et al. Elemental Analysis and In Vitro Evaluation of Antibacterial and Antifungal Activities of *Usnea barbata* (L.) Weber ex F.H. Wigg from C ă limani Mountains, Romania. *Plants* **2022**, *11*, 32. [CrossRef]
39. Cazacu, B.C.; Buzgar, N.; Iancu, O.G. Geochemical and spatial distribution of heavy metals in forest soils adjacent to the Tinovul Mare Poiana Stampei peat bog. *Rev. Chim.* **2018**, *69*, 434–438. [CrossRef]
40. Culicov, O.A.; Yurukova, L. Comparison of element accumulation of different moss- and lichen-bags, exposed in the city of Sofia (Bulgaria). *J. Atmos. Chem.* **2006**, *55*, 1–12. [CrossRef]
41. Jayasekera, R.; Rossbach, M. Background levels of heavy metals in plants of different taxonomic groups from a montane rain forest in Sri Lanka. *Environ. Geochem. Health* **1996**, *18*, 55–62. [CrossRef]
42. Conti, M.E.; Finoia, M.G.; Bocca, B.; Mele, G.; Alimonti, A.; Pino, A. Atmospheric background trace elements deposition in Tierra del Fuego region (Patagonia, Argentina), using transplanted *Usnea barbata* lichens. *Environ. Monit. Assess.* **2012**, *184*, 527–538. [CrossRef]
43. World Health Organisation. *WHO Guidelines on Good Manufacturing Practices (GMP) for Herbal Medicines 2007*; IRIS (Institutional Repository for Information Sharing); World Health Organisation: Geneva, Switzerland, 2007; Available online: https://apps.who.int/iris/handle/10665/43672 (accessed on 20 May 2022).
44. Popovici, V.; Bucur, L.; Popescu, A.; Schröder, V.; Costache, T.; Rambu, D.; Cucolea, I.E.; Gîrd, C.E.; Caraiane, A.; Gherghel, D.; et al. Antioxidant and cytotoxic activities of *Usnea barbata* (L.) f.h. wigg. dry extracts in different solvents. *Plants* **2021**, *10*, 909. [CrossRef]

45. Popovici, V.; Bucur, L.; Popescu, A.; Caraiane, A.; Badea, V. Determination of the content in usnic acid and polyphenols from the extracts of *Usnea barbata* L. And the evaluation of their antioxidant activity. *Farmacia* **2018**, *66*, 337–341.
46. Popovici, V.; Bucur, L.; Costache, T.; Gherghel, D.; Vochita, G.; Mihai, C.T.; Rotinberg, P.; Schroder, V.; Badea, F.C.; Badea, V. Studies on Preparation and UHPLC Analysis of the *Usnea Barbata* (L) F.H.Wigg Dry acetone extract. *Rev. Chim.* **2019**, *70*, 3775–3777. [CrossRef]
47. Stoicescu, I.; Lupu, E.C.; Radu, M.D.; Popescu, A.; Mihai, S. High-Performance Liquid Chromatography–Diode Array Detection (HPLC-DAD) Method for the Determination of Phenolic Compounds of Water Chesnut (*Trapa natans* L.). *Anal. Lett.* **2022**, *55*, 2147–2159. [CrossRef]
48. Salgado, F.; Albornoz, L.; Cortéz, C.; Stashenko, E.; Urrea-Vallejo, K.; Nagles, E.; Galicia-Virviescas, C.; Cornejo, A.; Ardiles, A.; Simirgiotis, M.; et al. Secondary metabolite profiling of species of the genus *Usnea* by UHPLC-ESI-OT-MS-MS. *Molecules* **2018**, *23*, 54. [CrossRef] [PubMed]
49. Goga, M.; Elečko, J.; Marcinčinová, M.; Ručová, D.; Bačkorová, M.; Bačkor, M. Lichen Metabolites: An Overview of Some Secondary Metabolites and Their Biological Potential. In *Reference Series in Phytochemistry*; Springer Science and Business Media B.V.: Berlin, Germany, 2020; pp. 175–209.
50. Elečko, J.; Vilková, M.; Frenák, R.; Routray, D.; Ručová, D.; Bačkor, M.; Goga, M. A Comparative Study of Isolated Secondary Metabolites from Lichens and Their Antioxidative Properties. *Plants* **2022**, *11*, 1077. [CrossRef]
51. Popovici, V.; Bucur, L.; Gîrd, C.E.; Popescu, A.; Matei, E.; Caraiane, A.; Botnarciuc, M. Phenolic Secondary Metabolites and Antiradical and Antibacterial Activities of Different Extracts of *Usnea barbata* (L.) Weber ex F.H. Wigg from C ă limani Mountains, Romania. *Pharmaceuticals* **2022**, *15*, 829. [CrossRef]
52. Kumar, M.; Prakash, S.; Radha; Kumari, N.; Pundir, A.; Punia, S.; Saurabh, V.; Choudhary, P.; Changan, S.; Dhumal, S.; et al. Beneficial role of antioxidant secondary metabolites from medicinal plants in maintaining oral health. *Antioxidants* **2021**, *10*, 1061. [CrossRef]
53. Popovici, V.; Bucur, L.; Popescu, A.; Caraiane, A.; Badea, V. Evaluation of the Antibacterial Action of the *Usnea barbata* L. Extracts on *Streptococcus* Species from the Oro-Dental Cavity. In Proceedings of the 17th Romanian National Congress of Pharmacy, Bucharest, Romania, 26–29 September 2018.
54. Popovici, V.; Bucur, L.; Popescu, A.; Caraiane, A.; Badea, V. Comparative study regarding antibacterial action if the *Usnea barbata* L. extracts on Gram-positive bacteria from the oro-dental cavity. In Proceedings of the 5th SGEM International Multidisciplinary Scientific Conferences on Social Sciences and Arts, Albena, Bulgaria, 24 August–2 September 2018.
55. Bucur, L.; Badea, V. Comparative Study between Antioxidant Activity and Antibacterial Effect of *Usnea barbata* (L.) F.H. Wigg Extracts and Volatile Oils Marked in Romania. *Ovidius. Univ. Ann. Econ. Sci. Ser.* **2020**, *2*, 246–251.
56. Lykkesfeldt, J. Malondialdehyde as biomarker of oxidative damage to lipids caused by smoking. *Clin. Chim. Acta* **2007**, *380*, 50–58. [CrossRef]
57. Cherian, D.; Peter, T.; Narayanan, A.; Madhavan, S.; Achammada, S.; Vynat, G. Malondialdehyde as a marker of oxidative stress in periodontitis patients. *J. Pharm. Bioallied Sci.* **2019**, *11*, S297–S300. [CrossRef]
58. Patel, V.M.; Prajapati, B.G.; Patel, M.M. Effect of hydrophilic polymers on buccoadhesive Eudragit patches of propranolol hydrochloride using factorial design. *AAPS Pharm. Sci. Tech.* **2007**, *8*, 119–126. [CrossRef] [PubMed]
59. Diaz del Consuelo, I.; Falson, F.; Guy, R.H.; Jacques, Y. Ex vivo evaluation of bioadhesive films for buccal delivery of fentanyl. *J. Control. Release* **2007**, *122*, 135–140. [CrossRef] [PubMed]
60. Gavriloaia, M.R.; Budura, E.A.; Toma, C.C.; Mitu, M.A.; Karampelas, O.; Arama, C.; Lupuleasa, D. In vitro evaluation of diffusion and rheological profiles for dexamethasone inclusion complexes with β-cyclodextrin or hydroxypropyl β-cyclodextrin. *Farmacia* **2012**, *60*, 895–904.
61. Mănescu, O.; Lupuleasa, D.; Miron, D.S.; Budura, E.A.; Rădulescu, F.Ş. In vitro drug release from topical antifungal pharmaceutical formulations. *Farmacia* **2011**, *59*, 15–23.
62. Guo, R.; Du, X.; Zhang, R.; Deng, L.; Dong, A.; Zhang, J. Bioadhesive film formed from a novel organic-inorganic hybrid gel for transdermal drug delivery system. *Eur. J. Pharm. Biopharm.* **2011**, *79*, 574–583. [CrossRef]
63. Nesseem, D.I.; Eid, S.F.; El-Houseny, S.S. Development of novel transdermal self-adhesive films for tenoxicam, an anti-inflammatory drug. *Life Sci.* **2011**, *89*, 430–438. [CrossRef] [PubMed]
64. Hashemi, M.; Ramezani, V.; Seyedabadi, M.; Ranjbar, A.M.; Jafari, H.; Honarvar, M.; Fanaei, H. Formulation and optimization of oral mucoadhesive patches of *Myrtus communis* by box behnken design. *Adv. Pharm. Bull.* **2017**, *7*, 441–450. [CrossRef]
65. Karki, S.; Kim, H.; Na, S.J.; Shin, D.; Jo, K.; Lee, J. Thin films as an emerging platform for drug delivery. *Asian J. Pharm. Sci.* **2016**, *11*, 559–574. [CrossRef]
66. Nair, A.B.; Kumria, R.; Harsha, S.; Attimarad, M.; Al-Dhubiab, B.E.; Alhaider, I.A. In vitro techniques to evaluate buccal films. *J. Control. Release* **2013**, *166*, 10–21. [CrossRef]
67. Esim, Ö. Preparation and in vitro evaluation of methylene blue films for treatment of oral mucosal diseases. *Gulhane Med. J.* **2019**, *61*, 109–113. [CrossRef]
68. Cao, N.; Yang, X.; Fu, Y. Effects of various plasticizers on mechanical and water vapor barrier properties of gelatin films. *Food Hydrocoll.* **2009**, *23*, 729–735. [CrossRef]
69. Bharkatiya, M.; Nema, R.K.; Bhatnagar, M. Designing and Characterization of Drug Free Patches for Transdermal Application. *Int. J. Pharm. Sci. Drug Res.* **2010**, *2*, 35.

70. Shaikh, R.; Raj Singh, T.; Garland, M.; Woolfson, A.; Donnelly, R. Mucoadhesive drug delivery systems. *J. Pharm. Bioallied Sci.* **2011**, *3*, 89–100. [PubMed]
71. Tedesco, M.P.; Monaco-Lourenço, C.A.; Carvalho, R.A. Characterization of oral disintegrating film of peanut skin extract—Potential route for buccal delivery of phenolic compounds. *Int. J. Biol. Macromol.* **2017**, *97*, 418–425. [CrossRef]
72. Repka, M.A.; McGinity, J.W. Bioadhesive properties of hydroxypropylcellulose topical films produced by hot-melt extrusion. *J. Control. Release* **2001**, *70*, 341–351. [CrossRef]
73. Ravi Kumar Reddy, J.; Indira Muzib, Y.; Chowdary, K.P.R. Development and in-vivo characterization of novel trans buccal formulations of Amiloride hydrochloride. *J. Pharm. Res.* **2013**, *6*, 647–652. [CrossRef]
74. Pilicheva, B.; Uzunova, Y.; Marudova, M. Polyelectrolyte Multilayer Films as a Potential Buccal Platform for Drug Delivery. *Polymers* **2022**, *14*, 734. [CrossRef]
75. Panomsuk, S.P.; Hatanaka, T.; Aiba, T.; Katayama, K.; Koizumi, T. A study of the hydrophilic cellulose matrix: Effect of drugs on swelling properties. *Chem. Pharm. Bull.* **1996**, *44*, 1039–1042. [CrossRef]
76. Gayathri, D.; Jayakumari, L.S. Evaluation of commercial arrowroot starch/CMC film for buccal drug delivery of glipizide. *Polimeros* **2019**, *29*, e2019047. [CrossRef]
77. Waghulde, S.; Kale, M.K.; Patil, V. Brine Shrimp Lethality Assay of the Aqueous and Ethanolic Extracts of the Selected Species of Medicinal Plants. *Proceedings* **2019**, *41*, 47.
78. Theda, C.; Hwang, S.H.; Czajko, A.; Loke, Y.J.; Leong, P.; Craig, J.M. Quantitation of the cellular content of saliva and buccal swab samples. *Sci. Rep.* **2018**, *8*, 4–11. [CrossRef] [PubMed]
79. Christopher, A.; Sarkar, D.; Shetty, K. Elicitation of Stress-Induced Phenolic Metabolites for Antimicrobial Applications against Foodborne Human Bacterial Pathogens. *Antibiotics* **2021**, *10*, 109. [CrossRef] [PubMed]
80. Chi, A.C.; Day, T.A.; Neville, B.W. Oral cavity and oropharyngeal squamous cell carcinoma-an update. CA. *Cancer J. Clin.* **2015**, *65*, 401–421. [CrossRef] [PubMed]
81. Prakash, S.; Radha; Kumar, M.; Kumari, N.; Thakur, M.; Rathour, S.; Pundir, A.; Sharma, A.K.; Bangar, S.P.; Dhumal, S.; et al. Plant-based antioxidant extracts and compounds in the management of oral cancer. *Antioxidants* **2021**, *10*, 1358. [CrossRef] [PubMed]
82. Hamidi, R.M.; Jovanova, B.; Kadifkova Panovska, T. Toxicological evaluation of the plant products using Brine Shrimp (*Artemia salina* L.) model. *Maced. Pharm. Bull.* **2014**, *60*, 9–18. [CrossRef]
83. Popovici, P.C.; Ancuceanu, V.R.; Olaru, T.O.; Stoicescu, C.-S.; Dinu, M. Toxicity Assessment of *Nephrolepis exaltata* (L.) Schott, Fam. Nephrolepidaceae. *Acta Biol. Marisiensis* **2018**, *1*, 27–36. [CrossRef]
84. Hovaneţ, M.V.; Ancuceanu, R.V.; Dinu, M.; Oprea, E.; Budura, E.A.; Negreş, S.; Velescu, B.Ş.; Duţu, L.E.; Anghel, I.A.; Ancu, I.; et al. Toxicity and anti-inflammatory activity of *Ziziphus jujuba* Mill. leaves. *Farmacia* **2016**, *64*, 802–808.
85. Iancu, I.M.; Bucur, L.A.; Schroder, V.; Mireșan, H.; Sebastian, M.; Iancu, V.; Badea, V. Phytochemical evaluation and cytotoxicity assay of *Lythri herba* extracts. *Farmacia* **2021**, *69*, 51–58. [CrossRef]
86. Nazir, S.; Ansari, F.L.; Hussain, T.; Mazhar, K.; Muazzam, A.G.; Qasmi, Z.U.H.; Makhmoor, T.; Noureen, H.; Mirza, B. Brine shrimp lethality assay 'an effective prescreen': Microwave-assisted synthesis, BSL toxicity and 3DQSAR studies-based designing, docking and antitumor evaluation of potent chalcones. *Pharm. Biol.* **2013**, *51*, 1091–1103. [CrossRef]
87. Arcanjo, D.; Albuquerque, A.; Melo-Neto, B.; Santana, L.; Medeiros, M.; Citó, A. Bioactivity evaluation against Artemia salina Leach of medicinal plants used in Brazilian Northeastern folk medicine. *Braz. J. Biol.* **2012**, *72*, 505–509. [CrossRef]
88. Redza-Dutordoir, M.; Averill-Bates, D.A. Interactions between reactive oxygen species and autophagy: Special issue: Death mechanisms in cellular homeostasis. *Biochim. Biophys. Actamol. Cell Res.* **2021**, *1868*, 119041. [CrossRef] [PubMed]
89. Kawanishi, S.; Ohnishi, S.; Ma, N.; Hiraku, Y.; Murata, M. Crosstalk between DNA damage and inflammation in the multiple steps of carcinogenesis. *Int. J. Mol. Sci.* **2017**, *18*, 1808. [CrossRef] [PubMed]
90. Kardeh, S.; Ashkani-Esfahani, S.; Alizadeh, A.M. Paradoxical action of reactive oxygen species in creation and therapy of cancer. *Eur. J. Pharmacol.* **2014**, *735*, 150–168. [CrossRef] [PubMed]
91. Redza-Dutordoir, M.; Averill-Bates, D.A. Activation of apoptosis signalling pathways by reactive oxygen species. *Biochim. Biophys. Actamol. Cell Res.* **2016**, *1863*, 2977–2992. [CrossRef] [PubMed]
92. Srinivas, U.S.; Tan, B.W.Q.; Vellayappan, B.A.; Jeyasekharan, A.D. ROS and the DNA damage response in cancer. *Redox Biol.* **2019**, *25*, 101084. [CrossRef] [PubMed]
93. Dos Santos, Á.; Cook, A.W.; Gough, R.E.; Schilling, M.; Olszok, N.A.; Brown, I.; Wang, L.; Aaron, J.; Martin-Fernandez, M.L.; Rehfeldt, F.; et al. DNA damage alters nuclear mechanics through chromatin reorganization. *Nucleic Acids Res.* **2021**, *49*, 340–353. [CrossRef]
94. Shah, M.A.; Rogoff, H.A. Implications of reactive oxygen species on cancer formation and its treatment. *Semin. Oncol.* **2021**, *48*, 238–245. [CrossRef]
95. Zaidieh, T.; Smith, J.R.; Ball, K.E.; An, Q. ROS as a novel indicator to predict anticancer drug efficacy. *BMC Cancer* **2019**, *19*, 1224. [CrossRef]
96. Păduraru, D.N.; Coman, F.; Ozon, E.A.; Gherghiceanu, F.; Andronic, O.; Ion, D.; Stănescu, M.; Bolocan, A. The use of nutritional supplement in romanian patients–attitudes and beliefs. *Farmacia* **2019**, *67*, 1060–1065. [CrossRef]
97. Favreau, J.T.; Ryu, M.L.; Braunstein, G.; Orshansky, G.; Park, S.S.; Coody, G.L.; Love, L.A.; Fong, T.L. Severe hepatotoxicity associated with the dietary supplement LipoKinetix. *Ann. Intern. Med.* **2002**, *136*, 590–595. [CrossRef]

98. Sanchez, W.; Maple, J.T.; Burgart, L.J.; Kamath, P.S. Severe hepatotoxicity associated with use of a dietary supplement containing usnic acid. *Mayo Clin. Proc.* **2006**, *81*, 541–544. [CrossRef] [PubMed]
99. Guo, L.; Shi, Q.; Fang, J.L.; Mei, N.; Ali, A.A.; Lewis, S.M.; Leakey, J.E.A.; Frankos, V.H. Review of usnic acid and *Usnea barbata* toxicity. *J. Environ. Sci. Healpart C Environ. Carcinog. Ecotoxicol. Rev.* **2008**, *26*, 317–338.

antioxidants

MDPI

Article

Evaluation of *Usnea barbata* (L.) Weber ex F.H. Wigg Extract in Canola Oil Loaded in Bioadhesive Oral Films for Potential Applications in Oral Cavity Infections and Malignancy

Violeta Popovici [1,†], Elena Matei [2,*], Georgeta Camelia Cozaru [2,3,†], Laura Bucur [4,†], Cerasela Elena Gîrd [5,†], Verginica Schröder [6,*], Emma Adriana Ozon [7,*], Oana Karampelas [7,*], Adina Magdalena Musuc [8,*], Irina Atkinson [8], Adriana Rusu [8], Simona Petrescu [8], Raul-Augustin Mitran [8], Mihai Anastasescu [8], Aureliana Caraiane [9], Dumitru Lupuliasa [7,‡], Mariana Aschie [2,3,‡] and Victoria Badea [1,‡]

[1] Department of Microbiology and Immunology, Faculty of Dental Medicine, Ovidius University of Constanta, 7 Ilarie Voronca Street, 900684 Constanta, Romania
[2] Center for Research and Development of the Morphological and Genetic Studies of Malignant Pathology, Ovidius University of Constanta, CEDMOG, 145 Tomis Blvd., 900591 Constanta, Romania
[3] Clinical Service of Pathology, Sf. Apostol Andrei Emergency County Hospital, 145 Tomis Blvd., 900591 Constanta, Romania
[4] Department of Pharmacognosy, Faculty of Pharmacy, Ovidius University of Constanta, 6 Capitan Al. Serbanescu Street, 900001 Constanta, Romania
[5] Department of Pharmacognosy, Phytochemistry, and Phytotherapy, Faculty of Pharmacy, Carol Davila University of Medicine and Pharmacy, 6 Traian Vuia Street, 020956 Bucharest, Romania
[6] Department of Cellular and Molecular Biology, Faculty of Pharmacy, Ovidius University of Constanta, 6 Capitan Al. Serbanescu Street, 900001 Constanta, Romania
[7] Department of Pharmaceutical Technology and Biopharmacy, Faculty of Pharmacy, Carol Davila University of Medicine and Pharmacy, 6 Traian Vuia Street, 020956 Bucharest, Romania
[8] "Ilie Murgulescu" Institute of Physical Chemistry, Romanian Academy, 202 Spl. Independentei, 060021 Bucharest, Romania
[9] Department of Oral Rehabilitation, Faculty of Dental Medicine, Ovidius University of Constanta, 7 Ilarie Voronca Street, 900684 Constanta, Romania
* Correspondence: sogorescuelena@gmail.com (E.M.); verginica.schroder@univ-ovidius.ro (V.S.); emma.budura@umfcd.ro (E.A.O.); oana.karampelas@umfcd.ro (O.K.); amusuc@icf.ro (A.M.M.)
† These authors contributed equally to this work.
‡ These authors contributed equally to this work.

check for updates

Citation: Popovici, V.; Matei, E.; Cozaru, G.C.; Bucur, L.; Gîrd, C.E.; Schröder, V.; Ozon, E.A.; Karampelas, O.; Musuc, A.M.; Atkinson, I.; et al. Evaluation of *Usnea barbata* (L.) Weber ex F.H. Wigg Extract in Canola Oil Loaded in Bioadhesive Oral Films for Potential Applications in Oral Cavity Infections and Malignancy. *Antioxidants* **2022**, *11*, 1601. https://doi.org/10.3390/antiox11081601

Academic Editors: Christof E Dörfer, Mohamed Mekhemar and Manoj Kumar

Received: 21 July 2022
Accepted: 17 August 2022
Published: 19 August 2022

Abstract: *Usnea* lichens are known for their beneficial pharmacological effects with potential applications in oral medicine. This study aims to investigate the extract of *Usnea barbata* (L.) Weber ex F.H. Wigg from the Călimani Mountains in canola oil as an oral pharmaceutical formulation. In the present work, bioadhesive oral films (F-UBO) with *U. barbata* extract in canola oil (UBO) were formulated, characterized, and evaluated, evidencing their pharmacological potential. The UBO-loaded films were analyzed using standard methods regarding physicochemical and pharmacotechnical characteristics to verify their suitability for topical administration on the oral mucosa. F-UBO suitability confirmation allowed for the investigation of antimicrobial and anticancer potential. The antimicrobial properties against *Staphylococcus aureus* ATCC 25923, *Pseudomonas aeruginosa* ATCC 27353, *Candida albicans* ATCC 10231, and *Candida parapsilosis* ATCC 22019 were evaluated by a resazurin-based 96-well plate microdilution method. The brine shrimp lethality assay (BSL assay) was the animal model cytotoxicity prescreen, followed by flow cytometry analyses on normal blood cells and oral epithelial squamous cell carcinoma CLS-354 cell line, determining cellular apoptosis, caspase-3/7 activity, nuclear condensation and lysosomal activity, oxidative stress, cell cycle, and cell proliferation. The results indicate that a UBO-loaded bioadhesive film's weight is 63 ± 1.79 mg. It contains 315 μg UBO, has a pH = 6.97 ± 0.01, a disintegration time of 124 ± 3.67 s, and a bioadhesion time of 86 ± 4.12 min, being suitable for topical administration on the oral mucosa. F-UBO showed moderate dose-dependent inhibitory effects on the growth of both bacterial and fungal strains. Moreover, in CLS-354 tumor cells, F-UBO increased oxidative stress, diminished DNA synthesis, and induced cell cycle arrest in G0/G1. All these properties led to considering UBO-loaded bioadhesive oral films as a suitable phytotherapeutic formulation with potential application in oral infections and neoplasia.

Keywords: *Usnea barbata* (L.) Weber ex F.H. Wigg; canola oil; bioadhesive oral films; poloxamer 407; antimicrobial activity; *Artemia salina*; blood cells; CLS-354 tumor cell line; anticancer activity

1. Introduction

Plants have been used in various disease therapies since ancient times; numerous individual cultures use specific plants for medicinal purposes. Traditional medicine—according to the World Health Organization (WHO)—is a sum of knowledge, skills, and practices based on beliefs, theories, and experiences indigenous to different cultures, used for maintaining health and involved in physical and mental illness diagnosis, treatment, amelioration, and prevention [1]. In their study [2], Davidson and Frank pointed out the significant differences between the most common terms belonging to this domain. Therefore, the medicinal use of numerous plants has been named plant medicine, while phytomedicine defines the current application of plant-based medicine. Phytopharmaceuticals are plant-based standardized extracts manufactured by authorized pharmaceutical producers [2]. In Europe, phytomedicine represents a part of the mainstream medical practice, and in hospitals, it is used primarily as adjuvant therapy. In addition, numerous general practitioners prescribe phytopharmaceuticals, and most of these prescriptions are supported by the public health insurance system in various European countries [2].

As medicinal plants, lichens are a promising source of antibiotic and anticancer drugs [3]. Auerbach's Wilderness Medicine Seventh Edition (2017) [2] includes the lichens from the genus *Usnea* (*Parmeliaceae*) in the North American Plant Medicines with therapeutical applications. *Usnea* sp. (old man's beard) has been used since ancient times, having a broad use across many cultures throughout the world: as an antiseptic (Argentina), eupeptic (Italy), wound healer (Canary Islands), antibacterial (Saudi Arabia), and antitumor agent (Chile) [2,4]. In Europe, *Usnea* lichens have been commonly used as a topical medication due to usnic acid's antibacterial, anti-inflammatory, and analgesic properties [5]. In addition to inhibitory effects on Gram-positive and Gram-negative bacteria, usnic acid has been shown to have other valuable activities (antiviral, antiprotozoal, and antiproliferative) consistent with its traditional use [6]. Soft and wispy *Usnea* sp. can be applied directly to the affected area and held in place by whatever means; dried lichen may be powdered and sprinkled directly on wounds, affording antimicrobial wound protection [2].

Usnic acid is the most studied lichen secondary metabolite and one of the few commercially available until recently. It was used as a dietary supplement for weight loss and associated with liver failure [7] and contact dermatitis [8,9]. For this reason, the current use is topical, including many different salves and creams with antimicrobial and anti-inflammatory action [10] and lozenges for oral cavity inflammation [2].

A recent literature review [11] also reported that studies on *Usnea* sp. bioactivities are limited compared to studies on its significant metabolite, usnic acid. The toxicity data examined by Sepahvand et al. (2021) evidenced that the use of pure usnic acid, mainly (−) enantiomer, is associated with the hepatotoxic effect. However, in most *Usnea* sp., usnic acid is identified as (+) enantiomer and based on their information, the extracts of *Usnea* sp. can be considered safer products [11].

In their study, Prateeksha et al. proved that *Usnea* lichens have valuable pharmacological potential and evidenced them as a potent phytomedicine [12]. Numerous studies investigated *Usnea* sp. extracts and displayed their antioxidant [13–15], antimicrobial [16–18], and anticancer effects [19–21]. Most authors have used chemical solvents for the preparation of these lichen extracts: ethanol, methanol, acetone, ethyl acetate, dimethyl ether, CCl_4, hexane, and CO_2 supercritical [22–24]. We propose to explore the properties of *U. barbata* extract in a green solvent—canola oil [25,26].

A recently published article [27] reported an oral product formulated as compressed tablets based on plant extracts/essential oils containing *U. barbata* supercritical CO_2 extract. This work investigates a different pharmaceutical formulation using *U. barbata* extract in canola oil, with potential application in oral medicine.

An interesting aspect for dental professionals is the presence of poloxamer 407 (P407) as an emulsifier for oil extract. Poloxamer 407 is a nonionic surfactant used in mouthwashes and toothpaste belonging to the most known brands: Listerine (Johnson & Johnson Healthcare Products Division of McNEIL-PPC, Inc., Fort Washington, PA, USA) and Colgate (Colgate-Palmolive Company, New York, NY, USA) [28] and other cosmetic products. P407 bioactivities were examined in our work, this compound being selected as a positive control for all performed studies.

The present study aimed to formulate and develop bioadhesive oral films loaded with canola oil extract of *U. barbata* (L.) F. H. Wigg and evaluate their antibacterial and antifungal properties. It also explored the F-UBO cytotoxicity on an animal model and in vitro anticancer activity.

2. Materials and Methods

2.1. Materials

This study's chemicals, reagents, and standards were of analytical grade. Usnic acid standard 98.1% purity, propidium iodide (PI) 1.0 mg/mL, dimethyl sulfoxide (DMSO), Poly (ethylene glycol)-block-poly (propylene glycol)-block-poly (ethylene glycol) (poloxamer 407), polyethylene glycol 400 (PEG 400), and hydroxypropyl methylcellulose (HPMC) and antibiotics mix solution—100 µL/mL with 10 mg streptomycin, 10,000 U penicillin, 25 µg amphotericin B per 1 mL—were provided by Sigma-Aldrich Chemie GmbH (Taufkirchen, Germany). Annexin V Apoptosis Detection Kit and flow cytometry staining buffer (FCB) were purchased from eBioscience™ (Frankfurt am Main, Germany) and RNase A 4 mg/mL from Promega Corporation (Madison, WI, USA). Magic Red® Caspase-3/7 Assay Kit, Reactive Oxygen Species (ROS) Detection Assay Kit, and EdU i-Fluor 488 Kit were supplied by Abcam (Cambridge, UK).

The OSCC cell line (CLS-354) growing culture and the culture medium—Dulbecco's Modified Eagle's Medium (DMEM) high glucose with 10% FBS, basic supplemented with 4.5 g/L glucose, 2 mM L-glutamine, and 10% fetal bovine serum (FBS)—were provided by CLS Cell Lines Service GmbH (Eppelheim, Germany). Trypsin-ethylenediamine tetra acetic acid (Trypsin EDTA) and the media for blood cells—Dulbecco's phosphate-buffered saline with $MgCl_2$ and $CaCl_2$, fetal bovine serum (FBS) and L-glutamine (200 mM) solution—were purchased from Gibco™ Inc. (Billings, MT, USA).

The blood samples were collected from a non-smoker healthy donor (B Rh+ blood type), according to Ovidius University of Constanta Ethical approval code 7080/10.06.2021 and Donor Consent code 39/30.06.2021.

U. barbata lichen was harvested in March 2021 from the branches of conifers in the forest localized in the Călimani Mountains (47°29′ N, 25°12′ E, and 900 m altitude). It was identified by the Department of Pharmaceutical Botany of the Faculty of Pharmacy, Ovidius University of Constanta, using standard methods. A voucher specimen is maintained in the Herbarium of Pharmacognosy Department, Faculty of Pharmacy, Ovidius University of Constanta (Popovici 3/2021, Ph-UOC). The canola seed oil for oil extract preparation was provided by TAF PRESSOIL SRL, Cluj, Romania.

Artemia salina eggs and Artemia salt (Dohse Aquaristik GmbH & Co., Gelsdorf, Germany) were purchased online from https://www.aquaristikshop.com/ (accessed on 5 May 2022).

The microbial cell lines (*S. aureus* ATCC 25923, *P. aeruginosa* ATCC 27353, *C. albicans* ATCC 10231, and *C. parapsilosis* ATCC 22019) were obtained from the Microbiology Department, S.C. Synevo Romania SRL, Constanta Laboratory, in partnership agreement No 1060/25.01.2018 with the Faculty of Pharmacy, Ovidius University of Constanta. Culture medium Mueller-Hinton agar (MHA) was supplied by Thermo Fisher Scientific, GmbH, Dreieich, Germany; RPMI 1640 medium and resazurin solution (from In Vitro Toxicology Assay Kit, TOX8-1KT, resazurin-based) were purchased from Sigma-Aldrich Chemie GmbH (Taufkirchen, Germany).

2.2. Formulation and Preparation of the UBO-Loaded Bioadhesive Oral Films

The *U. barbata* extract in canola oil (UBO) was obtained using a method adapted from that described by Basiouni et al. [29], from 20.2235 g dried and ground lichen and 500 mL cold-pressed canola seed oil [26] in darkness, at room temperature (21–22 °C). The container with both components was shaken daily for three months; then, UBO was filtered in another brown vessel with a sealed plug and preserved in a plant room, sheltered from sun rays. Both oil samples had a pH of 4.

For the development of the bioadhesive oral films containing *U. barbata* extract in canola oil (F-UBO), HPMC K100 (with a viscosity of 100 mPa) was selected as the film-forming polymer. It displays excellent hydrophilicity, water-absorbing ability, good biocompatibility, and biodegradability [30–32]. PEG 400 was included in the films' formulations as an external plasticizer for its high hydrophilic character and non-toxicity [33].

The non-ionic surfactant poloxamer 407 (P407) was chosen for emulsifying the oily phase to ensure the uniform incorporation of UBO in the polymer matrix.

Bioadhesive films, containing suitable excipients but no active ingredient load, were prepared and used as a reference (R) to prove the UBO activity and influence on the F-UBO pharmaceutical characteristics.

The formulation of the developed F-UBO is presented in Table 1.

Table 1. UBO-loaded bioadhesive oral film (F-UBO) vs. reference (R).

Ingredients	F-UBO	R
UBO	12.50	-
P407	5.00	5.00
PEG 400	5.00	5.00
HPMC 15% water dispersion (w/w)	77.8	90.00

R—reference (a film without UBO); F-UBO—UBO-loaded bioadhesive oral film; UBO—*U. barbata* extract in canola oil; PEG—polyethylene glycol; HPMC—hydroxypropyl methylcellulose; P407—poloxamer 407.

The UBO amount was selected according to the emulsifying ability of the poloxamer 407 (P407) and film-forming polymer. HPMC was weighed using a Mettler Toledo AT261 balance (Marshall Scientific, Hampton, NH, USA) with 0.01 mg sensitivity for the polymeric matrix system. Then, it was dispersed in water by stirring at 700 rpm and room temperature, using an MR 3001K magnetic stirrer (Heidolph Instruments GmbH & Co. K.G., Schwabach, Germany) and mixed with PEG 400. P407 was dissolved in the matrix, and UBO was included under continuous stirring for 1 h.

References (R) were realized by mixing P407 with the base system, and the formed gels were left overnight at room temperature for deaeration. The viscous dispersions were poured in a thin layer into Petri glass plates and dried in ambient conditions for 24 h. Finally, the dried films were peeled off the plate surface and cut into 1.5 × 2 cm patches.

The manufacturing process led to defining the concentration of UBO in the film formulation: F-UBO encloses 315 µg UBO.

2.3. Physico-Chemical Analysis of Bioadhesive Oral Films

2.3.1. SEM Analysis

A scanning electron microscope (SEM) in a high-resolution Quanta3D FEG (Thermo Fisher Scientific, GmbH, Dreieich, Germany) was used to investigate the bioadhesive oral film morphology.

2.3.2. Atomic Force Microscopy (AFM)

The bioadhesive oral film's morphology was obtained via atomic force microscopy (AFM). The AFM measurements were registered with an AFM XE-100 (Park Systems Corporate, Suwon, Korea) assisted with flexure-guided, crosstalk eliminated scanners in non-contact mode to minimize the tip–sample interaction. AFM images were registered with sharp tips (PPP-NCLR, from NANOSENSORS™, Neuchatel, Switzerland) having the following characteristics: less than 10 nm radius of curvature, 225 mm mean length, 38 mm mean width, ~48 N/m force constant, and a resonance frequency of 190 kHz. An XEI program (v 1.8.0—Park Systems Corporate, Suwon, Korea) was carried out to process the AFM images and to evaluate the roughness. The surface profile of the scanned samples (the dimensions of the selected particles indicated with red arrows along the selected line) shows the representative line scans presented below the AFM images in the so-called "enhanced contrast" mode.

2.3.3. FTIR Analysis

The infrared spectra of the materials (obtained as bioadhesive films) were registered using FTIR equipment (Nicolet Spectrometer 6700 FTIR from Thermo Electron Corporation, Waltham, MA, USA) assisted with a diamond-crystal ATR accessory. In transmittance mode, data were acquired in the spectral range of 400–4000 cm^{-1} (resolution of 4 cm^{-1} and a total of 32 scans per spectrum).

2.3.4. X-ray Diffraction Patterns

A Rigaku Ultima IV diffractometer (Rigaku Corporation, Tokyo, Japan) in parallel beam geometry was used to investigate the X-ray diffraction (XRD) patterns of bioadhesive films. A step size of 0.02 and a 2° (2θ)/min speed over 10–80° were used. The source of the X-rays was a CuKα tube (λ = 1.54056 Å) operating at 40 kV and 30 mA.

2.3.5. Thermogravimetric Analysis

The thermal investigations were conducted on a Mettler Toledo TGA/SDTA851e thermogravimetric analyzer (Mettler-Toledo GmbH, Greifensee, Switzerland). The non-isothermal measurements were performed in the 25–600 °C temperature range, under 80 mL min^{-1} synthetic air atmosphere at a constant heating rate of 10 °C min^{-1}.

2.4. Pharmacotechnical Analysis of Bioadhesive Oral Films

2.4.1. Weight Uniformity

The weight uniformity was evaluated on 20 bioadhesive oral films of each formulation (F-UBO and R). They were individually weighed, and the average weight was determined.

2.4.2. Thickness

This parameter was also measured on 20 bioadhesive films of each type (F-UBO and R) using a Yato digital micrometer (Yato China Trading Co., Ltd., Shanghai, China) with a measuring range of 0–25 mm and a resolution of 0.001 mm. Then, the mean value was calculated.

2.4.3. Folding Endurance

The bioadhesive films were repeatedly folded and rolled until they broke, or up to 300 times [5]. The folding times were registered and expressed as folding endurance values.

2.4.4. Tensile Strength and Elongation Ability

The film's tensile strength and elongation ability were determined using an L.R. 10K Plus digital tensile force tester for universal materials (Lloyd Instruments Ltd., West Sussex, United Kingdom). The analysis was performed from a 30 mm distance with a speed of 30 mm/min. Therefore, each film was placed in a vertical position between the two braces, and the breakage force was registered. The measurements were achieved in triplicate.

The following equations (Equations (1) and (2)) were used to calculate the tensile strength and the elongation at break:

$$\text{Tensile strength}\left(\text{kg}/\text{mm}^2\right) = \frac{\text{Force at breakage (kg)}}{\text{Film thickness (mm)} - \text{Film width (mm)}} \quad (1)$$

$$\text{Elongation \%} = \frac{\text{Increase in film length}}{\text{Initial film length}} \times 100 \quad (2)$$

2.4.5. Moisture Content

The moisture content was assessed as the loss on drying by the thermogravimetric method using an H.R. 73 halogen humidity analyzer (Mettler-Toledo GmbH, Greifensee, Switzerland) [6]. Five bioadhesive oral films of each formulation (F-UBO and R) were analyzed for moisture content determination.

2.4.6. Surface pH

Five films of each formulation (F-UBO and R) were moistened with 1 mL of distilled water (pH 6.5 ± 0.5) for 5 min at room temperature. Then, the pH value was measured with the CONSORT P601 pH-meter (Consort bvba, Turnhout, Belgium).

2.4.7. In Vitro Disintegration Time

The time required to disintegrate the F-UBO and R bioadhesive oral films, with no residual mass completely, was measured in simulated saliva phosphate buffer pH of 6.8 at 37 ± 2 °C, using an Erweka DT 3 apparatus (Erweka® GmbH, Langen, Germany) [34].

2.4.8. Swelling Rate

Six films of each formulation (F-UBO and R) were placed on 1.5% agar gel in Petri plates and incubated at 37 ± 1 °C. Every 30 min, for 6 h, the patches were weighed. The swelling rate was calculated according to Equation (3):

$$\text{Swelling rate} = \frac{\text{Wt} - \text{Wi}}{\text{Wi}} \times 100 \quad (3)$$

where w_t is the patch weight at time t after the incubation and w_i is the initial weight [35–38].

2.4.9. Ex Vivo Bioadhesion Time

The bioadhesion time [39] was measured through the method described by Gupta et al. [40] on a detached porcine buccal mucosa by removing the fat layer and any residual tissue. The buccal mucosa was washed with distilled water and a phosphate buffer (pH 6.8) at 37 °C and fixed on a glass plate. Each bioadhesive film was hydrated in the center with 15 µL phosphate buffer and brought on the mucosa surface by pressing it for 30 s. The glass plate was placed in 200 mL phosphate buffer pH 6.8 and maintained at 37 °C for 2 min. The suitable simulation of the oral cavity conditions was ensured using a paddle with a stirring rate of 28 rpm. Then, the necessary time for the entire film's erosion or detachment from the buccal mucosa surface was recorded [41]. This registered time represents the film's residence time [42] on the oral mucosa, known as a bioadhesion time [43]. This test was realized in triplicate.

2.5. F-UBO Antimicrobial Activity Evaluation by Resazurin-Based 96-Well Plate Microdilution Method

2.5.1. Inoculum Preparation

The bacterial inoculum was prepared by the direct colony suspension method [44]. Thus, bacterial colonies selected from a 24 h agar plate were suspended in M.H.A. medium, according to the 0.5 McFarland standard, measured at Densimat Densitometer (Biomerieux, Marcy-l'Étoile, France) with around 108 CFU/mL (CFU = colony-forming unit), The yeast inoculum was prepared using the same method, adjusting the RPMI 1640 with fungal colonies to the 1.0 McFarland standard, with 10^6 CFU/mL.

2.5.2. Samples and Standards

F-UBO was dissolved in 1 mL of diluted phosphate buffer. As standards, ceftriaxone (Cefort 1g Antibiotice SA, Iasi, Romania) solutions 30 mg/mL and 122 mg/mL in distilled water were used for bacteria. The Cefort powder was weighted at Partner Analytical balance (Fink & Partner GmbH, Goch, Germany) and dissolved in distilled water. Terbinafine solution 10.1 mg/mL (Rompharm Company SRL, Otopeni, Romania) was used as standard for *Candida* sp. As a positive control for antimicrobial activity evaluation, 5% P407 was selected, the emulsifier used for the UBO-loaded bioadhesive oral films formulation.

2.5.3. Microdilution Method

All successive steps were performed in an Aslair Vertical 700, laminar flow, microbiological protection cabinet (Asal Srl, Cernusco (MI), Italy). In four 96-well plates, we performed seven serial dilutions, adapting the protocol described by Fathi et al. [45].

All 96-well plates were incubated for 24 h at 37 °C for bacteria and 35 °C for yeasts in a My Temp mini Z763322 Digital Incubator (Benchmark Scientific Inc., Sayreville, NJ, USA).

2.5.4. Reading and Interpreting

After 24 h incubation, the plates were examined with a free eye to see the color differences between standard and samples [46]. The corresponding sample concentration activities were compared with the Standard antibiotic ones. For yeasts, the color chart of the resazurin dye reduction method was used [47,48].

2.6. Evaluation of UBO-Loaded Bioadhesive Oral Films Cytotoxicity on Animal Model

Aiming to evaluate the F-UBO cytotoxicity, we used *Artemia salina* as an animal model, adapting a previously described method [49].

F-UBO film was placed in a diluted buffer (1 mL) and incubated for 15 min at 37 °C, resulting in a homogenous dispersion.

2.6.1. Brine Shrimp Lethality Assay

The larvae were obtained from *A. salina* cysts through continuous light and aeration in a 0.35% saline solution at 20 °C. The brine shrimp larvae in the first stage (instar I) were introduced in 0.3% saline solution into experimental pots (with a volume of 1 mL) [26]. The analysis was compared to a blank (untreated nauplii) to obtain accurate results regarding the F-UBO cytotoxic effect. An amount of 5% P407 in water was a positive control. The nauplii have embryonic energy reserves as lipids, and they were not fed during the test, thus avoiding interference with the sample and positive control. Their evolution was analyzed after 24 h and 48 h, exploring the morphological changes induced by F-UBO and P407 [50,51].

2.6.2. Fluorescent Microscopy

The brine shrimp larvae were stained with 3% acridine orange (Merck Millipore, Burlington, MA, USA) for 5 min. The samples were subjected to drying for 15 min in darkness and placed on the microscope slides.

2.6.3. Data Processing

The microscopic images were realized using a VWR microscope VisiScope 300D (VWR International, Radnor, PA, USA) with a Visicam X3 camera (VWR International Radnor, PA, USA) at 40×, 100×, and 400× magnification. They were processed with VisiCam Image Analyzer 2.13.

Fluorescent microscopy images were achieved using an OPTIKA B-350 microscope (Ponteranica, BG, Italy) blue filter (λex = 450–490 nm; λem = 515–520 nm) and green filter (λex = 510–550 nm; λem = 590 nm). The FM images at 100× and 400× magnification were processed with Optikam Pro 3 Software (OPTIKA SRL, Ponteranica, BG, Italy).

All observations were performed in triplicate.

2.7. In Vitro Cytotoxicity of UBO-Loaded Bioadhesive Oral Films on Human Normal Blood Cells and CLS-354 Tumor Cells

2.7.1. Equipment

The present study platform for in vitro F-UBO cytotoxicity analysis was the Attune Acoustic focusing cytometer (Applied Biosystems, Bedford, MA, USA). Before cell analysis, the flow cytometer was first set by fluorescent beads—Attune performance tracking beads, labeling, and detection (Life Technologies, Europe BV, Bleiswijk, The Netherlands), with standard size (four intensity levels of beads population). The cell amount was established by counting cells below 1 µm [52]. Using forward scatter (FSC) and side scatter (SSC), more than 10,000 cells per sample for each analysis were gated.

2.7.2. Data Processing

Flow cytometry data were processed using Attune Cytometric Software v.1.2.5, Applied Biosystems, 2010 (Bedford, MA, USA).

2.7.3. Human Blood Cell Cultures

The blood samples were collected into heparin vacutainers, and the blood cell cultures were obtained according to a previously described method [53]. Then, the blood cells were treated with F-UBO and controls in Nunclon Vita Cell culture 6-well plates (Kisker Biotech GmbH & Co.KG, Steinfurt, Germany) and incubated in a Steri-Cycle™ i160 CO_2 Incubator (Thermo Fisher Scientific Inc., Waltham, MA, USA), at 37 °C, in 5% CO_2 for 24 h. All flow cytometry analyses were performed after this incubation time.

2.7.4. CLS-354 Cell Line

The human mouth squamous cell carcinoma cell line CLS-354 (CLS catalog number 300152) consists of epithelial cells established in vitro from the primary squamous carcinoma of a 51-year-old Caucasian male. The CLS-354 cells [54] were cultured in DMEM high glucose with 10% FBS, supplemented with antibiotic mix solution in humidity conditions of 5% CO_2 at 37 °C for 7 days. The cells were dissociated from the monolayer with trypsin–EDTA, centrifugated at 3000 rpm for 10 min in a Fisher Scientific GT1 centrifuge (Thermo Fisher Scientific Inc., Waltham, MA, USA), and distributed in Millicell™ 24-well cell culture microplates (Thermo Fisher Scientific Inc., Waltham, MA, USA). After treatment, they were incubated for 24 h in the same conditions. All the flow cytometry analyses were performed after this incubation period.

2.7.5. Samples and Control Solutions

F-UBOs were dissolved in the suitable culture media for both types of cells, with 1% DMSO. As positive controls, 5% P407 and usnic acid of 125 ug/mL in 1% DMSO were used, and as a negative control, 1% DMSO.

2.7.6. Annexin V-FITC Apoptosis Assay

The cells with annexin V-FITC and PI (20 µg/mL) were incubated in darkness, for 30 min, at room temperature [53]. Then, the viable, early apoptotic, late apoptotic, and necrotic cells were examined at a flow cytometer using a 488 nm excitation, green emission for annexin V-FITC (BL1 channel), and orange emission for PI (BL2 channel).

2.7.7. Evaluation of Caspase-3/7 Activity

The cells were well-mixed with Magic Red® Caspase-3/7 substrate solution and PI and incubated [53]. Then, the early stages of cell apoptosis by activating caspases-3/7

(DEVD-ases [55]) were analyzed through flow cytometry using a 488 nm excitation, red emission for MR-$(DEVD)_2$ (BL3 channel), and orange emission for PI (BL2 channel).

2.7.8. Evaluation of Nuclear Condensation and Lysosomal Activity

The cells were stained successively with Hoechst 33,342 and AO and incubated for 30 min at room temperature in darkness [53]. Then, they were examined at the flow cytometer, using UV excitation and blue emission for Hoechst 33,342 (VL2) at 488 nm and green emission for acridine orange (BL1 channel).

2.7.9. Cell Cycle Analysis

The cells with PI (20 µg/mL) and RNase A (30 µg/mL) were incubated at room temperature, into darkness, for 30 min [53]. Next, the cell cycle distribution was detected by flow cytometry, using a 488 nm excitation and orange emission for PI (BL2 channel) [56].

2.7.10. Evaluation of Total ROS Activity

ROS Assay Stain solution was well-mixed with cell cultures and incubated at 37 °C for 60 min [53]. Then, the cells were analyzed by flow cytometry, using a 488 nm excitation and green emission for ROS (BL1 channel).

2.7.11. Evaluation of Cell Proliferation

The cell cultures were incubated for 2 h with 50 µM EdU (500 µL) at 37 °C. Following a succession of previously described steps [53], they were prepared for flow cytometry examination at a 488 nm excitation and green emission for EdU-iFluor 488 (BL1).

2.8. Data Analysis

All analyses were effectuated in triplicate, and the data were registered as means values ± standard deviation (SD). The results are expressed as percent (%) in the case of cell apoptosis, caspase-3/7 activity, nuclear condensation, autophagy, cell cycle arrest, and DNA synthesis, and count ($\times 10^4$) for ROS levels. Data analysis was realized with SPSS v. 23 software, IBM, 2015. Paired *t*-test established the differences between F-UBO and controls, and $p < 0.05$ was considered statistically significant. The principal component analysis was performed with XLSTAT 2022.2.1. by Addinsoft (New York, NY, USA) and examined the correlations between variable parameters.

3. Results

3.1. Organoleptic Characteristics of Bioadhesive Oral Films

The organoleptic characteristics of the F-UBO and R films depend highly on the active ingredient state. Both bioadhesive films (R and F-UBO) are white, with the typical appearance of emulsified systems (Figure 1a,b). The films withstand normal handling and cutting processes without air bubbles, cracks, or imperfections. All formulations lead to homogenous, thin, and easy-to-peel bioadhesive oral films, with a uniform, smooth, and glossy surface (Figure 1a,b).

3.2. Physico-Chemical Characterization of Bioadhesive Oral Films

3.2.1. Morphology

Scanning electron microscopy (SEM) was performed to study the morphology of the bioadhesive films (Figure 1c,d). SEM image of R (Figure 1c) shows a denser surface containing few cavities and small spherically shaped protrusions. The F-UBO surface observed by SEM analysis (Figure 1d) is rough with deeper and interconnected pores compared to R.

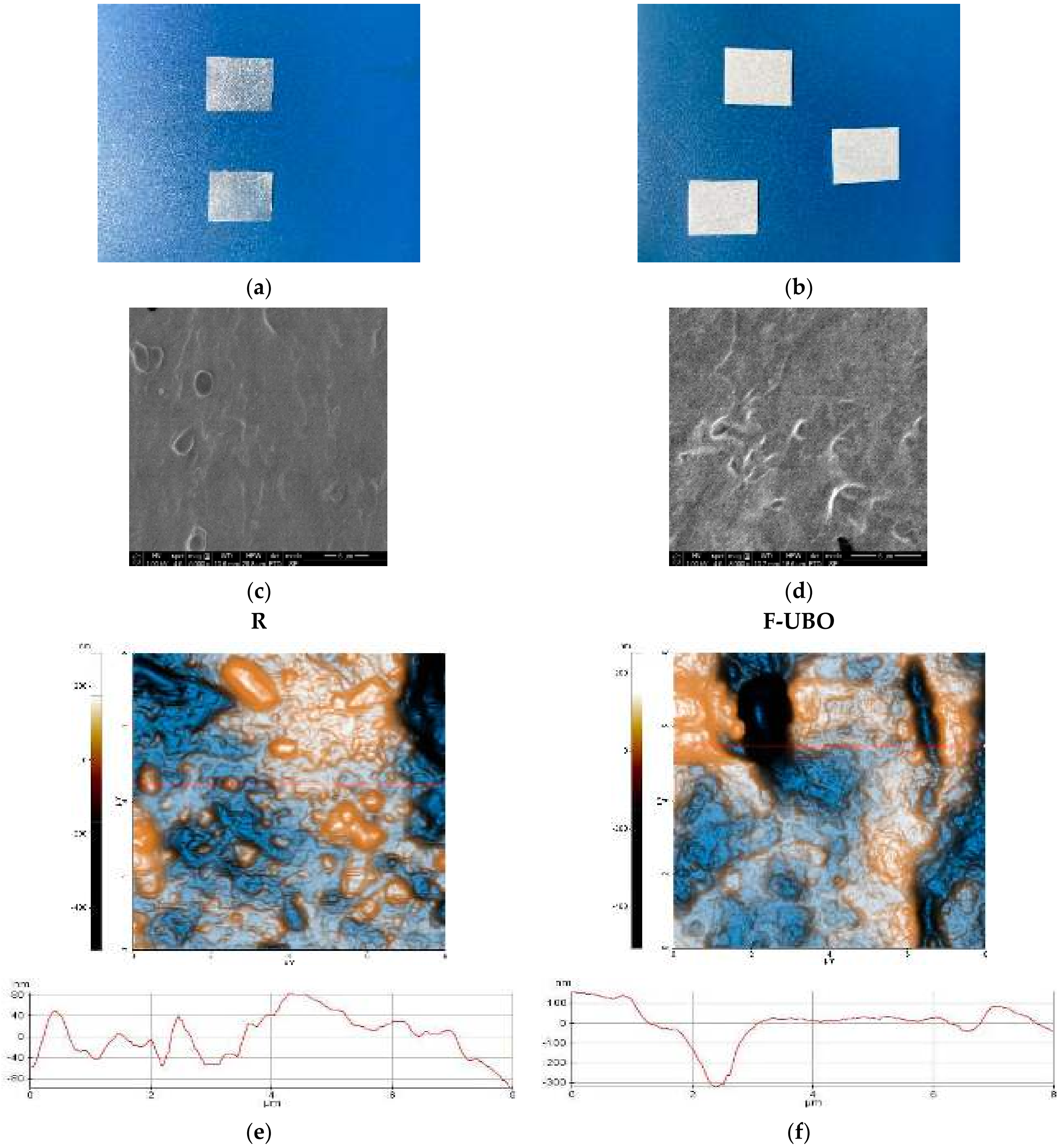
(**a**) (**b**)

(**c**) (**d**)

R **F-UBO**

(**e**) (**f**)

Figure 1. Bioadhesive oral films aspect (**a**,**b**): reference (**a**) and F-UBO (**b**). SEM images (**c**,**d**) of bioadhesive oral films: R (**c**) and F-UBO (**d**). The 2D-AFM images (**e**,**f**) of bioadhesive oral films in "enhanced contrast view" mode, at the scale of (8 × 8) μm^2, together with representative line scans for R (**e**) and F-UBO (**f**). R—reference (a film without UBO); F-UBO—UBO-loaded bioadhesive oral film; UBO—*U. barbata* extract in canola oil.

3.2.2. Atomic Force Microscopy

The AFM images are displayed in Figure 1e,f.

The reference (R) is corrugated, with a surface exhibiting large protruding particles (ranging from tens of nm up to microns—for example, see the upper, middle-left elongated particle in Figure 1e). Therefore, R is characterized by a higher global RMS roughness of 8.5 nm and an Rpv parameter of 804.5 nm. The line scan exhibits a vertical gradient (Δz level difference) of ~180 nm and more prominent surface features (Figure 1e).

F-UBO displays a rougher surface, having an RMS roughness of 98.5 nm and a peak-to-valley parameter of 480.6 nm (Figure 1f). The compact morphology is maintained similar to that of R; however, deep grooves and cavities are seen in the image, such as the one imaged along the red line, which is more than 300 nm deep. The surface features (such as pits, cavities, and grooves) create a clear surface corrugation, which could enhance the bioadhesive films' adherence to the targeted tissue.

3.2.3. FTIR Spectra

The FTIR spectra of R and F-UBO are illustrated in Figure 2.

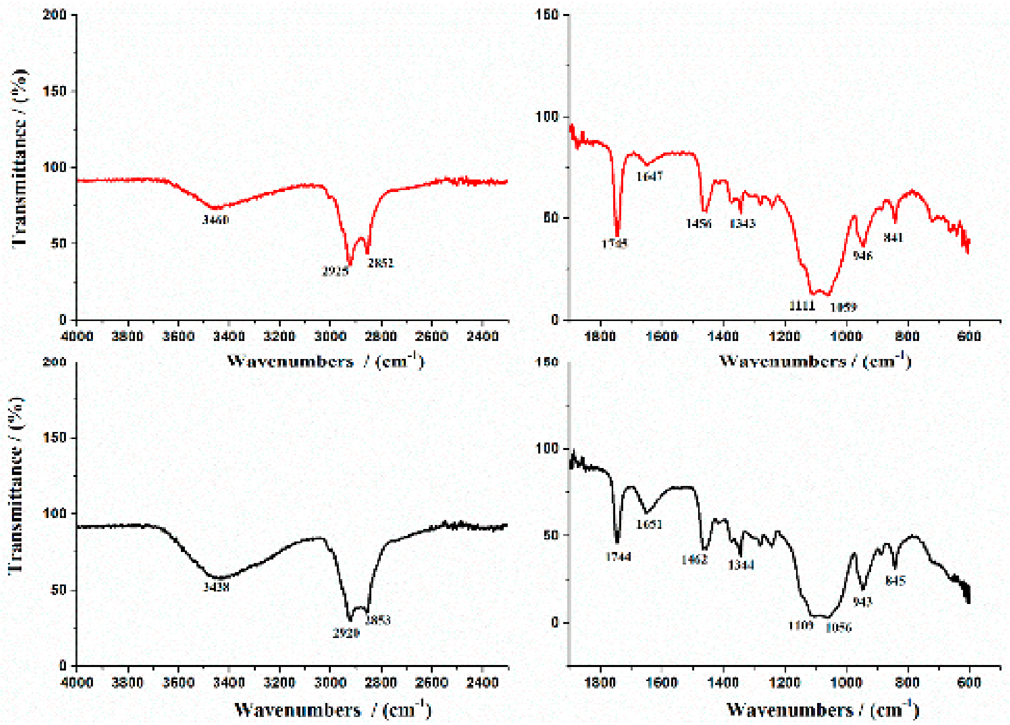

Figure 2. FTIR Spectra of bioadhesive oral films: R is shown with a red line and F-UBO with a black line. R—reference (a film without UBO); F-UBO—UBO-loaded bioadhesive oral film; UBO—*U. barbata* extract in canola oil.

The literature data showed that the main absorption peaks characterize the FTIR spectrum of P407 at 2893 cm^{-1} due to C-H stretch aliphatic, 1355 cm^{-1} corresponding to in-plane O-H bend, and 1124 cm^{-1} due to C-O stretch [57]. In addition, the FTIR spectrum of pure HPMC shows an absorption band at 3444 cm^{-1} assigned to the stretching frequency of the hydroxyl (-O.H.) group. The band at 1373 cm^{-1} is due to bending vibration of -O.H. Other stretching vibration bands related to C-H and C-O can be noted at 2929 cm^{-1} and 1055 cm^{-1}, respectively (Figure 2).

The prominent peaks of P407 and pure HPMC were shifted in R and F-UBO films due to the formation of bioadhesive film [58,59]. The main FTIR peaks of UBO [60] are superposed to the peaks of the polymer matrix.

On the other hand, the spectra exhibit the νO-H stretching vibration detected at 3460 cm^{-1} and νsim CH_2 at 2853 cm^{-1}, characteristic of P407. The band observed at 1050 cm^{-1} was assigned to the C-O group [61] (Figure 2). These findings are in accord with the assumption that F-UBO bioadhesive films are formed through UBO dispersion in the polymer matrix.

3.2.4. X-ray Diffractograms

The X-ray diffractograms of bioadhesive oral films are presented in Figure 3a.

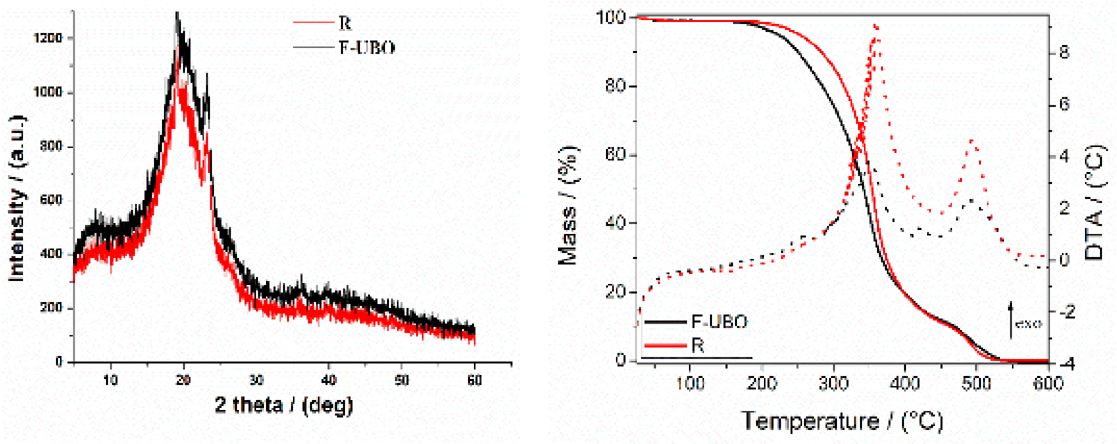

(**a**) (**b**)

Figure 3. (**a**) X-Ray diffractograms of bioadhesive oral films (R and F-UBO); (**b**) thermogravimetric analysis coupled with differential thermal analyses of R and F-UBO. R—reference (a film without UBO); F-UBO—UBO-loaded bioadhesive oral film; UBO—*U. barbata* extract in canola oil.

The X-ray diffractograms of R and F-UBO exhibited two peaks at $2\theta = 8^\circ$ and $2\theta = 20^\circ$. They represent the prominent HPMC XRD peaks, portraying their semicrystalline structure [62,63]. The peak at $2\theta = 22^\circ$ is attributed to P407 [64]. The X-ray diffraction pattern of F-UBO shows higher intensity peaks than the reference, proving the influence of UBO dispersion in the polymer matrix and correlated with the bioadhesive behavior.

3.2.5. Thermogravimetric Analysis

Thermogravimetric analysis coupled with differential thermal analysis was performed to characterize the film's thermal behavior and stability. Both materials (reference and F-UBO films) exhibit a similar behavior upon heating from 25 to 600 °C (Figure 3b). A 0.8–2.5% weight mass loss occurs on heating up to ~100 °C, which can be associated with the loss of residual solvent and physisorbed water. The decomposition process of the organic compounds takes place in two distinct steps, between 200–400 °C and 400–550 °C. Each decomposition step is accompanied by an exothermic thermal effect (Figure 3b). The mass losses associated with the solvent loss and first and second organic decomposition steps are presented in Table 2.

Table 2. Thermal parameters for the bioadhesive oral films (F-UBO and R) decomposition in air.

Film	**Solvent Mass Loss (%)**	**T (°C)/Mass Loss 1st Decomposition Step (%)**	**T (°C)/Mass Loss 2nd Decomposition Step (%)**
F-UBO	0.8	348.2 °C/87.3	488.8 °C/11.9
R	0.9	358.2 °C/86.4	A shoulder at 420 °C 495.3 °C/12.7

R—reference (films without UBO); F-UBO—UBO-loaded bioadhesive oral film; UBO—*U. barbata* extract in canola oil.

Figure 3b and Table 2 indicate that the first stage of both bioadhesive films (R and F-UBO) starts at a temperature below 100 °C due to the loss of adsorbed water. The second stage begins from 230 °C to 380 °C, corresponding to ~86% (for R) and ~87% (for F-UBO) weight loss. The third stage, with a maximum of 495.3 °C (for R) and 488.8 °C (for F-UBO) was due to the different organic part decomposition.

3.3. Pharmacotechnical Evaluation of Bioadhesive Oral Films

The results of pharmacotechnical evaluation of F-UBO and R are presented in Table 3. The film's weight varies depending on the active ingredient state and dispersion method. No significant differences are registered between the UBO-loaded films and the reference films (63 ± 1.79 vs. 62 ± 3.27 mg, $p > 0.05$).

Table 3. Pharmacotechnical [65] characterization of bioadhesive oral films (F-UBO and R).

Pharmacotechnical Parameter * [66]	**F-UBO**	**R**
Weight uniformity (mg)	63 ± 1.79	62 ± 3.27
Thickness (mm)	0.069 ± 0.006	0.065 ± 0.004
Folding endurance value	>300	>300
Tensile strength (kg/mm^2)	2.17 ± 0.49	2.36 ± 0.98
Elongation %	56.33 ± 0.92	52.16 ± 1.22
Moisture content % (*w*/*w*)	8.11 ± 0.78	8.42 ± 0.69
pH	6.97 ± 0.01	7.02 ± 0.04
Disintegration time (seconds)	124 ± 3.67	127 ± 4.81
Swelling rate (% after 6 h)	195 ± 5.24	202 ± 5.68
Ex vivo bioadhesion time (minutes)	86 ± 4.12	91 ± 3.79

* Expressed as mean value ± SD; R—reference (films without UBO); F-UBO—UBO-loaded bioadhesive oral film; UBO—*U. barbata* extract in canola oil; SD—standard deviation.

The thickness of F-UBO is similar to that of R (0.069 ± 0.006 vs. 0.065 ± 0.004 mm, $p > 0.05$). Low SD values registered in thickness measurements (Table 3) could also be observed.

Both films displayed a great folding endurance, with values above 300, proving suitable flexibility. The UBO-loaded films show a higher elongation and a lower tensile strength than the references (56.33 ± 0.92 vs. 52.16 ± 1.22, $p < 0.05$; 2.17 ± 0.49 vs. 2.36 ± 0.98, $p > 0.05$), proving the active ingredient's influence on the film's resistance and elasticity. The F-UBO's moisture content reported minor differences compared to that of R (8.11 ± 0.78 vs. 8.42 ± 0.69, $p > 0.05$). In addition, the pH measured on the film's surface shows approximately neutral and similar values for both formulations (6.97 ± 0.01 vs. 7.02 ± 0.04, $p > 0.05$). Furthermore, another three pharmacotechnical properties do not show significant differences between F-UBO and R: in vitro disintegration time in a simulated saliva medium (124 ± 3.67 vs. 127 ± 4.81, $p > 0.05$), swelling rate (195 ± 5.24 vs. 202 ± 5.68, $p > 0.05$), and bioadhesion time (86 ± 4.12 vs. 91 ± 3.79, $p > 0.05$).

The swelling rate over 6 h is presented in Figure 4.

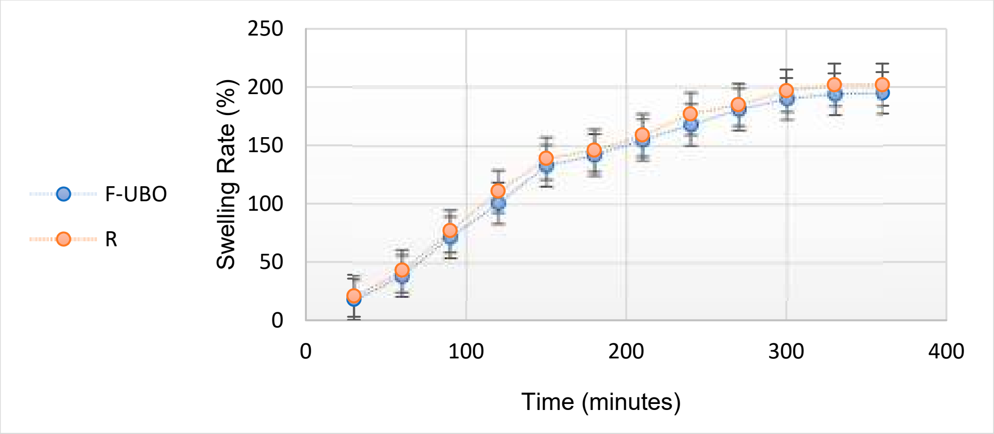

Figure 4. Swelling rate (%) over 6 h of F-UBO vs. R; F-UBO—UBO-loaded bioadhesive oral film; UBO—*U. barbata* extract in canola oil; R—reference (a film without UBO).

Figure 4 indicates that the swelling index increases linearly in the first 4 h (approximately 20% to every 30 min); then, the growth becomes slower, the differences between 330 and 360 min being insignificant. No films were eroded after 6 h, and no swelling could be detected after this time. With the oily active ingredient emulsified in the matrix, F-UBO displays a lower swelling behavior than R due to UBO's state and dispersion (Table 3).

3.4. Antimicrobial Activity

Data registered in Table 4 show the standard antibiotic (CTR), antifungal drug (TRF), P407, and F-UBO initial concentrations and microdilutions (mg/mL).

Table 4. Initial concentrations and microdilutions for standard antibacterial and antifungal drugs, positive control, and sample.

Micro-Dilution	**CTR (mg/mL)**		**TRF (mg/mL)**	**P407 (mg/mL)**	**F-UBO (mg/mL)**
	30.230 ± 0.630	**122.330 ± 0.850**	**10.050 ± 0.180**	**50.133 ± 1.305**	**63.533 ± 1.955**
1	1.511 ± 0.043	6.117 ± 0.042	0.500 ± 0.009	2.506 ± 0.065	3.176 ± 0.097
2	0.755 ± 0.022	4.893 ± 0.034	0.250 ± 0.004	1.253 ± 0.032	1.588 ± 0.048
3	0.377 ± 0.011	3.914 ± 0.027	0.125 ± 0.002	0.626 ± 0.016	0.794 ± 0.024
4	0.188 ± 0.005	3.131 ± 0.021	0.061 ± 0.001	0.315 ± 0.008	0.397 ± 0.012
5	0.094 ± 0.002	2.505 ± 0.017	0.031 ± 0.001	0.157 ± 0.004	0.199 ± 0.008
6	0.047 ± 0.002	2.004 ± 0.014	0.015 ± 0.001	0.078 ± 0.002	0.100 ± 0.004
7	0.023 ± 0.001	1.603 ± 0.011	0.007 ± 0.001	0.039 ± 0.001	0.049 ± 0.002

CTR—ceftriaxone; TRF—terbinafine; P407—poloxamer 407; F-UBO—bioadhesive oral films with *U. barbata* extract in canola oil.

The results obtained after 24 h incubation at 37 °C are displayed in Tables S1–S3 from the Supplementary Material.

Data from Table S1 indicate that the color showed by the standard antibiotic correlates with its inhibiting power and varies in a manner directly proportional to its concentration. CTR induced a "moderate" to "good" inhibition of bacterial strains' growth; the microdilutions [67,68] from 30.230 mg/mL CTR were less active than those from 122.330 mg/mL.

F-UBO exhibited inhibitory effects on both bacteria tested (Table S1). Comparing the colors of the well-plates with F-UBO and CTR, it can be observed that F-UBO of [3.176–0.100] mg/mL acts against *S. aureus*, similar to CTR of [0.047–0.023] mg/mL. F-UBO of [3.176–0.199] mg/mL inhibits *P. aeruginosa* proliferation, similar to CTR of [0.047–0.023] mg/mL (Table S1).

In the present study, 5% P407 had inhibitory effects against both bacteria tested (Table S2a–d), and its action was higher against *P. aeruginosa* than *S. aureus.* P407 of [2.506–0.626] mg/mL acted on *P. aeruginosa*, similar to CTR of [1.511—0.047] mg/mL. Moreover, P407 of [2.506–1.253] mg/mL inhibited *S. aureus* proliferation, similar to CTR of [0.047–0.023] mg/mL. Compared to F-UBO, 5% P407 reported similar effects on *S. aureus* and induced a slowly higher inhibition of *P. aeruginosa.*

Table S3 shows that terbinafine of [0.500–0.007] mg/mL exhibited the highest antifungal activity, having a fungicidal effect on both *Candida* sp.

F-UBO inhibited both *Candida* sp. proliferation. Thus, F-UBO of 3.176 mg/mL had the most significant inhibitory activity on both species, higher on *C. albicans* than on *C. parapsilosis.* The following decreasing F-UBO concentrations moderately inhibited the *Candida* sp. proliferation.

The antifungal activity of P407 is displayed in Table S2e–h. P407 of [2.506—0.078] mg/mL had a significant inhibitory effect, partially inducing the death of both fungal species [48]. The lowest concentration (0.039 mg/mL) similarly affected *C. albicans* and produced a moderate to fast proliferation of *C. parapsilosis* [48]. Moreover, Tables S2 and S3 show that 5% P407 had considerably higher inhibitory activity on both *Candida* sp. than F-UBO.

3.5. Evaluation of UBO-Loaded Bioadhesive Oral Films Cytotoxicity on Animal Model

A. salina nauplii were examined under the microscope to detect morphological changes after 24 and 48 h of exposure, compared to a blank and positive control (5% P407). All these data are illustrated in Figure 5.

After 24 h, all larvae were alive, swimming, and showing normally visible movements. However, F-UBO cytotoxicity was revealed after the first 24 h, even if the larvae were alive and apparently normal. Compared to untreated larvae (Figure 5a–d), the images 400× (Figure 5e–h) show the following processes in the early stage: penetration of emulsified lipids into tissues, depletion of cellular structures, and minimal detachment of the cuticle from the terminal portion of the digestive tract.

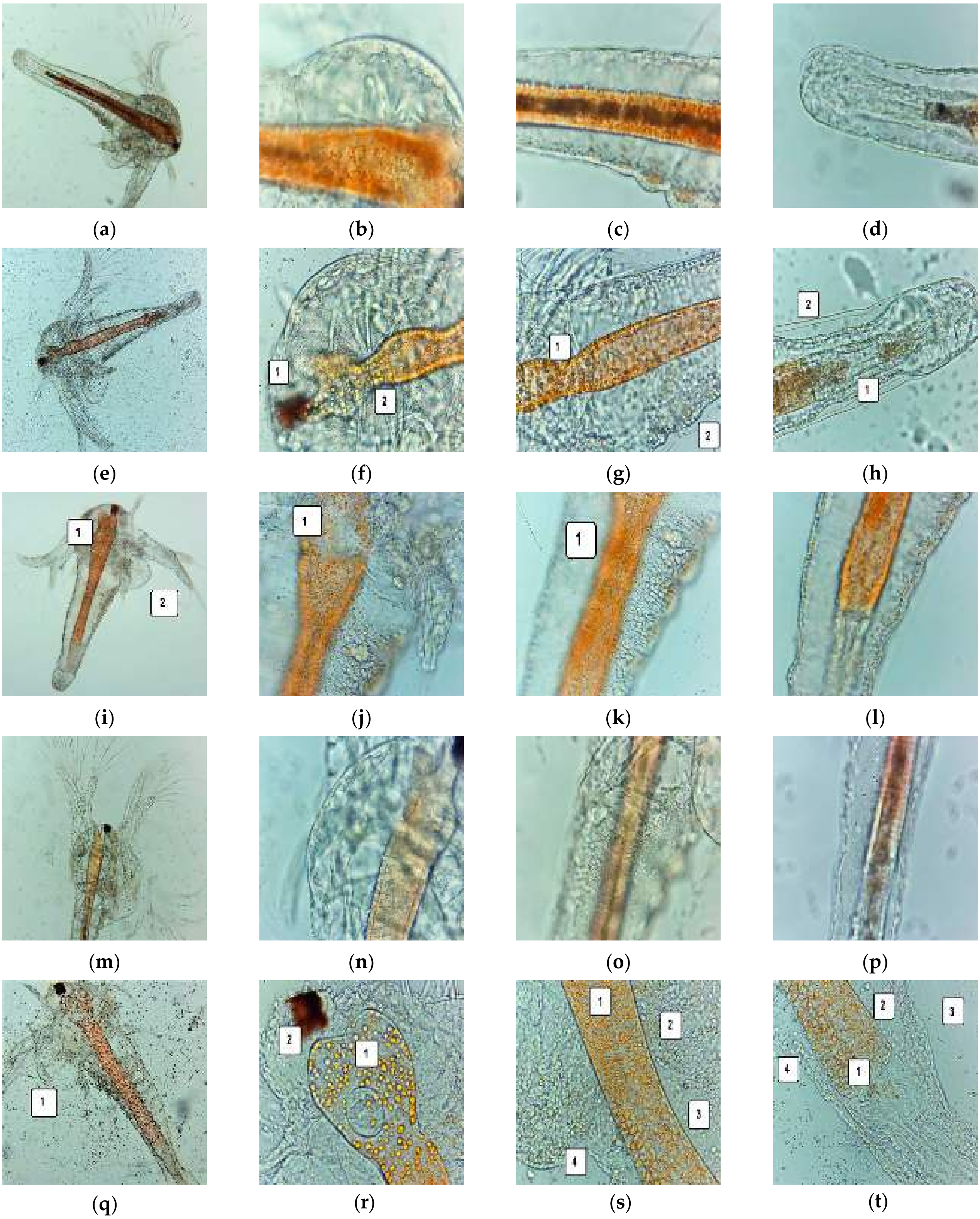

Figure 5. *Cont.*

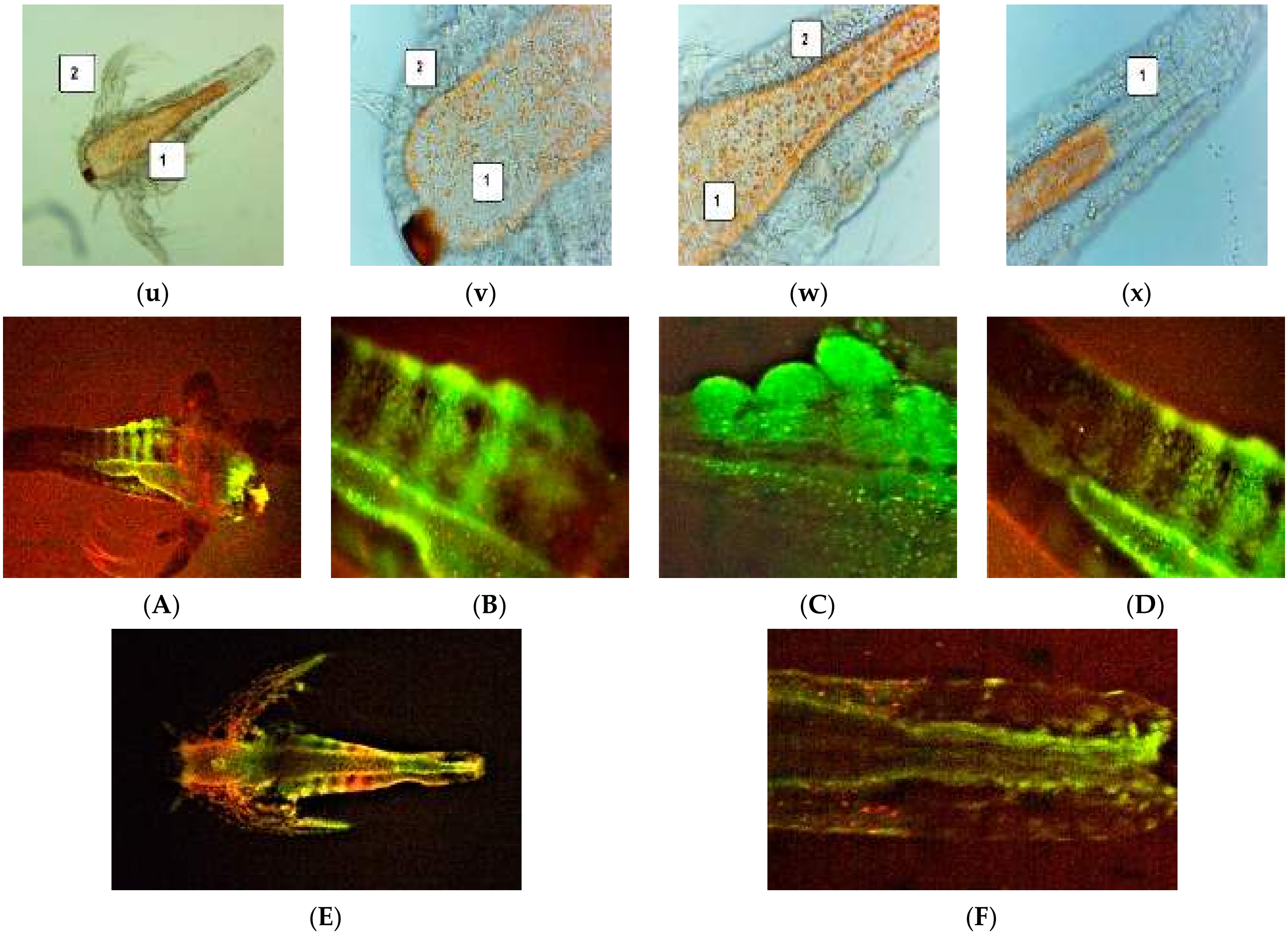

Figure 5. *A. salina* larvae after 24 and 48 h—microscopic images at 100× (**a**,**e**,**i**,**m**,**r**) and 400× (**b**–**d**,**f**–**h**,**j**–**l**,**n**–**p**,**s**–**u**). After 24 h: blank (**a**–**d**), F-UBO (**e**–**h**), 5% P407 (**i**–**l**); after 48 h: blank (**m**–**p**), F-UBO (**r**–**u**), 5% P407 (**v**–**x**). The following changes were observed compared to blank: (**f**) penetration of emulsified lipids into tissues (1); (**g**) penetration of emulsified lipids into tissues (1), depletion of cellular structures (2); (**h**) penetration of emulsified lipids into tissues (1), detachment of the cuticle from the terminal portion of the digestive tract (2); (**i**) increasing the volume of the digestive tube in the upper part (1); growth cessation—the brine shrimp larvae have not passed into the next stage of development (2); (**j**) different changes in the upper part of the digestive tube (1); (**k**) narrowing of the digestive tract in the lower half; (**q**) dead larvae (1); (**r**) massive penetration of small particles of emulsified lipids, into tissues (1), tissue damage (2); (**s**) blocked digestive tract due to accumulated lipids (1), accumulation of lipids in tissues (2), cell damage with large intercellular spaces (3), tissue destruction (4); (**t**) digestive tract blocked by accumulated lipids (1), cell damage with large intercellular spaces (2), massive detachment of the cuticle from larval tissues (3), tissue destruction (4); (**u**) intensifying the increase in the digestive tract's volume (1) and growth cessation (2); (**v**,**w**) intensifying the increase in the digestive tract's volume (1) and penetration of emulsified lipids into tissues (2); (**x**) penetration of emulsified lipids into tissues (1). *A. salina* larvae after 48 h exposure to F-UBO, stained with acridine orange 400× (**A**,**E**) and 200× (**B**–**D**,**F**): blank (**A**–**D**) and F-UBO (**E**,**F**). The red fluorescence shows intracellular lysosomes activated in cell death processes (**F**).

These morphological changes were intensified over the next 24 h, becoming incompatible with the brine shrimp nauplii survival. Hence, after 48 h, 64.81% of larvae were alive, and 11.11% were in the sublethal stage; the registered mortality was 25.92%.

Compared to blank (Figure 5i–l), the exposed larvae (Figure 5m–p) had blocked digestive transit due to accumulated lipids, cell damage with large intercellular spaces, tissue destruction, and massive detachment of the cuticle from larval tissues.

The *A. salina* larvae were alive and had normal movements after 24 and 48 h exposure at 5% P407. Microscopic examination after 48 h revealed a significant digestive tube volume increase, especially in the superior part, and low penetration of emulsified lipids into tissue (Figure 5v–x).

Moreover, at the intracellular level, FM images (Figure 5A–F) show activated lysosomes in cell death processes in brine shrimp larvae exposed to F-UBO (Figure 5F).

3.6. In Vitro Cytotoxicity of UBO-Loaded Bioadhesive Oral Films on Human Normal Blood Cells and CLS-354 Tumor Cells

3.6.1. Annexin V-FITC Apoptosis Assay

The effects of F-UBO on normal blood cells and CLS-354 tumor cells based on morphology and cell membrane integrity are illustrated in Figure 6.

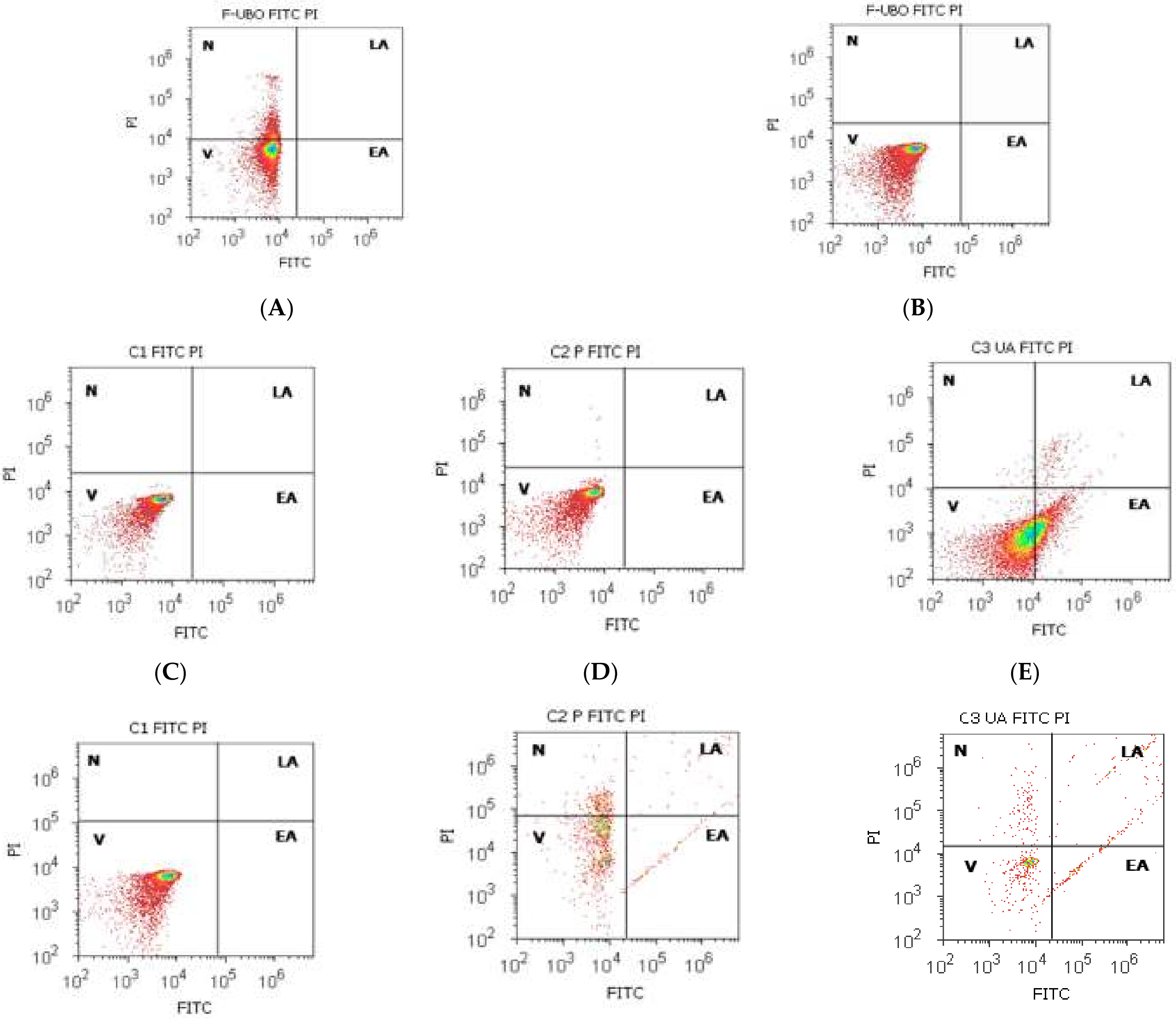

(**A**) (**B**)

(**C**) (**D**) (**E**)

(**F**) (**G**) (**H**)

Figure 6. *Cont.*

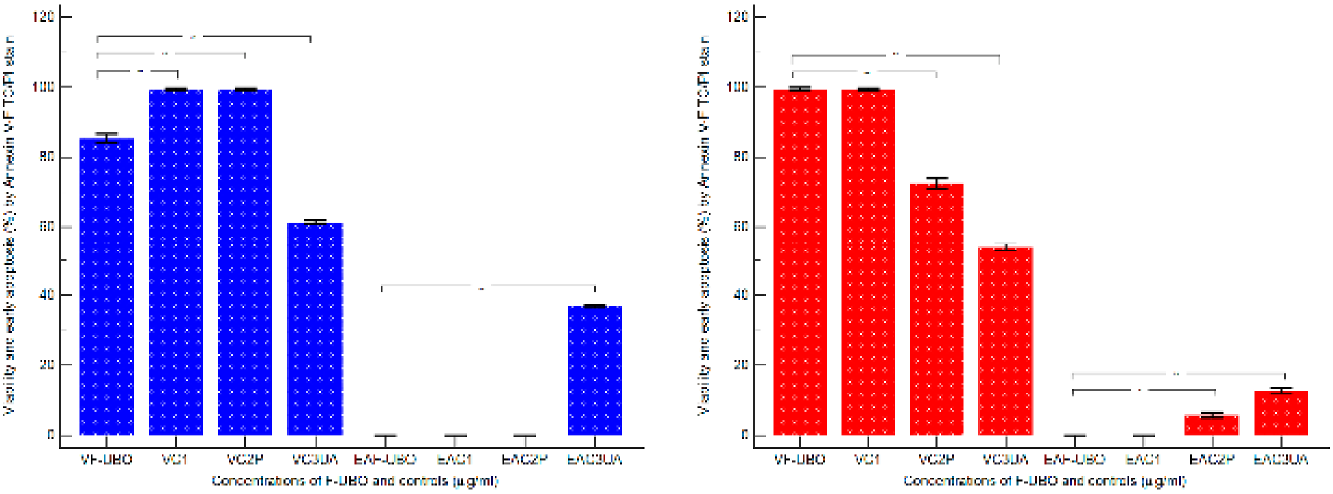

(**I**) (**J**)

Figure 6. Cell apoptosis models after 24 h treatment with F-UBO in normal blood cells (**A**,**C**–**E**) and CLS-354 tumor cells (**B**,**F**–**H**). Annexin V-FITC/PI patterns of F-UBO (**A**,**B**); 1% DMSO negative control (**C**,**F**); 5% poloxamer 407 positive control (**D**,**G**); 125 µg/mL UA positive control (**E**,**H**). Statistical analysis of cell apoptosis (**I**,**J**) in normal blood cells (**I**) and CLS-354 tumor cells. * $p < 0.05$ and ** $p < 0.01$ are significant statistical differences between controls and sample (F-UBO) made by paired samples *t*-test. V—viability; EA—early apoptosis; F-UBO—bioadhesive oral films loaded with *U. barbata* extract in canola oil; C1—negative control with 1% dimethyl sulfoxide; C2P—positive control with 5% poloxamer 407; C3UA—positive control with 125 µg/mL usnic acid.

After 24 h treatment with F-UBO, the normal blood cell's viability (V) was significantly higher compared to the C3UA positive control: 85.43 ± 2.01 vs. 61.43 ± 0.88, $p < 0.01$ (Figure 6A,E,I).

The viability of CLS-354 tumor cells treated with F-UBO was also appreciably increased compared to both positive controls: 99.50 ± 0.72 vs. C2P: 72.51 ± 2.51; C3UA: 54.05 ± 1.68, $p < 0.01$ (Figure 6B,G,H,J).

Moreover, Figure 6 shows that F-UBO did not induce early apoptosis in both cell types, thus reporting considerable differences compared to C3UA in normal blood cells (0.00 ± 0.00 vs. 37.04 ± 0.66, $p < 0.01$), and both positive controls in CLS-354 tumor cells (0.00 ± 0.00 vs. C2P: 5.88 ± 1.24, $p < 0.05$ and C3UA: 12.92 ± 1.35, $p < 0.01$).

3.6.2. Evaluation of Caspase-3/7 Activity

The pro-apoptotic signal induced by F-UBO in normal blood cells and CLS-354 tumor cells was achieved by measuring the effector caspase-3/7 (Figure 7).

(**A**) (**B**)

Figure 7. *Cont.*

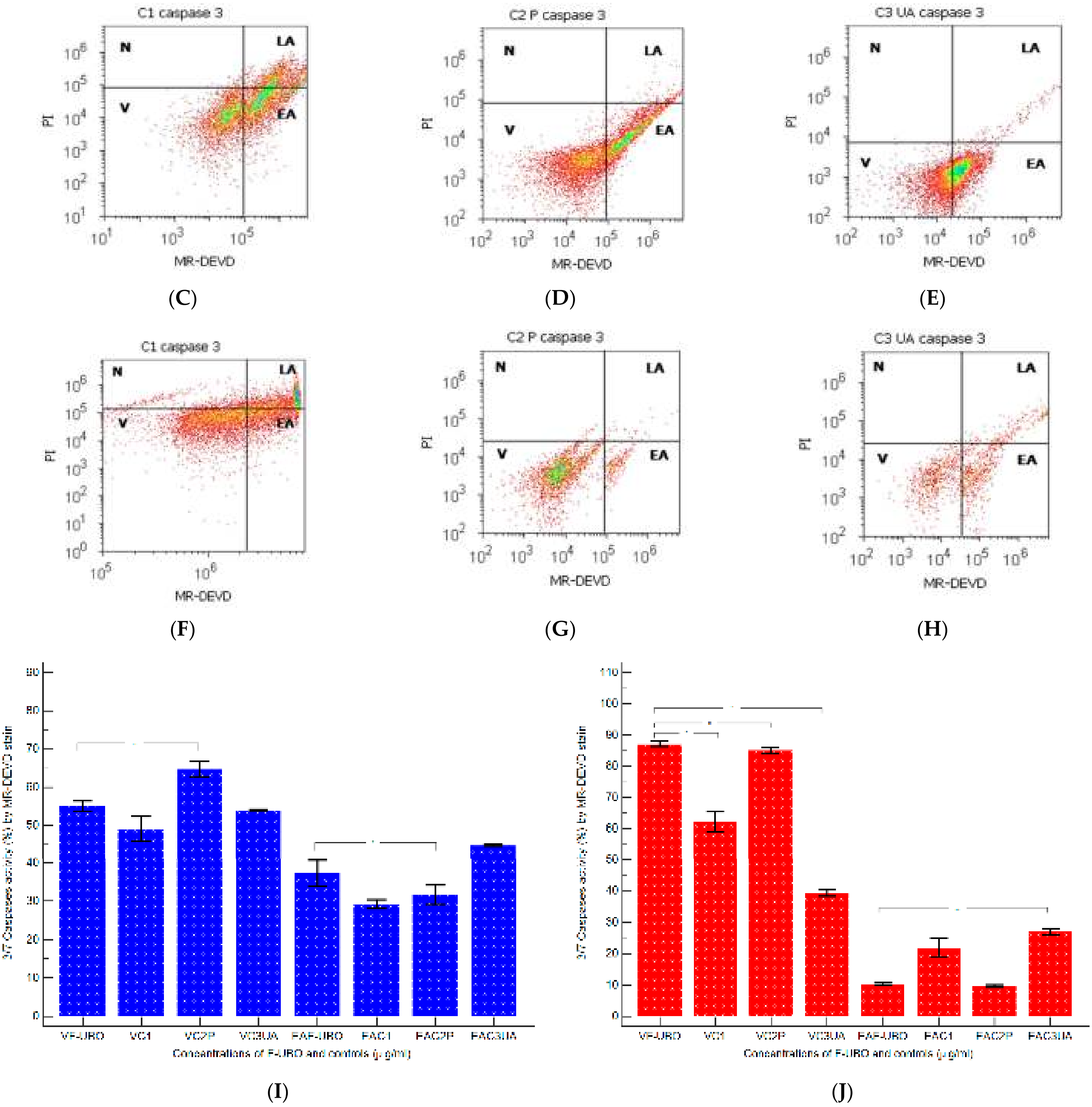

(**C**) (**D**) (**E**)

(**F**) (**G**) (**H**)

(**I**) (**J**)

Figure 7. Caspase-3/7 activity after 24 h treatment with F-UBO in normal blood cells (**A**,**C**–**E**) and CLS-354 tumor cells (**B**,**F**–**H**); MR-DEVD patterns of F-UBO (**A**,**B**), 1% DMSO negative control (**C**,**F**); 5% poloxamer 407 positive control (**D**,**G**); 125 µg/mL UA positive control (**E**,**H**). Statistical analysis of caspase-3/7 activity (**I**,**J**) in normal blood cells (**I**) and CLS-354 tumor cells (**J**). * $p < 0.05$ and ** $p < 0.01$ are significant statistical differences between controls and sample (F-UBO) made by paired samples *t*-test. V—viability; EA—early apoptosis; LA—late apoptosis; N—necrosis; F-UBO—bioadhesive oral films loaded with *U. barbata* extract in canola oil; C1—negative control with 1% dimethyl sulfoxide; C2P—positive control with 5% poloxamer 407; C3UA—positive control with 125 µg/mL usnic acid.

Caspase-3/7 activity in blood cells after 24 h treatment with F-UBO shows significantly increased values than 5% P407: EA: 37.31 ± 5.88 vs. 31.69 ± 4.33, $p < 0.05$. Consequently, the blood cell's viability was diminished considerably compared to the C2P positive control (55.06 ± 2.34 vs. C2P: 64.80 ± 3.41, $p < 0.01$, Figure 7A,D,I).

In CLS-354 tumor cells, the proapoptotic signal appreciably decreased compared with the C3UA positive control: 10.24 ± 0.76; vs. 27.02 ± 1.64, $p < 0.01$ (Figure 7B,H,J). The CLS-354 tumor cell's viability remained on significantly higher levels, compared to the C2P and C3UA controls: 87.14 ± 1.45 vs. C2P: 85.18 ± 1.59, $p < 0.05$; C3UA: 39.25 ± 1.88, $p < 0.01$ (Figure 7B,G,H,J).

3.6.3. Evaluation of Nuclear Condensation and Lysosomal Activity

Magic Red® Caspase-3/7 Assay Kit [69] contains Hoechst 33,342 and acridine orange stains. Hoechst 33,342 is a cell-permeant nuclear stain; when it is linked to double chain DNA, it emits blue fluorescence, highlighting condensed nuclei in apoptotic cells [70]. Acridine orange is a chelating dye for revealing the lysosomal activity [71]. Both processes triggered in normal blood cells and CLS-354 tumor cells after 24 h treatment with F-UBO are displayed in Figure 8.

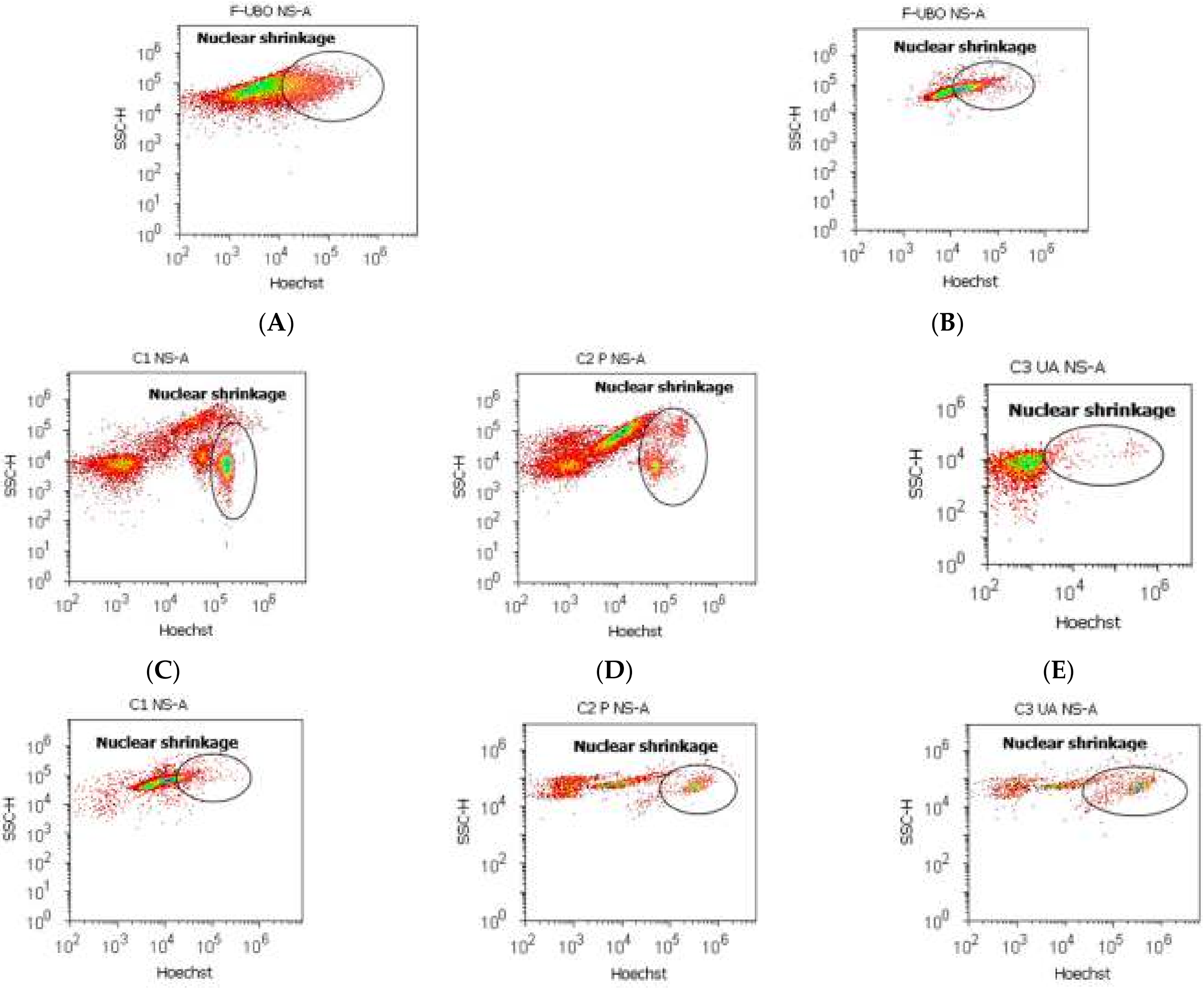

(A) (B)

(C) (D) (E)

(F) (G) (H)

Figure 8. *Cont.*

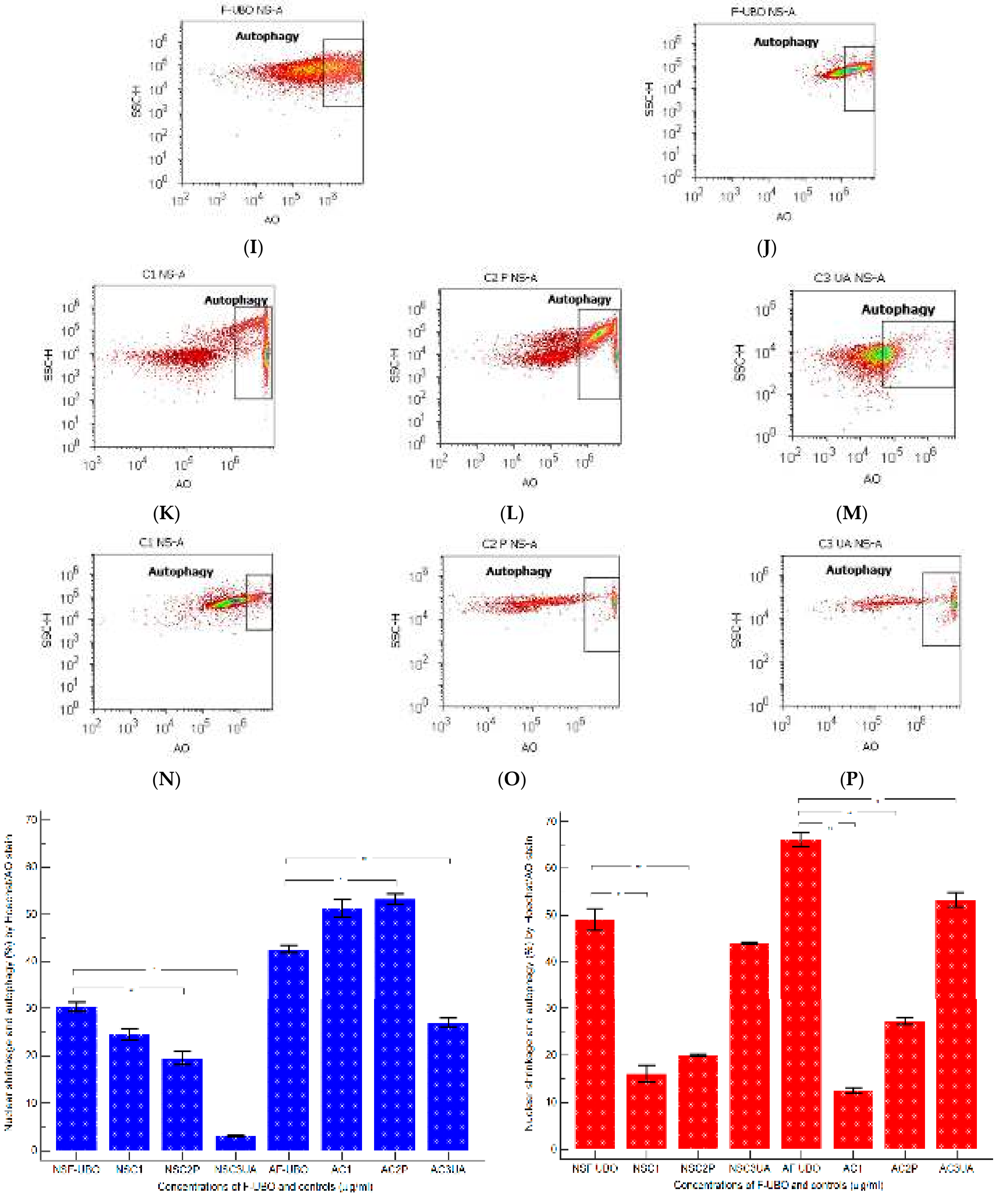

(I) (J)

(K) (L) (M)

(N) (O) (P)

(R) (S)

Figure 8. Nuclear shrinkage (**A**–**H**) and lysosomal activity (**I**–**P**) after 24 h treatment with F-UBO in normal blood cells (**A**,**C**–**E**,**I**,**K**–**M**) and CLS-354 tumor cells (**B**,**F**–**H**,**J**,**N**–**P**). Hoechst (**A**–**H**) and acridine orange (**I**–**P**) patterns of F-UBO (**A**,**B**,**I**,**J**); 1% DMSO negative control (**C**,**F**,**K**,**N**); 5% P407 positive control (**D**,**G**,**L**,**O**); 125 μg/mL UA positive control (**E**,**H**,**M**,**P**); Statistical analysis of nuclear shrinkage and autophagy (**R**,**S**) in normal blood cells (**R**) and CLS-354 tumor cells (**S**).* $p < 0.05$ and ** $p < 0.01$ represent significant statistical differences between controls and sample (F-UBO) made by paired samples *t*-test; NS—nuclear shrinkage; A—autophagy; F-UBO—bioadhesive oral films loaded with *U. barbata* extract in canola oil; C1—negative control with 1% dimethyl sulfoxide; C2P—positive control with 5% poloxamer 407; C3UA—positive control with 125 μg/mL usnic acid.

After 24 h treatment, F-UBO determined in normal blood cells significantly higher values of nuclear shrinkage compared to positive controls: 30.32 ± 1.73 vs. C2P: 19.53 ± 2.41, and C3UA: 3.19 ± 0.30, $p < 0.01$ (Figure 8A,D,E,R). The F-UBO-induced lysosomal activity is significantly lower than C2P: 42.66 ± 1.36 vs. 53.23 ± 1.99; $p < 0.05$ (Figure 8I,L,R). It is also considerably augmented compared to C3UA: 42.66 ± 1.36 vs. 27.05 ± 1.52; $p < 0.01$ (Figure 8I,M,R).

In CLS-354 tumor cells, F-UBO induced a substantially higher nuclear shrinkage than C1 negative and C2P positive controls: 49.04 ± 4.04 vs. C1: 16.11 ± 3.11, $p < 0.05$; C2P: 20.06 ± 0.37; $p < 0.01$ (Figure 8B,F,G,S). Moreover, F-UBO recorded a strong augmentation of tumor cell's lysosomal activity compared to all controls: 66.14 ± 2.67 vs. C1: 12.57 ± 0.92; C2P: 27.27 ± 1.37; $p < 0.01$, C3UA: 53.35 ± 2.63, $p < 0.05$ (Figure 8J,N,O,P,S).

3.6.4. Cell Cycle Analysis

The effects of F-UBO on the cell cycle of normal blood cells and CLS-354 tumor cells, evidenced with PI/RNase stain, are displayed in Figure 9.

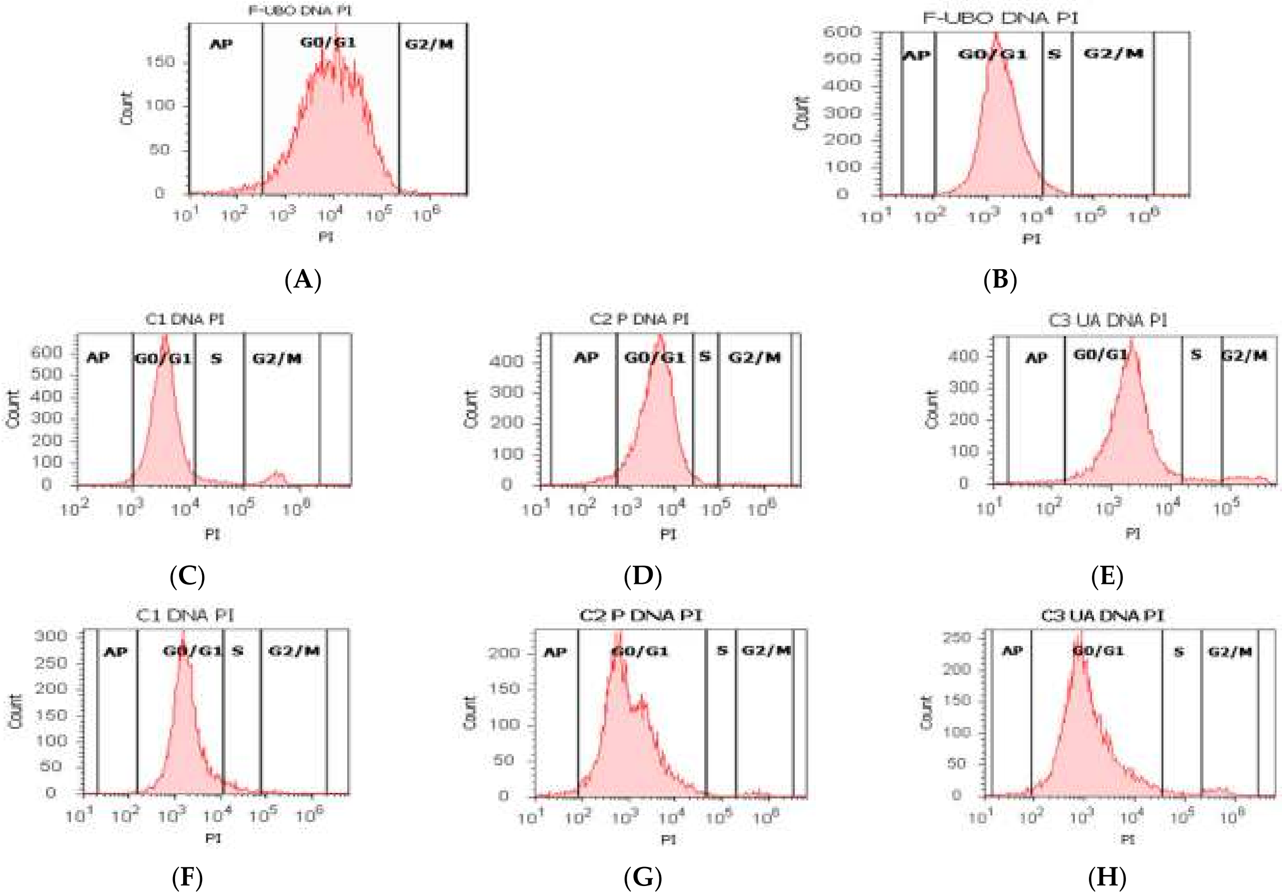

Figure 9. *Cont.*

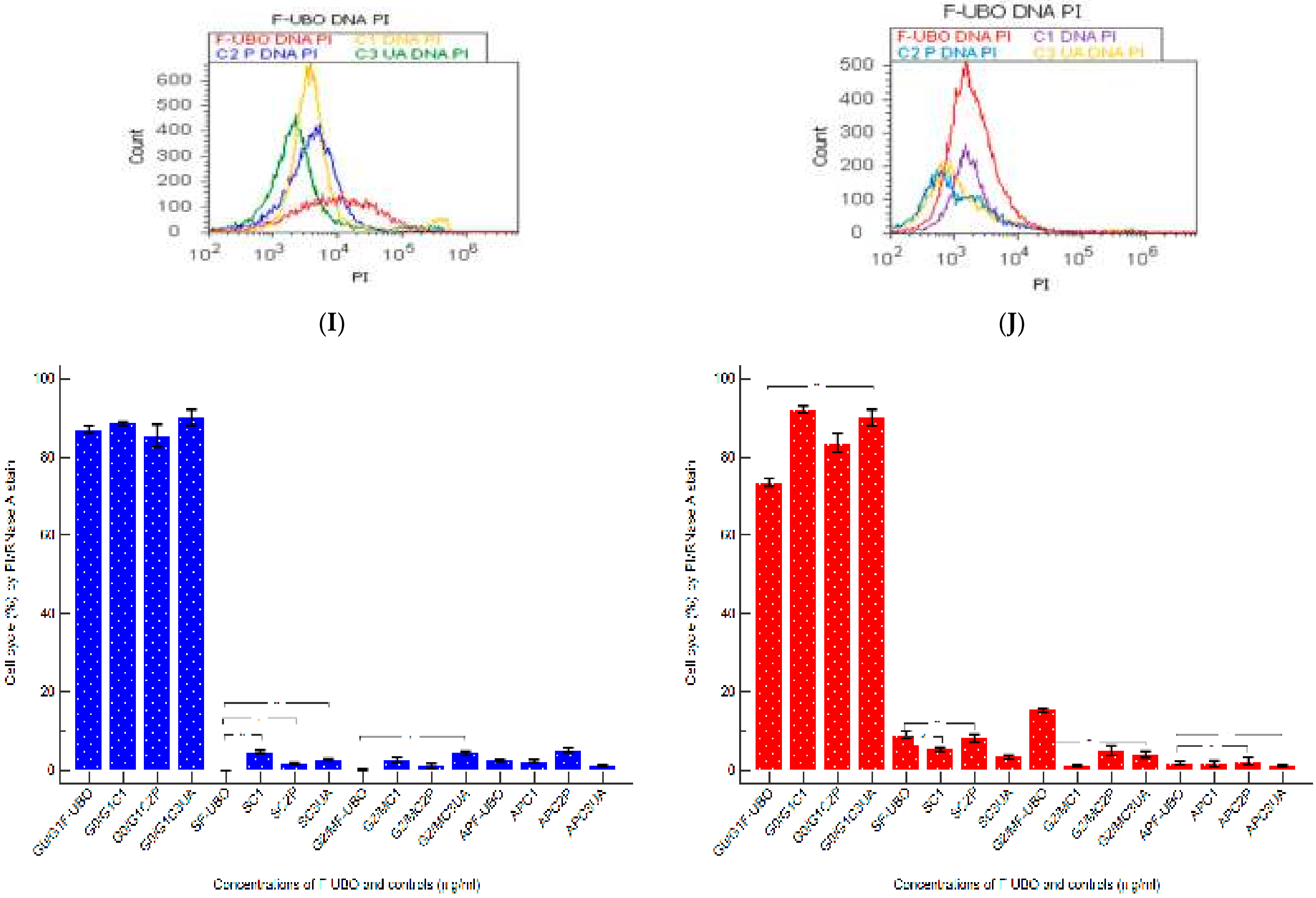

(I) (J)

(K) (L)

Figure 9. Cell cycle analysis after 24 h treatment with F-UBO in normal blood cells (**A**,**C**–**E**) and CLS-354 tumor cells (**B**,**F**–**H**). PI/RNase patterns of F-UBO (**A**,**B**); 1% DMSO negative control (**C**,**F**); 5% P407 positive control (**D**,**G**); 125 µg/mL UA positive control (**E**,**H**); F-UBO and controls extrapolated on PI axis (**I**,**J**); Statistical analysis of G0/G1, DNA synthesis (**S**), and G2/M phases of the cell cycle (**K**,**L**) in normal blood cells (**K**) and CLS-354 tumor cells (**L**). * $p < 0.05$ and ** $p < 0.01$ represent significant statistical differences between controls and sample (F-UBO) made by paired samples *t*-test; AP—apoptotic cell fraction (subG0/G1) [72]; PI—propidium iodide; S—synthesis of cell cycle phases; F-UBO—bioadhesive oral films loaded with *U. barbata* extract in canola oil; C1—negative control with 1% dimethyl sulfoxide; C2P—positive control with 5% poloxamer 407; C3UA—positive control with 125 µg/mL usnic acid.

In normal blood cells, F-UBO determined cell cycle arrest in G0/G1 without appreciable differences from controls: 86.99 ± 1.49 vs. C1: 88.52 ± 0.74, C2P: 85.38 ± 4.94, C3UA: 90.05 ± 3.45, $p \geq 0.05$ (Figure 9A,C–E,I,K). However, F-UBO blocked DNA-synthesis in normal blood cells: 0.00 ± 0.00 vs. C1: 4.76 ± 0.68, $p < 0.01$; C2P: 1.79 ± 0.36, $p < 0.05$; C3UA: 2.86 ± 0.23, $p < 0.01$ (Figure 9A,C–E,I,K).

F-UBO inhibited the CLS-354 tumor cell's growth through cell cycle arrest in G0/G1 and G2/M, registering significant differences from both positive controls. Thus, cell cycle arrest in G0/G1 is lower (73.51 ± 1.77 vs. C2P: 83.56 ± 4.20, $p < 0.05$; C3UA: 90.05 ± 3.45, $p < 0.01$) and in G2/M is higher (15.40 ± 0.72 vs. C2P: 5.12 ± 2.19, $p < 0.05$; C3UA: 4.06 ± 1.45, $p < 0.01$) compared to C2P and C3UA (Figure 9B,G,H,J,L).

3.6.5. Evaluation of Total ROS Activity

Total ROS activity evaluation measured the cellular oxidative stress induced by F-UBO in blood cells and CLS-354 tumor cells. The results are displayed in Figure 10.

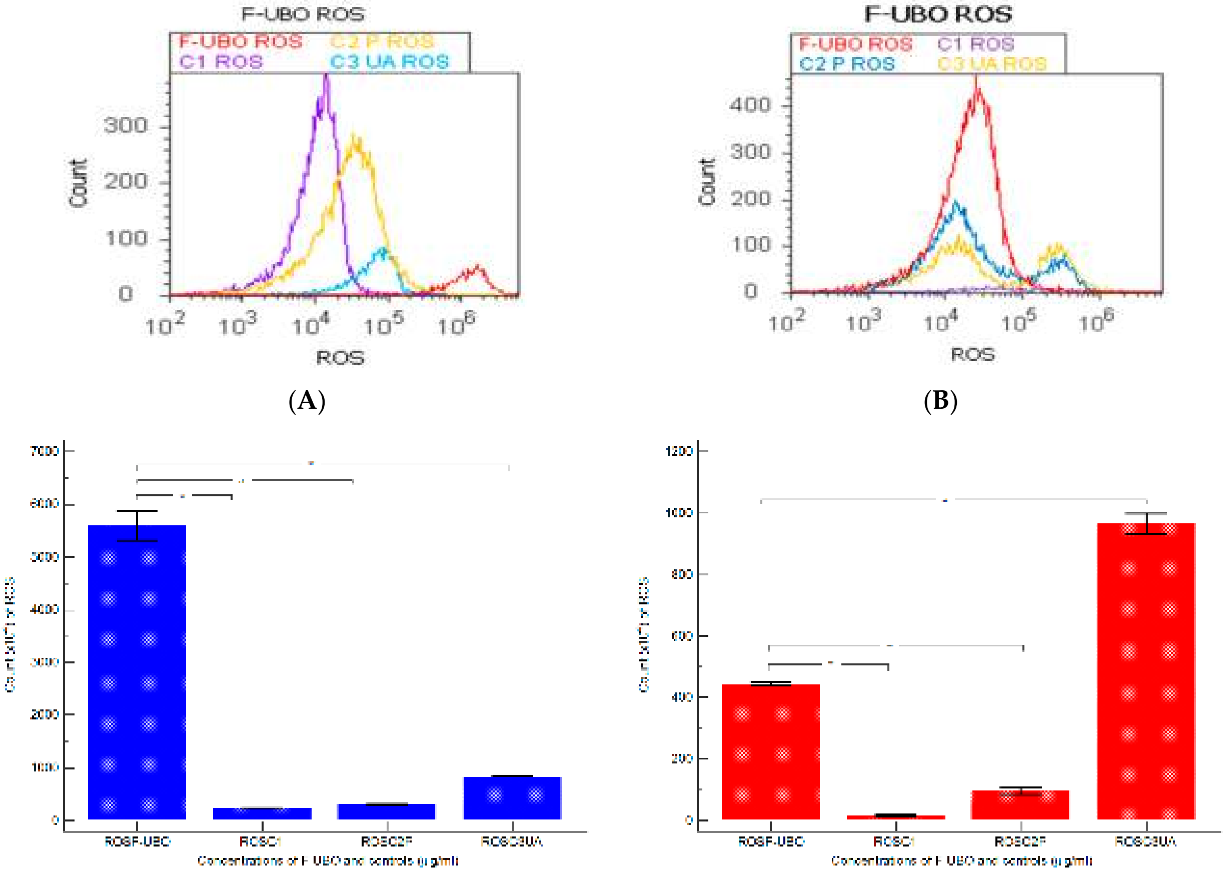

(**A**) (**B**)

(**C**) (**D**)

Figure 10. ROS levels after 24 h treatment with F-UBO in normal blood cells (**A**) and CLS-354 tumor cells (**B**) illustrated as F-UBO and controls extrapolated on the ROS axis. Statistical analysis of cellular oxidative stress (**C**,**D**) in normal blood cells (**C**) and CLS-354 tumor cells (**D**); ** $p < 0.01$ represents significant statistical differences between controls and sample (F-UBO) made by paired samples *t*-test; ROS—reactive oxygen species; F-UBO—bioadhesive oral films loaded with *U. barbata* extract in canola oil; C1—negative control with 1% dimethyl sulfoxide; C2P—positive control with 5% poloxamer 407; C3UA—positive control with 125 µg/mL usnic acid.

F-UBO-induced oxidative stress in normal blood cells was substantially higher compared to all controls: $5600 \times 10^4 \pm 500.00$; vs. C1: $242.00 \times 10^4 \pm 2.00$, C2P: $311 \times 10^4 \pm 9.64$; C3UA: $846.66 \times 10^4 \pm 5.77$, $p < 0.01$ (Figure 10A,C).

Moreover, ROS levels in CLS-354 cells treated with F-UBO considerably increased compared to C1 and C2P: $445.00 \times 10^4 \pm 8.66$ vs. C1: $15.66 \times 10^4 \pm 4.04$; and C2P: $96.66 \times 10^4 \pm 20.81$; $p < 0.01$ (Figure 10B,D). However, F-UBO-induced ROS levels were significantly lower than C3UA's: $966.66 \times 10^4 \pm 57.73$, $p < 0.01$ (Figure 10B,D).

3.6.6. Evaluation of Cell Proliferation

The F-UBO effects on DNA synthesis in normal blood cells and CLS-354 tumor cells were also assessed by EdU incorporation, and the results are presented in Figure 11.

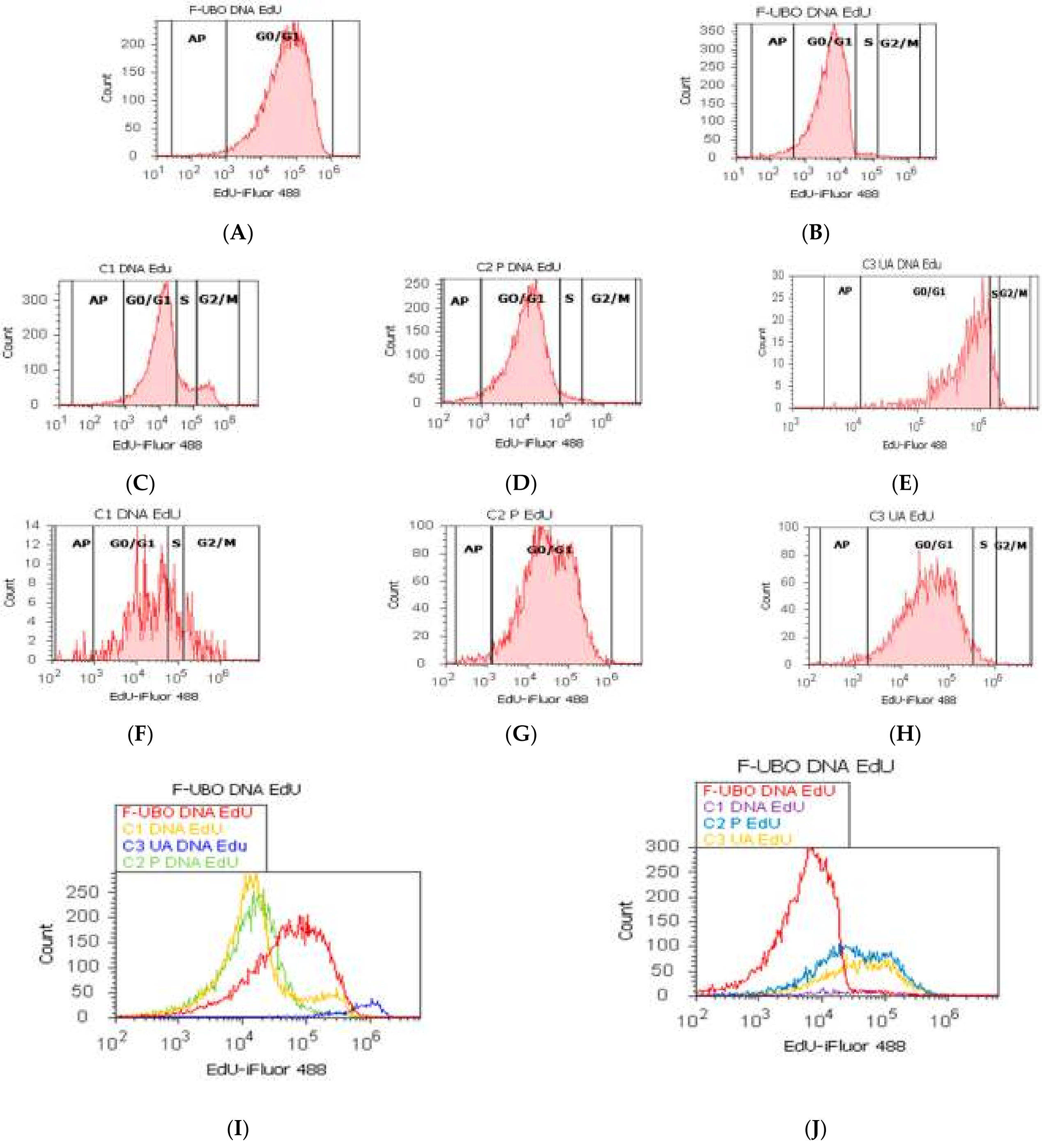

(**A**) (**B**)

(**C**) (**D**) (**E**)

(**F**) (**G**) (**H**)

(**I**) (**J**)

Figure 11. *Cont*.

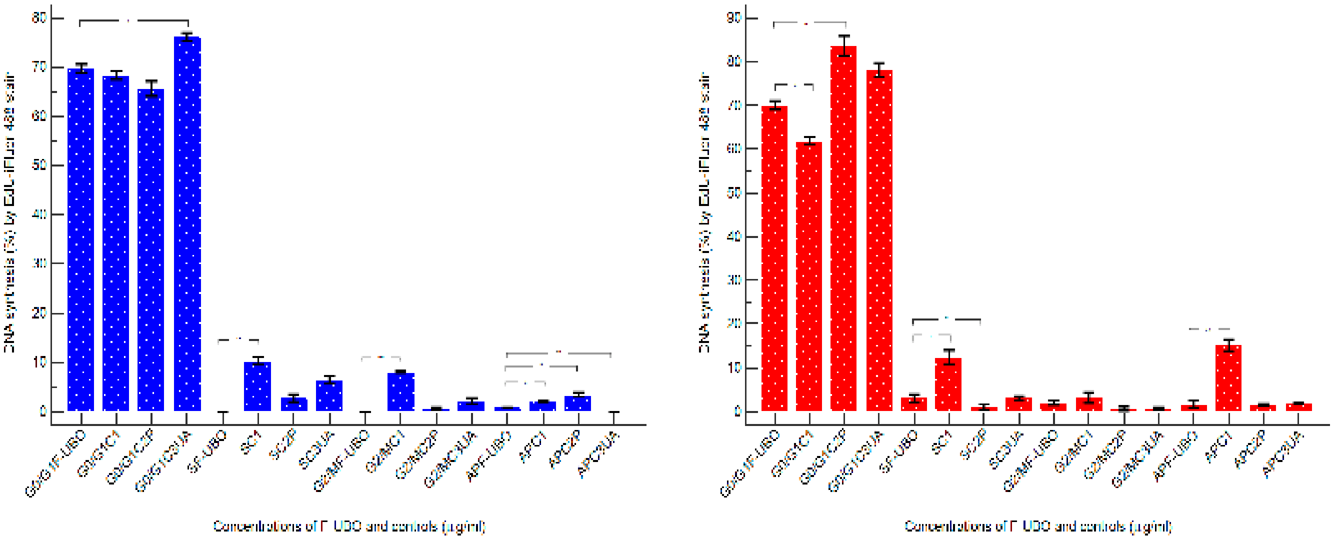

(**K**) (**L**)

Figure 11. DNA synthesis (S) in normal blood cells (**A**,**C**–**E**) and CLS-354 tumor cells (**B**,**F**–**H**) after 24 h treatment with F-UBO; EdU-iFluor 488 patterns of F-UBO (**A**,**B**); 1% DMSO negative control (**C**,**F**); 5% poloxamer 407 positive control (**D**,**G**); 125 µg/mL UA positive control (**E**,**H**); F-UBO and controls extrapolated on EdU-iFluor 488 axis (**I**,**J**); Statistical analysis of DNA synthesis (**K**,**L**) in normal blood cells (**K**) and CLS-354 tumor cells (**L**); * $p < 0.05$ and ** $p < 0.01$ represent significant statistical differences between controls and sample (F-UBO) made by paired samples *t*-test. AP—apoptotic cell fraction (subG0/G1) [73]; F-UBO—bioadhesive oral films loaded with *U. barbata* extract in canola oil; C1-negative control with 1% dimethyl sulfoxide; C2P—positive control with 5% poloxamer; C3UA—positive control with 125 µg/mL usnic acid.

In normal blood cells, F-UBO blocked DNA synthesis recording considerable differences from C1 negative control: 0.00 ± 0.00 vs. 10.36 ± 1.21; $p < 0.01$ (Figure 11A,C,I,K). As a result of DNA content diminution, the cell cycle arrest in subG0/G1 phase corresponds to apoptotic cell fraction; these cells have less DNA than healthy ones due to DNA fragmentation [72]. However, F-UBO induced apoptotic cell fraction (subG0/G1) [73] had significantly lower values compared with 1% DMSO (0.84 ± 0.09 vs. 2.01 ± 0.20, $p < 0.05$) and higher ones compared to UA (0.84 ± 0.09 vs. 0.00 ± 0.00, $p < 0.01$).

In CLS-354 tumor cells, F-UBO also significantly diminished DNA synthesis compared to C1 negative control: 3.09 ± 1.60 vs. C1: 12.44 ± 2.80, $p < 0.05$ (Figure 11B,F,J,L), but F-UBO-induced cell cycle arrest in subG0/G1 was still considerably lower than that of C1: 1.77 ± 1.37 vs. 15.18 ± 2.17, $p < 0.01$ (Figure 11B,F,J,L). Moreover, P407 reduced DNA synthesis in CLS-354 tumor cells higher than F-UBO: 1.16 ± 1.07 vs. 3.09 ± 1.60, $p < 0.05$ (Figure 11B,G,J,L), but apoptotic cell fraction also remained minimal.

3.6.7. Principal Component Analysis

The principal component analysis (PCA) was performed for F-UBO and controls (C1-DMSO, C2P407, and C3UA). It correlates the variable parameters determined in both cell types (normal blood cells and CLS-354 OSCC tumor cells) according to the correlation matrix and PCA-correlation circle from the Supplementary Materials. The results are displayed in Figure 12.

The two principal components explained 83.36% of total data variance, with 51.50% attributed to the first (PC1) and 31.85% to the second (PC2). PC1 was associated with C3UA, caspase-3/7 activity in normal blood cells and CLS-354 tumor cells, and ROS levels in CLS-354 tumor cells. At the same time, PC2 was related to F-UBO bioadhesive oral films, C1DMSO, and ROS levels in normal blood cells (Figure 12).

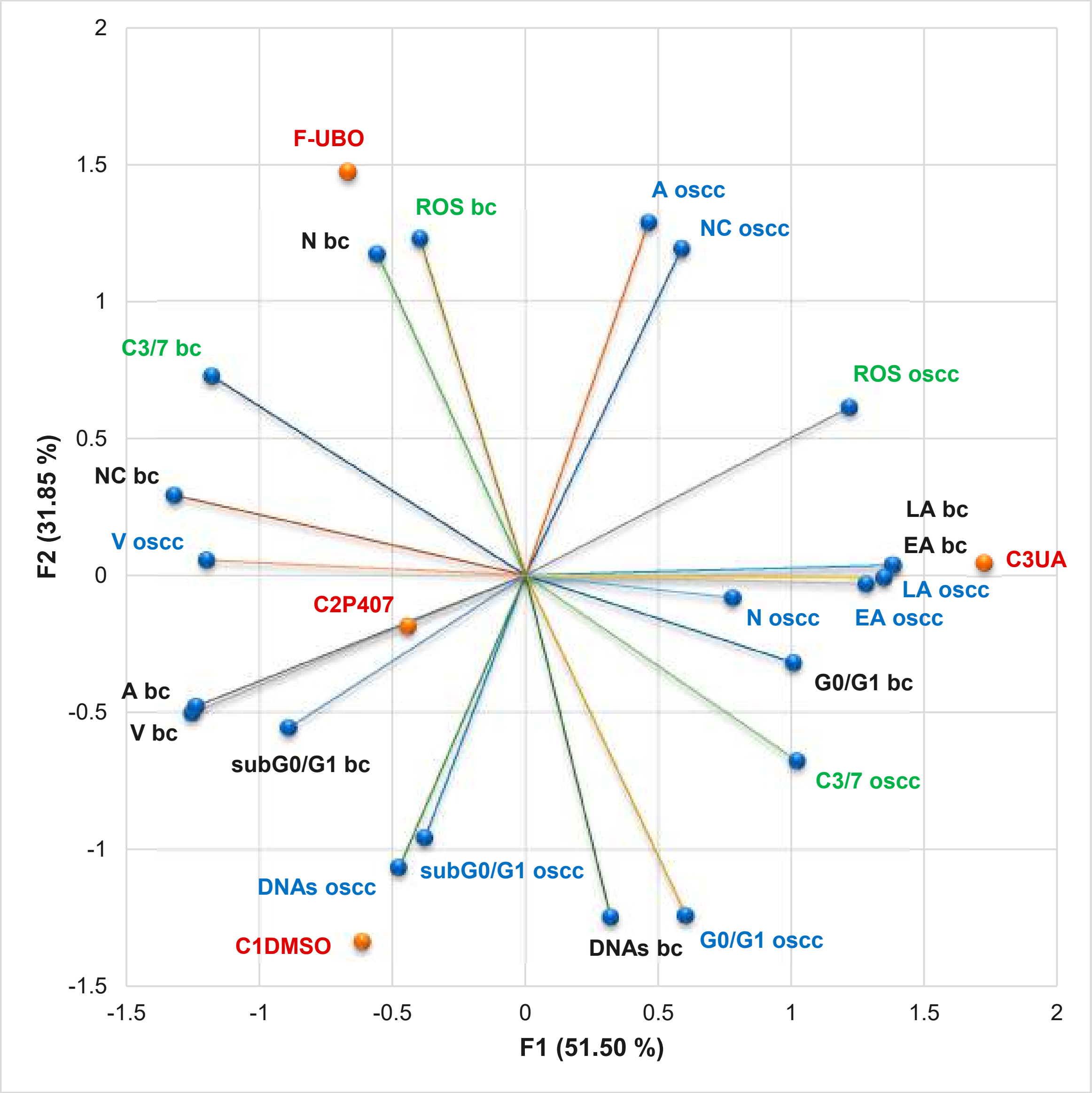

Figure 12. PCA-correlation biplot between mechanisms (caspase-3/7 activity and cellular oxidative stress) and processes induced by F-UBO and controls (C1DMSO, C2P407, and C2UA) in normal blood cells (bc) and CLS-354 tumor cells (oscc). V—viability; EA—early apoptosis; LA—late apoptosis; N—necrosis; NC—nuclear condensation; A—autophagy; DNAs—DNA synthesis; subG0/G1—apoptotic cell fraction; G0/G1—cell cycle arrest in G0/G1; ROS—oxidative stress; C3/7—caspase-3/7 activity.

In normal blood cells, caspase-3/7 activation shows a high positive correlation with nuclear condensation ($r = 0.921$, $p > 0.05$), a moderate one with necrosis ($r = 0.786$, $p > 0.05$), ROS levels ($r = 0.708$, $p > 0.05$), and autophagy ($r = 0.581$, $p > 0.05$), and a low one with apoptotic cell fraction (subG0/G1, $r = 0.382$, $p > 0.05$). This mechanism is highly negatively correlated with EA and LA (r = −0.835, $p > 0.05$) and moderate with a cell cycle arrest in G0/G1 phase and DNA synthesis (r = −0.741 and −0.669, $p > 0.05$). The cellular oxidative stress reported a considerable positive correlation with necrosis ($r = 0.992$, $p < 0.05$), and a low one with nuclear condensation ($r = 0.540$, $p > 0.05$).

In CLS-354 tumor cells, caspase-3/7 activation is highly positively correlated with cell cycle arrest in G0/G1 phase ($r = 0.800$, $p > 0.05$), and low with ROS level ($r = 0.513$, $p > 0.05$). However, oxidative stress (expressed as ROS level) shows a high and moderate positive correlation with the most damaging processes in OSCC cells. It displays a high correlation with late apoptosis and nuclear condensation ($r = 0.812$ and 0.802, $p > 0.05$), and a moderate one with early apoptosis and autophagy ($r = 0.739$ and 0.733, $p > 0.05$).

Data analysis shows that F-UBO acts on CLS-354 cells, inducing the highest levels of nuclear condensation and autophagy compared to all controls. Moreover, nuclear condensation and autophagy triggered by F-UBO display higher levels in OSCC cells than in normal blood ones. F-UBO also causes the most elevated oxidative stress in normal blood cells compared to controls. However, F-UBO significantly diminishes the apoptotic cell fraction (subG0/G1) and autophagy (A) and slowly decreases the cell cycle arrest in G0/G1, triggered in normal cells by 1% DMSO.

Usnic acid, the main secondary metabolite of *U. barbata* lichens, induced the highest oxidative stress and caspase-3/7 activation in OSCC cells, leading to the most substantial cellular apoptosis. It highlights a significant protective effect on normal blood cells, appreciably diminishing caspase-3/7 activation, nuclear condensation, and autophagy determined by 1% DMSO, thus reducing apoptotic cell fraction (subG0/G1).

In the present study, 5% P407, the emulsifier used in the F-UBO formulation, was selected as a positive control. It significantly acts on OSCC cells, determining cellular apoptosis by triggering all mechanisms that lead to cancer cell death. Moreover, it induces the highest DNA synthesis compared to F-UBO and controls. In normal blood cells, it generates oxidative stress and caspase-3/7 activation after 24 h of treatment, but the cell viability is not significantly affected.

By correlating and interpreting these data, the places of F-UBO and controls (C1DMSO, C2P407, and C3UA) in the PCA-correlation biplot (Figure 12) were justified, evidencing the corresponding processes triggered in CLS-354 cancer cells and normal blood cells.

4. Discussion

The previous UBO analysis measured the heavy metals content, quantified the active constituents (UA content = 0.915 ± 0.018 mg/g UBO), explored the antioxidant, cytotoxic, and rheological properties, and then proved its suitability for pharmaceutical formulation [26].

The use of HPMC in a 15% aqueous dispersion ensured the suitable film toughness, while 5% PEG 400 provided an elegant, glossy, smooth appearance and high flexibility. The film's homogeneity proved that the active ingredients were adequately incorporated into the polymer matrix, emulsifying the oil extract. All formulations led to a thin and uniform film, suitable characteristics for bioadhesive performance, and a comfortable administration.

The low variation in weight and thickness guarantees the efficiency of the formulation and applied method and provides a certain uniformity of content. The results obtained for film thickness agree with other developed studies on HPMC films [74]. Both types of formulations proved to have weight and thickness suitable for application to the oral mucosa [36,74,75].

Regarding the mechanical properties of both bioadhesive oral films (F-UBO and R), the differences between formulations are not substantial because they contain identical amounts of HPMC and PEG 400.

Thus, the film's flexibility is mandatory for easy handling and administration. It is induced by the plasticizer used in the formulation and the film-forming polymer [76]. Semalty M. et al. [77] proved that mixing HPMC with PEG 400 in 30% of the weight of the polymer leads to low folding endurance and that the optimal plasticizer is PEG, used in low concentrations. In the present study, using PEG 400 in a 5% concentration led to the excellent flexibility of both film types. The plasticizer reduces the film's rigidity by decreasing the intermolecular forces [78]. Still, it was proven that high amounts of plasticizer might diminish the film adhesive properties by over-hydration [79].

F-UBO contains the active ingredient emulsified in the polymer matrix, leading to its physical interruption and a suitable elasticity. The disruption of polymer molecular chains induces higher chain mobility, augmenting flexibility and diminishing rigidity. Maher et al. [80] proved the influence of the polymer type (including HPMC) on the film's tensile strength. It was also confirmed that the tensile strength increases with the film-forming polymer concentration. It was observed that 15% HPMC water dispersion conducts to the development of a strong matrix with a sufficiently dense network. The obtained results show that even if the film-forming agent and the plasticizer have the primary influence on the film's mechanical attributes, other factors, such as the active ingredient nature or concentration and its dispersion type, affect the bioadhesive film's strength. The data obtained in this study show that F-UBO's elongation and tensile strength are adequate to resist stress during handling [81].

The moisture content ensures the suitable film's mechanical properties. It influences the film's friability; however, both formulations (F-UBO and R) display good resistance. The moisture can be due to the solvent system used in the formulation or to the ingredients' hygroscopic properties, especially the plasticizer ones [82]. PEG 400 presents high hygroscopicity due to its hydrophilic hydroxyl groups interacting with water [83], providing more sites for interactions and leading to moisture retention in the films. HPMC also has hydrophilic hydroxypropyl substituents, but contains hydrophobic methoxyl groups and does not maintain excessive moisture [84]. Bioadhesive oral films must have a moderate moisture content to ensure their elasticity and protection from being brittle, dry, and easy to break [85], and F-UBO and R show suitable humidity.

Each ingredient influences the film's pH value in the formulation. The purpose is to properly select the components to obtain bioadhesive films with a surface pH close to the buccal one. F-UBO shows an approximately neutral pH on the surface, close to the oral cavity, ensuring good tolerability with no possible irritation of the buccal mucosa. In this work, both films have similar pH values, proving that the active ingredients do not modify the pH of the matrix system.

The formulation's disintegration time strongly depends on the polymer matrix. Shen et al. [86] demonstrated that the film's disintegration time rises directly proportional to HPMC concentration. The results show that F-UBO's rapid disintegration allows a fast release of active ingredients, suitable for in vitro studies.

The film's swelling properties are essential for bioadhesion [87] and highly depend on water diffusivity into the polymer [88]. The residence time [41,42] also depends on the film-forming polymer and the plasticizer's retention properties, being highly controlled by the ratio between them [89]. The disturbance of the polymer chains by including active ingredients in the matrix decreases the water content [90] and considerably influences the bioadhesive behavior. Adhesion is enhanced with increasing hydration until it reaches an optimum point. Overhydration causes the breaking of the polymer/tissue interface, thus decreasing the bioadhesive force. The values registered for ex vivo residence time are strongly related to the film's in vivo bioadhesive performance, and results were satisfactory for F-UBO.

Generally, the differences between UBO-loaded bioadhesive oral films and references are not statistically significant, proving that UBO does not considerably influence these previously mentioned properties.

On the other hand, P407, the emulsifier from the F-UBO formulation, is most known for its use as a surfactant in various oral hygiene products (dentifrices, mouthwashes, breath fresheners) in a concentration range of 0.3–20% [91]. Furthermore, it is particularly interesting in clinical use for surgical application due to its thermoreversible gelation and bactericidal effects on *S. aureus* [92]. Veyries et al. [93] revealed the potential of P407 for inhibiting the attachment of *S. aureus* and *S. epidermidis* and increasing their susceptibility to antibiotics once they are adherent. This study results show the significant antifungal potential of 5% P407 in water against *C. albicans* and *C. parapsilosis.*

Teanpaisan et al. [94] proposed a mixture of P407 and *Artocarpus lakoocha* (*Moraceae*) for endodontic treatment, proving its antibacterial activity against *E. fecalis.* Recently, another study proved antifungal activity of a hydroethanolic extract from *Astronium urundeuva* leaves loaded into a nanostructured lipid system with 0.5% P407® against *C. albicans* and *C. glabrata* [95]. Previous studies [96,97] included the most common oral cavity pathogens responsible for various opportunistic infections in immunocompromised patients, *S. aureus*, *P. aeruginosa*, and *C. albicans.* Our F-UBO oral biofilms revealed a dose-dependent inhibitory activity against *S. aureus*, *P. aeruginosa*, *C. albicans*, and *C. parapsilosis.*

The BSL cytotoxicity assay is one of the most known methods, using *Artemia* sp.—*A. salina* [26] and *A. franciscana* [98]. Together with phytotoxicity assay on *Triticum aestivum* L.—which evaluates the *Triticum* radicle growth [99], the BSL assay is considered a rapid, simple, low-cost, and effective test to estimate various natural products' safety for human use [100]. Okumu et al. [49] recently used *A. salina* as an animal model for the preliminary evaluation of snake-venom-induced toxicity. Nazir et al. [101] proved that the BSL assay is a significant antitumor prescreening in anticancer drug discovery. Rajabi et al. [102] described *Artemia salina* as a model organism in the toxicity assessment of nanoparticles. The present study used the BSL assay to evaluate the F-UBO cytotoxic potential, and the obtained results could be extrapolated to those on tumor cells.

Previous studies regarding the various poloxamer types' cytotoxicity on tumor cells reported a dose-dependent action. Thus, a concentration of 30 ± 10 mg/mL of poloxamer 188 inhibited 50% of HeLa (cervical cancer) cell growth, whereas a dose 10 times lower (2–5 mg/mL) was necessary to inhibit 50% of B-16 (mouse melanoma) cell growth [91]. In this study, 50 mg/mL P407 reduced the viability of CLS-354 (oral cancer) cells to 72.51 ± 2.51% after 24 h incubation. F-UBO dispersion led to 315 µg/mL UBO and 3.15 mg/mL P407; UBO penetrated rapidly through the cell wall in emulsified form, then the onset of apoptotic processes after 24 h of treatment could be explained. The F-UBO complex composition suggests a synergy between *U. barbata* secondary metabolites with pharmacological properties [103,104], canola oil's bioactive constituents [105], and P407 [106,107].

5. Conclusions

This study evaluated the pharmacological potential of the *U. barbata* (L.) Weber ex F.H. Wigg extract in canola oil (UBO) as an oral pharmaceutical formulation.

The UBO-loaded bioadhesive oral films were manufactured using P407, HPMC, and PEG 400 for their formulation. F-UBO suitability for topical administration on buccal mucosa was confirmed through complex physicochemical and pharmacotechnical analyses.

F-UBO antimicrobial and anticancer properties were investigated using P407 as a positive control. Data obtained revealed F-UBO and P407 dose-dependent inhibitory activity against the most common bacterial and fungal pathogens implied in immunosuppressed patients' oral infections. Moreover, they highlighted in vitro antitumor effects on oral epithelial squamous cell carcinoma (CLS-354 cell line).

The present research suggests that bioadhesive oral films with *U. barbata* extract in canola oil can be considered a phytotherapeutic formulation with potential applications against oral cavity infections and neoplasia. In vivo and clinical studies could be further steps in F-UBO analysis to confirm their medical benefits.

Supplementary Materials: The supporting information regarding principal component analysis and antimicrobial activity can be downloaded at: https://www.mdpi.com/article/10.3390/antiox11081601/s1: Table S1. The inhibitory activity of F-UBO on Gram-positive (*S. aureus*) and Gram-negative bacteria (*P. aeruginosa*) after 24 h incubation at 37 °C. CTR—ceftriaxone, F-UBO—bioadhesive oral film with *U. barbata* extract in canola oil; * results interpreted by using resazurin dye chart, adapted from Madushan et al. [46] as follows: blue—"excellent"; light blue—"very good"; violet—"good"; purple-pink—"moderate"; light pink—"low"; pink—"very low"; white—"no effect". Table S2. The antibacterial and antifungal activities of 5% P407. CTR—ceftriaxone, P407—poloxamer 407, TRF—terbinafine. * Results interpreted by using resazurin dye chart, adapted from Madushan et al. [46] as follows: blue—"excellent"; light blue—"very good"; violet—"good"; purple-pink—"moderate"; light pink—"low"; pink—"very low"; white—"no effect" (a–d). ** Results interpreting adapted from Bitacura et al. [48] (e–h). Table S3. The inhibitory activity of F-UBO on *C. albicans* and *C. parapsylosis* after 24 h incubation at 35 °C; the color score and signification [48]. TRF—terbinafine, F-UBO—bioadhesive films with *U. barbata* extract in canola oil. ** Results interpreting adapted from Bitacura et al. [48].

Author Contributions: Conceptualization, V.P., E.M., G.C.C., C.E.G., L.B., V.S. and E.A.O.; methodology, E.M., G.C.C., L.B., V.S., E.A.O., A.M.M., D.L. and M.A. (Mariana Aschie); software, V.P., E.M., V.S., E.A.O., O.K. and S.P.; validation, E.M., G.C.C., L.B., C.E.G., E.A.O., O.K., A.M.M. and V.B.; formal analysis, A.M.M., S.P., I.A., A.R., R.-A.M. and M.A. (Mihai Anastasescu); investigation, C.E.G., O.K., A.M.M., S.P., I.A., A.R. and R.-A.M.; resources, V.P., L.B., V.S., D.L. and M.A. (Mariana Aschie); data curation, G.C.C., O.K. and A.M.M.; writing—original draft preparation, V.P., E.M., E.A.O., V.S. and A.M.M.; writing—review and editing, V.P., E.M., E.A.O. and A.M.M.; visualization, G.C.C., L.B., C.E.G., A.C., D.L., M.A. (Mariana Aschie) and V.B.; supervision, G.C.C., L.B., C.E.G., D.L., M.A. (Mariana Aschie) and V.B.; project administration, V.B.; funding acquisition, V.P. and O.K. All authors have read and agreed to the published version of the manuscript.

Funding: This research was supported by the project ANTREPRENORDOC, in the framework of Human Resources Development Operational Programme 2014–2020, financed from the European Social Fund under the contract number 36355/23.05.2019 HRD OP/380/6/13—SMIS Code: 123847. The APC was funded by the Carol Davila University of Medicine and Pharmacy, Bucharest, Romania.

Institutional Review Board Statement: The study was conducted in accordance with the Declaration of Helsinki and approved by the Institutional Ethics Committee of Ovidius University of Constanta, code 7080/10.06.2021 for studies involving humans.

Informed Consent Statement: Written informed consent has been obtained from the blood donor to publish this paper, code 39/30.06.2021.

Data Availability Statement: Data are contained within the manuscript.

Acknowledgments: This project was performed in collaboration with the Department of Pharmaceutical Technology and Biopharmacy, and the Department of Pharmacognosy, Phytochemistry, and Phytotherapy, Faculty of Pharmacy, Carol Davila University of Medicine and Pharmacy, 6 Traian Vuia Street, 020956 Bucharest, Romania, the Institute of Physical Chemistry, Ilie Murgulescu, 202 Splaiul Independentei Street, 060021. Bucharest, Romania, and the Center for Research and Development of the Morphological and Genetic Studies of Malignant Pathology, Ovidius University of Constanta, CEDMOG, 145 Tomis Blvd., 900591 Constanta, Romania.

Conflicts of Interest: The authors declare no conflict of interest.

References

1. Mansoor, N.R.; Sanmugarajah, V. A Literature Review on Medicinal Plants that are being Used in Traditional Medicine for the Management of the Snake Bites in Sri Lanka. *Asian Plant Res. J.* **2018**, *1*, 1–18. [CrossRef]
2. Davison, K.J.; Marinelli, R. Ethnobotany: Plant-Derived Medical Therapy. In *Auerbach's Wilderness Medicine*, 7th ed.; Auerbach, P.S., Ed.; Elsevier, Inc.: Amsterdam, The Netherlands, 2017; pp. 1502–1528.
3. Shrestha, G.; St. Clair, L.L. Lichens: A promising source of antibiotic and anticancer drugs. *Phytochem. Rev.* **2013**, *12*, 229–244. [CrossRef]
4. Chae, H.J.; Kim, G.J.; Deshar, B.; Kim, H.J.; Shin, M.J.; Kwon, H.; Youn, U.J.; Nam, J.W.; Kim, S.H.; Choi, H.; et al. Anticancer activity of 2-o-caffeoyl alphitolic acid extracted from the lichen *Usnea barbata* 2017-kl-10. *Molecules* **2021**, *26*, 3937. [CrossRef] [PubMed]
5. Sharma, B.; Bhat, M. Ethnobiology, Phytochemistry and Pharmacology of *Usnea Longissima* a Review. *Int. J. Sci. Res. Biol. Sci.* **2019**, *6*, 263–269. [CrossRef]
6. Alahmadi, A.A. Usnic acid biological activity: History, evaluation and usage. *Int. J. Basic Clin. Pharmacol.* **2017**, *6*, 2752. [CrossRef]
7. Favreau, J.T.; Ryu, M.L.; Braunstein, G.; Orshansky, G.; Park, S.S.; Coody, G.L.; Love, L.A.; Fong, T.L. Severe hepatotoxicity associated with the dietary supplement LipoKinetix. *Ann. Intern. Med.* **2002**, *136*, 590–595. [CrossRef]
8. Pacheco, D.; Travassos, A.R.; Antunes, J.; Soares de Almeida, L.; Filipe, P.; Correia, T. Occupational airborne contact dermatitis caused by usnic acid in a domestic worker. *Allergol. Immunopathol.* **2014**, *42*, 80–82. [CrossRef]
9. Rafanelli, S.; Bacchillga, R.; Stanganelli, I.; Rafanelli, A. Contact dermatitis from usnic acid in vaginal ovules. *Contact Dermat.* **1995**, *33*, 271. [CrossRef]
10. Wakefield, M.E. Chinese Topical Herbal Treatments and Essential Oil Protocols. In *Constitutional Facial Acupuncture*; Churchill Livingstone: London, UK, 2014; pp. 277–334.
11. Sepahvand, A.; Studzińska-Sroka, E.; Ramak, P.; Karimian, V. *Usnea* sp.: Antimicrobial potential, bioactive compounds, ethnopharmacological uses and other pharmacological properties; a review article. *J. Ethnopharmacol.* **2021**, *268*, 113656. [CrossRef]
12. Prateeksha; Paliya, B.S.; Bajpai, R.; Jadaun, V.; Kumar, J.; Kumar, S.; Upreti, D.K.; Singh, B.R.; Nayaka, S.; Joshi, Y.; et al. The genus *Usnea:* A potent phytomedicine with multifarious ethnobotany, phytochemistry and pharmacology. *RSC Adv.* **2016**, *6*, 21672–21696. [CrossRef]

13. Popovici, V.; Bucur, L.; Popescu, A.; Schröder, V.; Costache, T.; Rambu, D.; Cucolea, I.E.; Gîrd, C.E.; Caraiane, A.; Gherghel, D.; et al. Antioxidant and cytotoxic activities of *Usnea barbata* (L.) F.H. Wigg. Dry extracts in different solvents. *Plants* **2021**, *10*, 909. [CrossRef] [PubMed]
14. Behera, B.C.; Verma, N.; Sonone, A.; Makhija, U. Optimization of culture conditions for lichen *Usnea ghattensis* G. Awasthi to increase biomass and antioxidant metabolite production. *Food Technol. Biotechnol.* **2009**, *47*, 7–12.
15. Ranjit, R.; Shrestha, R.; Paudel, S.; Maharjan, J.; Devkota, B.D.; Bhattarai, S.; Pandey, B.P. Evaluation of biological properties and isolation of metabolites of lichens of *Parmeliaceae* family from himalayan region of nepal. *Trop. J. Nat. Prod. Res.* **2019**, *3*, 265–271. [CrossRef]
16. Mesta, A.R.; N, R.; Kanivebagilu, V.S. Assessment of Antimicrobial Activity of Ethanolic Extraction of *Usnea Ghattensis* and Usnea Undulata. *Int. J. Res. Ayurveda Pharm.* **2020**, *11*, 75–77. [CrossRef]
17. Ivanovic, J.; Meyer, F.; Misic, D.; Asanin, J.; Jaeger, P.; Zizovic, I.; Eggers, R. Influence of different pre-treatment methods on isolation of extracts with strong antibacterial activity from lichen *Usnea barbata* using carbon dioxide as a solvent. *J. Supercrit. Fluids* **2013**, *76*, 1–9. [CrossRef]
18. Popovici, V.; Bucur, L.; Calcan, S.I.; Cucolea, E.I.; Costache, T.; Rambu, D.; Schröder, V.; Gîrd, C.E.; Gherghel, D.; Vochita, G.; et al. Elemental Analysis and in Vitro Evaluation of Antibacterial and Antifungal Activities of *Usnea barbata* (L.) Weber ex F.H. Wigg from C ă limani Mountains, Romania. *Plants* **2022**, *11*, 32. [CrossRef]
19. Çelikler Kasimoğullari, S.; Oran, S.; Ari, F.; Ulukaya, E.; Aztopal, N.; Sarimahmut, M.; Öztürk, Ş. Genotoxic, cytotoxic, and apoptotic effects of crude extract of Usnea filipendula Stirt. in vitro. *Turk. J. Biol.* **2014**, *38*, 940–947. [CrossRef]
20. Tram, N.T.T.; Anh, D.H.; Thuc, H.H.; Tuan, N.T. Investigation of chemical constituents and cytotoxic activity of the lichen *Usnea undulata*. *Vietnam J. Chem.* **2020**, *58*, 63–66. [CrossRef]
21. Zugic, A.; Jeremic, I.; Isakovic, A.; Arsic, I.; Savic, S.; Tadic, V. Evaluation of anticancer and antioxidant activity of a commercially available CO2 supercritical extract of old man's beard (*Usnea barbata*). *PLoS ONE* **2016**, *11*, e0146342. [CrossRef]
22. Matvieieva, N.A.; Pasichnyk, L.A.; Zhytkevych, N.V.; Jacinto, P.G.; Pidgorskyi, V.S. Antimicrobial Activity of Extracts from Ecuadorian Lichens. *Mikrobiol. Z.* **2015**, *77*, 23–27. [CrossRef]
23. Prabhu, S.S.; Sudha, S.S. Evaluation of the antibacterial properties of some Lichen species against human pathogens. *Int. J. Adv. Res. Biol. Sci.* **2015**, *2*, 177–181.
24. Žugić, A.; Isaković, A.; Jeremić, I.; Savić, S.; Tadić, V. Cytotoxic activity of supercritical CO2 extract of old man's beard in L929 fibrosarcoma cell line. *Lek. Sirovine* **2019**, *39*, 30–34. [CrossRef]
25. Nandasiri, R.; Eskin, N.A.M.; Eck, P.; Thiyam-Höllander, U. Application of Green Technology on Extraction of Phenolic Compounds in Oilseeds (Canola). In *Cold Pressed Oils*; Ramadan, M.F., Ed.; Elsevier Inc.: Amsterdam, The Netherlands, 2020; pp. 81–96.
26. Popovici, V.; Bucur, L.; Gîrd, C.E.; Rambu, D.; Calcan, S.I.; Cucolea, E.I.; Costache, T.; Ungureanu-Iuga, M.; Oroian, M.; Mironeasa, S.; et al. Antioxidant, Cytotoxic, and Rheological Properties of Canola Oil Extract of *Usnea barbata* (L.) Weber ex F.H. Wigg from Călimani Mountains, Romania. *Plants* **2022**, *11*, 854. [CrossRef]
27. Tadić, V.; Žugić, A.; Đorđević, S.; Žižović, I.; Homšek, I.; Mišić, D.; Nešić, I. The RP-HPLC method for analysis of usnic acid as potential marker of herbal drugs-based formulations containing *Usnea barbata*. *J. Serbian Chem. Soc.* **2022**, *71*, 45. [CrossRef]
28. Al-Ani, E.; Heaselgrave, W. The Investigation of Thymol Formulations Containing Poloxamer 407 and Hydroxypropyl Methylcellulose to Inhibit Candida Biofilm Formation and Demonstrate Improved Bio-Compatibility. *Pharmaceuticals* **2022**, *15*, 71. [CrossRef]
29. Basiouni, S.; Fayed, M.A.A.; Tarabees, R.; El-Sayed, M.; Elkhatam, A.; Töllner, K.R.; Hessel, M.; Geisberger, T.; Huber, C.; Eisenreich, W.; et al. Characterization of sunflower oil extracts from the lichen *Usnea barbata*. *Metabolites* **2020**, *10*, 353. [CrossRef]
30. Ding, C.; Zhang, M.; Li, G. Preparation and characterization of collagen/hydroxypropyl methylcellulose (HPMC) blend film. *Carbohydr. Polym.* **2015**, *119*, 194–201. [CrossRef]
31. Gavriloaia, M.R.; Budura, E.A.; Toma, C.C.; Mitu, M.A.; Karampelas, O.; Arama, C.; Lupuleasa, D. In vitro evaluation of diffusion and rheological profiles for dexamethasone inclusion complexes with β-cyclodextrin or hydroxypropyl β-cyclodextrin. *Farmacia* **2012**, *60*, 895–904.
32. Mănescu, O.; Lupuleasa, D.; Miron, D.S.; Budura, E.A.; Rădulescu, F.Ş. In vitro drug release from topical antifungal pharmaceutical formulations. *Farmacia* **2011**, *59*, 15–23.
33. Domján, A.; Bajdik, J.; Pintye-Hódi, K. Understanding of the plasticizing effects of glycerol and PEG 400 on chitosan films using solid-state NMR spectroscopy. *Macromolecules* **2009**, *42*, 4667–4673. [CrossRef]
34. Musuc, A.M.; Anuta, V.; Atkinson, I.; Sarbu, I.; Popa, V.T.; Munteanu, C.; Mircioiu, C.; Ozon, E.A.; Nitulescu, G.M.; Mitu, M.A. Formulation of chewable tablets containing carbamazepine-β-cyclodextrin inclusion complex and f-melt disintegration excipient. The mathematical modeling of the release kinetics of carbamazepine. *Pharmaceutics* **2021**, *13*, 915. [CrossRef] [PubMed]
35. Nafee, N.A.; Ismail, F.A.; Boraie, N.A.; Mortada, L.M. Mucoadhesive buccal patches of miconazole nitrate: In vitro/in vivo performance and effect of ageing. *Int. J. Pharm.* **2003**, *264*, 1–14. [CrossRef]
36. Perioli, L.; Ambrogi, V.; Angelici, F.; Ricci, M.; Giovagnoli, S.; Capuccella, M.; Rossi, C. Development of mucoadhesive patches for buccal administration of ibuprofen. *J. Control. Release* **2004**, *99*, 73–82. [CrossRef] [PubMed]
37. Don, T.M.; Huang, M.L.; Chiu, A.C.; Kuo, K.H.; Chiu, W.Y.; Chiu, L.H. Preparation of thermo-responsive acrylic hydrogels useful for the application in transdermal drug delivery systems. *Mater. Chem. Phys.* **2008**, *107*, 266–273. [CrossRef]

38. Derle, D.; Joshi, O.; Pawar, A.; Patel, J.; Perdeshi, V. Effect of tablet excipients on mucoadhesive properties of polyoxyethylene and Carbopol 971P. *Int. J. Pharm. Pharm. Sci.* **2009**, *1*, 198–205.
39. Ahuja, M.; Kumar, S.; Kumar, A. Evaluation of mucoadhesive potential of gum cordia, an anionic polysaccharide. *Int. J. Biol. Macromol.* **2013**, *55*, 109–112. [CrossRef]
40. Gupta, A.; Garg, S.; Khar, R.K. Measurement of bioadhesive strength of mucoadhesive buccal tablets: Design of an in-vitro assembly. *Indian Drugs* **1993**, *30*, 1–6.
41. Samanthula, K.S.; Cb, M.K.; Bairi, A.G.; Satla, S.R. Development, in-Vitro and ex-Vivo Evaluation of Muco-Adhesive Buccal Tablets of Hydralazine Hydrochloride. *Braz. J. Pharm. Sci.* **2022**, *58*, e18635. [CrossRef]
42. Baus, R.A.; Haug, M.F.; Leichner, C.; Jelkmann, M.; Bernkop-Schnürch, A. In Vitro-in Vivo Correlation of Mucoadhesion Studies on Buccal Mucosa. *Mol. Pharm.* **2019**, *16*, 2719–2727. [CrossRef]
43. Estrellas, K.M.; Fiecas, M.; Azagury, A.; Laulicht, B.; Cho, D.Y.; Mancini, A.; Reineke, J.; Furtado, S.; Mathiowitz, E. Time-dependent mucoadhesion of conjugated bioadhesive polymers. *Colloids Surf. B Biointerfaces* **2019**, *173*, 454–469. [CrossRef]
44. Schug, A.R.; Bartel, A.; Scholtzek, A.D.; Meurer, M.; Brombach, J.; Hensel, V.; Fanning, S.; Schwarz, S.; Feßler, A.T. Biocide susceptibility testing of bacteria: Development of a broth microdilution method. *Vet. Microbiol.* **2020**, *248*, 108791. [CrossRef] [PubMed]
45. Fathi, F.; Ghobeh, M.; Tabarzad, M. Anti-Microbial Peptides: Strategies of Design and Development and their Promising Wound-Healing Activities. *Mol. Biol. Rep.* **2022**, *8*, 1–12. [CrossRef] [PubMed]
46. Madushan, R.; Vidanarachchi, J.K.; Prasanna, P.H.P.; Werellagama, S.; Priyashantha, H. Use of natural plant extracts as a novel microbiological quality indicator in raw milk: An alternative for resazurin dye reduction method. *LWT* **2021**, *144*, 111221. [CrossRef]
47. Cox, K.D.; Quello, K.; Deford, R.J.; Beckerman, J.L. A rapid method to quantify fungicide sensitivity in the brown rot pathogen Monilinia fructicola. *Plant Dis.* **2009**, *93*, 328–331. [CrossRef] [PubMed]
48. Bitacura, J.G. The Use of Baker's Yeast in the Resazurin Reduction Test: A Simple, Low-Cost Method for Determining Cell Viability in Proliferation and Cytotoxicity Assays. *J. Microbiol. Biol. Educ.* **2018**, *19*, jmbe-19–87. [CrossRef]
49. Okumu, M.O.; Mbaria, J.M.; Gikunju, J.K.; Mbuthia, P.G.; Madadi, V.O.; Ochola, F.O.; Jepkorir, M.S. *Artemia salina* as an animal model for the preliminary evaluation of snake venom-induced toxicity. *Toxicon X* **2021**, *12*, 100082. [CrossRef]
50. Schröder, V.; Arcus, M.; Anghel, A.H.; Busuricu, F.; Lepadatu, A.C. Cell differentiation process of *Artemia* sp. larvae tools for natural products testing. *Sci. Pap. Ser. D Anim. Sci.* **2019**, *62*, 149–153.
51. Iancu, I.M.; Bucur, L.A.; Schroder, V.; Mireșan, H.; Sebastian, M.; Iancu, V.; Badea, V. Phytochemical evaluation and cytotoxicity assay of *Lythri herba* extracts. *Farmacia* **2021**, *69*, 51–58. [CrossRef]
52. Matei, E.; Aschie, M.; Mitroi, A.F.; Ghinea, M.M.; Gheorghe, E.; Petcu, L.; Dobrin, N.; Chisoi, A.; Mihaela, M. Biomarkers involved in evaluation of platelets function in South-Eastern Romanian patients with hematological malignancies subtypes. *Medicine* **2021**, *100*, e25944. [CrossRef]
53. Popovici, V.; Matei, E.; Cozaru, G.C.; Aschie, M.; Bucur, L.; Rambu, D.; Costache, T.; Cucolea, I.E.; Vochita, G.; Gherghel, D.; et al. Usnic acid and *Usnea barbata* (L.) F.H. Wigg. dry extracts promote apoptosis and DNA damage in human blood cells through enhancing ROS levels. *Antioxidants* **2021**, *10*, 1171. [CrossRef]
54. Utaipan, T.; Athipornchai, A.; Suksamrarn, A.; Jirachotikoon, C.; Yuan, X.; Lertcanawanichakul, M.; Chunglok, W. Carbazole alkaloids from Murraya koenigii trigger apoptosis and autophagic flux inhibition in human oral squamous cell carcinoma cells. *J. Nat. Med.* **2017**, *71*, 158–169. [CrossRef] [PubMed]
55. Staib, P.; Tiehen, J.; Strunk, T.; Schinköthe, T. Determination of caspase-3 activation fails to predict chemosensitivity in primary acute myeloid leukemia blasts. *BMC Cancer* **2005**, *5*, 60. [CrossRef] [PubMed]
56. Ionescu, C.; Aschie, M.; Matei, E.; Cozaru, G.C.; Deacu, M.; Mitroi, A.F.; Baltatescu, G.I.; Nicolau, A.; Mazilu, L.; Tuta, L.A.; et al. Characterization of the Tumor Microenvironment and the Biological Processes with a Role in Prostatic Tumorigenesis. *Biomedicines* **2022**, *10*, 1672. [CrossRef] [PubMed]
57. Garala, K.; Joshi, P.; Patel, J.; Ramkishan, A.; Shah, M. Formulation and evaluation of periodontal in situ gel. *Int. J. Pharm. Investig.* **2013**, *3*, 29. [CrossRef] [PubMed]
58. Iqbal, F.M.; Ahmad, M.; Tulain, U.R. Microwave radiation induced synthesis of hydroxypropyl methylcellulose-graft-(polyvinylalcohal-co-acrylic acid) polymeric network and its in vitro evaluation. *Acta Pol. Pharm. -Drug Res.* **2017**, *74*, 527–541.
59. Shetty, G.R.; Rao, B.L.; Asha, S.; Wang, Y.; Sangappa, Y. Preparation and characterization of silk fibroin/hydroxypropyl methyl cellulose (HPMC) blend films. *Fibers Polym.* **2015**, *16*, 1734–1741. [CrossRef]
60. Popovici, V.; Bucur, L.; Gîrd, C.E.; Calcan, S.I.; Cucolea, E.I.; Costache, T.; Rambu, D.; Oroian, M.; Mironeasa, S.; Schröder, V.; et al. Advances in the Characterization of *Usnea barbata* (L.) Weber ex F.H. Wigg from Călimani Mountains, Romania. *Appl. Sci.* **2022**, *12*, 4234. [CrossRef]
61. Kamoun, E.A.; Youssef, M.E.; Abu-Saied, M.A.; Fahmy, A.; Khalil, H.F.; Abdelhai, F. Ion conducting nanocomposite membranes based on PVA-HA-HAP for fuel cell application: II. Effect of modifier agent of PVA on membrane properties. *Int. J. Electrochem. Sci.* **2015**, *10*, 6627–6644.
62. Zhang, L.; Lu, Y.Q.; Peng, Y.L.; Yu, Y.X.; Zhao, Y.; Ma, Y.; Qian, J.Y. Microstructures and properties of photophobic films composed of hydroxypropyl methylcellulose and different salts. *Int. J. Biol. Macromol.* **2018**, *120*, 945–951. [CrossRef]

63. Jillani, U.; Mudassir, J.; Ijaz, Q.A.; Latif, S.; Qamar, N.; Aleem, A.; Ali, E.; Abbas, K.; Wazir, M.A.; Hussain, A.; et al. Design and Characterization of Agarose/HPMC Buccal Films Bearing Ondansetron HCl in Vitro and in Vivo: Enhancement Using Iontophoretic and Chemical Approaches. *BioMed Res. Int.* **2022**, *2022*, 1662194. [CrossRef]
64. Ellakwa, T.E.; Fahmy, A.; Ellakwa, D.E. Influence of poloxamer on the dissolution properties of mosapride and its pharmaceutical tablet formulation. *Egypt. J. Chem.* **2017**, *60*, 443–451.
65. Vlad, R.A.; Antonoaea, P.; Todoran, N.; Muntean, D.L.; Rédai, E.M.; Silași, O.A.; Tătaru, A.; Bîrsan, M.; Imre, S.; Ciurba, A. Pharmacotechnical and analytical preformulation studies for cannabidiol orodispersible tablets. *Saudi Pharm. J.* **2021**, *29*, 1029–1042. [CrossRef]
66. European Economic Community. *Specifications and Control Tests on the Test Procedures Batch Analysis Specifications and Control Tests*; European Medicines Agency: Amsterdam, The Netherlands, 1992; pp. 83–94.
67. Kavanagh, A.; Ramu, S.; Gong, Y.; Cooper, M.A.; Blaskovich, M.A.T. Effects of microplate type and broth additives on microdilution MIC susceptibility assays. *Antimicrob. Agents Chemother.* **2019**, *63*, e01760-18. [CrossRef] [PubMed]
68. Golus, J.; Sawicki, R.; Widelski, J.; Ginalska, G. The agar microdilution method—A new method for antimicrobial susceptibility testing for essential oils and plant extracts. *J. Appl. Microbiol.* **2016**, *121*, 1291–1299. [CrossRef] [PubMed]
69. Thirusangu, P.; Pathoulas, C.L.; Ray, U.; Xiao, Y.; Staub, J.; Jin, L.; Khurana, A.; Shridhar, V. Quinacrine-induced autophagy in ovarian cancer triggers cathepsin-l mediated lysosomal/mitochondrial membrane permeabilization and cell death. *Cancers* **2021**, *13*, 2004. [CrossRef] [PubMed]
70. Bucevičius, J.; Lukinavičius, G.; Gerasimaite, R. The use of hoechst dyes for DNA staining and beyond. *Chemosensors* **2018**, *6*, 18. [CrossRef]
71. Thomé, M.P.; Filippi-Chiela, E.C.; Villodre, E.S.; Migliavaca, C.B.; Onzi, G.R.; Felipe, K.B.; Lenz, G. Ratiometric analysis of Acridine Orange staining in the study of acidic organelles and autophagy. *J. Cell Sci.* **2016**, *129*, 4622–4632. [CrossRef]
72. Kntayya, S.B.; Ibrahim, M.D.; Ain, N.M.; Iori, R.; Ioannides, C.; Abdull Razis, A.F. Induction of apoptosis and cytotoxicity by isothiocyanate sulforaphene in human hepatocarcinoma HepG2 cells. *Nutrients* **2018**, *10*, 718. [CrossRef]
73. Choi, H.S.; Seo, H.S.; Kim, J.H.; Um, J.Y.; Shin, Y.C.; Ko, S.G. Ethanol extract of paeonia suffruticosa Andrews (PSE) induced AGS human gastric cancer cell apoptosis via fas-dependent apoptosis and MDM2-p53 pathways. *J. Biomed. Sci.* **2012**, *19*, 82. [CrossRef]
74. Priya, S.; Rathnanand, M.; Nayanabhirama, U.; Ongole, R.; Sumanth, K.N.; Joshi, U. Preparation and evaluation of buccal mucoadhesive patch of betamethasone sodium phosphate for the treatment of Oral submucous fibrosis. *J. Chem. Pharm. Res.* **2011**, *3*, 56–65.
75. Cao, N.; Yang, X.; Fu, Y. Effects of various plasticizers on mechanical and water vapor barrier properties of gelatin films. *Food Hydrocoll.* **2009**, *23*, 729–735. [CrossRef]
76. Peh, K.; Khan, T.; Ch'ng, H. Mechanical, bioadhesive strength and biological evaluations of chitosan films for wound dressing. *J. Pharm. Pharm. Sci.* **2000**, *3*, 303–311. [PubMed]
77. Semalty, M.; Semalty, A.; Kumar, G. Formulation and characterization of mucoadhesive buccal films of glipizide. *Indian J. Pharm. Sci.* **2008**, *70*, 43–48. [CrossRef] [PubMed]
78. Karki, S.; Kim, H.; Na, S.J.; Shin, D.; Jo, K.; Lee, J. Thin films as an emerging platform for drug delivery. *Asian J. Pharm. Sci.* **2016**, *11*, 559–574. [CrossRef]
79. Kaur, G.; Singh, D.; Brar, V. Bioadhesive okra polymer based buccal patches as platform for controlled drug delivery. *Int. J. Biol. Macromol.* **2014**, *70*, 408–419. [CrossRef]
80. Maher, E.M.; Ali, A.M.A.; Salem, H.F.; Abdelrahman, A.A. In vitro/in vivo evaluation of an optimized fast dissolving oral film containing olanzapine co-amorphous dispersion with selected carboxylic acids. *Drug Deliv.* **2016**, *23*, 3088–3100. [CrossRef]
81. Mandal, U.K.; Chatterjee, B.; Senjoti, F.G.; Adebisi, A.O.; Laity, P.R.; Conway, B.R.; Rajab, M.; Jouma, M.; Neubert, R.H.H.; Dittgen, M.; et al. A Review on Buccal Mucoadhesive Drug Delivery Systems. *AAPS PharmSciTech* **2006**, *7*, 197–208.
82. Elshafeey, A.H.; El-Dahmy, R.M. Formulation and development of oral fast-dissolving films loaded with nanosuspension to augment paroxetine bioavailability: In vitro characterization, ex vivo permeation, and pharmacokinetic evaluation in healthy human volunteers. *Pharmaceutics* **2021**, *13*, 1869. [CrossRef] [PubMed]
83. Vedala, H.; Huang, J.; Zhou, X.Y.; Kim, G.; Roy, S.; Choi, W.B. Effect of PVA functionalization on hydrophilicity of Y-junction single wall carbon nanotubes. *Appl. Surf. Sci.* **2006**, *252*, 7987–7992. [CrossRef]
84. Mali, S.; Sakanaka, L.S.; Yamashita, F.; Grossmann, M.V.E. Water sorption and mechanical properties of cassava starch films and their relation to plasticizing effect. *Carbohydr. Polym.* **2005**, *60*, 283–289. [CrossRef]
85. Londhe, V.; Shirsat, R. Formulation and Characterization of Fast-Dissolving Sublingual Film of Iloperidone Using Box–Behnken Design for Enhancement of Oral Bioavailability. *AAPS PharmSciTech* **2018**, *19*, 1392–1400. [CrossRef] [PubMed]
86. Shen, C.; Shen, B.; Xu, H.; Bai, J.; Dai, L.; Lv, Q.; Han, J.; Yuan, H. Formulation and optimization of a novel oral fast dissolving film containing drug nanoparticles by Box-Behnken design-response surface methodology. *Drug Dev. Ind. Pharm.* **2014**, *40*, 649–656. [CrossRef] [PubMed]
87. Peh, K.K.; Wong, C.F. Polymeric films as vehicle for buccal delivery: Swelling, mechanical, and bioadhesive properties. *J. Pharm. Pharm. Sci.* **1999**, *2*, 53–61. [PubMed]
88. Singh, S.; Jain, S.; Muthu, M.S.; Tiwari, S.; Tilak, R. Preparation and evaluation of buccal bioadhesive films containing clotrimazole. *AAPS PharmSciTech* **2008**, *9*, 660–667. [CrossRef] [PubMed]

89. Castán, H.; Ruiz, M.A.; Clares, B.; Morales, M.E. Design, development and characterization of buccal bioadhesive films of Doxepin for treatment of odontalgia. *Drug Deliv.* **2015**, *22*, 869–876. [CrossRef]
90. Pagano, C.; Puglia, D.; Luzi, F.; Michele, A.D.; Scuota, S.; Primavilla, S.; Ceccarini, M.R.; Beccari, T.; Iborra, C.A.V.; Ramella, D.; et al. Development and characterization of xanthan gum and alginate based bioadhesive film for pycnogenol topical use in wound treatment. *Pharmaceutics* **2021**, *13*, 324. [CrossRef]
91. McLain, V.C. Safety assessment of poloxamers 101, 105, 108, 122, 123, 124, 181, 182, 183, 184, 185, 188, 212, 215, 217, 231, 234, 235, 237, 238, 282, 284, 288, 331, 333, 334, 335, 338, 401, 402, 403, and 407, poloxamer 105 benzoate, and poloxamer 182 dibenzoate as used in cosmetics. *Int. J. Toxicol.* **2008**, *27*, 93–128.
92. Beard, M.C.; Cobb, L.H.; Grant, C.S.; Varadarajan, A.; Henry, T.; Swanson, E.A.; Kundu, S.; Priddy, L.B. Autoclaving of Poloxamer 407 hydrogel and its use as a drug delivery vehicle. *J. Biomed. Mater. Res. -Part B Appl. Biomater.* **2021**, *109*, 338–347. [CrossRef]
93. Veyries, M.L.; Faurisson, F.; Joly-Guillou, M.L.; Rouveix, B. Control of staphylococcal adhesion to polymethylmethacrylate and enhancement of susceptibility to antibiotics by poloxamer 407. *Antimicrob. Agents Chemother.* **2000**, *44*, 1093–1096. [CrossRef]
94. Teanpaisan, R.; Ruangkiatkul, P.; Thammasitboon, K.; Puripattanavong, J.; Faroongsarng, D. Effectiveness of Artocarpus lakoocha extract, poloxamer 407, on Enterococcus faecalis in vitro. *J. Investig. Clin. Dent.* **2013**, *4*, 219–224. [CrossRef]
95. Bonifácio, B.V.; Vila, T.V.M.; Masiero, I.F.; da Silva, P.B.; da Silva, I.C.; de Oliveira Lopes, É.; dos Santos Ramos, M.A.; de Souza, L.P.; Vilegas, W.; Pavan, F.R.; et al. Antifungal Activity of a Hydroethanolic Extract from *Astronium urundeuva* Leaves Against *Candida albicans* and *Candida glabrata*. *Front. Microbiol.* **2019**, *10*, 2642. [CrossRef] [PubMed]
96. Jardón-Romero, E.A.; Lara-Carrillo, E.; González-Pedroza, M.G.; Sánchez-Mendieta, V.; Salmerón-Valdés, E.N.; Toral-Rizo, V.H.; Olea-Mejía, O.F.; López-González, S.; Morales-Luckie, R.A. Antimicrobial Activity of Biogenic Silver Nanoparticles from *Syzygium aromaticum* against the Five Most Common Microorganisms in the Oral Cavity. *Antibiotics* **2022**, *11*, 834. [CrossRef] [PubMed]
97. Rafey, A.; Amin, A.; Kamran, M.; Haroon, U.; Farooq, K.; Foubert, K.; Pieters, L. Analysis of plant origin antibiotics against oral bacterial infections using in vitro and in silico techniques and characterization of active constituents. *Antibiotics* **2021**, *10*, 1504. [CrossRef]
98. Popovici, P.C.; Ancuceanu, V.R.; Olaru, T.O.; Stoicescu, C.-S.; Dinu, M. Toxicity Assessment of *Nephrolepis exaltata* (L.) Schott, Fam. Nephrolepidaceae. *Acta Biol. Marisiensis* **2018**, *1*, 27–36. [CrossRef]
99. Hovaneţ, M.V.; Ancuceanu, R.V.; Dinu, M.; Oprea, E.; Budura, E.A.; Negreş, S.; Velescu, B.Ş.; Duţu, L.E.; Anghel, I.A.; Ancu, I.; et al. Toxicity and anti-inflammatory activity of *Ziziphus jujuba* Mill. leaves. *Farmacia* **2016**, *64*, 802–808.
100. Păduraru, D.N.; Coman, F.; Ozon, E.A.; Gherghiceanu, F.; Andronic, O.; Ion, D.; Stănescu, M.; Bolocan, A. The use of nutritional supplement in romanian patients—Attitudes and beliefs. *Farmacia* **2019**, *67*, 1060–1065. [CrossRef]
101. Nazir, S.; Ansari, F.L.; Hussain, T.; Mazhar, K.; Muazzam, A.G.; Qasmi, Z.U.H.; Makhmoor, T.; Noureen, H.; Mirza, B. Brine shrimp lethality assay 'an effective prescreen': Microwave-assisted synthesis, BSL toxicity and 3DQSAR studies-based designing, docking and antitumor evaluation of potent chalcones. *Pharm. Biol.* **2013**, *51*, 1091–1103. [CrossRef] [PubMed]
102. Rajabi, S.; Ramazani, A.; Hamidi, M.; Naji, T. Artemia salina as a model organism in toxicity assessment of nanoparticles. *DARU J. Pharm. Sci.* **2015**, *23*, 20. [CrossRef] [PubMed]
103. Da Costa Júnior, S.D.; Da Silva, W.R.C.; Da Silva, A.M.C.M.; Maciel, M.A.V.; Cavalcanti, I.M.F. Synergistic Effect between Usnic Acid and Polymyxin B against Resistant Clinical Isolates of *Pseudomonas aeruginosa*. *Evid. -Based Complement. Altern. Med.* **2020**, *2020*, 9852145. [CrossRef]
104. Guney Eskiler, G.; Eryilmaz, I.E.; Yurdacan, B.; Egeli, U.; Cecener, G.; Tunca, B. Synergistic effects of hormone therapy drugs and usnic acid on hormone receptor-positive breast and prostate cancer cells. *J. Biochem. Mol. Toxicol.* **2019**, *33*, e22338. [CrossRef]
105. Zhang, J.; Li, L.; Wang, X.; Wang, Z.; Zheng, C.; Zhang, H.; Wang, H.; Li, P.; Zhai, X.; Li, H.; et al. Inhibitory mechanism against oxidative stress and biological activities of canolol. *Acta Pol. Pharm. -Drug Res.* **2017**, *74*, 25–29.
106. Alakhova, D.Y.; Kabanov, A.V. Pluronics and MDR reversal: An update. *Mol. Pharm.* **2014**, *11*, 2566–2578. [CrossRef] [PubMed]
107. Smith, A.J.; Morrison, D.; Robertson, D.; Tang, M.K.; Al-Doori, Z. Efficacy of oral hygiene products against MRSA and MSSA isolates. *J. Antimicrob. Chemother.* **2003**, *52*, 738–739. [CrossRef] [PubMed]

biomedicines

MDPI

Article

Characterization of the Tumor Microenvironment and the Biological Processes with a Role in Prostatic Tumorigenesis

Cristina-Anita Ionescu [1,2], Mariana Aschie [2,3,4], Elena Matei [3,*], Georgeta Camelia Cozaru [3,4], Mariana Deacu [2,4], Anca Florentina Mitroi [3,4], Gabriela Isabela Baltatescu [3,4], Antonela-Anca Nicolau [3,4], Laura Mazilu [2,5], Liliana Ana Tuta [2,6], Ionut Ciprian Iorga [2,7], Alina Stanigut [2,6] and Manuela Enciu [2,4]

[1] Chemical Carcinogenesis and Molecular Biology Laboratory, Institute of Oncology "Prof. Dr. Alexandru Trestioreanu", 022328 Bucharest, Romania; anitaionescu7@gmail.com
[2] Medicine Faculty, "Ovidius" University of Constanta, 1 Universitatii Street, 900470 Constanta, Romania; aschiemariana@yahoo.com (M.A.); deacu_mariana@yahoo.com (M.D.); lauragrigorov@gmail.com (L.M.); tutaliliana@yahoo.com (L.A.T.); ionut_iorga@yahoo.com (I.C.I.); asburlan29@yahoo.com (A.S.); iftimemanuela@yahoo.com (M.E.)
[3] Center for Research and Development of the Morphological and Genetic Studies of Malignant Pathology, "Ovidius" University of Constanta, 145 Tomis Blvd., 900591 Constanta, Romania; drcozaru@yahoo.com (G.C.C.); ank_mitroi@yahoo.com (A.F.M.); gabrielabaltatescu@yahoo.com (G.I.B.); ancanicolau@rocketmail.com (A.-A.N.)
[4] Clinical Service of Pathology, "Sf. Apostol Andrei" Emergency County Hospital, 145 Tomis Blvd., 900591 Constanta, Romania
[5] Oncology Department, "Sf. Apostol Andrei" Emergency County Hospital, 145 Tomis Blvd., 900591 Constanta, Romania
[6] Nephrology Department, "Sf. Apostol Andrei" Emergency County Hospital, 145 Tomis Blvd., 900591 Constanta, Romania
[7] Urology Department, "Sf. Apostol Andrei" Emergency County Hospital, 145 Tomis Blvd., 900591 Constanta, Romania
[*] Correspondence: sogorescuelena@gmail.com; Tel.: +40-723-943-559

Abstract: Prostate intratumoral heterogeneity, driven by epithelial–mesenchymal plasticity, contributes to the limited treatment response, and it is therefore necessary to use the biomarkers to improve patient prognostic survival. We aimed to characterize the tumor microenvironment (T lymphocyte infiltration, intratumoral CD34, and KI-67 expressions) by immunohistochemistry methods and to study the biological mechanisms (cell cycle, cell proliferation by adhesion glycoproteins, cell apoptosis) involved in the evolution of the prostate tumor process by flow-cytometry techniques. Our results showed that proliferative activity (S-phase) revealed statistically significant lower values of prostate adenocarcinoma (PCa) and benign prostatic hyperplasia (BPH) reported at non-malignant adjacent cell samples (PCa 4.32 ± 4.91; BPH 2.35 ± 1.37 vs. C 10.23 ± 0.43, $p < 0.01$). Furthermore, 68% of BPH cases and 88% of patients with PCa had aneuploidy. Statistically increased values of cell proliferation (CD34+ CD61+) were observed in prostate adenocarcinoma and hyperplasia cases reported to non-malignant adjacent cell samples (PCa 28.79 ± 10.14; BPH 40.65 ± 11.88 vs. C 16.15 ± 2.58, $p < 0.05$). The CD42b+ cell population with a role in cell adhesion, and metastasis had a significantly increased value in PCa cases (38.39 ± 11.23) reported to controls (C 26.24 ± 0.62, $p < 0.01$). The intratumoral expression of CD34 showed a significantly increased pattern of PCa tissue samples reported to controls (PCa 26.12 ± 6.84 vs. C 1.50 ± 0.70, $p < 0.01$). Flow cytometric analysis of the cell cycle, apoptosis, and adhesion glycoproteins with a critical role in tumoral cell proliferation, T cell infiltrations, Ki-67, and CD 34 expressions by IHC methods are recommended as techniques for the efficient means of measurement for adenocarcinoma and hyperplasia prostate tissue samples and should be explored in the future.

Keywords: prostate carcinogenesis; cell cycle; apoptosis; CD34; CD61; CD42b glycoproteins; T cell infiltrations; Ki-67 expression

check for updates

Citation: Ionescu, C.-A.; Aschie, M.; Matei, E.; Cozaru, G.C.; Deacu, M.; Mitroi, A.F.; Baltatescu, G.I.; Nicolau, A.-A.; Mazilu, L.; Tuta, L.A.; et al. Characterization of the Tumor Microenvironment and the Biological Processes with a Role in Prostatic Tumorigenesis. *Biomedicines* **2022**, *10*, 1672. https://doi.org/10.3390/biomedicines10071672

Academic Editors: Cecilia M. P. Rodrigues, Fernando Capela e Silva and Christos K. Kontos

Received: 2 June 2022
Accepted: 6 July 2022
Published: 12 July 2022

1. Introduction

Prostate adenocarcinoma (PCa) is the most common cancer in men in the world, being the leading cause of death. Despite its high incidence, PCa prognosis for patients is good when the carcinoma is detected in stages when androgen deprivation, prostatectomy, or/and radiation therapies are implemented [1–3]. Prostate intratumoral heterogeneity, driven by epithelial–mesenchymal plasticity, contributes to the limited treatment response; therefore, it is necessary to use the biomarkers to highlight this efficiently and quickly to improve patient prognostic survival. Flow cytometric analysis of ploidy and the cell cycle, together with adhesion glycoproteins with an essential role in tumoral cell proliferation and cell apoptosis, represent the rapid and efficient means of measurement for the microenvironment (TME) of the PCa and benign prostatic hyperplasia (BPH). DNA content observes the cell frequency in the G0/G1, S, and G2/M phases of the cell cycle and assesses DNA ploidy. The evidence of aneuploidy represents a marker of the tumor presence, being a prognostic indicator of tumor progression and the treatment outcome [4]. DNA ploidy and cell proliferation have provided prognostic information for prostate cancer [5]. Aneuploidy represents a human cancer characteristic, being a tumorigenesis driver [6]. Aneuploidy may arise during tumor initiation via polyploidization because unstable tetraploid intermediates determinate chromosomal gains, losses, and translocations [7–9]. Polyploid cells also occur in cancer, but aneuploidy cells are found in various tumors, often indicating higher malignancy. Flow cytometric analysis of aneuploidy has been used as a prognostic indicator in prostate, colon, and breast tumors, and it highlights that aneuploidy results from deletion or replication of specific chromosomes, with a different process from normal chromosome replication [10]. Cell adhesion molecules (glycoproteins) are essential in cancer progression and metastasis. Interactions between tumor cells, platelets, and leukocytes contribute to cancer cell adhesion, extravasation, and the establishment of metastatic lesions [11]. CD61 transmembrane glycoproteins (β3 integrin) attach the cells to the extracellular matrix (ECM), inducing cluster formation with signaling molecules (focal adhesions kinase), which result in cell adhesion and cell migration. Changes in integrin gene expression were shown in various malignancies, including prostate adenocarcinoma [12–15]. CD34 is a transmembrane phosphoglycoprotein associated with the proliferative capacity of multipotent mesenchymal stromal cells (MSC) [16,17]. In addition, CD34 represents a biomarker of vascular endothelial progenitor cells [18]. Noncirculating adult endothelial cells were represented by the CD34+ cell population, located within smaller blood vessels, while most endothelial cells from larger veins and arteries are part of the CD34- cell population. CD34+ endothelial cells are involved in migration and adhesion [17]. The integrin αIIb/β3 (CD61 complex) is involved in prostate cancer metastasis [19]. In addition, integrin α5β1 (GPIB-V complex) is vital in cell adhesion in prostate cancer cells [20]. T lymphocyte infiltration into the tumor microenvironment plays an important role in antitumor immunity [21]. T lymphocyte infiltration into malignant tumors in controlling cancer progression and survival of patients with cancer was described in [22]. Other authors suggest that patients with tumors with increased T lymphocyte infiltration have a survival advantage, but it appears that the mechanisms that contributed to escape the tumor cells originated from immune responses [3,23,24].

Our study presents the DNA content and cell apoptosis related to adhesion glycoprotein expressions and T lymphocyte infiltration in PCa and BPH tissue in a report with non-malignant adjacent tissue samples. DNA content was measured by flow cytometry to show cell distribution within the G0/G1, S, and G2/M phases of the cell cycle, to estimate the frequency of apoptotic cells with the fractional DNA content (subG0/G1), and to calculate the DNA ploidy of the observed cell population, being made by a PI stain. Adhesion glycoproteins made by dual stain CD34 Alexa Fluor 488 and CD61-PE reveal mesenchymal and endothelial cell proliferation and platelet and T cell aggregation to tumoral and endothelial cells (CD34+ CD61+). The CD42b-PE stain observed the platelet aggregation in tumor and endothelial cells. T lymphocytes, especially CD3 (total T lymphocytes), CD4 (helper T lymphocytes), and CD8 (cytotoxic T lymphocytes), were analyzed by immunohistochemistry methods (IHC) to observe the infiltration degrees of leucocytes in tissue samples. In addition, the intratumoral expression of CD34 and cell proliferation by Ki-67 expression in PCa and BPH tissue samples were reported to controls by ICH analysis.

2. Materials and Methods

2.1. Cases Selection

All tissue samples (n = 75) were recovered from patients (who signed informed consent forms, agreeing to participate in this study) from the Clinical Service of Pathology, Sf. Apostol Andrei Clinical Emergency County Hospital in Constanta, Romania. In agreement with WHO classifications, the patients were divided into two experimental groups: (1) patients with PCa without treatment (n = 25); (2) patients with BPH without treatment (n = 25); (3) controls for experimental groups using non-malignant adjacent tissue samples recovered from patients with PCa or BPH (n = 25, C, controls).

Tissue samples of PCa, BPH, and control, excised by transurethral resection of the prostate (TURP), were divided into two parts: (1) samples used to evaluate the T cell infiltrations, CD 34, and Ki-67 cell proliferation by IHC methods at Clinical Service of Pathology, Sf. Apostol Andrei Clinical Emergency County Hospital, Constanta, Romania; (2) samples mechanically homogenized with TissueRuptor II (Qiagen, USA), used for flow cytometry determinations (DNA content, cell apoptosis, CD34, CD61, and CD42b biomarkers at the Cell Biology Department, CEDMOG, Ovidius University of Constanta, Romania). Our selection criteria were applied to identify and establish the clinical efficiency of the human PCa and BPH biomarkers by flow cytometry and IHC methods, highlighting the characterization of the tumor microenvironment in conformity with references [25].

2.2. Morphological Evaluation of Tissue Samples

After the macroscopic description, the prostate tissue specimens were fixed in 10% formaldehyde, paraffin-embedded, sectioned, and stained in the usual laboratory stains. For the microscopic evaluation, by the Gleason classification, primary prostate adenocarcinomas were divided into three categories: (1) well-differentiated—Gleason score (GS) 6; (2) moderately differentiated—Gleason score 7; (3) poorly differentiated—Gleason scores 8–10. The second classification of PCa cases in the function of the prognostic grade of the patient survival was made in accordance with the references: (1) Group I—Gleason score ≤ 6 (n = 1); (2) Group II—Gleason score 3 + 4 = 7 (n = 16); (3) Group III—Gleason score 4 + 3 = 7; (4) Group IV—Gleason score 4 + 4 = 8 (n = 3); (5) Group V—Gleason score 9–10 (n = 5) [26–28]. After the T stage (pTNM), the third classification identified two risk groups: (1) patients with T1-T2 stage; (2) patients with T3-T4 stage [29].

2.3. Reagents and Equipment

Our study analyses used a flow cytometer (Attune, Acoustic focusing cytometer, Applied Biosystems, part of Life Technologies, Bedford, MA, USA). The flow cytometer was set using fluorescent beads (Attune performance tracking beads, labeling, and detection, Life Technologies, Europe BV, Bleiswijk, The Netherlands) with standard size (four intensity levels of beads population). The quantity was established by enumerating cells below 1 μm; 10,000 cells per sample for each analysis were gated by Forward Scatter (FSC) and Side Scatter (SSC). Flow cytometry data were collected using Attune Cytometric Software v.1.2.5, Applied Biosystems, 2010. Annexin V-FITC/PI (Bender MedSystems GmbH, Wien, Austria) was used to observe the apoptotic cells. Propidium iodide (PI) (1.0 mg/mL, Sigma-Aldrich, Chemie GmbH, Taufkirchen, Germany) and RNase A (4 mg/mL, Promega, Madison, WI, USA) were used in cell cycle analysis. Anti-CD42b-PE (HIP1) and anti-CD61-PE (integrin beta 3, Invitrogen, eBioscience) monoclonal antibodies conjugated with phycoerythrin (PE) were used to assess platelet glycoproteins expressions of GPIba and GPIIIa. CD34 Antibody, conjugate Alexa Fluor 488 (4H11(APG), Thermo Scientific, Waltham, MA, USA) was used for glycoprotein expression of CD34. Anti-CD4 (EP204 clone), anti-CD 8 (SP16 clone), anti-CD3 (EP41 clone), anti-CD34 (QB-End/10 clone), and anti-Ki67 (SP6 clone, Master

Diagnostica, Sao Paolo, Brazil) monoclonal antibodies were used for immunohistochemistry (IHC) methods to evaluate the T cell infiltration, intratumoral expression of CD34, and cell proliferation in PCa and BPH tissue samples reported to controls. We used formalin-fixed, paraffin-embedded tissue for IHC assessment, sectioned at 4 µm thickness. We followed the staining protocol, as recommended by the producers. Master Diagnostica protocols included dewaxing using xylene and decreasing grades of alcohol, HIER in ph8 Master Diagnostica EDTA buffer in a pressure cooker incubating the ready-to-use monoclonal antibodies at room temperature for 10 min. For detection, we used the Master Polymer Plus Detection System (HRP) (DAB included), counterstained with hematoxylin, and mounted the glass cover slides.

2.4. Cell Cycle Analysis

In the darkness, the homogenized cells (100 µL) were introduced into flow cytometry tubes and fixed with 100 µL ethanol for 30 min. After this process, the cells were treated with 20 µL of PI (20 mg/mL) and 30 µL of RNase A (30 mg/mL) and incubated for 30 min at room temperature into darkness. Then, 1 mL flow cytometry stain buffer (FCB, eBioscienceTM, Life Technologies Europe BV, Bleiswijk, The Netherlands) was added, and the cell cycle distribution was detected with the flow cytometer using a 488 nm excitation and orange emission for PI (BL2 channel).

2.5. Adhesion Glycoproteins Determinations

The homogenized cells (100 µL for each tube) spread: (1) CD61-PE and CD34+ -Alexa Flour 488 dual stain; (2) CD42b-PE stain; (3) control negative-IgG stain. In the tubes with cells were introduced 5µL of CD61-PE and 5µL of CD34-Alexa Flour 488. In the other tubes with cells were added 5 µL of CD42b-PE. A control tube with cells and 5 µL of the negative control (mouse IgG) were realized for each experimental sample. All work tubes were vortexed and incubated into darkness for 25 min at 37 °C. Then, 1 ml of FCB was added into each tube and vortexed for 1 min before analysis. Flow cytometry identified adhesion glycoproteins based on the size and specificity of CD34, CD61, and CD42b expressions, using the BL1 channel for Alexa Fluor 488 and the BL2 channel for PE.

2.6. Cell Apoptosis Assay

The homogenized cells from each sample were introduced in flow cytometry tubes with 2 µL of Annexin V-FITC and 2 µL PI (20 mg/mL) for 30 min at room temperature in darkness. After incubation, 1 mL of FCB was added. Viable cells, early apoptotic cells, late apoptotic cells, and necrotic cells were examined with a flow cytometer using 488 nm excitation, green emission for Annexin V-FITC (BL1 channel), and orange emission for PI (BL2 channel).

2.7. Surface Glycoproteins of T Cell Analysis

The expressions of the CD4, CD3, and CD8 biomarkers were evaluated semi-quantitatively as the number of lymphocytes (less or greater than 50 cells) on 400× magnification by microscope examination. Immunolabeling was considered brown positive at the membrane level. Lymphocytes from the peritumoral stroma were evaluated, either as single cells or as cell aggregates and intraepithelial cells. Tonsils were used as a positive control. Thus, the degree of inflammation in the tissue samples was assessed and divided into three categories depending on the lymphocyte's percentage: (1) slight inflammation, when the inflammatory infiltrates were equal to or less than 10% (n = 39); (2) moderate inflammation, with infiltrates between 10 and 20 (n = 14); (3) severe inflammation, when the percentage of infiltrates was equal to or greater than 20 (n = 22) [30].

2.8. Intratumoral Expression of CD34

Vascularity was evaluated by an average of CD34-positive numbers of stained vessels in cases with non-malignant tissue, HBP tissue, and PCa tissue samples. CD34 expression was assessed in both small vessels within the prostate tumor tissue, which is more likely to be formed during tumor angiogenesis, and in pre-existing stromal vessels. For evaluation, the expression was observed by brown positivity in the monolayer endothelial cells, which line the lumen of small vessels. Each section was initially examined with a low power field of 100× to mark the area of MDV (microvessel density) and then with a large, high power field of 400×. They were evaluated as vascular spaces, lumen-centered structures, endothelial cell groups, or CD34-positive cell clusters that were considered a microvessel. In the situation where at least two clusters or foci were observed, which seemed to belong to the same vascular structure, they were also considered a microvessel. MVD count was established as the sum of the three highest counts, in the hot spots, at 0.18 mm^2 [29,31].

2.9. Ki-67 Cell Proliferation

The evaluation was quantified at the nuclear level by strong brown staining as the percentage of cells that react with the antibody. Positive cells were counted from 500 cells evaluated on the magnification of 400 (HPF—high power field). We used as reference for interpretation the following values: below 2%, negative (n = 50); below 25%, score 1+ (n = 25); 26–50%, score 2+; 51–75%, score 3+; 76–100%, score 4+ [32].

2.10. Statistical Analysis

We analyzed the cell cycle, adhesion glycoproteins, cell apoptosis, T cell infiltrations, and intratumoral expression of CD34 for all tissue samples, and the obtained results were presented as mean values with standard deviations, made by SPSS v. 23 software, IBM, Armonk, NY, USA, 2015. Data were analyzed by the Levene test for homogeneity of the sample variances, an independent t test was used to show the differences between cases, and $p < 0.05$ was considered statistically significant. The Pearson correlations were made between DNA content, cell apoptosis, glycoproteins parameters, tissue inflammation grade, and Ki-67 cell proliferation in PCa and HP tissue in a report with non-malignant adjacent tissue samples. Figures 1–4 were produced with Attune Cytometric Software v.1.2.5, Applied Biosystems, Bedford, MA, USA, 2010.

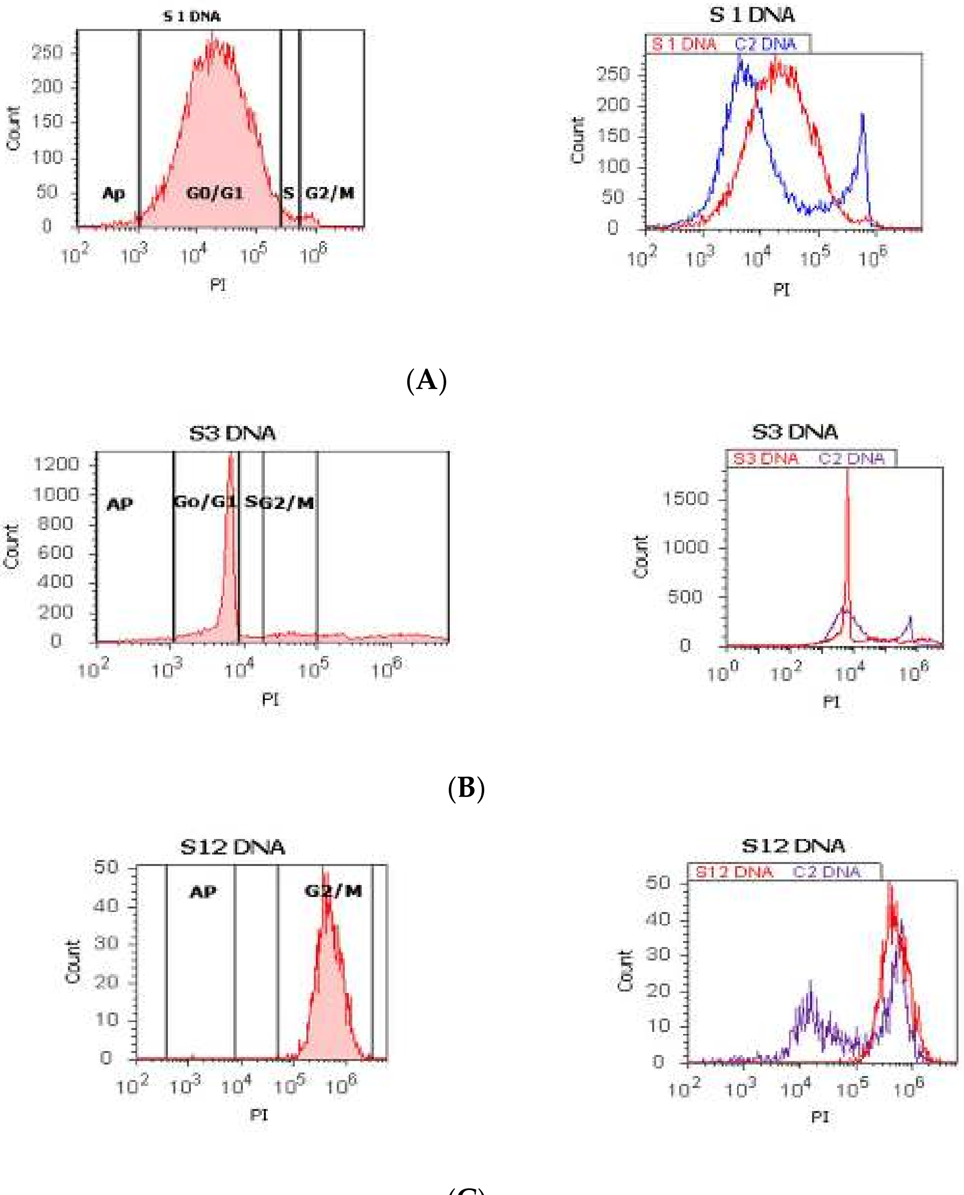

(**A**)

(**B**)

(**C**)

Figure 1. Cell cycle, ploidy, and DNA fragmentation (AP, subG0/G1) represented by propidium iodide stain (PI). Control DNA extrapolate on the PI ax. *G0/G1 phase* = (**A**) 95.48%; (**B**) 2c 59.44%; 4c 10.87%; 8c 6.52%; 16c 12.68%; (**C**) 0.00%; *S phase* = (**A**) 1.27%; (**B**) 0.00%; (**C**) 0.00%; *G2/M phase* = (**A**) 1.13%; (**B**) 0.00%; (**C**) 99.92%; *subG0/G1:* (**A**) 1.05%; (**B**) 3.31%; (**C**) 0.07%. Legend: AP, cell apoptosis; (**A**) malignant tumor tissue with an invasion of the prostatic urethra (hyperdiploid, cell cycle arrest in G0/G1 phase); (**B**) adenoleiomyoma prostate tissue, chronic inflammation hyperplasia (tetrapoliploidy); (**C**) benign prostatic tissue hyperplasia (aneuploid, present only the G2/M phase).

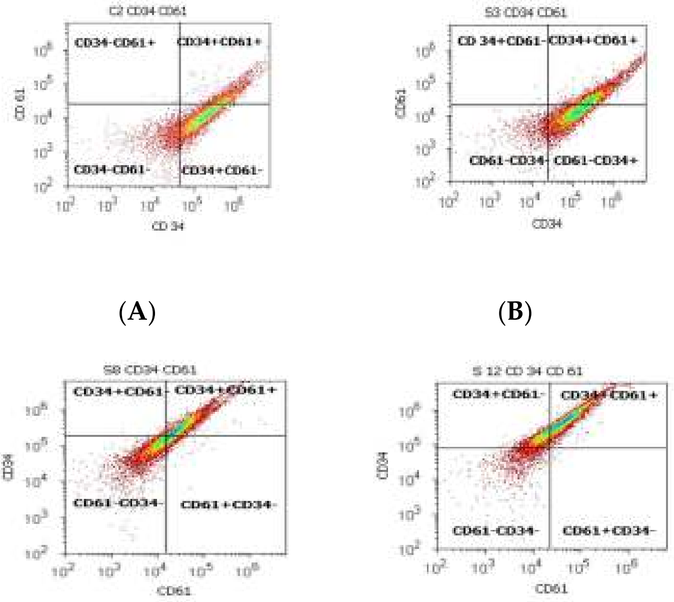

(**A**) (**B**)

(**C**) (**D**)

Figure 2. Cell proliferation highlights the double-positive populations of glycoprotein expression (CD34+ CD61+) with CD34- Alexa Fluor 488 and CD 61-PE dual stain. Cell adhesion is interpreted by the CD34 + CD61+ population: (**A**) 17.98%; (**B**) 33.63%; (**C**) 45.71%; (**D**) 59.68%. Legend: (**A**) non-malignant prostate tissue adjacent to nodular hyperplastic tissue; (**B**) adenoleiomyoma prostate tissue, chronic inflammation hyperplasia; (**C**) malignant prostate tumor tissue; (**D**) benign prostatic tissue hyperplasia.

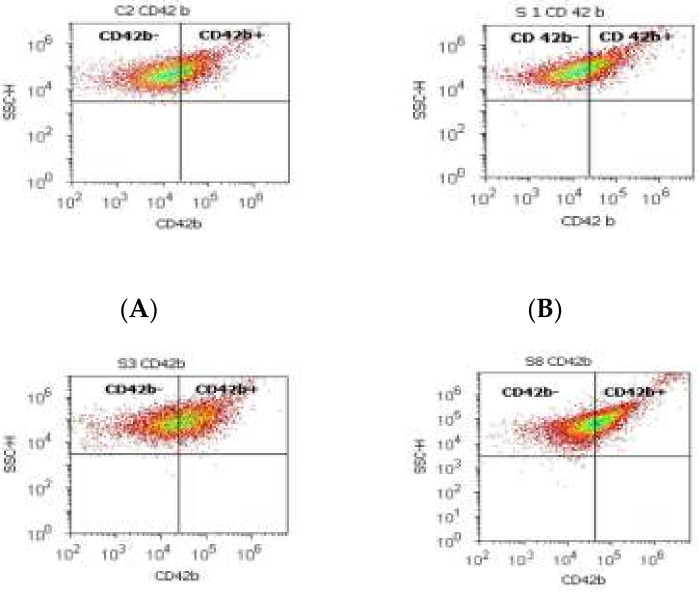

(**A**) (**B**)

(**C**) (**D**)

Figure 3. Integrin mediation of platelet aggregation to tumoral and endothelial cells by highlighting the positive and negative glycoprotein populations (CD42b-/CD42b+) with CD 42b-PE stain. CD42b+ population: (**A**) 25.80 %; (**B**) 16.79%; (**C**) 41.10%; (**D**) 39.74%; CD42b- population: (**A**) 73.08%; (**B**) 82.88%; (**C**) 57.58%; (**D**) 57.23%. Legend: (**A**) non-malignant prostate tissue adjacent to nodular hyperplastic tissue; (**B**) adenoleiomyoma prostate tissue, chronic inflammation hyperplasia; (**C**) malignant prostate tumor tissue; (**D**) benign prostatic tissue hyperplasia.

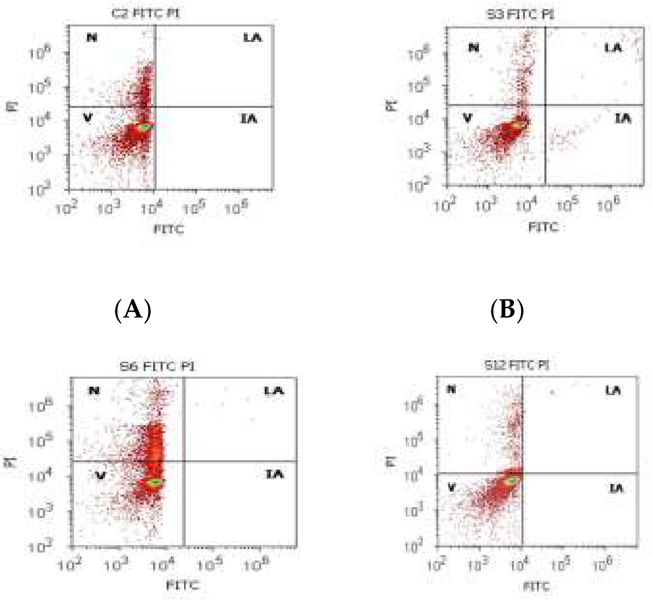

(**A**) (**B**)

(**C**) (**D**)

Figure 4. Cell apoptosis by Annexin V- FITC/ propidium iodide (PI) dual stain. Viability (V): (**A**) 83.50%; (**B**) 94.72%; (**C**) 68.79%; (**D**) 87.90%; Incipient apoptosis (IA): (**A**) 0.00%; (**B**) 0.54%; (**C**) 0.005%; (**D**) 0.025%; Late apoptosis (LA): (**A**) 0.00%; (**B**) 0.49%; (**C**) 0.07%; (**D**) 0.22%; Necrosis (*n*): (**A**) 17.12%; (**B**) 4.23%; (**C**) 31.13%; (**D**) 11.85%. Legend: A, non-malignant prostate tissue adjacent to nodular hyperplastic tissue; B, adenoleiomyoma prostate tissue, chronic inflammation hyperplasia; C, malignant prostate tumor tissue; D, benign prostatic tissue hyperplasia.

3. Results

3.1. DNA Content, CD34, CD61, CD42 b Glycoproteins Expressions, Cell Apoptosis by Flow Cytometry Analysis in PCa and BPH Tissue Reported to Non-Malignant Adjacent Tissue Samples

The proliferative activity (S-phase) revealed statistically significant lower values of prostate adenocarcinoma and hyperplasia reported at non-malignant adjacent cell samples (PCa 4.32 ± 4.91; BPH 2.35 ± 1.37 vs. C 10.23 ± 0.43, $p < 0.01$, Table 1, Figure 1). Furthermore, 68% of BPH cases presented aneuploidy, 88% of patients with prostate adenocarcinoma had aneuploidy, 4% of cases from these highlighted hypodiploid and hyperdiploid cell heterogeneity, and 4% of cases showed polyploidy (tetrapoliploidy).

Table 1. Cell cycle phases, ploidy index, and DNA fragmentation at prostate adenocarcinoma, benign prostatic hyperplasia, and non-malignant adjacent tissue samples.

Number	Parameters	Control X ± SD	PCa X ± SD	Control X ± SD	BPH X ± SD
1	G0/G1 phase	68.67 ± 1.51	76.84 ± 20.68	68.67 ± 1.51	66.74 ± 34.38
	p values		0.14		0.86
2	S phase	10.23 ± 0.43 **	4.32 ± 4.91 **	10.23 ± 0.43 **	2.35 ± 1.37 **
	p values		**0.00**		**0.00**
3	G2/M phase	14.64 ± 2.99	8.81 ± 14.23	14.64 ± 2.99	20.42 ± 33.03
	p values		0.19		0.60
4	DNA index	1.00 ± 0.01 *	1.38 ± 0.51 *	1.00 ± 0.01 *	1.19 ± 0.20 *
	p values		**0.01**		**0.03**
5	subG0/G1	1.43 ± 0.11 *	4.63 ± 2.69 *	1.43 ± 0.11	2.19 ± 2.74
	p values		**0.01**		0.40

Legend: X, obtained results mean; SD, standard deviation; PCa, prostate adenocarcinoma; BPH, benign prostatic hyperplasia; ** $p \leq 0.01$ and * $p < 0.05$ represent statistically significant differences between controls and experimental samples made by independent *t* test.

Index of ploidy presented significantly increased values at PCa and BPH cases reported to control cases (PCa 1.38 ± 0.51; BPH 1.19 ± 0.20 vs. C 1.00 ± 0.01, $p < 0.01$). DNA fragmentation (subG0/G1) had a significantly increased percentage in PCa tissue (4.63 ± 2.69) compared to control tissue samples (1.43 ± 0.11, $p < 0.01$, Table 1, Figure 1).

Statistically increased values of cell proliferation (CD34+ CD61+) were observed in prostate adenocarcinoma and hyperplasia cases reported to non-malignant adjacent cell samples (PCa 28.79 ± 10.14; PH-40.65 ± 11.88 vs. C 16.15 ± 2.58, $p < 0.05$, Table 2, Figure 2).

Table 2. CD34 and CD61 glycoprotein expressions implied in cell proliferation in prostate adenocarcinoma, benign prostatic hyperplasia, and non-malignant adjacent tissue samples.

Number	Parameters	Control X ± SD	PCa X ± SD	Control X ± SD	BPH X ± SD
1	CD61T	86.90 ± 4.39 *	70.59 ± 15.30 *	86.90 ± 4.39	91.15 ± 4.76
	p values	**0.019**		0.273	
2	CD34 + CD61+	16.15 ± 2.58 **	28.79 ± 10.14 **	16.15 ± 2.58 *	40.65 ± 11.88 *
	p values	**0.005**		**0.019**	
3	CD61+	16.26 ± 2.52 **	37.81 ± 16.21 **	16.26 ± 2.52 **	36.50 ± 13.55 **
	p values	**0.000**		**0.002**	
4	CD61-	83.49 ± 2.72 **	59.89 ± 17.38 **	83.49 ± 2.72 **	62.49 ± 13.57 **
	p values	**0.000**		**0.001**	
5	CD34T	87.29 ± 5.20	75.43 ± 14.20	87.29 ± 5.20	90.55 ± 6.38
	p values	0.090		0.532	
6	CD34+	54.49 ± 0.72	57.81 ± 14.22	54.49 ± 0.72 **	66.31 ± 11.28 **
	p values	0.369		**0.009**	
7	CD34-	45.25 ± 0.52	39.95 ± 13.36	45.25 ± 0.52 **	32.69 ± 11.30 **
	p values	0.136		**0.007**	

Legend: X, obtained results mean; SD, standard deviation; PCa, prostate adenocarcinoma; BPH, benign prostatic hyperplasia; CD61 T, total CD61 glycoproteins expression; CD34 T, total CD34 glycoproteins expression; ** $p \leq 0.01$ and * $p < 0.05$ represent statistically significant differences between controls and experimental samples made by independent *t* test.

CD 61+ cell population, characteristically for platelets and T cell aggregation to tumoral cells and endothelium, presented significantly increased levels of PCa (37.81 ± 16.21) and BPH (36.50 ± 13.55) samples reported in controls (16.26 ± 2.52, $p < 0.01$). Mesenchymal cell proliferation represented by the CD34+ cell population revealed a significant increase in BPH cases reported to controls (66.31 ± 11.28 vs. 54.49 ± 0.72, $p < 0.01$). In addition, benign prostatic hyperplasia showed a significantly lower pattern for the CD34- cell population reported to control cases (32.69 ± 11.30 vs. 45.25 ± 0.52, $p < 0.01$, Table 2), which characterized the tumoral cells' adhesion to endothelial cells from larger veins and arteries.

A significant increase in the CD42b+ cell population with a role in cell adhesion and metastasis was observed in PCa cases (38.39 ± 11.23) reported to controls (26.24 ± 0.62, $p < 0.01$). Instead, the CD42b- cell population presented significantly lower values in PCa and BPH tissue samples compared to non-malignant adjacent cell samples (PCa 59.26 ± 12.02; BPH 59.97 ± 17.15 vs. C 73.14 ± 0.08; $p < 0.01$; $p < 0.05$, Table 3, Figure 3).

Cell viability had increased values without significant differences on PCa and control tissue samples (81.30 ± 16.42; 86.95 ± 5.75, $p > 0.05$, Table 4, Figure 4), but the obtained results for BPH cases showed a significantly lower value of this on BPH tissue samples reported to controls (BPH 64.26 ± 22.68 vs. 86.95 ± 5.75, $p < 0.05$). Necrosis presented a statistical increase of values in BPH cases compared with control cases (BPH 26.76 ± 6.32 vs. C 13.04 ± 5.76), and incipient cell apoptosis had a statistical increase in PCa tissue samples (7.08 ± 10.46) reported to non-malignant adjacent tissue samples (0.10 ± 0.01, $p < 0.05$, Table 4, Figure 4).

Table 3. CD42b glycoprotein expression at prostate adenocarcinoma, benign prostatic hyperplasia, and non-malignant adjacent tissue samples.

Number	Parameters	Control X ± SD	PCa X ± SD	Control X ± SD	BPH X ± SD
1	CD42bT	86.98 ± 5.23	76.07 ± 12.95	86.98 ± 5.23	77.75 ± 17.37
	p values	0.113		0.209	
2	CD42b+	26.24 ± 0.62 **	38.39 ± 11.23 **	26.24 ± 0.62	38.06 ± 17.43
	p values	**0.001**		0.061	
3	CD42b-	73.14 ± 0.08 **	59.26 ± 12.02 **	73.14 ± 0.08 *	59.97 ± 17.15 *
	p values	**0.000**		**0.038**	

Legend: X, obtained results mean; SD, standard deviation; PCa, prostate adenocarcinoma; BPH, benign prostatic hyperplasia; CD42b T, total CD42b glycoprotein expression; ** $p \leq 0.01$ and * $p < 0.05$ represent statistically significant differences between controls and experimental samples made by independent *t* test.

Table 4. Cell apoptosis at prostate adenocarcinoma and benign prostatic hyperplasia cases reported to control cases.

Number	Parameters	Control X ± SD	PCa X ± SD	Control X ± SD	BPH X ± SD
1	Viability	86.95 ± 5.75	81.30 ± 16.42	86.95 ± 5.75 *	64.26 ± 22.68 *
	p values	0.396		**0.037**	
2	Necrosis	13.04 ± 5.76	8.56 ± 13.40	13.04 ± 5.76 *	26.76 ± 6.32 *
	p values	0.470		**0.030**	
3	Incipient apoptosis	0.10 ± 0.01 *	7.08 ± 10.46 *	0.10 ± 0.01	6.67 ± 10.14
	p values	**0.025**		0.105	
4	Late apoptosis	0.00 ± 0.00	2.96 ± 6.55	0.00 ± 0.00	2.28 ± 5.58
	p values	0.115		0.286	

Legend: X, obtained results mean; SD, standard deviation; PCa, prostate adenocarcinoma; BPH, benign prostatic hyperplasia; IA, incipient apoptosis; LA, late apoptosis; * $p < 0.05$ represents a statistically significant difference between controls and experimental samples made by independent *t* test.

3.2. Surface Glycoproteins of T Cells, Intratumoral Expression of CD34, and Ki-67 Cell Proliferation by ICH Analysis in PCa and BPH Tissue Reported to Non-Malignant Adjacent Tissue Samples

This study presented prostate tissue samples with T cell infiltrates from areas of PCa and BPH versus non-malignant adjacent tissue regions. PCa samples presented similar patterns for CD3+, CD4+, and CD8 lymphocytes that formed clusters adjacent to adenocarcinoma areas, which appeared separated from the lymphocytic infiltration. Healthy prostate tissue samples contain CD3+, CD4+, and CD8+ lymphocytes dispersed in the interstitial stroma without cluster formation. BPH tissue samples presented CD3+, CD4+, and CD8 lymphocytes with their distribution, such as healthy tissue, but they sometimes may form significantly smaller clusters than those of the adenocarcinoma tissue. The total CD3 lymphocytes presented slightly higher patterns without significant differences in PCa and BPH reported in non-malignant tissue samples (59.00 ± 22.43, 57.70 ± 25.48 vs. 44.00 ± 22.62, $p > 0.05$). The cytotoxic CD8 lymphocytes had slightly lower PCa and BHP tissue sample values without significant differences in controls (PCa 31.25 ± 17.55 and BPH 26.00 ± 14.49 vs. C 45.00 ± 28.28, $p > 0.05$, Table 5, Figure 5).

Table 5. Evaluation of T lymphocyte biomarkers and intratumoral expression of CD34 in prostate adenocarcinoma, benign prostatic hyperplasia, and non-malignant adjacent tissue samples.

Number	Parameters	Control X ± SD	PCa X ± SD	Control X ± SD	BPH X ± SD
1	CD3+	44.00 ± 22.62	59.00 ± 22.43	44.00 ± 22.62	57.70 ± 25.48
	p values		0.386		0.499
2	CD4+	66.00 ± 48.08	54.68 ± 21.09	66.00 ± 48.08	66.00 ± 26.11
	p values		0.533		0.919
3	CD8+	45.00 ± 28.28	31.25 ± 17.55	45.00 ± 28.28	26.00 ± 14.49
	p values		0.334		0.166
4	CD34+	1.50 ± 0.70 **	26.12 ± 6.84 **	1.50 ± 0.70	2.60 ± 1.07
	p values		**0.000**		0.204

Legend: X, obtained results mean; SD, standard deviation; PCa, prostate adenocarcinoma; BPH, benign prostatic hyperplasia; CD3, total lymphocytes; CD4, T helper lymphocytes; CD8, cytotoxic T lymphocytes; CD34, intratumoral CD34 glycoproteins; ** $p \leq 0.01$ represents statistically significant differences between controls and experimental samples made by independent *t* test.

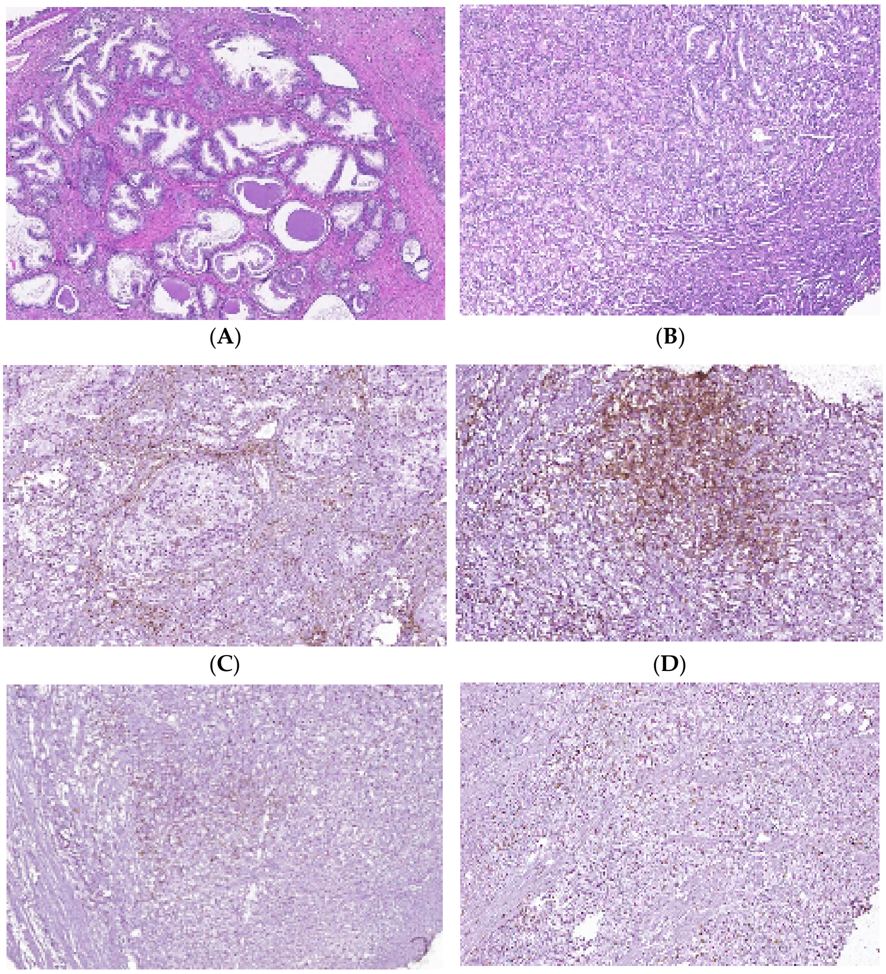
(**A**) (**B**)
(**C**) (**D**)
(**E**) (**F**)

Figure 5. T cell infiltrates from areas of PCa and BPH tissue samples. Legend: (**A**) Microscopic appearance of benign prostatic hyperplasia, usual staining (×20); (**B**) prostate adenocarcinoma, usual staining, Gleason score 3 + 4 (×20); (**C**) CD4-positive peritumoral lymphocytes, more than 50 cells/HPF, prostate adenocarcinoma, Gleason score 3 + 4 (×20); (**D**) CD4-intensely positive in the peritumoral stroma, more than 50 cells/HPF, prostate adenocarcinoma, Gleason score 4 + 5 (×20); (**E**) CD3-positive (adenocarcinoma, Gleason score 4 + 5), less than 50 cells /HPF (×20); (**F**) CD8-positive (adenocarcinoma, Gleason score 4 + 4), more than 50 cells /HPF (×20).

The intratumoral expression of CD34 showed a significantly increased pattern of PCa tissue samples reported to controls (26.12 ± 6.84 vs. 1.50 ± 0.70, $p < 0.01$, Table 5, Figure 6). In addition, Ki-67 was expressed in only PCa tissue samples, the score of cell proliferation being below 25% (score 1+) for all studied PCa cases (Figure 6).

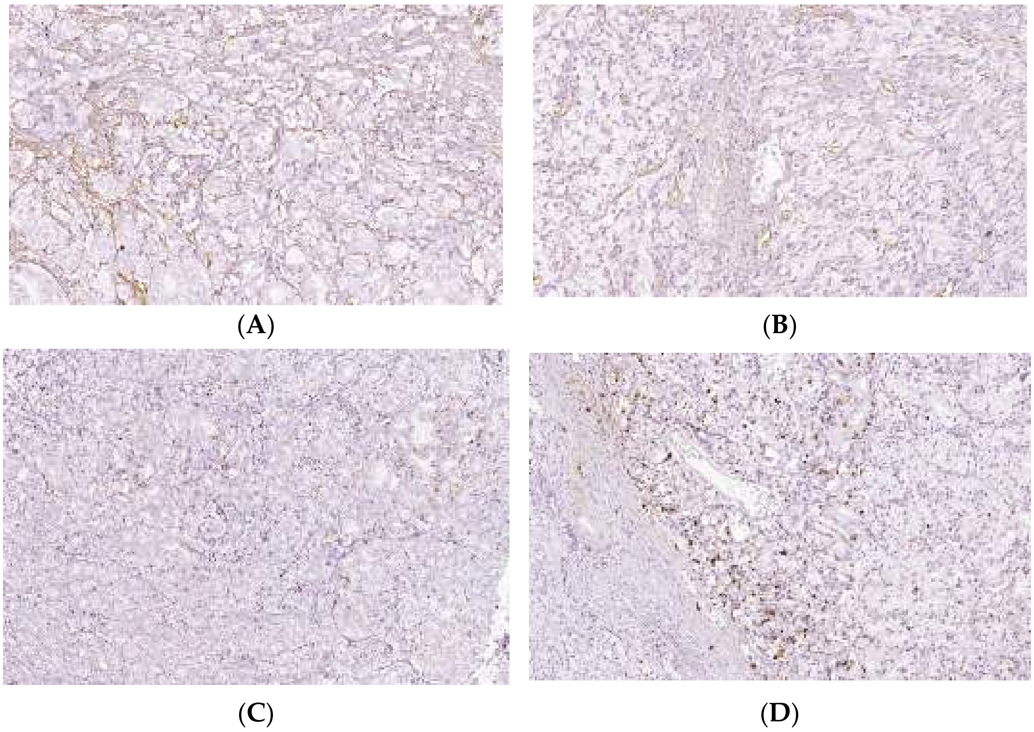

Figure 6. Intratumoral CD34 and Ki-67 expressions of PCa and BPH tissue samples. Legend: (**A**) CD34 positive vascular endothelial, intratumoral, 10–20 vessels/HPF, prostate adenocarcinoma, Gleason score 4 + 3 (×20); (**B**) CD34 positive intratumoral vasculature, 20–30 vessels/HPF adenocarcinoma, Gleason score 4 + 4 (×20); (**C**) Ki67 nuclear positive, score 1+, less than 25% of tumor cell proliferation 9 (×40); (**D**) Ki67 nuclear positive, score 1+, less than 25% of tumor cell proliferation (×40).

3.3. Correlations between DNA Content, Cell Apoptosis, Adhesion Glycoproteins Expressions, Tissue Inflammation Grade, and Ki-67 Cell Proliferation in Tissue Samples

Relationships between the DNA content and adhesion glycoproteins are presented in Table 6. Pearson correlations were observed between the G0/G1 phase of cell cycle and CD34+ CD61+ glycoproteins (r = −0.514; $p < 0.01$), and CD42b+ cell population (r = −0.475; $p < 0.05$), between G2/M phase of cell cycle and CD34+ CD61+ glycoproteins (r = 0.513; $p < 0.01$), and CD42b+ cell population (r = 0.446; $p < 0.05$), between S phase and CD61+ cell population (r = −0.430; $p < 0.05$, Table 6).

Table 6. DNA content and adhesion glycoproteins expressions correlations.

Cell Cycle	CD34 + CD61+	CD61+	CD61-	CD42b+	CD42b-
G0/G1 phase	−0.514 **	−0.150	0.121	−0.475 *	0.490 **
p values	**0.005**	0.447	0.539	**0.011**	**0.008**
S phase	−0.236	−0.430 *	0.431 *	−0.121	0.151
p values	0.226	**0.023**	**0.022**	0.539	0.444
G2/M phase	0.513 **	0.226	−0.200	0.446 *	−0.470 *
p values	**0.005**	0.247	0.307	**0.017**	**0.012**

Legend: * $p < 0.05$ and ** $p < 0.01$ represent statistically significant differences between cases made by Pearson correlations.

Double-positive population of glycoproteins (CD34+ CD61+) were positively correlated with total CD61 and CD34 glycoprotein levels (r = 0.512; r = 0.503, $p < 0.01$), CD61+, CD34+, and CD42b+ cells populations (r = 0.589; r = 0.500; r = 0.623; $p < 0.01$), and were negatively correlated with CD61-, CD34-, and CD42b- cell populations (r = −0.550; r = −0.516; r = −0.641; $p < 0.01$, Table 7).

Table 7. Correlations between glycoprotein levels implied in cell proliferation.

Glycoproteins	CD61T	CD61+	CD61-	CD34T	CD34+	CD34-	CD42b+	CD42b-
CD34+ **CD61+**	0.512 *	0.589 *	−0.550 *	0.503 *	0.500 *	−0.516 *	0.623 *	−0.641 *
p values	**0.005**	**0.001**	**0.002**	**0.006**	**0.007**	**0.005**	**0.000**	**0.000**

Legend: * $p < 0.01$ represents a statistically significant difference between cases made by Pearson correlations.

The grade of tissue inflammation by T lymphocytes was directly correlated with CD 61, CD42b-positive cell populations (r = 0.544; $p < 0.05$; r = 0.664, $p < 0.01$), late apoptosis (r = 0.528; $p < 0.05$) and was inversely correlated with CD 61, CD42b-negative cell populations (r = −0.535; $p < 0.05$; r = −0.639, $p < 0.01$), and cell viability (r = −0.632; $p < 0.01$, Table 8).

Table 8. Tissue inflammation grade (TIG) correlated with adhesion glycoproteins expressions, cell viability, and late cell apoptosis.

Parameters	CD61+	CD61-	CD42b+	CD42b-	Viability	LA
TIG	0.544 *	−0.535 *	0.664 **	−0.639 **	−0.632 *	0.528 *
p values	0.024	0.027	0.004	0.006	0.011	0.043

Legend: ** $p < 0.01$ and * $p < 0.05$ represent statistically significant differences between cases made by Pearson correlations; LA, late apoptosis.

Cell proliferation by Ki-67 expression was positively correlated with cell viability (r = 0.548; $p < 0.05$) and intratumoral CD34 expression (r = 0.611; $p < 0.01$), and was negatively correlated with necrosis (r = −0.682; $p < 0.01$, Table 9).

Table 9. Ki-67 cell proliferation correlates with viability, necrosis, and intratumoral CD34 expression.

Parameters	Viability	Necrosis	CD34 IT
Ki-67 expression	0.548 *	−0.682 **	0.611 **
p values	0.034	0.005	0.009

Legend: ** $p < 0.01$ and * $p < 0.05$ represent statistically significant differences between cases made by Pearson correlations; CD34 IT, intratumoral CD34 glycoproteins expression.

4. Discussion

The cell cycle is characterized by the interphase and mitosis phases. Interphase is represented by three sub-phases, G1, S, and G2. In G1, cells based on internal/external signals lead to a decision of DNA replication or not [4]. The S phase is defined by the ability to synthesize genomic DNA. G2 is the second gap between S and Mitosis, with a function such as DNA damage repair and preparation for entering into Mitosis (M phase). G0/G1, S, and G2/M phases of the cell cycle are quantitatively identified by the flow cytometry method based on propidium iodide stain and RNase.

Ploidy and cell cycle analyses were the first flow cytometry applications, being rapid and efficient measurement methods [33,34]. DNA ploidy is defined as DNA index (DI), and for normal cells in the G0/G1 phase of the cell cycle, DI is 1.0. Aneuploid/polyploid cell populations are divided by DI distribution into categories such as hypodiploid (DI < 0.95), hyperdiploid (DI = 1.15−1.91), tetraploid (DI = 1.92−2.04), hypertetraploid (DI ≥ 2.05), and multiploid (DNA content histogram has ≥2 peaks corresponding to aneuploid/polyploid cell population) [35]. Apoptotic cell frequency that is characterized by fractional DNA content is defined as a subG0/G1 cell population [4].

In our study, 68% of BPH cases present aneuploidy. In addition, 88% of PCa patients had aneuploidy, including hypodiploid and hyperdiploid cell heterogeneity and tetrapoliploidy. PCa samples presented modified cell cycle phases, represented by cell cycle arrest in G0/G1 and a low S phase.

The authors proposed to gain prognostic information by dividing the S proliferative phase (S-phase) into three prognostic categories: low (<7.0%), intermediate (7.0−11.9%), and high (≥12%). These categories allow for the grouping of the patients according to their level of risk. The risk of death or recurrence for diploid and aneuploid cases is 50% higher for the high S-phase category, and 50% higher for the intermediate category than for the low category. Despite different techniques (the tissue samples are fresh, frozen, or paraffin-embedded), a higher S phase of the cell cycle is correlated with worse tumor grade and larger tumors in breast cancer tissue samples [35]. Lower values of the S-phase for PCa and BPH cases were observed in our study, included in the first category of prognostics reported by the references. In addition, we observed a significant negative correlation between the S-phase and CD 61 cell positive population, which means a better survival rate for the patients.

Adhesion glycoproteins from this study, represented by the increased values of double-positive populations of CD34/CD61, and the platelets, T cell aggregation to tumoral cells and endothelium, represented by the CD61+ cell population, observed at PCa and BPH cases, support adhesion, migration, and cell proliferation and are in accord with the following references.

Integrins, the transmembrane glycoprotein receptor superfamily, are represented in our study by the CD61 and CD42b glycoproteins with a role in cancer progression. Altered cell adhesion leads to cell proliferation, migration, and metastasis correlated to the different stages of human tumors and pathological outcomes (metastasis, recurrence, survival) [36–44].

Other integrins, with roles in tumoral cell adhesion and metastasis, such as the CD42b+ cell population had increased values in PCa cases, conforming to the following references. β integrins are transmembrane protein receptors that attach cells to the ECM or bind ligands secreted by other cells. The type I membrane glycoproteins (CD42b) play essential roles in cell signaling networks, growth, differentiation, mobility, and survival [12,15,45].

Integrins are essential in acquiring and maintaining the neoplastic phenotype by escaping from cell apoptosis and maintaining cell proliferation. Integrin expression is modified upon the normal-to-neoplastic transition. Activated platelet integrins αIIbβ3 help the cancer cells of blood circulating from induced tumor cell arrest by binding to leukocytes and platelets to survive a long time [46].

α1β1, α2β1, and α5β1 integrin activation stimulates vascular endothelial growth factor (VEGF) expression, promotes VEGF receptor activation, and increases the adhesion of endothelial cells to ligands (angiogenic effect) [11,47,48].

Other authors observed that cell platelet interactions are mediated either by *p*-selectin or platelet integrin αIIbβ3 in metastasis. αIIbβ3 integrins or *p*-selectin inhibition by function-blocking antibodies determine lower platelet-tumor cell interaction and tumor cell adhesion on activated endothelium [11]. A bridging factor between platelet αIIbβ3 integrins and tumoral cells was identified as a fibrinogen that facilitates tumor cell arrest in the vasculature and metastasis to various tissues [46]. The authors investigated the role of β1 integrins in tumor growth and metastasis and observed that β integrin overexpression correlated with the metastatic spread of these cells to the lung and liver [11].

Metastasis is the common cause of cancer-related deaths because it is based on the complex formation process of the migratory cells, named the epithelial–mesenchymal transition (EMT). The cell-to-cell and cell-to-matrix adhesion molecule expressions are essential to metastasis formation. The leukocytes/cancer cells’ attachment to the endothelium is mediated by different integrins [49]. L1-CAM ligands interact with integrins such as α5ß1, αVß5, αVß1, αVß3, and αIIbß3 with a role in the adhesion process in tumor cell extravasation [50]. In agreement with the references presented above, we observed that

CD61+/CD34+ glycoproteins were positive and significantly correlated with the biomarker of cell metastasis (CD42b+). In BPH cases, mesenchymal cell proliferation is represented by higher values of the CD34+ cell population. According to the references, the characterization of the tumoral cells' adhesion to endothelial cells from larger veins and arteries is represented by a lower pattern for the CD34- cell population.

Mesenchymal cells (MSC) present in *in vitro* mesenchymal differentiation potential, which is well reported by the references. These are associated with properties such as paracrine wound healing, niche forming abilities, immune privilege, and immunomodulation [51,52]. Is was reported that the freshly extracted stromal cells from various tissues contain a CD34+ cells population with distinct characteristics from the total MSC population [53]. CD34+ cells were associated with MSC biomarkers such as CD271 and Stro-1 and biomarkers such as CD45 and CD133 [16,53–56]. CD34+ cells have a greater tendency for endothelial transdifferentiation [57,58]. CD34 was found on embryonic stem cell-derived MSC, suggesting that it is a marker of early human MSC [59]. In addition, CD34 expression was observed on the luminal membrane of cellular processes and the abluminal membrane of cells found at the tips of vascular sprouts [15].

PCa has a lower proliferative capacity, which renders apoptosis induction important for targeted therapies, especially for studying the apoptotic signaling mechanisms responsible for apoptosis evasion [60]. In our study, cell viability was increased for PCa samples, without significant differences reported to the controls. An easily increased but significant value of incipient cell apoptosis was observed in PCa cases. Instead, BPH cases presented a lower pattern of cell viability and a higher necrosis value reported to controls. Our observations are essential to understanding the molecular mechanisms implied in cell apoptosis in PCa and BPH cases because they seem to be different. Cancer progression results from an imbalance in cell proliferation and apoptosis.

Anoikis represents a form of cell apoptosis based on the detachment of cells from the extracellular matrix (ECM), which is evaded by tumor cells to spread [60,61]. This is a developed strategy by the tumor cells in the metastatic spread and therapeutic resistance. Tumor cells undergoing EMT can evade the anoikis based on cellular reprogramming. Pro-EMT molecules such as transcriptional repressors SNAIL and SLUG and cell adhesion molecules confer the resistance of tumoral cells to anoikis [62].

Prostate cancer cells can modify their integrin expressions to lead to an anoikis-resistant phenotype. Integrins in the prostate and other cancers confer a migratory phenotype. Anoikis and EMT processes contribute to chemoresistance, immune evasion, and metastasis [61]. Biochemical recurrence of prostate cancer (bcr) and metastasis prediction after PCa curative treatment were shown by the references for other molecular tests [63].

Another objective of our study was to observe lymphocyte infiltrations, their activation status, and their distribution in PCa and BPH tissues compared to non-malignant prostate tissue samples. T cell infiltrations provide information about the immune system–tumoral cell interactions and the immune evasion mechanisms, which are necessary for developing anti-tumoral immunotherapies.

T cell infiltration in PCa samples forms the clusters adjacent to adenocarcinoma areas, separated from lymphocytic infiltration. The T lymphocytes are dispersed in the interstitial stroma in controls without cluster formation. In addition, T lymphocyte distribution in BPH cases is similar to non-malignant tissue. Analysis of lymphocyte distribution in the tumor environment was described for different tumors [22,64]. An intense infiltration of CD3+ cells is related to slow progression and better prognosis. Our study presented directly correlated T cell infiltrations and CD61+ and CD42b+ adhesion glycoproteins. We observed that an intense T cell infiltration contributes to the generally small tumor size of PCa. A similar association was observed in small-cell lung cancer, where a high number of T cells was associated with a significantly smaller tumor size [65]. The immune cells' recruitment and interactions with the prostate microenvironment promote PCa progression. Studies about the profiles of the prostate tumor-infiltrating lymphocytes are limited. It has been reported that the immune response might have anti- or pro-tumorigenic potential, depending on cell phenotypes and the tumor microenvironment. Distribution and inflammatory cell interactions in the PCa and BPH represent promising indicators of the potential response of the target cell populations in immunotherapies and biomarkers to measure therapeutic efficacy [66,67]. The causal relationship between tumor proliferation and inflammation is widely studied, and in this regard, chronic inflammation has a vital role in developing malignant epithelial tumors [68]. A causal link between inflammation in normal prostate tissue and samples with a diagnosis of malignancy was also observed [66]. In this regard, tumor cells, including prostate malignant neoplastic cells, are modified, atypical cells that can induce a strong immune response in the body, which during the inflammatory process, are consumed, and the lymphocyte-mediated antitumor immune response is gradually reduced [69–71].

Intense tumor neovascularization is closely associated with tumor growth and metastasis. Angiogenesis is thereby a crucial factor affecting the prognosis of cancer patients. The analysis of microvessel density (MVD) by CD34, made in our study, showed a significant increase in the number of microvessels in PCa compared to BPH and non-malignant tissue samples. Intratumoral CD34 represents a biomarker for the IHC visualization of microvessels in benign and malignant prostate tissue. The authors observed that in PCa, a sensitive biomarker for newly derived blood vessels was CD34, and IHC analysis and MVD quantification within the tumor represents the basis for understanding the effects of antiangiogenic treatment [72]. CD34, a myeloid progenitor cell antigen also expressed by endothelial cells of arteries and venules, is considered the most sensitive and stable vascular marker, with a high positive rate and expression level [73]. In addition, the expression of CD34 in new vessels—tiny ones, compared to large ones, considered to be old vessels—in the tumor microscopic field suggests and strengthens the idea that this vascular marker plays a crucial role in the process of tumor neoangiogenesis [74]. Angiogenesis represents a prognostic factor by using CD34 as an endothelial biomarker in various solid tumors, including prostate adenocarcinoma [75–77]. A high immunoexpression of CD34 in the vessels of tumor tissue indicates intensive neoplastic neovascularization and increased MVD. According to some authors, increased MVD was associated with increased PSA and Gleason scores and later clinical stage, which may be due to rapid tumor growth induced by a high nutrient supply rate of newly formed blood vessels [29]. The authors observed a strong correlation between GS and therapeutic response to cabazitaxel in metastatic castration-resistant prostate cancer patients [78].

As men are diagnosed with prostate cancer at an older age than other malignancies, more attention should be paid to markers of anti-angiogenic activity. Combining anti-angiogenic drugs with other drugs of different classes may open a door for more promising clinical results [79].

Another studied biomarker, Ki-67 cell proliferation, was expressed only in prostate adenocarcinoma tissue samples, agreeing with authors who also observed that this biomarker is expressed in PCa reported in BPH tissue samples [29,80,81]. In addition, a significant positive correlation between Ki-67 staining and intratumoral CD34 expression was observed. It was reported that Ki 67 as a proliferating biomarker has higher accuracy in the early diagnosis of PCa [82], although qualifying it as an independent prognostic marker in prostate adenocarcinoma is still controversial. According to some authors, the Ki-67 index is more expressed in adenocarcinoma tissues than in benign prostate hyperplasia and is still higher in metastatic than non-metastatic cases. Thus, an increased Ki-67 value may indicate a poor prognosis of the disease [32]. Our study observed a direct correlation between Ki 67 cell proliferation and intratumoral CD34 expression, but no correlation between Ki67 expression and Gleason scores, as observed in the study [81], which concluded that this nuclear biomarker could be a prognostic factor for prostate cancer.

In this study, the principal limitation to developing the utility of cell cycle, apoptosis, and adhesion glycoproteins, T cell infiltrations, Ki-67, and CD 34 expressions by flow cytometry and IHC methods in adenocarcinoma and hyperplasia prostate cases was a small number of samples recovered from the patients. Another limitation of our study may be represented by the heterogeneity of the PCa tissue samples. With the macro-dissection technique, it is difficult to purify the tumor and non-malignant parts because some cancer parts may still have BPH tissue. For the ideal cases, micro-dissection with laser captures may be needed, but in Romania, only macro-dissection is used to separate the tumoral from the non-malignant parts of tissue samples made by experienced pathologists.

Future directions in this research area will be to study the importance of these biomarkers in many malignant affections because there is a promise to be critical regarding diagnostic biomarkers for diseases and uses to improve patient prognostic survival. In addition, these biomarkers may be studied in the prostate cell line co-culture system, which may provide more information about the biological mechanisms implied in the characterization of the tumoral microenvironment.

5. Conclusions

Biological mechanisms implied in the prostate tumor microenvironment characterization represented by the cell cycle, apoptosis, adhesion glycoproteins, T lymphocytes infiltrations, Ki-67, and intratumoral CD 34 biomarkers provide efficient means of measurement by flow cytometry and IHC techniques for PCa and BPH tissue samples and should be explored in the future not only for diagnostics but also for therapeutic purposes.

Author Contributions: All authors contributed equally to this study and shared the first authorship. Conceptualization, E.M., M.E., C.-A.I., M.A., L.A.T., L.M. and G.C.C.; methodology, E.M., M.E., M.A., G.I.B., A.-A.N., A.F.M., M.D. and C.-A.I.; software, E.M.; validation, M.E.; formal analysis, C.-A.I. and M.E.; investigation C.-A.I., M.E., I.C.I., A.S. and G.C.C.; resources, M.E. and L.A.T.; data curation, M.E.; writing—original draft preparation, E.M., C.-A.I., M.E. and G.C.C.; writing—review and editing, E.M. and M.E.; visualization, G.C.C.; supervision, A.S., L.A.T., M.D., L.M. and M.A.; project administration, L.A.T. and M.E.; funding acquisition, L.A.T. and M.E. All authors have read and agreed to the published version of the manuscript.

Funding: This study is part of the result indicators assumed within the PROMETEU grant, contract number 06/October 20th, 2021. This grant was won in the biomedical competition organized into the CNFIS-FDI-2021-0447 project entitled "Excellence, performance, and competitiveness in biomedical research at the Ovidius University of Constanta".

Institutional Review Board Statement: All aspects of ethics approval and consent to participate of patients in this study are made in conformity with the declaration of Helsinki 2000 and approved by the Ethics Committee of "Ovidius" University of Constanta, Romania, 1430/4 February 2022.

Informed Consent Statement: Informed consent was obtained from all parents of subjects involved in the study.

Data Availability Statement: Data are contained within the article.

Conflicts of Interest: The authors declare that they have no conflict of interest.

References

1. Jemal, A.; Siegel, R.; Ward, E.; Murray, T.; Xu, J.; Smigal, C.; Thun, M.J. Cancer statistics, 2006. *CA Cancer J. Clin.* **2006**, *56*, 106–130. [CrossRef] [PubMed]
2. Hsing, A.W.; Tsao, L.; Devesa, S.S. International trends and patterns of prostate cancer incidence and mortality. *Int. J. Cancer (Pred. Oncol.)* **2000**, *85*, 60–67. [CrossRef]
3. Ebelt, K.; Babaryka, G.; Figel, M.A.; Pohla, H.; Buchner, A.; Stief, C.G.; Eisenmenger, W.; Kirchner, T.; Schendel, J.D.; Noessner, E. Dominance of CD4+ Lymphocytic Infiltrates with Disturbed Effector Cell Characteristics in the Tumor Microenvironment of Prostate Carcinoma. *Prostate* **2008**, *68*, 1–10. [CrossRef] [PubMed]
4. Darzynkiewicz, Z.; Halicka, H.D.; Zhao, H. Analysis of cellular DNA content by flow and laser scanning cytometry. *Adv. Exp. Med. Biol.* **2010**, *676*, 137–147.
5. So, M.J.; Cheville, J.C.; Katzmann, J.A.; Riehle, D.L.; Lohse, B.S.C.M.; Pankratz, B.S.S.V.; Sebo, T.J. Factors That Influence the Measurement of Prostate Cancer DNA Ploidy and Proliferation in Paraffin Embedded Tissue Evaluated by Flow Cytometry. *Mod. Pathol.* **2001**, *14*, 906–912. [CrossRef]
6. Duesberg, P. Does aneuploidy or mutation start cancer? *Science* **2005**, *307*, 41. [CrossRef]
7. Ganem, N.J.; Storchova, Z.; Pellman, D. Tetraploidy, aneuploidy and cancer. *Curr. Opin. Genet. Dev.* **2007**, *17*, 57–162. [CrossRef]

8. Ganem, N.J.; Pellman, D. Limiting the proliferation of polyploid cells. *Cell* **2007**, *131*, 437–440. [CrossRef]
9. Roh, M.; Franco, O.E.; Hayward, S.W.; van der Meer, R.; Abdulkadir, S.A. A Role for Polyploidy in the Tumorigenicity of Pim-1-Expressing Human Prostate and Mammary Epithelial Cells. *PLoS ONE* **2008**, *3*, e2572. [CrossRef]
10. Zimmet, J.; Ravid, K. Polyploidy: Occurrence in nature, mechanisms, and significance for the megakaryocyte-platelet system. *Exp. Hematol.* **2000**, *28*, 3–16. [CrossRef]
11. Bendas, G.; Borsig, L. Cancer Cell Adhesion and Metastasis: Selectins, Integrins, and the Inhibitory Potential of Heparins. *Int. J. Cell Biol.* **2012**, *2012*, 676731. [CrossRef] [PubMed]
12. Goel, H.; Li, J. Integrins in Prostate Cancer Progression. *Endocr. Relat. Cancer* **2008**, *15*, 657–664. [CrossRef] [PubMed]
13. Winograd-Katz, S.E.; Fässler, R.; Geiger, B.; Legate, K.R. The Integrin Adhesome: From Genes and Proteins to Human Disease. *Nat. Rev. Mol. Cell Biol.* **2014**, *15*, 273–288. [CrossRef]
14. Horton, E.R.; Byron, A.; Askari, J.A.; Ng, D.H.J.; Millon-Frémillon, A.; Robertson, J.; Koper, E.J.; Paul, N.R.; Warwood, S.; Knight, D.; et al. Definition of a Consensus Integrin Adhesome and Its Dynamics during Adhesion Complex Assembly and Disassembly. *Nat. Cell Biol.* **2015**, *17*, 1577–1587. [CrossRef]
15. Juan-Rivera, M.C.; Martínez-Ferrer, M. Integrin Inhibitors in Prostate Cancer. *Cancers* **2018**, *10*, 44. [CrossRef]
16. Quirici, N.; Soligo, D.; Bossolasco, P.; Servida, F.; Lumini, C.; Deliliers, G.L. Isolation of bone marrow mesenchymal stem cells by anti-nerve growth factor receptor antibodies. *Exp. Hematol.* **2002**, *30*, 783–791. [CrossRef]
17. Sidney, L.E.; Branch, M.J.; Dunphy, S.E.; Dua, H.S.; Hopkinson, A. Concise Review: Evidence for CD34 as a Common Marker for Diverse Progenitors. *Stem Cells* **2014**, *32*, 1380–1389. [CrossRef] [PubMed]
18. Hristov, M.; Weber, C. Endothelial progenitor cells in vascular repair and remodeling. *Pharmacol. Res.* **2008**, *58*, 148–151. [CrossRef]
19. Collins, A.T.; Habib, F.K.; Maitland, N.J.; Neal, D.E. Identification and isolation of human prostate epithelial stem cells based on alpha (2) beta (1)-integrin expression. *J. Cell Sci.* **2001**, *114*, 3865–3872. [CrossRef]
20. Stachurska, A.; Elbanowski, J.; Kowalczynska, H.M. The role of α5β1and αvβ3 integrins in relation to adhesion and spreading dynamics of prostate cancer cells interacting with fibronectin under in vitro conditions. *Cell Biol. Int.* **2012**, *36*, 883–892. [CrossRef]
21. Rosenberg, S.A. Progress in human tumour immunology and immunotherapy. *Nature* **2001**, *411*, 380–384. [CrossRef] [PubMed]
22. Sato, E.; Olson, S.H.; Ahn, J.; Bundy, B.; Nishikawa, H.; Qian, F.; Jungbluth, A.A.; Frosina, D.; Gnjatic, S.; Ambrosone, C.; et al. Intraepithelial, CD8þ tumor-infiltrating lymphocytes and a high CD8+/regulatory T cell ratio is associated with favourable prognosis in ovarian cancer. *Proc. Natl. Acad. Sci. USA* **2005**, *102*, 18538–18543. [CrossRef] [PubMed]
23. Marincola, F.M.; Jaffee, E.M.; Hicklin, D.J.; Ferrone, S. Escape of human solid tumors from T-cell-recognition: Molecular mechanisms and functional significance. *Adv. Immunol.* **2000**, *74*, 181–273.
24. Radoja, S.; Frey, A.B. Cancer-induced defective cytotoxic T lymphocyte effector function: Another mechanism how antigenic tumors escape immune-mediated killing. *Mol. Med.* **2000**, *6*, 465–479. [CrossRef] [PubMed]
25. Ferro, M.; Lucarelli, G.; de Cobelli, O.; del Giudice, F.; Musi, G.; Mistretta, F.A.; Luzzago, S.; Busetto, G.M.; Buonerba, C.; Sciarra, A.; et al. The emerging landscape of tumor marker panels for the identification of aggressive prostate cancer: The perspective through bibliometric analysis of an Italian translational working group in uro-oncology. *Minerva Urol. Nephrol.* **2021**, *73*, 442–451. [CrossRef]
26. Van Leenders, G.J.L.H.; van der Kwast, T.H.; Grignon, D.J.; Evans, A.J.; Kristiansen, G.; Kweldam, C.F.; Litjens, G.; McKenney, J.K.; Melamed, J.; Mottet, N.; et al. ISUP Grading Workshop Panel Members. The 2019 International Society of Urological Pathology (ISUP) Consensus Conference on Grading of Prostatic Carcinoma. *Am. J. Surg. Pathol.* **2020**, *44*, e87–e99. [CrossRef]
27. Epstein, J.I.; Egevad, L.; Amin, M.B.; Delahunt, B.; Srigley, J.R.; Humphrey, P.A.; Grading Committee. The 2014 International Society of Urological Pathology (ISUP) Consensus Conference on Gleason Grading of Prostatic Carcinoma: Definition of Grading Patterns and Proposal for a New Grading System. *Am. J. Surg. Pathol.* **2016**, *40*, 244–252. [CrossRef]
28. Pierorazio, P.M.; Walsh, P.C.; Partin, A.W.; Epstein, J.I. Prognostic Gleason grade grouping: Data based on the modified Gleason scoring system. *BJU Int.* **2013**, *111*, 753–760. [CrossRef]
29. Wang, Y.; Dong, X.; Qu, Z.; Peng, K.; Sun, X.; Chen, R. Correlation between peripheral blood neutrophil-lymphocyte ratio and CD34 expression in prostate cancer. *BMC Cancer* **2020**, *20*, 900. [CrossRef]
30. Davidsson, S.; Ohlson, A.L.; Andersson, S.O.; Fall, K.; Meisner, A.; Fiorentino, M.; Andrén, O.; Rider, J.R. CD4 helper T cells, CD8 cytotoxic T cells, and FOXP3 + regulatory T cells with respect to lethal prostate cancer. *Mod. Pathol.* **2013**, *26*, 448–455. [CrossRef]
31. Gautama, K.A.; Singhb, A.N.; Srivastavc, A.N.; Sankhwar, S.N. Angiogenesis in prostate cancer and benign prostatic hyperplasia assessed by VEGF and CD-34 IHC: A comparative clinico-pathological study. *Afr. J. Urol.* **2018**, *24*, 98–103. [CrossRef]
32. Madani, S.H.; Ameli, S.; Khazaei, S.; Kanani, M.; Izadi, B. Frequency of Ki-67 (MIB-1) and P53 expressions among patients with prostate cancer. *Indian J. Pathol. Microbiol.* **2011**, *54*, 688–691. [PubMed]
33. Darzynkiewicz, Z.; Traganos, F.; Zhao, H.; Halicka, H.D.; Li, J. Cytometry of DNA replication and RNA synthesis: Historical perspective and recent advances based on "click chemistry". *Cytom. Part A* **2011**, *79*, 328–337. [CrossRef]
34. López-Otero, A.; Ruiz-Delgado, G.J.; Hernández-Arizpe, A.; Ruiz-Argüelles, A.; Ruiz-Argüelles, G.J. The flow-cytometric DNA content of the plasma cells of patients with multiple myeloma is a prognostic factor: A single institution experience. *Hematology* **2010**, *15*, 378–381. [CrossRef] [PubMed]
35. Gerashchenko, B.I.; Huna, A.; Erenpreisa, J. Characterization of breast cancer DNA content profiles as a prognostic tool. *Exp. Oncol.* **2014**, *36*, 219–225. [PubMed]

36. Mitchell, K.; Svenson, K.B.; Longmate, W.M.; Gkirtzimanaki, K.; Sadej, R.; Wang, X.; Zhao, J.; Eliopoulos, A.G.; Berditchevski, F.; DiPersio, C.M. Suppression of integrin alpha3beta1 in breast cancer cells reduces cyclooxygenase-2 gene expression and inhibits tumorigenesis, invasion, and cross-talk to endothelial cells. *Cancer Res.* **2010**, *70*, 6359–6367. [CrossRef]
37. Saito, Y.; Sekine, W.; Sano, R.; Komatsu, S.; Mizuno, H.; Katabami, K.; Shimada, K.; Oku, T.; Tsuji, T. Potentiation of cell invasion and matrix metalloproteinase production by alpha3beta1 integrin-mediated adhesion of gastric carcinoma cells to laminin-5. *Clin. Exp. Metastasis* **2010**, *27*, 197–205. [CrossRef]
38. Tsuji, T.; Kawada, Y.; Kai-Murozono, M.; Komatsu, S.; Han, S.A.; Takeuchi, K.; Mizushima, H.; Miyazaki, K.; Irimura, T. Regulation of melanoma cell migration and invasion by laminin-5 and alpha 3 beta 1 integrin (VLA-3). *Clin. Exp. Metastasis* **2002**, *19*, 127–134. [CrossRef]
39. Pontes-Junior, J.; Reis, S.T.; Dall'Oglio, M.; Neves de Oliveira, L.C.; Cury, J.; Carvalho, P.A.; Ribeiro-Filho, L.A.; Leite, K.R.M.; Srougi, M. Evaluation of the expression of integrins and cell adhesion molecules through tissue microarray in lymph node metastases of prostate cancer. *J. Carcinog.* **2009**, *8*, 3–9. [CrossRef]
40. Rolli, M.; Fransvea, E.; Pilch, J.; Saven, A.; Felding-Habermann, B. Activated integrin alphavbeta3 cooperates with metalloproteinase MMP-9 in regulating migration of metastatic breast cancer cells. *Proc. Natl. Acad. Sci. USA* **2003**, *100*, 9482–9487. [CrossRef]
41. Reinmuth, N.; Liu, W.; Ahmad, S.A.; Fan, F.; Stoeltzing, O.; Parikh, A.A.; Bucana, C.D.; Gallick, G.E.; Nickols, M.A.; Westlin, W.F.; et al. $\alpha v\beta 3$ integrin antagonist S247 decreases colon cancer metastasis and angiogenesis and improves survival in mice. *Cancer Res.* **2003**, *63*, 2079–2087. [PubMed]
42. Gillan, L.; Matei, D.; Fishman, D.A.; Gerbin, C.S.; Karlan, B.Y.; Chang, D.D. Periostin secreted by epithelial ovarian carcinoma is a ligand for $\alpha V\beta 3$ and $\alpha V\beta 5$ integrins and promotes cell motility. *Cancer Res.* **2002**, *62*, 5358–5364.
43. Ramirez, N.E.; Zhang, Z.; Madamanchi, A.; Boyd, K.L.; O'Rear, L.D.; Nashabi, A.; Li, Z.; Dupont, W.D.; Zijlstra, A.; Zutter, M.M. The α 2 β 1 integrin is a metastasis suppressor in mouse models and human cancer. *J. Clin. Investig.* **2011**, *121*, 226–237. [CrossRef] [PubMed]
44. Hall, C.L.; Dubyk, C.W.; Riesenberger, T.A.; Shein, D.; Keller, E.T.; van Golen, K.L. Type I collagen receptor ($\alpha 2\beta 1$) signaling promotes prostate cancer invasion through RhoC GTPase. *Neoplasia* **2008**, *10*, 797–803. [CrossRef]
45. Ryu, S.; Park, K.M.; Lee, S.H. Gleditsia Sinensis Thorn Attenuates the Collagen-Based Migration of PC3 Prostate Cancer Cells through the Suppression of Integrin Expression. *Int. J. Mol. Sci.* **2016**, *17*, 328. [CrossRef]
46. Felding-Habermann, B.; O'Toole, T.E.; Smith, J.W.; Fransvea, E.; Ruggeri, Z.M.; Ginsberg, M.H.; Hughes, P.E.; Pampori, N.; Shattil, S.J.; Saven, A.; et al. Integrin activation controls metastasis in human breast cancer. *Proc. Natl. Acad. Sci. USA* **2001**, *98*, 1853–1858. [CrossRef]
47. Byzova, T.V.; Goldman, C.K.; Pampori, N.; Thomas, K.A.; Bett, A.; Shattil, S.J.; Plow, E.F. A mechanism for modulation of cellular responses to VEGF: Activation of the integrins. *Mol. Cell* **2000**, *6*, 851–860. [CrossRef]
48. Francis, S.E.; Goh, K.L.; Hodivala-Dilke, K.; Bader, B.L.; Stark, M.; Davidson, D.; Hynes, R.O. Central roles of alpha 5 beta 1 integrin and fibronectin in vascular development in mouse embryos and embryoid bodies. *Arterioscler. Thromb. Vasc. Biol.* **2002**, *22*, 927–933. [CrossRef]
49. Sökeland, G.; Schumacher, U. The functional role of integrins during intra- and extravasation within the metastatic cascade. *Mol. Cancer* **2019**, *18*, 12. [CrossRef]
50. Kiefel, H.; Bondong, S.; Hazin, J.; Ridinger, J.; Schirmer, U.; Riedle, S.; Altevogt, P. L1CAM: A major driver for tumor cell invasion and motility. *Cell Adhes. Migr.* **2012**, *6*, 374–384. [CrossRef]
51. Phinney, D.G.; Prockop, D.J. Concise review: Mesenchymal stem/multipotent stromal cells: The state of transdifferentiation and modes of tissue repair—Current views. *Stem Cells* **2007**, *25*, 2896–2902. [CrossRef] [PubMed]
52. Chamberlain, G.; Fox, J.; Ashton, B.; Middleton, J. Concise review: Mesenchymal stem cells: Their phenotype, differentiation capacity, immunological features, and potential for homing. *Stem Cells* **2007**, *25*, 2739–2749. [CrossRef] [PubMed]
53. Ferraro, G.A.; de Francesco, F.; Nicoletti, G.; Paino, F.; Desiderio, V.; Tirino, V.; D'Andrea, F. Human adipose CD34 (1) CD90 (1) stem cells and collagen scaffold constructs grafted in vivo fabricate loose connective and adipose tissues. *J. Cell. Biochem.* **2013**, *114*, 1039–1049. [CrossRef] [PubMed]
54. Kuci, S.; Kuci, Z.; Kreyenberg, H.; Deak, E.; Pütsch, K.; Huenecke, S.; Amara, C.; Koller, S.; Rettinger, E.; Grez, M.; et al. CD271 antigen defines a subset of multipotent stromal cells with immunosuppressive and lymphohematopoietic engraftment promoting properties. *Haematologica* **2010**, *95*, 651–659. [CrossRef]
55. Nielsen, J.S.; McNagny, K.M. CD34 is a key regulator of hematopoietic stem cell trafficking to bone marrow and mast cell progenitor trafficking in the periphery. *Microcirculation* **2009**, *16*, 487–496. [CrossRef] [PubMed]
56. Kaiser, S.; Hackanson, B.; Follo, M.; Mehlhorn, A.; Geiger, K.; Ihorst, G.; Kapp, U. BM cells giving rise to MSC in culture have a heterogeneous CD34 and CD45 phenotype. *Cytotherapy* **2007**, *9*, 439–450. [CrossRef]
57. De Francesco, F.; Tirino, V.; Desiderio, V.; Ferraro, G.; D'Andrea, F.; Giuliano, M.; Libondi, G.; Pirozzi, G.; de Rosa, A.; Papaccio, G. Human CD34/CD90 ASCs are capable of growing as sphere clusters, producing high levels of VEGF and forming capillaries. *PLoS ONE* **2009**, *4*, e6537. [CrossRef]
58. Miranville, A.; Heeschen, C.; Sengenes, C.; Curat, C.A.; Busse, R.; Bouloumie, A. Improvement of postnatal neovascularization by human adipose tissue-derived stem cells. *Circulation* **2004**, *110*, 349–355. [CrossRef]

59. Kopher, R.A.; Penchev, V.R.; Islam, M.S.; Hill, K.L.; Khosla, S.; Kaufman, D.S. Human embryonic stem cell-derived CD341 cells function as MSC progenitor cells. *Bone* **2010**, *47*, 718–728. [CrossRef]
60. Rennebeck, G.; Martelli, M.; Kyprianou, N. Anoikis and survival connections in the tumor microenvironment: Is there a role in prostate cancer metastasis? *Cancer Res.* **2005**, *65*, 11230–11235. [CrossRef]
61. Nakazawa, M.; Paller, C.; Kyprianou, N. Mechanisms of Therapeutic Resistance in Prostate Cancer. *Curr. Oncol. Rep.* **2017**, *19*, 13. [CrossRef] [PubMed]
62. Frisch, S.M.; Screaton, R.A. Anoikis mechanisms. *Curr. Opin. Cell Biol.* **2001**, *13*, 555–562. [CrossRef]
63. Govers, T.M.; Hessels, D.; Vlaeminck-Guillem, V.; Schmitz-Dräger, B.J.; Stief, C.G.; Martinez-Ballesteros, C.; Ferro, M.; Borque-Fernando, A.; Rubio-Briones, J.; Sedelaar, J.P.M.; et al. Cost-effectiveness of SelectMDx for prostate cancer in four European countries: A comparative modeling study. *Prostate Cancer Prostatic Dis.* **2019**, *22*, 101–109. [CrossRef] [PubMed]
64. Tsuta, K.; Ishii, G.; Kim, E.; Shiono, S.; Nishiwaki, Y.; Endoh, Y.; Kodama, T.; Nagai, K.; Ochiai, A. Primary lung adenocarcinoma with massive lymphocyte infiltration. *Am. J. Clin. Pathol.* **2005**, *123*, 547–552. [CrossRef]
65. Eerola, A.K.; Soini, Y.; Paakko, P. A high number of tumor infiltrating lymphocytes are associated with a small tumor size, low tumor stage and a favourable prognosis in operated small cell lung carcinoma. *Clin. Cancer Res.* **2000**, *6*, 1875–1881.
66. Gurel, B.; Lucia, M.S.; Thompson, I.M., Jr.; Goodman, P.J.; Tangen, C.M.; Kristal, A.R.; Parnes, H.L.; Hoque, A.; Lippman, S.M.; Sutcliffe, S.; et al. Chronic inflammation in benign prostate tissue is associated with high-grade prostate cancer in the placebo arm of the prostate cancer prevention trial. *Cancer Epidemiol. Biomark. Prev.* **2014**, *23*, 847–856. [CrossRef]
67. Pepe, P.; Aragona, F. Does an inflammatory pattern at primary biopsy suggest a lower risk for prostate cancer at repeated saturation prostate biopsy? *Urol. Int.* **2011**, *87*, 171–174. [CrossRef]
68. Brower, V. Feeding the flame: New research adds to role of inflammation in cancer development. *J. Natl. Cancer Inst.* **2005**, *97*, 251–253. [CrossRef]
69. Gokce, M.I.; Tangal, S.; Hamidi, N.; Suer, E.; Ibis, M.A.; Beduk, Y. Role of neutrophil to-lymphocyte ratio in prediction of Gleason score upgrading and disease upstaging in low-risk prostate cancer patients eligible for active surveillance. *Can. Urol. Assoc. J.* **2016**, *10*, E383–E387. [CrossRef]
70. Grivennikov, S.I.; Greten, F.R.; Karin, M. Immunity, inflammation, and cancer. *Cell* **2010**, *140*, 883–899. [CrossRef]
71. Sharaiha, R.Z.; Halazun, K.J.; Mirza, F.; Port, J.L.; Lee, P.C.; Neugut, A.I.; Altorki, N.K.; Abrams, J.A. Elevated preoperative neutrophil:lymphocyte ratio as a predictor of postoperative disease recurrence in esophageal cancer. *Ann. Surg. Oncol.* **2011**, *18*, 3362–3369. [CrossRef] [PubMed]
72. Trojan, L.; Daniel, T.; Friedrich, D.; Grobholz, R.; Knoll, T.; Alken, P.; Michel, M.S. Expression of Different Vascular Endothelial Markers in Prostate Cancer and BPH Tissue: An Immunohistochemical and Clinical Evaluation. *Anticancer Res.* **2004**, *24*, 1651–1656. [CrossRef]
73. Teo, N.B.; Shoker, B.S.; Jarvis, C.; Martin, L.; Sloane, J.P.; Holcombe, C. Vascular density and phenotype around ductal carcinoma in situ (DCIS) of the breast. *Br. J. Cancer* **2002**, *86*, 905–911. [CrossRef]
74. Miyata, Y.; Mitsunari, K.; Asai, A.; Takehara, K.; Mochizuki, Y.; Sakai, H. Pathological significance and prognostic role of microvessel density, evaluated using CD31, CD34, and CD105 in prostate cancer patients after radical prostatectomy with neoadjuvant therapy. *Prostate* **2015**, *75*, 84–91. [CrossRef] [PubMed]
75. Poon, R.T.; Fan, S.T.; Wong, J. Clinical significance of angiogenesis in gastrointestinal cancers: A target for novel prognostic and therapeutic approaches. *Ann. Surg.* **2003**, *238*, 9–28. [CrossRef] [PubMed]
76. Kato, T.; Kameoka, S.; Kimura, T.; Nishikawa, T.; Kobayashi, M. The combination of angiogenesis and blood vessel invasion as a prognostic indicator in primary breast cancer. *Br. J. Cancer* **2003**, *88*, 1900–1908. [CrossRef]
77. Jemaa, A.B.; Bouraoui, Y.; Sallami, S.; Banasr, A.; Rais, N.B.; Ouertani, L.; Nouira, Y.; Horchani, A.; Oueslati, R. Co-expression and impact of prostate specific membrane antigen and prostate specific antigen in prostatic pathologies. *J. Exp. Clin. Cancer Res.* **2010**, *29*, 171. [CrossRef]
78. Buonerba, C.; Pond, G.R.; Sonpavde, G.; Federico, P.; Rescigno, P.; Puglia, L.; Bosso, D.; Virtuoso, A.; Policastro, T.; Izzo, M.; et al. Potential value of Gleason score in predicting the benefit of cabazitaxel in metastatic castration-resistant prostate cancer. *Future Oncol.* **2013**, *9*, 889–897. [CrossRef]
79. Bilusic, M.; Wong, Y.N. Anti-angiogenesis in prostate cancer: Knocked down but not out. *Asian J Androl.* **2014**, *16*, 372–377.
80. Nikoleishvili, D.; Pertia, A.; Trsintsadze, O.; Gogokhia, N.; Managadze, L.; Chkhotua, A. Expression of p27 ((Kip1)), cyclin D3 and Ki67 in BPH, prostate cancer and hormone-treated prostate cancer cells. *Int. Urol. Nephrol.* **2008**, *40*, 953–959. [CrossRef]
81. Rashed, H.E.; Kateb, M.I.; Ragab, A.A.; Shaker, S.S. Evaluation of minimal prostate cancer in needle biopsy specimens using AMACR (p504s), p63 and Ki-67. *Life Sci.* **2012**, *9*, 12–21.
82. Zhong, D.W.; Peng, J.; He, H.C.; Wu, D.; Han, Z.D.; Bi, X.C.; Dai, Q.S. Ki-67 and PCNA expression in prostate cancer and benign prostatic hyperplasia. *Clin. Investig. Med.* **2008**, *31*, E8–E15. [CrossRef] [PubMed]

pharmaceuticals

MDPI

Article

Phenolic Secondary Metabolites and Antiradical and Antibacterial Activities of Different Extracts of *Usnea barbata* (L.) Weber ex F.H.Wigg from Călimani Mountains, Romania

Violeta Popovici [1,†], Laura Bucur [2,*], Cerasela Elena Gîrd [3,*], Antoanela Popescu [2,†], Elena Matei [4,†], Georgeta Camelia Cozaru [4,5,†], Verginica Schröder [6,*], Emma Adriana Ozon [7,*], Ancuța Cătălina Fița [7,*], Dumitru Lupuliasa [7,‡], Mariana Aschie [4,5,‡], Aureliana Caraiane [8,‡], Mihaela Botnarciuc [9,‡] and Victoria Badea [1,‡]

[1] Department of Microbiology and Immunology, Faculty of Dental Medicine, Ovidius University of Constanta, 7 Ilarie Voronca Street, 900684 Constanta, Romania; violeta.popovici@365.univ-ovidius.ro (V.P.); victoria.badea@365.univ-ovidius.ro (V.B.)
[2] Department of Pharmacognosy, Faculty of Pharmacy, Ovidius University of Constanta, 6 Capitan Al. Serbanescu Street, 900001 Constanta, Romania; antoanela.popescu@365.univ-ovidius.ro
[3] Department of Pharmacognosy, Phytochemistry, and Phytotherapy, Faculty of Pharmacy, Carol Davila University of Medicine and Pharmacy, 6 Traian Vuia Street, 020956 Bucharest, Romania
[4] Center for Research and Development of the Morphological and Genetic Studies of Malignant Pathology, Ovidius University of Constanta, CEDMOG, 145 Tomis Blvd., 900591 Constanta, Romania; sogorescuelena@gmail.com (E.M.); drcozaru@yahoo.com (G.C.C.); aschiemariana@yahoo.com (M.A.)
[5] Clinical Service of Pathology, Sf. Apostol Andrei Emergency County Hospital, 145 Tomis Blvd., 900591 Constanta, Romania
[6] Department of Cellular and Molecular Biology, Faculty of Pharmacy, Ovidius University of Constanta, 6 Capitan Al. Serbanescu Street, 900001 Constanta, Romania
[7] Department of Pharmaceutical Technology and Biopharmacy, Faculty of Pharmacy, Carol Davila University of Medicine and Pharmacy, 6 Traian Vuia Street, 020956 Bucharest, Romania; dumitru.lupuliasa@umfcd.ro
[8] Department of Oral Rehabilitation, Faculty of Dental Medicine, Ovidius University of Constanta, 7 Ilarie Voronca Street, 900684 Constanta, Romania; aureliana.caraiane@365.univ-ovidius.ro
[9] Department of Microbiology, Faculty of Medicine, Ovidius University of Constanta, 1 University Street, 900470 Constanta, Romania; mihaela.botnarciuc@365.univ-ovidius.ro
* Correspondence: laurabucur@univ-ovidius.ro (L.B.); cerasela.gird@umfcd.ro (C.E.G.); verginica.schroder@univ-ovidius.ro (V.S.); emma.budura@umfcd.ro (E.A.O.); catalina.fita@umfcd.ro (A.C.F.)
† These authors contributed equally to this work.
‡ These authors contributed equally to this work.

check for updates

Citation: Popovici, V.; Bucur, L.; Gîrd, C.E.; Popescu, A.; Matei, E.; Cozaru, G.C.; Schröder, V.; Ozon, E.A.; Fița, A.C.; Lupuliasa, D.; et al. Phenolic Secondary Metabolites and Antiradical and Antibacterial Activities of Different Extracts of *Usnea barbata* (L.) Weber ex F.H.Wigg from Călimani Mountains, Romania. *Pharmaceuticals* **2022**, *15*, 829. https://doi.org/10.3390/ph15070829

Academic Editors: Fernando Calzada and Miguel Valdes

Received: 6 June 2022
Accepted: 1 July 2022
Published: 4 July 2022

Abstract: Phenolic compounds represent an essential bioactive metabolites group with numerous pharmaceutical applications. Our study aims to identify and quantify phenolic constituents of various liquid and dry extracts of *Usnea barbata* (L.) Weber ex F.H. Wigg (*U. barbata*) from Calimani Mountains, Romania, and investigate their bioactivities. The extracts in acetone, 96% ethanol, and water with the same dried lichen/solvent ratio (w/v) were obtained through two conventional techniques: maceration (*m*UBA, *m*UBE, and *m*UBW) and Soxhlet extraction (*d*UBA, *d*UBE, and *d*UBW). High-performance liquid chromatography with diode-array detection (HPLC-DAD) was performed for usnic acid (UA) and different polyphenols quantification. Then, the total phenolic content (TPC) and 2,2-diphenyl-1-picrylhydrazyl (DPPH) free-radical scavenging activity (AA) were determined through spectrophotometric methods. Using the disc diffusion method (DDM), the antibacterial activity was evaluated against Gram-positive and Gram-negative bacteria known for their pathogenicity: *Staphylococcus aureus* (ATCC 25923), *Streptococcus pneumoniae* (ATCC 49619), *Pseudomonas aeruginosa* (ATCC 27853), and *Klebsiella pneumoniae* (ATCC 13883). All extracts contain phenolic compounds expressed as TPC values. Five lichen extracts display various UA contents; this significant metabolite was not detected in *d*UBW. Six polyphenols from the standards mixture were quantified only in ethanol and water extracts; *m*UBE has all individual polyphenols, while *d*UBE shows only two. Three polyphenols were detected in *m*UBW, but none was found in *d*UBW. All *U. barbata* extracts had antiradical activity; however, only ethanol and acetone extracts proved inhibitory activity against *P. aeruginosa*, *S. pneumoniae*, and *S. aureus*. In contrast, *K. pneumoniae* was strongly resistant (IZD = 0). Data analysis evidenced a high positive correlation between the phenolic constituents and bioactivities of each *U. barbata* extract. Associating these extracts' properties with both conventional techniques used for their preparation revealed the extraction conditions' significant influence on lichen extracts metabolites profiling, with a powerful impact on their pharmacological potential.

Keywords: *Usnea barbata* (L.) Weber ex F.H. Wigg extracts; phenolic secondary metabolites; usnic acid; polyphenols; DPPH free-radical scavenging activity; antibacterial activity

1. Introduction

Phenolic compounds are essential plant secondary metabolites with numerous pharmaceutical applications [1]. As unique symbionts between fungi and algae, lichens are distinguished in the plants' world by their specific secondary metabolites with phenolic structures (depsides, depsidones, dibenzofurans, anthraquinones, and xanthones) [2]. These constituents are deposited as crystals on fungal hyphae in the cortex or medulla; the different distribution in the thallus layers is correlated with their biological actions [3]. The lichen's most significant pharmacological activities are antioxidant [4], antimicrobial [5], anticancer [6], photoprotective [7], and anti-inflammatory [8]. Therefore, they are considered important representatives with biopharmaceutical potential [9]. Due to remarkable antioxidant [10] and antibacterial [11] properties, lichens represent a promising source of protective [12–14] and antibiotic drugs [15–17].

With numerous pharmacological activities, the lichens of the genus *Usnea* (*Parmeliaceae*) are appreciated as powerful phytomedicines, used for therapeutical purposes for thousands of years [18]. The most known secondary metabolite in *Usnea* sp. is usnic acid—a phenolic compound with a dibenzofuran structure. As yellow crystals, it is found on cortex fungal hyphae, exhibiting a photoprotective action [19]. Usnic acid is found as a (+) enantiomer in *Usnea* lichens [20]. A valuable representative of this genus, known for its antioxidant [21], antibacterial [22], and photoprotective [7] effects, is *U. barbata*. Usnic acid is the main secondary metabolite responsible for its pharmacological potential [23]. The pharmaceutical applications of UA as an antibacterial agent are limited by its poor water solubility [24] and significant hepatotoxicity [25]. Therefore, the nanosystems with usnic acid must be able to increase its bio-disponibility, tolerance, and antibacterial effects [26]. Interesting nanoformulations were performed: liposomal UA-cyclodextrin inclusion complexes, which increase usnic acid solubility in water [27], glycosylated cationic liposomes, promoting usnic acid penetration in the bacterial biofilm matrix [28], and magnetic nanoparticles [29] with antimicrobial activity and antibiofilm activity against Gram-positive bacteria (*S. aureus* and *E. faecalis*) and Gram-negative ones (*P. aeruginosa*). Balaz et al. [30] recently proposed a bio-mechanochemical synthesis of silver nanoparticles using *U. antarctica* and other lichen species. Using $AgNO_3$ (as a silver precursor) and lichens (as reduction agents), they performed techniques of mechanochemistry (ball milling) and obtained nanoparticles with an intense antibacterial effect against *S. aureus*. This described procedure overcomes the lichen secondary metabolites' low solubility in water. Siddiqi et al. [31] demonstrated the antimicrobial properties of *U. longissima*-driven silver nanoparticles through the denaturation of ribosomes, leading to enzyme inactivation and protein denaturation, resulting in bacterial apoptosis.

U. barbata also contains bioactive polyphenols with pharmaceutical applications; different nanotechnologies were described to enhance their bioavailability and biocompatibility [32]. They can be used as nanoparticles to increase their antioxidant and antibacterial potential or other activities [33–38].

Numerous studies investigated the antibacterial effects of *Usnea* sp. Extracts—obtained through conventional and green extraction techniques—for pharmaceutical applications [39]. Thus, Tosun et al. [40] explored the antimycobacterial action of *U. barbata* fractions in petroleum ether, chloroform, methanol, and water. Bate et al. [41] studied the antibacterial activity of *U. articulata* and *U. florida* methanol macerates against MDR bacteria (*Staphylococcus* sp., *P aeruginosa*, *Salmonella* sp., and *E. coli*). Zizovic et al. [42] proved the strong antibacterial action of *U. barbata* supercritical fluid extracts (SFE). One year later, Ivanovic et al. [43] analyzed the influence of various extraction conditions (temperature, pressure) and pre-treatment methods on bactericidal effects against *S. aureus* strains. Basiouni et al. [44] evaluated the *U. barbata* sunflower oil extract inhibitory activity on bacterial strains isolates from poultry. In a previous study, Matvieva et al. [15] analyzed the antimicrobial properties of the ethanol, isopropanol, acetone, DMSO, and water extracts of *Usnea* sp against *S. aureus*, *B. subtilis*, and *E coli.*

We propose to investigate the antibacterial and antiradical properties of *U barbata* extracts in the same solvents, obtained by two low-cost and easy-to-use conventional techniques. Our study novelty consists of a comparative analysis of fluid and dry *U. barbata* extracts in ethanol, acetone, and water, obtained by maceration and Soxhlet extraction [34], determining their phenolic constituents and evaluating the free radical scavenging activity and antibacterial effects. Our results revealed that, despite the same ratio between the dried lichen and the solvent (*w*/*v*), all *U. barbata* extracts display significant differences in the phenolic metabolites' diversity and amount due to extraction conditions, with a substantial impact on their bioactivities.

2. Results

2.1. Lichen Extracts

All data regarding the obtained *U. barbata* extracts are displayed in Table 1 and Figure S1 from Supplementary Materials.

Table 1. Extraction conditions and *U. barbata* extracts color.

Extraction Solvent	*U. barbata* Extract	Temperature of Extraction (°C)	Yield (%)	*U. barbata* Extract's Color
Acetone	*d*UBA	55–60	5.55 ^{b}	Yellow-brown
	*m*UBA	20–22	n/a	Yellow
Ethanol	*d*UBE	75–80	11.15 ^{a}	Light brown
	*m*UBE	20–22	n/a	Light brown
Water	*d*UBW	95–100	1.76 ^{c}	Dark brown-reddish
	*m*UBW	20–22	n/a	Brown reddish

UBA—*U. barbata* acetone extract, UBE—*U. barbata* ethanol extract, UBW—*U. barbata* water extract; *m*—macerate, *d*—dry extract, n/a—not applicable. The yield values followed by superscript letters are statistically significant ($p < 0.05$).

Data from Table 1 show that the extraction temperature for liquid extracts was 20–22 °C, and their color varies from yellow (*m*UBA) to light brown (*m*UBE) and brown-reddish (*m*UBW).

At Soxhlet extraction, the temperature value increased from *d*UBA (55–60 °C) to *d*UBE (75–80 °C) and *d*UBW (95–100 °C). The highest yield (11.15%) was obtained for *d*UBE; its value decreased to 5.55% for *d*UBA and 1.76% for *d*UBW. Moreover, the dry extracts color changed from yellow-brown (*d*UBA) to light brown (*d*UBE) and dark brown-reddish (*d*UBW).

2.2. HPLC-DAD Determination of Usnic Acid Content

The usnic acid contents in all *U. barbata* extracts are displayed in Table 2.

All liquid extracts contain UA. Thus, *m*UBA had the highest UA content (211.9 mg/g extract equivalent to 21.19 mg/g dried lichen), following in decreasing order *m*UBE (0.257 mg/g, corresponding to 0.025 mg/g dried lichen) and *m*UBW (0.045 mg/g corresponding to 0.004 mg/g dried lichen). According to https://pubchem.ncbi.nlm.nih.gov/compound/Usnic-acid (accessed on 20 May 2022), usnic acid solubility significantly decreases in order: acetone > ethanol > water; these data can explain our results.

Table 2. Usnic acid content in fluid and dry *U. barbata* extracts.

***U. barbata* Extract**		**UAC**	
		mg/g Lichen Extract	**mg/g Dried Lichen**
Acetone	*m*UBA	211.900 ± 0.002 ^{b}	21.190 ^{f}
	*d*UBA	241.830 ± 0.172 ^{a}	13.418 ^{g}
Ethanol	*m*UBE	0.257 ± 0.002 ^{d}	0.025 ^{i}
	*d*UBE	108.742 ± 0.703 ^{c}	12.125 ^{h}
Water	*m*UBW	0.045 ± 0.002 ^{e}	0.004 ^{j}
	*d*UBW	ND	n/a

UAC—usnic acid content, UBA—*U. barbata* acetone extract, UBE—*U. barbata* ethanol extract, UBW—*U. barbata* water extract; *m*—macerate, *d*—dry extract, ND—non-detected, n/a—not applicable; the mean values followed by superscript letters are statistically significant ($p < 0.05$).

The chromatograms of usnic acid standard and *U. barbata* extracts in all three solvents are displayed in Figure 1.

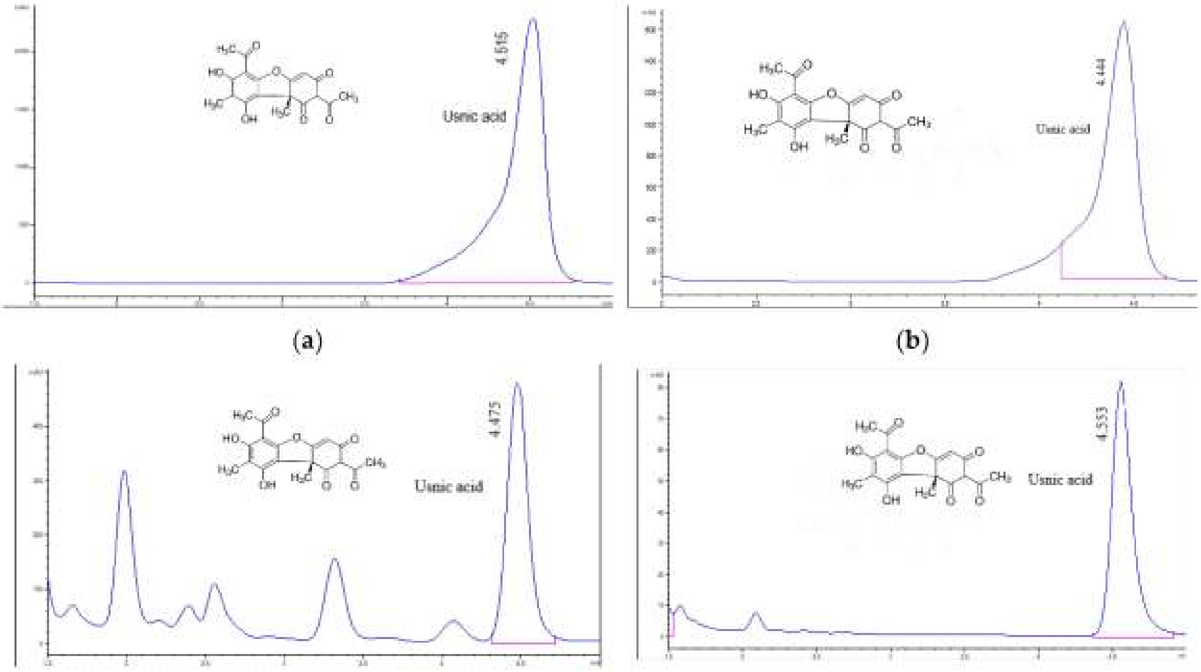

(**a**) (**b**) (**c**) (**d**)

Figure 1. Chromatograms of usnic acid standard (**a**), *m*UBA (**b**), *m*UBE (**c**), *m*UBW (**d**). The red lines mark the significant peak areas.

Data from Table 2 show that only two dry extracts contain UA because in *d*UBW it was non-detected. Dry acetone extract contains UA of 241.773 mg/g, corresponding to 13.418 mg/g dried lichen. The usnic acid content in *d*UBE is 108.752 mg/g (12.125 mg/g dried lichen).

2.3. HPLC-DAD Determination of Polyphenols

The polyphenols contents are displayed in Table 3.

The chromatograms of *U. barbata* extracts are displayed in Figures 2–5.

Table 3. Polyphenols contents in *U. barbata* fluid and dry extracts in ethanol and water.

U. barbata **Extracts**	***m*****UBE**	***m*****UBW**	***d*****UBE**	***d*****UBW**
Polyphenols	**Polyphenols Content mg/g Lichen Extract**			
Caffeic acid (CA)	0.414 ± 0.005	ND	ND	ND
p-coumaric acid (pCA)	0.312 ± 0.001 ^{b}	0.749 ± 0.049 ^{a}	ND	ND
Ellagic acid (EA)	230.819 ± 0.264 ^{c}	ND	0.605 ± 0.007 ^{d}	ND
Chlorogenic acid (ChA)	0.512 ± 0.006 ^{f}	0.627 ± 0.006 ^{e}	ND	ND
Gallic acid (GA)	27.487 ± 0.459 ^{h}	60.358 ± 0.363 ^{g}	0.870 ± 0.008 ^{k}	ND
Cinnamic acid (CiA)	17.948 ± 0.114	ND	ND	ND

UBA—*U. barbata* acetone extract, UBE—*U. barbata* ethanol extract, UBW—*U. barbata* water extract; *m*—macerate, d—dry; pCA—*p*-coumaric acid, ChA—chlorogenic acid, CA—caffeic acid, CiA—cinnamic acid, EA—ellagic acid, GA—gallic acid, ND—non-detected; the mean values followed by superscript letters are statistically significant ($p < 0.05$).

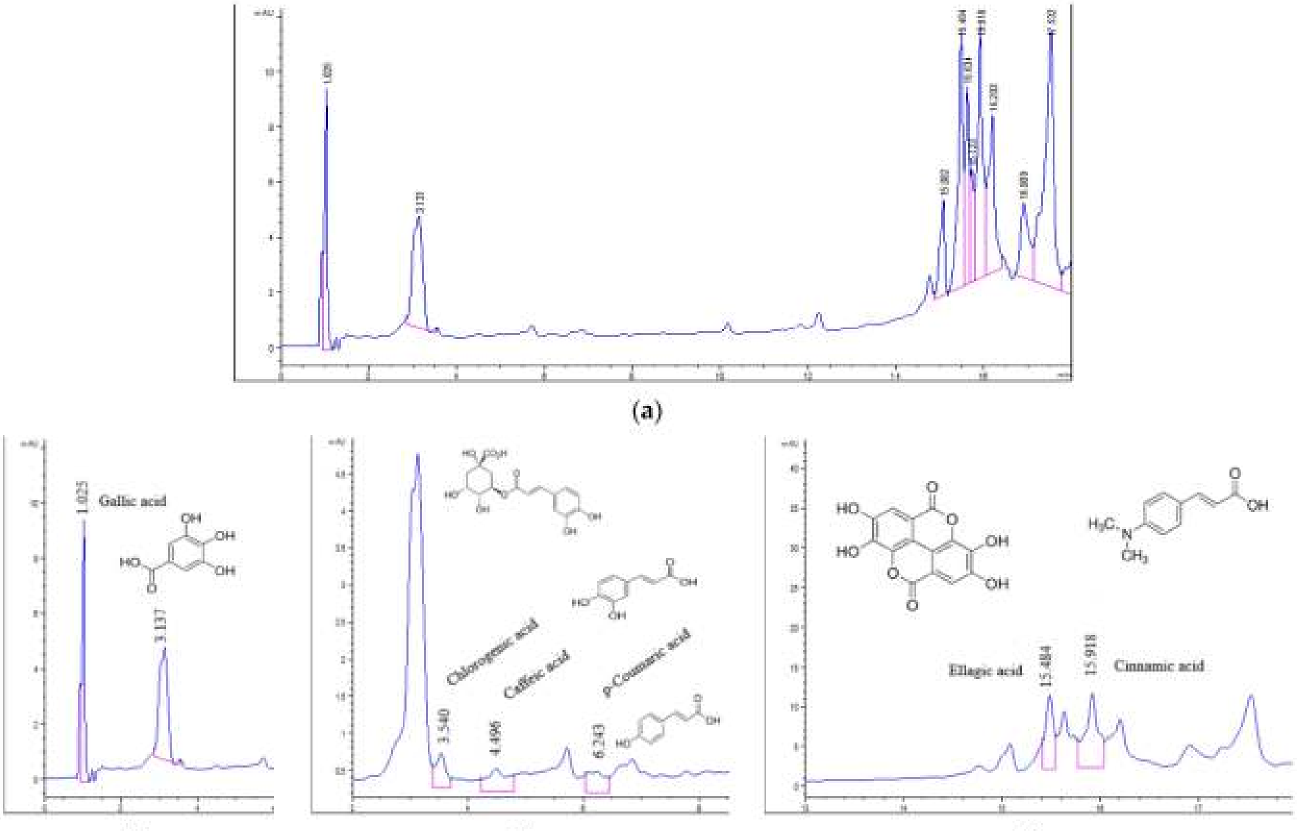

(**a**)

(**b**) (**c**) (**d**)

Figure 2. Chromatograms of *m*UBE (**a**); polyphenols in *m*UBE: gallic acid (**b**); chlorogenic, caffeic, and *p*-coumaric acids (**c**); ellagic and cinnamic acids (**d**). The red lines mark the significant peak areas, UBE—*U. barbata* ethanol extract, *m*—macerate.

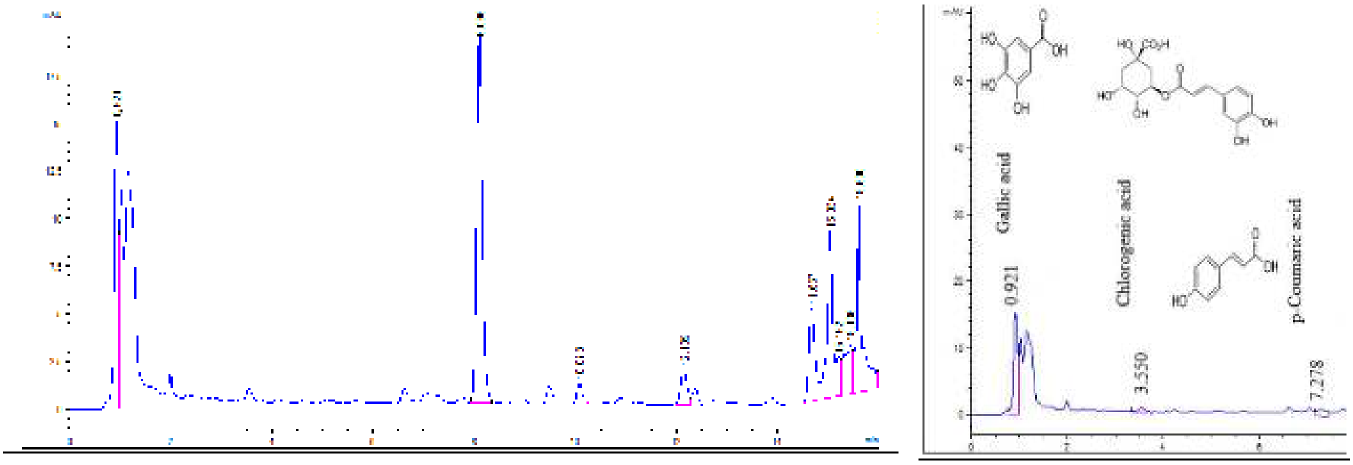

(**a**) (**b**)

Figure 3. Chromatograms of *m*UBW (**a**); polyphenols in *m*UBW (**b**). The red lines mark the significant peak areas; UBW—*U. barbata* water extract, *m*—macerate.

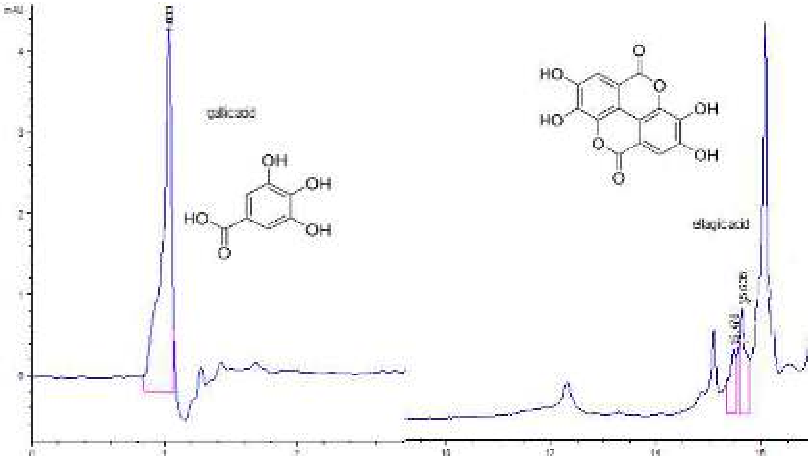

Figure 4. Gallic acid and ellagic acid in *d*UBE. The red lines mark the significant peak areas.

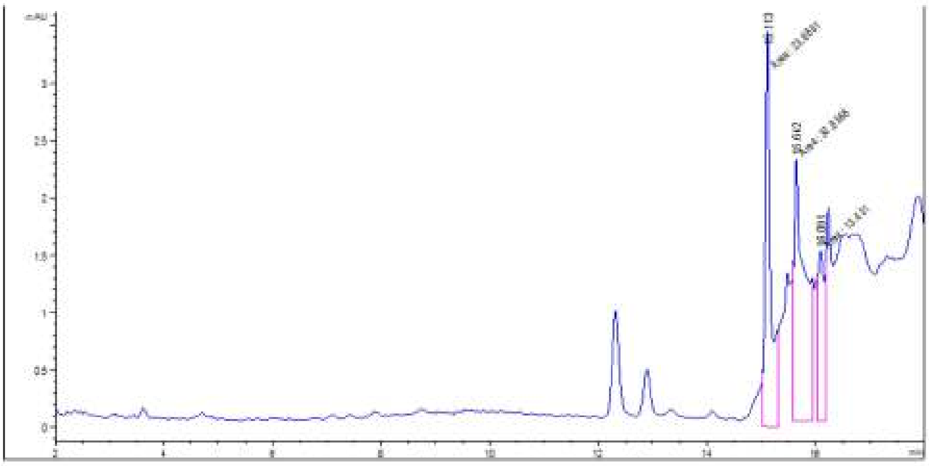

Figure 5. Chromatogram of *d*UBW. The red lines mark the significant peak areas.

As can be seen, six polyphenols of the standard mixture were identified only in ethanol and water fluid extracts; their high solubility in polar solvents could justify their absence in acetone extracts (Table 3 and Figures 2 and 3).

Of all six polyphenols identified in *m*UBE: caffeic acid (CA), *p*-coumaric acid (pCA), ellagic acid (EA), chlorogenic acid (ChA), gallic acid (GA), and cinnamic acid (CiA), only two (EA and GA) were found in *d*UBE, and three (pCA, ChA, and GA) in *m*UBW (Figures 2–4). The common polyphenol for all three extracts is GA, with the highest content in *m*UBW (60.358 mg/g), followed by *m*UBE (27.487 mg/g) and *d*UBE (0.870 mg/g). Ellagic acid content is 230.819 mg/g in *m*UBE and 0.605 mg/g in *d*UBE (Table 3, Figure 4).

The common polyphenols for *m*UBW and *m*UBE were pCA and ChA; their amounts were higher in *m*UBW (0.749 and 0.627 mg/g) than *m*UBE (0.312 and 0.512 mg/g). The other two polyphenols—CA (0.414 mg/g) and CiA (17.948 mg/g)—were identified exclusively in *m*UBE (Table 3, Figure 2).

The *d*UBW chromatogram (Figure 5) shows three peaks at the following retention times (RT): 15.113 min, 15.642 min, and 16.091 min; these RT values differed from standard polyphenols' ones. Their absence in *d*UBW could be due to their thermolability; the Soxhlet extraction involves prolonged heating for 8 h at 95–100 °C [45].

The polyphenols from the standard mixture were also non-detected in both *U. barbata* acetone extracts (Table 3) because their solubility is lower in this solvent than in ethanol or water.

2.4. Total Phenolic Content

It can be observed that the highest total phenolic content (TPC) values belong to dry *U. barbata* extracts (Table 4). The *d*UBA had the highest TPC (862.843 mg PyE/g); it is followed in decreasing order by *d*UBE (573.234 mg PyE/g) and *d*UBW (111.626 mg PyE/g). The TPC values in fluid extracts decreased in the following order: *m*UBE (276.603 mg PyE/mL), *m*UBA (220.597 mg PyE/mL), and *m*UBW (176.129 mg PyE/mL). TPC includes usnic acid, identified polyphenols, and unidentified phenolic constituents of each *U. barbata* extract.

Table 4. Total phenolic content (TPC) and free-radical scavenging activity of *U. barbata* extracts.

***U. barbata* Extract**		**TPC (mg PyE/g Extract)**	**DPPH-Free Radical Scavenging%**
Acetone	*m*UBA	220.597 ± 24.527 ^{d}	11.146 ± 0.577 ^{k}
	*d*UBA	862.843 ± 33.727 ^{a}	15.471 ± 0.629 ^{h}
Ethanol	*m*UBE	276.603 ± 15.025 ^{c}	12.162 ± 0.396 ^{j}
	*d*UBE	573.234 ± 42.308 ^{b}	16.728 ± 0.284 ^{g}
Water	*m*UBW	176.129 ± 24.169 ^{e}	6.429 ± 0.286 ^{l}
	*d*UBW	111.626 ± 11.132 ^{f}	3.951 ± 0.297 ^{m}

TPC—total phenolic content, UBA—*U. barbata* acetone extract, UBE—*U. barbata* ethanol extract, UBW—*U. barbata* water extract; *m*—macerate, *d*—dry extract, mg PyE—mg equivalents pyrogallol. The mean values followed by superscript letters are statistically significant ($p < 0.05$).

2.5. Free-Radical Scavenging Activity Assay

The results are displayed in Table 4.

Data from Table 4 show that all *U. barbata* extracts have antiradical activity. This effect was higher for dry ethanol and acetone extracts (16.728% for *d*UBE, 15.471% for *d*UBA) than fluid ones (12.162% for *m*UBE, 11.146% for *m*UBA). Only for water extracts, the antiradical activity of *d*UBW (3.951%) is lower than the *m*UBW one (6.429%).

2.6. Antibacterial Activity

The obtained results proved that the negative control (DMSO 0.1%) has no inhibitory effect on the bacteria tested (IZD = 0 mm). Only *U. barbata* extracts in acetone and ethanol inhibited bacterial strains' growth. (Figure S2, Supplementary Materials). Neither UBWs have any inhibitory effect on the tested bacteria (IZD = 0 mm).

Given that usnic acid is the major secondary metabolite of the genus *Usnea*, we considered this phenolic compound as a positive control. For the optimal interpretation of the obtained IZD values, we used two bactericidal antibiotics with different mechanisms of action and breakpoints: ofloxacin (OFL) and ceftriaxone (CTR).

The data displayed in Table 5 show the IZD values (mm) for all *U. barbata* extracts, UA, and standard antibiotics drugs (OFL and CTR).

Table 5. Antibacterial activity of *U. barbata* extracts.

Bacteria		***S. aureus***	***S. pneumoniae***	***P. aeruginosa***	***K. pneumoniae***
		Inhibition Zone Diameter—IZD (mm)			
UA		16.33 ± 0.82	17.33 ± 0.47	16.67 ± 0.47	0
Liquid extracts					
*m*UBA		12.00 ± 0.82 ^{b}	17.67 ± 0.47	17.33 ± 1.25	0
*m*UBE		11.00 ± 0.82 ^{d}	18.67 ± 0.47	20.33 ± 1.70	0
*m*UBW		0	0	0	0
Dry extracts					
*d*UBA		13.66 ± 0.47 ^{a}	18.00 ± 1.63	17.00 ± 1.63	0
*d*UBE		12.33 ± 1.25 ^{c}	18.33 ± 0.47	20.00 ± 1.63	0
*d*UBW		0	0	0	0
Standard antibacterial drugs inhibitory activity					
OFL 5		26.33 ± 1.70	19.00 ± 1.63	19.33 ± 1.70	30.00 ± 0.82
CTR 30		25.00 ± 2.45	32.33 ± 2.05	21.00 ± 2.16	32.33 ± 2.49
Standard antibacterial drugs breakpoints *					
Ofloxacin					
OFL 5	S *	≥18 *	≥16 *	≥16 *	≥16 *
	I *	17–15 *	15–13 *	15–13 *	15–13 *
	R *	≤14 *	≤12 *	≤12 *	≤12 *
Ceftriaxone					
CTR 30	S *	≥21 *	≥26 *	≥18 *	≥23 *
	I *			17–15 *	22–20 *
	R *	≤20 *	≤25 *	≤14 *	≤19 *

UBA—*U. barbata* acetone extract, UBE—*U. barbata* ethanol extract, UBW—*U. barbata* water extract; *m*—macerate, *d*—dry extract, UA—usnic acid (positive control), * Data adapted from CLSI breakpoints analyzed by Humphries et al. [46]; OFL—ofloxacin, CTR—ceftriaxone; 5, 30 µg—the antibiotic amount from the standard antibiotic disc; S—sensitivity, I—intermediate (dose-dependent action), R—resistance. The superscripts letters noted the statistically significant IZD mean values ($p < 0.05$).

Therefore, comparing the IZD values of the *U. barbata* extracts to those of both standard antibiotics on *S. aureus*, none had antibacterial action (IZD = 11.00–13.66 mm). Only usnic acid has an IZD (16.33 mm) in the "I" range of ofloxacin (17–15 mm); this means that antibacterial activity on *S. aureus* is dose dependent. Compared to ceftriaxone, the IZD value for UA belongs to the resistance range (<20 mm).

S. pneumoniae is sensitive to all *U. barbata* extracts as well as to usnic acid (IZD = 17.33–18.67 mm) when IZD values are compared to ofloxacin (S ≥ 16 mm *). However, it could be considered resistant when IZD values were compared to CTR (S ≥ 26 mm *).

Among Gram-negative bacteria, *P. aeruginosa* proves the highest sensitivity; all lichen extracts showed antibacterial action on *P. aeruginosa* (IZD = 16.77–20.33 mm), compared to ofloxacin (*S* ≥ 16 mm *). Only ethanol extracts (IZD = 20.00–20.33 mm) had an antibacterial effect related to ceftriaxone (S ≥ 18 mm *); the others are active in a dose-dependent manner (I = 17–15 mm). Contrariwise, no *U. barbata* extract inhibited the growth of *K. pneumoniae* colonies (IZD = 0 mm).

Considering the data registered in Table 5, we calculated the antibacterial activity index (AI), reporting the IZD values (mm) of lichen extracts to the ones of the standard antibiotic drugs [47]. It can be noted that dry and fluid *U. barbata* acetone and ethanol extracts had similar inhibitory effects (Table 6).

Table 6. Antibacterial activity index of *U. barbata* extracts and UA compared to both standard antibiotic drugs.

Bacteria	AI Values (Adim)					AB
	*m*UBA	*d*UBA	*m*UBE	*d*UBE	UA	
S. aureus	0.455 0.480	0.519 0.546	0.417 0.440	0.468 0.490	0.620 0.693	OFL5 CTR30
S. pneumoniae	0.930 ^{a} 0.546 ^{b}	0.947 ^{a} 0.556 ^{b}	0.982 ^{a} 0.577 ^{b}	0.964 ^{a} 0.566 ^{b}	0.912 ^{a} 0.536 ^{b}	OFL5 CTR30
P. aeruginosa	0.896 0.825	0.879 0.809	1.051 0.968	1.034 0.952	0.862 0.793	OFL5 CTR30

AI—antibacterial activity index, adim—without measure unit, UBA—*U. barbata* acetone extract, UBE—*U. barbata* ethanol extract, *m*—macerate, *d*—dry extract, UA—usnic acid, AB—standard antibiotic drug, OFL—ofloxacin, CTR—ceftriaxone. 5, 30 µg—the antibiotic amount from the standard antibiotic disc. The AI values noted with superscripts letters are statistically significant ($p < 0.05$).

The presence of similar bioactive secondary metabolites, the fluid extracts used after solvent evaporation, and the additional presence of the polyphenols known for their strong antibacterial action could explain the results registered in Tables 5 and 6. Thus, UA had the highest inhibitory activity on *S. aureus*, showing a dose-dependent antibacterial effect and the highest AI values; the following are the extracts with a high usnic acid content, respectively UBA. *U. barbata* ethanol extracts show the lowest inhibitory effect because usnic acid is known for its highest inhibition levels on *S. aureus*; both UBEs have lower UAC values than the corresponding UBAs ones (Table 5).

On *S. pneumoniae* and *P. aeruginosa*, the lichen extracts in ethanol indicated the most significant inhibitory levels. Antibacterial activities of individual polyphenols could justify these results. They showed an antibacterial action against *S. pneumoniae* similar to ofloxacin. On *S. pneumoniae*, the AI values compared to OFL are statistically different from those linked to CTR (Table 6). In this case, for all *U. barbata* extracts, AI ≥ 0.912, proving that their antibacterial activity is similar to OFL. Against *P. aeruginosa*, *m*UBA and *d*UBA reported AI values higher than OFL (AI > 1) and similar to CTR (AI ≥ 0.952) (Table 6).

2.7. Data Analysis

We obtained *U. barbata* extracts performing two easy-to-use and low-cost conventional techniques mentioned in Romanian Pharmacopoeia X [48]: maceration for fluid extracts and Soxhlet extraction for dry ones. They have been one of the most used extraction procedures for herbal bioactive compounds [49]. According to the green chemistry concept, the solvents used for lichen extraction are "preferable," having low toxicity and significant safety [50]. Our entire study's data were synthesized in Table 7.

From the beginning, the same ratio—1:10 (w/v) between dried lichen and solvent—was maintained for all extracts. The fluid extracts were obtained at room temperature (20–22 °C). The Soxhlet extraction was performed by prolonged heating, and the requested temperature values registered in Table 7 were maintained for 8 h.

The phenolic metabolites contents were strongly influenced by extraction conditions, as shown in Table 7. Usnic acid content and TPC significantly increase in acetone and ethanol dry extracts than in fluid ones; UBAs have higher UAC and TPC than UBEs. The *m*UBW had the lowest TPC and UAC. However, after 8 h of Soxhlet extraction at 100 °C, *d*UBW shows diminished TPC values and no UAC.

The individual polyphenols were quantified only in ethanol and water *U. barbata* extracts. The *m*UBE contains all six polyphenols (CA, CiA, pCA, EA, GA, and ChA) and *m*UBW—only three (pCA, GA, and ChA). Regarding the corresponding dry extracts, in *d*UBE only two polyphenols (EA and GA) were found in lower content than *m*UBE; *d*UBW has no polyphenols.

Table 7. Characteristics of *U. barbata* extracts in ethanol, acetone, and water obtained by two different conventional techniques, regarding the extraction conditions, phenolic metabolites, and bioactivities.

U. barbata **Extract**		***m*UBE**	***d*UBE**	***m*UBA**	***d*UBA**	***m*UBW**	***d*UBW**
		Extraction conditions					
Solvent		96% ethanol		Acetone		Water	
Ratio (w/v)		1:10					
Temperature (°C)		20–22	75–80	20–22	55–60	20–22	95–100
Yield (%)			11.150		5.550		1.760
		Phenolic metabolites (mg/g extract)					
TPC		276.603	573.234	220.597	862.843	176.129	111.626
UA	mg/g extract	0.257	108.74	211.190	241.830	0.045	
	% in dried lichen	0.002	1.212	2.119	1.341	0.0004	
CA		0.414					
pCA		0.312				0.749	
EA		230.820	0.605				
GA		27.487	0.870			60.358	
CiA		17.948					
ChA		0.513				0.627	
		Antibacterial activity—IZD (mm)					
S.a.		11.000	12.330	12.000	13.670		
S.p.		18.670	18.330	17.670	18.000		
P.a.		20.330	20.000	17.330	17.000		
		DPPH free radical scavenging activity (%)					
AA		12.162	16.728	11.146	15.471	6.429	3.951

pCA—*p*-coumaric acid, ChA—chlorogenic acid, CA—caffeic acid, CiA—cinnamic acid, EA—ellagic acid, GA—gallic acid, UA—usnic acid, TPC—total phenolic content, AA—antiradical activity, P.a.—inhibitory activity against *P. aeruginosa*, S.a.—inhibitory activity against *S. aureus*, S.p.—inhibitory activity against *S. pneumoniae;* UBA—*U. barbata* acetone extract, UBE—*U. barbata* ethanol extract, UBW—*U. barbata* water extract; *m*UBE, *m*UBA, *m*UBW—obtained by maceration; *d*UBE, *d*UBA, *d*UBW—obtained by Soxhlet extraction.

These detailed aspects could be explained in the first step by the solubility differences of phenolic compounds in each extraction solvent. Polyphenols are soluble in polar solvents (ethanol, water); however, they are affected by prolonged heating [45]; thus, it can justify their decreasing or absence in the dry extracts after Soxhlet extraction for 8 h at 75–80 °C (*d*UBE) and 95–100 °C (*d*UBA). The lowest solubility of usnic acid in water underlies the minimal UAC value in *m*UBW. The high temperature of extraction (100 °C for 8 h) affects usnic acid stability; thus, the absence of UA in *d*UBW could be justified. According to https://www.biocrick.com/Usnic-acid-BCN4306.html (accessed on 2 May 2022), usnic acid storage requests desiccation and freezing (−20 °C); this information supports our results.

On the other hand, it can be seen that the dry extracts are obtained with a considerably low yield. When all UAC values are reported to the dried lichen amount used for each extract preparation, 2.119% corresponds to *m*UBA and only 1.341% for *d*UBA.

Principal Component Analysis

Principal component analysis (PCA) was performed for all *U. barbata* liquid and dry extracts and variable parameters—according to the correlation matrix from Supplementary Materials—and illustrated in Figure 6.

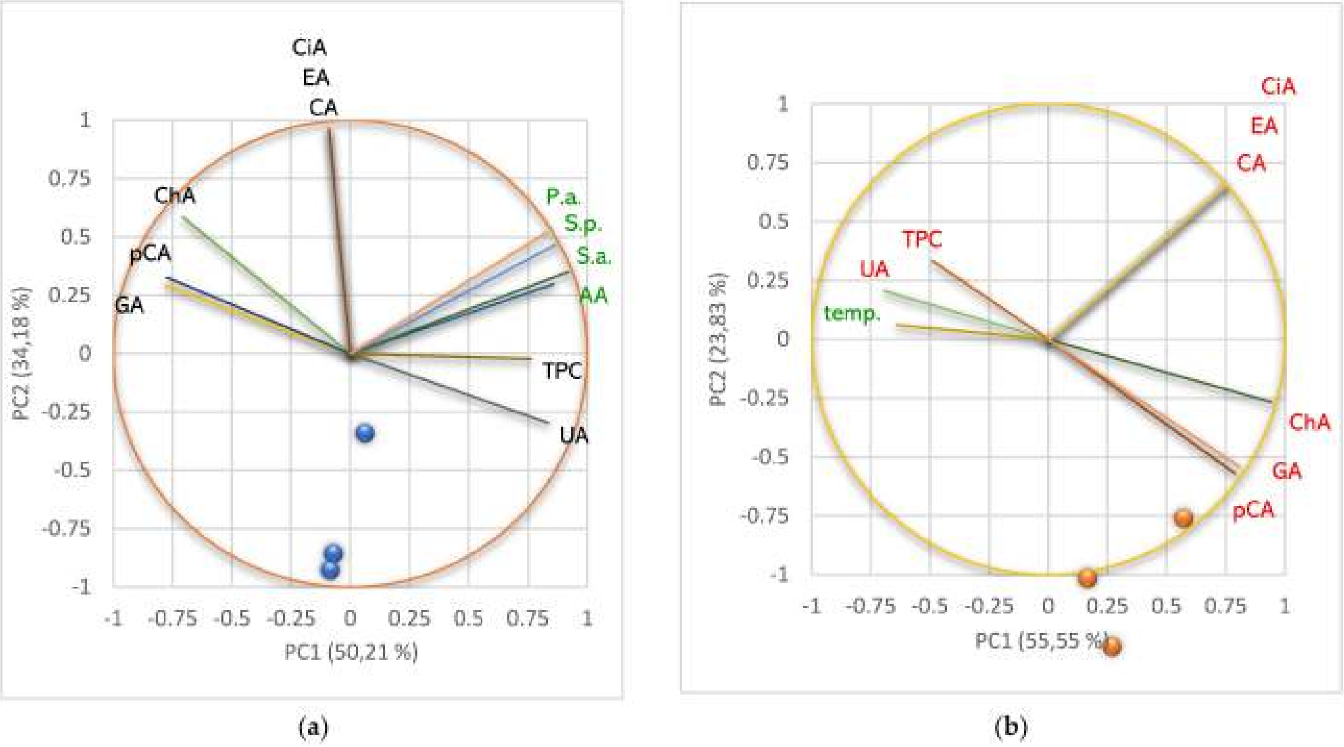

Figure 6. Principal component analysis (PCA): PCA-Correlation circle between phenolic metabolites and bioactivities of *U. barbata* extracts (**a**); PCA-Correlation circle between phenolic metabolites and extraction temperature (**b**). pCA—*p*-coumaric acid, ChA—chlorogenic acid, CA—caffeic acid, CiA—cinnamic acid, EA—ellagic acid, GA—gallic acid, UA—usnic acid, TPC—total phenolic content, AA—antiradical activity, P.a.—inhibitory activity against *P. aeruginosa*, S.a.—inhibitory activity against *S. aureus*, S.p.—inhibitory activity against *S. pneumoniae*, temp—extraction temperature.

The PCA-Correlation circle from Figure 6a explains 84.40% of the data variances [51] and correlates the lichen extracts metabolites with their bioactivities. It can be observed that the horizontal axis (PC1) is linked to pCA, GA, and ChA, usnic acid content, TPC, AA, and antibacterial activities. PC2 is associated with CA, EA, and CiA. Figure 6a shows that UA moderately correlates with the lichen extracts bioactivities: AA ($r = 0.626$, $p > 0.05$), S.a. ($r = 0.728$, $p > 0.05$), S.p. ($r = 0.625$, $p > 0.05$), and P.a. ($r = 0.545$, $p > 0.05$). TPC displays a good positive correlation with AA ($r = 0.822$, $p < 0.05$) and the moderate ones with antibacterial activities—r values decrease from 0.693 (S.a.) to 0.603 (S.p.) and 0.563 (P.a.), $p > 0.05$. We can also observe that AA is highly correlated with antibacterial activities—r values are 0.923 (S.a.), 0.900 (S.p.), and 0.897 (P.a.), $p < 0.05$—because in both effects involve the phenolic metabolites, with their phenolic -OH groups (Figure 6a). The individual polyphenols are insignificantly (positively or negatively) correlated with both bioactivities for all lichen extracts because these compounds were quantified only in three *U. barbata* extracts (Figure 6a).

The PCA-Correlation circle from Figure 6b explains 79.38% of the data variances and correlates the lichen extracts metabolites with extraction temperature. All parameters (except TPC, $r = 0.209$) are negatively correlated with the temperature ($p > 0.05$). The temperature values moderately correlate with pCA ($r = -0.587$), ChA ($r = 0.652$) and GA ($r = 0.594$). Other variable parameters reported a low negative correlation with extraction temperature (detailed data in Supplementary Materials). Usnic acid with temperature registered the lowest negative correlation ($r = -0.042$).

The lichen extracts' phytoconstituents significantly influence their pharmacological potential. Hence, we explored the metabolites content to explain the differences in the obtained results regarding antiradical and antibacterial effects. Then, we determined the correlations between these bioactivities and phenolic metabolites quantified in each lichen extract. All data are displayed in Figures 7–10 and detailed in Supplementary Materials.

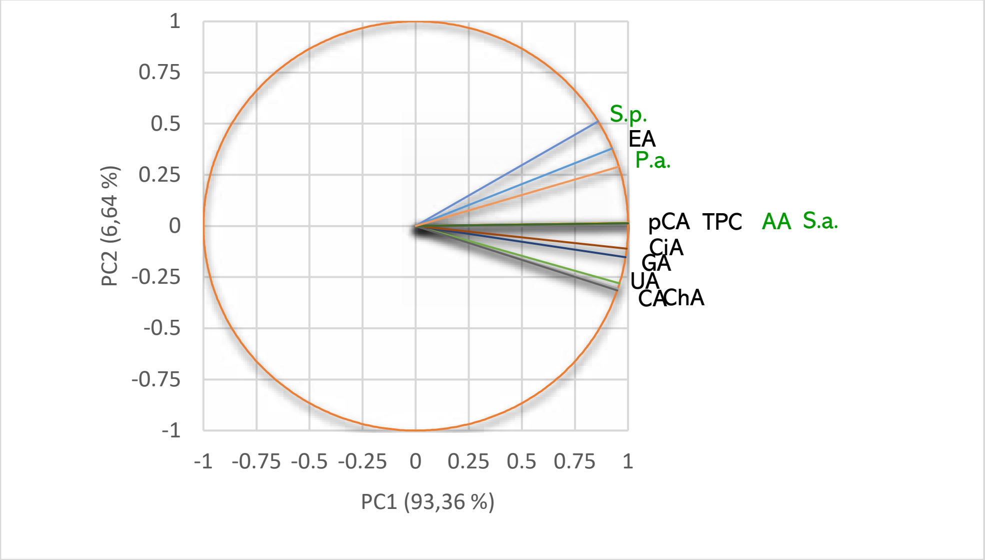

Figure 7. PCA-Correlation circle between TPC, UA, and individual polyphenols in *m*UBE and antibacterial and antiradical activities. *m*UBE—*U. barbata* liquid ethanol extract, pCA—*p*-coumaric acid, ChA—chlorogenic acid, CA—caffeic acid, CiA—cinnamic acid, EA—ellagic acid, GA—gallic acid, UA—usnic acid, TPC—total phenolic content, AA—antiradical activity, P.a.—inhibitory activity against *P. aeruginosa*, S.a.—inhibitory activity against *S. aureus*, S.p.—inhibitory activity against *S. pneumoniae*.

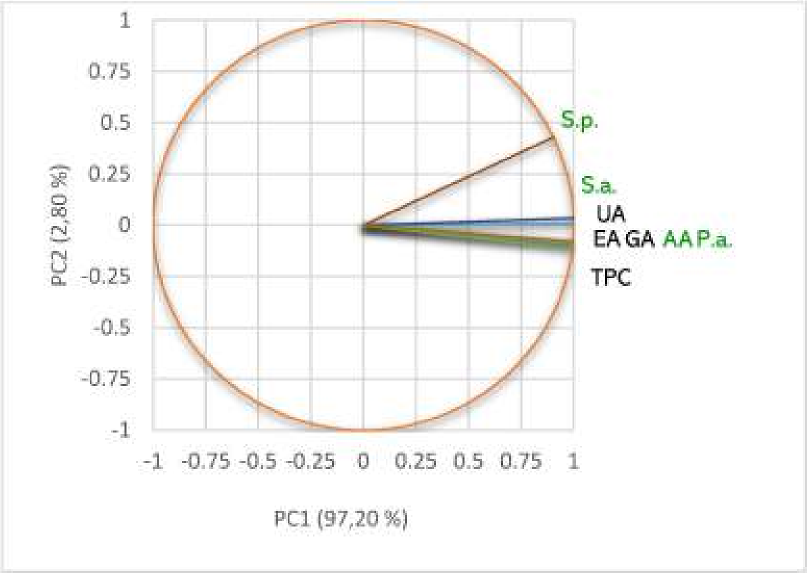

Figure 8. PCA-Correlation circle between TPC, UA, and individual polyphenols in *d*UBE and antibacterial and antiradical activities. *d*UBE—*U. barbata* dry ethanol extract, EA—ellagic acid, GA—gallic acid, UA—usnic acid, TPC—total phenolic content, AA—antiradical activity, P.a.—inhibitory activity against *P. aeruginosa*, S.a.—inhibitory activity against *S. aureus*, S.p.—inhibitory activity against *S. pneumoniae*.

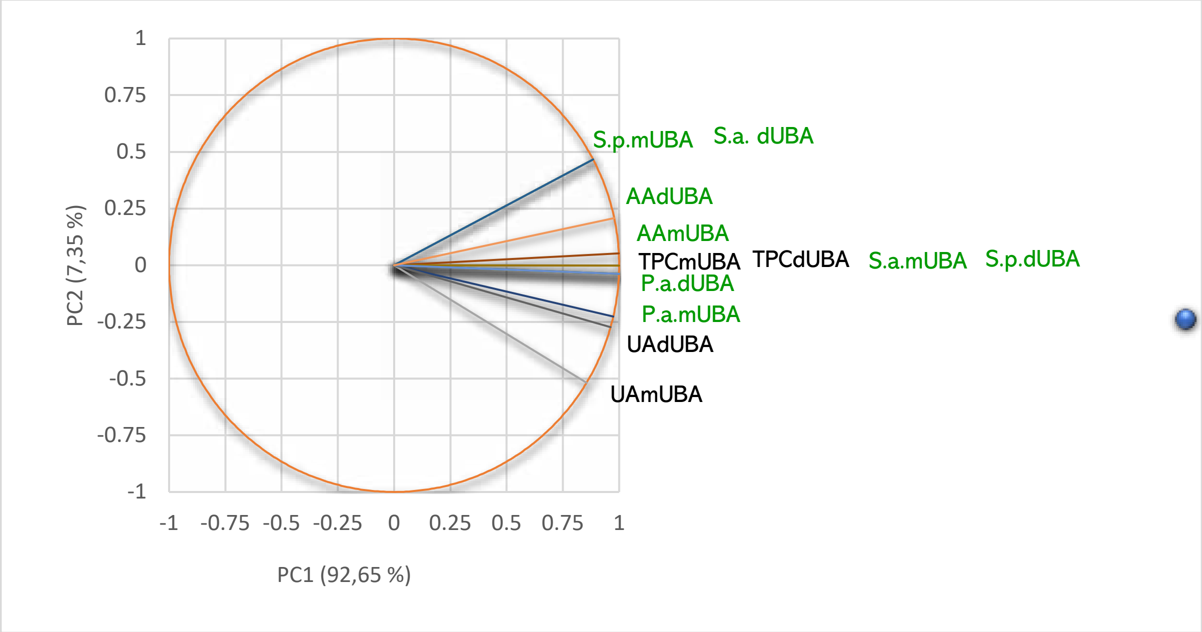

Figure 9. PCA-Correlation circle between TPC, UA, and individual polyphenols in *m*UBA and *d*UBA and antibacterial and antiradical activities; UBA—*U. barbata* acetone extract, *m*—macerate, *d*—dry; UA—usnic acid, TPC—total phenolic content, AA—antiradical activity, P.a.—inhibitory activity against *P. aeruginosa*, S.a.—inhibitory activity against *S. aureus*, S.p.—inhibitory activity against *S. pneumoniae*.

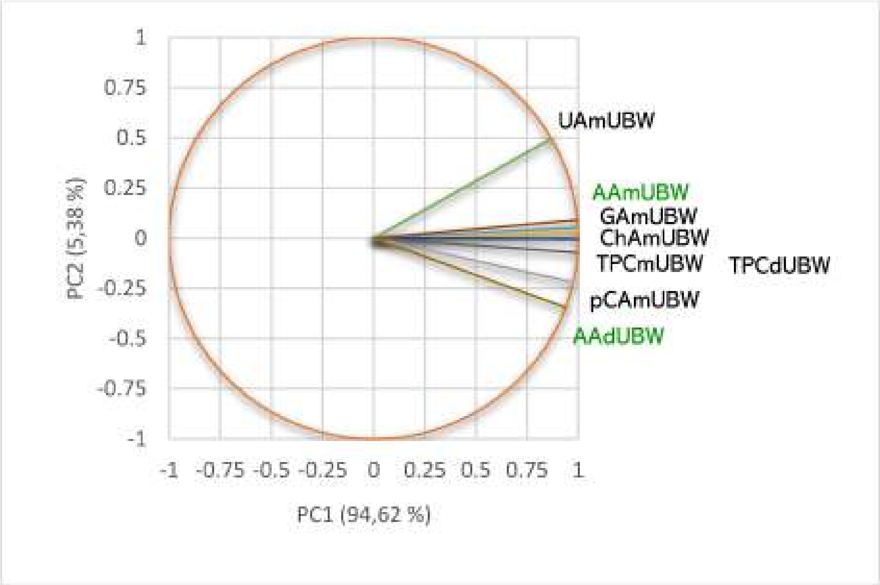

Figure 10. PCA-Correlation circle between TPC, UA, and individual polyphenols in *m*UBW and only between TPC in *d*UBW and antiradical activities; UBW—*U. barbata* water extract, *m*—macerate, *d*—dry; pCA—*p*-coumaric acid, ChA—chlorogenic acid, GA—gallic acid, UA—usnic acid, TPC—total phenolic content, AA—antiradical activity.

In *m*UBE, all quantified phenolic secondary metabolites significantly correlate with DPPH free radical scavenging ability (AA, $r \geq 0.930$) and antibacterial activities (Figure 7).

As expected, Figure 7 shows a high correlation ($r = 0.999$, $p < 0.05$) between pCA and TPC and AA and S.a. Ellagic acid remarkably correlates with AA ($r = 0.930$, $p > 0.05$) and all antibacterial effects—r value decreases from 0.996 (P.a.) to 0.989 (S.p.) and 0.930 (S.a.), $p > 0.05$. The phenolic compounds correlate with the inhibitory effect against *S. aureus* registering the highest correlation index values ($r \geq 0.930$, $p > 0.05$), followed by the one against *P. aeruginosa* ($r = 0.817$–0.996, $p > 0.05$) and *S. pneumoniae* (in the most cases, a moderate correlation, $r = 0.655$–0.867, $p > 0.05$). UA shows the highest correlation with S.a. ($r = 0.945$, $p > 0.05$), followed by P.a. ($r = 0.817$, $p > 0.05$) and S.p. ($r = 0.655$, $p > 0.05$). Moreover, AA is considerably correlated with all antibacterial activities, S.a. ($r = 0.999$, $p < 0.05$), P.a. ($r = 0.961$, $p > 0.05$) and S.p. ($r = 0.866$, $p > 0.05$).

In *d*UBE, we identified two polyphenols (gallic acid and ellagic acid) and UA. The phenolic metabolites remarkably correlate with both bioactivities ($r \geq 0.848$, p </> 0.05, Figure 8).

Data illustrated in Figure 8 highlight the strongest correlation ($r = 0.999$, $p < 0.05$) between phenolic compounds (EA, GA, and TPC) and AA and P.a. On *P. aeruginosa*, the powerful action of ellagic acid and gallic acid is due to phenolic compound general mechanisms and biofilm inhibition [52]. The same correlation ($r = 0.999$, $p < 0.05$) can be noticed between UA and S.a.; UA is a valuable antibacterial compound against *S. aureus* and, as a positive control, had a dose-dependent antibacterial effect. Both activities—AA and P.a.—are also highly correlated ($r = 0.999$, $p < 0.05$).

TPC of *m*UBA and *d*UBA are positively correlated with antibacterial effects (Figure 9). In *m*UBA, TPC correlates with S.a. ($r = 0.999$, $p < 0.05$); it also corellates with S.p. and P.a. in *d*UBA. UA moderately corellates with S.p. ($r = 0.515$, $p < 0.05$) in *m*UBA and S.a. in *d*UBA ($r = 0.723$, $p > 0.05$). In both UBAs, UA ($r = 0.827$ and 0.884, $p > 0.05$) and TPC ($r = 0.996$ and 0.978, $p > 0.05$) display a high correlation with AA. These correlations are evidenced in Figure 9. Furthermore, in both UBAs, DPPH free-radical scavenging activity and antibacterial effects are strongly correlated ($r = 0.906$, 0.962 and 0.970, $p > 0.05$, Figure 9).

These correlations associated with the bio-activities of all quantified metabolites could explain the similar inhibitory activity on bacterial strains growing of both *U barbata* extracts in ethanol and acetone. Moreover, in these extracts, all phenolic metabolites could synergistically act.

The PCA-correlation circle for UBWs is displayed in Figure 10.

Data from Figure 10 show that usnic acid ($r = 0.910$, $p > 0.05$) and individual polyphenols—pCA ($r = 0.951$, $p > 0.05$), GA and ChA ($r = 0.999$, $p < 0.05$) highly correlate with AA in liquid water extract. Furthermore, in both UBWs, TPC show a powerful correlation with AA ($r = 0.995$, and 0.961, $p < 0.05$). However, because the phenolic compounds with known antibacterial action were extracted in water in minimal quantities, both UBWs did not exhibit any inhibitory effect on bacteria tested (IZD = 0).

Our study deeply analyzed six *U. barbata* extracts in three solvents, from the description of extraction conditions to phenolic constituents' determination and the evaluation of their biological activities. A detailed data analysis was performed on the correlations between phenolic metabolites and biological activities for each *U. barbata* extract, aiming to explain the obtained results. We correlated phenolic metabolites with antiradical and antibacterial activities and with extraction temperature for all six *U. barbata* extracts. The extraction temperature's significant role was highlighted by comparing the liquid and dry extracts in the same solvent. Thus, we evidenced the strong influence of the extraction temperature on phenolic metabolites diversity and content and, consequently, the strong impact on antiradical and antibacterial activities.

Correlating and interpreting all data, we made each lichen extract characterization, highlighting the similar and different properties compared to the others (Figure 11).

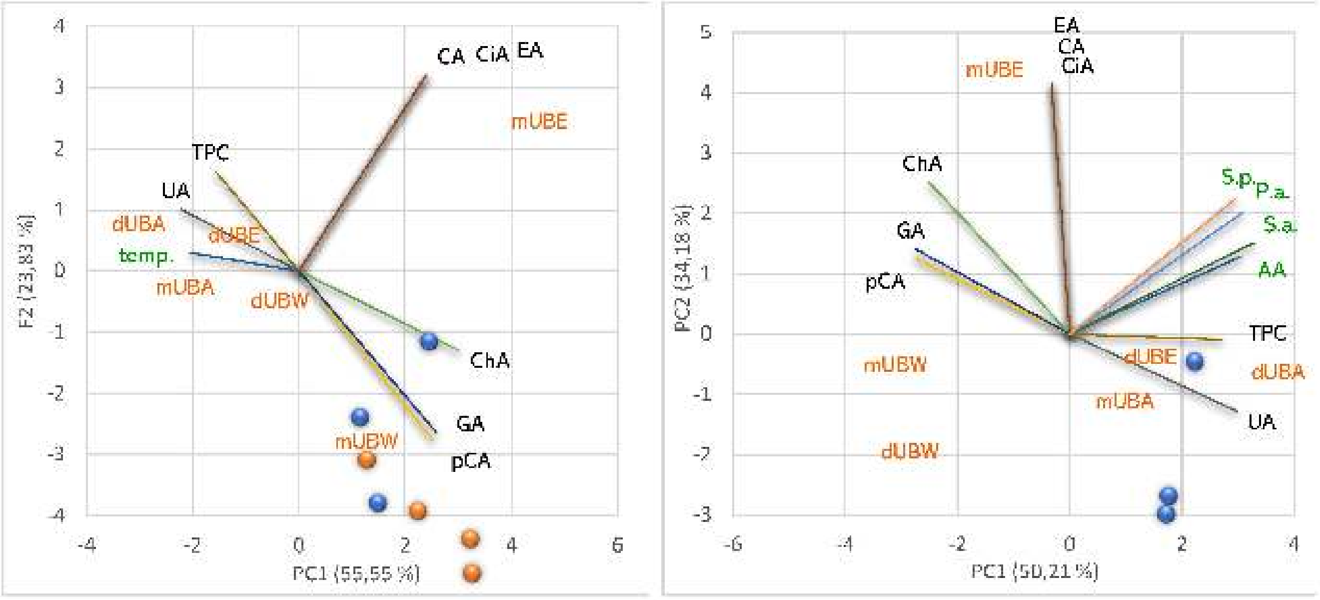

(a) (b)

Figure 11. Characterization of *U. barbata* extracts by positioning each lichen extract according to its phenolic metabolites correlated with temperature (**a**) and bioactivities (**b**). pCA—*p*-coumaric acid, ChA—chlorogenic acid, CA—caffeic acid, CiA—cinnamic acid, EA—ellagic acid, GA—gallic acid, UA—usnic acid, TPC—total phenolic content, AA—antiradical activity; P.a.—inhibitory activity against *P. aeruginosa*, S.a.—inhibitory activity against *S. aureus*, S.p.—inhibitory activity against *S. pneumoniae;* temp—extraction temperature. UBA—*U. barbata* acetone extract, UBE—*U. barbata* ethanol extract, UBW—*U. barbata* water extract; *m*—macerate, *d*—dry extract.

Figure 11a shows that the fluid UBE (obtained at room temperature) contains UA in a low content and all six polyphenols in an appreciable amount. It can be noticed that CA, EA, and CiA are associated exclusively with *m*UBE; moreover, it shares ChA, GA, and pCA with *m*UBW. Individual polyphenols contribute considerably to the *m*UBE's TPC value (Figure 11a). These constituents could synergistically act, leading to their significant antiradical and antibacterial potential (Figure 11b). The Soxhlet extraction at 75–80 °C significantly diminished the polyphenols content; thus, *d*UBE reported low concentrations of only two polyphenols (EA and GA, Figure 11a). Moreover, UA and other phenolic secondary metabolites were resistant to prolonged heating and detected in dry acetone extract (Figure 11a). Therefore, *d*UBE shows a higher AA than *m*UBE and similar antibacterial effects. The fluid water extract (*m*UBW) shows the lowest content of phenolic metabolites compared to other macerates. It contains three individual polyphenols (pCA, GA, ChA) and usnic acid (Figure 11a). Despite the antibacterial properties of all phenolic constituents, their content is too low, and *m*UBW does not inhibit bacterial strains' growth; it has only moderate antiradical activity (Figure 11b). The prolonged heating at 100 °C during Soxhlet extraction diminished phenolics content; UA and individual polyphenols from *m*UBW were not detected in *d*UBW (Figure 11a), and AA decreased.

Both acetone extracts (*m*UBA and *d*UBA) have the same metabolites (UA and TPC) and bioactivities (Figure 11b); the temperature and yield have a quantitative influence, increasing UAC and TPC in *d*UBA. Therefore, AA augments and antibacterial properties are similar. In Figure 11a,b, both UBAs and *d*UBE are positioned at low distances; both UBWs are located in the same quarter of the PCA–biplot, thus evidencing their similar properties.

3. Discussion

The low yields associated with diminished UAC in dried lichen can also be observed in other studies on *U. barbata* extracts obtained in various conditions [42,43,53,54]. The most relevant data are displayed in Table 8.

Table 8. Various *U. barbata* extracts with different extraction conditions correlated with the yield and usnic acid content expressed as mg/g extract, and % UA in dried lichen.

***U. barbata* Extract**	**Extraction Solvent**	**Conditions of Extraction**				**Yield %**	**UAC (mg/g in Extract)**	**% UA in Dried Lichen ***
		Pressure (Mpa)	**Temperature (°C)**	**CO_2 Pressure (m^3/kg)**	**Pretreatment**			
UBDEA [a]	Ethyl acetate		75–80			6.27	376.73	2.362
UB-SFE [b]	99% CO_2	30	60			0.38	594.80	2.226
UB-SFE [b]	99% CO_2	30	40			0.60	364.90	2.190
UBO [c]	Canola oil		22				0.915	2.162
UBDA [a]	Acetone		55–60			6.36	282.78	1.798
UBDE [a]	96% ethanol		75–80			12.52	127.21	1.592
UBDM [a]	Methanol		65			11.29	137.60	1.553
UB-SFE [d]	99% CO_2	50	40	992	CM	2.28	545	1.243
					RM	1.67	585	0.977
					UM + RGD	1.50	645	0.968
		30	40	911	UM	1.27	617	0.806
					UM + RGD	1.46	423	0.618
					UM	0.85	648	0.551
					RM	0.78	634.5	0.481
					CM	0.86	558.1	0.479

UB SFE—*U. barbata* extract obtained by supercritical fluid extraction with CO_2, UBDEA—*U. barbata* dry extract in ethyl acetate, UBDA—*U. barbata* dry extract in acetone, UBDE—*U. barbata* dry extract in ethanol, UBDM—*U. barbata* dry extract in methanol, UBO—*U. barbata* extract in canola oil, RM—roller mill; UM—ultra-centrifugal mill; CM—cutting mill; RGD—rapid gas decompression. * Data registered in decreasing order; superscript letters evidenced the data adapted from: [a] [53], [b] [42], [c] [54], [d] [43].

The data from Table 8 indicate that the UAC (%) in dried lichen generally decreases directly proportional to the extraction yield when the same solvent is used.

The usnic acid chemical structure strongly relates to *U. barbata* antiradical and antibacterial activities [22]. Due to protonophore and uncoupling action, all three phenolic OH groups of UA are essential [55], leading to bacterial membrane potential dissipation, associated with bacterial colonies growing inhibition. Maciag-Dorszynska et al. [56] proved that usnic acid produces a rapid and strong inhibition of nucleic acids synthesis in Gram-positive bacteria (*S. aureus* and *B. subtilis*). It could also inhibit Group A Streptococcus (*Streptococcus pyogenes*) biofilm formation [57], reducing biofilm biomass and depleting the biofilm-forming cells' proteins and fatty acids. Sinha et al. [58] proved that UA could act synergistically with norfloxacin and modify *S. aureus* methicillin-resistant (MRSA) drug resistance. This effect involves efflux pump inhibition, oxidative stress induction, and down-regulation of peptidoglycans and fatty acids biosynthesis. These mechanisms alter membrane potential and perturb cell respiration and metabolic activity.

The polyphenols could synergistically act with usnic acid and other secondary metabolites in *U. barbata* extracts' antiradical and antibacterial activities. The antibacterial effects of polyphenols implicate various mechanisms. Thus, Lou et al. [59] proved that the *p*-coumaric acid bactericidal effect against *S. aureus* and *S. pneumoniae* involves irreversible permeability changes in bacterial cell walls and binding to bacterial genomic DNA; as a result, it occurs cell function inhibition followed by bacteria cell death. Caffeic acid (CA) acts as an antibacterial drug through various mechanisms; it produces cell membrane depolarization and disruption, reduces the respiratory activity of bacteria, decreases efflux activity, affects intracellular redox processes, donates protons, and increases intracellular acidity [34]. Moreover, CA proved to have an appreciable inhibitory effect against *S. aureus* (IZD = 12 mm) [34]. Cinnamic acid (CiA) preferentially acts against Gram-negative bacteria (*P. aeruginosa*), determining cell membrane damage, affecting its lipidic profile, and leading to protein loss and denaturation [60]. Chlorogenic acid (ChA) antibacterial mechanisms involve outer cell membrane bounding and disrupting, intracellular potential exhausting, and loss of cytoplasm macromolecules, leading to cell death [61]. On *S. pneumoniae*, ChA inhibits a key virulence factor (neuraminidase) [62]. Gallic acid (GA) has a significant antibacterial effect against Gram-positive bacteria (*S. aureus*, *Streptococcus* sp.), increasing their ability to accept electrons. On Gram-negative bacteria, this property could decrease, indicating that GA is an electrophilic compound interacting with bacterial surface components [63–65]. Ellagic acid (EA) acts on *S. aureus* damaging the bacteria cell membrane, leading to significant leakage of proteins and nucleic acids. Its antibacterial activity could inhibit protein synthesis, inducing great morphological changes in bacterial cell structure [66]. Both phenolic acids (GA and EA) also proved bactericidal effects against *P. aeruginosa* [52]. In encapsulated form, their antibacterial potential could increase [38].

Numerous researchers analyzed the antibacterial activity of *U. barbata* and *Usnea* sp.; generally, their results were similar to those obtained in our study [39]. The sensibility of Gram-positive bacteria to usnic acid and various *Usnea* sp. extracts is most known. Idamokoro et al. [67] analyzed the effect of *U. barbata* extracts in methanol and ethyl-acetate against 13 isolated *Staphylococcus* sp. involved in cow mastitis. They evidenced ethyl-acetate extract's lower inhibitory activity than methanol ones. On *S. aureus*, they reported an IZD value = 14 mm for methanol extract, similar to our *d*UBA (IZD = 13.66 mm). Mesta et al. [68] indicated the IZD values of 12 mm—for *U. ghatensis* ethanol extract 15 mg/mL against *S. aureus*—and 18 mm—for *U. undullata* ethanol extract 15 mg/mL on *S. pneumoniae*; both values are similar to those for *m/d*UBE obtained in the present study. In a previous study [69], we evaluated the antibacterial activity of *U. barbata* liquid extracts against two other *Streptococcus* sp. (*S. oralis* and *S. intermedius*) isolated from the oral cavity. Those obtained IZD values proved that *m*UBE had a stronger action for both *Streptococcus* sp. than *m*UBA; *m*UBW did not show any inhibitory effect. No inhibitory effects (IZD = 0) displayed the extracts of *U. pectinata*, *U. coraline*, and *U. baileyi* in methanol and dichloromethane against *K. pneumoniae* [5]. The methanol extracts of *U. articulata* (IZD = 28 mm) and *U. florida* (IZD = 18 mm) highlighted a remarkable antibacterial action against *P. aeruginosa* [41]. *U. florida* extract in methanol also proved significant activity on *S. aureus* (IZD = 30). Boisova et al. [70] optimized the conditions of UA SFE extraction from *U. subfloridana* (for 80 min, at a temperature of 85 °C and pressure of 150 atm). Their obtained extract proved an intense antibacterial activity against *S. aureus*.

4. Materials and Methods

4.1. Materials

Our study's chemicals, reagents, and standards were of analytical grade. Usnic acid standard 98.1% purity, phenolic standards (Z-resveratrol, caffeic acid, E-resveratrol, chlorogenic acid, ferulic acid, gallic acid, ellagic acid, p-coumaric acid, vanillin, 3-methyl gallic acid, cinnamic acid) were purchased from Sigma (Sigma-Aldrich Chemie GmbH., Taufkirchen, Germany). Folin–Ciocâlteu reagent, Pyrogallol, DPPH, acetone, and ethanol were supplied by Merck (Merck KGaA, Darmstadt, Germany).

The bacterial lines were obtained from Microbiology Department, S.C. Synevo Romania SRL, Constanta Laboratory, in partnership agreement No 1060/25.01.2018 with the Faculty of Pharmacy, Ovidius University of Constanta. Culture media Mueller–Hinton agar simple and one with 5% defibrinated sheep blood were supplied by Thermo Fisher Scientific, GmbH, Dreieich, Germany.

4.2. Lichen Extracts

U. barbata was harvested from Călimani Mountains, Romania (47°28′ N, 25°10′ E, 900 m altitude) in March 2021. The lichen was dried at a constant temperature below 25 °C in an airy room, protected from the sunlight. After drying, the obtained herbal product was preserved for a long time in the same conditions for use in subsequent studies. The lichen was identified using standard methods by the Department of Pharmaceutical Botany of the Faculty of Pharmacy, Ovidius University of Constanta. A voucher specimen (*Popovici 3/2021 Ph/UOC*) [71] can be found at the Department of Pharmacognosy, Faculty of Pharmacy, Ovidius University of Constanta.

The dried lichen was ground in an LM 120 laboratory mill (PerkinElmer, Waltham, MA, USA) and passed through the no. 5 sieve [19]. The obtained moderately fine lichen powder (particle size $\leq$ 315 µm) was subjected to extraction in acetone, 96% ethanol, and water (dried lichen: solvent ratio (w/v) = 1:10) using two conventional techniques.

The first procedure was maceration—three samples of 10 g ground dried lichen were extracted with 100 mL solvent (water, acetone, and 96% ethanol) in a dark place at room temperature (20–22 °C) for 10 days, with manual shaking 3–4 times/day. The resulting extractive solutions were filtered and made up of a 100 mL volumetric flask with each solvent. These fluid extracts (*m*UBA, *m*UBE, and *m*UBW) were preserved in dark-glass recipients with sealed plugs in the same conditions until processing.

The second one was Soxhlet extraction for 8 h, with the temperature values around each solvent's boiling point. Thus, three samples of 20 g ground dried lichen were refluxed at Soxhlet for eight hours with 200 mL of each solvent. Acetone and 96% ethanol were evaporated at the rotary evaporator TURBOVAP 500 (Caliper Life Sciences Inc., Hopkinton, MA, USA). Then, these extracts were kept for 16 h in a chemical exhaust hood for optimal solvent evaporation. After filtration with filter paper, UBW was concentrated on a Rotavapor R-215 with a vacuum controller V-850 (BÜCHI Labortechnik AG, Flawil, Switzerland), and lyophilized with a freeze-dryer Christ Alpha 1-2L (Martin Christ Gefriertrocknungsanlagen GmbH, Osterode am Harz, Germany) connected to a vacuum pump RZ 2.5 (VACUUBRAND GmbH, Wertheim, Germany) [72]. All these dry extracts (*d*UBA, *d*UBE, *d*UBW) were transferred in sealed-glass containers and preserved in freezer (Sirge® Elettrodomestici—S.A.C. Rappresentanze, Torino, Avigliana, Italy) at −18 °C [73] until processing.

4.3. HPLC-DAD Determination of Usnic Acid Content

A previously validated HPLC-DAD method was adapted for quantifying usnic acid [53].

4.3.1. Equipment and Chromatographic Conditions

This analytic method used an Agilent 1200 HPLC (Agilent Technologies, Santa Clara, CA, USA) with a G1311 quaternary pump, Agilent 1200 G1315B diode array detector (DAD), G1316 thermostatted column compartment, G1322 vacuum degassing system, G1329 autosampler.

The system has a Zorbax C18 analytical column 150 mm/4.6 mm; 5 µm (Agilent Technologies, Santa Clara, CA, USA). As a mobile phase, isocratic methanol: water: acetic acid = 80:15:5 was selected for 6 min per run, at an injection volume of 20 µL at a flow rate = 1.5 mL/min. The oven temperature was established at 25 °C, and the detection was performed at 282 nm.

4.3.2. Sample, Blank, Standard Solutions

All requested solutions were prepared using acetone as a solvent. The standard was usnic acid dissolved in acetone at concentrations of 2.5, 5, 10, 20, 50 µg/mL, with which the calibration curve (Figure S3, Supplementary Materials) was drawn ($y = 39.672x - 3.8228$; $R^2 = 0.999$). Each dilution was injected 6 times (20 µL) in the chromatographic system, and the obtained retention time value was 4.463 ± 0.008 min.

4.3.3. Data Processing

Data processing was achieved using the Waters Empower 2 chromatography data software with ICS 1.05 (Waters Corporation, Milford, MA, USA).

4.4. HPLC-DAD Determination of Polyphenols

The polyphenols quantification was achieved using a standardized HPLC method. It was described by the USP 30-NF25 monograph and previously validated [74].

4.4.1. Equipment and Chromatographic Conditions

The Agilent HPLC-DAD system was the analytical platform, with the same Zorbax C18 column, 150 mm 4.6 mm; 5 µm. As a mobile phase, two solutions were used: solution A: 0.1% phosphoric acid and solution B: acetonitrile, with gradient elution, at 22 min per run, with the same injection volume and flow The temperature was set at 35 °C and the detection was performed at UV 310 nm.

4.4.2. Sample, Blank, Standard Solutions

The standard solutions were 70% methanol solutions with various concentrations of: Z-resveratrol (0.22 mg/mL), caffeic acid (0.36 mg/mL), E-resveratrol (0.37 mg/mL), chlorogenic acid (0.37 mg/mL), ferulic acid (0.38 mg/mL), gallic acid (0.39 mg/mL), ellagic acid (0.40 mg/mL), p-coumaric acid (0.41 mg/mL), vanillin (0.42 mg/mL), 3-methyl gallic acid (0.51 mg/mL), cinnamic acid (0.58 mg/mL). The retention time values (minutes), established after 6 injections with each standard were displayed in Figure S4 and Table S1, Supplementary Materials; all phenolic standards have R^2 values > 0.99, as admissibility condition. The samples were the *U. barbata* extracts in different solvents (their preparation was mentioned in the Section 4.2).

4.5. Total Phenolic Content

The total phenolic content was determined using Folin–Ciocâlteu reagent through a spectrophotometric method detailed in a previous study [53]. Pyrogallol was selected as the standard, the TPC values being calculated as mg of pyrogallol equivalents (PyE) per gram extract.

4.6. DPPH Free-Radical Scavenging Activity Assay

The *U. barbata* extracts free radical scavenging activity (AA) was determined spectrophotometrically through the DPPH free-radical scavenging assay previously described [19].

4.7. Antibacterial Activity

The antibacterial effects were evaluated by an adapted disc diffusion method (DDM) from the Clinical and Laboratory Standard Institute (CLSI) [75], previously described [76].

4.7.1. Microorganisms and Media

We obtained all bacteria strains from the American Type Culture Collection (ATCC). Their identification was performed at the Department of Microbiology and Immunology, Faculty of Dental Medicine, Ovidius University of Constanta. The Gram-positive bacteria were *S. aureus* (ATCC 25923) and *S. pneumoniae* (ATCC 49619); the Gram-negative ones were *Pseudomonas aeruginosa* (ATCC 27853) and *K. pneumoniae* (ATCC 13883). As a culture medium for all bacterial strains, Mueller–Hinton agar was used.

4.7.2. Inoculum Preparation

We prepared the bacterial inoculum using the direct colony suspension method (CLSI). Thus, we obtained a 0.9% saline suspension of bacterial colonies selected from a 24 h agar plate, according to the 0.5 McFarland standard, with around 10^8 CFU/mL (CFU—colony-forming unit).

4.7.3. Lichen Samples Preparations

The fluid extracts were subjected to solvent evaporation in the rotary evaporator TURBOVAP 500. These concentrated extracts were kept for 2 h in a chemical exhaust hood for each optimal solvent evaporation. Then, all *U. barbata* extracts were redissolved in 0.1% DMSO [77], obtaining a final solution of 15 mg/mL concentration.

The dry lichen extracts were dissolved in 0.1% DMSO, resulting in 15 mg/mL concentration solutions.

4.7.4. Disc Diffusion Method

The 15 mg/mL lichen extracts in 0.1% DMSO were applied on Whatman® filter paper discs (6 mm, Merk KGaA, Darmstadt, Germany). The negative control was the solvent (0.1% DMSO); UA of 15 mg/mL in 0.1% DMSO was the positive control for all extracts. We impregnated each filter paper disc with 10 μL control and sample solutions. The standard antibiotic discs (6 mm) with ofloxacin 5 μg and ceftriaxone 30 μg (Oxoid, Thermo Fisher Scientific GmbH, Dreieich, Germany) were selected for antimicrobial activity evaluation. These blank discs were stored in a freezer at −14 °C and incubated for 2 h before analysis at room temperature.

Each inoculum was applied over the entire surface of the plate with the suitable culture media using a sterile cotton swab. After 15 min of drying, the filter paper discs were applied to the inoculated plates; they were incubated at 37 °C for 24 h.

4.7.5. Reading Plates

Circular zones of a microorganism growing inhibition around several discs could be observed, examining the plates after 24 h incubation. The results of the disc diffusion assay are expressed in the inhibition zone diameter (IZD) measured in mm. These IZD values quantify bacterial strains' susceptibility levels after 24 h incubation [78].

4.7.6. Interpretation of Disc Diffusion Method results

Usnic acid and *U. barbata* extracts' IZD were compared to the IZD values of the positive controls represented by the blank antibiotic discs, ofloxacin 5 ug and ceftriaxone 30 ug [78]. In DDM, IZD values inversely correlate with minimum inhibitory concentrations (MIC) from standard dilution tests. According to CLSI [78], the interpretive categories are as follows: susceptible ("S"), intermediate—dose-dependent susceptibility ("I"), and resistant ("R") [46].

4.7.7. Activity Index

The activity index (AI) [47] is calculated using the following formula:

$$AI = \frac{\text{IZD sample}}{\text{IZD standard}} \tag{1}$$

where IZD sample—inhibition zone diameter for each *U. barbata* extract, and IZD standard—inhibition zone diameter for each antibacterial drug, used as standard.

4.8. Data Analysis, Software

All analyses were accomplished in triplicate, and the results are expressed as the mean (n = 3) ± SD, calculated by Microsoft 365 Office Excel (Redmond, Washington, DC, USA). The p-values were calculated with the one-way ANOVA test; when the p-value was <0.05, the differences between the obtained mean values were considered significant. The principal component analysis (PCA) [51] was performed using XLSTAT 2022.2.1. by Addinsoft (New York, NY, USA) [79].

5. Conclusions

Our study analyzed the phenolic constituents and bioactivities of six *U. barbata* lichen extracts obtained through two low-cost conventional techniques widely used in pharmaceutical laboratories. Despite the same ratio between the dried lichen and the solvent (w/v), all lichen extracts displayed significant differences regarding the phenolic metabolites' diversity and amount due to extraction conditions, with a substantial impact on their bioactivities. All *U. barbata* extracts show antiradical activity; the antibacterial study proves that the *U. barbata* extracts in acetone and ethanol obtained through both methods considerably inhibit bacterial colony growth. Both Gram-positive bacteria and *P. aeruginosa* of Gram-negative ones reveal the highest sensibility.

Our results suggest that further research could extend the antibacterial studies, exploring their effects on other bacteria species. Future studies could optimize both extraction processes to obtain *U. barbata* extracts with valuable bioactivities for potential pharmaceutical applications.

Supplementary Materials: The following supporting information can be downloaded at: https://www.mdpi.com/article/10.3390/ph15070829/s1, Figure S1. (a). *U. barbata* fluid extracts: A. *m*UBW, B. *m*UBA, C. *m*UBE; (b–d) *U. barbata* dry extracts: (b) *d*UBW, (c) *d*UBA, (d) *d*UBE; Figure S2. Antibacterial activity of usnic acid (1) and *U. barbata* extracts: *m*UBA (2), *d*UBA (3), *m*UBE (4), *d*UBE (5), *m*UBW (6), on *S. aureus* (a), *S. pneumoniae* (b), *P. aeruginosa* (c), *K. pneumoniae* (d); Figure S3. Calibration curve for usnic acid; Figure S4. Polyphenols standards: mixture (a), ellagic acid (b), *p*-coumaric acid (c), cis-resveratrol, and trans-resveratrol (d); Table S1. Concentration, retention time, and correlation coefficient (R^2) values for all phenolic standards used in the HPLC-DAD method.

Author Contributions: Conceptualization, V.P., L.B. and A.P.; methodology, L.B., C.E.G., A.P., E.M., G.C.C., M.A., V.S., E.A.O., A.C.F., D.L. and V.B.; software, V.P., L.B. and A.P.; validation, L.B., C.E.G., A.P., M.B. and V.B.; formal analysis, C.E.G., E.M., G.C.C., M.A., V.S. and D.L.; investigation, E.M., G.C.C., M.A., E.A.O., A.C.F., D.L., A.C. and M.B.; resources, V.P., L.B., C.E.G., A.P., E.M., G.C.C., M.A., E.A.O., A.C.F., D.L., M.B. and V.B.; data curation, E.M., G.C.C., M.A., E.A.O., V.S. and A.C.; writing—original draft preparation, V.P., L.B., C.E.G., A.P. and V.B.; writing—review and editing, V.P., L.B., C.E.G., E.A.O., A.C.F. and V.B.; visualization, L.B., C.E.G., A.P., E.M., G.C.C., M.A., V.S., E.A.O., A.C.F., D.L., A.C., M.B. and V.B.; supervision, L.B., C.E.G., A.P., E.A.O., A.C.F., D.L., A.C. and V.B.; project administration, V.B.; funding acquisition, V.P. All authors have read and agreed to the published version of the manuscript.

Funding: This work is supported by the project ANTREPRENORDOC, in the framework of Human Resources Development Operational Programme 2014–2020, financed from the European Social Fund under the contract number 36355/23.05.2019 HRD OP/380/6/13—SMIS Code: 123847.

Institutional Review Board Statement: Not applicable.

Informed Consent Statement: Not applicable.

Data Availability Statement: Data are contained within the article.

Acknowledgments: This project is performed in collaboration with the Department of Pharmacognosy, Phytochemistry, and Phytotherapy, and Department of Pharmaceutical Technology and Biopharmacy, Faculty of Pharmacy, Carol Davila University of Medicine and Pharmacy, 6 Traian Vuia Street, 020956 Bucharest, Romania, and Center for Research and Development of the Morphological and Genetic Studies of Malignant Pathology, Ovidius University of Constanta, CEDMOG, 145 Tomis Blvd., 900591 Constanta, Romania.

Conflicts of Interest: The authors declare no conflict of interest.

References

1. Ge, L.; Li, S.P.; Lisak, G. Advanced sensing technologies of phenolic compounds for pharmaceutical and biomedical analysis. *J. Pharm. Biomed. Anal.* **2020**, *179*, 112913. [CrossRef] [PubMed]
2. Albornoz, L.; Torres-Benítez, A.; Moreno-Palacios, M.; Simirgiotis, M.J.; Montoya-Serrano, S.A.; Sepulveda, B.; Stashenko, E.; García-Beltrán, O.; Areche, C. Phylogenetic Studies and Metabolite Analysis of *Sticta* Species from Colombia and Chile by Ultra-High Performance Liquid Chromatography-High Resolution-Q-Orbitrap-Mass Spectrometry. *Metabolites* **2022**, *12*, 560. [CrossRef] [PubMed]
3. Stocker-Wörgötter, E.; Cordeiro, L.M.C.; Iacomini, M. Accumulation of potential pharmaceutically relevant lichen metabolites in lichens and cultured lichen symbionts. In *Studies in Natural Products Chemistry*; Atta-ur-Rahman, Ed.; Elsevier: Amsterdam, The Netherlands, 2013; Volume 39, pp. 337–380.
4. Fernández-Moriano, C.; Gómez-Serranillos, M.P.; Crespo, A. Antioxidant potential of lichen species and their secondary metabolites. A systematic review. *Pharm. Biol.* **2016**, *54*, 1–17. [CrossRef] [PubMed]
5. Jha, B.N.; Shrestha, M.; Pandey, D.P.; Bhattarai, T.; Bhattarai, H.D.; Paudel, B. Investigation of antioxidant, antimicrobial and toxicity activities of lichens from high altitude regions of Nepal. *BMC Complement. Altern. Med.* **2017**, *17*, 282. [CrossRef]
6. Kello, M.; Kuruc, T.; Petrova, K.; Goga, M.; Michalova, Z.; Coma, M.; Rucova, D.; Mojzis, J. Pro-apoptotic potential of *Pseudevernia furfuracea* (L.) Zopf extract and isolated physodic acid in acute lymphoblastic leukemia model in vitro. *Pharmaceutics* **2021**, *13*, 2173. [CrossRef]
7. Varol, M.; Tay, T.; Candan, M.; Türk, A.; Koparal, A.T. Evaluation of the sunscreen lichen substances usnic acid and atranorin. *Biocell* **2015**, *39*, 25–31.
8. Varol, M. Lichens as a Promising Source of Unique and Functional Small Molecules for Human Health and Well-Being. In *Studies in Natural Products Chemistry*; Atta-ur-Rahman, Ed.; Elsevier: Amsterdam, The Netherlands, 2018; Volume 60, pp. 425–458.

9. Tas, I.; Yildirim, A.B.; Ozkan, E.; Ozyigitoglu, G.C.; Yavuz, M.Z.; Turker, A.U. Evaluation of pharmaceutical potential and phytochemical analysis of selected traditional lichen species. *Farmacia* **2021**, *69*, 1101–1106. [CrossRef]
10. Elečko, J.; Vilková, M.; Frenák, R.; Routray, D.; Ručová, D.; Bačkor, M.; Goga, M. A Comparative Study of Isolated Secondary Metabolites from Lichens and Their Antioxidative Properties. *Plants* **2022**, *11*, 1077. [CrossRef]
11. Gunasekaran, S.; Pillai Rajan, V.; Ramanathan, S.; Murugaiyah, V.; Samsudin, M.W.; Din, L. Antibacterial and Antioxidant Activity of Lichens *Usnea rubrotincta, Ramalina dumeticola, Cladonia verticillata* and Their Chemical Constituents. *Malays. J. Anal. Sci.* **2016**, *20*, 1–13. [CrossRef]
12. Areche, C.; Parra, J.R.; Sepulveda, B.; Garc, O.; Simirgiotis, M.J. UHPLC-MS Metabolomic Fingerprinting, Antioxidant, and Enzyme Inhibition Activities of *Himantormia lugubris* from Antarctica. *Metabolites* **2022**, *12*, 560. [CrossRef]
13. Odabasoglu, F.; Cakir, A.; Suleyman, H.; Aslan, A.; Bayir, Y.; Halici, M.; Kazaz, C. Gastroprotective and antioxidant effects of usnic acid on indomethacin-induced gastric ulcer in rats. *J. Ethnopharmacol.* **2006**, *103*, 59–65. [CrossRef] [PubMed]
14. Fitriani, L.; Fista, B.; Ismed, F.; Zaini, E. Membrane of Usnic Acid in Solid Dispersion and Effectiveness in Burn Healing. *Adv. Health Sci. Res.* **2021**, *40*, 323–329.
15. Matvieieva, N.A.; Pasichnyk, L.A.; Zhytkevych, N.V.; Pabón, G.G.; Pidgorskyi, V.S. Antimicrobial Activity of Extracts from Ecuadorian Lichens. *Mikrobiol. Z.* **2015**, *77*, 23–27. [CrossRef] [PubMed]
16. Oh, J.M.; Kim, Y.J.; Gang, H.S.; Han, J.; Ha, H.H.; Kim, H. Antimicrobial Activity of Divaricatic Acid Isolated from the Lichen *Evernia mesomorpha* against Methicillin-Resistant *Staphylococcus aureus*. *Molecules* **2018**, *23*, 3068. [CrossRef]
17. Fitriani, L.; Afifah; Ismed, F.; Bakhtiar, A. Hydrogel formulation of usnic acid and antibacterial activity test against *Propionibacterium acne*. *Sci. Pharm.* **2019**, *87*, 1. [CrossRef]
18. Prateeksha Paliya, B.S.; Bajpai, R.; Jadaun, V.; Kumar, J.; Kumar, S.; Upreti, D.K.; Singh, B.N.R.; Nayaka, S.; Joshi, Y.; Brahma Singh, N.; et al. The genus *Usnea*: A potent phytomedicine with multifarious ethnobotany, phytochemistry and pharmacology. *RSC Adv.* **2016**, *6*, 21672–21696. [CrossRef]
19. Popovici, V.; Bucur, L.; Gîrd, C.E.; Calcan, S.I.; Cucolea, E.I.; Costache, T.; Rambu, D.; Oroian, M.; Mironeasa, S.; Schröder, V.; et al. Advances in the Characterization of *Usnea barbata* (L.) Weber ex F.H. Wigg from Călimani Mountains, Romania. *Appl. Sci.* **2022**, *12*, 4234. [CrossRef]
20. Galanty, A.; Paśko, P.; Podolak, I. Enantioselective activity of usnic acid: A comprehensive review and future perspectives. *Phytochem. Rev.* **2019**, *18*, 527–548. [CrossRef]
21. Maulidiyah, M.; Darmawan, A.; Ahmad, E.; Musdalifah, A.; Wibowo, D.; Salim, L.O.A.; Arham, Z.; Mustapa, F.; Nurdin, I.F.A.; Nurdin, M. Antioxidant activity-guided isolation of usnic acid and diffractaic acid compounds from lichen genus *Usnea* sp. *J. Appl. Pharm. Sci.* **2021**, *11*, 075–083. [CrossRef]
22. Bachtiar, E.; Hermawati, E.; Juliawaty, L.D.; Syah, Y.M. Antibacterial properties of usnic acid against vibriosis. *Res. J. Chem. Environ.* **2020**, *24*, 100–101.
23. White, P.A.S.; Oliveira, R.C.M.; Oliveira, A.P.; Serafini, M.R.; Araújo, A.A.S.; Gelain, D.P.; Moreira, J.C.F.; Almeida, J.R.G.S.; Quintans, J.S.S.; Quintans-Junior, L.J.; et al. Antioxidant activity and mechanisms of action of natural compounds isolated from lichens: A systematic review. *Molecules* **2014**, *19*, 14496–14527. [CrossRef] [PubMed]
24. Kristmundsdóttir, T.; Jónsdóttir, E.; Ögmundsdóttir, H.M.; Ingólfsdóttir, K. Solubilization of poorly soluble lichen metabolites for biological testing on cell lines. *Eur. J. Pharm. Sci.* **2005**, *24*, 539–543. [CrossRef] [PubMed]
25. Kwong, S.P.; Wang, C. Review: Usnic acid-induced hepatotoxicity and cell death. *Environ. Toxicol. Pharmacol.* **2020**, *80*, 103493. [CrossRef] [PubMed]
26. Macedo, D.C.S.; Almeida, F.J.F.; Wanderley, M.S.O.; Ferraz, M.S.; Santos, N.P.S.; López, A.M.Q.; Santos-Magalhães, N.S.; Lira-Nogueira, M.C.B. Usnic acid: From an ancient lichen derivative to promising biological and nanotechnology applications. *Phytochem. Rev.* **2021**, *20*, 609–630. [CrossRef]
27. Lira, M.C.B.; Ferraz, M.S.; da Silva, D.G.V.C.; Cortes, M.E.; Teixeira, K.I.; Caetano, N.P.; Sinisterra, R.D.; Ponchel, G.; Santos-Magalhães, N.S. Inclusion complex of usnic acid with β-cyclodextrin: Characterization and nanoencapsulation into liposomes. *J. Incl. Phenom. Macrocycl. Chem.* **2009**, *64*, 215–224. [CrossRef]
28. Francolini, I.; Giansanti, L.; Piozzi, A.; Altieri, B.; Mauceri, A.; Mancini, G. Glucosylated liposomes as drug delivery systems of usnic acid to address bacterial infections. *Colloids Surf. B Biointerfaces* **2019**, *181*, 632–638. [CrossRef]
29. Grumezescu, A.M.; Cotar, A.I.; Andronescu, E.; Ficai, A.; Ghitulica, C.D.; Grumezescu, V.; Vasile, B.S.; Chifiriuc, M.C. In vitro activity of the new water-dispersible Fe_3O_4@usnic acid nanostructure against planktonic and sessile bacterial cells. *J. Nanoparticle Res.* **2013**, *15*, 1766. [CrossRef]
30. Baláž, M.; Goga, M.; Hegedüs, M.; Daneu, N.; Kováčová, M.; Tkáčiková, L.; Balážová, L.; Bačkor, M. Biomechanochemical Solid-State Synthesis of Silver Nanoparticles with Antibacterial Activity Using Lichens. *ACS Sustain. Chem. Eng.* **2020**, *8*, 13945–13955. [CrossRef]
31. Siddiqi, K.S.; Rashid, M.; Rahman, A.; Husen, A.; Rehman, S. Biogenic fabrication and characterization of silver nanoparticles using aqueous-ethanolic extract of lichen (*Usnea longissima*) and their antimicrobial activity. *Biomater. Res.* **2018**, *22*, 23. [CrossRef]
32. Mariadoss, A.V.A.; Saravanakumar, K.; Sathiyaseelan, A.; Karthikkumar, V.; Wang, M.H. Smart drug delivery of p-Coumaric acid loaded aptamer conjugated starch nanoparticles for effective triple-negative breast cancer therapy. *Int. J. Biol. Macromol.* **2022**, *195*, 22–29. [CrossRef]

33. Mitrea, D.R.; Malkey, R.; Florian, T.L.; Filip, A.; Clichici, S.; Bidian, C.; Moldovan, R.; Hoteiuc, O.A.; Toader, A.M.; Baldea, I. Daily oral administration of chlorogenic acid prevents the experimental carrageenan-induced oxidative stress. *J. Physiol. Pharmacol.* **2020**, *71*, 74–81.
34. Khan, F.; Bamunuarachchi, N.I.; Tabassum, N.; Kim, Y.M. Caffeic Acid and Its Derivatives: Antimicrobial Drugs toward Microbial Pathogens. *J. Agric. Food Chem.* **2021**, *69*, 2979–3004. [CrossRef] [PubMed]
35. Boo, Y.C. *p*-coumaric acid as an active ingredient in cosmetics: A review focusing on its antimelanogenic effects. *Antioxidants* **2019**, *8*, 275. [CrossRef] [PubMed]
36. Abozaid, O.A.R.; Moawed, F.S.M.; Ahmed, E.S.A.; Ibrahim, Z.A. Cinnamic acid nanoparticles modulate redox signal and inflammatory response in gamma irradiated rats suffering from acute pancreatitis. *Biochim. Biophys. Acta—Mol. Basis Dis.* **2020**, *1866*, 165904. [CrossRef] [PubMed]
37. Yu, Z.; Song, F.; Jin, Y.C.; Zhang, W.M.; Zhang, Y.; Liu, E.J.; Zhou, D.; Bi, L.L.; Yang, Q.; Li, H.; et al. Comparative pharmacokinetics of gallic acid after oral administration of Gallic acid monohydrate in normal and isoproterenol-induced myocardial infarcted rats. *Front. Pharmacol.* **2018**, *9*, 328. [CrossRef]
38. De Souza Tavares, W.; Pena, G.R.; Martin-Pastor, M.; de Sousa, F.F.O. Design and characterization of ellagic acid-loaded zein nanoparticles and their effect on the antioxidant and antibacterial activities. *J. Mol. Liq.* **2021**, *341*, 116915. [CrossRef]
39. Cansaran, D.; Kahya, D.; Yurdakulol, E.; Atakol, O. Identification and quantitation of usnic acid from the lichen *Usnea* species of Anatolia and antimicrobial activity. *Z. Fur Naturforsch.—Sect. C. J. Biosci.* **2006**, *61*, 773–776. [CrossRef]
40. Tosun, F.; Kizilay, Ç.A.; Şener, B.; Vural, M. The evaluation of plants from Turkey for in Vitro antimycobacterial activity. *Pharm. Biol.* **2005**, *43*, 58–63. [CrossRef]
41. Bate, P.N.N.; Orock, A.E.; Nyongbela, K.D.; Babiaka, S.B.; Kukwah, A.; Ngemenya, M.N. In vitro activity against multi-drug resistant bacteria and cytotoxicity of lichens collected from Mount Cameroon. *J. King Saud Univ.—Sci.* **2020**, *32*, 614–619. [CrossRef]
42. Zizovic, I.; Ivanovic, J.; Misic, D.; Stamenic, M.; Djordjevic, S.; Kukic-Markovic, J.; Petrovic, S.D. SFE as a superior technique for isolation of extracts with strong antibacterial activities from lichen *Usnea barbata* L. *J. Supercrit. Fluids* **2012**, *72*, 7–14. [CrossRef]
43. Ivanovic, J.; Meyer, F.; Misic, D.; Asanin, J.; Jaeger, P.; Zizovic, I.; Eggers, R. Influence of different pre-treatment methods on isolation of extracts with strong antibacterial activity from lichen Usnea barbata using carbon dioxide as a solvent. *J. Supercrit. Fluids* **2013**, *76*, 1–9. [CrossRef]
44. Basiouni, S.; Fayed, M.A.A.; Tarabees, R.; El-Sayed, M.; Elkhatam, A.; Töllner, K.R.; Hessel, M.; Geisberger, T.; Huber, C.; Eisenreich, W.; et al. Characterization of sunflower oil extracts from the lichen *Usnea barbata*. *Metabolites* **2020**, *10*, 353. [CrossRef] [PubMed]
45. Ghafoor, K.; Ahmed, I.A.M.; Doğu, S.; Uslu, N.; Gbemisola Jamiu, F.; Al Juhaimi, F.; Babiker, E.E.; Özcan, M.M. The Effect of Heating Temperature on Total Phenolic Content, Antioxidant Activity, and Phenolic Compounds of Plum and Mahaleb Fruits. *Int. J. Food Eng.* **2019**, *15*, 11–12. [CrossRef]
46. Humphries, R.M.; Abbott, A.N.; Hindler, J.A. Understanding and addressing CLSI breakpoint revisions: A primer for clinical laboratories. *J. Clin. Microbiol.* **2019**, *57*, e00203–e00219. [CrossRef] [PubMed]
47. Shiromi, P.S.A.I.; Hewawasam, R.P.; Jayalal, R.G.U.; Rathnayake, H.; Wijayaratne, W.M.D.G.B.; Wanniarachchi, D. Chemical Composition and Antimicrobial Activity of Two Sri Lankan Lichens, *Parmotrema rampoddense*, and *Parmotrema tinctorum* against Methicillin-Sensitive and Methicillin-Resistant Staphylococcus aureus. *Evid.—Based Complement. Altern. Med.* **2021**, 9985325. [CrossRef]
48. Farmacopeea Rom. 10th ed. 1993; pp. 419–421. Available online: https://ro.scribd.com/doc/215542717/Farmacopeea-Romana-X (accessed on 26 May 2022).
49. Malik, J.; Mandal, S.C. Extraction of herbal biomolecules. In *Herbal Biomolecules in Healthcare Applications*; Mandal, S.C., Nayak, A.K., Dhara, A.K., Eds.; Academic Press: Cambridge, MA, USA, 2022; pp. 21–46.
50. Joshi, D.R.; Adhikari, N. An Overview on Common Organic Solvents and Their Toxicity. *J. Pharm. Res. Int.* **2019**, *28*, 1–18. [CrossRef]
51. Sawicki, T.; Starowicz, M.; Kłębukowska, L.; Hanus, P. The Profile of Polyphenolic Compounds, Contents of Total Phenolics and Flavonoids, and Antioxidant and Antimicrobial Properties of Bee Products. *Molecules* **2022**, *27*, 1301. [CrossRef]
52. Kosuru, R.Y.; Aashique, M.; Fathima, A.; Roy, A.; Bera, S. Revealing the dual role of gallic acid in modulating ampicillin sensitivity of *Pseudomonas aeruginosa* biofilms. *Future Microbiol.* **2018**, *13*, 297–312. [CrossRef]
53. Popovici, V.; Bucur, L.; Popescu, A.; Schröder, V.; Costache, T.; Rambu, D.; Cucolea, I.E.; Gîrd, C.E.; Caraiane, A.; Gherghel, D.; et al. Antioxidant and cytotoxic activities of *Usnea barbata* (L.) F.H. Wigg. dry extracts in different solvents. *Plants* **2021**, *10*, 909. [CrossRef]
54. Popovici, V.; Bucur, L.; Gîrd, C.E.; Rambu, D.; Calcan, S.I.; Cucolea, E.I.; Costache, T.; Ungureanu-Iuga, M.; Oroian, M.; Mironeasa, S.; et al. Antioxidant, Cytotoxic, and Rheological Properties of Canola Oil Extract of *Usnea barbata* (L.) Weber ex F. H. Wigg from Călimani Mountains, Romania. *Plants* **2022**, *11*, 854. [CrossRef]
55. Antonenko, Y.N.; Khailova, L.S.; Rokitskaya, T.I.; Nosikova, E.S.; Nazarov, P.A.; Luzina, O.A.; Salakhutdinov, N.F.; Kotova, E.A. Mechanism of action of an old antibiotic revisited: Role of calcium ions in protonophoric activity of usnic acid. *Biochim. Biophys. Acta—Bioenerg.* **2019**, *1860*, 310–316. [CrossRef] [PubMed]

56. Maciag-Dorszyńska, M.; Wegrzyn, G.; Guzow-Krzemińska, B. Antibacterial activity of lichen secondary metabolite usnic acid is primarily caused by inhibition of RNA and DNA synthesis. *FEMS Microbiol. Lett.* **2014**, *353*, 57–62. [CrossRef] [PubMed]
57. Nithyanand, P.; Beema Shafreen, R.M.; Muthamil, S.; Karutha Pandian, S. Usnic acid, a lichen secondary metabolite inhibits Group A *Streptococcus* biofilms. *Antonie Van Leeuwenhoek Int. J. Gen. Mol. Microbiol.* **2015**, *107*, 263–272. [CrossRef] [PubMed]
58. Sinha, S.; Gupta, V.K.; Kumar, P.; Kumar, R.; Joshi, R.; Pal, A.; Darokar, M.P. Usnic acid modifies MRSA drug resistance through down-regulation of proteins involved in peptidoglycan and fatty acid biosynthesis. *FEBS Open Bio.* **2019**, *9*, 2025–2040. [CrossRef] [PubMed]
59. Lou, Z.; Wang, H.; Rao, S.; Sun, J.; Ma, C.; Li, J. P-Coumaric acid kills bacteria through dual damage mechanisms. *Food Control* **2012**, *25*, 550–554. [CrossRef]
60. Vasconcelos, N.G.; Croda, J.; Simionatto, S. Antibacterial mechanisms of cinnamon and its constituents: A review. *Microb. Pathog.* **2018**, *120*, 198–203. [CrossRef]
61. Lou, Z.; Wang, H.; Zhu, S.; Ma, C.; Wang, Z. Antibacterial activity and mechanism of action of chlorogenic acid. *J. Food Sci.* **2011**, *76*, 398–403. [CrossRef]
62. Guan, S.; Zhu, K.; Dong, Y.; Li, H.; Yang, S.; Wang, S.; Shan, Y. Exploration of binding mechanism of a potential *Streptococcus pneumoniae* neuraminidase inhibitor from herbaceous plants by molecular simulation. *Int. J. Mol. Sci.* **2020**, *21*, 1003. [CrossRef]
63. Selim, S.; Abdel-Mawgoud, M.; Al-Sharary, T.; Almuhayawi, M.S.; Alruhaili, M.H.; Al Jaouni, S.K.; Warrad, M.; Mohamed, H.S.; Akhtar, N.; Abdelgawad, H. Pits of date palm: Bioactive composition, antibacterial activity and antimutagenicity potentials. *Agronomy* **2022**, *12*, 54. [CrossRef]
64. Štumpf, S.; Hostnik, G.; Primožič, M.; Leitgeb, M.; Bren, U. Generation Times of *E. coli* Prolong with Increasing Tannin Concentration while the Lag Phase Extends Exponentially. *Plants* **2020**, *9*, 1680. [CrossRef]
65. Štumpf, S.; Hostnik, G.; Primožič, M.; Leitgeb, M.; Salminen, J.P.; Bren, U. The effect of growth medium strength on minimum inhibitory concentrations of tannins and tannin extracts against *E coli*. *Molecules* **2020**, *25*, 2947. [CrossRef] [PubMed]
66. Zhou, D.; Liu, Z.H.; Wang, D.M.; Li, D.W.; Yang, L.N.; Wang, W. Chemical composition, antibacterial activity and related mechanism of valonia and shell from *Quercus variabilis* Blume (Fagaceae) against Salmonella paratyphi a and Staphylococcus aureus. *BMC Complement. Altern. Med.* **2019**, *19*, 271. [CrossRef] [PubMed]
67. Idamokoro, E.M.; Masika, P.J.; Muchenje, V.; Falta, D.; Green, E. In-vitro antibacterial sensitivity of *Usnea barbata* lichen extracted with methanol and ethyl-acetate against selected Staphylococcus species from milk of cows with mastitis. *Arch. Anim. Breed.* **2014**, *57*, 25. [CrossRef]
68. Mesta, A.R.; Rajeswari, N.; Kanivebagilu, V.S. Assessment of Antimicrobial Activity of Ethanolic Extraction of *Usnea ghattensis* and *Usn Undulata*. *Int. J. Res. Ayurveda Pharm.* **2020**, *11*, 75–77. [CrossRef]
69. Popovici, V.; Bucur, L.; Popescu, A.; Caraiane, A.; Badea, V. Evaluation of the Antibacterial Action of the *Usnea barbata* L. Extracts, on Streptococcus Species from the Oro-Dental Cavity. In Proceedings of the Romanian National Congress of Pharmacy, Bucharest, Romania, 26–29 September 2018. 17th ed..
70. Boitsova, T.A.; Brovko, O.S.; Ivakhnov, A.D.; Zhil'tsov, D.V. Optimizing Supercritical Fluid Extraction of Usnic Acid from the Lichen Species *Usn Subfloridana*. *Russ. J. Phys. Chem. B* **2020**, *14*, 1135–1141. [CrossRef]
71. Stern, W.L.; Chambers, K.L. The Citation of Wood Specimens and Herbarium Vouchers in Anatomical. *Int. Assoc. Plant Taxon.* **2018**, *9*, 7–13. Available online: https://www.jstor.org/stable/1217349 (accessed on 20 May 2022). [CrossRef]
72. Popovici, V.; Bucur, L.; Costache, T.; Gherghel, D.; Vochita, G.; Mihai, C.T.C.T.; Rotinberg, P.; Schroder, V.; Badea, F.C.F.C.; Badea, V.; et al. Studies on Preparation and UHPLC Analysis of the *Usnea barbata* (L.) F.H.Wigg Dry acetone extract. *Rev. Chim.* **2019**, *70*, 3775–3777. [CrossRef]
73. Ranković, B.; Kosanić, M.; Stanojković, T.; Vasiljević, P.; Manojlović, N. Biological activities of *Toninia candida* and *Usnea barbata* together with their norstictic acid and usnic acid constituents. *Int. J. Mol. Sci.* **2012**, *13*, 14707–14722. [CrossRef]
74. Popovici, V.; Bucur, L.; Popescu, A.; Caraiane, A.; Badea, V. Determination of the content in usnic acid and polyphenols from the extracts of *Usnea barbata* L. and the evaluation of their antioxidant activity. *Farmacia* **2018**, *66*, 337–341.
75. Hudzicki, J. Kirby-Bauer Disk Diffusion Susceptibility Test Protocol Author Information. *Am. Soc. Microbiol.* **2009**, *15*, 55–63.
76. Popovici, V.; Bucur, L.; Calcan, S.I.; Cucolea, E.I.; Costache, T.; Rambu, D.; Schröder, V.; Gîrd, C.E.; Gherghel, D.; Vochita, G.; et al. Elemental Analysis and In Vitro Evaluation of Antibacterial and Antifungal Activities of *Usnea barbata* (L.) Weber ex F.H. Wigg from C ă limani Mountains, Romania. *Plants* **2022**, *11*, 32. [CrossRef] [PubMed]
77. Timm, M.; Saaby, L.; Moesby, L.; Hansen, E.W. Considerations regarding use of solvents in in vitro cell based assays. *Cytotechnology* **2013**, *65*, 887–894. [CrossRef] [PubMed]
78. Kassim, A.; Omuse, G.; Premji, Z.; Revathi, G. Comparison of Clinical Laboratory Standards Institute and European Committee on Antimicrobial Susceptibility Testing guidelines for the interpretation of antibiotic susceptibility at a University teaching hospital in Nairobi, Kenya: A cross-sectional study. *Ann. Clin. Microbiol. Antimicrob.* **2016**, *15*, 21. [CrossRef] [PubMed]
79. Vidal, N.P.; Manful, C.F.; Pham, T.H.; Stewart, P.; Keough, D.; Thomas, R.H. The use of XLSTAT in conducting principal component analysis (PCA) when evaluating the relationships between sensory and quality attributes in grilled foods. *MethodsX* **2020**, *302*, 125326. [CrossRef] [PubMed]

antioxidants

MDPI

Article

Usnic Acid and *Usnea barbata* (L.) F.H. Wigg. Dry Extracts Promote Apoptosis and DNA Damage in Human Blood Cells through Enhancing ROS Levels

Violeta Popovici [1], Elena Matei [2,*], Georgeta Camelia Cozaru [2,3], Mariana Aschie [2,3], Laura Bucur [4,*], Dan Rambu [5], Teodor Costache [5], Iulia Elena Cucolea [5], Gabriela Vochita [6], Daniela Gherghel [6], Aureliana Caraiane [7] and Victoria Badea [1]

[1] Department of Microbiology and Immunology, Faculty of Dental Medicine, Ovidius University of Constanta, 7 Ilarie Voronca Street, 900684 Constanta, Romania; violeta.popovici@365.univ-ovidius.ro (V.P.); victoria.badea@365.univ-ovidius.ro (V.B.)

[2] Center for Research and Development of the Morphological and Genetic Studies of Malignant Pathology, Ovidius University of Constanta, CEDMOG, 145 Tomis Blvd., 900591 Constanta, Romania; drcozaru@yahoo.com (G.C.C.); aschiemariana@yahoo.com (M.A.)

[3] Clinical Service of Pathology, Sf. Apostol Andrei Emergency County Hospital, 145 Tomis Blvd., 900591 Constanta, Romania

[4] Department of Pharmacognosy, Faculty of Pharmacy, Ovidius University of Constanta, 6 Capitan Al. Serbanescu Street, 900001 Constanta, Romania

[5] Research Center for Instrumental Analysis SCIENT, 1E Petre Ispirescu Street, Tancabesti, 077167 Ilfov, Romania; dan.rambu@scient.ro (D.R.); teodor.costache@scient.ro (T.C.); iulia.cucolea@scient.ro (I.E.C.)

[6] NIRDBS, Institute of Biological Research Iasi, 47 Lascar Catargi Street, 700107 Iasi, Romania; gabriela.vochita@icbiasi.ro (G.V.); daniela.gherghel@icbiasi.ro (D.G.)

[7] Department of Oral Rehabilitation, Faculty of Dental Medicine, Ovidius University of Constanta, 7 Ilarie Voronca Street, 900684 Constanta, Romania; aureliana.caraiane@365.univ-ovidius.ro

* Correspondence: sogorescuelena@gmail.com (E.M.); laurabucur@univ-ovidius.ro (L.B.); Tel.: +40-72-394-3559 (E.M.); +40-72-152-8446 (L.B.)

Abstract: Nowadays, numerous biomedical studies performed on natural compounds and plant extracts aim to obtain highly selective pharmacological activities without unwanted toxic effects. In the big world of medicinal plants, *Usnea barbata* (L) F.H. Wigg (*U. barbata*) and usnic acid (UA) are well-known for their therapeutic properties. One of the most studied properties is their cytotoxicity on various tumor cells. This work aims to evaluate their cytotoxic potential on normal blood cells. Three dry *U. barbata* extracts in various solvents: ethyl acetate (UBEA), acetone (UBA), and ethanol (UBE) were prepared. From UBEA we isolated usnic acid with high purity by semipreparative chromatography. Then, UA, UBA, and UBE dissolved in 1% dimethyl sulfoxide (DMSO) and diluted in four concentrations were tested for their toxicity on human blood cells. The blood samples were collected from a healthy non-smoker donor; the obtained blood cell cultures were treated with the tested samples. After 24 h, the cytotoxic effect was analyzed through the mechanisms that can cause cell death: early and late apoptosis, caspase 3/7 activity, nuclear apoptosis, autophagy, reactive oxygen species (ROS) level and DNA damage. Generally, the cytotoxic effect was directly proportional to the increase of concentrations, usnic acid inducing the most significant response. At high concentrations, usnic acid and *U. barbata* extracts induced apoptosis and DNA damage in human blood cells, increasing ROS levels. Our study reveals the importance of prior natural products toxicity evaluation on normal cells to anticipate their limits and benefits as potential anticancer drugs.

Keywords: *Usnea barbata*; usnic acid; secondary metabolites; blood cells; DNA damage; apoptosis; cytotoxic effect; oxidative stress

check for updates

Citation: Popovici, V.; Matei, E.; Cozaru, G.C.; Aschie, M.; Bucur, L.; Rambu, D.; Costache, T.; Cucolea, I.E.; Vochita, G.; Gherghel, D.; et al. Usnic Acid and *Usnea barbata* (L.) F.H. Wigg. Dry Extracts Promote Apoptosis and DNA Damage in Human Blood Cells through Enhancing ROS Levels. *Antioxidants* **2021**, *10*, 1171. https://doi.org/10.3390/antiox10081171

Academic Editors: Maria A. Livrea and Mario Allegra

Received: 2 July 2021
Accepted: 19 July 2021
Published: 23 July 2021

1. Introduction

Natural products have a significant role in modern drug development, especially as antitumor agents [1]. Since discovering that plant secondary metabolites have been elaborated for adaptive reasons [2] within living systems [3], they are often understood as exhibiting more drug-likeness and biological friendliness [4] than totally synthetic molecules [5]. Complex biomedical studies performed on isolated natural compounds and plant extracts aim to obtain high therapeutic activity to treat various diseases without unwanted effects [6]. Especially in oncological pathology, in vitro and in vivo studies have as their principal objective a selective cytotoxic action against tumor cells without affecting the normal ones [7].

In the big world of medicinal plants, lichens are symbiotic organisms [8] between a fungus and microalgae/cyanobacteria [9], known since ancient times for their biological effects [10]. As an important representative of this plant group, *Usnea barbata* (L) F.H. Wigg (*U. barbata*) is a fruticose thalli lichen with interesting therapeutic properties [11]; this species has been used for thousands of years in traditional medicine worldwide to treat various diseases [12]. The wide range of bio-activities (antioxidant [13], antimicrobial [14], anti-inflammatory [15], anticancer [16], cytotoxic [17], pro-oxidant [18]) is due to the content of active secondary metabolites [19] synthesized by the mycobiont (lichen-forming fungus) [20]. The phytochemical profile of *U. barbata* is already known. The metabolomics of this species belongs to different classes of chemical compounds: depsides (barbatic acid, methyl-8-hydroxy-4-*O*-demethylbarbatate, baeomycesic acid, 8-hydroxybarbatic acid), depsidones (connorstictic acid, fumarprotocetraric acid, hypoconstictic acid, lobaric acid), lipids (polyhydroxylated lipids), and dibenzofurans (usnic acid, placodiolic acid) [21]. Of all these lichen secondary metabolites, usnic acid [22] is by far the best known [23] and responsible for most bio-activities [24] of the *U. barbata* and, at the same time, of all lichens of the *Usnea* genus [25].

Usnic acid is an extensively studied lichen metabolite with controversial [26,27] results related to its benefits in relationship with the extraction method and the lichen species [28]. It was used to induce human weight loss [29], although unwanted hepatotoxic effects were also triggered [30]. In addition, UA highlights antimicrobial [31], insecticidal [32], anticholinergic [33], antioxidant [34], pro-oxidant [35], antigenotoxic [36], genotoxic [37], teratogenic [38], anti-inflammatory [39], analgesic and antipyretic [40], mutagenic and carcinogenic [41], anticancer [42], and cytotoxic [43] activities. Numerous researchers have shown the pharmacological actions of usnic acid and *Usnea* sp. extracts, especially cytotoxic activity, on different types of tumor cells [44].

The most important event resulting from the cytotoxic activity is cell death, which consists of morphological alterations [45]. Hence, the highly described mechanism in usnic acid and *Usnea* sp. anticancer activity is apoptosis [46]. This programmed cell death (PCD) is associated with DNA fragmentation and recognized by morphological characteristics as well as cytoplasmic condensation, nuclear pyknosis, chromatin condensation, cell rounding, membrane blebbing, and cytoskeletal collapse. In addition, membrane-bound apoptotic bodies are formed; macrophages rapidly digest them without activating the immune response [47]. In apoptosis, biochemical events through two distinct pathways (extrinsic and intrinsic) are correlated with these morphological changes [48]. Thus, the common extrinsic pathway (receptor-mediated) begins with receptor binding and activation of the initiator caspase-8. The following step is caspase-3 activation by caspase-8 or Bid-a B-cell lymphoma 2 (Bcl-2) pro-apoptotic protein-cleavage. Bid splitting brings mitochondrial cytochrome *c* leakage and apoptosomes formation. The intrinsic (mitochondrial) apoptotic pathway consists of cytochrome *c* release by Bcl-2 pro-apoptotic proteins action. Next, cytochrome *c* interacts with Apaf-1, dATP, and procaspase 9, generating apoptosomes. As a result, caspase-9 and -3 activation follows in both pathways. Moreover, various cell apoptosis can occur through common or specific biochemical processes [48,49]; for instance, a considerable diversity of molecular mechanisms involved in this PCD was highlighted in the different blood cells types. Thereby, nucleus-free platelets exhibit increasing mitochondrial functions in ATP synthesis, energy metabolism, cells survival and apoptosis activation [49]. Thereby, the major apoptotic pathway is the intrinsic one, with overexpression of Bcl-2 pro-apoptotic proteins, depolarization of the mitochondrial membrane potential, and cytochrome *c* release [50]. The extrinsic apoptotic pathway is initiated by tumor necrosis factor (TNF) death ligands binding to platelets surface TNF receptors. Finally, caspase-3 activation induces phosphatidylserine (PS) exposure and platelet microparticles (PMPs) formation, generating thrombotic phenomena [51].

Otherwise, mammalian erythrocytes (red blood cells, RBCs) have been considered unable to undergo apoptosis because they contain neither mitochondria nor nucleus. However, RBCs contain procaspase-3 and procaspase-8 levels comparable with those found in Jurkat cells [52]. They can express caspase-3 and caspase-8 [53], but they do not display other elements of the apoptotic machinery, such as Apaf-1, cytochrome *c*, and caspases-2, -6, -7 and -9 [54]. Klatt et al. (2018) reported that significant receptors belonging to the tumor necrosis factors (TNF) family (CD95 [55] and Fas [56]) signaling in RBCs are known to induce a particular type of programmed cell death, similar to the apoptotic death of nucleated cells named eryptosis [57], by caspase-3 activation, leading to cell shrinkage and cell membrane scrambling [58] with PS externalization [59]. The major trigger of eryptosis is the increase of cytosolic Ca^{2+} activity resulting from Ca^{2+} entry through Ca^{2+}-permeable unselective cation channels (permeable to both Na^{+} and Ca^{2+}) [60]. Instead, Ca^{2+} entry and Ca^{2+}-dependent RBCs membrane scrambling do not require caspases activation [61,62].

Leucocytes (white blood cells, WBCs) apoptosis displays morphological features like in other nucleated cells; however, this PCD involves distinct molecular mechanisms in various WBCs types. For instance, the extrinsic apoptosis pathway in monocytes is modulated by CD95, Fas, and TNF-cell surface apoptosis-triggering receptors (TRAIL-R1 and TRAIL-R2); it recruits cytoplasmic adaptor proteins, forming a death-inducing signaling complex (DISC) [63]. Moreover, various apoptotic agents (including commonly used chemotherapeutic drugs) induce the release of cytochrome *c* and the second mitochondria-derived activator of caspase/direct inhibitor of apoptosis-binding protein (Smac/DIABLO) in the intrinsic pathway; both proteins determine caspase-3 activation [63] in this WBCs type.

Therefore, we aim to explore cell death mechanisms in our study, analyzing the cytotoxic effects of usnic acid and *U. barbata* extracts. Usnic acid can be obtained by organic synthesis, but it can be isolated from various lichens extracts [64]. A previous report has described UA extraction from *U. barbata* acetone extract [65]; however, this present study proposes to show usnic acid isolation from UBEA. Because relatively few studies are focused exclusively on proving their effects on normal cells [66], the cytotoxicity of isolated UA and *U. barbata* dry extracts (UBA and UBE) on human blood cells cultures was evaluated in our work. Consequently, our study aims to investigate cell death mechanisms, analyzing cellular apoptosis, caspase 3/7 activity, nuclear shrinkage, lysosomal activity, ROS levels, cell cycle, and DNA synthesis by flow cytometry techniques. Finally, we suggest a relationship overview between UA, UBA, UBE concentrations, and cytotoxic activity on human blood cells cultures.

2. Materials and Methods

2.1. Lichen Samples and Usnic Acid Isolation

U. barbata was harvested from the Călimani Mountains (900 m altitude, Suceava County, Romania). Three dry extracts were obtained in different solvents: ethyl acetate (Chemical Company S.A., Iasi, Romania), acetone and ethanol (Chimreactiv SRL Bucharest, Romania) using a method described in detail in our previous study [13]. The dry extract in ethyl acetate was used only for usnic acid isolation. Further, in vitro studies were performed with isolated UA, UBA and UBE dissolved in 1% dimethyl sulfoxide (DMSO). Therefore, we prepared sample solutions with different concentrations: UA of 25, 50, 75, 125 μg/mL and both UBA and UBE of 75, 125, 250, 500 μg/mL.

2.1.1. Usnic Acid Isolation by Semi-Preparative Chromatography

This process consists of usnic acid extraction by ultra-high performance liquid chromatography (UHPLC) with photodiode array detector (PDA), followed by collecting the separated fraction. A semi-preparative technique was adapted by our UHPLC analytical method previously validated [13]. The PerkinElmer® Flexar® FX-15 UHPLC system was equipped with a Flexar FX PDA-Plus photodiode array detector (PerkinElmer®Waltham, MA, USA) and a Cosmosil 5-C18-AR-2 chromatographic column with a length of 150 mm and an inner diameter of 20 mm (producer: Nacalai Tesque, Kyoto, Japan); in addition, a Gilson FC 203B fraction collector (Gilson Co, Middleton, WI, USA) was used. More detailed data can be found in the supplementary material. Working conditions consisted of flow rate = 10 mL/min, column compartment temperature = 25 °C, injection volume = 400 µL, analysis time = 18 min. The mobile phase was an isocratic system of methanol/water/glacial acetic acid (80:15:5); the detection was performed at 282 nm and 254 nm. The samples were prepared at 3 mg/mL (282 nm), and 8 mg/mL (254 nm). The retention time of the usnic acid is reported around 13 min, at a flow rate of 10 mL/min.

The usnic acid peak was collected manually between 12.5 and 13.5 min (on approximately 15% of its height, preserving the peak purity) after four successive injections (4 × 400 µL 8 mg/mL UBEA in DMSO) at 254 nm. Its identity was confirmed by comparing the retention time of the most significant peak of the sample solution with the reference one [13]. Furthermore, the solution was collected in a previously weighed vial (supplementary material, video sequence S1). The solvent was evaporated under a nitrogen stream and the vial was placed in an oven for 30 min at 105 °C. After cooling in a desiccator to remove the last solvent traces, a yellow solid matter was obtained. Finally, the isolated usnic acid amount was calculated by subtracting the empty vial mass from the whole mass. The isolated UA was dissolved in 1% DMSO (Sigma-Aldrich Chemie GmbH, Taufkirchen, Germany) and used for in vitro analyses.

2.1.2. Determination of the Purity of Isolated Usnic Acid

The purity of previously isolated UA was determined using the UHPLC-PDA analytical method [13]. First, the sample resulting from drying was weighed and brought to a final concentration of 160 µg/mL. Then, three standard usnic acid solutions were prepared simultaneously (160 µg/mL). Finally, all solutions were injected in the same sequence. The purity was calculated according to the following formula:

$$\mathrm{Ps\%} = \mathrm{As}/\mathrm{Astd} \times \mathrm{Cstd}/\mathrm{Cs} \times 100,$$

$$\mathrm{Cstd} = \mathrm{Mstd}/\mathrm{d} \times \mathrm{Pstd\%} \times 1000,$$

$$\mathrm{Cs} = \mathrm{Ms}/\mathrm{d} \times 1000,$$

where, Ps% = sample purity %, As = area of the sample, Astd = area of the standard solution, Cstd = standard solution concentration (µg/mL); Cs = sample solution concentration of the sample solution (µg/mL), Mstd = standard mass weighed (mg), d = dilution, P% std = standard purity %, Ms = sample weighed mass (mg). The previously isolated usnic acid was diluted with DMSO to a 160 µg/mL concentration. Then, this sample solution was injected into the chromatographic system according to the method described in our previous study [13]. The analyzed sequence was represented by the sample solution in DMSO, and three standard solutions of 160 µg/mL (usnic acid in DMSO) considering the average aria. Next, the precision of the area expressed in % relative standard deviation (RSD) was determined. Following the calculation, the purity value (concerning an external standard) and an RSD value = 0.66% was obtained. Finally, the identity of isolated usnic acid was certified by the retention time [13] (supplementary material).

2.2. *In Vitro Analysis of the Biological Effects of UA, UBA, and UBE on Human Blood Cells*

2.2.1. Human Blood Cell Cultures

Blood samples from non-smoker healthy donor (B Rh+ blood type) were collected into heparin tubes and used throughout the experiment. The heparinized blood (1.0 mL) in 6.0 mL of Dulbecco's phosphate buffered saline with $MgCl_2$ and $CaCl_2$ medium (Sigma-Aldrich Chemie GmbH, Taufkirchen, Germany) supplemented with 10% bovine fetal serum (Sigma-Aldrich, Chemie GmbH, Taufkirchen, Germany), 1% L-glutamine (Merck, KGaA, Darmstadt, Germany), and antibiotics mix solution (100 µL/mL, 10,000 U penicillin, 10 mg streptomycin, 25 µg amphotericin B per 1 mL, Sigma-Aldrich, Chemie GmbH, Taufkirchen, Germany) added in 6 wells untreated Nuncleon plates were incubated in a 37 °C incubator with 5% CO_2. After 72 h of incubation, blood cell cultures were treated with UA, UBA and UBE dissolved in 1% DMSO. Human blood samples were treated with final concentrations of 25, 50, 75, and 125 µg/mL of UA. Higher concentrations (75, 125, 250, and 500 µg/mL) of both UBA and UBE were used to treat the human blood cell cultures. In addition, the blood cells were treated with 1% DMSO as the negative control (solvent control).

2.2.2. Reagents and Equipment

Our study analyses used the flow cytometer (Attune, Acoustic focusing cytometer, Applied Biosystems, part of Life Technologies, Bedford, MA, USA). Before blood cells analysis, the flow cytometer was first set by using fluorescent beads (Attune performance tracking beads, labelling and detection, Life Technologies, Europe BV, Bleiswijk, Netherlands), with standard size (four intensity levels of beads population), and the quantity was established by enumerating cells below 1 µm [67]; 10,000 cells per sample for each analysis were gated by Forward Scatter (FSC) and Side Scatter (SSC). Flow cytometry data were collected using Attune Cytometric Software v.1.2.5, Applied Biosystems, 2010.

Annexin V-FITC/PI (Bender MedSystems GmbH, Vienna, Austria) was used to observe the apoptotic cells. Activating caspases 3/7 enzymes that determine a series of reactions triggered in response to proapoptotic signals were observed with Red Magic Methodology (MR-DEVD, Caspase-3/7 Assay Kit, Abcam, Shanghai, China). Nuclear apoptosis and lysosomal activity, dual stain with Hoechst 33,342 and acridine orange from MR-DEVD, Caspase-3/7 Assay Kit were analyzed. Total ROS level evaluation was performed using ROS Assay Kit 520 nm (Life Technologies Europe BV, Bleiswijk, The Netherlands). Propidium iodide (PI) (1.0 mg/mL, Sigma-Aldrich, Chemie GmbH, Taufkirchen, Germany) and RNase A (4 mg/mL, Promega, Madison, USA) were used in cell cycle analysis. Cell proliferation assay was performed using EdU proliferation kit, iFluor 488 (Abcam, Shanghai, China). Negative control was 1% DMSO (PanBiotech, Aidenbach, Germany).

2.2.3. Apoptosis Assay

After 24 h incubation, the treated blood cells with each tested solution reported to the negative control were double-stained with Annexin V-FITC/PI. Next, blood cells were incubated in flow cytometry tubes with 2 µL Annexin V-FITC and 2 µL PI (20 µg/mL) for 30 min, at room temperature, in darkness. After incubation, 1 mL of flow cytometry staining buffer (FCB) (eBioscience^{TM}, Life Technologies Europe BV, Bleiswijk, The Netherlands) was added. Viable cells, early apoptotic cells, late apoptotic cells, and necrotic cells were examined at flow cytometer, using a 488 nm excitation, green emission for Annexin V-FITC (BL1 channel), and orange emission for PI (BL2 channel).

2.2.4. Caspase 3/7 Assay

After 24 h incubation, 300 µL of blood cell culture was transferred to flow cytometry tubes, 20 µL of MR-DEVD solution was added and mixed with the cells. Next, 20 µL of PI was added. After incubation, was added 1 mL FCB. The early stages of cell apoptosis by activating caspase 3/7 were analyzed by flow cytometry, using a 488 nm excitation, red emission for MR-DVD (BL3 channel), and orange emission for PI (BL2 channel).2.2.5. Nuclear Condensation and Lysosomal Activity Assay

After 24 h of treatment with the tested solutions, 300 µL of blood cell culture was introduced in flow cytometry tubes, 2 µL of Hoechst 33,342 stain was added, and blood cells were mixed well. After this process, 50 µL of acridine orange (AO) 1.0 µM was added, and the cells were incubated 30 min at room temperature into darkness. After incubation, 1 mL FCB was added; the cells were examined at flow cytometer. UV excitation and blue emission for Hoechst 33,342 (VL2) at 488 nm, and green emission acridine orange (BL1 channel) were used for examination.

2.2.5. Total ROS Activity Assay

After 24 h treatments with the tested solutions, 100 µL of ROS Assay Stain solution was added for each 1 mL of blood cell culture in flow cytometry tubes and mixed well. Next, the cells were incubated for 60 min at 37 °C, in an incubator with 5% CO_2. After incubation, the blood cells were analyzed by flow cytometry, using a 488 nm excitation and green emission for ROS (BL1 channel).

2.2.6. Cell Cycle Analysis

Blood cells were treated with UA (25–125 µg/mL), UBA and UBE (75–500 µg/mL) and incubated for 24 h; 1 mL of each cell culture was washed in FCB, introduced in flow cytometry tubes, and fixed with 50 µL ethanol for 10 min. After this process, the cells were treated with PI (20 µg/mL) and RNase A (30 µg/mL) and incubated for 30 min at room temperature, into darkness. After this time, 1 mL FCB was added, and the cell cycle distribution was detected at flow cytometer, using a 488 nm excitation and orange emission for PI (BL2 channel).

2.2.7. Cell Proliferation Assay

After 24 h of treatment, 1 mL of blood cell culture was incubated with 50 µM EdU (500 µL), at 37 °C, for 2 h. Then, the cells were fixed (100 µL of 4% paraformaldehyde in PBS) and permeabilized (100 µL of Triton X-100 1×). After washing in 3% BSA in flow cytometry (2 mL) and centrifuging at 300× *g* for 5 min, at 4 °C, the blood cells were incubated with a reaction mix (500 µL), 30 min at room temperature, into darkness. After washing in permeabilization buffer (2 mL) and centrifuging (300× *g*, 5 min, at 4 °C), 1 mL FCB was added. Finally, the blood cells were examined by flow cytometry, using a 488 nm excitation and green emission for EdU-iFluor 488 (BL1).

2.2.8. Statistical Analysis

All analyses were performed in triplicate, and the obtained results were presented as means values ± standard deviation (SD). Our results are presented as percent (%) of cell and nuclear apoptosis, caspase 3/7 activity, autophagy, cell cycle, DNA synthesis, and count ($\times 10^4$) of oxidative cellular stress after flow cytometry analyses were performed with SPSS v. 23 software, IBM, 2015. The Levene test was analyzed for homogeneity of variances of samples, while paired *t*-test, ANOVA [68], was used to establish the differences between samples and controls, and $p < 0.05$ was considered statistically significant. Figures 2, 4, 6, 7, 9, 11 and 13 were made with Attune Cytometric Software v.1.2.5, Applied Biosystems, 2010 (Bedford, MA, USA). Figures 3, 5, 8, 10, 12 and 14 were made by the v. 14.8.1, 2014 of MedCalc program (Ostend, Belgium).

3. Results

3.1. Usnea Barbata Dry Extracts and Usnic Acid Isolation

The obtained chromatograms in both UHPLC determinations from Sections 2.1.1 and 2.1.2 are presented in Figure 1. From 12.8 mg UBEA, 3.6 mg of isolated usnic acid (Figure 1d) with 89.36% purity was obtained. The yield of this process was 28.15%.

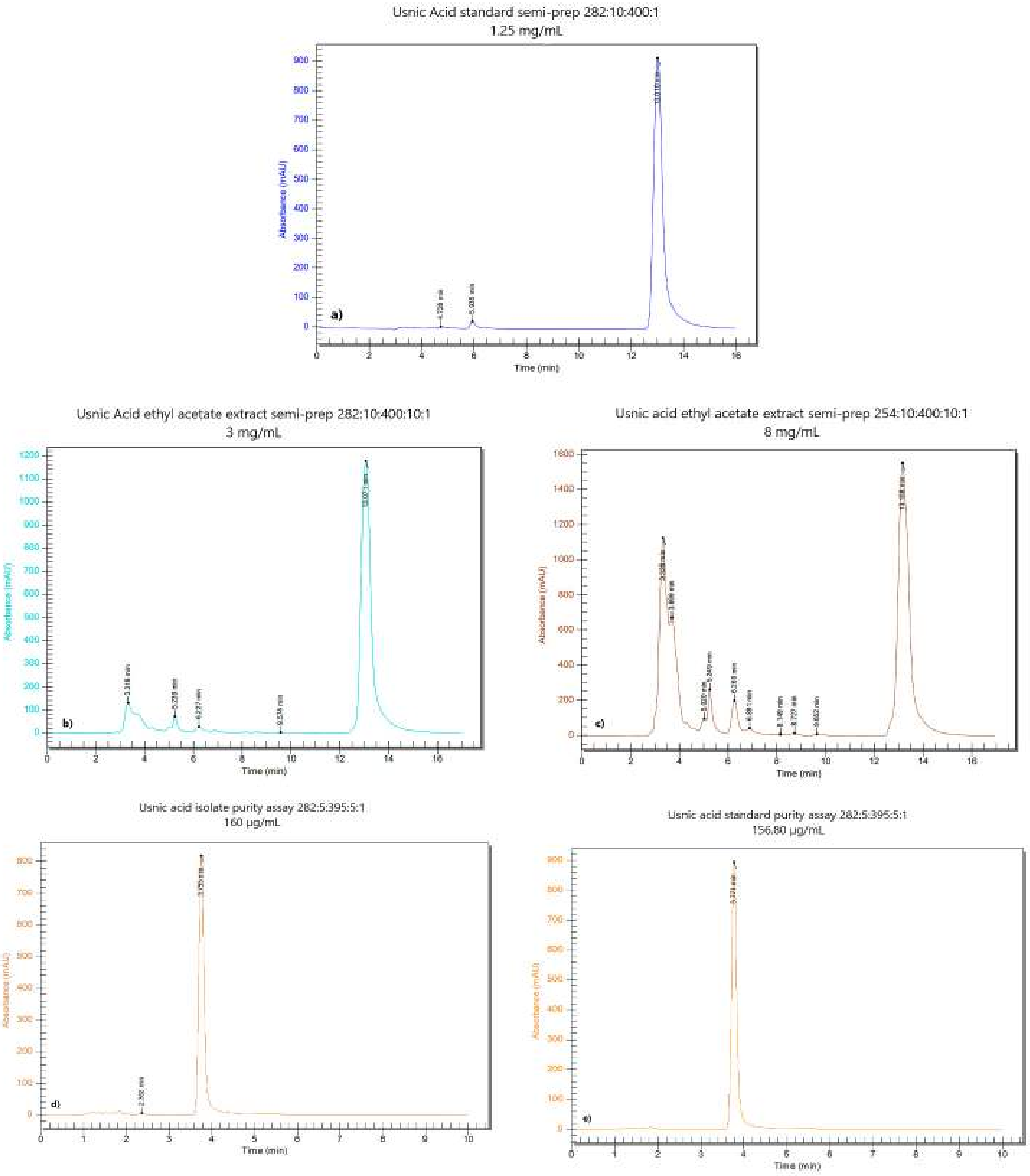

Figure 1. The chromatograms of usnic acid and sample solution for usnic acid separation; (**a**–**c**) chromatograms of usnic acid from semi-preparative chromatography, at the same flow rate (10 mL/min) and different wavelengths and concentrations: (**a**) usnic acid standard at 282 nm and 1.25 mg/mL; (**b**) usnic acid in UBEA at 282 nm and 3 mg/mL; (**c**) usnic acid in UBEA at 254 nm and 8 mg/mL; (**d**,**e**) chromatograms obtained at 282 nm from purity determination of isolated usnic acid: (**d**) sample solution (usnic acid isolate) (**e**) usnic acid standard solution.

3.2. *In Vitro Analysis of the Biological Effects of UA, UBA, and UBE on Human Blood Cells*

3.2.1. Cell Apoptosis Assay

Cell apoptosis induced by UA, UBA, and UBE treatments was determined based on morphology and cell membrane integrity in blood cell cultures. The obtained results are illustrated in Figure 2A–C and Figure 3a–c (V-cell viability, EA-early apoptosis, LA-late apoptosis, N-necrosis).

The influence of UA (25, 50, 75, 125 µg/mL) on blood cells viability and apoptosis is presented in Figure 2A(b–e) and Figure 3a.

It can be noted that the viability of blood cells treated with 25 µg/mL of UA (Figure 2A(a,b)) insignificantly decreased in comparison with the solvent control: 96.45 ± 0.27% vs. 96.89 ± 0.14% ($p \geq 0.05$, Figure 3a). On the other hand, a concentration of 50 µg/mL of UA on blood cell cultures (Figure 2A(a,c)) determined reduced cell viability reported to 1% DMSO: 95.75 ± 0.63% vs. 96.89 ±0.14% ($p < 0.05$, Figure 3a).

Likewise, these low concentrations of UA (25 and 50 µg/mL) induce insignificant differences of early apoptosis (Figure 2A(a–c)) collated to control: 3.12 ± 0.26%; 3.69 ± 0.71% vs. 2.72 ± 0.16% ($p \geq 0.05$, Figure 3a).

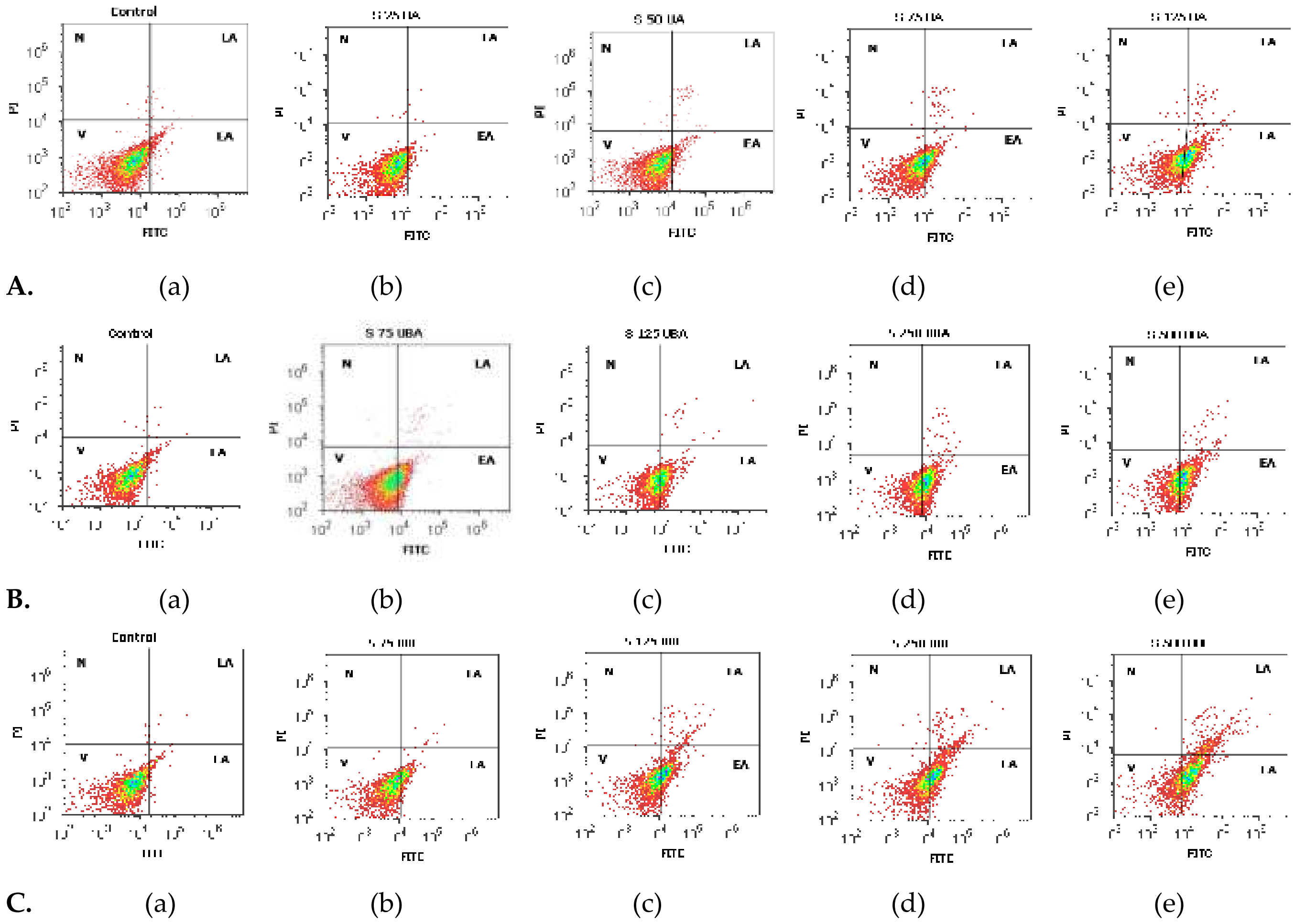

Figure 2. Cell apoptosis models of usnic acid (UA), *U. barbata* acetone (UBA), and *U. barbata* ethanol (UBE) treatments in normal blood cell cultures. Annexin V-FITC/PI patterns of 1% dimethyl sulfoxide (DMSO) Negative Control (**A**(**a**), **B**(**a**), **C**(**a**)); **A**(**b**–**e**) UA 25, 50, 75, 125 µg/mL; **B**(**b**–**e**) UBA 75, 125, 250, 500 µg/mL; and **C**(**b**–**e**) UBE 75, 125, 250, 500 µg/mL.

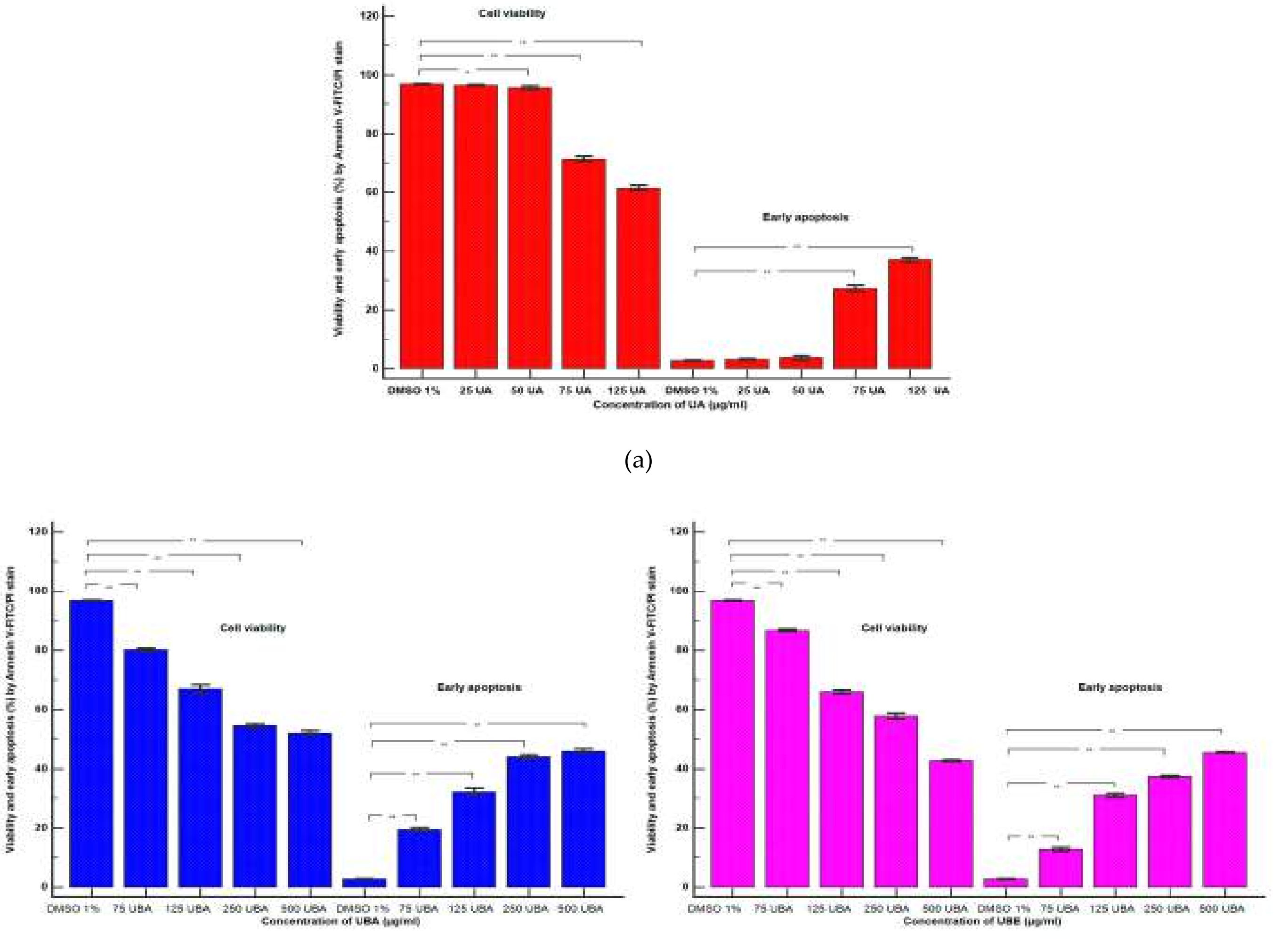

(a)

(b) (c)

Figure 3. Statistical analysis of cell apoptosis: (**a**) UA; (**b**) UBA; (**c**) UBE. * $p < 0.05$ and ** $p \leq 0.001$ represent significant statistical differences between control and samples made by paired samples *t*-test.

Moreover, higher concentrations of UA (75 and 125 µg/mL) significantly influenced both parameters (Figure 2A(a,d,e)). They induced an evident decline of cell viability (71.34 ± 0.90%; 61.43 ± 0.88% vs. 96.89 ±0.14%, $p < 0.001$), and an augmentation of early apoptosis (27.27 ± 1.00%; 37.04 ± 0.66% vs. 2.72 ± 0.16%, $p < 0.001$, Figure 3a).

UBA activity (75, 125, 250, 500 µg/mL) on blood cells viability and apoptosis compared with 1% DMSO is shown in Figure 2B(a–e) and Figure 3b.

The obtained data revealed that 75 µg/mL of UBA (Figure 2B(a,b)) determined a diminution in cell viability: 80.16 ± 0.57% vs. 96.89 ± 0.14%, ($p < 0.001$); also, it induced an increase of cell apoptosis: 19.45 ± 0.60% vs. 2.72 ± 0.16% ($p < 0.001$, Figure 3b).

Higher concentrations of UBA (125, 250, and 500 µg/mL) remarkably reduced blood cells viability, triggering apoptosis (Figure 2B(c–e)). Hence, previously mentioned concentrations of UBA had a significant cytotoxic effect on blood cells, with diminishing viability compared with solvent control: 66.93 ± 1.37%; 54.57 ± 0.65%; 52.15 ± 0.81%; vs. 96.89 ± 0.14% ($p < 0.001$, Figure 3b). Moreover, these results indicated high rise of early apoptosis: 32.18 ± 1.22%; 43.99 ± 0.66%; 45.98 ± 0.78% vs. 2.72 ± 0.16% ($p < 0.001$, Figure 3b).

The flow cytometry results regarding UBE effects on the apoptosis process are indicated in Figure 2C(b–e) and Figure 3c.

It can be seen that 75 µg/mL of UBE (Figure 2C(a,b)) determined a diminution of blood cell viability reported to 1% DMSO: 86.66 ± 0.45% vs. 96.89 ± 0.14%, $p < 0.001$; therefore, it raised their apoptosis: 12.81 ± 0.66% vs. 2.72 ± 0.16% ($p < 0.001$, Figure 3c).

In addition, higher concentrations of UBE (125, 250, and 500 µg/mL) had a considerable cytotoxic effect on blood cells (Figure 2C(a,c–e)); viability has substantial reduced values, compared with the solvent control: 65.96 ± 0.68%; 57.91 ± 0.96%; 42.65 ± 0.32% vs. 96.89 ± 0.14% ($p < 0.001$, Figure 3c). In addition, our results indicate that UBE at the same concentrations promoted significantly augmented levels of early apoptosis reported to 1% DMSO: 30.19 ± 0.77%; 30.99 ± 0.77%; 45.52 ± 0.18% vs. 2.72 ± 0.16% ($p < 0.001$, Figure 3c).

Finally, Figure 2 indicates that insignificant late apoptosis and necrosis phenomena occurred in blood cell cultures after 24 h treatment.

3.2.2. Caspase 3/7 Activity Assay

The apoptotic effects of UA, UBA, and UBE evaluated by measuring the caspase-3/7 activity compared with 1% DMSO, were registered in Figure 4A–C and Figure 5a–c.

We noted that the minimum concentration of UA (25 µg/mL) induces a low increase of cell apoptosis (Figure 4A(a,b)) reported to control (3.75 ± 0.36% vs. 1.38 ± 0.03%, $p < 0.01$, Figure 5a). Forwards, a remarkable increase of caspase-3/7 activation was registered on blood cell cultures treated with 50, 75, and 125 µg/mL of UA (Figure 4A(a,c–e)) in comparison with 1% DMSO: 6.81 ± 0.43%; 29.49 ± 1.96%; 44.74 ± 0.41% vs. 1.38 ± 0.03% ($p < 0.001$, Figure 5a).

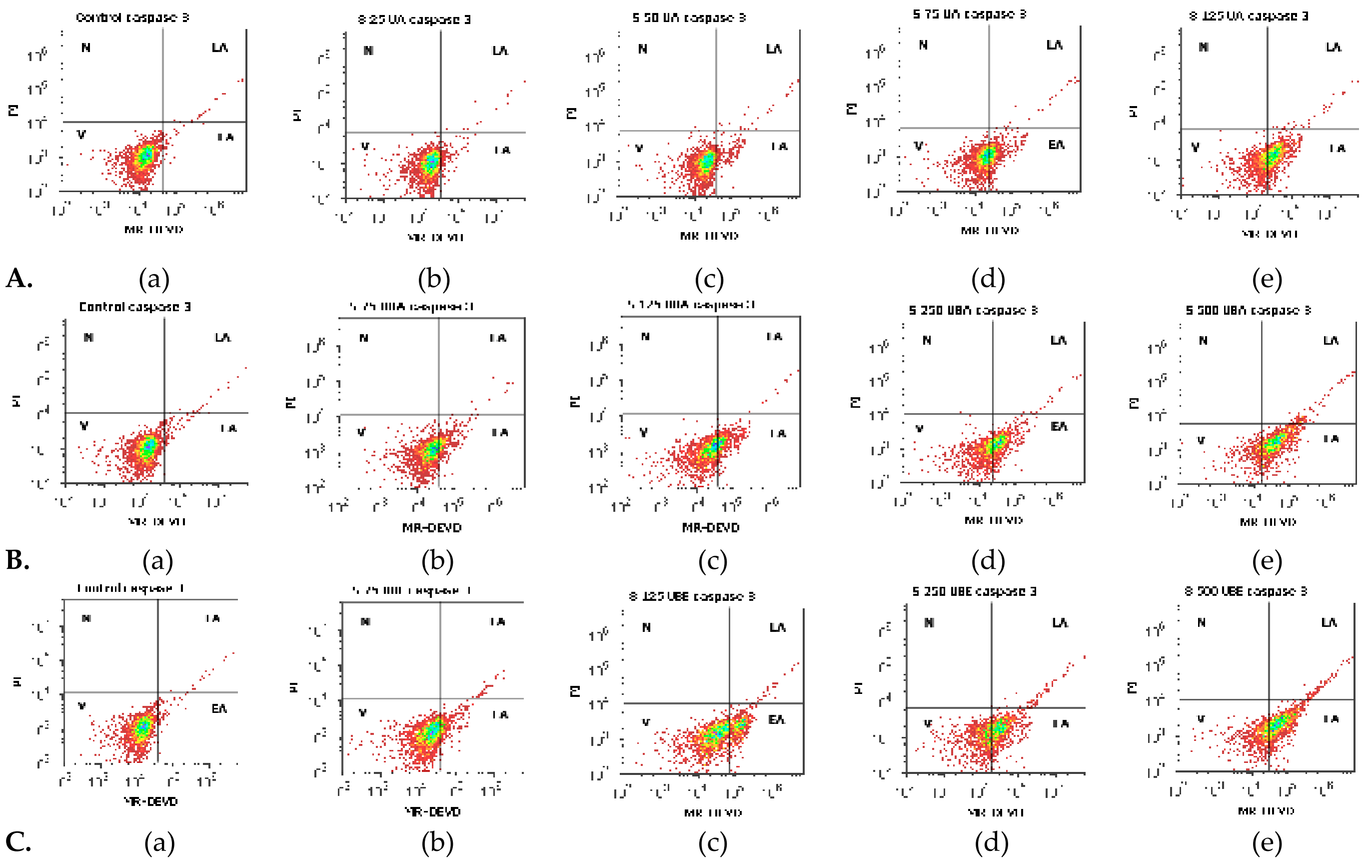

(a) (b) (c) (d) (e)

Figure 4. Caspase 3/7 activity status of UA, UBA, and UBE treatments in normal blood cell cultures. MR-DEVD/PI patterns of 1% DMSO as Negative Control (**A**(**a**), **B**(**a**), **C**(**a**)); **A**(**b**–**e**) UA 25, 50, 75, 125 µg/mL; **B**(**b**–**e**) UBA 75, 125, 250, 500 µg/mL; **C**(**b**–**e**) UBE 75, 125, 250, 500 µg/mL.

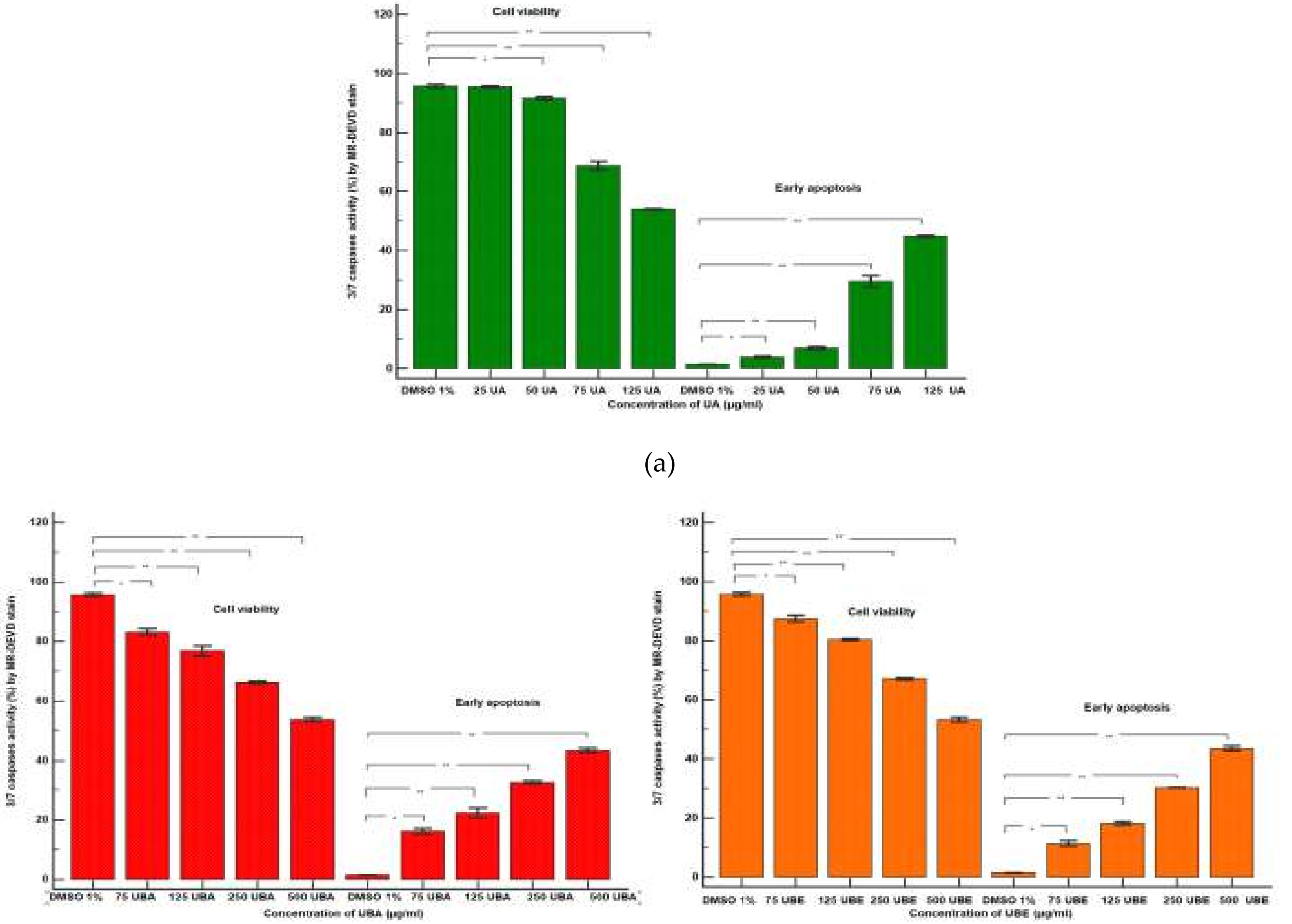

(a)

(b) (c)

Figure 5. Statistical analysis of caspase 3/7 activity: (**a**) UA; (**b**) UBA; (**c**) UBE. * $p < 0.01$ and ** $p < 0.001$ represent significant statistical differences between the control and samples made by paired samples *t*-test.

Remarkably, the lowest UBA concentration (75 µg/mL, Figure 4B(a,b)) induces mild apoptosis in blood cells cultures: 16.16 ± 0.93% vs. 1.38 ± 0.03% ($p < 0.01$, Figure 5b). Furthermore, we aimed to confirm that 125, 250, and 500 µg/mL of UBA produce significant blood cells apoptosis (Figure 4B(c–e)). Consequently, we evaluated the intracellular activity of effector caspase 3/7, and we observed that the biochemical cascade of reactions implied into pro-apoptotic signal has considerably increased more than 1% DMSO: 22.35 ± 1.58%; 32.53 ± 0.57%; 43.57 ± 0.73% vs. 1.38 ± 0.03%, ($p < 0.001$, Figure 5b).

Similarly, 75 µg/mL of UBE (Figure 4C(a,b)) induced a low apoptosis in blood cells cultures: 11.25 ± 0.96% vs. 1.38 ± 0.03% ($p < 0.01$, Figure 5c). Higher UBE concentrations (125, 250, and 500 µg/mL) triggered proapoptotic signal with considerable increased values (Figure 4C(a,c–e)) compared with solvent control: 18.15 ± 0.52%; 30.18 ± 0.09%; 43.54 ± 0.72% vs. 1.38 ± 0.03% ($p < 0.001$, Figure 5c).

Our results indicate a similar trend to the previous assay in UA, UBA, and UBE activity on blood cell cultures (Figure 2). The effect on caspase 3/7 activity is directly proportional with the sample concentration, which registers significantly increased levels at high doses, and decreases in the order of: usnic acid, *U. barbata* dry extract in acetone, and ethanol (Figures 4 and 5).

3.2.3. Nuclear Condensation and Lysosomal Activity Assay

Apoptosis is the mode of cell death that includes pyknosis; in this assay, pyknotic nuclei were stained with Hoechst 33,342 on blood cell cultures. Another aimed objective was an evaluation of lysosomal activity directly related to autophagy.

Therefore, blood cells were also colored with acridine orange (AO). The obtained results were synthesized in Figures 6 and 7.

The lowest concentration of UA (25 μg/mL, Figure 6A(a,b)) induced an insignificant increase of nuclear condensation: 1.36 ± 0.20% vs. 1.03 ± 0.03% ($p \geq 0.05$, Figure 8a) and a mild increase of lysosomal activity (Figure 7A(a,b)) reported to solvent control: 6.59 ± 0.33% vs. 1.04 ± 0.04% ($p \leq 0.01$, Figure 8a).

The higher concentrations of UA (50, 75, and 125 μg/mL, Figure 6A(a,c–e)) continued to have directly proportional effects on nuclear shrinkage: 1.49 ± 0.02%; 3.00 ± 0.10%; 3.19 ± 0.30% vs. 1.03 ± 0.03% ($p \leq 0.01$; $p < 0.001$, Figure 8a). In addition, the same UA concentrations (Figure 7A(a,c–e)) induced a substantial increase of the autophagy levels compared with 1% DMSO: 12.97 ± 1.55%; 21.72 ± 0.38%; 27.05 ± 1.52% vs. 1.04 ± 0.04% ($p \leq 0.01$; $p < 0.001$, Figure 8a).

Nuclear shrinkage and autophagy were concomitantly examined to evaluate the mechanism of UBA cytotoxicity on blood cells cultures. Thereby, it can be noted that 75 μg/mL of UBA had minimal effects on both processes (Figure 6B(a,b) and Figure 7B(a,b)) compared with 1% DMSO: nuclear condensation 1.41 ± 0.09% vs. 1.03 ± 0.03%, ($p < 0.05$, Figure 8b), and autophagy 4.64 ± 0.38% vs. 1.04 ± 0.04% ($p \leq 0.01$, Figure 8b).

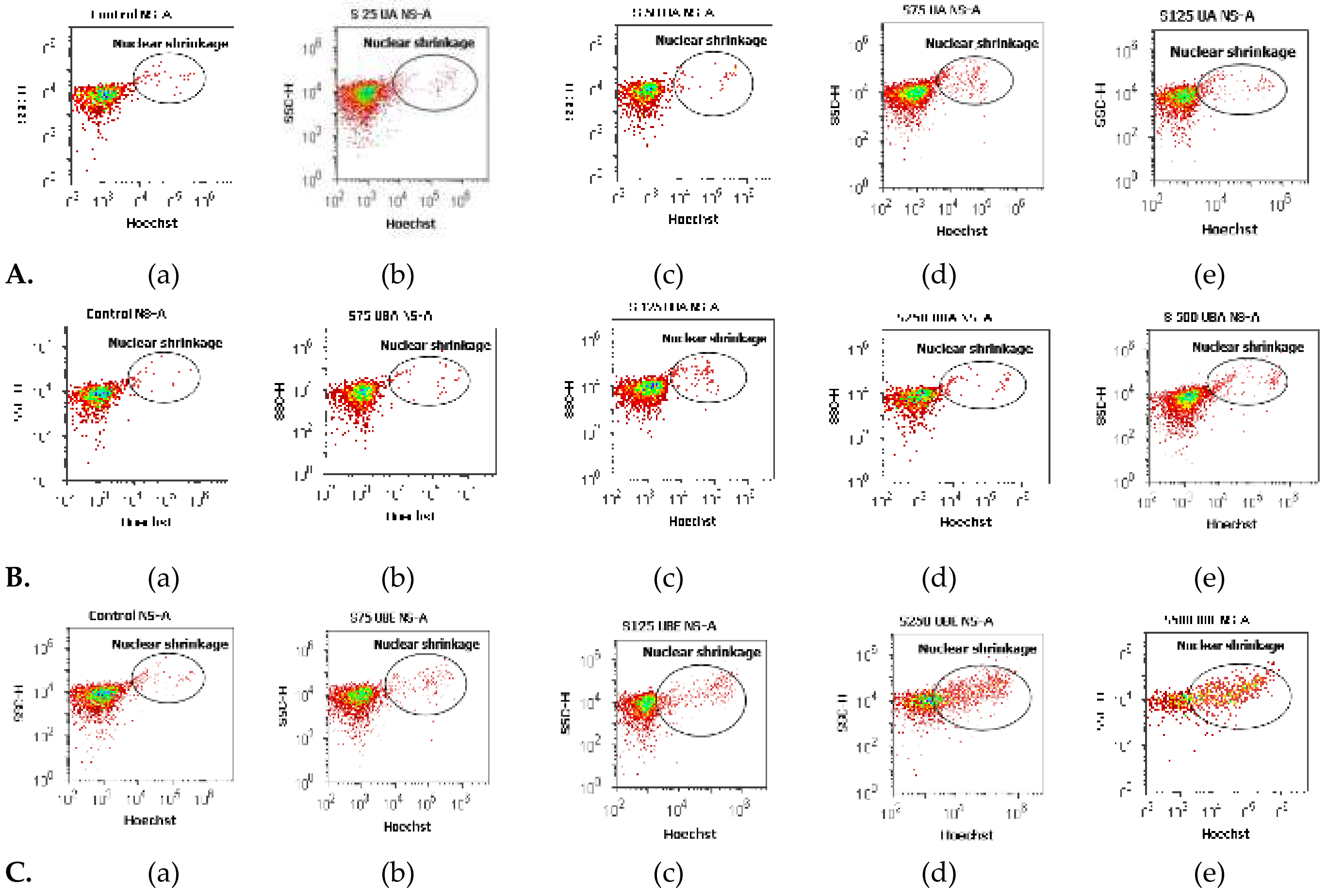

Figure 6. Nuclear shrinkage status of UA, UBA, and UBE treatments in normal blood cell cultures. Hoechst patterns of UA 25, 50, 75, 125 μg/mL **A**(**b**–**e**); **B**(**b**–**e**) UBA 75, 125, 250, 500 μg/mL; **C**(**b**–**e**) UBE 75, 125, 250, 500 μg/mL reported to 1% DMSO (**A**(**a**), **B**(**a**), **C**(**a**)).

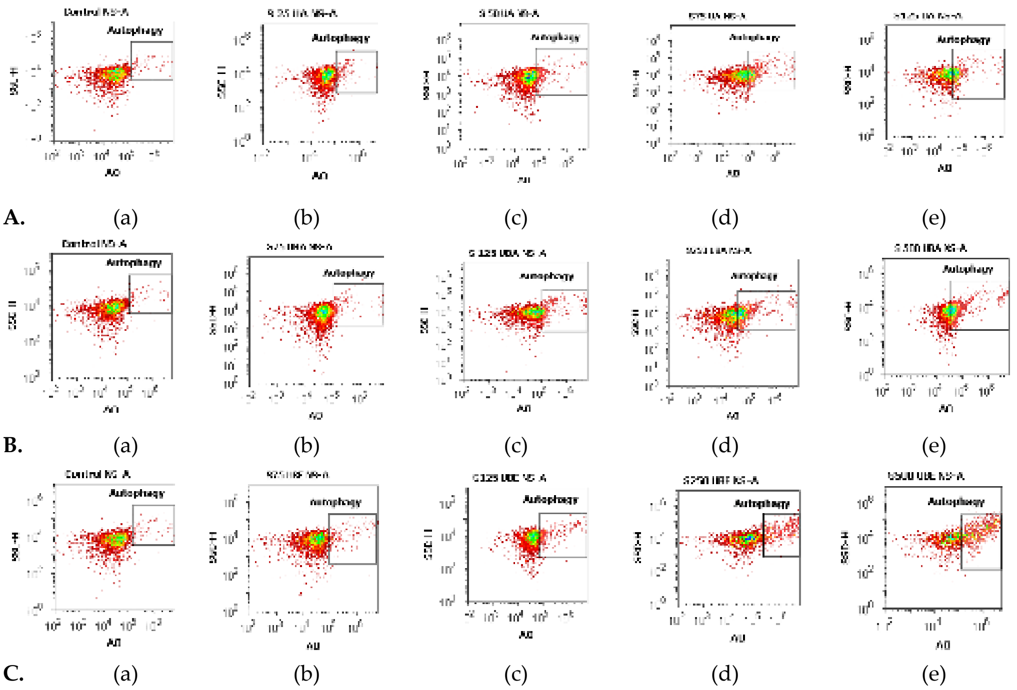

Figure 7. Autophagy status of UBA, UBA, and UBE treatments in normal blood cell cultures. Acridine orange patterns of UA 25, 50, 75, 125 μg/mL **A**(**b**–**e**); **B**(**b**–**e**) UBA 75, 125, 250, 500 μg/mL; **C**(**b**–**e**) UBE 75, 125, 250, 500 μg/mL reported to 1% DMSO (**A**(**a**), **B**(**a**), **C**(**a**)).

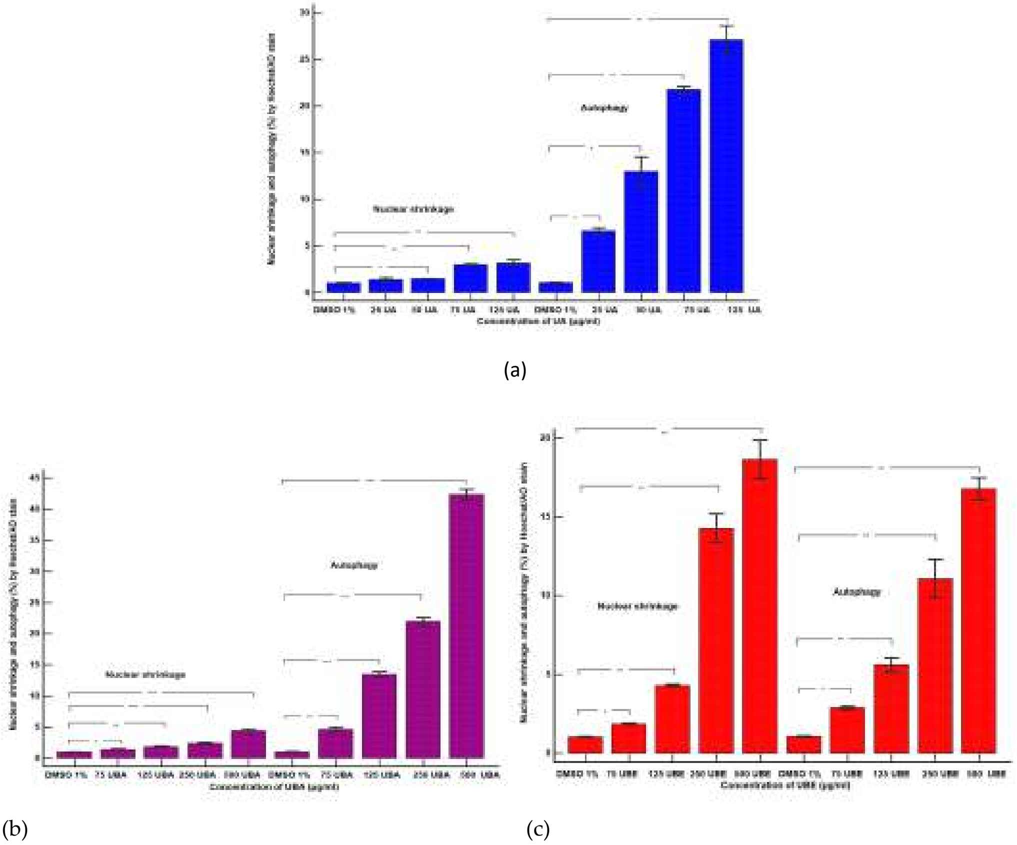

(a)

(b)

(c)

Figure 8. Statistical analysis of nuclear shrinkage and autophagy: (**a**) UA; (**b**) UBA; (**c**) UBE. * $p < 0.05$. ** $p \leq 0.01$, and *** $p < 0.001$ represent significant statistical differences between the control and samples made by paired samples *t*-test.

On nuclear condensation, the following concentrations of UBA: 125, 250, and 500 µg/mL (Figure 6B(a,c–e)) continued to show mild effects reported to control: 1.85 ± 0.10%; 2.36 ± 0.16%; 4.41 ± 0.32% vs. 1.03 ± 0.03% ($p < 0.01$, $p \leq 0.001$, Figure 8b). In addition, previously mentioned concentrations of UBA (Figure 7B(a,c–e)) significantly increased autophagy: 13.49 ± 0.45%; 21.99 ± 0.57%; 42.32 ± 0.85% vs. 1.04 ± 0.04% ($p \leq 0.001$, Figure 8b).

Finally, 75 µg/mL UBE (Figure 6C(a,b)) showed a similar effect on nuclear contraction with UBA (Figure 7B(a,b)) at the same concentration as the solvent control: 1.85 ± 0.03% vs. 1.03 ± 0.03% ($p \leq 0.01$, Figure 8c).

However, this effect considerably increases at the following UBE higher concentrations (125, 250 and 500 µg/mL, Figure 6C(a,c–e)) reported to control: 4.29 ± 0.06%; 14.27 ± 0.93%; 18.64 ± 1.22% vs. 1.03 ± 0.03% ($p \leq 0.001$, Figure 8c)

Besides, UBE acted slowly, inducing a moderate increase of the lysosomal activity (Figure 7C(a–e)) from 75 µg/mL to 500 µg/mL reported to 1% DMSO: 2.87 ± 0.09%; 5.59 ± 0.44%; 11.08 ± 1.21%; 16.77 ± 0.69% vs. 1.04 ± 0.04% ($p \leq 0.01$, $p \leq 0.001$, Figure 8c).

3.2.4. Total ROS Activity Assay

The ranges 25–125 µg/mL UA and 75–500 µg/mL UBA and UBE were selected to evaluate oxidative stress in blood cells by ROS level determination.

As shown in Figure 9A–C(a–e), except for 1% DMSO, all samples (UA, UBA, and UBE) induced ROS generation, highlighted by the moving of the peaks to the right of the graph. Hence, the lowest concentration of UA (25 µg/mL) slowly stimulated ROS production (Figure 9A(a,b)) reported to 1% DMSO: $34.33 \times 10^4 \pm 4.04$ vs. $10.40 \times 10^4 \pm 1.00$ ($p < 0.01$, Figure 10a). A remarkable increase in ROS levels was observed in blood cells treated with 50, 75, and 125 µg/mL of UA (Figure 9A(a,c–e)) compared with the negative control: $56.33 \times 10^4 \pm 1.52$; $80.33 \times 10^4 \pm 0.57$; $84.67 \times 10^4 \pm 0.57$ vs. $10.40 \times 10^4 \pm 1.00$ ($p < 0.001$, Figure 10a).

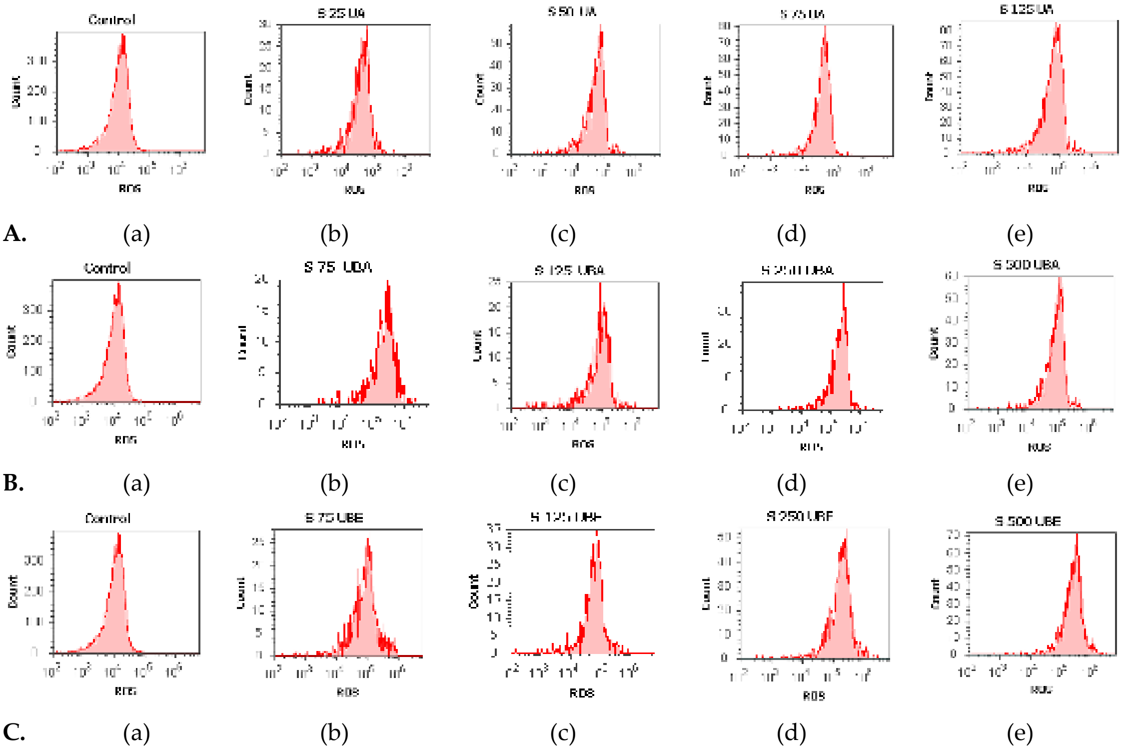

Figure 9. Reactive oxygen species (ROS) status of UA, UBA, and UBE treatments in normal blood cell cultures. ROS patterns of UA 25, 50, 75, 125 µg/mL **A**(**b**–**e**); **B**(**b**–**e**) UBA 75, 125, 250, 500 µg/mL; **C**(**b**–**e**) UBE 75, 125, 250, 500 µg/mL reported to 1% DMSO (**A**(**a**), **B**(**a**), **C**(**a**)).

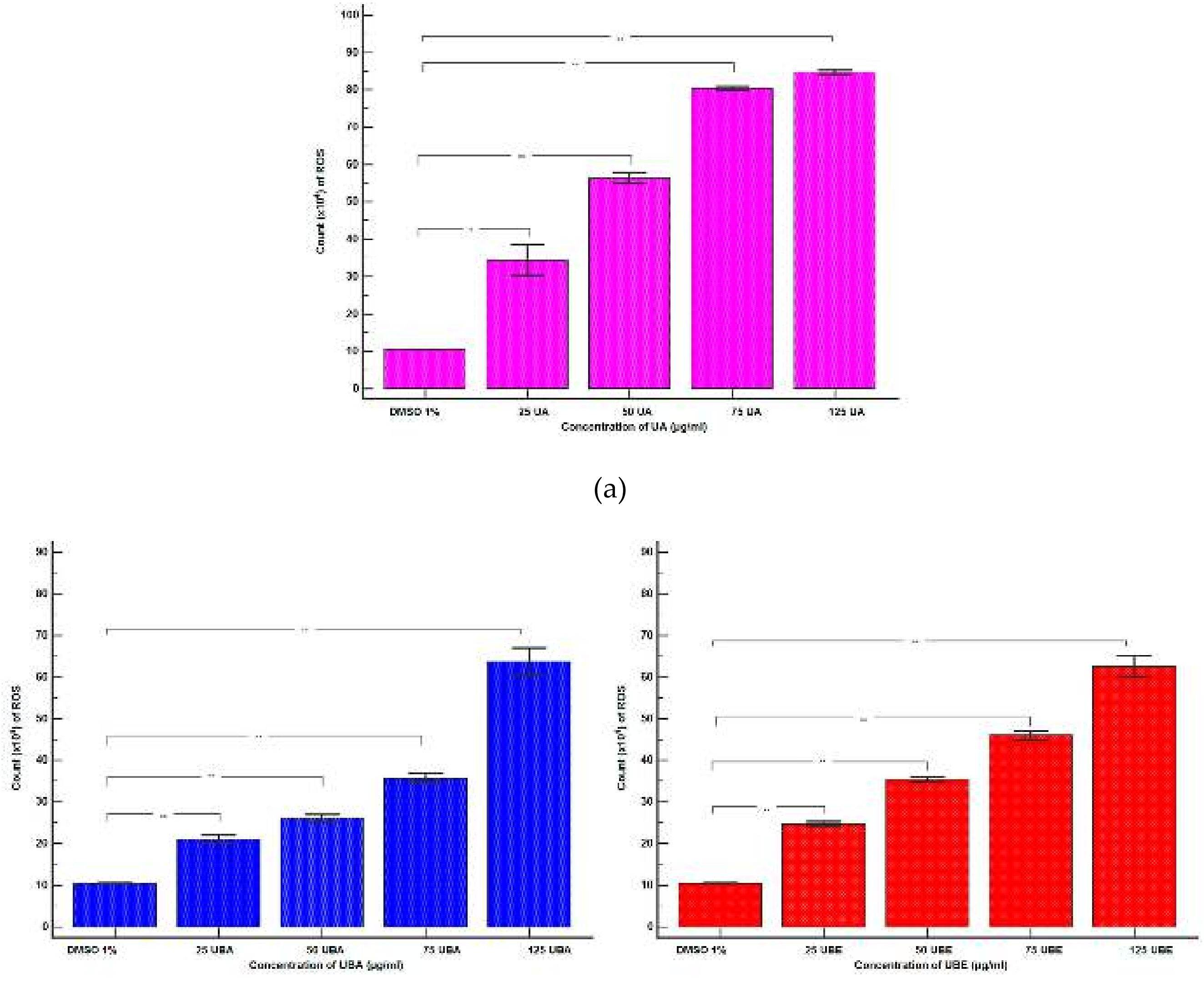

(a)

(b)

(c)

Figure 10. Statistical analysis of cellular oxidative stress: (**a**) UA; (**b**) UBA; (**c**) UBE. * $p < 0.01$ and ** $p < 0.001$ represent significant statistical differences between the control and samples made by paired samples *t*-test.

The lowest concentration of UBA (75 µg/mL) slightly stimulated ROS production (Figure 9B(a,b)) compared with 1% DMSO: $21.00 \times 10^4 \pm 1.00$ vs. $10.40 \times 10^4 \pm 1.00$ ($p < 0.001$, Figure 10b).

Subsequent higher concentrations of UBA (125, 250, and 500 µg/mL) continued to increase ROS levels (Figure 9B(a,c–e)) and the differences reported to solvent control remained significant: $26.00 \times 10^4 \pm 1.00$; $35.66 \times 10^4 \pm 1.15$; $63.66 \times 10^4 \pm 3.21$ vs. $10.40 \times 10^4 \pm 1.00$ ($p < 0.001$, Figure 10b).

Likewise, 75, 125, 250, and 500 µg/mL UBE considerably stimulated ROS production in blood cells, directly proportional with the concentrations (Figure 9C(a–d)).

Our results showed that ROS levels in blood cells compared with the negative control were as follows: $24.66 \times 10^4 \pm 0.57$; $35.63 \times 10^4 \pm 0.57$; $46.00 \times 10^4 \pm 1.00$; $62.53 \times 10^4 \pm 2.50$ vs. $10.40 \times 10^4 \pm 1.00$ ($p < 0.001$, Figure 10c).

3.2.5. Cell Cycle Analysis

To explore the effects of UA, UBA, and UBE on cell cycle distribution on blood cell cultures, the DNA content was evaluated. Propidium iodide/RNase A staining was performed using flow cytometry analyses for DNA content (Figure 11A–C).

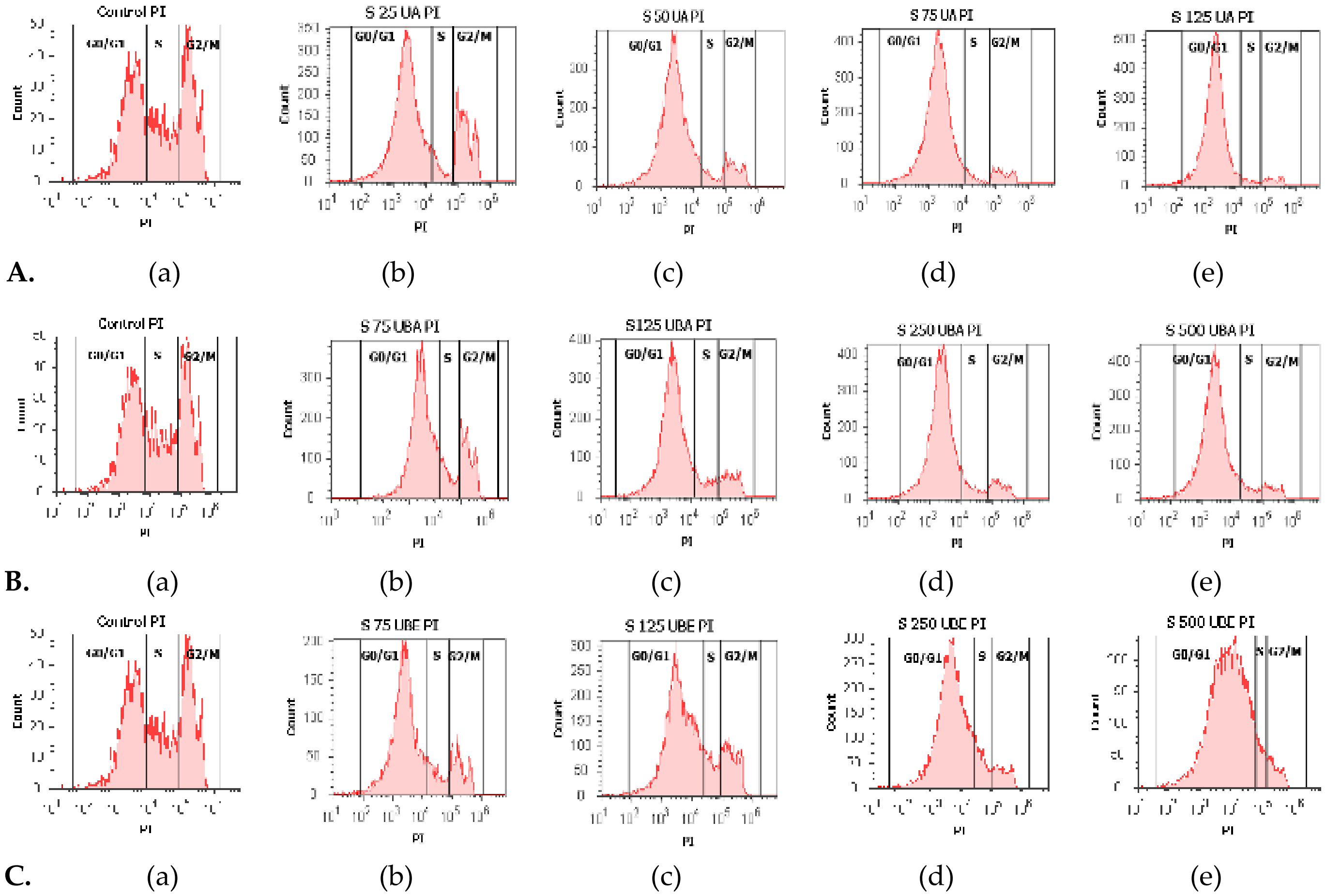

Figure 11. Cell cycle model of UA, UBA, and UBE treatments in normal blood cell cultures. PI/RNase A patterns of UA 25, 50, 75, 125 µg/mL **A**(**b**–**e**); **B**(**b**–**e**) UBA 75, 125, 250, 500 µg/mL; **C**(**b**–**e**) UBE 75, 125, 250, 500 µg/mL reported to 1% DMSO (Negative Control, **A**(**a**), **B**(**a**), **C**(**a**)).

As shown in Figure 11A(a–e) and Figure 12a, UA concentrations of 25, 50, 75, and 125 µg/mL induce a noteworthy cell cycle arrest in the G1/G0 phase: 64.13 ± 1.55%; 78.52 ± 0.87%; 81.91 ± 1.41%; 88.09 ± 0.98% vs. 39.29 ± 0.76%; $p < 0.01$, $p < 0.001$ compared to solvent control. This activity is directly proportional to UA concentrations.

To understand whether the cell growth inhibition was due to cell cycle arrest, blood cells were treated with UBA of 75–500 µg/mL concentrations (Figure 11B(a–e)). *U. barbata* dry extracts exhibited a noticeable cell cycle arrest in G0/G1 phase reported to 1% DMSO: 65.13 ± 0.15%; 76.35 ± 0.94%; 78.93 ± 0.54%; 81.86 ± 1.11%; vs. 39.29 ± 0.76% ($p < 0.01$, $p < 0.001$, Figure 12b).

Thereby, 75, 125, 250, and 500 µg/mL of UBE (Figure 11C(a–e)) induced cell cycle arrest in G0/G1 phase reported to the negative control as follows: 68.16 ± 0.14%; 68.47 ± 0.58%; 76.06 ± 0.68%; 82.75 ± 0.55% vs. 39.29 ± 0.76% ($p < 0.001$, Figure 12c).

Finally, it can be observed that UA proved the highest effect on cell cycle arrest in G0/G1, followed by UBA and UBE with similar activities.

In this study, we observed that the lowest concentration (25 μg/mL) of UA determined an increase of DNA synthesis (Figure 13A(a,b)) in comparison with 1% DMSO (17.25 ± 0.36% vs. 11.43 ± 1.04%, $p < 0.05$, Figure 14a).

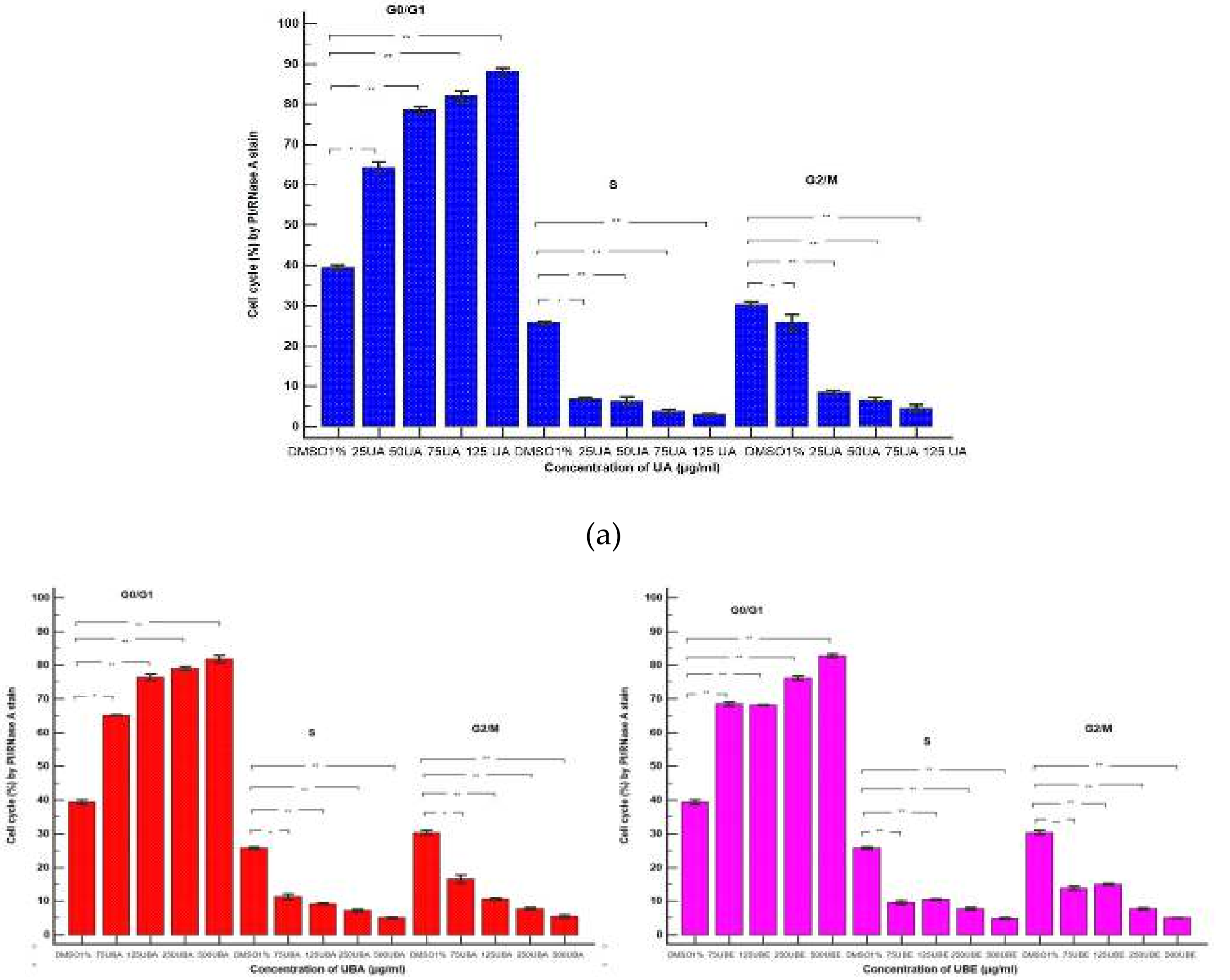

(a)

(b) (c)

Figure 12. Statistical analysis of DNA content: (**a**) UA; (**b**) UBA; (**c**) UBE. * $p < 0.01$, and ** $p < 0.001$ represent significant statistical differences between control and samples made by paired samples *t*-test.

3.2.6. Cell Proliferation Assay

Flow cytometry analyses with EdU incorporation were used for examining DNA synthesis in blood cells (Figure 13).

Instead, UA at 50, 75 and 125 μg/mL did not significantly alter DNA synthesis (Figure 13A(a,c–e)) relative to the control (11.25 ± 0.83%; 10.32 ± 0.64%; 6.49 ± 1.25% vs. 11.43 ± 1.04%, $p \geq 0.05$, Figure 14a).

The lowest concentration of UBA (75 μg/mL) did not significantly modify the DNA synthesis (Figure 13B(a,b)) more than 1% DMSO: 12.78 ± 0.67% vs. 11.43 ± 1.04% ($p \geq 0.05$, Figure 14b).

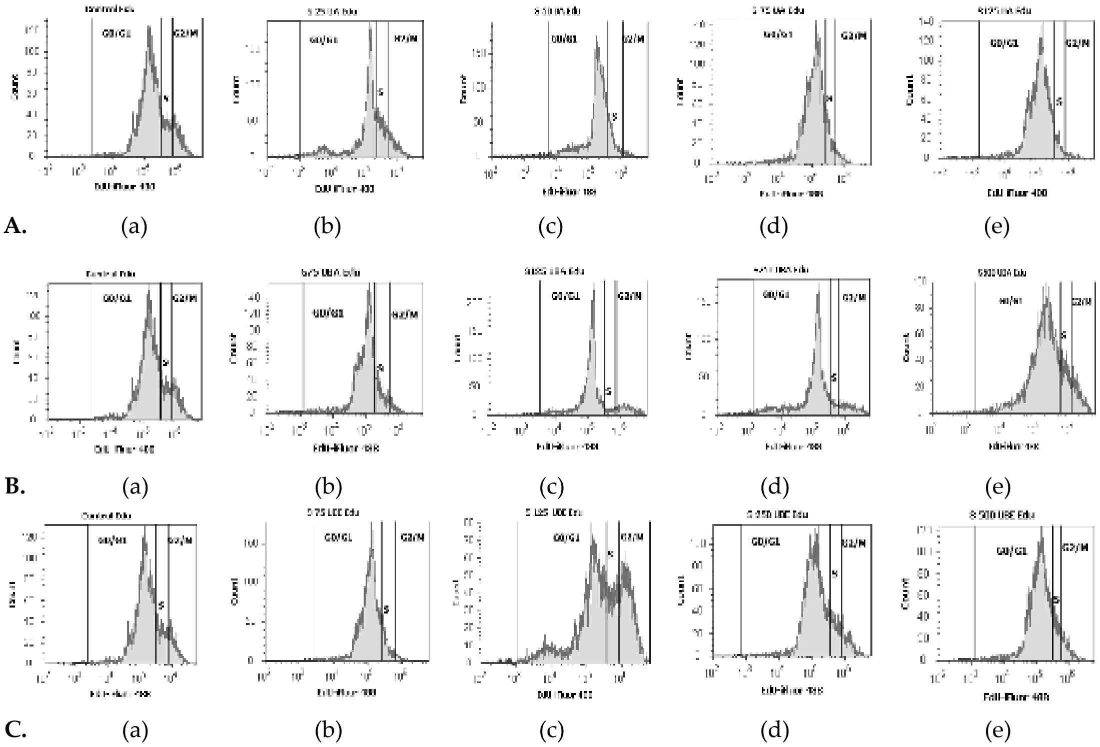

A. (a) (b) (c) (d) (e)

B. (a) (b) (c) (d) (e)

C. (a) (b) (c) (d) (e)

Figure 13. Cell proliferation status of UA, UBA, and UBE treatments in normal blood cell cultures. EdU-iFluor 488 patterns of UA 25, 50, 75, 125 μg/mL (**A**(**b**–**e**)); (**B**(**b**–**e**)) UBA 75, 125, 250, 500 μg/mL; (**C**(**b**–**e**)) UBE 75, 125, 250, 500 μg/mL reported to 1% DMSO (**A**(**a**), **B**(**a**), **C**(**a**)).

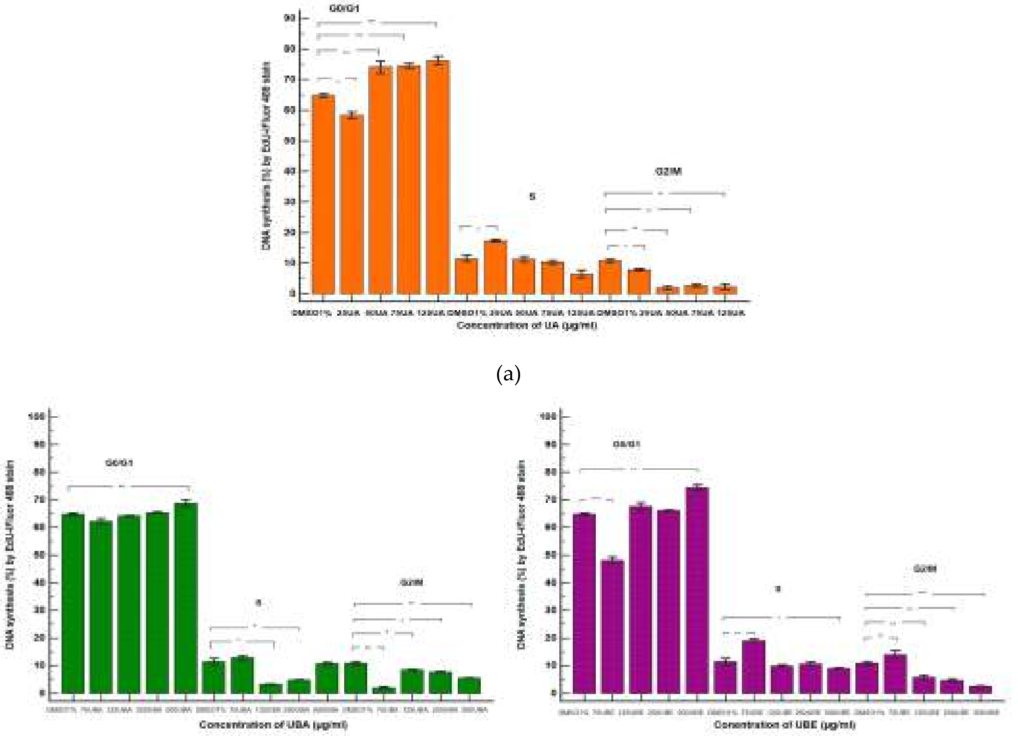

(a)

(b) (c)

Figure 14. Statistical analysis of DNA synthesis: (**a**) UA; (**b**) UBA; (**c**) UBE. * $p < 0.05$, ** $p < 0.01$, and *** $p \leq 0.001$ represent significant statistical differences between the control and samples made by paired samples *t*-test.

Regarding higher concentrations of UBA (125 and 250 μg/mL), a decrease of DNA synthesis (Figure 13B(a,c,d)) was registered, compared with 1% DMSO, with moderate differences: 3.12 ± 0.18%; 4.81 ± 0.15% vs. 11.43 ± 1.04% ($p < 0.05$, Figure 14b).

Finally, the highest UBA concentration (500 μg/mL) did not significantly affect DNA synthesis (Figure 13B(a,e)) more than the solvent control: 10.77 ± 0.43% vs. 11.43 ± 1.04% ($p \geq 0.05$, Figure 14b).

In blood cells treated with 75 μg/mL UBE, an evident higher stimulation of DNA synthesis reported to solvent control (19.05 ± 0.64% vs. 11.43 ± 1.04%, $p < 0.01$) was registered (Figure 13C(a,b) and Figure 14c).

The treatment with 125 and 250 μg/mL of UBE (Figure 13a,d) did not significantly alter DNA synthesis in comparison with 1% DMSO: 9.92 ± 0.43%; 10.60 ± 0.63% vs. 11.43 ± 1.04%, ($p \geq 0.05$, Figure 14c).

Furthermore, 500 μg/mL of UBE produced a lower DNA synthesis stimulation (Figure 13C(a,e)) than the negative control: 8.89 ± 0.30% vs. 11.43 ± 1.04% ($p < 0.05$, Figure 14c).

4. Discussion

Our previous study analyzed five *U. barbata* dry extracts in different solvents [13]; we calculated the yield and evaluated the usnic acid, total polyphenols, and tannins content of each obtained extract. Therefore, we opted only for three lichen dry extracts for the present study: in ethyl acetate, acetone, and ethanol.

The highest usnic acid content (376.73 μg/mg) was the reason for selecting UBEA in the first phase of our study-usnic acid isolation. Then, isolated usnic acid was purified in the sample matrix. As a result, we obtained usnic acid with 89.36% purity and a yield of 28.15%. Ranković et al. (2012) obtained 95 mg usnic acid with 98.6% purity from 500 mg *U. barbata* dry acetone extract [59]. The purity value difference could be due to the solvents used. We used only DMSO, while in the previously mentioned study, dry acetone extract was dissolved in benzene and then, usnic acid was recrystallized using chloroform/ethanol. We can state that our isolated usnic acid is (+)-UA because *Usnea* sp. tends to produce this enantiomer exclusively; in addition, (+)-UA registers antiviral, insecticidal, and phytotoxic activities significantly higher than (−)-UA [69].

Isolated UA and both UBA and UBE were used to evaluate their cytotoxic activity on blood cells. We opted for UBA because it contains an appreciable usnic acid amount (282.78 μg/mg) and other secondary metabolites. In addition, only 127.21 μg/mg of UA were extracted in UBE and a wider lichen secondary metabolites variety. UBE also had the highest extraction yield (12.52%) compared with UBA (6.36%) and UBEA (6.27%) [13]. Consequently, the obtained biological effects could be correlated with the secondary metabolites content.

The present study proved that UA generally induced a significant cytotoxic effect on normal blood cells, more intense than both *U. barbata* extracts, UBA, and UBE. Hence, in early apoptosis events, the appearance of PS residues (commonly hidden within the plasma membrane) on the surface of the cells can be used to detect and measure this PCD. In our flow cytometry method, we opted for annexin V as staining to detect apoptotic cells due to its ability of PS-binding [70]. Moreover, translocation of PS to the external cell surface can occur during apoptosis and necrosis. The difference between these two forms of cell death is that the cell membrane remains intact in early apoptosis; however, it loses integrity and becomes permeable when necrosis is installed [71]. Shlomovitz et al. (2019) showed that PS externalization is also available in necroptosis [72]. However, in RBCs, this process corresponds to eryptosis (quasi-apoptosis) [73]. The intact cells membrane consists of the bilayer with choline-containing phospholipids (phosphatidylcholine and sphingomyelin) in the outer layer and amine-containing phospholipids (phosphatidylethanolamine and PS) in the inner layer. This normal disposition is known as phospholipid asymmetry. Lipid asymmetry is disturbed when the erythrocytes enter into eryptosis, and PS is exposed on RBCs surface [74]. This process involves three ATP and Ca^{2+} -dependent transporters activation (flippase [75], floppase [76], and scramblase [77]). In addition, spectrin [78,79] oxidation and increasing cytoplasmic Ca^{2+} [80] concentration lead to membrane proteins denaturation [81]. Usnic acid oxidative stress-induced plays an essential role in all blood cells PCD, triggering these various molecular mechanisms [35]. One of the prominent protein families that regulate and execute programmed cell death is caspases; they cleave a subset of essential cellular proteins to promote apoptotic cell death [82].

In all blood cells types PCD involves caspases [50,52,53,59,63,73,83–86]. In response to apoptotic stress, the activated initiator caspases (caspase-2, 8, 9) cleave and activate the effector caspases (caspase-3, 6, 7), which execute the death process [87]. They regulate the extrinsic (receptor-mediated) apoptosis pathway involving receptor binding, followed by activation of the initiator caspase, caspase-8, which activates caspase-3 or amplifies caspase-3 activation cleaving BH3 Interacting Domain Death Agonist protein. Bid cleavage induces mitochondrial cytochrome *c* release, forming a protein complex (apoptosome) and activating caspase-9 [88]. During apoptosis, caspase-3 is also actively transported to the nucleus through the nuclear pores, playing a significant role in its disintegration by processing several nuclear substrates. Caspase-7 plays a significant role in cell viability loss [89]. According to Sundquist et al. (2006), the late apoptotic events occur after activating the effector caspases. Late apoptosis includes exposure of phosphatidylserine on the external surface of the plasma membrane (which can be measured by annexin V binding), cleavage of poly (ADP-ribose) polymerase (PARP), and internucleosomal DNA fragmentation [48]. McComb et al. (2019) revealed that efficient apoptosis requires feedback amplification of upstream apoptotic signals by effector caspase-3 or -7 [90]. For this reason, we aimed to evaluate the influence of our tested samples on caspase 3/7 apoptosis pathway. The obtained results showed that caspase 3/7 activity was significantly stimulated during PCD process.

During apoptosis, caspase-3 is actively transported to the nucleus through the nuclear pores, playing a significant role in its disintegration by processing several nuclear substrates [89]. Nuclear apoptosis is characterized by chromatin condensation and progressive DNA cleavage into high-molecular-weight fragments and oligo-nucleosomes [91]. We analyzed the nuclear shrinkage to validate that UA, UBA, and UBE caused apoptosis; this process occurs only in white blood cells [92], RBCs, and platelets being enucleate. Chromatin condensation and fragmentation of nuclei are included in PCD [93]; exclusively, UA at high concentrations showed an appreciable stimulatory effect compared with the solvent control and UBA, and UBE samples.

Various studies have recently shown that lysosomes have been implicated in the regulation of cell death. Increasing their membrane permeability, released hydrolytic enzymes can contact cytosolic targets and contribute to apoptotic cell death [94]. Furthermore, lysosomal activity is directly associated with autophagy, another decisive process for cell death [95]. Various studies from accessed scientific literature analyze autophagy in platelets [96,97] and different WBCs [98–100].

Moreover, according to numerous studies, mitochondrial dysfunction consists of structural alteration, membrane potential disruption, and electron transport reaction instability. These events generate ROS overproduction, caspase cascades activation, and apoptosis pathway initiation [101]. The mitochondrial apoptotic pathway is available only at platelets [102,103], and WBCs [104].

In addition, low ROS concentration can promote cell proliferation, whereas excessive ROS levels cause DNA oxidative damage, consequently inducing cell death [105]. ROS levels are implicated in all blood cell lines death: platelets [106,107], RBCs [108,109], and WBCs [110,111].

It is known that the cell cycle consists of few successive phases in mammals: synthesis (S) with DNA replication and mitosis (M) with repartition of replicated DNA into two daughter cells. Separation of DNA replication from mitosis is performed by two gap phases (G1 and G2). In G1, the cell increasing size, RNA, and protein synthesis occurs, while in G2, after DNA synthesis, the cell grows and synthesizes proteins. Only in RBCs cell cycle arrest occurs in G1 [112]. After division, the cell enters the resting phase, known as the G0 gap phase [113]. Thus, cell cycle arrest represents the first response to DNA damage and one of the first steps in cell apoptosis. However, nucleate WBCs proliferation is a tightly controlled process, and DNA replication is essential [114].

According to the obtained results, the high ROS levels produced by 75 and 125 µg/mL of UA in blood cells triggers a series of consecutive events: cell apoptosis, effector caspases 3/7 activation, pyknosis, autophagy, and cell-cycle arrest in the G0/G1 phase. Furthermore, many studies on numerous cell types proved apoptosis induction by ROS [115].

We have also shown that 125, 250, and 500 µg/mL concentrations of UBA and UBE triggered blood cells apoptosis by caspase 3/7 pathway, oxidative stress, and accumulation of cells in G0/G1. Moreover, altered cell-cycle checkpoints and cell apoptosis parameters conformed with references [116].

Our results proved that UA and UBE at the lowest concentrations stimulated DNA replication (S-phase of the cell cycle). At higher concentrations, they highlighted inhibitory activity on blood cell proliferation. In great measure, these opposite effects manifested at low and high concentrations and can be associated with ROS levels, as previously mentioned. Similar data are mentioned by Damiano et al. (2019), revealing ROS dual function in skeletal muscle: at low levels, they improve muscle force and adaptation to exercise, while at high levels, they decrease muscle performance [117].

However, relatively few studies from the accessed scientific literature are focused exclusively on proving the effects of *Usnea* sp. extracts and usnic acid on normal cells [60,118]. A few years ago, dietary supplements containing usnic acid used for weight loss (Lipokinetix, [119]) reported severe hepatotoxic effects [120–122]. Fujimoto et al. (2010) reported that in vitro usnic acid hepatotoxicity involves oxidative stress, mitochondrial toxicant depletion of glycogen [123], and potential ATP biosynthesis inhibition mediated by mitochondrial electron transport chain [124], triggering necrotic death of hepatocytes. The structural properties of usnic acid can explain these molecular mechanisms. Thus, usnic acid is a lipophilic compound that can easily pass the mitochondrial membranes into the matrix, releasing a proton. Next, usniate anion diffuses into the intermembrane space to bind to a proton to restore usnic acid. The resulting cycle causes a proton leak that could dissipate the proton grad across the membrane, altering ATP levels and changing mitochondrial membrane potential [125]. Usnic acid can induce structural changes in intracellular glutathione molecules, decreasing its reduced form (GSH) [126]. In the same mode, usnic acid can perform spectrin oxidation with cell membrane shrinkage and PS exposure during apoptosis. Thus, usnic acid prooxidant potential can induce oxidative stress and liver cell death signaling. Concomitantly, using natural or synthetic antioxidants to neutralize the prooxidative activity of UA might also be a cell-protecting measure. Due to high hepatotoxicity induced by usnic acid, FDA released a Safety Alerts for Human Medical Products about Lipokinetix [119]. This notification is also current and supports the necessity for identification of natural or synthetic compounds to ensure the safe use of AU as potential anticancer drug.

Instead, the most numerous researchers pointed out these activities on various tumor cell lines [127]. For instance, Ozturk et al. (2019) reported several extract types of different *Usnea* sp. which determine cell apoptosis and DNA damage on cancer cells [128]. In addition, methanol extracts of *U. barbata* induced cell apoptosis, as evidenced by the increasing Annexin V expression and pan-caspase activation in human breast and lung cancer cells [16]. Additionally, Disoma et al. (2018) mentioned caspase 3/7 activation as an apoptotic mechanism on colon cancer cells proved by *U. filipendula* extracts [129]. In their study, Koparal et al. (2006) examined usnic acid effects on two types of lung cells (normal and tumor cells). They described usnic acid cytotoxic activity on both cell types and highlighted that cancer cells are more sensitive than normal cells [130]. Geng et al. (2018) reported that usnic acid induces cycle arrest, apoptosis, and autophagy in gastric cancer cells types in vitro and in vivo [131]. In another study, Wang et al. (2019) proved antileukemia action of (+) usnic acid derivatives, inhibiting pan-Pim kinases [116]. Besides, Rabelo et al. (2012) suggested that usnic acid displays variable redox-active properties, acting as an antioxidant and prooxidant agent, according to different system conditions and cellular environment [27]. High cytotoxic effects on cancer cells and minimal unwanted effects on normal cells represent the essential quality of an antitumor agent. High cytotoxicity levels on cancer cells and low damage on normal cells represent the meaningful purpose in antitumor activity. Finally, Tram et al. (2020) evidenced the highly different cytotoxicity of the same compound against tumor and normal cells [23].

Our study highlights the relationship between concentration and biological effect on normal blood cells. Thereby, usnic acid at a minimal concentration (25 μg/mL) shows low cytotoxicity on human blood cells, slowly inducing cell apoptosis, caspases 3/7 activation, mild ROS level and stimulating DNA synthesis. On the other hand, higher concentrations (50–125 μg/mL) of UA progressively display significant cytotoxic effects: increasing cell apoptosis, effector caspases 3/7 proapoptotic signal, nuclear condensation, autophagy, oxidative stress, and causing cell-cycle arrest in G1/G0 phase.

U. barbata dry extracts in acetone and ethanol, at low concentration (75 μg/mL), exhibit minor cytotoxicity, inducing cell and nuclear apoptosis, autophagy, and increased DNA synthesis. In contrast, higher concentrations (125–500 μg/mL) of UBA and UBE report directly proportional significant toxic effects on blood cells, enhancing cell and nuclear apoptosis, autophagy, ROS levels and promoting cell-cycle arrest G1/G0 phase.

5. Conclusions

The novelty of our study consists of analyzing *U. barbata* and usnic acid cytotoxic effects on human normal blood cells cultures. The principal points of this complex activity have been highlighted, exploring the cell and nuclear apoptosis, caspase 3/7 activity, autophagy, oxidative cellular stress, cell cycle, and DNA synthesis.

High cytotoxicity levels on cancer cells and relatively lower damage to the normal blood cells represent the meaningful purpose in antitumor activity. Based on this statement, our study can offer essential data to target the previously mentioned objective by evaluating the blood cells sensitivity to various concentrations of *U. barbata* dry extracts and usnic acid. The obtained results suggest that future researches may select several concentration domains to evaluate their various pharmacological activities. Moreover, exploring anticancer potential, we can select which extracts highlight optimal and exclusive cytotoxicity on a broad domain of cancer cells, also displaying minimal or no side effects on normal cells.

Supplementary Materials: The following are available online at https://www.mdpi.com/article/10.3390/antiox10081171/s1: video S1 Isolated usnic acid.

Author Contributions: All authors contributed equally to this study and shared the first authorship. Conceptualization, V.P., E.M. and L.B.; methodology, E.M., L.B., T.C., D.R., I.E.C., software, E.M. and D.R.; validation, E.M., L.B. and D.R.; formal analysis, G.C.C. and M.A.; investigation, A.C.; resources, V.P.; data curation, G.C.C. and M.A.; writing—original draft preparation, V.P., E.M. and D.R.; writing—review and editing, V.P., E.M., G.V. and D.G.; visualization, G.C.C., G.V. and D.G.; supervision, L.B., G.C.C. and V.B.; project administration, V.B.; funding acquisition, V.P. All authors have read and agreed to the published version of the manuscript.

Funding: This work is supported by the project ANTREPRENORDOC, in the framework of Human Resources Development Operational Program 2014–2020, financed from the European Social Fund under the contract number 36355/23.05.2019 HRD OP/380/6/13–SMIS Code: 123847.

Institutional Review Board Statement: All aspects of ethics approval and consent of the patients to participate in this study are made in conformity with the declaration of Helsinki 2000, and are approved by the Ethics Committee of "Ovidius" University of Constanta, Romania, 7080/10.06.2021.

Informed Consent Statement: Informed consent was obtained from all subjects involved in the study.

Data Availability Statement: Data is contained within the article and supplementary material.

Acknowledgments: This study was performed in collaboration with the Center for Research and Development of the Morphological and Genetic Studies of Malignant Pathology (CEDMOG), "Ovidius" University of Constanta, 145 Tomis Blvd., 900591, Constanta, Romania, Research Centre of Instrumental Analysis SCIENT, 1E Petre Ispirescu Street, 77167, Tancabesti, Romania, and Institute of Biological Research Iasi, branch of NIRDBS, 47 Lascar Catargi Street, 700107 Iasi, Romania.

Conflicts of Interest: The authors declare no conflict of interest.

References

1. Atanasov, A.G.; Waltenberger, B.; Pferschy-Wenzig, E.M.; Linder, T.; Wawrosch, C.; Uhrin, P.; Temml, V.; Wang, L.; Schwaiger, S.; Heiss, E.H.; et al. Discovery and resupply of pharmacologically active plant-derived natural products: A review. *Biotechnol. Adv.* **2015**, *33*, 1582–1614. [CrossRef] [PubMed]
2. Mitrović, T.; Stamenković, S.; Cvetković, V.; Nikolić, M.; Tošić, S.; Stojičić, D. Lichens as source of versatile bioactive compounds. *Biol. Nyssana* **2011**, *2*, 1–6.
3. Mazid, M.; Khan, T.A.; Mohammad, F. Role of secondary metabolites in defense mechanisms of plants. *Biol. Med.* **2011**, *3*, 232–249.
4. Mukherjee, P.K.; Ponnusankar, S.; Venkatesh, P. Synergy in herbal medicinal products: Concept to realization. *Indian J. Pharm. Educ. Res.* **2011**, *45*, 210–217.
5. Lahlou, M. The Success of Natural Products in Drug Discovery. *Pharmacol. Pharm.* **2013**, *4*, 17–31. [CrossRef]
6. Veeresham, C. Natural products derived from plants as a source of drugs. *J. Adv. Pharm. Technol. Res.* **2012**, *3*, 200–201. [CrossRef]
7. Yin, J.; Li, Q.; Sun, L.D.; Yang, Q.; Zhao, Z.; Ran, Q.S.; Weng, X.G.; Chen, Y.; Wang, Y.J.; Li, Y.J.; et al. Research advancement in natural anti-cancer product. *Zhongguo Zhong Yao Za Zhi* **2019**, *44*, 19–27.
8. Elkhateeb, W.A.; Daba, G.M.; Sheir, D.; Nguyen, T.-D.; Hapuarachchi, K.K.; Thomas, P.W. Mysterious World of Lichens: Highlights on Their History, Applications, and Pharmaceutical Potentials. *Nat. Prod. J.* **2020**, *10*, 1–13. [CrossRef]
9. Aschenbrenner, I.A.; Cernava, T.; Berg, G.; Grube, M. Understanding microbial multi-species symbioses. *Front. Microbiol.* **2016**, *7*, 180. [CrossRef]
10. Molnár, K.; Farkas, E. Current results on biological activities of lichen secondary metabolites: A review. *Z. Nat. C* **2010**, *65*, 157–173. [CrossRef]
11. Prateeksha; Paliya, B.S.; Bajpai, R.; Jadaun, V.; Kumar, J.; Kumar, S.; Upreti, D.K.; Singh, B.R.; Nayaka, S.; Joshi, Y.; et al. The genus Usnea: A potent phytomedicine with multifarious ethnobotany, phytochemistry and pharmacology. *RSC Adv.* **2016**, *6*, 21672–21696. [CrossRef]
12. Sepahvand, A.; Studzińska-Sroka, E.; Ramak, P.; Karimian, V. *Usnea* sp.: Antimicrobial potential, bioactive compounds, ethnopharmacological uses and other pharmacological properties; a review article. *J. Ethnopharmacol.* **2021**, *268*, 113656. [CrossRef] [PubMed]
13. Popovici, V.; Bucur, L.; Popescu, A.; Schröder, V.; Costache, T.; Rambu, D.; Cucolea, I.E.; Gîrd, C.E.; Caraiane, A.; Gherghel, D.; et al. Antioxidant and Cytotoxic Activities of *Usnea barbata* (L.) F.H. Wigg. Dry Extracts in Different Solvents. *Plants* **2021**, *10*, 909. [CrossRef]
14. Idamokoro, E.M.; Masika, P.J.; Muchenje, V.; Falta, D.; Green, E. In-vitro antibacterial sensitivity of *Usnea barbata* lichen extracted with methanol and ethyl-acetate against selected *Staphylococcus* species from milk of cows with mastitis. *Arch. Anim. Breed.* **2014**, *57*, 1–9. [CrossRef]
15. Engel, K.; Schmidt, U.; Reuter, J.; Weckesser, S.; Simon-Haarhaus, B.; Schempp, C.M. Usnea barbata extract prevents ultraviolet-B induced prostaglandin E2 synthesis and COX-2 expression in HaCaT keratinocytes. *J. Photochem. Photobiol. B* **2007**, *89*, 9–14. [CrossRef]
16. Zugic, A.; Jeremic, I.; Isakovic, A.; Arsic, I.; Savic, S.; Tadic, V. Evaluation of anticancer and antioxidant activity of a commercially available CO_2 supercritical extract of old man's beard (*Usnea barbata*). *PLoS ONE* **2016**, *11*, e0146342. [CrossRef] [PubMed]
17. Popovici, V.; Bucur, L.A.; Schröder, V.; Gherghel, D.; Mihai, C.T.; Caraiane, A.; Badea, F.C.; Vochița, G.; Badea, V. Evaluation of the Cytotoxic Activity of the *Usnea barbata* (L.) F. H. Wigg Dry Extract. *Molecules* **2020**, *25*, 1865. [CrossRef]
18. Tang, J.Y.; Wu, K.H.; Wang, Y.Y.; Farooqi, A.A.; Huang, H.W.; Yuan, S.S.F.; Jian, R.I.; Tsao, L.Y.; Chen, P.A.; Chang, F.R.; et al. Methanol Extract of *Usnea barbata* Induces Cell Killing, Apoptosis, and DNA Damage against Oral Cancer Cells through Oxidative Stress. *Antioxidants* **2020**, *9*, 694. [CrossRef]
19. Ranković, B. *Lichen Secondary Metabolites: Bioactive Properties and Pharmaceutical Potential*; Springer International Publishing: Cham, Switzerland, 2015; pp. 1–29.
20. Pizarro, D.; Divakar, P.K.; Grewe, F.; Crespo, A.; Grande, F.D.; Lumbsch, H.T. Genome-wide analysis of biosynthetic gene cluster reveals correlated gene loss with absence of usnic acid in lichen-forming fungi. *Genome Biol. Evol.* **2020**, *12*, 1858–1868. [CrossRef]
21. Salgado, F.; Albornoz, L.; Cortéz, C.; Stashenko, E.; Urrea-Vallejo, K.; Nagles, E.; Galicia-Virviescas, C.; Cornejo, A.; Ardiles, A.; Simirgiotis, M.; et al. Secondary metabolite profiling of species of the genus usnea by UHPLC-ESI-OT-MS-MS. *Molecules* **2017**, *23*, 54. [CrossRef]
22. Mesta, A.R.; Rajeswari, N.; Kanivebagilu, V.S. Distribution of bioactive compounds in usneoid lichens from Western Ghats. *Plant Arch.* **2019**, *19*, 2163–2168.
23. Tram, N.T.T.; Anh, D.H.; Thuc, H.H.; Tuan, N.T. Investigation of chemical constituents and cytotoxic activity of the lichen Usnea undulata. *Vietnam J. Chem.* **2020**, *58*, 63–66. [CrossRef]
24. Alahmadi, A.A. Usnic acid biological activity: History, evaluation and usage. *Int. J. Basic Clin. Pharmacol.* **2017**, *6*, 2752–2759. [CrossRef]

25. White, P.A.S.; Oliveira, R.C.M.; Oliveira, A.P.; Serafini, M.R.; Araújo, A.A.S.; Gelain, D.P.; Moreira, J.C.F.; Almeida, J.R.G.S.; Quintans, J.S.S.; Quintans-Junior, L.J.; et al. Antioxidant Activity and Mechanisms of Action of Natural Compounds Isolated from Lichens: A Systematic Review. *Molecules* **2014**, *19*, 14496–14527. [CrossRef]
26. Leandro, L.F.; Munari, C.C.; Sato, V.L.; Alves, J.M.; de Oliveira, P.F.; Mastrocola, D.F.; Martins Sde, P.; Moraes Tda, S.; de Oliveira, A.I.; Tozatti, M.G.; et al. Assessment of the genotoxicity and antigenotoxicity of (+)-usnic acid in V79 cells and Swiss mice by the micronucleus and comet assays. *Mutat Res.* **2013**, *753*, 101–106. [CrossRef]
27. Rabelo, T.K.; Zeidán-Chuliá, F.; Vasques, L.M.; dos Santos, J.P.A.; da Rocha, R.F.; de Bittencourt Pasquali, M.A.; Rybarczyk-Filho, J.L.; Araújo, A.A.S.; Moreira, J.C.F.; Gelain, D.P. Redox characterization of usnic acid and its cytotoxic effect on human neuron-like cells (SH-SY5Y). *Toxicol. Vitr.* **2012**, *26*, 304–314. [CrossRef] [PubMed]
28. Basiouni, S.; Fayed, M.A.A.; Tarabees, R.; El-Sayed, M.; Elkhatam, A.; Töllner, K.-R.; Hessel, M.; Geisberger, T.; Huber, C.; Eisenreich, W.; et al. Characterization of Sunflower Oil Extracts from the Lichen *Usnea barbata*. *Metabolites* **2020**, *10*, 353. [CrossRef]
29. Neff, G.W.; Rajender Reddy, K.; Durazo, F.A.; Meyer, D.; Marrero, R.; Kaplowitz, N. Severe hepatotoxicity associated with the use of weight loss diet supplements containing ma huang or usnic acid. *J. Hepatol.* **2004**, *6*, 1062–1064. [CrossRef] [PubMed]
30. Moreira, C.T.; Oliveira, A.L.; Comar, J.F.; Peralta, R.M.; Bracht, A. Harmful effects of usnic acid on hepatic metabolism. *Chem. Biol. Interact.* **2013**, *203*, 502–511. [CrossRef]
31. Kartsev, V.; Lichitsky, B.; Geronikaki, A.; Petrou, A.; Smiljkovic, M.; Kostic, M.; Radanovic, O.; Soković, M. Design, synthesis and antimicrobial activity of usnic acid derivatives. *Med. Chem. Comm.* **2018**, *9*, 870–882. [CrossRef]
32. Cetin, H.; Tufan-Cetin, O.; Turk, A.O.; Tay, T.; Candan, M.; Yanikoglu, A.; Sumbul, H. Insecticidal activity of major lichen compounds, (-)- and (+)-usnic acid, against the larvae of house mosquito, *Culex pipiens* L. *Parasitol. Res.* **2008**, *102*, 1277–1279. [CrossRef] [PubMed]
33. Cakmak, K.C.; Gülçin, İ. Anticholinergic and antioxidant activities of usnic acid-an activity-structure insight. *Toxicol. Rep.* **2019**, *6*, 1273–1280. [CrossRef] [PubMed]
34. Odabasoglu, F.; Cakir, A.; Suleyman, H.; Aslan, A.; Bayir, Y.; Halici, M.; Kazaz, C. Gastroprotective and antioxidant effects of usnic acid on indomethacin-induced gastric ulcer in rats. *J. Ethnopharmacol.* **2006**, *103*, 59–65. [CrossRef] [PubMed]
35. Kohlhardt-Floehr, C.; Boehm, F.; Troppens, S.; Lademann, J.; Truscott, T.G. Prooxidant and antioxidant behaviour of usnic acid from lichens under UVB-light irradiation—Studies on human cells. *J. Photochem. Photobiol. B Biol.* **2010**, *101*, 97–102. [CrossRef] [PubMed]
36. Prokopiev, I.A.; Filippov, E.V.; Filippova, G.V.; Zhanataev, A.K. Pro/Antigenotoxic Activity of Usnic Acid Enantiomers In vitro. *Bull. Exp. Biol. Med.* **2018**, *164*, 312–315. [CrossRef] [PubMed]
37. Prokopiev, I.; Filippova, G.; Filippov, E.; Voronov, I.; Sleptsov, I.; Zhanataev, A. Genotoxicity of (+)- and (−)-usnic acid in mice. *Mutat. Res. Genet. Toxicol. Environ. Mutagen.* **2019**, *839*, 36–39. [CrossRef]
38. Silva, C.R.; Marinho, K.S.N.; Silva, T.D.S.; Ferreira, D.K.S.; Aguiar, G.M.; Martins, M.C.B.; Santos, K.R.P.; Aguiar Júnior, F.C.A.; Santos, N.P.S.; Pereira, E.C.; et al. Teratogenic Effect of Usnic Acid from Cladonia substellata Vainio during Organogenesis. *BioMed Res. Int.* **2017**, *2017*, 5948936. [CrossRef]
39. Erfani, S.; Valadbeigi, T.; Aboutaleb, N.; Karimi, N.; Moghimi, A.; Khaksari, M. Usnic acid improves memory impairment after cerebral ischemia/ reperfusion injuries by anti-neuroinflammatory, anti-oxidant, and anti-apoptotic properties. *Iran. J. Basic Med. Sci.* **2020**, *23*, 1225–1231.
40. Okuyama, E.; Umeyama, K.; Yamazaki, M.; Kinoshita, Y.; Yamamoto, Y. Usnic acid and diffractaic acid as analgesic and antipyretic components of Usnea diffracta. *Planta Med.* **1995**, *61*, 113–115. [CrossRef]
41. Machado, N.M.; de Rezende, A.A.A.; Nepomuceno, J.C.; Tavares, D.C.; Cunha, W.R.; Spanó, M.A. Evaluation of mutagenic, recombinogenic and carcinogenic potential of (+)-usnic acid in somatic cells of Drosophila melanogaster. *Food Chem. Toxicol.* **2016**, *96*, 226–233. [CrossRef]
42. Einarsdóttir, E.; Groeneweg, J.; Björnsdóttir, G.G.; Haroardottir, G.; Omarsdóttir, S.; Ingólfsdóttir, K.; Ögmundsdóttir, H.M. Cellular mechanisms of the anticancer effects of the lichen compound usnic acid. *Planta Med.* **2010**, *76*, 969–974. [CrossRef]
43. Kwong, S.P.; Wang, C. Review: Usnic acid-induced hepatotoxicity and cell death. *Environ. Toxicol. Pharmacol.* **2020**, *80*, 103493. [CrossRef] [PubMed]
44. Solárová, Z.; Liskova, A.; Samec, M.; Kubatka, P.; Büsselberg, D.; Solár, P. Anticancer Potential of Lichens' Secondary Metabolites. *Biomolecules* **2020**, *10*, 87. [CrossRef]
45. Galluzzi, L.; Vitale, I.; Aaronson, S.A.; Abrams, J.M.; Adam, D.; Agostinis, P.; Alnemri, E.S.; Altucci, L.; Amelio, I.; Andrews, D.W.; et al. Molecular mechanisms of cell death: Recommendations of the Nomenclature Committee on Cell Death 2018. *Cell Death Differ.* **2018**, *25*, 486–541. [CrossRef]
46. Wong, R.S.Y. Apoptosis in cancer: From pathogenesis to treatment. *J. Exp. Clin. Cancer Res.* **2011**, *30*, 87. [CrossRef] [PubMed]
47. Li, J.; Yuan, J. Caspases in apoptosis and beyond. *Oncogene* **2008**, *27*, 6194–6206. [CrossRef]
48. Sundquist, T.; Moravec, R.; Niles, A.; O'Brien, M.; Riss, T. Timing your apoptosis assays. *Cell Notes* **2006**, *16*, 18–21.
49. Melchinger, H.; Jain, K.; Tyagi, T.; Hwa, J. Role of Platel et Mitochondria: Life in a Nucleus-Free Zone. *Front. Cardiovasc. Med.* **2019**, *6*, 153. [CrossRef]
50. Leytin, V. Apoptosis in the anucleate platelet. *Blood Rev.* **2012**, *26*, 51–63. [CrossRef]
51. Nguyen, K.A.; Hamzeh-Cognasse, H.; Palle, S.; Anselme-Bertrand, I.; Arthaud, C.A.; Chavarin, P.; Pozzetto, B.; Garraud, O.; Cognasse, F. Role of siglec-7 in apoptosis in human platelets. *PLoS ONE* **2014**, *9*, e10623. [CrossRef]

52. Berg, C.P.; Engels, I.H.; Rothbart, A.; Lauber, K.; Renz, A.; Schlosser, S.F.; Schulze-Osthoff, K.; Wesselborg, S. Human mature red blood cells express caspase-3 and caspase-8, but are devoid of mitochondrial regulators of apoptosis. *Cell Death Differ.* **2001**, *8*, 1197–1206. [CrossRef]
53. Bratosin, D.; Tcacenco, L.; Sidoroff, M.; Cotoraci, C.; Slomianny, C.; Estaquier, J.; Montreuil, J. Active caspases-8 and -3 in circulating human erythrocytes purified on immobilized annexin-V: A cytometric demonstration. *Cytom. Part A* **2009**, *75A*, 236–244. [CrossRef]
54. Holcik, M. Do mature red blood cells die by apoptosis? *Trends Genet.* **2002**, *18*, 121. [CrossRef]
55. Peter, M.E.; Krammer, P.H. The CD95(APO-1/Fas) DISC and beyond. *Cell Death Differ.* **2003**, *10*, 26–35. [CrossRef] [PubMed]
56. Mita, E.; Hayashi, N. Molecular biology of Fas antigen-Fas ligand system. *Nippon Rinsho* **1996**, *54*, 1736–1740.
57. Lang, E.; Pozdeev, V.I.; Xu, H.C.; Shinde, P.V.; Behnke, K.; Hamdam, J.M.; Lehnert, E.; Scharf, R.E.; Lang, F.; Häussinger, D.; et al. Storage of erythrocytes induces suicidal erythrocyte death. *Cell. Physiol. Biochem.* **2016**, *39*, 668–676. [CrossRef]
58. Vaschenko, V.I.; Vil'yaninov, V.N. Eryptosis (quasi-apoptosis) the human red blood cells. Its role in medicinal therapy. *Rev. Clin. Pharmacol. Drug Ther.* **2019**, *17*, 5–38. [CrossRef]
59. Klatt, C.; Krüger, I.; Zey, S.; Krott, K.J.; Spelleken, M.; Gowert, N.S.; Oberhuber, A.; Pfaff, L.; Lückstädt, W.; Jurk, K.; et al. Platelet-RBC interaction mediated by FasL/FasR induces procoagulant activity important for thrombosis. *J. Clin. Investig.* **2018**, *128*, 3906–3925. [CrossRef] [PubMed]
60. Pretorius, E.; Du Plooy, J.N.; Bester, J. A Comprehensive Review on Eryptosis. *Cell. Physiol. Biochem.* **2016**, *39*, 1977–2000. [CrossRef]
61. Restivo, I.; Attanzio, A.; Tesoriere, L.; Allegra, M. Suicidal erythrocyte death in metabolic syndrome. *Antioxidants* **2021**, *10*, 154. [CrossRef]
62. Lang, E.; Lang, F. Triggers, inhibitors, mechanisms, and significance of eryptosis: The suicidal erythrocyte death. *Biomed. Res. Int.* **2015**, *2015*, 513518. [CrossRef] [PubMed]
63. Parihar, A.; Eubank, T.D.; Doseff, A.I. Monocytes and macrophages regulate immunity through dynamic networks of survival and cell death. *J. Innate Immun.* **2010**, *2*, 204–215. [CrossRef]
64. Galanty, A.; Paśko, P.; Podolak, I.; Zagrodzki, P. Optimization of usnic acid extraction conditions using fractional factorial design. *Lichenologist* **2020**, *52*, 397–401. [CrossRef]
65. Ranković, B.; Kosanić, M.; Stanojković, T.; Vasiljević, P.; Manojlović, N. Biological Activities of *Toninia candida* and *Usnea barbata* Together with Their Norstictic Acid and Usnic Acid Constituents. *Int. J. Mol. Sci.* **2012**, *13*, 14707–14722. [CrossRef]
66. Guo, L.; Shi, Q.; Fang, J.L.; Mei, N.; Ali, A.A.; Lewis, S.M.; Leakey, J.E.; Frankos, V.H. Review of usnic acid and Usnea barbata toxicity. *J. Environ. Sci. Health C Environ. Carcinog Ecotoxicol. Rev.* **2008**, *26*, 317–338. [CrossRef] [PubMed]
67. Matei, E.; Aschie, M.; Mitroi, A.F.; Ghinea, M.M.; Gheorghe, E.; Petcu, L.; Dobrin, N.; Chisoi, A.; Manea, M. Biomarkers involved in evaluation of platelets function in South-Eastern Romanian patients with hematological malignancies subtypes. *Medicine* **2021**, *100*, e25944. [CrossRef]
68. Gibson, M.G.; Miller, R.G. Beyond ANOVA: Basics of Applied Statistics. *J. R. Stat. Soc. Ser. D Stat.* **1986**, *35*, 566–567. [CrossRef]
69. Galanty, A.; Paśko, P.; Podolak, I. Enantioselective activity of usnic acid: A comprehensive review and future perspectives. *Phytochem. Rev.* **2019**, *18*, 527–548. [CrossRef]
70. Van Engeland, M.; Nieland, L.J.W.; Ramaekers, F.C.S.; Schutte, B.; Reutelingsperger, C.P.M. Annexin V-affinity assay: A review on an apoptosis detection system based on phosphatidylserine exposure. *Cytometry* **1998**, *31*, 1–9. [CrossRef]
71. Vermes, I.; Haanen, C.; Steffens-Nakken, H.; Reutellingsperger, C. A novel assay for apoptosis Flow cytometric detection of phosphatidylserine expression on early apoptotic cells using fluorescein labelled Annexin V. *J. Immunol. Methods* **1995**, *184*, 39–51. [CrossRef]
72. Shlomovitz, I.; Speir, M.; Gerlic, M. Flipping the dogma—Phosphatidylserine in non-apoptotic cell death. *Cell Commun. Signal.* **2019**, *17*, 139. [CrossRef]
73. Gusev, G.P.; Govekar, R.; Gadewal, N.; Agalakova, N.I. Understanding quasi-apoptosis of the most numerous enucleated components of blood needs detailed molecular autopsy. *Ageing Res. Rev.* **2017**, *35*, 46–62. [CrossRef]
74. Sathi, A.; Viswanad, V.; Aneesh, T.P.; Kumar, B.A. Pros and cons of phospholipid asymmetry in erythrocytes. *J. Pharm. Bioallied Sci.* **2014**, *6*, 81–85.
75. Jing, W.; Yabas, M.; Bröer, A.; Coupland, L.; Gardiner, E.E.; Enders, A.; Bröer, S. Calpain cleaves phospholipid flippase ATP8A1 during apoptosis in platelets. *Blood Adv.* **2019**, *3*, 219–229. [CrossRef]
76. Groen, A.; Romero, M.R.; Kunne, C.; Hoosdally, S.J.; Dixon, P.H.; Wooding, C.; Williamson, C.; Seppen, J.; Van Den Oever, K.; Mok, K.S.; et al. Complementary functions of the flippase ATP8B1 and the floppase ABCB4 in maintaining canalicular membrane integrity. *Gastroenterology* **2011**, *141*, 1927–1937.e4. [CrossRef] [PubMed]
77. Williamson, P. Phospholipid Scramblases. *Lipid Insights* **2015**, *8*, 41–44. [CrossRef] [PubMed]
78. Djinovic-Carugo, K.; Gautel, M.; Ylänne, J.; Young, P. The spectrin repeat: A structural platform for cytoskeletal protein assemblies. *FEBS Lett.* **2002**, *513*, 119–123. [CrossRef]
79. Machnicka, B.; Grochowalska, R.; Bogusławska, D.M.; Sikorski, A.F.; Lecomte, M.C. Spectrin-based skeleton as an actor in cell signaling. *Cell. Mol. Life Sci.* **2012**, *69*, 191–201. [CrossRef] [PubMed]

80. Bissinger, R.; Petkova-Kirova, P.; Mykhailova, O.; Oldenborg, P.A.; Novikova, E.; Donkor, D.A.; Dietz, T.; Bhuyan, A.A.M.; Sheffield, W.P.; Grau, M.; et al. Thrombospondin-1/CD47 signaling modulates transmembrane cation conductance, survival, and deformability of human red blood cells. *Cell Commun. Signal.* **2020**, *18*, 155. [CrossRef] [PubMed]
81. Fadok, V.A.; De Cathelineau, A.; Daleke, D.L.; Henson, P.M.; Bratton, D.L. Loss of phospholipid asymmetry and surface exposure of phosphatidylserine is required for phagocytosis of apoptotic cells by macrophages and fibroblasts. *J. Biol. Chem.* **2001**, *276*, 1071–1077. [CrossRef]
82. Robertson, J.D.; Orrenius, S.; Zhivotovsky, B. Review: Nuclear events in apoptosis. *J. Struct. Biol.* **2000**, *129*, 346–358. [CrossRef] [PubMed]
83. Gyulkhandanyan, A.V.; Allen, D.J.; Mykhaylov, S.; Lyubimov, E.; Ni, H.; Freedman, J.; Leytin, V. Mitochondrial Inner Membrane Depolarization as a Marker of Platelet Apoptosis: Disclosure of Nonapoptotic Membrane Depolarization. *Clin. Appl. Thromb.* **2017**, *23*, 139–147. [CrossRef]
84. Lauber, K.; Bohn, E.; Kröber, S.M.; Xiao, Y.J.; Blumenthal, S.G.; Lindemann, R.K.; Marini, P.; Wiedig, C.; Zobywalski, A.; Baksh, S.; et al. Apoptotic cells induce migration of phagocytes via caspase-3-mediated release of a lipid attraction signal. *Cell* **2003**, *113*, 717–730. [CrossRef]
85. El Kebir, D.; Filep, J.G. Modulation of neutrophil apoptosis and the resolution of inflammation through β2 integrins. *Front. Immunol.* **2013**, *4*, 60. [CrossRef]
86. Fox, S.; Leitch, A.E.; Duffin, R.; Haslett, C.; Rossi, A.G. Neutrophil apoptosis: Relevance to the innate immune response and inflammatory disease. *J. Innate Immun.* **2010**, *2*, 216–227. [CrossRef] [PubMed]
87. Walsh, J.G.; Cullen, S.P.; Sheridan, C.; Lüthi, A.U.; Gerner, C.; Martin, S.J. Executioner caspase-3 and caspase-7 are functionally distinct proteases. *Proc. Natl. Acad. Sci. USA* **2008**, *105*, 12815–12819. [CrossRef]
88. Elmore, S. Apoptosis: A Review of Programmed Cell Death. *Toxicol. Pathol.* **2007**, *35*, 495–516. [CrossRef] [PubMed]
89. Faleiro, L.; Lazebnik, Y. Caspases Disrupt the Nuclear-Cytoplasmic Barrier. *J. Cell Biol.* **2000**, *151*, 951–959. [CrossRef]
90. McComb, S.; Chan, P.K.; Guinot, A.; Hartmannsdottir, H.; Jenni, S.; Dobay, M.P.; Bourquin, J.P.; Bornhauser, B.C. Efficient apoptosis requires feedback amplification of upstream apoptotic signals by effector caspase-3 or -7. *Sci. Adv.* **2019**, *5*, eaau9433. [CrossRef]
91. Lecoeur, H. Nuclear apoptosis detection by flow cytometry: Influence of endogenous endonucleases. *Exp. Cell Res.* **2002**, *277*, 1–14. [CrossRef]
92. Simons, M.P.; Nauseef, W.M.; Griffith, T.S.; Apicella, M.A. Neisseria gonorrhoeae delays the onset of apoptosis in polymorphonuclear leukocytes. *Cell. Microbiol.* **2006**, *8*, 1780–1790. [CrossRef] [PubMed]
93. Prasad, C.V.; Nayak, V.L.; Ramakrishna, S.; Mallavadhani, U.V. Novel menadione hybrids: Synthesis, anticancer activity, and cell-based studies. *Chem. Biol. Drug Des.* **2018**, *91*, 220–233. [CrossRef]
94. Kågedal, K.; Johansson, A.C.; Johansson, U.; Heimlich, G.; Roberg, K.; Wang, N.S.; Jürgensmeier, J.M.; Ollinger, K. Lysosomal membrane permeabilization during apoptosis–involvement of Bax? *Int. J. Exp. Path.* **2005**, *86*, 309–321. [CrossRef]
95. Jung, S.; Jeong, H.; Yu, S.W. Autophagy as a decisive process for cell death. *Exp. Mol. Med.* **2020**, *52*, 921–930. [CrossRef] [PubMed]
96. Ouseph, M.M.; Huang, Y.; Banerjee, M.; Joshi, S.; MacDonald, L.; Zhong, Y.; Liu, H.; Li, X.; Xiang, B.; Zhang, G.; et al. Autophagy is induced upon platelet activation and is essential for hemostasis and thrombosis. *Blood* **2015**, *126*, 1224–1233. [CrossRef]
97. Feng, W.; Chang, C.; Luo, D.; Su, H.; Yu, S.; Hua, W.; Chen, Z.; Hu, H.; Liu, W. Dissection of autophagy in human platelets. *Autophagy* **2014**, *10*, 642–651. [CrossRef] [PubMed]
98. Skendros, P.; Mitroulis, I.; Ritis, K. Autophagy in neutrophils: From granulopoiesis to neutrophil extracellular traps. *Front. Cell Dev. Biol.* **2018**, *6*, 109. [CrossRef]
99. Vural, A.; Kehrl, J.H. Autophagy in Macrophages: Impacting Inflammation and Bacterial Infection. *Scientifica* **2014**, *2014*, 825463. [CrossRef]
100. Rodríguez-Vargas, J.M.; Oliver-Pozo, F.J.; Dantzer, F. PARP1 and poly(ADP-ribosyl)ation signaling during autophagy in response to nutrient deprivation. *Oxid. Med. Cell. Longev.* **2019**, *2019*, 2641712. [CrossRef] [PubMed]
101. Zaidieh, T.; Smith, J.R.; Ball, K.E.; An, Q. ROS as a novel indicator to predict anticancer drug efficacy. *BMC Cancer* **2019**, *19*, 1224. [CrossRef] [PubMed]
102. Lin, K.H.; Hsiao, G.; Shih, C.M.; Chou, D.S.; Sheu, J.R. Mechanisms of resveratrol-induced platelet apoptosis. *Cardiovasc. Res.* **2009**, *83*, 575–585. [CrossRef]
103. Leytin, V.; Gyulkhandanyan, A.V.; Freedman, J. Platelet Apoptosis Can Be Triggered Bypassing the Death Receptors. *Clin. Appl. Thromb. Hemost.* **2019**, *25*, 1076029619853641. [CrossRef] [PubMed]
104. Park, K.-S.; Lee, M.-G. Effects of unaccustomed downhill running on muscle damage, oxidative stress, and leukocyte apoptosis. *J. Exerc. Nutr. Biochem.* **2015**, *19*, 55–63. [CrossRef] [PubMed]
105. Nita, M.; Grzybowski, A. The Role of the Reactive Oxygen Species and Oxidative Stress in the Pathomechanism of the Age-Related Ocular Diseases and Other Pathologies of the Anterior and Posterior Eye Segments in Adults. *Oxid. Med. Cell. Longev.* **2016**, *2016*, 3164734. [CrossRef]
106. Dziedzic, A.; Morel, A.; Miller, E.; Bijak, M.; Sliwinski, T.; Synowiec, E.; Ceremuga, M.; Saluk-Bijak, J. Oxidative Damage of Blood Platelets Correlates with the Degree of Psychophysical Disability in Secondary Progressive Multiple Sclerosis. *Oxid. Med. Cell. Longev.* **2020**, *2020*, 2868014. [CrossRef] [PubMed]

107. Lopes-Pires, M.E.; Ahmed, N.S.; Vara, D.; Gibbins, J.M.; Pula, G.; Pugh, N. Zinc regulates reactive oxygen species generation in platelets. *Platelets* **2021**, *32*, 368–377. [CrossRef]
108. Kosmachevskaya, O.V.; Novikova, N.N.; Topunov, A.F. Carbonyl Stress in Red Blood Cells and Hemoglobin. *Antioxidants* **2021**, *10*, 253. [CrossRef]
109. Matarrese, P.; Straface, E.; Pietraforte, D.; Gambardella, L.; Vona, R.; Maccaglia, A.; Minetti, M.; Malorni, W. Peroxynitrite induces senescence and apoptosis of red blood cells through the activation of aspartyl and cysteinyl proteases. *FASEB J.* **2005**, *19*, 1–27. [CrossRef]
110. Haag, F.; Janicova, A.; Xu, B.; Powerski, M.; Fachet, M.; Bundkirchen, K.; Neunaber, C.; Marzi, I.; Relja, B.; Sturm, R. Reduced phagocytosis, ROS production and enhanced apoptosis of leukocytes upon alcohol drinking in healthy volunteers. *Eur. J. Trauma Emerg. Surg.* **2021**. [CrossRef]
111. Jacinto, T.A.; Meireles, G.S.; Dias, A.T.; Aires, R.; Porto, M.L.; Gava, A.L.; Vasquez, E.C.; Pereira, T.M.C.; Campagnaro, B.P.; Meyrelles, S.S. Increased ROS production and DNA damage in monocytes are biomarkers of aging and atherosclerosis. *Biol. Res.* **2018**, *51*, 33. [CrossRef]
112. Heredia, A.; Davis, C.; Amoroso, A.; Dominique, J.K.; Le, N.; Klingebiel, E.; Reardon, E.; Zella, D.; Redfield, R.R. Induction of G 1 cycle arrest in T lymphocytes results in increased extracellular levels of-chemokines: A strategy to inhibit R5 HIV-1. *Proc. Natl. Acad. Sci. USA* **2003**, *100*, 4179–4184. [CrossRef]
113. Gérard, C.; Goldbeter, A. The balance between cell cycle arrest and cell proliferation: Control by the extracellular matrix and by contact inhibition. *Interface Focus* **2014**, *4*, 20130075. [CrossRef]
114. Nikbakht, M.; Pakbin, B.; Brujeni, G.N. Evaluation of a new lymphocyte proliferation assay based on cyclic voltammetry; an alternative method. *Sci. Rep.* **2019**, *9*, 4503. [CrossRef]
115. Uchihara, Y.; Tago, K.; Taguchi, H.; Narukawa, Y.; Kiuchi, F.; Tamura, H.; Funakoshi-Tago, M. Taxodione induces apoptosis in BCR-ABL-positive cells through ROS generation. *Biochem. Pharmacol.* **2018**, *154*, 357–372. [CrossRef] [PubMed]
116. Wang, W.; Niu, S.; Qiao, L.; Wei, F.; Yin, J.; Wang, S.; Ouyang, Y.; Chen, D. Usnea Acid as Multidrug Resistance (MDR) Reversing Agent against Human Chronic Myelogenous Leukemia K562/ADR Cells via an ROS Dependent Apoptosis. *Biomed. Res. Int.* **2019**, *2019*, 8727935. [CrossRef] [PubMed]
117. Damiano, S.; Muscariello, E.; La Rosa, G.; Di Maro, M.; Mondola, P.; Santillo, M. Dual role of reactive oxygen species in muscle function: Can antioxidant dietary supplements counteract age-related sarcopenia? *Int. J. Mol. Sci.* **2019**, *20*, 3815. [CrossRef] [PubMed]
118. Araújo, A.A.S.; De Melo, M.G.D.; Rabelo, T.K.; Nunes, P.S.; Santos, S.L.; Serafini, M.R.; Santos, M.R.V.; Quintans, L.J.; Gelain, D.P. Review of the biological properties and toxicity of usnic acid. *Nat. Prod. Res.* **2015**, *29*, 2167–2180. [CrossRef] [PubMed]
119. Favreau, J.T.; Ryu, M.L.; Braunstein, G.; Orshansky, G.; Park, S.S.; Coody, G.L.; Love, L.A.; Fong, T.L. Severe hepatotoxicity associated with the dietary supplement LipoKinetix. *Ann. Intern. Med.* **2002**, *136*, 590–595. [CrossRef]
120. Hsu, L.M.; Huang, Y.S.; Chang, F.Y.; Lee, S.D. "Fat burner" herb, usnic acid, induced acute hepatitis in a family. *J. Gastroenterol. Hepatol.* **2005**, *20*, 1138–1139. [CrossRef]
121. Yellapu, R.K.; Mittal, V.; Grewal, P.; Fiel, M.; Schiano, T. Acute liver failure caused by "fat burners" and dietary supplements: A case report and literature review. *Can. J. Gastroenterol.* **2011**, *25*, 157–160.
122. Sanchez, W.; Maple, J.T.; Burgart, L.J.; Kamath, P.S. Severe hepatotoxicity associated with use of a dietary supplement containing usnic acid. *Mayo Clin. Proc.* **2006**, *81*, 541–544. [CrossRef] [PubMed]
123. Fujimoto, K.; Kishino, H.; Hashimoto, K.; Watanabe, K.; Yamoto, T.; Mori, K. Biochemical profiles of rat primary cultured hepatocytes following treatment with rotenone, FCCP, or (+)-usnic acid. *J. Toxicol. Sci.* **2020**, *45*, 339–347. [CrossRef] [PubMed]
124. Han, D.; Matsumaru, K.; Rettori, D.; Kaplowitz, N. Usnic acid-induced necrosis of cultured mouse hepatocytes: Inhibition of mitochondrial function and oxidative stress. *Biochem. Pharmacol.* **2004**, *67*, 439–451. [CrossRef]
125. Bessadottir, M.; Egilsson, M.; Einarsdottir, E.; Magnusdottir, I.H.; Ogmundsdottir, M.H.; Omarsdottir, S.; Ogmundsdottir, H.M. Proton-Shuttling Lichen Compound Usnic Acid Affects Mitochondrial and Lysosomal Function in Cancer Cells. *PLoS ONE* **2012**, *7*, e51296. [CrossRef] [PubMed]
126. Chen, C.; Zhao, D.; Fang, S.; Chen, Q.; Cheng, B.; Fang, X.; Shu, Q. TRIM22-Mediated Apoptosis is Associated with Bak Oligomerization in Monocytes. *Sci. Rep.* **2017**, *7*, 39961. [CrossRef] [PubMed]
127. Bačkorová, M.; Bačkor, M.; Mikeš, J.; Jendželovský, R.; Fedoročko, P. Variable responses of different human cancer cells to the lichen compounds parietin, atranorin, usnic acid and gyrophoric acid. *Toxicol. Vitr.* **2011**, *25*, 37–44. [CrossRef] [PubMed]
128. Ozturk, S.; Erkisa, M.; Oran, S.; Ulukaya, E.; Celikler, S.; Ari, F. Lichens exerts an anti-proliferative effect on human breast and lung cancer cells through induction of apoptosis. *Drug Chem. Toxicol.* **2021**, *44*, 259–267. [CrossRef]
129. Disoma, C.; Erkisa, M.; Oran, S.; Aloglou, I.; Ulkaya, E.; Ari, F. Usnea filipendula Induces Apoptosis in Human Colon Cancer Cell Lines. *Indian J. Pharm. Sci.* **2018**, *80*, 1078–1085. [CrossRef]
130. Koparal, A.T.; Tüylü, B.A.; Türk, H. In vitro cytotoxic activities of (+)-usnic acid and (−)-usnic acid on V79, A549, and human lymphocyte cells and their non-genotoxicity on human lymphocytes. *Nat. Prod. Res.* **2006**, *20*, 1300–1307. [CrossRef]
131. Geng, X.; Zhang, X.; Zhou, B.; Zhang, C.; Tu, J.; Chen, X.; Wang, J.; Gao, H.; Qin, G.; Pan, W. Usnic acid induces cycle arrest, apoptosis, and autophagy in gastric cancer cells in vitro and in vivo. *Med. Sci. Monit.* **2018**, *24*, 556–566. [CrossRef]

Observational Study

Medicine®

OPEN

The diagnostic value of miR-92a, -143, and -145 expression levels in patients with colorectal adenocarcinoma from Romania

Costel Brînzan, PhD[a,b], Mariana Aşchie, MD, PhD[a], Georgeta Cozaru, MD, PhD[a,b], Eugen Dumitru, MD, PhD[b,c], Anca Mitroi, MD, PhD[a,b,*]

Abstract

MicroRNAs (miRNAs) refers to a small, short non-coding RNA of endogenous class. They have shown to have an increasingly altered expression in many types of cancer, including colorectal cancer (CRC).

In the present study, miRNA TaqManMGB and qRT-PCR was used to quantify the expression and clinical significance of 3 mature human miRNA in 82 pairs of colorectal adenocarcinoma tissues and normal adjacent tissue samples (NATS) collected from patients of the south-east part of Romania. Differences between CRC and NATS were analyzed using Wilcoxon test, while correlations between miRNAs expression levels and clinicopathological features were examined using non-parametric tests. In addition, the ability of selected miRNAs to function as biomarkers and, as potential indicators in CRC prognosis was also examined.

When the miRNA expression was compared in CRC related NATS, miR-143, and miR-145 were significantly underexpressed (4.99±–1.02 vs –5.66±–1.66, $P<.001$; –4.85±–0.59 vs –9.27±–1.51, $P<.001$, respectively), while the pattern of miR-92a was significantly overexpressed (–5.55±–2.83 vs –4.92±–2.44, $P<.001$). Moreover, the expression levels of selected miRNAs were identified to be correlated with gradual increases in fold change expression with the depth of tumor invasion, lymph node invasion, and maximal increases with distant metastasis. Furthermore, the receiver operating characteristic analysis demonstrated that potential diagnostic of miR-143, miR-145, and miR-92a in discriminating CRC from NATS, with the area under the curve of 0.74, 0.85, and 0.84 respectively. The Kaplan–Meier and the log-rank test showed that a high level of miR-92a and low levels of miR-143 and miR-145 predicted poor survival rate in our cohorts.

In conclusion, we can summarize that miR-145 and miR-143 are decreased, while miR-92 is increased in CRC compared to NATS, and associated with different stages of CRC pathogenesis. Thus, the expression of selected miRNAs can represent potential diagnostic and prognostic tools in patients with CRC from Romania.

Abbreviations: AUC = area under the curve, CI = 95% interval of confidence, CRC = colorectal cancer, miRNA = microRNA, ncRNAs = non-coding RNAs, NATS = normal adjacent tissue samples, qRT-PCR = real-time quantitative polymerase chain reaction analysis, ROC = receiver operating characteristic, RT = room temperature, TNM = tumor-node-metastasis, UTR = 3’ noncoding region, WHO = World Health Organization.

Keywords: colorectal cancer, miR-92a, miR-143, miR-145, real-time quantitative polymerase chain reaction analysis, expression profiling

1. Introduction

Among all ranges of tumors, colorectal cancer (CRC) is one of the most common malignancies and a significant public health burden. Moreover, the incidence rate of CRC is 9.7%, thereby making it the third most common form of cancer worldwide and it is the fourth leading cause of cancer-related mortality.[1] As per the findings of the Global Burden of Cancer Reports in the Romania population, the relative incidence of CRC increased from 8.660 in 2012 to 11.076 in 2018, thus representing the second most common malignancy, after lung/bronchus cancers in

---

Editor: Lishuang Shen.

All authors contributed equally to this work and are the co-first authors.

Experiments of molecular biology was performed at the Research Center for the Morphologic and Genetic Study in Malignant Pathology, CEDMOG, from Ovidius University.

The authors have no funding and conflicts of interest to disclose.

The datasets generated during and/or analyzed during the current study are available from the corresponding author on reasonable request.

[a] Pathology Department, Sf. Apostol Andrei Clinical Emergency County Hospital, [b] CEDMOG Center, Ovidius University, [c] Gastroenterology Department, Sf. Apostol Andrei Clinical Emergency County Hospital, Constanta, Romania.

[*] Correspondence: Anca Mitroi, CEDMOG Center, Ovidius University, 145 Tomis Bdv, Constanta 900591, Romania. (e-mail: ank_mitroi@yahoo.com).

How to cite this article: Brînzan C, Aşchie M, Cozaru G, Dumitru E, Mitroi A. The diagnostic value of miR-92a, -143, and -145 expression levels in patients with colorectal adenocarcinoma from Romania. Medicine 2020;99:35(e21895).

Received: 3 December 2019 / Received in final form: 17 May 2020 / Accepted: 19 July 2020

http://dx.doi.org/10.1097/MD.0000000000021895

men and breast cancer in women.[2] CRC is a multifactorial disease characterized by a sequential process associated with alteration of the molecular architecture in oncogene or tumor suppressor gene regulatory networks, mainly due to genomic mutation or epigenetic alterations and the involvement of small noncoding RNA species, named microRNAs (miRNAs) and long noncoding RNAs.[3,4]

In this regard, numerous studies and resources have been devoted to elucidating the molecular mechanisms of the CRC, however, the underlying mechanisms are not yet well understood. Therefore, improving the survival rate of patients with CRC requires a better understanding of tumor biology as well as the development of novel therapeutic and diagnostic strategies. A rapidly developing field of cancer research is the examination of miRNAs genes in CRC carcinogenesis. Molecules that are widespread and differentially expressed in CRC samples when compared to normal non-cancerous samples and may provide new insights into the mechanisms involved.

Functionally, miRNAs represent a novel class of small, non-coding RNAs (ncRNAs), found in plants, animals, and humans that use endogenous RNA interference pathways in order to modulate gene expression networks. Typically, miRNA genes are initially transcribed into the nucleus as longer primary transcripts guided by RNA polymerase II (pri-miRNAs), which are subsequently enzymatically cleaved by the Drosha into small miRNAs precursor (pre-miRNA). These pre-miRNAs are comprised of 70 nucleotides with hairpin stem-loop structures and are translocated into the cytoplasm through the assistance of Exportin-5 to undergo final maturation, within a functional miRNA to approximately 22 nucleotides catalyzed via RNase III endonuclease Dicer.[5] Predominantly, miRNAs exert their functionality in post-transcriptional modulation of gene expression through direct binding to the 3' untranslated region (UTR) of specific messenger RNA targets, thereby leading to cleavage and degradation or suppression of translation.[5] The latest version of the miRBase database contains – 1.917 entries of mature human miRNAs (http://www.mirbase.org), which can be classified into clusters and families based on seed sequence or genomic relatedness, able to regulate the expression of one-third of human protein-coding genes.

It is now widely accepted that the altered functionality of miRNAs plays an important role in various biological and cancer-related processes, such as control of cellular homeostasis, differentiation, cell growth, and apoptosis. In colorectal tumorigenesis, the specific expression patterns of human miRNAs have been used by many researchers to understand the involvement of these regulatory molecules in the diagnosis and prognosis of this type of cancer.[6] Some of these deregulated mature miRNAs, due to high tissue specificity, altered stability, and unique expression in tumor development, might help distinguish CRC from other colon-related diseases, representing a new field of molecular diagnosis and prognosis of CRC. For instance, deregulation of miR-92a, miR-143, and miR-145 have been documented in plenty of pathophysiological events, including neoplastic diseases.[22,24] This suggests that miRNAs clusters function as oncogenic, respectively tumor suppressor genes and their inadequate expression is the result of excessive or deficient processing, and that ultimately leads to altered cellular homeostasis, essential events of tumorigenesis. In light of these data, miRNA genes have relevant biological and biomedical consequences in the detection and evolution of cancer, and their inadequate expression is an almost universal feature in human malignancies.

The present research aimed to investigate the signature of 3 mature human miRNAs involving miR-143, miR-145, and miR-92a in 82 pairs of colorectal adenocarcinoma tissues in the normal adjacent tissue samples (NATS) collected from patients in south-east Romania. The ability of the selected miRNAs to function as potential biomarkers, discriminating between CRC and NATS and, their potential as indicators in CRC prognosis was also examined. The miRNAs were selected based on previous studies on their clinical relevance in complex mechanisms of carcinogenesis.[17–27]

2. Materials and methods

2.1. Case selection

This study included 82 selected patients diagnosed with CRC at the Pathology Department of the Clinical Emergency County Hospital in Constanta, Romania. the Local Ethics Commission for the Approval of Clinical and Research Developmental Studies approved the study and all eligible patients provided written informed consent. Immediately after the surgical resection, CRC tissues and NATS (located at least 5 cm from the tumor site) were stabilized in RNAlater solution (Invitrogen by Thermo Fisher Scientific, USA) and frozen at –80 °C until further processing. A section of each sample (tumor and non-tumor) was stained with hematoxylin and eosin and evaluated by an experienced pathologist. All tumor specimens used in this study were histologically classified as colon or rectum adenocarcinoma. The histological tumor stage and differentiation grade was classified using the tumor-node-metastasis staging system of the American Joint Committee on Cancer, in accordance with standards set by World Health Organization.[7] Subsequently, clinicopathological features of patients were obtained from observation sheets and pathology reports and included age, sex, tumor location, tumor-node-metastasis stage, tumor differentiation degree, and eventual metastasis.

2.2. RNA extraction

Total RNA including miRNA molecules was isolated from the tissue samples using a miRNeasy kit (Qiagen, Germany) closely following the manufacturer's recommendations. We started with 30 mg of tissue which was thoroughly homogenized in 750 μl QIAzol Lysis Reagent for 90 seconds. Thereafter, 140 μL of chloroform was added to tissue homogenate and after 5 minutes incubation at room temperature, the sample was centrifuged for 15 minutes at 12.000 rpm at 4 °C. The upper aqueous phase containing RNA was transferred and precipitated in a new Eppendorf tube by adding 1.5 volumes of 100% ethanol. Approximately 650 μL of the precipitated sample was transferred to a RNeasy Mini column placed in an appropriate collection tube and centrifuged at 12.000 rpm for 1 minute at room temperature. After centrifugation, the filtrate was discarded and then 700 μL wash buffer RW1 was pipetted and centrifuged at 12.000 rpm for 1 minute. Next, 500 μL of wash buffer RPE was pipetted and centrifuged at 12.000 rpm for 1 minute at room temperature. To dry the membrane, the column was centrifuged at maximum speed for 1 minute. Following this, the column was placed in a new tapered collection tube, and 30 μL RNase-free water was added and centrifuged at maximum speed for 1 minute to collect an eluate.

The purity and yield of the RNA solutions were assessed by measuring the optical density at 260/280 nm using a NanoDrop

Table 1

The mature miRNA sequences.

miRNA	Lot ID	Mature miRNA Sequence
hsa-miR-143	P170309-001 H08	GGUGCAGUGCUGCAUCUCUGGU
hsa-miR-145	P170206-005 H09	GGAUUCCUGGAAAUACUGUUCU
hsa-miR-92a	P161221-005 H03	UAUUGCACUUGUCCCGGCCUGU
hsa-miR-26b	P161118-006-G01	UUCAAGUAAUUCAGGAUAGGU
RNU44	P181019-000 G11	UAUUGCACUUGUCCCGGCCUG

One Spectrophotometer (Thermo Fisher Scientific, USA), where a ratio A260/A280 = 2 to 2.1, and A260/A230 > 2 was considered acceptable. The concentration of the samples was measured with Qubit 3.0 Fluorometer (Thermo Fisher Scientific) using the Qubit RNA HR (High-Range) Assay Kit. Furthermore, the RNA integrity number was conducted using the 2200 TapeStation Bioanalyzer (Agilent Technologies GmbH, Germany) with an RNA HS ScreenTape kit.

2.3. Reverse transcription of miRNA to complementary cDNA and qPCR reaction

Selected human miRNAs were reverse-transcribed to complementary DNA (cDNA) using the TaqMan MiRNA Reverse Transcription Kit (Applied Biosystems, San Diego, CA). Each reaction was initiated using an RNA-specific stem-looped for reverse transcription (RT) (Table 1). The RNA concentration was set between 1 to 10 ng per 15 μL of RT reaction. Each 15 μL RT reaction consist of 7 μL master mix (0.15 μL dNTP mix, 1 μL Multiscribe RT enzyme, 1.5 μL 10 x RT Buffer, 0.19 μL RNase inhibitor and 4.16 μL Nuclease-free water), 3 μL primer, and 5 μL RNA sample. Samples were incubated in a thermocycler with the following parameters: 16 °C for 30 minutes, 42 °C for 30 minutes, 85 °C for 5 mintes, and then cooled to 4 °C.

The complementary DNA strand for selected targets of miRNAs was synthesized using a specific sequence TaqManMGB Assay (Applied Biosystems, San Diego, CA). For the 20 μL reaction mix, 10 μL of TaqMan 2 × Universal PCR Master Mix was added to 1.33 μL of the product from the RT reaction, 7.67 μL of RNase-free dH_2O, and 1 μL of TaqMan Small RNA assay (20X). The quantitative real-time polymerase chain reaction analysis (qPCR) was performed in triplicate for each sample using the ABI 7500 Fast qPCR instrument for 40 cycles, where each cycle contained denaturation step at 95 °C for 3 seconds, and an annealing step at 60 °C for 30 seconds, followed by the extension of the primers with cleavage of the probe. Fluorescence was detected at the end of each cycle. A negative control without a template was used with all the qRT-PCR runs.

The average of cycle threshold (Ct) values obtained from triplicates of each miRNAs and endogenous control (miR-26b/RNU44) was calculated using an automatic baseline/threshold setting (7500 Fast Real-Time PCR software, version 2.3, Applied Biosystems, San Diego, CA) in concordance with the equation of Livak, Fold-change (FC) = $2^{-\Delta\Delta Ct}$, where $\Delta\Delta Ct = \Delta Ct\ (Ct_{miR\ target} - Ct_{miR26b/RUN44})_{tumoral\ tissue} - \Delta Ct\ (Ct_{miR\ target} - Ct_{miR26b/RNU44})_{normal\ tissue}$.[8] A fold change value <1 meant that the miRNAs were downregulated, where a value > 1 meant that the miRNAs were upregulated in the CRC relative to NATS. Thus, the results were expressed as FC in comparison with the calibrator sample, which was considered the normal value and assumed to equal 1.

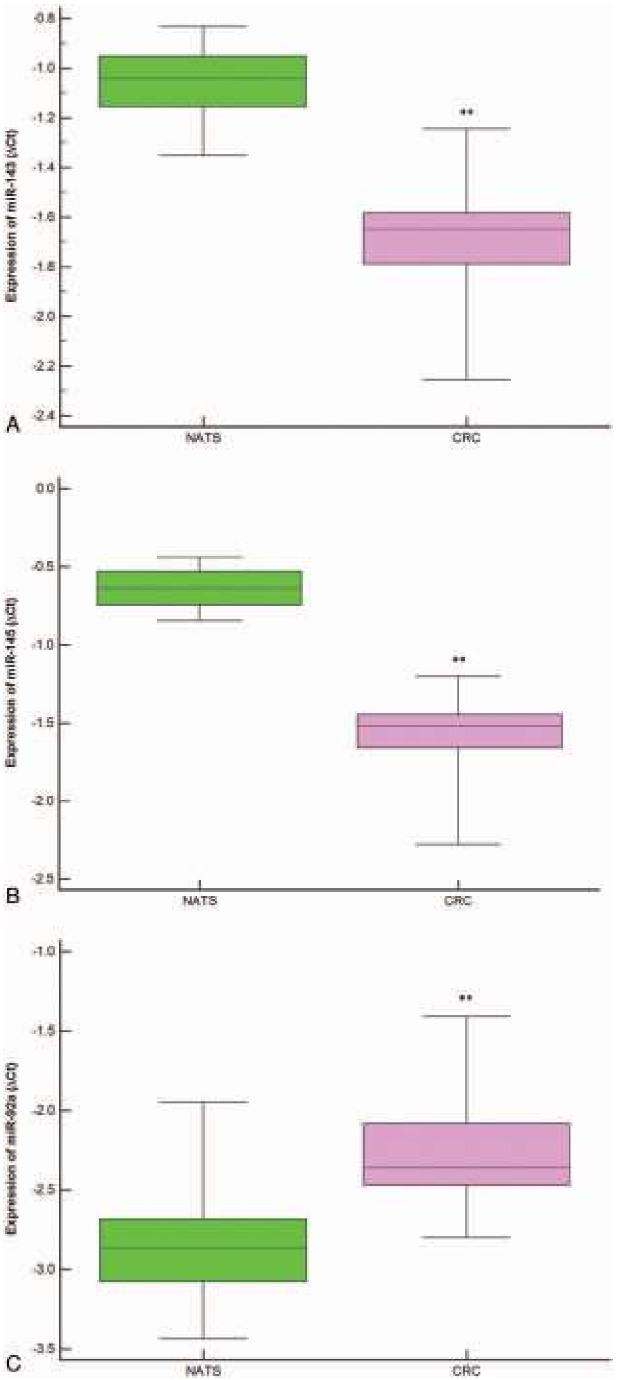

Figure 1. Expression levels of each microRNAs (ΔCt) in colorectal cancer tissue relative to normal adjacent tissue samples are normalized using RNU44 and miR-26b as endogenous controls. The statistically significant difference between colorectal cancer tissue and normal adjacent tissue samples samples was calculated using the Wilcoxon test ($^{**}P < .001$).

2.4. Statistical Analysis

Data obtained were analyzed and graphs were constructed using SPSS version 20.0 software (SPSS, Chicago, IL) and MedCalc version 19.0.3 software (MedCalc, Ostend, Belgium). Differences between CRC and NATS were analyzed by the Wilcoxon test, while correlations between miRNAs expression

Table 2

Analysis of miR-143, miR-145, and miR-92a with the clinicopathologic features of CRC patients.

Clinicopathological variables N (%)	FC⁺ miR-143 median (95% CI for median)	FC⁺ miR-145 median (95% CI for median)	FC⁺ miR-92a median (95% CI for median)
Age (yr)			
≤65–17 yr (20.73)	1.46 (0.81–2.24)	1.75 (1.50–2.66)	1.56 (0.85–1.97)
>65–65 yr (79.26)	1.60 (1.38–3.13)	2.08 (1.58–3.26)	2.00 (1.59–2.47)
Test statistic Z	–1.77	–1.24	–1.85
P-value (2-tailed)	.07†	.21†	.06†
Gender			
Female–38 (46.34)	1.46 (1.15–1.83)	2.13 (1.53–4.65)	1.76 (1.15–2.33)
Male–44 (53.65)	1.60 (1.39–3.13)	1.75 (1.51–2.87)	1.78 (1.56–2.24)
Test statistic Z	–1.04	0.95	–0.47
P-value (2-tailed)	.29†	.34†	.63†
Tumor location			
Proximal colon–30 (36.58)	1.60 (1.41–2.88)	2.08 (1.63–3.16)	2.07 (1.46–2.89)
Distal colon–30 (36.58)	1.54 (0.80–4.62)	2.77 (1.03–4.68)	2.77 (1.03–4.68)
Rectum–22 (26.84)	1.46 (1.06–2.03)	1.58 (1.26–2.07)	1.76 (0.97–3.08)
Test statistic Z	0.02	0.80	0.90
P-value (2-tailed)	.09‡	.31‡	.34‡
Tumor size			
≤5–59 cm (71.95)	1.94 (1.41–2.96)	2.13 (1.66–3.03)	1.73 (1.56–2.22)
>5 cm–23 cm (28.05)	1.41 (1.00–1.58)	1.58 (1.30–2.41)	1.74 (1.57–2.23)
Test statistic Z	1.41	0.98	–0.01
P-value (2-tailed)	.15†	.32†	1.01†
Histological grade			
G1–12 (14.63)	2.48 (0.81–3.13)	1.50 (1.25–3.21)	1.56 (1.27–2.25)
G2–60 (73.17)	1.56 (1.37–2.07)	1.75 (1.57–2.29)	1.76 (1.42–2.15)
G3–10 (12.20)	3.65 (1.05–46.3)	6.30 (1.08–27.06)	2.26 (1.79–5.18)
Test statistic Z	1.55	1.84	1.73
P-value (2-tailed)	.38‡	.13‡	.07‡
Depth of tumor invasion			
T1-T2–14 (17.07)	0.87 (0.66–1.38)	1.53 (0.79–1.89)	0.86 (0.68–1.35)
T3-T4–68 (82.93)	1.60 (1.37–2.96)	3.05 (1.70–3.39)	2.47 (2.11–2.97)
Test statistic Z	3.68	2.97	6.42
P-value (2-tailed)	<.001†	<.001†	<.001†
Nodal status			
N0–37 (45.12)	1.56 (1.15–1.67)	1.58 (1.38–1.88)	1.46 (0.82–1.87)
N1-N2–45 (54.87)	1.94 (1.35–4.63)	3.21 (2.07–9.76)	2.15 (1.77–2.56)
Test statistic Z	2.17	2.49	3.24
P-value (2-tailed)	.02†	<.01†	<.001†
Distant metastasis			
M0–49 (59.75)	1.54 (1.20–1.67)	1.63 (1.50–2.07)	1.58 (1.11–1.76)
M1–33 (40.24)	4.62 (1.23–7.02)	4.70 (1.60–12.47)	2.21 (2.01–2.91)
Test statistic Z	2.27	2.30	2.70
P-value (2-tailed)	.02†	.02†	<.001†

† Mann–Whitney *U* Test.
‡ Kruskal–Wallis H Test.
⁺ Fold change expression.
CI = 95% interval of confidence.

levels as well as clinicopathological features were examined using the Mann–Whitney *U* test for 2 independent groups and Kruskal–Wallis H test for three independent groups. Survival rates for each miRNA were estimated using the Kaplan–Meier method and differences between low and high expression were calculated by using log-rank tests. The diagnostic efficacy of selected miRNAs to function as prognostic biomarkers were evaluated by using Receiver operating characteristics (ROC). Similarly, the area under the curve(AUC) was plotted to assess to evaluate the power of selected miRNAs to functions as a diagnostic tool in order to discriminate CRC from NATS. Sensitivity and specificity were then defined by the optimal cut-off point, which refers to the maximized value of the area under the ROC (Youden index). The univariate prognostic analysis revealed the parameters which affected the prognosis of CRC patients, as miRNAs expression levels and clinicopathological characteristics.

3. Results

3.1. Dysregulated expression levels of miRNAs in tumors and NATS from CRC patients

In the present study, 82 patients with colorectal adenocarcinoma along with their NATS, were investigated. This included 30 of proximal colon cases, 30 of distal colon cases, as well as 22 of rectal cases. In order to evaluate the miRNAs expression patterns in tumor tissue, the quantitative reverse transcription real-time polymerase chain reaction (qRT-PCR) was used. Additionally, it was observed that miR-143 and miR-145 were down-regulated, whereas miR-92a was up-regulated (Fig. 1).

Consequently, the expression levels of miR-143 and miR-145 were found to decrease in 75.60% of CRC cases (–4.99 ± –1.02 vs –5.66 ± –1.66, $P < .001$) and 83% of cases, respectively (–4.85 ± –0.59 vs –9.27 ± –1.51, $P < .001$). On the other hand, the mean FC level expressions of miR-143 and miR-145 in CRC samples were downregulated around 8.21 times less and around 11.66 times less, respectively. In a similar vein, miR-92a expression level was upregulated in 78.00% of cases of CRC as compared to NATS (–5.55 ± –2.83 vs –4.92 ± –2.44, $P < .001$), with its fold increase being 2.32.

3.2. Selected miRNAs expression and association with clinicopathological characteristics

Associations with clinicopathological characteristics were determined in order to explore the clinical relevance of selected miRNAs. Some of these clinicopathological features were grouped, such as histological grade (G1, G2, and G3), pT stage (T1–T2 and T3–T4), pN stage (N0 and N1–N2) and pM stage (M0 and M1). As illustrated in Table 2, the higher expression of miR-92a was found to be closely associated with the depth of tumor invasion ($P = .03$), the involvement of regional lymph node ($P < .001$), and distant metastasis ($P < .001$).

In addition, expression levels of miR-143 and miR-145 were tended to be associated with late-stage tumor invasion ($P = .04$, $P < .001$, respectively), involvement of lymph's node ($P = .02$, $P < .001$, respectively) and with distant metastasis ($P < .001$) as illustrated in Figure 2.

Moreover, no significant statistical differences were observed between selected miRNAs expression levels and gender, age, locations of tumor, tumor size, or tumor differentiation, respectively.

3.3. Correlation between deregulated expression levels of miRNAs and prognosis of CRC patients

In our study, the survival condition of the patients was followed and recorded, beginning from surgery to death or until the date of the last observation (censored data). The follow-up period ranging from 12 to 60 months and was monitored through the Oncology Department. In accordance with the relative expression levels of miR-92a, miR-143, and miR-145, patients were divided based on median values into high-expression groups and low-expression groups. The median survival time in CRC patients with high expression levels of miR-92a was found to be 36 months, which was significantly statistically lower than that median survival time in the low expression group (51 months, $\chi 2 = 10.28$; $P < .01$) (Fig. 3).

In addition, the survival probability of 5 years in the high expression group of miR-143 was 48 months significantly higher than that in the low expression group (36 months, $\chi 2 = 4.43$; $P = .03$). Moreover, the median survival rates of CRC patients in the low expression group of miR-145 was 35 months, significantly lower than that in the high expression group (48 months, $\chi 2 = 7.05$; $P < .01$). According to the univariate analysis of the overall survival rate, the level of miR-92a expression was an independent prognostic indicator for CRC ($P < .01$, Table 3).

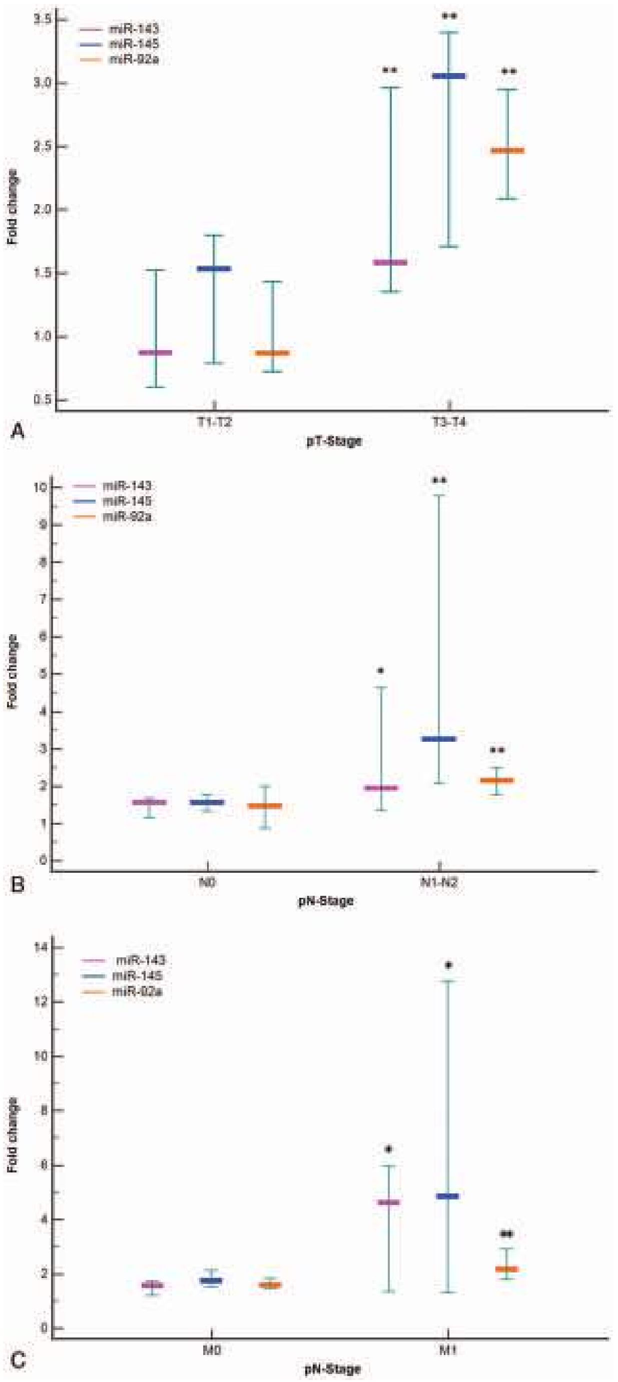

Figure 2. Fold change of miR-143, miR-145, and miR-92a in Romanian patients with colorectal cancer tissue according to different clinical stages. A boxplot showing fold change represented as median and 95% interval of confidence of the median, exhibited that the expressions of analyzed microRNAs increased with increasing pT stage- pT-stage (Fig. A), nodal metastasis - pN-stage (Fig. B), and distant metastasis - pM-stage (Fig. C). All experiments were conducted in triplicate ($^{*}P < .05$, $^{**}P < .001$).

3.4. ROC analysis

Analysis of the ROC curves and AUCs revealed that expression levels of miR-92a, miR-143, and miR-145 could help distinguish tumor tissue from normal adjacent tissues with very good specificity

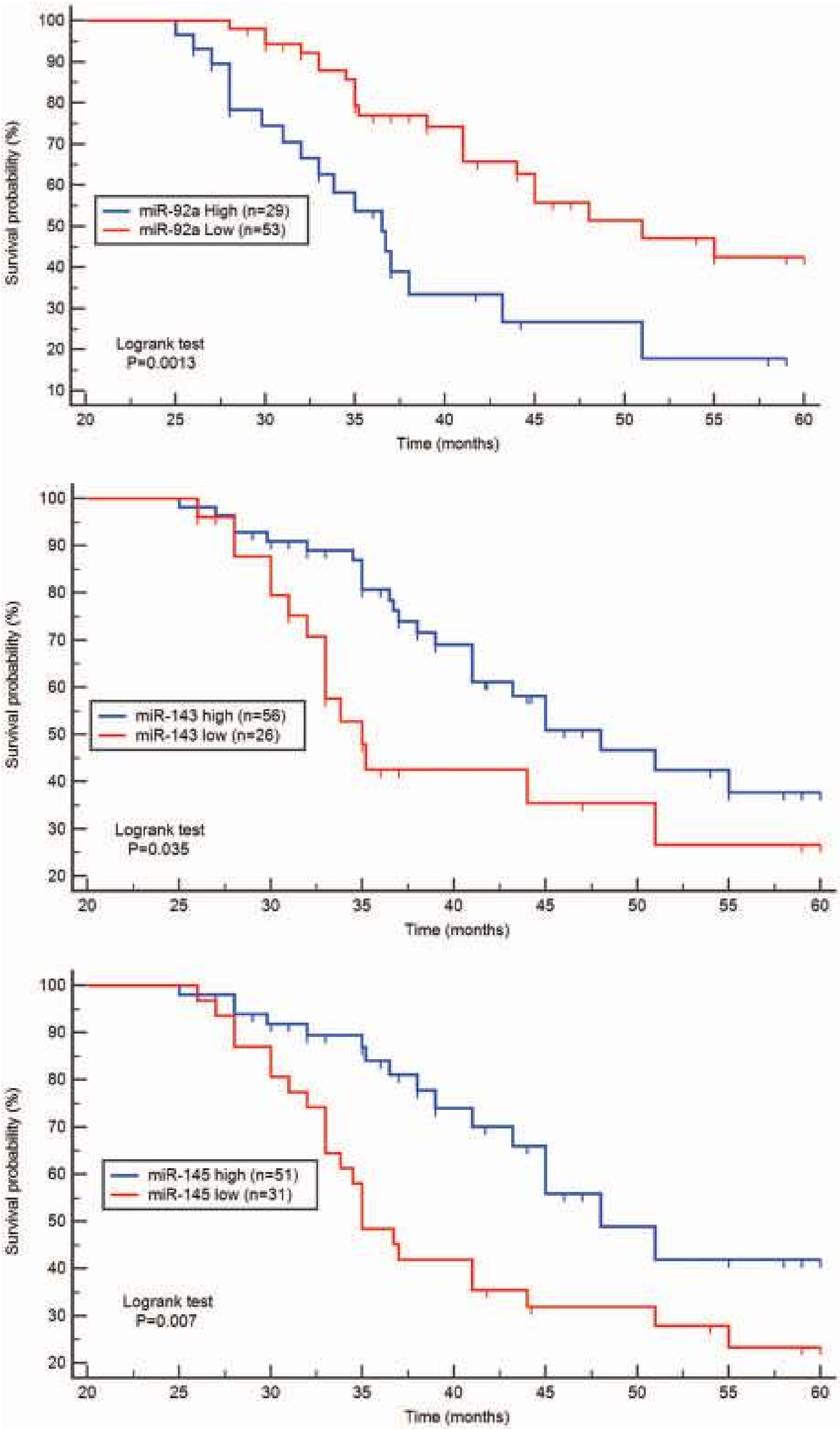

Figure 3. Kaplan–Meier survival curves for CRC patients. CRC patients with high miR-92a expression levels had a significant statistically poorer prognosis than those with low expression ($P<.001$). Moreover, the 5 yr survival probability in the low expression groups of miR-143 and miR-145 had a significant statistically poorer prognosis than in the high expression groups ($P<.01$, $P<.001$ respectively).

and sensitivity (Fig. 4). With regard to the AUC of miR-92a was 0.84 (95% interval of confidence (CI): 0.77 – 0.89, $P<.001$), the specificity was 80.49% and the sensitivity was 71.95% at a cut off value of 0.52. For miR-143 the specificity was 80.49% and the sensitivity was 60.98% at a cut off value of 0.41 and AUC of 0.74% (95% CI: 0.67 – 0.81, $P<.001$). Meanwhile the miR-145 exhibited a specificity of 85.37% and a sensitivity of 82.93% at a cut off value of 0.68 and AUC of 0.85 (95% CI: 0.78 – 0.91; $P<.001$).

Table 3

Logistic regression of prognostic values of microRNAs associated with the clinicopathological features in colorectal cancer tissue patients.

Parameters	Subset	HR	95% CI	*P*-value
Age	<65/>65 yr	1.05	1.01–1.09	<.01*
Gender	Female/Male	0.86	0.48–1.51	.60
Location of tumor	Proximal colon/distal colon/rectum	1.09	0.77–1.54	.60
Grading	G1/G2/G3	1.03	0.51–2.08	.91
pT	T1-T2/T3-T4	0.85	0.44–1.63	.62
pN	N0/N1-N2	1.10	0.78–1.55	.55
pM	M0/M1	1.29	0.64–2.60	.46
miR-143	Low/high expression	0.60	0.31–1.18	.14
miR-145	Low/high expression	0.90	0.44–1.82	.77
miR-92a	Low/high expression	0.27	0.13–0.54	<.01*

* *P*-values <.01 were considered significant statistically.
HR = hazard ratio, CI = 95% interval of confidence.

4. Discussion

CRC continues to be a major cause of mortality induced by cancer worldwide. However, since conventional strategies for CRC treatments have not yet been deemed satisfactory, and an ideal therapeutic target should be associated with the causality of disease. Over the past few decades, numerous studies and resources have identified the involvement of ncRNAs in carcinogenesis and tumor progression.[9] Among all types of ncRNAs, miRNAs have received particular attention and have been proposed as useful diagnostic and prognostic biomarkers. This is attributed to the fact that their profile of tumor tissue has been found to have a close association with a tissue of origin, due to their ability to resist degradation by endogenous ribonuclease, as well as their ease of quantitation involving several methods (e.g., qRT-PCR, microarray or sequencing technology).[10–13]

Dysregulated expressions of miRNAs with oncogenic or tumor suppressor activities have been reported in cancer development, metastasis, angiogenesis and drug resistance.[14,15] In CRC, a large variety of miRNAs are up- or down-regulated as compared to normal tissues. MiRNAs that are consistently found to be down-regulated in CRC act as tumor suppressor genes and are accordingly termed “mirsupps.” In contrast, miRNAs that are consistently found to be upregulated in CRC act as oncogenes and are referred to as “oncomirs”. Against this backdrop, studying the specific function of miRNAs in human carcinogenesis will help characterize new targets for cancer research, diagnosis, and treatment of cancer at the molecular level.

In the present study, we demonstrated that the expression profiles of miRNAs were significantly altered in the selected group of CRC patients from the south-eastern region of Romania. This was done by using the qRT-PCR method and miRNA specific hydrolysis probes TaqManMGB. Moreover, 2 miRNAs, namely, the miR-143 and miR-145, exhibited significantly lower expression, while 1 miRNA, namely the miR-92a, showed increased expression in CRC than in the NATS.

The miR-143 and miR-145 genes are situated in close proximity to each other in a ~1.7 kb region on chromosome 5q32-33. In addition, they are co-transcribed together from a single bicistronic unit, thereby suggesting that they originate from

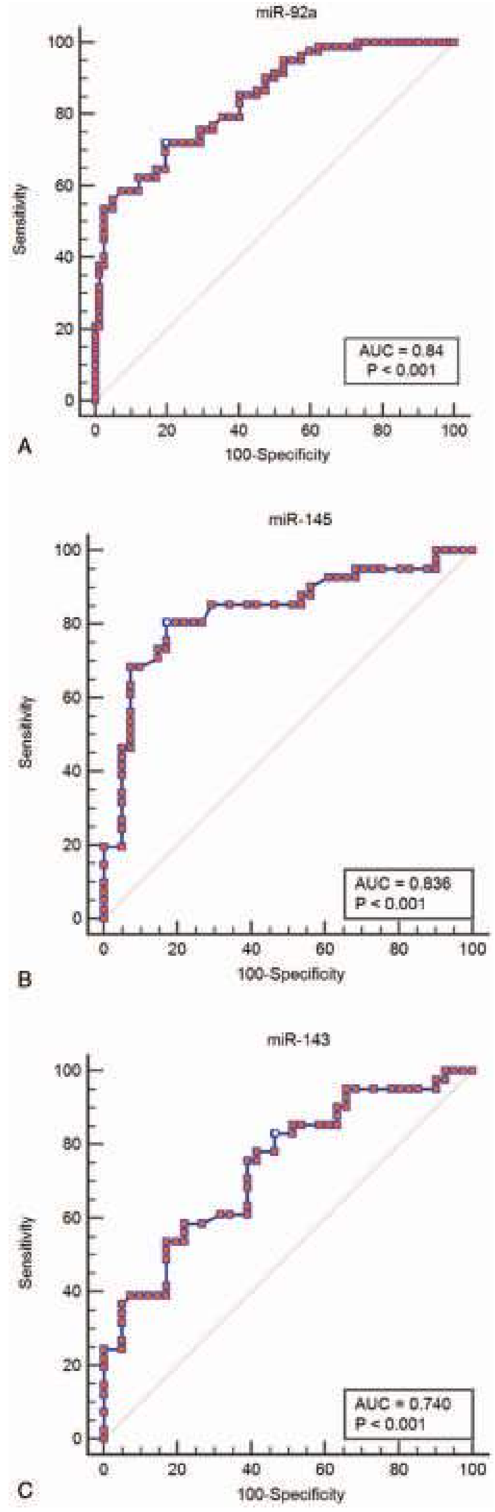

Figure 4. Receiver operating characteristic curves were analyzed to evaluate the miR-92a, miR-143, miR-145 expression levels as potential biomarkers in colorectal cancer tissue detection. area under the curve of upregulated miR-92a (A) expression was 0.84 (sensitivity: 71.95%, specificity: 80.49%; $P < .001$). For downregulated miR-145 (B), and miR-143 (C) expressions, the area under the curves were 0.85 (sensitivity: 82.93%, specificity: 85.37%; $P < .001$), and 0.74 (sensitivity: 60.98%, specificity: 80.49%, $P < .001$).

the same primary transcript and they could be involved in similar functions.[16] Michael et al were the first authors to report the correlation between miRNAs and CRC by uncovering the downregulation of miR-143 and miR-145 in both precancerous and cancer neoplasia tissues as compared to normal colon epithelium in CRC patients.[17]

In most studies, miR-143 and miR-145 have been presented as independent miRNAs and were not considered as concomitant re-expression genes. On the other hand, co-expression of both miRNAs has been shown to be an early event in the course of cancer development, with anti-oncogenic activities by targeting the same genes, or different genes that regulating the same pathway.[18] Functionally, miR-143/miR-145 cluster expression regulates cell proliferation and differentiation in the Lovo cells by inhibiting the KRAS gene.[19] It is notable that miR-143 and miR-145 could suppress cancer cell proliferation through target sites of the 3'-UTR of insulin-like growth factor 1 receptor and regulate their expression.[20]

In our study, an 8.21-fold decreased expression level of miR-143 in the colorectal samples was observed, as compared to the NATS. However, in the present study in consonance with other authors, we found a significant association between expression of miR-143 and different stages of CRC pathogenesis, including depth of invasion, lymph node metastasis, and distant metastasis.[21,22]

Also, miR-145 expression was decreased 11.66-folds in CRC tissue compared with NATS. Furthermore, we found that miR-145 expression was correlated with a depth of the tumor invasion, lymph node involvement, and distant metastases in CRC patients. Our observation that miR-143 and miR-145 were downregulated in CRC patients was confirmed by other reports.[23–26]

On the other hand, many studies had indicated that dysregulated miR-143, and miR-145 expressions in CRC, are often associated with the CRC progression, and metastasis, which may create a new opportunity to develop the ways of disease mechanism understand, and the potential diagnostic and/or the prognostic biomarkers. Moreover, our obtained results for the expression levels of these miRNAs from CRC samples, are suggesting their use as biomarkers for the diagnostic of the disease with a good performance indicators values (miR-143: 80.49% of specificity and 60.98% of sensitivity; miR-145: 85.37% of specificity and 82.93% of sensitivity, respectively). In addition, the 5 years survival probability time of CRC patients with low expression of miR-143 was shorter than that with the high expression of miR-143. The same difference in survival time was observed in patients with low expression of miR-143 who had a poor prognosis and it can be used as a potential indicator of CRC prognosis.

In CRC research, the role of miR-92a becomes important, as they belong to the miR-17-92 polycistronic cluster, which resides at chromosome 13q13, a region known to be frequently implicated in the proliferation of cancer cells, by suppressing carcinoma cells apoptosis whilst accelerating the progression of the tumor in CRC.[27] Abnormal expression of miR-92a has been known to play a decisive role in various diseases, including breast cancer, CRC, and leukemia.[22,28,29]

Meanwhile, the upregulation of miR-92a plays a pivotal role In CRC pathogenesis, which leads to up-regulation of β-catenin and vimentin, along with the down-regulation of E-cadherin during the regulation of epithelial-mesenchymal transition by specifically targeting phosphatase and tensin homolog, which denotes inhibitory enzyme that is known to block the pathway of PI3K/Akt.[30]

Our study showed that miR-92a was upregulated in CRC, noticing a 2.32-fold increase in colorectal tumors of patients as compared to usual adjacent tissue samples. Furthermore, heightened expression of miR-92a was found to have a significant correlation with the late stage of tumor invasion, lymph node metastasis, and development of distant metastasis in CRC patients.

According to the research carried out by Zhou et al, the upregulation of miR-92a has prognosis prediction in CRC patients; moreover, it was linked to worsening clinical variables and poor rate of survival.[31] Similar conclusions were drawn by our study, which demonstrated that the CRC patients mean survival time was 36 months with a high expression of miR-92a, which is significantly lower as compared to low expression 51 months, respectively. This implies the use of miR-92a as a potentially feasible indicator of prognosis CRC. Meanwhile, Chen et al showed that as an oncomir, diagnostic biomarker miR-92a plays a pivotal role in CRC. In addition, its regulating network may potentially facilitate the mechanism of CRC pathogenesis.[34] When it comes to distinguishing between NATS and CRS, the high specificity (80.49%) and sensitivity (71.95%) of miR-92a expression indicate the potential use of this miRNA as a potential biomarker for CRC diagnosis, which is in alignment with the views of earlier authors.[32,33]

Notably, our study has some limitations. First, because of the small number of cases investigated. The second limitation in agreement with the assumption that abnormal expression levels of selected messenger RNAs were examined only in tissue samples without matching their expression in cell cultures and sera. Therefore, further investigations are needed to confirm our findings.

5. Conclusion

In conclusion, we may summarize that patterns of selected miRNAs are differentially expressed in colorectal adenocarcinoma compared with their normal counterparts with 2 miRNAs decreased (miR-145 and miR-143) and 1 increased (miR-92). Furthermore, the expression levels of selected miRNAs were correlated with gradual increases in fold change expression with different stages of CRC pathogenesis, including depth of tumor invasion, lymph node invasion, and maximal increases with distant metastasis. In addition, ROC analysis and AUC demonstrates the ability of selected miRNAs to discriminating CRC from NATS with good performance of specificity and sensitivity. Prognosis indicators of CRC were also examined using Kaplan–Meier curves and the log-rank test which showed that 5-year overall survival of patients with a high level of miR-92a and low levels of miR-143 and miR-145 are significantly associated with poor prognosis in our cohorts.

Author contributions

All authors contributed equally to this study.
Conceptualization: Mariana Aşchie, Costel Brînzan, Anca Mitroi.
Data curation: Costel Brînzan.
Formal analysis: Costel Brînzan.
Investigation: Costel Brînzan, Anca Mitroi.
Methodology: Costel Brînzan, Anca Mitroi, Georgeta Cozaru.

Software: Costel Brînzan.
Supervision: Mariana Aşchie, Eugen Dumitru.
Validation: Georgeta Cozaru.
Writing – original draft: Costel Brînzan, Georgeta Cozaru.
Writing – review & editing: Costel Brînzan, Anca Mitroi, Eugen Dumitru.

References

[1] Siegel R, Desantis C, Jemal A. Colorectal cancer statistics. CA Cancer J Clin 2014;64:104–17.
[2] World Health Organization - cancer country profiles 2014, Romania, http://www.who.int/cancer/country-profiles/rou_en.pdf?ua=1MaL. Accessed November 25, 2019.
[3] Brînzan C, Aşchie M, Grasa CN, et al. The mutation profiles of Kras and Braf genes in a Romanian colorectal cancer cohort. Rev Chim 2019;70:1346–50.
[4] Brînzan C, Aşchie M, Matei E, et al. Molecular expression profiles of selected microRNAs in colorectal adenocarcinoma in patients from south-eastern part of Romania. Medicine 2019;98:e18122.
[5] Bartel DP. MicroRNAs: genomics, biogenesis, mechanism, and function. Cell 2004;116:281–97.
[6] Almeida MI, Reis RM, Calin GA. MicroRNA history: discovery, recent applications, and next frontiers. Mutat Res 2011;717:1–8.
[7] Edge SB, Byrd DR, Compton CC, et al. AJCC cancer staging manual-seventh edition. Springer 2010;7:143–59.
[8] Livak KJ, Schmittgen TD. Analysis of relative gene expression data using real-time quantitative PCR and the 2(-delta delta C(T)) method. Methods 2001;25:402–8.
[9] Seton-Rogers S. Non-coding RNAs: the cancer X factor. Nat Rev Cancer 2013;13:224–5.
[10] Xiao B, Guo J, Miao Y, et al. Detection of miR-106a in gastric carcinoma and its clinical significance. Clin Chim Acta 2009;400:97–102.
[11] Schetter AJ, Leung SY, Sohn JJ, et al. MicroRNA expression profiles associated with prognosis and therapeutic outcome in colon adenocarcinoma. JAMA 2008;299:425–36.
[12] Calin GA, Croce CM. MicroRNA signatures in human cancers. Nat Rev Cancer 2006;6:857–66.
[13] Waldman SA, Terzic A. Translating microRNA discovery into clinical biomarkers in cancer. JAMA 2007;297:1923–5.
[14] Esquela-Kerscher A, Slack FJ. Oncomirs- microRNAs with a role in cancer. Nat Rev Cancer 2006;6:259–69.
[15] Tong AW, Nemunaitis J. Modulation of miRNA activity in human cancer: a new paradigm for cancer gene therapy? Cancer Gene Ther 2008;15:341–55.
[16] Cordes KR, Sheehy NT, White MP, et al. MiR-145 and miR-143 regulate smooth muscle cell fate and plasticity. Nature 2009;460:705–10.
[17] Michael MZ, O' Connor SM, van Holst Pellekaan NG, et al. Reduced accumulation of specific microRNAs in colorectal neoplasia. Mol Cancer Res 2003;1:882–91.
[18] Sempere LF, Christensen M, Silahtaroglu A, et al. Altered microRNA expression confined to specific epithelial cell subpopulations in breast cancer. Cancer Res 2007;67:11612–20.
[19] Chen X, Guo X, Zhang H, et al. Role of miR-143 targeting KRAS in colorectal tumorigenesis. Oncogene 2009;28:1385–92.
[20] Su J, Liang H, Yao W, et al. MiR-143 and miR-145 regulate IGF1R to suppress cell proliferation in colorectal cancer. PLoS One 2014;9:e1144–220.
[21] Secil AK, Tunca B, Tezcan G, et al. MicroRNA expression patterns of tumors in early-onset colorectal cancer patients. J Surg Res 2014;191:113–22.
[22] Nishida N, Nagahara M, Sato T, et al. Microarray analysis of colorectal cancer stromal tissue reveals upregulation of two oncogenic miRNA clusters. Clin Cancer Res 2012;18:3054–70.
[23] Akao Y, Nakagawa Y, Hirata I, et al. Role of anti-oncomirs miR-143 and -145 in human colorectal tumors. Cancer Gene Ther 2010;17:398–408.
[24] Bandres E, Cubedo E, Agirre X, et al. Identification by real-time PCR of 13 mature microRNAs differentially expressed in colorectal cancer and non-tumoral tissues. Mol Cancer 2006;5:29.
[25] Lanza G, Ferracin M, Gafa R, et al. MRNA/microRNA gene expression profile in microsatellite unstable colorectal cancer. Mol Cancer 2007;6:54.
[26] Cummins JM, He Y, Leary RJ, et al. The colorectal microRNAome. Proc Natl Acad Sci USA 2006;103:3687–92.
[27] Wang LG, Gu J. Serum microRNA-29a is a promising novel marker for early detection of colorectal liver metastasis. Cancer Epidemiol 2012;36:e61–7.
[28] Sharifi M, Salehi R, Gheisari Y, et al. Inhibition of microRNA miR-92a induces apoptosis and necrosis in human acute promyelocytic leukemia. Adv Biomed Res 2014;3:61.
[29] Si H, Sun X, Chen Y, et al. Circulating microRNA-92a and microRNA-21 as novel minimally invasive biomarkers for primary breast cancer. J Cancer Res Clin Oncol 2013;139:223–9.
[30] Lu C, Shan Z, Hong J, et al. MicroRNA-92a promotes epithelial-mesenchymal transition through activation of PTEN/PI3K/AKT signaling pathway in non-small cell lung cancer metastasis. Int J Oncol 2017;51:235–44.
[31] Zhou T, Zhang G, Liu Z, et al. Over expression of miR-92a correlates with tumor metastasis and poor prognosis in patients with colorectal cancer. Int J Colorectal Dis 2013;28:19–24.
[32] Yang X, Zeng Z, Hou Y, et al. MicroRNA-92a as a potential biomarker in diagnosis of colorectal cancer: a systematic review and meta-analysis. PLoS One 2014;9:e88745.
[33] Chang PY, Chen CC, Chang YS, et al. MicroRNA-223 and microRNA-92a in stool and plasma samples act as complementary biomarkers to increase colorectal cancer detection. Oncotarget 2016;7:10663–75.
[34] Chen E, Li Q, Wang H, et al. MiR-92a promotes tumorigenesis of colorectal cancer, a transcriptomic and functional based study. Biomed Pharmacother 2018;106:1370–7.

Observational Study

Medicine® OPEN

Molecular expression profiles of selected microRNAs in colorectal adenocarcinoma in patients from south-eastern part of Romania

Costel Brînzan, PhD[a,b], Mariana Aşchie, MD, PhD[b,a], Elena Matei, PhD[b], Anca Mitroi, MD, PhD[a,b,*], Georgeta Cozaru, MD, PhD[a,b]

Abstract

MicroRNAs (miRNAs) are endogenous, non-coding class of RNAs with functions in the regulation of genes expressions. Dysregulated expressions of miRNAs play important roles in carcinogenesis and cancer progression by targeting various oncogenes and tumor-suppressor genes. miRNAs represent a new field for molecular diagnosis and prognosis of colorectal cancer (CRC) due to their high tissue specificity, their stability, and their dysregulated expression in tumor development.

This study aimed to investigate using the qRT-PCR method the expression profile and prognostic value of 11 mature miRNAs in a cohort of 82 Romanian patients diagnosed with CRC. The relationship between the expression levels of selected miRNAs and clinicopathologic features were evaluated using ANOVA and Pearson test. In addition, the receiver operating characteristic (ROC) and area under the curve (AUC) were used to assess the diagnostic values of the miRNAs to discriminate cancerous from non-cancerous states of the samples.

The expression levels of miR-30c, miR-144, miR-375, miR-214, and miR-195 in CRC tissue were significantly downregulated (all $P < .05$; Paired T-Test) than that in normal adjacent tissue sample (NATS), while the expression of miR-141, miR-182, miR-183, miR-21, and miR-370 in CRC tissue were significantly upregulated (all $P < .001$) than that in NATS. Moreover, the expression levels of miR-182, miR-183, miR-141, and miR-21 were demonstrated to be associated with a gradual increase in fold change expression with depth of tumor invasion (all $P < .05$), lymph node invasion (all $P < .001$), and maximal increase with distant metastasis (all $P < .001$). Moreover, the analysis of ROC curves revealed that AUC (95% CI) of miR-182, miR-183, miR-141, and miR-21 in diagnosis of CRC was 0.76 (0.66–0.87), 0.85 (0.78–0.94), 0.77 (0.62–0.92), 0.83 (0.73–0.90), respectively. The univariate and multivariate Cox-proportional hazard regression for all variables revealed that the nodal status, distant metastasis, miR-21, miR-141, miR-182, and miR-183 were independent prognostic markers of CRC.

In conclusion, altered expressions of miR-21, miR-141, miR-182, and miR-183 in CRC varies at different stages of CRC development and may serve as potential diagnosis molecular biomarkers in Romanian patients with CRC. Further investigations are needed to confirm our findings.

Abbreviations: AJCC = American Joint Committee on Cancer, AUC = area under the curve, Cdc25a = cell division cycle 25 homolog A, CI = 95% interval of confidence, CRC = colorectal cancer, EMT = epithelial to mesenchymal transition, FC = fold change, miRNA = microRNA, miRNAs = microRNAs, mRNA = messenger RNA, NATS = normal adjacent tissue samples, NPV = negative predictive value, PDCD4 = programmed cell death4, PPV = positive predictive value, PTEN = phosphatase and tensin homolog, qRT-PCR = real-time quantitative polymerase chain reaction analysis, RECK = reversion-inducing cysteine-rich protein with kazal motifs, RIN = RNA integrity number, ROC = receiver operating characteristic, RT = room temperature, TNM = tumor-node-metastasis, TPM1 = tropomyosin 1, UTR = 3′ noncoding region, WHO = World Health Organization, ZEB1/2 = E-box-binding homeobox factors.

Keywords: colorectal, depth of tumor invasion, distant metastasis, lymph node, miRNAs, qRT-PCR

Editor: Chun Gao.

All authors made an equal contribution and share the first authorship.

The authors declare no conflict of interests.

[a] *Pathology Department, Sf. Apostol Andrei Clinical Emergency County Hospital Constanta,* [b] *CEDMOG Center, Ovidius University, Constanta, Romania.*

[*] *Correspondence: Anca Mitroi, Spitalul Clinic Judetean De Urgenta Constanta Constanta, Romania (e-mail: ank_mitroi@yahoo.com).*

How to cite this article: Brînzan C, Aşchie M, Matei E, Mitroi A, Cozaru G. Molecular expression profiles of selected microRNAs in colorectal adenocarcinoma in patients from south-eastern part of Romania. Medicine 2019;98:47(e18122).

Received: 12 June 2019 / Received in final form: 9 October 2019 / Accepted: 28 October 2019

http://dx.doi.org/10.1097/MD.0000000000018122

1. Introduction

Colorectal cancer (CRC) is one of the most common types of malignant tumors. Worldwide, CRC poses a major threat to human life and continues to be a significant economic burden.[1] The incidence of CRC is 9.7%, making it the third most common form of cancer after lung and breast cancers and the fourth leading cause of death.[2] According to the results of the Global Burden of Cancer reports, CRC is the second most common malignancy in Romania, after lung cancer in men and breast cancer in women, with 8.660 new cases diagnosed in 2012.[3] Although, in recent years, substantial progress has been made in the prevention, diagnosis, and treatment options as a result of improved clinical management and treatment efficiency. However, CRC remains a public health issue due to the increased prevalence of risk factors associated with Westernization, including unhealthy diets, obesity, and smoking.[2] Colorectal carcinogenesis is linked to the activation of oncogene gene-signaling pathways and the inactivation of tumor suppressor genes, mainly due to genetic mutation and epigenetic changes, including germline or somatic mutation, DNA methylation, histone acetylation, and the involvement of noncoding RNAs, such as those of microRNAs (miRNAs) and long noncoding RNAs.[4]

The discovery of miRNAs took place in the early 1990s when Ambrose et al identified a small RNA that exerted regulatory functions on a specific messenger RNA (mRNA), resulting in the suppression of its action.[5] miRNAs form a class of small, single-stranded, highly conserved, noncoding RNA molecules containing approximately 19 to 24 nucleotides. They bind directly to the 3' noncoding region (UTR) of the target mRNA and act as negative regulators in the expression of the majority of human protein-coding genes.[6]

Currently, a total of 1917 annotated human miRNA precursor genes have been identified, which are processed into ~2654 mature sequences (http://www.mirbase.org), and are able to regulate the expression of one-third of the human genome. miRNAs bind to their mRNA targets by achieving an almost perfect complementarity between the base pairs. A perfect match between base pairs is essential only in the central region of the miRNA and mRNA target to enable the degradation and destabilization or inhibition of mRNA translation and the suppression of the gene expression.[7]

The role of miRNAs in cancer development is well studied, but their biogenesis and mode of action have not yet been fully elucidated. However, it is known that miRNA mediates translation repression and is involved in almost all cellular processes (e.g., proliferation, differentiation, development, cell cycle regulation, metabolism, apoptosis, and carcinogenesis).[8] Pathological alterations in the expression of miRNAs are commonly associated with the occurrence of various diseases, and their expression patterns are used to diagnose various types of cancer, such as breast, lung, pancreatic, and ovarian cancer, as well as colorectal carcinoma.[9–13]

Specific miRNA expressions patterns help distinguish cases of CRC from other colon-related diseases, where they may function either as tumor suppressor or oncogenic genes; however, the mechanisms underlying their potential involvement in proliferation and tumor cell survival are unclear.[14]

In the present study, we aimed to analyze the expression of 11 mature humans miRNA species in colorectal cancer tissues and normal adjacent tissue samples (NATS) collected from 82 Romanian patients and to further explore their association with clinicopathological features. We also examined the ability of selected miRNAs to function as potential biomarkers, discriminating between CRC and NATS states of samples. The miRNAs were selected from a literature review based on their clinical relevance to the complex mechanisms of carcinogenesis.[22–28]

2. Material and methods

2.1. Case selection

Tumor samples with paired adjacent normal tissues (harvested at >5 cm from the cancer tissue) were collected from 82 patients diagnosed with CRC at the Clinical Emergency County Hospital in Constanta, Romania. The study was approved by the Local Ethics Commission for the Approval of Clinical and Research Developmental Studies and informed consent was signed by all patients. Specimens were processed and evaluated by an experienced pathologist according to standard protocols, and only adenocarcinoma types were selected for the miRNA expression analysis. All samples were preserved in RNAlater solution until the total RNA was extracted. The tumor staging of the cancer was classified using the tumor-node-metastasis (TNM) staging system of the American Joint Committee on Cancer (AJCC), in accord with World Health Organization (WHO) standards.[15] The clinicopathological features of the CRC patients were obtained from observation sheets and pathology reports, including age, gender, tumor location, tumor type, tumor size, TNM stage, tumor grade, and eventual metastasis.

2.2. RNA isolation

Small RNA molecules were isolated from the CRC and NATS by using a miRNeasy kit (Qiagen, Germany) according to the manufacturer's instructions. About 30 mg of tissue was homogenized in 700 μlQIAzol lysis buffer for 90 seconds. After 5 minutes of incubation at room temperature (RT), 140 μl chloroform was added and it was centrifuged for 15 minutes at 12.000 rpm at 4°C. The upper aqueous phase was transferred and precipitated in a new Eppendorf tube by the addition of 530 μl 100% ethanol. Approximately 700 μl of the precipitated sample was transferred to a RNeasy Mini column and centrifuged at 12.000 rpm for 1 minute at RT. After centrifugation, the filtrate was discarded and then 700 μl wash buffer 1 was pipetted and centrifuged at 12.000 rpm for 1 minute. Next, 500 μl wash buffer 2 was pipetted and centrifuged at 12.000 rpm for 1 minute at RT. The column was then placed in a new tapered collection tube, and 30 μLRNase-free water was added and centrifuged at maximum speed for 1 minute to collect an eluate.

The purity of the RNA solutions was assessed by measuring the optical density at 260/280 nm using a NanoDrop One Spectrophotometer (Thermo Fisher Scientific, Waltham, MA, USA). The concentration of the samples was measured using the Qubit3.0 (Thermo Fisher Scientific, Waltham, MA, USA), and RNA integrity number (RIN) was conducted using 2200 TapeStation Bioanalyzer (Agilent Technologies GmbH, Waldbronn, Germany) with an RNA ScreenTape kit.

2.3. Reverse transcription of miRNA to complementary cDNA and qRT-PCR

miRNA molecules were reverse transcribed to complementary DNA (cDNA) using the TaqMan MicroRNA Reverse Transcription Kit (Applied Biosystems, San Diego, CA). Each reaction was initiated using a miRNA-specific stem-looped RT primer, with the aim of prolonging the target of the miRNAs from ~22 bp to over 60 bp (Table 1). The RNA concentration was set between 1 and 10 ng in a final volume of 15 μl of the reaction mixture used. Reverse transcription reagents were combined with total RNA and incubated in a thermocycler with the following parameters: 16°C for 30 minutes, 42°C for 30 minutes, 85°C for 5 minutes, and then cooled to 4°C.

In the second step, the complementary cDNA strand was synthesized using TaqManMicroRNA Assays Inventoried (Applied Biosystems, San Diego, CA). For the 20 μl reaction mix, 10 μl of TaqMan 2 × Universal PCR Master Mix was added to 1.33 μl of the product from the reverse transcription reaction, 7.67 μl of RNase-free dH_2O, and 1 μl of TaqMan microRNA assay. The real-time quantitative polymerase chain reaction analysis (qRT-PCR) was performed in triplicate for each sample using the ABI 7500 Fast qPCR instrument for 40 cycles, where each cycle contained a denaturation step at 95°C for 3 seconds, and an annealing step at 60°C for 30 seconds, followed by the extension of the primers with cleavage of the probe. Fluorescence was detected at the end of each cycle. A negative control without a template was used with all the qRT-PCR runs.

The Ct fluorescent level of each miRNAs was calculated using an automatic baseline/threshold setting (7500 Fast Real-Time PCR software, version 2.3) in concordance with the equation $2^{-\Delta\Delta Ct}$, which represents the fold change (FC) between samples.[16] The miR-26b and miR-92N were selected as reference genes in our experiments, and both were found to be stably expressed in all samples. An FC value < 1 meant that the miRNAs were downregulated. An FC value > 1 meant that the miRNAs were upregulated in the cancer tissue relative to the normal mucosa. Thus, the results were expressed as FC in comparison with the calibrator sample, which was considered the normal value and assumed to equal 1.

2.4. Statistical analysis

Results obtained were analyzed with SPSS version 20 software and GraphPad Prism version 8.0 software. Paired-Samples T Tests were applied to determine the statistical difference of miRNA species between CRC and NATS. Differences between miRNA expression levels and clinicopathological features of colorectal cancer were analyzed using 2 tests (One-Way ANOVA and Pearson correlations), where *P* value <.05 was considered to be statistically significant. Furthermore, univariate and multivariate Cox-proportional hazard regression were performed to determine the prognostic values of selected miRNA expressions and the clinicopathological features in CRC patients. Receiver operating characteristic (ROC) and area under the curve (AUC) were used to evaluate the sensitivity and specificity and to establish the accuracy of the biomarkers in CRC diagnosis. We defined the sensitivity and specificity of the optimal threshold cut-off point as the values that maximized the area under the ROC curve.

Table 1

The mature miRNA sequence.

miRNA	Mature miRNA Sequence
hsa-miR-30c	UGUAAACAUCCUACACUCUCAGC
hsa-miR-182	UUUGGCAAUGGUAGAACUCACACU
hsa-miR-183	UAUGGCACUGGUAGAAUUCACU
hsa-miR-21	UAGCUUAUCAGACUGAUGUUGA
hsa-miR-195	UAGCAGCACAGAAAUAUUGGC
hsa-miR-144	GGAUAUCAUCAUAUACUGUAAG
hsa-miR-141	CAUCUUCCAGUACAGUGUUGGA
hsa-miR-375	UUUGUUCGUUCGGCUCGCGUGA
hsa-miR-370	GCCUGCUGGGGUGGAACCUGGU
hsa-miR-214	UGCCUGUCUACACUUGCUGUGC
hsa-miR-299	UAUGUGGGAUGGUAAACCGCUU
hsa-miR-92N	UAUUGCACUUGUCCCGGCCUG
hsa-miR-26b	UUCAAGUAAUUCAGGAUAGGU

3. Results

3.1. miRNAs expressions in tumor and normal adjacent tissue samples from CRC patients

Among the 82 patients included in our study, 42 patients (51.21%) were males and 40 patients (48.78%) were females; between 48 years and 89 years with a median age of 63.00 years. The tumor site location was the proximal colon for 36.58% of patients (n = 30), the distal colon for 34.14% of cases (n = 28), and the rectum for 29.26% of cases (n = 24).

When the miRNA expressions were compared in the CRC relative to the NATS, 5 miRNAs (miR-21, miR-141, miR-182, miR-183, and miR-370) were found to be overexpressed, and 6 (miR-30c, miR-144, miR-375, miR-214, miR-195, and miR-299) were found to be underexpressed in the CRC samples (Fig. 1). The overexpressions of miR-182, miR-183, and miR-370 and the underexpressions of miR-30c, miR-375, and miR-195 presented the most significant changes in expression.

Among the miRNAs that were overexpressed in the CRC samples, miR-21 was overexpressed in 84% of cases (69/82; *P* = .02), miR-141 in 75% of cases (62/82; *P* = .02), miR-182 in 92% of cases (76/82; *P* < .001), miR-183 in 90% of cases (74/52; *P* < .001), and miR-370 in 86% of cases (71/82; *P* < .001, Table 2). The mean FC level expressions of miR-182, miR-183 and miR-370 in the tumor samples as compared to the NATS were the most significantly overexpressed. Indeed, miR-182 was expressed by about 4.3 times, miR-183 by about 6.1 times, and miR-370 by about 6.0 times, whereas the miR-141 overexpression was only 1.86 times.

Quantification analyses were shown that levels of miR-30c, miR-144, miR-375, miR-214, miR-195, and miR-299 were significantly downregulated in CRC relative to NATS. Thus miR-30c was underexpressed in 75% of cases (62/82; *P* < .001), miR-144 in 75% of cases (62/82; *P* = .04), miR-375 in 78% of cases (64/82; *P* < .001), miR-214 in 70% of cases (58/82; *P* = .04), miR-299 in 73.1% of cases (60/82; *P* = .32), and miR-195 in 90% of cases (74/82; *P* < .001). The mean FC level expressions of miR-375, miR-195, and miR-144 in tumor samples were the most underexpressed. Indeed, miR-375 was downregulated by about 38.1 times, miR-195 by about 4.6 times, and miR-144 was expressed 2.2 times less frequently in the tumor samples as compared to the NATS. The relative expression ratio for miR-299 suggested that it was also underexpressed in CRC by about 1.7 times; however, the statistical analysis did not reveal any significant differences.

3.2. Correlations between expression of miRNAs and clinicopathological features of CRC patients

Expression of selected miRNAs in CRC patients was not significantly correlated with age, gender, tumor size, tumor grade, and tumor locations. Among all miRNAs studied, we

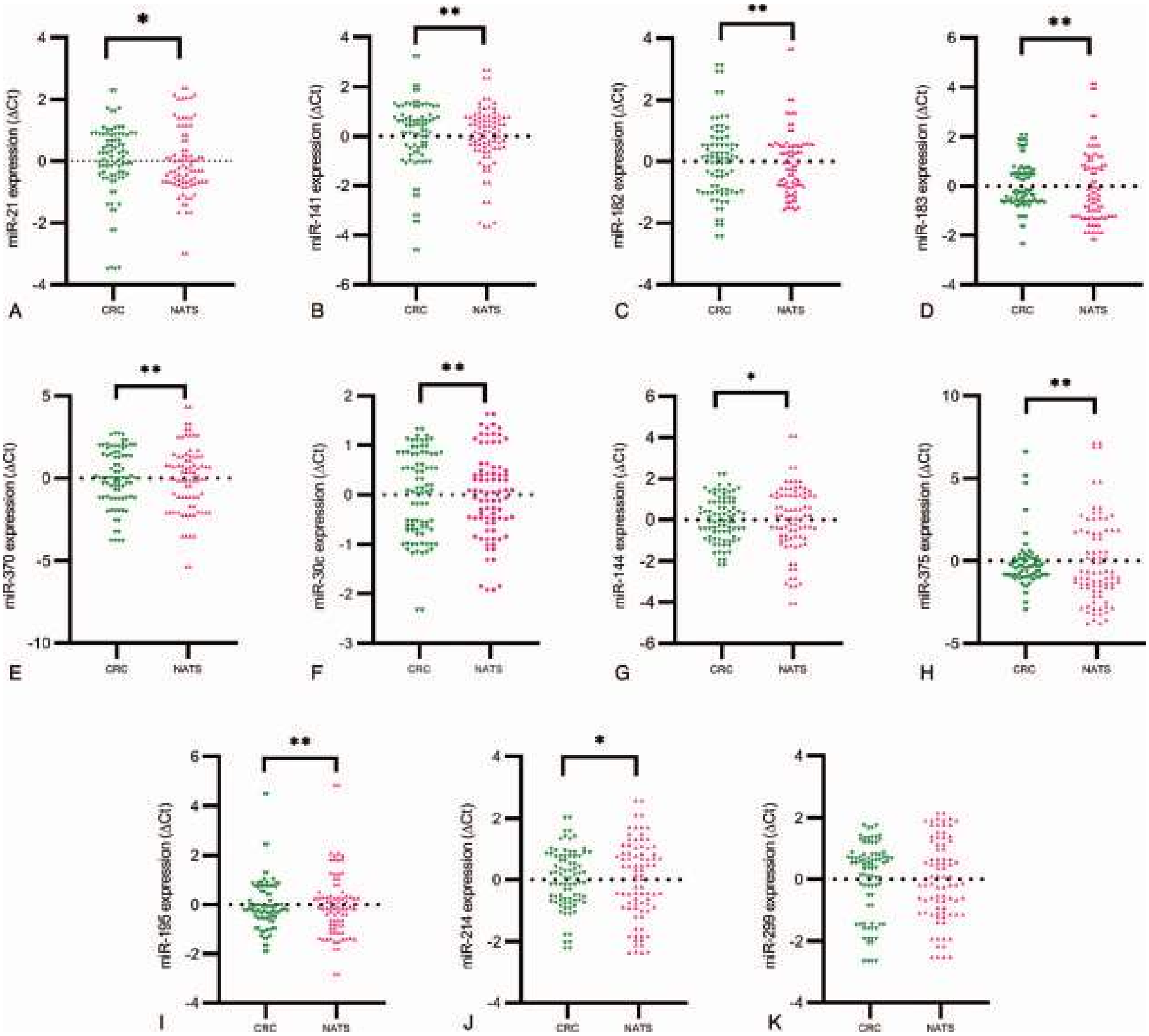

Figure 1. Dots-plot showing the results of deregulated miRNAs' expressions in colorectal cancer tissue (CRC) in relation to normal adjacent tissue samples (NATS). ΔCt values of upregulated miRNAs' expression: (A) miR-21, (B) miR-141, (C) miR-182, (D) miR-183, (E) miR-370. Downregulated miRNAs' expressions levels (ΔCt): (F) miR-30c, (G) miR-144, (H) miR-375, (I) miR-195, (J) miR-214, and (K) miR-299. The statistical difference ranks between the two groups, were calculated using Paired-Samples T-Test, were *$P < .05$, **$P < .001$.

Table 2

MiRNAs overexpressed or underexpressed in CRC relative to NATS.

miRNA species	Relative expression[*] in NATS[§] (Mean ± SD)	95% CI[§] of the difference in NATS[§] Lower	Upper	Relative expression[*] in CRC[‡] (Mean ± SD)	95% CI[§] of the difference in CRC[‡] Lower	Upper	Fold increase/ decrease in CCR[†]	*P* value
miR-141	−0.43 ± 0.86	−0.70	0.16	0.01 ± 0.95	−0.28	0.31	1.86	.02
miR-21	−3.11 ± 1.14	−3.48	2.74	−2.25 ± 1.22	−2.65	1.86	3.21	.02
miR-182	7.2 ± 1.07	6.89	7.56	8.69 ± 1.22	8.30	9.07	4.34	<.001
miR-183	7.29 ± 1.99	6.58	7.99	8.93 ± 1.11	8.54	9.33	6.16	<.001
miR-370	8.92 ± 2.05	8.19	9.64	10.5 ± 1.73	9.94	11.1	6.07	<.001
miR-30c	1.55 ± 0.86	1.28	1.82	0.90 ± 0.82	0.62	1.18	1.91	<.001
miR-144	10.0 ± 1.75	9,48	10.5	9.29 ± 1.39	8.86	9.73	2.29	.04
miR-375	2.55 ± 2.64	1.72	3.39	0.52 ± 1.86	−0.06	1.11	38.1	<.001
miR-214	7.61 ± 1.27	7.21	8.02	7.11 ± 0.96	6.81	7.42	1.96	.04
miR-299	10.2 ± 1.27	9.78	10.6	9.85 ± 1.09	9.48	10.21	1.76	.32
miR-195	9.97 ± 1.29	9.56	10.3	8.51 ± 0.80	8.25	8.76	4.65	<.001

[*] ΔCT;

[†] $2^{-\Delta\Delta CT}$;

[‡] Colorectal cancer;

[§] Normal adjacent tissue sample;

[†] Confidence interval.

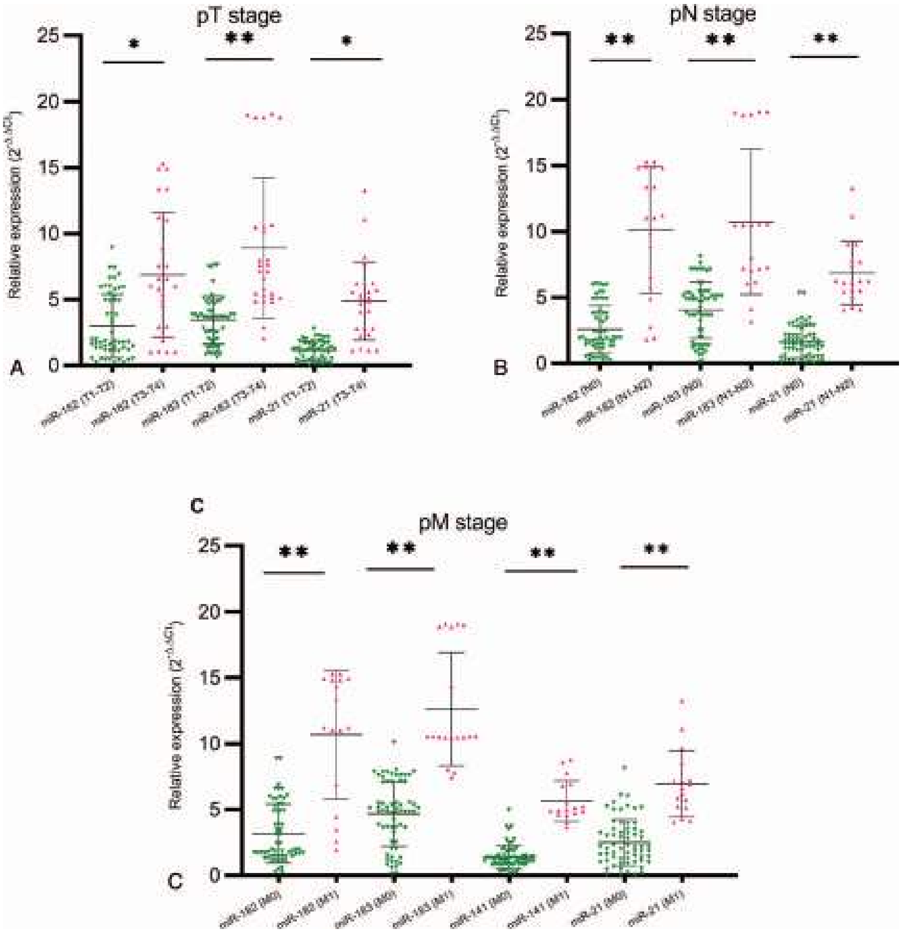

Figure 2. Fold change of the 4 miRNAs genes in Romanian patients with CRC at different clinical stages. The dot plots (using $2^{-\Delta\Delta Ct}$ method) represent mean ± standard deviation of miR-182, miR-183, miR-141, and miR-21 according to the depth of tumor invasion - pT-stage (Fig. A), nodal metastasis - pN-stage (Fig. B), and distant metastasis - pM-stage (Fig. C). All experiments were conducted in triplicate (*$P < .05$**$P < .001$).

found that the miR-183, miR-182, miR-141, and miR-21 levels were positively correlated with some clinicopathological characteristics (Fig. 2 and Table 3).

The ANOVA test indicated a tendency of associations between higher expression of miR-182 in CRC tissue relative to NATS in advanced T stages (T3–T4: 6.85 ± 4.70 vs T1–T2: 2.90 ± 2.30; $P = .02$), with the metastasis stage (M1: 10.14 ± 5.76 vs M0: 3.04 ± 2.13; $P < .001$), and nodal status (N1–N2: 10.13 ± 4.82 vs N0: 2.57 ± 1.82; $P < .001$). In addition, miR-183 expression was significantly higher in advanced tumor stages (T3–T4: 8.26 ± 3.58 vs T1–T2: 3.44 ± 2.23; $P < .001$), lymph node metastasis (N1–N2: 10.5 ± 4.01 vs N0: 4.01 ± 2.17; $P < .001$), and in extension of metastases (M1: 12.6 ± 4.29 vs M0: 4.63 ± 2.49; $P < .001$). The miR-141 was upregulated in CRC compared with NATS, and its expression was higher in patients in M1 stage relative to those in M0 stage (M1: 5.63 ± 1.90 vs M0: 1.39 ± 0.89; $P < .001$).

The advanced stage of distant metastasis (M1: 7.01 ± 2.22 vs M0: 2.66 ± 3.58; $P < .001$), the late stages of tumor invasion (T3–T4: 4.86 ± 3.91 vs T1–T2: 1.14 ± 0.61; $P = .011$) and lymph node involvement (N1-N2: 7.08 ± 3.83 vs N0: 1.67 ± 1.14; $P < .001$) all presented higher values for miR-21 expression in CRC patients.

Furthermore, in univariate and multivariate analysis (Cox regression), nodal status, distant metastasis, miR-30c, miR-144, miR-375, miR-214, miR-21, miR-195, miR-141, miR-182, miR-183, and miR-370 were independent and significant predictor factors associated with CRC (Table 4).

Table 3

Pearson correlations between miRNAs expressions and clinicopathological features in tumor samples at CRC patients.

Clinicopathological features	miR-21	miR-182	miR-183	miR-141
Depth of tumor invasion				
r	0.41	0.34	0.36	0.11
P-value	<.001	.029	.019	.48
Nodal status				
r	0.71	0.62	0.65	0.25
P-value	<.001	<.001	<.001	.10
Distant metastasis				
r	0.54	0.63	0.63	0.36
P-value	<.001	<.001	<.001	.019

3.3. ROC curve analysis

ROC curve analyses were performed to determine the sensitivity and specificity of selected miRNAs and used as a discriminatory

Table 4

Logistic regression of prognostic values of miRNAs associated with the clinicopathological features in CRC patients.

	Univariate analysis			Multivariate analysis		
Clinical variables	**Hazard ratio**	**95% CI***	***P* value**	**Hazard ratio**	***P* value**	**95% CI***
Age	1.65	0.73–3.98	.32	–	–	–
Gender	1.23	1.07–3.50	.32	–	–	–
Tumor Location	1.52	1.28–3.79	.63	–	–	–
Depth of tumor invasion	1.23	1.26–3.86	.063	–	–	–
Nodal Status	2.83	0.88–7.29	.035	3.86	.012	0.77–3.90
Distant metastasis	6.32	0.79–1.17	.023	3.29	.035	1.00–3.54
Tumor size	2.62	0.10–9.31	.32	2.17	.047	1.29–3.79
miR-30c	3.62	1.02–5.31	.032	4.97	.012	1.02–5.24
miR-144	3.23	0.81–5.06	.028	3.31	.016	0.80–5.51
miR-375	3.22	0.65–5.90	.012	2.06	.035	0.88–5.22
miR-214	3.95	0.54–5.88	.023	4.90	.014	1.00–3.54
miR-21	3.76	1.00–5.20	<.001	1.88	.042	1.29–3.79
miR-195	2.86	0.82–5.56	<.001	2.20	.034	1.24–3.86
miR-141	2.41	0.79–6.17	.035	1.00	.023	0.80–5.51
miR-182	2.32	0.10–7.31	.035	3.98	.023	0.88–5.22
miR-183	2.42	0.73–4.97	.023	4.50	.042	0.76–6.14
miR-370	2.53	1.02–4.31	.011	3.79	.031	1.75–5.62

* Confidence interval

tool to classify tissues in CRC and NATS. Analysis of the ROC curves and AUCs revealed that miR-183, miR-182, miR-141, and miR-21 expressions could be potential diagnostic biomarkers in CRC patients. The AUC of miR-182 was 0.76 (95% interval of confidence - CI: 0.66–0.87; $P < .001$), the specificity was 80.8% and the sensitivity was 66.6%. For miR-183, the AUC was 0.85% (95% CI: 0.78–0.94, $P < .001$), the specificity was 85.0% and the sensitivity was 80.9%. The AUC for miR-141 was 0.77 (95% CI: 0.62–0.92; $P < .001$), the specificity was 75%, and the sensitivity was 84%. The specificity of miR-21 was 87.5%, the sensitivity was 73.8%, and the AUC was 0.83 (95% CI: 0.73–0.90; $P < .001$, Table 5 and Fig. 3). All 4 miRNAs were able to distinguish tumor tissue from normal mucosal tissues with good specificity and sensitivity.

4. Discussion

Now-a-days, the dysregulated expression of miRNAs is observed in almost all types of cancer. This may be attributed to genomic alterations/mutations, inadequate biogenesis of miRNA, transcriptional disorders, or epigenetic silencing.[17] Predominantly, miRNAs play an essential role in the post-transcriptional regulation of gene expression by targeting several oncogenes or tumor suppressor genes that are critical in the pathogenesis of cancer.[18] In CRC, a large variety of miRNAs have been found to be either upregulated or downregulated in tumor tissues as compared to healthy tissues. Upregulated miRNAs in CRC essentially act as oncogenes and are termed “oncomiRs”, while downregulated miRNAs act as tumor suppressor genes and are termed ”tsmiRNAs".

Wang et al evaluated the expression of 3 miRNAs (miR-34a, miR-155, and miR-200c) in 109 pairs of tumor and non-tumor tissues using qRT-PCR. They found that the selected miRNAs were overexpressed in most cases of CRC.[19] Al-Sheikh et al investigated the expression of 4 mature miRNAs (miR-145, miR-195, miR-29, and miR-92) in the plasma and tissues of a group of 20 patients with CRC using qRT-PCR.[20] In a study conducted by Ahmed et al when compared with 27 healthy control patients, upregulated patterns of miR-92a and downregulated patterns of miR-375 and miR-760 were found in the sera of 64 CRC patients.[21] Similarly, in the present study, we demonstrated that the expression profiles of miRNAs were significantly altered in the selected group of Romanian CRC patients. This was determined using the TaqManMGB qRT-PCR method. Moreover, 5 miRNAs namely miR-21, miR-141, miR-182, miR-183, and miR-370, showed increased expression, while 6 miRNAs, namely miR-30c, miR-144, miR-375, miR-195, miR-214, and miR-299 showed significantly lower expression in the CRC than in the NATS. It should be noted that other studies previously revealed expression profiles of miRNAs species examined in CRC.[22–28] In the present study, we focused our attention on

Table 5

Receiver operating characteristic (ROC) analysis of selected miRNAs in CRC.

miRNAs	AUC	95% CI*	*P* value	Youden J index	Cut-off value	Sensitivity	Specificity	PPV %	NPV %
miR-183	0.85	0.78–0.94	<.001	0.65	>4.70	80.95	85.00	92.68	81.71
miR-182	0.76	0.66–0.87	<.001	0.46	>5.44	66.75	80.89	70.73	87.56
miR-141	0.77	0.62–0.92	<.001	0.59	>2.08	84.00	75.00	58.54	73.17
miR-21	0.83	0.73–0.90	<.001	0.61	>3.68	73.81	87.50	71.95	78.05

AUC = area under the curve, NPV = negative predictive value, PPV = positive predictive value, ROC = receiver operating characteristic.
* Confidence interval; Youden J = sensitivity + specificity – 100.

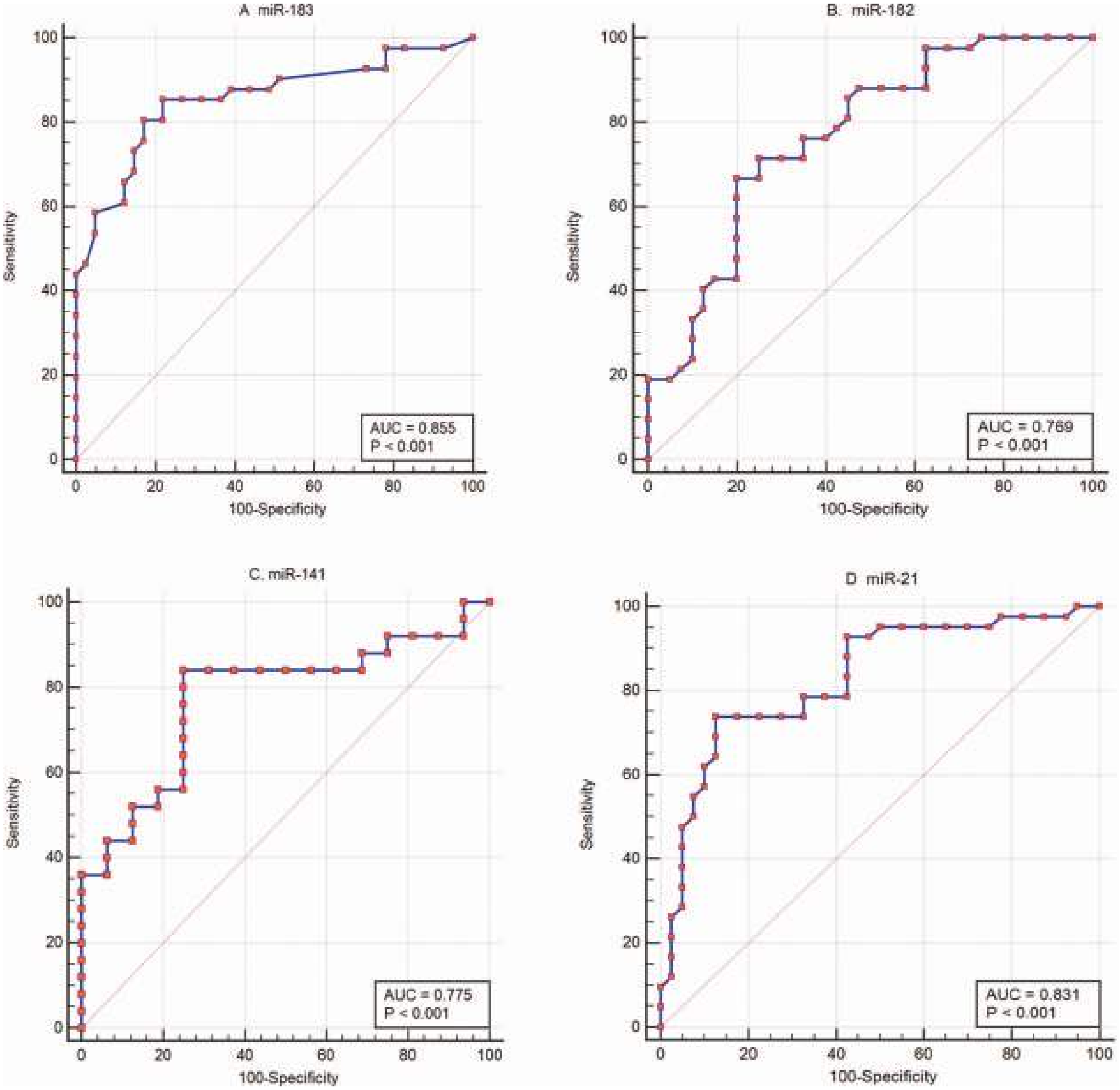

Figure 3. The miR-182, miR-183, miR-141, and miR-21 expressions levels as potential biomarkers in CRC diagnosis. Receiver operating curve (ROC) analyses were generated from 82 patients had a value of the area under the curve (AUC) for miR-183 of 0.85 (sensitivity: 80.95%, specificity: 85%; *P* < .001), for miR-182, miR-141, and miR-21, the AUC were 0.76 (sensitivity: 66.75%, specificity: 80.89%; *P* < .001), 0.77 (sensitivity: 84%, specificity: 75%, *P* < .001), and 0.83 (sensitivity: 73.81%, specificity: 87.50%; *P* < .001), respectively.

miR-21, miR-141, miR-183, and miR-182, which are positively correlated with clinicopathological features. In addition, ROC curves analysis revealed that they could function as potentially useful diagnostic tools in differentiating between colorectal cancer tissue and adjacent non-cancerous tissues.

miR-21 is regarded as an oncomiR and is frequently overexpressed in many types of solid tumors, including CRC.[29] Slaby et al, indicated that the presence of increased levels of miR-21 correlated significantly with clinicopathological features, including lymph node involvement and the development of distant metastases. This indicated a potential role for miR-21 in initiating, progressing and metastasizing CRC.[13] Overexpression of miR-21 may increase cell proliferation, migration, invasion and survival in a variety of cancer cell lines through the targeting and repression of the expression of several tumor suppressor genes. These include programmed cell death4 (PDCD4), phosphatase and tensin homolog (PTEN), cell division cycle 25 homolog A (Cdc25a), reversion-inducing cysteine-rich protein with kazal motifs (RECK), and tropomyosin 1 (TPM1).[30–34] Upregulation of miR-21 has been demonstrated to promote metastasis, invasion and intravasation in CRC cells through the repression of the PTEN/PI-3K/Akt signaling pathway.[35]

Our findings demonstrated that miR-21 levels were significantly upregulated in CRC tissue than in paired NATS, and Pearson statistical analysis revealed a marked correlation between the expression of miR-21 and the depth of tumor invasion (r – 0.41; *P* < .001), lymph node metastasis (r – 0.71;

$P < .001$), and the development of distant metastasis ($r - 0.54$; $P < .001$). Moreover, the analysis of the ROC curve revealed that the miR-21 expression level could discriminate between CRC and NATS with a sensitivity of 73.8%, specificity of 87.5%, positive predictive value (PPV) of 71.9% and negative predictive value (NPV) of 78% at a cutoff value greater than 3.68 ($P < .001$). All of these are in accordance with prior studies.[36–37]

miR-141 is part of the miR-200 family, which includes the following 4 members: miR-200a, miR-200b, miR-200c, and miR-429. The miR-200 family is organized into 2 clusters with different genomic loci localizations. Cluster 1 (miR-200a, miR-200b, and miR-429) are located on chromosome 1 (1p36.3), whereas cluster 2 (miR-200c and miR-141) are located on chromosome 12 (12p.13.3).[38] Previous studies have demonstrated the role of the miR-200 family in cancer where they are associated with tumorigenesis and the progression of various types of human malignancies.[39–41] Downregulation of miR-141 and miR-200b regulates the epithelial to mesenchymal transition (EMT) by directly targeting the zinc finger E-box-binding homeobox factors (ZEB1/2), which are repressors of E-cadherin and vimentin transcription.[42] miR-141 as part of the miR-200 family is dysregulated in various types of human malignancies. This demonstrates the dual role it can play in carcinogenesis, where it can either act as an oncogene or a tumor suppressor gene. Previous studies have shown that miR-141 and miR-200c are highly expressed in the plasma of patients with CRC ($n = 54$) and that miR-141 levels are increased in patients with liver metastases compared to non-metastatic patients. This suggests that the expression of miR-141 may be used as an indicator of CRC metastasis.[43] In another study, Cheng et al demonstrated that an increased plasma level of miR-141 in 102 patients with stage IV CRC was associated with poor survival. In addition, they found that miR-141 may be a new, useful, non-invasive biomarker in the detection of CRC with distant metastases.[44]

In the present study, miR-141 expression was shown to be significantly upregulated in CRC compared to NATS, and its expression was increased in patients in stage M1 relative to those in stage M0 ($r - 0.36$; $P = .019$). Since increased expression of miR-141 is associated with an epithelial phenotype, it can be assumed that miR-141 expression varies at different stages of carcinogenesis, increasing in primary tumors, and decreasing during the metastatic process when cells acquire mesenchymal characteristics. It may be overexpressed again in metastases where the cells again exhibit epithelial features.[45] Furthermore, the miR-141 expression level at a cutoff value greater than 2.08 ($P < .001$) could discriminate between tumoral tissue and NATS samples among CRC patients with a sensitivity of 84% and specificity of 75%, PPV of 58%, and NPV of 73.1%.

miR-182 and miR-183 belong to the miR-183–96–182 family, which is a highly conserved polycistronic cluster across species and is located within a 5-kb region on chromosome 7q32.2.[46] Either individually, or as a cluster, expression levels of the miR-183 family have been demonstrated to be deregulated in diverse types of malignant tumor. In CRC, the miR-183 family is overexpressed and acts as an oncomiR cluster by promoting cell proliferation, inhibition of apoptosis, accelerated tumor progression and metastasis, with phenotypes that are essential for carcinogenesis.[47] Elevated levels of miR-183 were found by Zhou et al, in 94 CRC specimens relative to their adjacent normal pairs. In relation to clinicopathological features, in the same study, the authors demonstrated that increased expression of miR-183 tends to correlate with lymph node metastasis, depth of tumor invasion, and distant metastasis, suggesting that miR-183 could be considered a promising biomarker for the prognosis or the aggressiveness of CRC.[48]

Similarly, in this study, we found that miR-183 expression was significantly upregulated in CRC relative to NATS, in accordance with prior authors.[49–50] Furthermore, our data showed that increased levels of miR-183 were correlated with advanced clinical stage T ($r - 0.36$; $P = .019$), lymph node involvement ($r - 0.65$; $P < .001$), and distant metastases ($r - 0.63$; $P < .001$) in CRC patients. Moreover, miRNA-183 presented the best diagnostic performance in discriminating CRC tissue from NATS at a cutoff value greater than 4.70 ($P < .001$) with a sensitivity of 80.8% and specificity of 85%, PPV of 92.6%, and NPV of 81.7%.

miR-182 is involved in several key steps of tumorigenesis, including EMT, cell cycle regulation, proliferation, survival, migration, aggressiveness, and drug resistance.[51–52] A study by Hui et al, showed that the expression of miR-182 is higher in CRC compared to adjacent noncancerous tissues, and its overexpression correlates positively with the TNM stage, lymph node metastasis and tumor size, representing an independent prognostic factor for CRC patients.[53] In this study, miR-182 was also found to be upregulated in the CRC samples and the higher expression was positively correlated with the advanced clinical stage T ($r - 0.34$; $P = .029$), with lymph node involvement ($r - 0.62$; $P < .001$) and with distant metastases ($r - 0.63$; $P < .001$). In addition, miR-182 at a cutoff value higher than 5.44 ($P < .001$) could predict patients with tumoral status from those with non-tumoral status among CRC patients with a sensitivity of 66.6% and specificity of 80.8%, PPV of 70.7% and NPV 87.5%. This finding agrees with those of prior authors.[54]

miRNAs have some features that make them attractive as biomarkers of malignancy, offering new opportunities for improving diagnosis, prognosis, and the management of CRC. Their suitability includes the altered expression of miRNAs in malignant vs normal tissue, their ability to resist degradation by endogenous ribonuclease, their ease of quantitation using several methods (e.g., qRT-PCR, microarray, or sequencing technology), and especially their differentiated expression in different types of tumor.[54] Furthermore, the ROC curve analysis demonstrated that miR-21, miR-183, miR-182, and miR-141 are useful tools for differentiating between tumor samples and normal adjacent tissues in CRC patients, with a sensitivity of between 66.7% to 84.0% and a specificity between 75.0% to 87.5%, suggesting the clinical relevance of these biomarkers.

Nevertheless, this study has several limitations. First of all, the small number of patients enrolled. Second, all selected humans miRNAs were based on a review of literature, and perhaps other miRNAs may be more prominently deregulated in Romanian patients. Third, the panels of miRNAs were investigated only in tumor tissue samples, without matching their expression in sera samples so as to ensure dysregulated expression pattern in both tissues and sera. The fourth limitation is represented by normalization strategies based on endogenous miRNAs control. In the present study we used a combination of 2 careful selected controls (miR-2b and miR-92N), which we consider to reduce the effects of intra- and inter-variability in the qRT-PCR assay.

5. Conclusions

In conclusion, the present study demonstrated that the selected miRNAs species were shown to be differently expressed in colorectal cancer tissue as compared to normal adjacent tissue samples in a cohort of 82 Romanian patients. Furthermore, altered expression levels of 4 miRNAs genes (miR-21, miR-141, miR-182, and miR-183) in CRC varies at different stages of CRC development. In addition, evaluating expression of these 4 genes in tumor tissue could be a valuable tool in the diagnosis of Romanian patients with colorectal cancer. Therefore, further investigations are needed to confirm our findings.

Acknowledgments

The molecular biology experiments were carried out within the Research Center for the Morphological and Genetic Study in Malignant Pathology - CEDMOG from Ovidius University

Author contributions

Conceptualization: Costel Brînzan, Mariana Aşchie, Anca Mitroi, Georgeta Cozaru.

Formal analysis: Costel Brînzan, Elena Matei.

Investigation: Costel Brînzan.

Methodology: Costel Brînzan, Mariana Aşchie, Anca Mitroi, Georgeta Cozaru.

Software: Costel Brînzan, Elena Matei.

Supervision: Costel Brînzan.

Validation: Costel Brînzan, Mariana Aşchie.

Writing – original draft: Costel Brînzan, Elena Matei, Anca Mitroi, Georgeta Cozaru.

Writing – review & editing: Costel Brînzan, Mariana Aşchie, Elena Matei, Anca Mitroi, Georgeta Cozaru.

References

[1] Mariotto AB, Yabroff KR, Shao YE, et al. Projections of the cost of cancer care in the United States: 2010–2020. J Natl Cancer Inst 2011;103:117–28.

[2] Bray F, Ferlay J, Soerjomataram I, et al. Global cancer statistics: GLOBCAN estimates of incidence and mortality wordwide for 36 cancers in 185 countries. CA Cancer J Clin 2018;68:394–424.

[3] World Health Organization - Cancer Country Profiles 2014, Romania, http://www.who.int/cancer/country-profiles/rou_en.pdf?ua=1MasL

[4] Srivastava K, Srivastava A. Comprehensive review of genetic association studies and meta-analyses on miRNA polymorphisms and cancer risk. PLoS One 2012;7:e50966.

[5] Lee RC, Feinbaum RL, Ambros V, et al. elegans heterochronic gene lin-4 encodes small RNAs with antisense complementarity to lin-14. Cell 1993;75:843–54.

[6] Bartel DP. MicroRNAs: Genomics, biogenesis, mechanism, and function. Cell 2004;116:281–97.

[7] Filipowicz W, Bhattacharyya SN, Sonenberg N. Mechanisms of post-transcriptional regulation by microRNAs: are the answers in sight? Nat Rev Genet 2008;9:102–14.

[8] Calin GA, Croce CM. MicroRNA signatures in human cancers. Nat Rev Cancer 2006;6:857–66.

[9] Huang GL, Zhang XH, Guo GL, et al. Clinical significance of miR-21 expression in breast cancer: SYBR-Green I-based real-time RT-PCR study of invasive ductal carcinoma. Oncol Rep 2009;21:673–9.

[10] Yanaihara N, Caplen N, Bowman E, et al. Unique microRNA molecular profiles in lung cancer diagnosis and prognosis. Cancer Cell 2006;9:189–98.

[11] Mees ST, Mardin WA, Wendel C, et al. EP300 - a miRNA-regulated metastasis suppressor gene in ductal adenocarcinomas of the pancreas. Int J Cancer 2010;126:114–24.

[12] Iorio MV, Visone R, Di Leva G, et al. MicroRNA signatures in human ovarian cancer. Cancer Res 2007;67:8699–707.

[13] Slaby O, Svoboda M, Fabian P, et al. Altered expression of miR-21, miR-31, miR-143 and miR-145 is related to clinicopathologic features of colorectal cancer. Oncology 2007;72:397–402.

[14] Edge SB, Byrd DR, Compton CC, et al. AJCC Cancer Staging Manual-Seventh edition. Springer 2010;7:143–59.

[15] Livak KJ, Schmittgen TD. Analysis of relative gene expression data using real-time quantitative PCR and the 2(-Delta DeltaC(T)) method. Methods 2001;25:402–8.

[16] Kent OA, Mendell JT. A small piece in the cancer puzzle: microRNAs as tumor suppressors and oncogenes. Oncogene 2006;25:6188–96.

[17] Dalmay T, Edwards DR. MicroRNAs and the hallmarks of cancer. Oncogene 2006;25:6170–5.

[18] Wang M, Zhang P, Li Y, et al. The quantitative analysis by stem-loop real-time PCR revealed the microRNA-34a, microRNA-155 and microRNA-200c overexpression in human colorectal cancer. Med Oncol 2012;29:3113–8.

[19] Al-Sheikh YA, Ghneim HK, Softa KI, et al. Expression profiling of selected microRNA signatures in plasma and tissues of Saudi colorectal cancer patients by qPCR. Oncol Lett 2016;11:1406–12.

[20] Ahmed Elshafei , Olfat Shaker , et al. The expression profiling of serum miR-92a, miR-375, and miR-760 in colorectal cancer: an Egyptian study. Tumor Biol 2017;1-14:

[21] Zhang Q, Yu L, et al. Role of microRNA-30c targeting ADAM19 in colorectal cancer. PLoS One 2015;10:e0120698.

[22] Iwaya T, Yokobori T, Nishidan , et al. Downregulation of miR-144 is associated with colorectal cancer progression via activation of mTOR signaling pathway. Carcinogenesis 2012;33:2391–7.

[23] Dai X, Chiang Y, Wang Z, et al. Expression levels of microRNA-375 in colorectal carcinoma. Mol Med Rep 2012;5:1299–304.

[24] Wang X, Wang J, Ma H, et al. Downregulation of miR-195 correlates with lymph node metastasis and poor prognosis in colorectal cancer. Med Oncol 2012;29:919–27.

[25] Bandres E, Cubedo E, Agirre X, et al. Identification by Real-time PCR of 13 mature microRNAs differentially expressed in colorectal cancer and non-tumoral tissues. Mol Cancer 2006;5:29.

[26] Wu K, Ma J, Zhan Y, et al. Down-Regulation of MicroRNA-214 Contributed to the Enhanced Mitochondrial Transcription Factor A and Inhibited Proliferation of Colorectal Cancer Cells. Cell Physiol Biochem 2018;49:545–54.

[27] Fateh A, Feizi MAH, Safaralizadeh R, et al. Importance of miR-299-5p in colorectal cancer. Ann Gastroenterol 2017;30:1–5.

[28] Kulda V, Pesta M, Topolcan A, et al. Relevance of miR-21 and miR-143 expression in tissue samples of colorectal carcinoma and its liver metastases. Cancer Genet Cytogenet 2010;200:154–60.

[29] Frankel LB, Christoffersen NR, Jacobsen A, et al. Programmed cell death 4 (PDCD4) is an important functional target of the microRNA miR-21 in breast cancer cells. J Biol Chem 2008;283:1026–33.

[30] Meng F, Henson R, Wehbe-Janek H, et al. MicroRNA-21 regulates expression of the PTEN tumor suppressor gene in human hepatocellular cancer. Gastroenterology 2007;133:647–58.

[31] Peng W, Fangdong Z, Xiaodong Z, et al. MicroRNA-21 negatively regulates Cdc25A and cell cyce progression in cancer cells. Cancer Res 2009;69:8157–65.

[32] Han L, Yue X, Zhou X, et al. MicroRNA-21 expression is regulated by (-catenin/STAT3 pathway and promotes glioma cell invasion by direct targeting RECK. CNS Neurosci Ther 2012;18:573–83.

[33] Zhu S, Si ML, Wu H, et al. MicroRNA-21 targets the tumor suppressor gene tropomyosin 1 (TPM1). J Biol Chem 2007;282:14328–36.

[34] Xiong B, Cheng Y, Ma L, et al. MiR-21 regulates biological behavior through the PTEN/PI-3K/Akt signaling pathway in human colorectal cancer cells. Int J Oncol 2013;42:219–28.

[35] Shibuya H, Iinuma H, Shimada R, et al. Clinicopathological and prognostic value of microRNA-21 and microRNA-155 in colorectal cancer. Oncoogy 2010;79:313–220.

[36] Xia X, Yang B, Zhai X, et al. Prognostic role of microRNA-21 in colorectal cancer: a meta-analysis. PLoS One 2013;8:e80426.

[37] Altuvia Y, Landgraf P, Lithwick G, et al. Clustering and conservation patterns of human microRNAs. Nucleic Acids Res 2005;33:2697–706.

[38] Zhang L, Deng T, Li X, et al. microRNA-141 is involved in a nasopharyngeal carcinoma-related genes network. Carcinogenesis 2010;31:559–66.

[39] Mohr AM, Bailey JM, Lewallen ME, et al. MUC1 regulates expression of multiple microRNAs involved in pancreatic tumor progression, including the miR-200c/141 cluster. PLoS One 2013;8:e73306.

[40] Li X, Roslan S, Johnstone CN, et al. miR-200 can repress breast cancer metastasis through ZEB1-independent but moesin-dependent pathways. Oncogene 2014;33:4077–88.

[41] Park SM, Gaur AB, Lengyel E, et al. The miR-200 family determines the epithelial phenotype of cancer cells by targeting the E-cadherin repressors ZEB1 and ZEB2. Genes Dev 2008;22:894–907.
[42] Hur K, Toiyama Y, Takahashi M, et al. MicroRNA-200c modulates epithelial-to-mesenchymal transition (EMT) in human colorectal cancer metastasis. Gut 2013;62:1315–26.
[43] Cheng H, Zhang L, Cogdell DE, et al. Circulating plasma MiR-141 is a novel biomarker for metastatic colon cancer and predicts poor prognosis. PLoS One 2011;6:e17745.
[44] Baffa R, Fassan M, Volinia S, et al. MicroRNA expression profiling of human metastatic cancers identifies cancer gene targets. J Pathol 2009;219:214–21.
[45] Dambal S, Shah M, Mihelich B, et al. The microRNA-183 cluster: The family that plays together stays together. Nucleic Acids Res 2015;43: 7173–88.
[46] Zhang Q, Ren W, Huang B, et al. MicroRNA-183/182/96 cooperatively regulates the proliferation of colon cancercells. Mol Med Rep 2015; 12:668–74.
[47] Zhou T, Zhang GJ, Zhou H, et al. Overexpression of microRNA-183 in human colorectal cancer and its clinical significance. Eur J Gastroenterol Hepatol 2014;26:229–33.
[48] Stiegelbauer V, Perakis S, Deutsch A, et al. MicroRNAs as novel predictive biomarkers and therapeutic targets in colorectal cancer. World J Gastroenterol 2014;20:11727–35.
[49] Nugent M, Miller N, Kerin MJ. MicroRNAs in colorectal cancer: function, dysregulation and potential as novel biomarkers. Eur J Surg Oncol 2011;37:649–54.
[50] Pignot G, Cizeron-Clairac G, Vacher S, et al. MicroRNA expression profile in a large series of bladder tumors: identification of a 3-miRNA signature associated with aggressiveness of muscle-invasive bladder cancer. Int J Cancer 2013;132:2479–91.
[51] Cekaite L, Rantala JK, Bruun J, et al. MiR-9, -31, and -182 deregulation promote proliferation and tumor cell survival in colon cancer. Neoplasia 2012;14:868–79.
[52] Liu H, Du L, Wen Z, et al. Up-regulation of miR-182 expression in colorectal cancer tissues and its prognostic value. Int J Colorectal Dis 2013;28:697–703.
[53] Kunz M. MicroRNAs in melanoma biology. Adv Exp Med Biol 2013;774:103–20.
[54] Chen X, Ba Y, Ma L, et al. Characterization of microRNAs in serum: a novel class of biomarkers for diagnosis of cancer and other diseases. Cell Res 2008;18:997–1006.